

Dissertation  
Submitted to the  
Combined Faculties for Natural Sciences and for Mathematics  
of the Ruperto-Carola University of Heidelberg, Germany  
for the degree of  
Doctor of Natural Sciences

Put forward by:  
MPhys Denis Pöhler  
Born in: Erfurt, Germany

Oral Examination: July 20, 2010



# Determination of two dimensional trace gas distributions using tomographic LP- DOAS measurements in the city of Heidelberg, Germany



Referees: Prof. Dr. Ulrich Platt  
Prof. Dr. Thomas Wagner



## **Determination of two dimensional trace gas distributions using tomographic LP- DOAS measurements in the city of Heidelberg, Germany**

### **Abstract:**

Tomographic Long path Differential Optical Absorption Spectroscopy (LP-DOAS) allows two and three dimensional determination of trace gas distributions by measuring the average concentration along 10 to 20 intersecting light paths and applying tomographic inversion techniques. In this thesis such a setup was developed and applied for the first time to determine the horizontal distribution of several trace gases in the open atmosphere. The measurements took place in the city of Heidelberg, Germany from 2005 to 2007 and focused on the trace gases NO<sub>2</sub>, SO<sub>2</sub>, O<sub>3</sub>, HCHO and HONO, which play a major role in the polluted atmosphere. The setup consisted of three Multi Beam LP-DOAS instruments and 20 retro reflector arrays all installed on different buildings in the city. The 20 realised intersecting light paths covered an area of 4 × 4 km<sup>2</sup> with different emission sources. The retrieved horizontal trace gas distributions had a temporal resolution of up to 15 minutes with best results for NO<sub>2</sub>, SO<sub>2</sub> and O<sub>3</sub>. The highest trace gas concentrations (except for O<sub>3</sub>) and spatial variations arose during low wind situations. Emission sources varying in space and time could be distinguished and identified mainly as emissions from traffic (NO<sub>2</sub> with O<sub>3</sub> depletion) and power plants / industry (SO<sub>2</sub>). Several insights into chemical processes in the atmosphere could be gained by studying the interrelationship of the measured trace gases. HONO, for example, displayed much lower spatial variability than NO<sub>2</sub> and was thus not directly emitted by the same source but rather formed in heterogeneous reactions. Transport processes of plumes were also investigated.

## **Bestimmung von zwei-dimensionalen Spurengasverteilungen mittels tomographischen LP-DOAS Messungen in der Stadt Heidelberg, Deutschland**

### **Zusammenfassung**

Tomographische Langpfad Differentielle Optische Absorptions Spektroskopie (LP-DOAS) ermöglicht die zwei und dreidimensionale Bestimmung von Spurengasverteilungen durch das Messen der mittleren Konzentration entlang von 10 bis 20 sich überschneidenden Lichtwegen und der anschließenden Anwendung tomographischer Inversionsverfahren. In dieser Arbeit wurde ein solcher Aufbau entwickelt und erstmalig angewandt um die horizontale Spurengasverteilung in der offenen Atmosphäre zu bestimmen. Die Untersuchungen fanden in der Stadt Heidelberg, Deutschland von 2005 bis 2007 statt und konzentrierten sich auf die Spurengase NO<sub>2</sub>, SO<sub>2</sub>, O<sub>3</sub>, HCHO und HONO, welche eine wichtige Rolle in der verschmutzten Atmosphäre spielen. Der Aufbau bestand aus drei Multibeam LP-DOAS Instrumenten und 20 Retroreflektorarrays installiert auf verschiedenen Gebäuden in der Stadt. Die 20 realisierten Lichtwege überspannten ein Gebiet von 4 × 4 km<sup>2</sup> mit verschiedenen Emissionsquellen. Die bestimmten horizontalen Spurenstoffverteilungen hatten eine Zeitauflösung von bis zu 15 Minuten mit den besten Ergebnissen für NO<sub>2</sub>, SO<sub>2</sub> und O<sub>3</sub>. Höchste Konzentrationen (außer für O<sub>3</sub>) und stärkste räumliche Variabilität traten bei schwachem Wind auf. Sich stark räumlich und zeitlich ändernde Emissionsquellen konnten im Wesentlichen bestimmt werden als Verkehr (NO<sub>2</sub> mit O<sub>3</sub> Abbau) und Kraftwerke / Industrie (SO<sub>2</sub>). Verschiedene Einblicke in die Abläufe in der Atmosphäre konnten gewonnen werden durch die Untersuchung der Zusammenhänge der gemessenen Spurenstoffe. HONO, z.B., zeigte eine viel geringere räumliche Variabilität auf als NO<sub>2</sub> und wurde daher nicht direkt durch dieselben Quellen emittiert, sondern in heterogenen Reaktionen gebildet. Transportprozesse von Abgasfahnen wurden ebenfalls untersucht.



# Table of Contents

<b>1</b>	<b>Introduction</b> .....	<b>1</b>
<b>2</b>	<b>Chemistry and Physics of the Troposphere</b> .....	<b>7</b>
<b>2.1</b>	<b>Nitrogen Oxides (NO<sub>x</sub>)</b> .....	<b>8</b>
2.1.1	Sources of Nitrogen Oxides.....	9
2.1.2	Chemistry of Nitrogen Oxides in the Troposphere.....	12
2.1.3	Tropospheric Sinks for Nitrogen Oxides .....	13
2.1.4	Annual Cycle of Nitrogen Dioxide .....	15
<b>2.2</b>	<b>Ozone (O<sub>3</sub>)</b> .....	<b>15</b>
2.2.1	Annual Cycle of Ozone .....	19
<b>2.3</b>	<b>Nitrous Acid (HONO)</b> .....	<b>20</b>
<b>2.4</b>	<b>Formaldehyde (HCHO)</b> .....	<b>22</b>
<b>2.5</b>	<b>Sulphur Dioxide (SO<sub>2</sub>)</b> .....	<b>24</b>
<b>2.6</b>	<b>Trace Gas Distributions on Local Scale</b> .....	<b>26</b>
<b>2.7</b>	<b>Atmospheric Dynamics of the Planetary Boundary Layer</b> .....	<b>28</b>
2.7.1	The Structure of the Planetary Boundary Layer .....	29
2.7.2	Diurnal Variations of the Planetary Boundary Layer .....	31
2.7.3	Transport Processes in the Planetary Boundary Layer .....	33
<b>3</b>	<b>Differential Optical Absorption Spectroscopy (DOAS)</b> .....	<b>37</b>
<b>3.1</b>	<b>Absorption Spectroscopy</b> .....	<b>38</b>
<b>3.2</b>	<b>The Principle of DOAS</b> .....	<b>41</b>
<b>3.3</b>	<b>Mathematical Description of a DOAS Spectrum</b> .....	<b>43</b>
<b>3.4</b>	<b>Conversion to Concentrations and Mixing Ratios</b> .....	<b>46</b>
<b>3.5</b>	<b>Evaluation Procedure</b> .....	<b>47</b>
<b>3.6</b>	<b>Measurement Accuracy and Error Estimation</b> .....	<b>49</b>
3.6.1	Systematic Errors.....	50
3.6.2	Photon Noise ( $\sigma_p$ ).....	50
3.6.3	Optical Noise ( $\sigma_o$ ) .....	52
3.6.4	Instrument Noise ( $\sigma_i$ ) .....	52
3.6.5	Estimate the Measurement Errors.....	53
3.6.6	Averaging Data Points .....	55
<b>3.7</b>	<b>Detection Limit</b> .....	<b>56</b>
<b>3.8</b>	<b>Measurable Trace Gases</b> .....	<b>57</b>
<b>3.9</b>	<b>Spectral Sampling and Aliasing Problems</b> .....	<b>58</b>
<b>3.10</b>	<b>Measurement Concepts</b> .....	<b>59</b>
<b>4</b>	<b>DOAS Tomography</b> .....	<b>61</b>
<b>4.1</b>	<b>Principle of LP-DOAS Tomography</b> .....	<b>64</b>
<b>4.2</b>	<b>Tomographic Reconstruction</b> .....	<b>67</b>
<b>4.3</b>	<b>Iterative Solution of the Least-Square Problem</b> .....	<b>70</b>
<b>4.4</b>	<b>Algebraic Reconstruction Methods</b> .....	<b>72</b>
<b>4.5</b>	<b>Measurement Geometry</b> .....	<b>72</b>
<b>4.6</b>	<b>Reconstruction Grid</b> .....	<b>73</b>

4.7	<b>Limits of LP-DOAS Tomography.....</b>	<b>73</b>
<b>5</b>	<b><i>Measurement Instruments.....</i></b>	<b>75</b>
5.1	<b>The Principle of Long Path-DOAS and Multibeam Instruments (MBI) .....</b>	<b>76</b>
5.2	<b>The Multibeam Instrument (MBI) Setup.....</b>	<b>80</b>
5.2.1	The “Cube” MBI Telescope.....	81
5.2.2	The External Mirrors.....	82
5.2.3	The Controlling of the Instruments .....	87
5.2.4	Lamp Reference Measurement with a Shortcut System .....	88
5.2.5	Quartz Fibre and Mode Mixer .....	89
5.3	<b>Spectrograph and Detector .....</b>	<b>91</b>
5.3.1	Czerny Turner Spectrograph.....	92
5.3.2	Spectrograph Shutter.....	94
5.3.3	CCD Camera (Detector) .....	100
5.3.4	Characterisation of the Measurement Quality (Noise Tests) .....	103
5.4	<b>Retro Reflectors.....</b>	<b>107</b>
5.4.1	Investigation of Reflectivity with Changing Incident Angle .....	107
5.4.2	Comparison of Retro Reflectors of Different Size .....	111
5.5	<b>Tomographic LP-DOAS Measurement Software .....</b>	<b>112</b>
5.6	<b>New Generation of LP-DOAS Instruments .....</b>	<b>114</b>
5.6.1	Application of New LP-DOAS Instruments for Tomographic Observations .....	116
5.7	<b>In situ monitors .....</b>	<b>118</b>
5.7.1	Chemiluminescence NO / NO <sub>2</sub> monitor.....	118
5.7.2	UV- absorption ozone monitor .....	118
5.8	<b>Weather stations.....</b>	<b>119</b>
<b>6</b>	<b><i>Heidelberg Tomographic LP-DOAS Setup.....</i></b>	<b>123</b>
6.1	<b>Facts About Heidelberg.....</b>	<b>123</b>
6.1.1	City Districts .....	124
6.1.2	Transport Sector.....	125
6.1.3	Power Plants and Small Heating Systems.....	126
6.1.4	Industry .....	127
6.1.5	Spatial Characterisations of Urban Areas .....	127
6.2	<b>Measurement Geometry and Setup.....</b>	<b>129</b>
6.3	<b>Local Instrument Setup.....</b>	<b>131</b>
6.3.1	Institute of Environmental Physics (IUP) .....	131
6.3.2	SAS .....	133
6.3.3	Heidelberger Druckmaschinen AG (HD-Druck) .....	135
<b>7</b>	<b><i>Data Evaluation and Simulations .....</i></b>	<b>139</b>
7.1	<b>DOAS Measurements and Data Evaluation .....</b>	<b>139</b>
7.1.1	Spectrograph Calibration, Mercury Spectrum and Instrument Function .....	141
7.1.2	Trace Gas Reference Spectra and Fit Preparation.....	142
7.1.3	Atmospheric Spectra Measured Along Different Light Paths.....	144
7.1.4	Lamp Reference Spectrum (Shortcut).....	144
7.1.5	Background Corrections .....	146
7.1.6	High Pass Filter.....	149
7.1.7	DOAS Fit with DOASIS.....	151
7.2	<b>Interpolating and Averaging of Measurement Data.....</b>	<b>153</b>
7.2.1	Averaging to Time Bases .....	153
7.2.2	Averaging to Daily, Weekly and Annual Cycles .....	155
7.3	<b>Retrieval of Trace Gas Profiles from LP-DOAS Data.....</b>	<b>155</b>
7.4	<b>Tomographic Inversion .....</b>	<b>157</b>

7.4.1	Reconstruction Grid.....	158
7.4.2	Reconstruction of Simulated Trace Gas Distributions.....	160
7.4.3	Determination of the Optimal Iteration Number .....	165
7.4.4	Artefacts in the Tomographic Reconstruction .....	169
7.4.5	Quality Measure for Tomographic Retrieval.....	173
<b>7.5</b>	<b>Plotting Trace Gas Distributions.....</b>	<b>173</b>
<b>8</b>	<b><i>Tomographic Measurement Results</i> .....</b>	<b>175</b>
<b>8.1</b>	<b>An Exemplary Day with High Trace Gas Concentrations.....</b>	<b>177</b>
<b>8.2</b>	<b>NO<sub>2</sub> and O<sub>3</sub> Distributions.....</b>	<b>184</b>
8.2.1	NO <sub>2</sub> Cycle at High O <sub>3</sub> Concentrations.....	184
8.2.2	NO <sub>2</sub> Cycle at Medium O <sub>3</sub> Concentrations .....	188
8.2.3	NO <sub>2</sub> Cycle at Low O <sub>3</sub> Concentrations .....	190
8.2.4	Local NO <sub>2</sub> Concentration Minimum at IUP .....	192
8.2.5	Influence of High Wind Speeds on NO <sub>2</sub> and O <sub>3</sub> Concentrations and Distributions .....	193
8.2.6	Passing NO <sub>2</sub> Plumes .....	196
<b>8.3</b>	<b>Nitrous Acid (HONO) Distributions .....</b>	<b>197</b>
8.3.1	Influence of Solar Radiation, Temperature and Wind Speed .....	198
8.3.2	HONO to NO <sub>2</sub> Correlation .....	199
8.3.3	HONO Distributions at Sunrise .....	200
8.3.4	HONO Distributions at Sunset .....	201
8.3.5	Characterisation of HONO Distributions .....	202
<b>8.4</b>	<b>Formaldehyde (HCHO) Distributions .....</b>	<b>203</b>
8.4.1	Influence of Solar Radiation, Temperature and Wind Speed .....	203
8.4.2	HCHO Correlation to NO <sub>2</sub> and O <sub>3</sub> .....	205
8.4.3	HCHO Daily Cycle.....	206
8.4.4	Variation of HCHO due to Direct Emissions .....	208
8.4.5	Characterisation of HCHO Distributions.....	209
<b>8.5</b>	<b>SO<sub>2</sub> Distributions .....</b>	<b>210</b>
8.5.1	SO <sub>2</sub> Plume Emissions .....	211
8.5.2	SO <sub>2</sub> from Heating and Traffic.....	213
8.5.3	SO <sub>2</sub> Transported to Heidelberg.....	215
8.5.4	Influence of High Wind Speeds on SO <sub>2</sub> Concentration and Distributions .....	215
<b>8.6</b>	<b>Trace Gas Concentrations During Fireworks.....</b>	<b>216</b>
<b>8.7</b>	<b>Mean Daily Cycle.....</b>	<b>218</b>
<b>8.8</b>	<b>Mean Weekly Cycle .....</b>	<b>224</b>
<b>8.9</b>	<b>Mean Annual Cycle .....</b>	<b>228</b>
<b>8.10</b>	<b>Trace Gas Profiles.....</b>	<b>231</b>
<b>8.11</b>	<b>Influence of Wind Direction on trace gas Concentrations and Distributions .....</b>	<b>232</b>
<b>8.12</b>	<b>Comparison with In-Situ Monitors .....</b>	<b>237</b>
8.12.1	Comparison for NO <sub>2</sub> .....	238
8.12.2	Comparison for O <sub>3</sub> .....	241
8.12.3	Comparison for SO <sub>2</sub> .....	241
<b>8.13</b>	<b>Comparison to Vehicle Measurements .....</b>	<b>242</b>
<b>8.14</b>	<b>Comparison to Power Plant Emissions .....</b>	<b>243</b>
<b>8.15</b>	<b>Comparison to Ship Emissions .....</b>	<b>244</b>
<b>8.16</b>	<b>Long Term Measurement Data and Data DVD .....</b>	<b>246</b>
<b>9</b>	<b><i>Conclusions and Outlook</i> .....</b>	<b>249</b>
<b>9.1</b>	<b>Instrumentation and Developments .....</b>	<b>249</b>

9.2	Measurement Setup and Data Evaluation .....	250
9.3	Observations of Trace Gas Distributions.....	251
9.4	Final Remarks .....	253
10	<i>References</i> .....	255
11	<i>Acknowledgements &amp; Danksagung</i> .....	267
12	<i>Appendix</i> .....	269
12.1	Data September 2005 (selected plots).....	270
12.2	Data October 2005 (selected plots) .....	273
12.3	Data November 2005 (selected plots).....	276
12.4	Data December 2005 (selected plots).....	279
12.5	Data January 2006 (selected plots) .....	282
12.6	Data February 2006 (selected plots) .....	285
12.7	Data September 2006 (selected plots).....	288
12.8	Data October 2006 (selected plots) .....	292
12.9	Data November 2006 (selected plots).....	295
12.10	Data December 2006 (selected plots).....	298
12.11	Data January 2007 .....	301
12.12	Data February 2007 (selected plots).....	310
12.13	Data March 2007 (selected plots) .....	313
12.14	Data June/July 2007 (selected plots) .....	316
12.15	Data August 2007 (selected plots).....	319
12.16	Data September 2007 (selected plots).....	322

# 1 Introduction

From the beginning of industrialisation mankind began to destroy their environment on a large scale by emitting pollutants with unpredictable consequences. First reports of the so-called “London smog” caused by the widespread use of high-sulphur coal for domestic heating even date back to the 17<sup>th</sup> century [by John Evelyn reported in Finlayson-Pitts and Pitts, 2000]. Serious public health problems occurred with a high rate of mortality. The pollution also affected the quality of water, buildings and clothes. These reports were mainly phenomenological. The actual pollutants or combination of pollutants responsible for the “London smog” were not identified at that time. Today it is known that high sulphur dioxide (SO<sub>2</sub>) and particle levels in combination with strong meteorological inversions that concentrated the pollutants in a relative small volume in the lowest 100m of the atmosphere. Such heavy smog events arose regularly every few years. The “Great Smog” of 1952 even led to more than 4000 deaths [Finlayson-Pitts and Pitts, 2000].

Contrary to the “London smog” phenomenon, which arises in winter at low temperatures, the “Los Angeles smog” was observed during hot summer days and bright sunshine. For the first time reported in the late 1940s, the ambient air around Los Angeles contained strongly oxidising, eye-watering and plant-killing pollutants [Finlayson-Pitts and Pitts, 2000 and references therein]. This phenomenon could be reproduced in the laboratory by irradiating plants with sunlight and simultaneously exposing them to synthetic polluted air containing nitrogen dioxide (NO<sub>2</sub>) and alkenes which produce ozone. Similar effects could be found with car exhausts which contain NO<sub>x</sub> (NO<sub>x</sub> = NO + NO<sub>2</sub>) and a variety of hydrocarbons (HC). In contrast to stratospheric ozone, tropospheric ozone has a negative impact on the health of living organisms. Since the “Los Angeles smog”, high ozone levels have been observed throughout the world. It is a problem in areas where volatile organic compounds (VOC) and NO<sub>x</sub> emissions from major mobile and stationary sources are “trapped” by thermal inversions and irradiated by sunlight.

Health and ecological problems have increased with ongoing industrialisation. In the second part of the 20<sup>th</sup> century, first serious attempts were made to protect the environment and to increase the health-related quality of life. To improve the air quality it is necessary to understand the processes which determine the composition of the atmosphere. Measurements of chemical and physical parameters are crucial for the understanding of these processes.

Great efforts were made to improve the air quality in industrialised countries. Germany implemented strong regulations in the 70’s and 80’s of the last century, and concentrations of many pollutants could be reduced. Nowadays the European Union (EU) regulates the allowed pollutant threshold values to protect public health in Europe. New limits are valid since 2010. The latest data for 2009 show, that 55% of the German city measurement stations close to streets display an annual average concentration of NO<sub>2</sub> above the new maximum permissible value of 40 µg/m<sup>3</sup> (~20.9 ppb) [Umweltbundesamt, 2010]. Also for ozone, 15% of the measurement stations observed levels above the new recommended threshold of 120 µg/m<sup>3</sup> (~60 ppb, for an 8 hour average value). Thus still large attempts are required to reduce the exposure of these pollutants. Additionally, several pollutants on the list of hazardous air pollutants, like formaldehyde and aromatic compounds, are in general not monitored [EPA,

2010] and thus their exposure is unclear. New technologies are required for their observation. The main constituents of the ambient air are inert or slowly reacting substances like molecular nitrogen (~78.084 vol%), molecular oxygen (~20.946 vol%), argon (~0.934 vol%) and carbon dioxide (~0.035 vol%) [Baumüller and Kapp, 2000]. In addition, the atmosphere contains innumerable so-called trace gases which are present at much lower concentrations and occupy volume ratios of several parts per trillion ( $10^{-12}$ ) up to a few parts per million ( $10^{-6}$ ) molecules per air molecule. Since many of these gases are very reactive, they control the chemical reaction cycles in the atmosphere. Due to the complex mixture of species and their temporal and spatial variability on small scales, it is difficult to determine the composition of the atmosphere. In the lower troposphere, the variability is particularly large due to non-uniform distribution of emission sources and sinks, geographical influences and complex transport processes. The current knowledge of the basic chemical processes in urban areas, including the trace gases relevant for this thesis, like nitrogen oxides, ozone and sulphur dioxide are given in *Chapter 2*. The concentration of these trace gases in urban areas mainly depends on anthropogenic emissions, primarily from industry, cars and heating systems. They also depend on geographical conditions and local transport processes. The knowledge of the exact concentration and their distribution on regional or local scale is necessary for several reasons. First, it is required to assess the quality of chemical transport models on microscales. Second, the distributions are required to quantify total emissions from sources and distinguish between them. Third, such data is necessary to analysis different local exposures of pollutants. A brief discussion of trace gas distributions and basical physical processes in the atmosphere is given in *Chapter 2.6* and *2.7*. Measurements of trace gases are either point measurements (in-situ) or remote sensing. In-situ techniques are widely used in urban air monitoring and provide concentration values on site. Thus they are sensitive to local and temporal fluctuations but do not have to be representative for a point close by. A solution could be a close grid of measurement points, which is however often not realistic in practice. Remote sensing by absorption spectroscopy along long measurement light paths of several kilometres [e.g. Platt and Perner, 1983, Platt und Stutz, 2008] yields path integrated mean values and is called Long path Differential Optical Absorption Spectroscopy (LP-DOAS). For the quantification of atmospheric trace gases, LP-DOAS gives more representative concentrations than point measurements, but can also not resolve concentration differences.

To obtain two- or even three-dimensional trace gas distributions, path integrating LP-DOAS measurements along several paths can be combined with tomographic retrieval methods. This technique does not only open a new era of trace gas monitoring, which can improve our knowledge of the sources, distribution and transport of trace gases, but also gives new insights of atmospheric processes.

First tomographic measurements employing the LP-DOAS technique were carried out to investigate the emission of a motorway [Pundt et al. 2005] applying two telescopes and 16 light paths. They retrieved the  $\text{NO}_2$  concentration field perpendicular to the motorway, which was in good agreement with model expectations [Laeppele et al. 2004]. The best achieved temporal resolution was four hours. Unfortunately this resolution is too low for strongly varying emission sources as they are found in urban areas. Thus these measurements are not directly applicable for other tomographic observations. In an indoor experiment, horizontal LP-DOAS measurements and tomographic reconstructions were tested over an area of

15×10m<sup>2</sup> [Mettendorf et al., 2006]. 39 relatively homogeneously distributed light paths crossed this area, which was temporally filled with one or two NO<sub>2</sub> cells to simulate locally confined concentration fields, e.g. plumes emitted by a point source. The derived distributions from the measurement could reflect the artificial distributions very well.

In the frame work of this thesis this new methods was applied for the first time to determine the concentration distribution of atmospheric trace gases in an urban area of several square kilometres. Due to logistical reasons the city of Heidelberg in Germany was chosen as measurement site. The path integrating measurements are based on the LP-DOAS technique determining the absorption of different trace gases along a light path. The principle of this measurement method is presented in *Chapter 3.1*. Other used trace gas measurement techniques are shortly discussed in the *Chapter 5.7*. Overall, 20 absorption light paths were applied for the DOAS measurements using three telescopes and 20 retro reflectors located on the roofs of different buildings in the city. If the trace gases feature absorption structures in the measured wavelength interval, the average concentrations can be obtained along each light path [e.g. Platt, 1994, Platt und Stutz, 2008]. For the chosen wavelength range from 285 to 365 nm, the trace gases NO<sub>2</sub>, O<sub>3</sub>, SO<sub>2</sub>, HCHO and HONO can be measured in urban areas. These gases play a major role in the chemistry of the polluted atmosphere, e.g. contributing to photo smog. Therefore they are already discussed in *Chapter 2*.

Trace gas distributions can be reconstructed from the optimised and well selected measurement geometry and combined with tomographic inversion techniques [e.g. Hartl et al., 2006]. This new method is called LP-DOAS tomography. The tomographic principle and inversion techniques are outlined in *Chapter 4*. The difficult task for such tomographic inversions of horizontal distributions is that no a-priori of the trace gas distribution can be made. Neither localised plumes nor defined concentration gradients can be assumed. Thus, sophisticated inversion routines and parameters are necessary to avoid artefacts.

The instrumental setup needed to fulfil the requirements of tomographic measurements is complex. The tomographic technique is based on several simultaneous LP-DOAS measurements. In this thesis, three Multibeam Instruments (MBI) [Pundt and Mettendorf, 2005] are used which were especially designed for this purpose. Each of them could simultaneously measure along four light paths. Several modifications of the system were necessary in order to make the instruments suitable for outdoor application and guarantee stable long term measurements [e.g. Pöhler, 2009]. Since the tomographic reconstruction relies on small variations of the determined concentration between different light paths, it was necessary to improve the measurement quality and stability of the system. The system was fully automated and the developed software controls all processes and corrects misalignment automatically. All technical details of these instruments are described in *Chapter 5*.

The first tomographic measurements in the framework of this thesis were performed in Heidelberg, Germany. Some background information about the city are reflected in *Chapter 6.1*. The three instruments were installed at three different sites in 2005. Together with 20 retro reflectors which were installed all over the city on top of different buildings, in total 20 measurement light paths could be realised and covered almost an area of 4×4 km<sup>2</sup>. The set-up in Heidelberg is presented in *Chapter 6.2* and *6.3*. Tomographic measurements were carried out between summer 2005 and spring 2007.

The trace gas concentration of NO<sub>2</sub>, O<sub>3</sub>, SO<sub>2</sub>, HCHO and HONO were obtained for each light path. The spectral evaluation algorithm was adapted to the characteristics of the instrument. The amount of collected data does not allow a manual optimisation of the evaluation for each light path, as it is typically done, so a nearly fully automatic evaluation was developed. Only this approach allowed guaranteeing optimal evaluation results for the large amount of obtained data. Additionally, corrupt spectra were automatically removed from the evaluation by a careful selection process. The evaluation process is presented in *Chapter 7*. The data of the whole long term time series are appended in a digital form on the data DVD (*Chapter 8.16*) and some selected data are shown in the *Appendix*. The reconstruction process of the trace gas distribution applying tomographic inversion techniques is presented in *Chapter 7.4*. The results are displayed as two dimensional distributions over the city of Heidelberg for the trace gases NO<sub>2</sub>, SO<sub>2</sub>, O<sub>3</sub>, HCHO and HONO. First results are published in Pöhler et al. [2007]. The reconstruction is especially difficult, as the irregular measurement geometry due to local restriction require special treatment. The applied reconstruction grid and reconstruction parameters have to be sensitive tested prior to their application. Several simulations were applied and presented in *Chapter 7.4.2*. With them the tomographic reconstruction was further optimised and automated to improve the reconstruction quality. The finally derived results are presented in *Chapter 8*, in the *Appendix* and on the the data DVD (*Chapter 8.16*). First, the time series of the trace gas distributions were created. The best achieved temporal resolution was 15 minutes. They allow studying transport and single emission events. As for several analyses such a high resolution is not required, the produced averaged data products range from hours to days. These data are used to study sources and chemical processes of the trace gas concentrations. Additionally, daily, weekly and annual averaged cycles are studied. They directly show the influence of changing anthropogenic emissions. Further the influence of wind speed and wind direction on the spatial distribution is investigated. Some selected results are presented and analysed in *Chapter 8*. The interpretation and discussion are reflected in corresponding sub chapters for the according trace gases. It is shown that such tomographic measurements can be used to achieve information about emissions and transport of trace gases. They can also be useful for the validation of small-scaled chemical transport models.

This thesis represents the first application of the described new method to environmental trace gas measurements above urban areas. The gained experience could help to develop an improved setup for tomographic measurements in the future. LP-DOAS instruments, which were used in this thesis, are rather complicated, expensive and require intensive support, thus their application would be limited. New developments were performed which use a new design of LP-DOAS instruments based on fibre optic [Merten et al., 2010; Pöhler et al., 2008] and LED light sources [Kern et al., 2006; Sihler et al., 2009]. They allow constructing a smaller, cheaper and handier LP-DOAS instrument. The combination of several of these instruments, similar to the applied setup of this thesis, allows performing tomographic LP-DOAS measurements and thus multidimensional trace gas observations [Pöhler et al., 2008]. The newly developed instruments, which are a basis for future tomographic setups, are presented in the *Chapter 5.6*. They have already been used in several other campaigns for the measurement of urban pollution trace gases e.g. in Heidelberg [Landwehr, 2010], Spain (El Arensillo, 2008), Hong Kong (2009 – 2010) and Mexico City [Merten, 2008]. They were also

applied for Halogen measurements in Mace Head, Ireland [Seitz et al. 2009], Arctic [Pöhler et al. 2010] as well as in volcanic plumes [Kern et al., 2009]. These measurements demonstrate that the simplified LP-DOAS set-up is suitable for atmospheric measurements and can in principle also be applied to LP-DOAS tomography. The combination of LP-DOAS tomography with passive DOAS measurements like Multi-Axis (MAX) DOAS, gives the possibility to retrieve three dimensional trace gas distributions and potentially even aerosol distributions [Pöhler et al., 2008; Platt et al., 2009a].

In *Chapter 9*, a summary of the most important findings of this thesis is given with a short outlook of different future applications of the applied technique. It is shown that tomographic LP-DOAS measurements are also interesting for studying natural atmospheric chemistry processes like the release of halogens in the arctic or in marine environments.

Due to the public interest of the here presented measurements of trace gas concentrations in Heidelberg, articles appeared at two local newspapers [RNZ, 2006; UniSpiegel, 2007].



## 2 Chemistry and Physics of the Troposphere

In addition to the main components of the atmosphere such as nitrogen (78.084 %), oxygen (20.946 %), argon (0.934 %) and carbon dioxide (0.035 %) [e.g. Baumüller and Kapp, 2000], many so-called trace gases with concentrations less than 1 molecule per million air molecules (1 part per million, ppm) are nowadays of major interest in air quality monitoring and for the scientific understanding of the atmosphere<sup>1</sup>. Nowadays it is known that innumerable trace species exist in the atmosphere with concentrations in the ppt range and even below. Most of them occur naturally, but since mankind increasingly pollutes the atmosphere, many compounds exceed their natural level. They do not only have a strong impact on the chemical and physical processes in the atmosphere but some of them, e.g. ozone, nitrogen oxides and sulphur dioxide, also directly affect human health.

Air pollutants can either be emitted directly into the ambient air (primary pollutants) or they arise due to chemical transformations in the atmosphere (secondary pollutants). The emission and transformation typically take place in the lowest ~1000 m of the troposphere, the planetary boundary layer (PBL) (*Chapter 2.7*). Exceptions can be found like the formation of the ozone hole. The trace gas concentrations in the PBL are not only influenced by the emission and transformation, but also by variation of physical conditions, e.g. the structure of the boundary layer, topography and the presence and intensity of solar radiation. An overview of important trace gas sources, including natural and anthropogenic is shown in Figure 2-1.

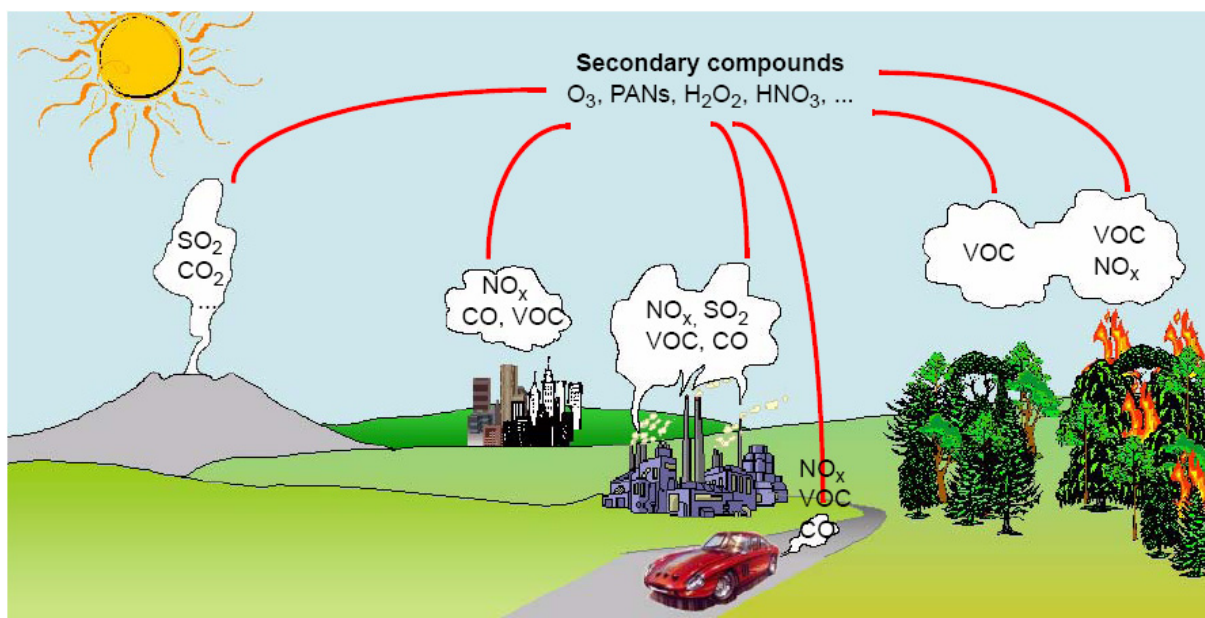


**Figure 2-1: Trace gases, emitted by anthropogenic and natural sources, react in the atmosphere under the influence of solar radiation. The sources of most trace gases are located near the surface. [adapted from Hak, 2006]**

<sup>1</sup> The units “ppm”, “ppb” and “ppt” are widely used in science as the unit for mixing ratios of atmospheric compounds. 1  $\mu\text{mol}$  per mol is defined as mixing ratio of 1 ppm. Lower mixing ratios are defined as 1ppb ( $1 \times 10^{-9}$  mol per mole) and 1ppt ( $1 \times 10^{-12}$  mol per mole).

Under the influence of solar radiation, the emitted gases are converted into a mixture of secondary compounds (like  $O_3$ ,  $H_2O_2$ , PANs and other). An example is the photochemical smog formed in the chemical reaction of sunlight, nitrogen oxides ( $NO_x$ ) and volatile organic compounds (VOC). As the atmospheric lifetime of some first and secondary compounds can be in the order of hours to days, they affect not only the emission areas but can also be transported into regions with little or no emission. For example, since the industrialisation, acid rain was observed both in rural and in urban areas. The direct result was forest dieback and damage to buildings. In former days, sulphuric acid, generated from  $SO_2$  emissions from industry, was mainly causing the acid rain. The so-called “London smog” was a consequence of high concentrations of  $SO_2$  and particulate matter (smoke) in combination with dense fog and low inversions. In Europe nowadays most problems with  $SO_2$  are solved due to effective filters in emission stacks and reduced sulphur concentrations in the petrol. Thus the acid deposition today is mainly due to nitric acid ( $HNO_3$ ), the final oxidized form of all nitrogen oxides (see *Chapter 2.1.3*).

In order to improve the air quality and reduce man-made pollutants (primary and secondary), there is a large effort in scientific research to study these trace gases and their transformation processes. In this thesis, measurements of the following air components were performed using the DOAS technique: nitrogen dioxide ( $NO_2$ ), ozone ( $O_3$ ), sulphur dioxide ( $SO_2$ ), formaldehyde (HCHO) and nitrous acid (HONO). A short introduction of these trace gases, their sources, chemical transformation and diurnal variation are given in the *Chapter 2.1 - 2.5*. *Chapter 2.6* discusses in more detail why trace gas concentration distributions arise and why measurements are important not only for scientific, but also for environmental monitoring reasons. As the trace gas concentration, mixing and transport are also strongly dependent on physical parameters and metrological conditions. The processes and their influence are described in *Chapter 2.7*.

## 2.1 Nitrogen Oxides ( $NO_x$ )

Many pollution phenomena and processes in the atmosphere are directly or indirectly linked to nitrogen oxides [e.g. Finlayson-Pitts and Pitts, 2000]. The most well-known examples are the “ozone hole” in the stratosphere, “acid rain” in the lee of industrial centres and the “summer smog” in urban areas. The  $NO_x$  concentration has a strong influence on the concentration of hydroxyl radicals (OH), which is responsible for the oxidation processes of most trace gases.

The expression “nitrogen oxides” include all chemical combinations of  $N_aO_b$ . The most important components of the atmospheric chemistry are NO and  $NO_2$ , which are summarized as  $NO_x$ .

$$NO_x = \{NO, NO_2\}$$

All reactive nitrogen containing species are summarized by the term  $NO_y$ .

$\text{NO}_y = \{\text{NO}, \text{NO}_2, \text{NO}_3, \text{N}_2\text{O}_5, \text{HNO}_3, \text{HONO}, \text{PAN}^2, \text{etc.}\}$

All  $\text{NO}_y$  species mainly originate in NO, which is primarily emitted into the atmosphere by natural and anthropogenic sources. For anthropogenic emissions about 90 % originate as NO, which is a result of the combustion processes. NO is then converted in the troposphere to higher oxidised nitrogen oxides through different chemical processes. Photolysis during the day can convert the higher nitrogen oxides back to NO (for details see *Chapter 2.1.3* and Figure 2-6).

$\text{NO}_2$  also has an impact on climate change as it is a source for tropospheric ozone which is a green house gas. Ozone also directly affects human health.

### 2.1.1 Sources of Nitrogen Oxides

The concentration of nitrogen oxides in urban areas is mainly dominated by anthropogenic sources and can reach concentrations of over one hundred ppb. Main emissions arise from all kinds of fossil fuel consumption processes, e.g. car traffic, power generation or heating. Biomass burning is also a large anthropogenic source. Natural emissions are dominated by natural fires, lightning and soil emission. During the last decades many publications have discussed the sources and sinks of nitrogen oxides [e.g. Logan, 1983]. An overview of the global sources is given in Table 2-1. Large uncertainties still exist, indicating a limited knowledge of all the processes. No matter if the source is anthropogenic or natural, the largest emissions arise from all kinds of burning processes. Nowadays, atmospheric concentrations have risen several times above preindustrial values. Hammeed and Dignon [1992] still estimated an increase of 350 % since 1983.

$\text{NO}_x$ -Sources	Emission ( $10^{12}$ g/a)	Uncertainty ( $10^{12}$ g/a)
Industry and Traffic	22.00	13.00-31.00
Biomass Burning	7.90	3.00-15.00
Soil Emission	7.00	4.00-12.00
Thunderstorm	5.00	2.00-20.00
Air Traffic	0.80	0.59-0.95
Stratospheric Production	0.64	0.40-1.00
Total	44.00	23.00-8.00

**Table 2-1: Main anthropogenic and natural sources for global tropospheric  $\text{NO}_x$  [Lee et al., 1997]**

Based on new measurements from satellites, it has recently been possible to estimate nitrogen dioxide concentrations on a global scale with resolutions in the range of several 10 kilometres [e.g. Beirle et al., 2003]. Figure 2-2 illustrates the estimated vertical column density over the period of 18 months from January 2003 to June 2004 [Beirle et al., 2004] measured by the SCIAMACHY (Scanning Imaging Absorption Spectrometer for Atmospheric Chartography) instrument on board of the European Space Agency's Envisat satellite. Areas with high  $\text{NO}_2$  concentration directly correlate to areas with strong urban pollution and arise from

<sup>2</sup> Peroxyacyl nitrates

anthropogenic sources. Approximately three quarters of the total  $\text{NO}_x$  emissions are generated by anthropogenic sources [Müller, 1992]. Measurements from satellites are very limited in temporal and spatial resolution. Thus they give an overview of concentration distributions on global scale, but do not allow studying distributions on a local scale which are often necessary to investigate sources and sinks. The low temporal resolution (depending on the satellite, but often not better than one distribution a day) is insufficient to investigate evolution processes. Also the determination of absolute concentrations is difficult. In order to study atmospheric chemistry processes in more detail, ground based measurements are necessary.

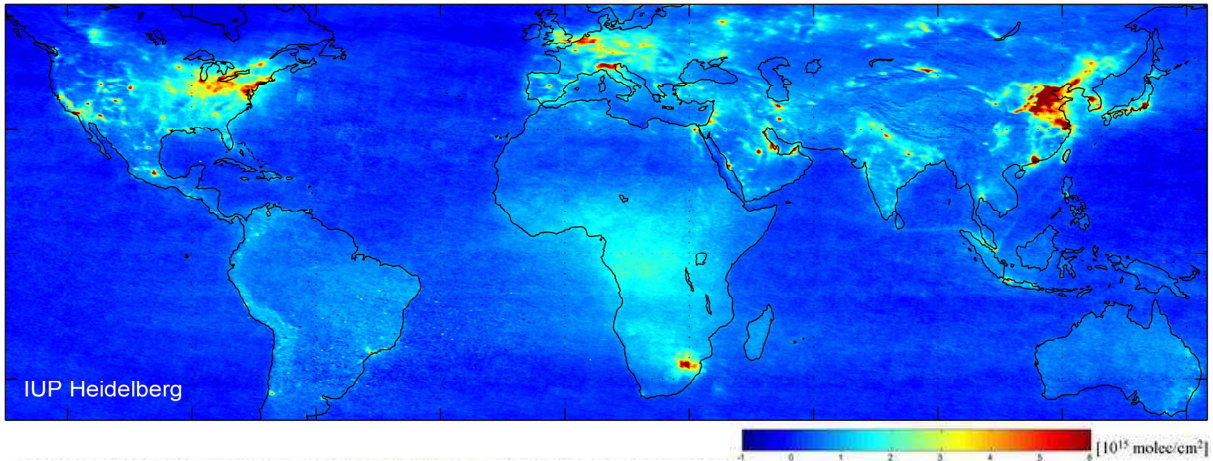


**Figure 2-2: Satellite averaged measurement of tropospheric  $\text{NO}_2$  vertical column density (VCD) from Sciamachy (January 2003 – June 2004) [Beirle et al., 2004].**

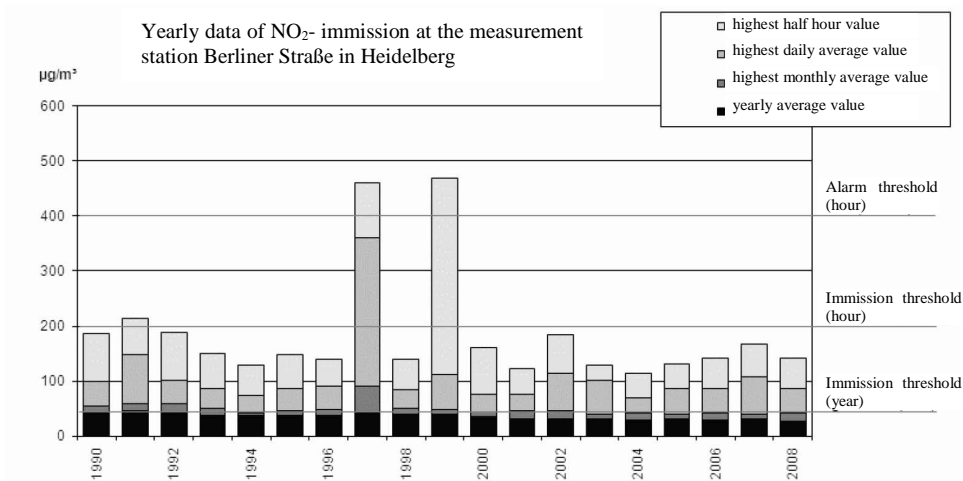


**Figure 2-3: One year averaged data of  $\text{NO}_2$  from 1990 to 2008 for the LUBW measurement station in “Berliner Straße” in Heidelberg (see map in Figure 6-2). The yearly average concentrations have slightly decreased over the last two decades, whereas the maximum observed concentrations varying from year to year due to the strong influence of metrology.  $100 \mu\text{g}/\text{m}^3$  correspond to  $\sim 52 \text{ ppb}$ . [Heidelberg, 2009a]**

Today  $\text{NO}_x$  emissions still remain one of the most problematic pollution sources in industrialised countries, even if a lot of effort has already been made towards their reduction. Till the 1990’s in urban areas all over the world the concentrations increased a few times above the background one. However during the last decades these  $\text{NO}_x$  emissions slowly started to decrease in most industrialised countries. In the United States the  $\text{NO}_2$  concentration decreased by 40 % (from 1990 to 2007) and a reduction of emission by 33% could be reached

[EPA, 2007]. In Germany reductions are much lower. The concentration remains constant or even increases as observed between 2000 and 2006 by the city measurement stations located close to roads with high traffic loads in cities all over Germany. On average the concentration increased there by 7 % [Umweltbundesamt, 2006]. During the last years a slight reduction could be observed [Umweltbundesamt, 2009]. But new data for 2009 show that still 55% of the city measurement stations close to streets display an annual average concentration above the maximum permissible value in the European Union, valid from 2010, which is  $40 \mu\text{g}/\text{m}^3$  ( $\sim 20.9$  ppb) [Umweltbundesamt, 2010]. It is therefore expected that most of these stations will not fulfil the EU criteria in 2010. At 6 measurement stations the maximum permitted concentration of  $200 \mu\text{g}/\text{m}^3$  ( $\sim 104.5$  ppb) was exceeded more than the allowed 18 times. In comparison to the year 2008, the nitrogen dioxide concentration was unchanged.

The yearly average  $\text{NO}_2$  concentration for Heidelberg, Germany, where the measurements of this thesis were performed, has slightly decreased between 1990 and 2008 (Figure 2-3). This is mainly due to increase in public transport, bicycles, a slight reduction of car numbers and a replacement of old cars by newer ones. Still the values are very high and close to the EU maximum permissible value. The maximum concentration for hourly or daily average concentration also strongly depends on the metrology, and thus can still reach the respective threshold levels.

In Heidelberg city the total  $\text{NO}_x$  emission is dominated by traffic (Figure 2-4), as only very few emitting industries are present. It is interesting that 10% of the  $\text{NO}_x$  emission arise from shipping traffic which are investigated in *Chapter 8.15*. During the winter month's emissions from heating systems also become important.

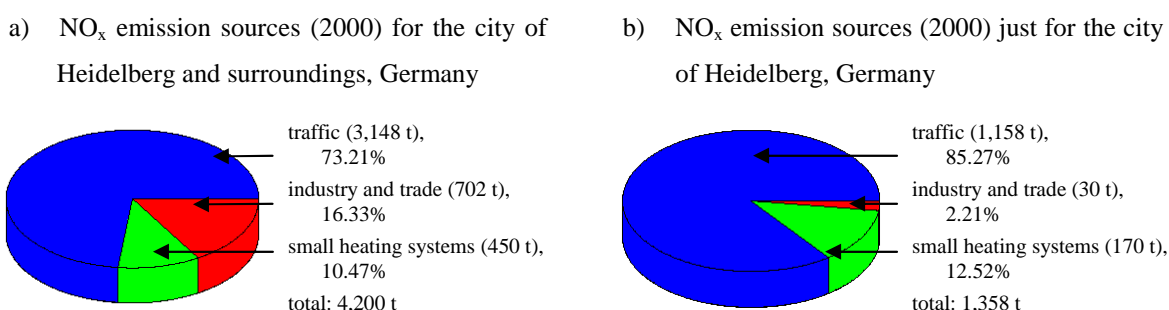
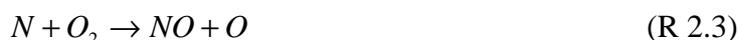
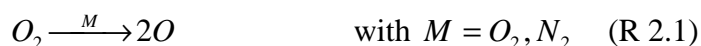


**Figure 2-4: Anthropogenic sources for  $\text{NO}_x$  in Heidelberg, Germany, for the year 2000 [Umweltbundesamt, 2000]**

$\text{NO}_x$  is preliminary emitted in the form of  $\text{NO}$  (typically  $> 90\%$ ) from processes taking place at temperatures high enough to dissociate the triple bond of the nitrogen ( $\text{N}_2$ ) molecule. The process forming  $\text{NO}$  is known as the Zel'dovich Process [Zel'dovich, 1967].



The back reactions require similarly high activation energies and can be eliminated by fast cooling. The highest  $\text{NO}$  concentrations can therefore be found in processes which occur at high temperature and are followed by fast cooling of the gas, e.g. burning in internal combustion engines or electric discharge.

## 2.1.2 Chemistry of Nitrogen Oxides in the Troposphere

The transformation pathways between the different nitrogen compounds are coupled to the reactions of ozone (see *Chapter 2.2*) and to the cycles of hydrogen radicals (OH and HO<sub>2</sub>). In the troposphere, NO reacts with ozone to NO<sub>2</sub>. The speed of this reaction depends on the concentration of ozone.



The reaction constant  $k_{NO+O_3}$  is  $1.8 \cdot 10^{-14} \frac{\text{cm}^3}{\text{molecule} \cdot \text{s}}$  at 298 K and at a pressure of 1 atm [Atkinson, 2004]. In the presence of UV light (wavelength below 420 nm), NO<sub>2</sub> photodissociates to NO and atomic oxygen.



The photolysis rate of nitrogen dioxide  $J(\text{NO}_2)$  therefore depends on UV/ Visible solar radiation which is strongly influenced by the solar zenith angle, clouds and aerosols. On sunny days the lifetime of NO<sub>2</sub> can decrease to 2 minutes with photolysis frequencies around  $J(\text{NO}_2) = 0.008 \text{ s}^{-1}$  [Junkermann et al., 1989].

This reaction is followed by the rapid recombination of the atomic oxygen with molecular oxygen to form ozone. Thus for each NO<sub>2</sub> molecule, an ozone molecule is formed.

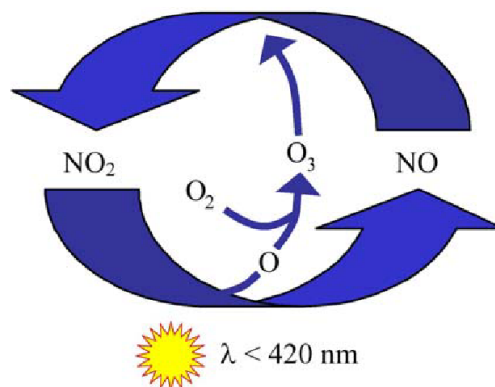


**Figure 2-5: The photo-stationary state between NO, NO<sub>2</sub> and O<sub>3</sub> excluding organic compounds. [adapted from Veitel, 2002]**

Close to the earth's surface other reactions can be neglected, therefore the three mentioned reactions form a photochemical stationary state between NO, NO<sub>2</sub> and O<sub>3</sub> (Figure 2-5).

The reaction R 2.6 is much faster than R 2.4 and R 2.5 (lifetime of atomic oxygen  $\sim 10^{-5} \text{ s}$ ) and can therefore be ignored for the calculation of the photochemical stationary ratio between NO and NO<sub>2</sub>, the so-called Leighton ratio [Leighton, 1961].

$$L := \frac{[NO]}{[NO_2]} = \frac{J(NO_2)}{k_{NO+O_3} \cdot [O_3]} \quad (\text{R 2.7})$$

For typical ozone mixing ratios of 30 ppb, the  $[\text{NO}]/[\text{NO}_2]$  ratio near the ground during daytime is in the order of unity.

During the night, other processes are of importance. The oxidation of NO to  $\text{NO}_2$  with the degradation of ozone (R 2.4) still takes place, but another reaction becomes important, the reaction of  $\text{NO}_2$  with ozone to form the  $\text{NO}_3$  radical.



$\text{NO}_3$  can react with NO or  $\text{NO}_2$ . The reaction with  $\text{NO}_2$  creates a temperature dependent stationary state between  $\text{NO}_2$ ,  $\text{NO}_3$  and  $\text{N}_2\text{O}_5$ .



During the night,  $\text{NO}_3$  is important for the oxidation of organic components. During daylight, it rapidly photodissociates (lifetime in the order of seconds) to NO and  $\text{O}_2$ .

$\text{N}_2\text{O}_5$  is believed to play a significant role in tropospheric chemistry [Finlayson-Pitts and Pitts, 2000]. Its concentration can also be estimated by the measured  $\text{NO}_2$  and  $\text{NO}_3$  concentration and the equilibrium constant for the  $\text{N}_2\text{O}_5$  formation. Peak concentrations up to 10 – 15 ppb in a polluted atmosphere have been calculated [Atkinson et al., 1986].

### 2.1.3 Tropospheric Sinks for Nitrogen Oxides

The main sink (~90 %) of tropospheric nitrogen oxides is the conversion to the water soluble species nitric acid ( $\text{HNO}_3$ ) or nitrous acid ( $\text{HONO}$ ). The most important sink of  $\text{NO}_x$  is the wet deposition, e.g. on water droplets from rain, and it is therefore a major constituent of acid rain. The dry deposition of the “sticky”  $\text{HNO}_3$  molecule, e.g. adsorption on aerosols or the ground, is expected to be responsible for 16 % up to 40 % of the total nitrogen flux to the surface, as estimated by [Russell et al., 1993] and [Nielsen et al., 1996], respectively [Trick, 2004].

One of the main reactions leading to the formation of nitric acid is the degradation of  $\text{NO}_2$  by reaction with OH radicals to form  $\text{HNO}_3$ .



During the night, a major loss process of  $\text{NO}_2$  appears in the form of the hydrolysis of the nitrogen oxides (R 2.9 and R 2.10) and subsequently the dry or wet deposition of the formed  $\text{N}_2\text{O}_5$  [Mentel et al., 1996].



It is suggested that these reactions are both first and second order reactions in water [Mentel et al., 1996]. In the northern hemisphere, 50 to 90 % of the  $\text{HNO}_3$  formation occurs by the reactions R 2.12 and R 2.13 and the adsorption of  $\text{NO}_3$  on wet surfaces [Dentener and

Crutzen, 1993]. Therefore,  $\text{N}_2\text{O}_5$  has to be seen as a major sink of nitrogen oxides in the polluted troposphere as discussed in detail by Alicke [2000]. Also other formation reaction processes of  $\text{HNO}_3$  exist: the reaction of  $\text{NO}_3$  and aldehydes [Morris and Niki, 1974], alkenes [Hoshino et al., 1978] or with dimethylsulfide (DMS) in the marine boundary layer [Alicke, 2000].

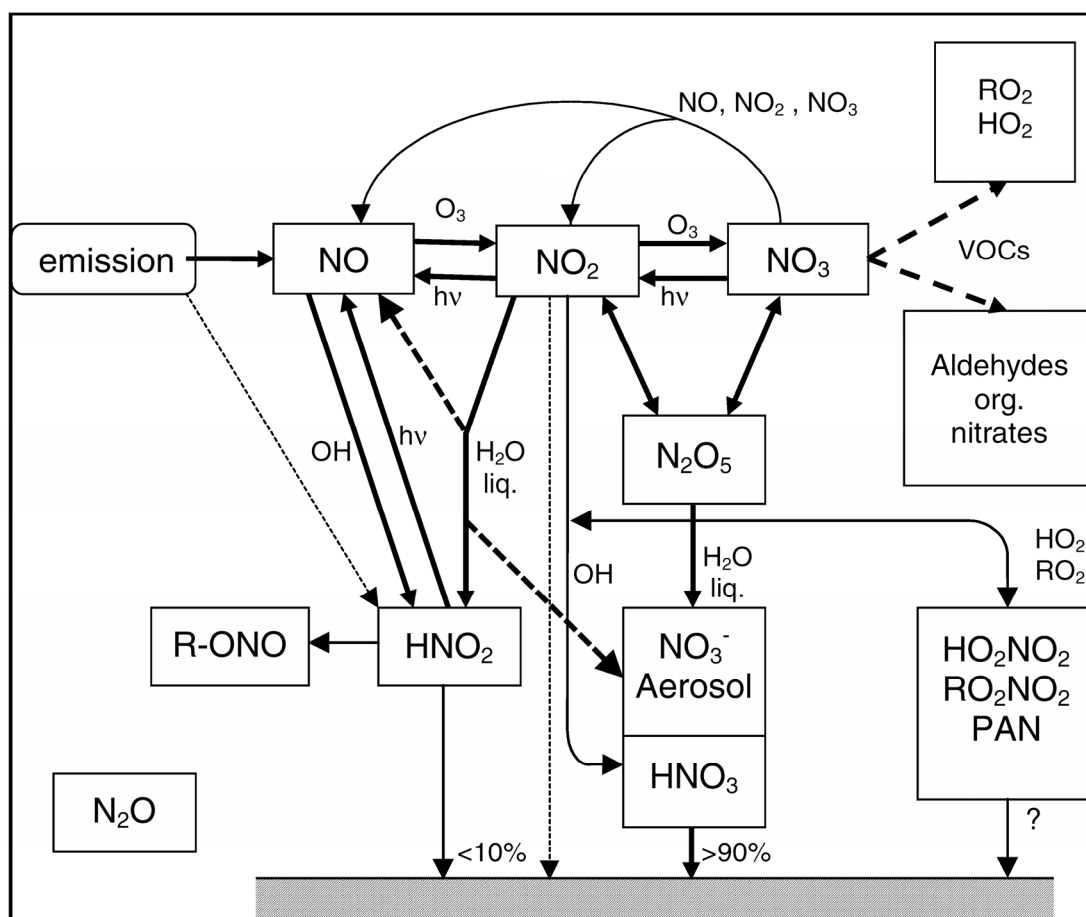


**Figure 2-6: Overview of the nitrogen oxide chemistry in the troposphere. The trace gases next to the arrows indicate the necessary components for the reaction [adapted from Platt and Stutz, 2008].**

It should be mentioned that the formation of  $\text{NO}_3$  by the reaction of  $\text{NO}_2$  with  $\text{O}_3$  (R 2.8) is another  $\text{NO}_2$  (and thus  $\text{NO}_x$ ) sink. Even if the rate constant of this reaction is small at 296K ( $k_{R\ 2.8} = 3.2 \times 10^{17} \text{ cm}^3 \text{ molec}^{-1} \text{ s}^{-1}$ ), it is important in areas featuring high  $\text{O}_3$  concentrations at night. If an  $\text{O}_3$  concentration of 100 ppb is assumed, which is below the European alarm threshold of 120 ppb for at least 3 hours, the lifetime of  $\text{NO}_2$  with respect to  $\text{O}_3$  is only 3.5 hours [Finlayson-Pitts and Pitts, 2000].

The loss of nitrogen oxides through the formation of HONO and its decomposition is described in *Chapter 2.3*.

An overview of the nitrogen oxide processes is given in Figure 2-6.  $\text{NO}_x$  plays the central role in the tropospheric nitrogen chemistry, which is primarily emitted in the form of  $\text{NO}$  and presents the supply for most nitrogen oxides.

As the  $\text{NO}_2$  concentration strongly depends on emissions and different reaction pathways, it can have a very strongly varying spatial distribution, which is often unknown especially in urban areas. Measurements of the  $\text{NO}_2$  distribution are required to quantitatively estimate the exposure to humans and plants for chemical and public health reasons.

## 2.1.4 Annual Cycle of Nitrogen Dioxide

NO<sub>2</sub> displays only a weak yearly cycle in urban areas (Figure 2-7), in contrast to the significant daily cycle (see *Chapter 8.7*). First of all, the anthropogenic sources vary only slightly with the season. In winter, higher emissions arise due to heating and more traffic emissions. But the conversion of the emitted NO to NO<sub>2</sub> in winter is often limited due to depletion in ozone. Thus it is only converted later if it is mixed with ozone containing air, outside the urban area. In summer during daytime, due to higher solar radiation, more of the NO<sub>2</sub> is converted to NO and ozone, than in winter. This fact reduces the NO<sub>2</sub> concentrations during the day. Typically the highest concentrations arise during days, when a metrological inversion exists (see *Chapter 2.7*). In this situation, the air does not mix with the air above the PBL and emissions are trapped. This mostly occurs during cold winter days or cold cloud free nights. Therefore, the highest NO<sub>2</sub> concentrations arise in winter (Figure 2-7) and are responsible for the winter smog.

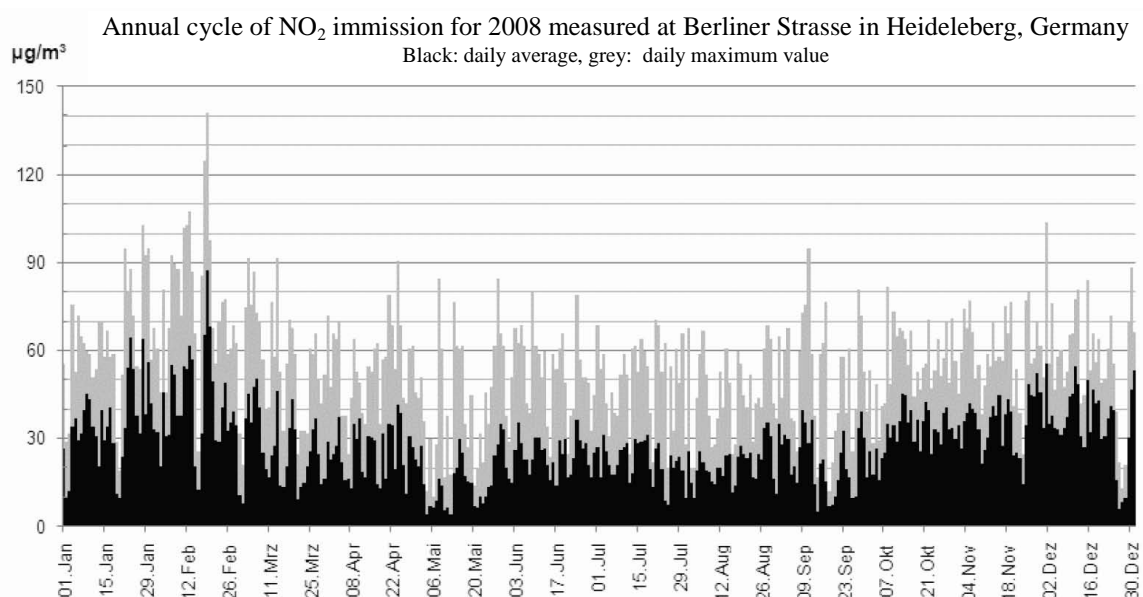


**Figure 2-7: Annual cycle of NO<sub>2</sub> for 2008 measured at the LUBW station in Berliner Strasse in Heidelberg, Germany. Only a weak yearly cycle can be found, as emissions do not vary significantly. In summer the concentration is reduced due to enhanced photolysis. Highest concentrations arise if a metrological inversion occurs and nitrogen oxides are trapped what often arise in winter. 100 µg/m<sup>3</sup> correspond to ~ 52 ppb. [Heidelberg, 2009b]**

## 2.2 Ozone (O<sub>3</sub>)

The highest concentration of O<sub>3</sub> can be found in the ozone layer in the stratosphere, at altitudes between 15 and 30 km. The absorption of O<sub>3</sub> in the ultra violet (UV) wavelength range protects the earth from dangerous UV radiation. Only 10 % of the total O<sub>3</sub> is located in the troposphere. This ozone is a strong greenhouse gas [Kiehl and Trenberth, 1997]. The radiative forcing is about 25 % that of CO<sub>2</sub> [IPCC, 2001]. Due to its short lifetime it is not as homogeneously distributed as the most important green house gases CO<sub>2</sub>, CH<sub>4</sub>, N<sub>2</sub>O and CFC. Ozone is not directly emitted and for a long time it was assumed that transport from the

stratosphere is the origin of tropospheric ozone. Since the late 70's of the 20<sup>th</sup> century however we know that only ~15 % of tropospheric ozone has its origin in the stratosphere. It is mostly created in the troposphere by processes including OH- and NO<sub>x</sub>-catalysis [Fishman and Crutzen, 1978; Finlayson-Pitts and Pitts, 2000].

High ozone concentrations are responsible for damages to plants and irritations of human and animal eyes and respiratory systems [Haagen-Smit et al., 1952]. They arise during summer smog events if high UV radiation is present in combination with the emission of NO<sub>x</sub>, H<sub>2</sub>O<sub>2</sub>, CO or VOC. This phenomenon was first observed during the Los Angeles smog where the arising high ozone values even resulted in damages to rubber. Extremely high concentrations of ozone of up to 400 ppb have since then been detected in many sunny urban areas around the world, including Sydney, Mexico City and Athens.

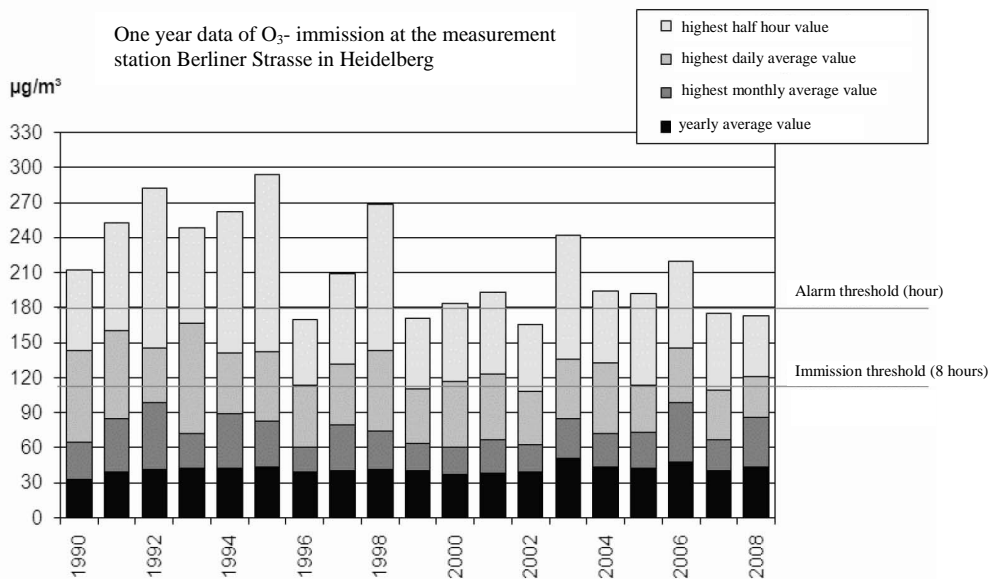


**Figure 2-8: One year data of O<sub>3</sub> from 1990 to 2008 for the LUBW measurement station in the “Berliner Straße” in Heidelberg (see map in Figure 6-2). The maximum concentrations have slightly decreased over the last two decades, whereas the yearly average concentrations remain constant. 100 µg/m<sup>3</sup> correspond to ~ 50 ppb. [Heidelberg, 2009c]**

Over the last decades ozone concentrations have only slightly decreased in industrialised cities. In Germany highest concentrations arose in the 80's and 90's. During warm summers, levels of 300 µg/m<sup>3</sup> (~ 150 ppb) are reached regularly. Due to a reduction of the sources NO<sub>2</sub> and VOC, also the ozone concentrations could be reduced in the last decade. As the ozone formation strongly depends on the metrological conditions, strong fluctuations from year to year arise. Hot dry summers always result in higher ozone levels. During the extreme hot summer of 2003, much higher levels were reached, and several cities exceed the recommended exposure limit of 180 µg/m<sup>3</sup> (~ 90 ppb) for one hour average or even the threshold level of 240 µg/m<sup>3</sup> (~120 ppb) [Umweltbundesamt, 2005]. During the last years, episodes of increased ozone levels did not occurred, as no equivalent hot summer with similar high solar radiation arosed. In 2009 however, 15 % of the measurement stations observed O<sub>3</sub> concentrations exceeding 120 µg/m<sup>3</sup> (~ 60 ppb, for an 8 hour average value) [Umweltbundesamt, 2010]. This is the new threshold level (since 2010) which should be exceeded on a maximum of 25 days per year.

In Heidelberg, the very high concentrations detected on hot summer days could slightly be reduced, but the overall concentration remained constant (Figure 2-8). Even restrictive measures in the 90's like a ban on driving during high ozone concentrations (above 240  $\mu\text{g}/\text{m}^3$ ) did not show significant improvement.

Ozone levels can only be reduced efficiently if the emission of  $\text{NO}_x$  and VOC are reduced. The fact that the ozone levels recently remain below the highest values of the last century, although these were very hot summers is due to reductions in the emitted VOC. Ozone still remains one of the most important pollutants in industrialised areas.

The initial reaction, which is involved in the production of ozone in the troposphere, is the photodissociation of  $\text{NO}_2$  (R 2.5) to  $\text{NO}$ . The formed atomic oxygen then reacts with molecular oxygen to ozone (R 2.6). The reverse reaction is also possible and a photostationary state, the Leighton ratio, is produced as described in *Chapter 2.1.2*. These reaction cycles do not lead to a net formation of ozone.

However, if other relevant oxidising species exist, which can catalytically oxidise  $\text{NO}$  to  $\text{NO}_2$  without the destruction of  $\text{O}_3$ , they can lead to a net ozone production. Most relevant are the hydroperoxyl radical  $\text{HO}_2$  and the hydroxyl radical  $\text{OH}$ , collectively represented as  $\text{HO}_x$ . The  $\text{HO}_2$  (or  $\text{RO}_2$ ) radical reacts with  $\text{NO}$  to form  $\text{OH}$  and  $\text{NO}_2$ . Furthermore the  $\text{OH}$  radical reacts with  $\text{CO}$  or  $\text{HC}$  and is converted to  $\text{HO}_2$  or  $\text{RO}_2$  radicals, thus closing the  $\text{HO}_x$  (or  $\text{RO}_x$ ) cycle.



Together with the reactions R 2.5 and R 2.6 this leads to the following net reaction:



The concentrations of  $\text{OH}$ ,  $\text{HO}_2$  and  $\text{NO}$  are not influenced by these reactions, which lead to a catalytic production of ozone during daylight, by converting the carbon monoxide ( $\text{CO}$ ) to carbon dioxide ( $\text{CO}_2$ ). The process shown in Figure 2-9 displays the formation of ozone and the chemistry of  $\text{NO}_x$ ,  $\text{O}_3$ ,  $\text{OH}$  and hydrocarbons. Analogue to  $\text{CO}$ , ozone production is also possible with volatile organic compounds (VOCs) (for details see Sillman et al. [1990]).

Because  $\text{HO}_x$  and  $\text{NO}_x$  are recycled, the formation of ozone can be very efficient [Crutzen, 1970]. The catalytic production is only interrupted if either a  $\text{NO}_x$  or a  $\text{HO}_x$  is removed, for example by the reaction of  $\text{OH}$  with  $\text{NO}_2$ , or the self-reaction of  $\text{HO}_2$  and  $\text{RO}_2$ .

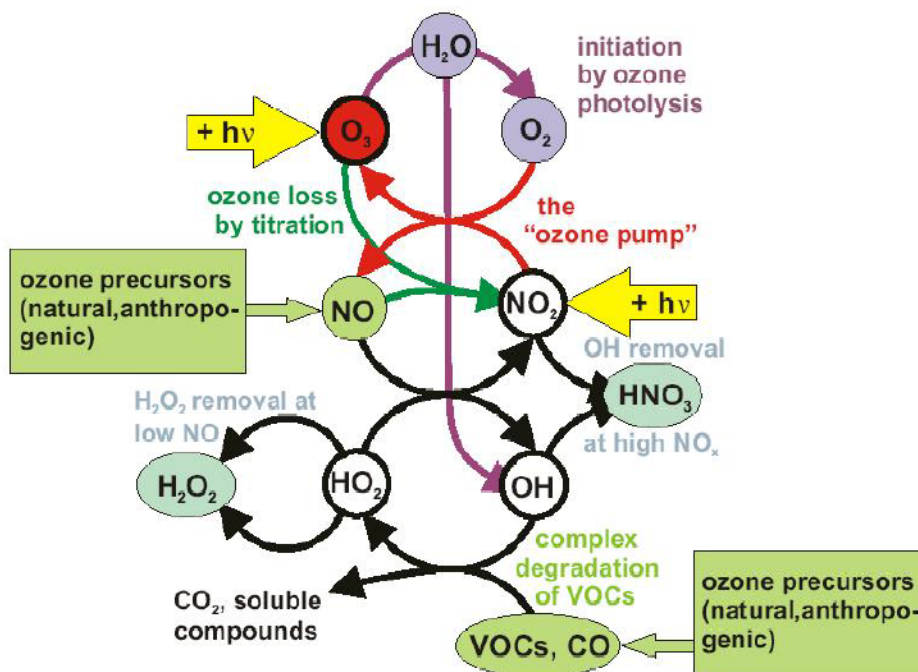


Figure 2-9: Overview of the formation of tropospheric ozone including the most relevant precursors [adapted from Beirle, 2004].

The formed ozone molecules can photodissociate and form hydroxyl radicals. Atomic oxygen in the excited state  $O(^1D)$  is created if high radiation energies are present. The direct transition to the ground state  $O(^3P)$  is forbidden but occurs due to collisions with other molecules.  $O(^3P)$  then reacts with  $O_2$  to regenerate ozone. According to [Finlayson-Pitts and Pitts, 2000], 10 % of the  $O(^1D)$  reacts with water vapour at typical weather conditions (50 % relative humidity, 300 K) creating two hydroxyl radicals. The average lifetime of ozone is about 10 hours.



OH radicals can also be formed in the photodissociation of HONO (R 2.20) and formaldehyde (R 2.30 or R 2.31) plus the reaction with ozone which are described in *Chapter 2.3* and *2.4*.

In urban areas, typically car exhausts dominate the emission of pollution (Figure 2-4). Home heating and industry can also contribute considerably. The sources emit large amounts of  $NO_x$  (mostly in the form of NO) and VOC, the main precursors of ozone. Thus, ozone formation can be orders of magnitudes higher than in slightly polluted areas. However, effective ozone sinks are also present in urban centres such as the reaction with emitted NO or olefins. Therefore, the ozone lifetime can be quite short (few hours) and high diurnal fluctuations arise in these areas. In fact, the ozone level near the ground can reach zero a few hours after sunset and remain at zero until sunrise. In the morning the enhanced vertical mixing replenishes some ozone from higher layers thus initiating the radical chemistry again.

The photolysis of HONO (R 2.20) and HCHO (R 2.30 and R 2.31) can significantly speed up the radical process and thus the growth of  $O_3$  in the morning. In fact, the ozone production or reduction depends on the initial concentration of  $NO_x$  and hydrocarbons. If too many nitrogen oxide molecules or if only a few of them are available, ozone production is reduced. This

dependency of the ozone production on the initial  $\text{NO}_x$  and hydrocarbon concentration is shown in Figure 2-10. The maximum ozone production arises for a special  $\text{NO}_x$  to VOCs ratio.

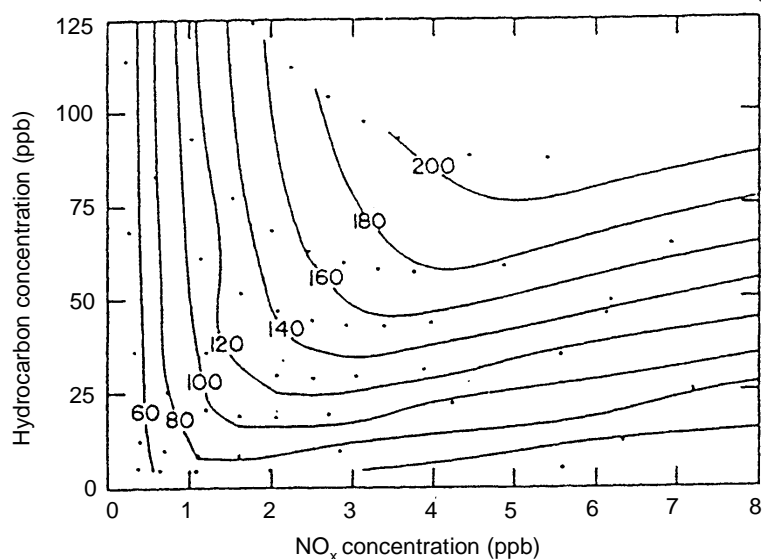


**Figure 2-10: Ozone isopleths in ppb as a function of the concentration of  $\text{NO}_x$  and hydrocarbons [Sillman et al., 1990]. The dots result from individual runs of the computer simulations with emission rates as input parameters.**

For a fixed initial hydrocarbon concentration the ozone concentration increases with higher  $\text{NO}_x$  concentration until it reaches a maximum. If the  $\text{NO}_x$  concentration increases further, the ozone concentration decreases again. Only an increase of hydrocarbons would increase the ozone concentration, therefore this situation is called “VOCs limited case”.

In the other case of constant initial  $\text{NO}_x$  concentration, the ozone concentration increases with increasing hydrocarbons but the ozone production converges to a constant value which is called “ $\text{NO}_x$ -limited” [Sillman et al., 1990].

In order to improve air quality in heavily polluted areas, the profound knowledge of the actual situation is important. In many polluted cities the situation is “VOCs limited”, and therefore the attempt to improve air quality by reducing  $\text{NO}_x$  would actually result in an ozone increase. As the lifetimes of  $\text{NO}_x$  and VOCs are different, the ratio changes for an air-mass with time. Additionally biogenic VOC emissions can change the ratio. Also the formation of ozone takes several hours. Thus, highest ozone levels are typically found downwind of urban or industrial areas.

### 2.2.1 Annual Cycle of Ozone

As ozone is formed due to photolysis of  $\text{NO}_2$ , the highest concentration arises if high  $\text{NO}_2$  and VOC emissions are combined with high solar radiation. This is the case for warm summer days in urban areas like the city of Heidelberg, e.g. May 2008 in Figure 2-11. During days with low solar radiation, like in winter, ozone is depleted, due to emissions of NO which convert ozone to oxygen and a low photolysis rate of  $\text{NO}_2$ . If the air mass is trapped, e.g. due

to an inversion, a complete depletion of ozone can sometimes occur, e.g December 2008 in Figure 2-11.

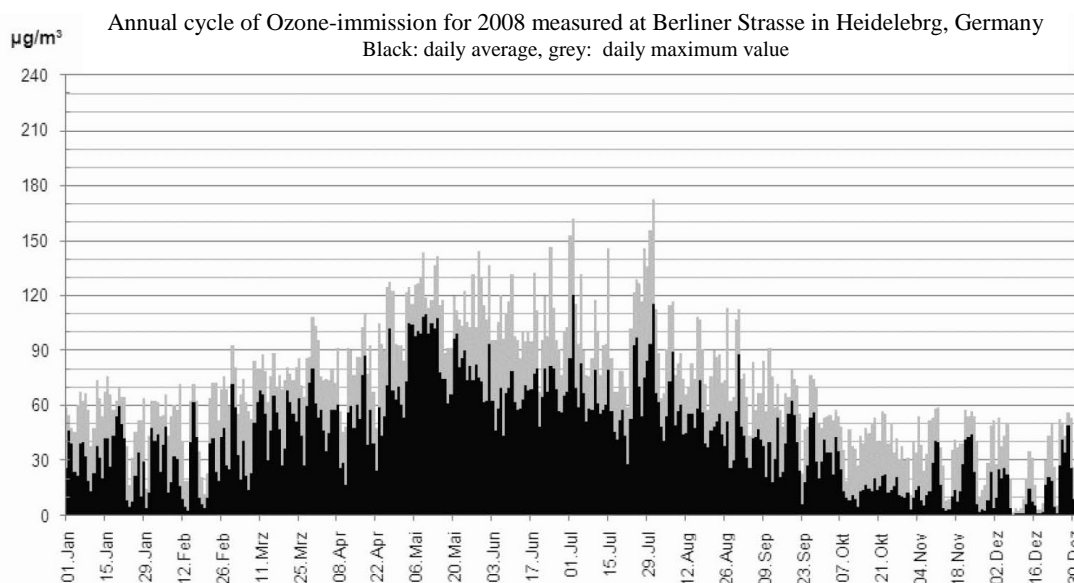


**Figure 2-11: Annual cycle of O<sub>3</sub> for 2008 measured at the LUBW station in Berliner Strasse in Heidelberg, Germany. A strong yearly cycle can be found, as the formation of ozone strongly depends on the photolysis of NO<sub>2</sub>. In winter ozone can often be completely depleted due to emissions of NO and trapped air masses due to inversion situations. 100 µg/m<sup>3</sup> correspond to ~ 50 ppb. [Heidelberg, 2009d]**

## 2.3 Nitrous Acid (HONO)

The role of nitrous acid for the atmospheric chemistry has been underestimated for a long time and has been neglected in many models. The photolysis of nitrous acid (HONO) is an important source for OH radicals, the most important daytime oxidizing species [Perner and Platt, 1979; Platt et al., 1980]. Under certain circumstances it is even the major source of OH radicals, e.g. in polluted areas it can contribute to 1/3 of the total 24 hour production, and in the morning hours it can be the dominant OH source [Alicke et al., 2002]. Maximum HONO mixing ratios in urban areas of up to 15 ppb are reported [Winner and Biermann, 1994; Alicke, 2002 and References therein]. Generally, nitrous acid concentrations scale with the NO<sub>2</sub> level, thus approximately with the degree of pollution. The diurnal variation is characterised by photolysis causing lower values during the day. In the night the level increases, often reaching a constant level in the early morning. The amount of HONO formed is often correlated with the stability of the nocturnal boundary layer (see *Chapter 2.7*).

The photolysis of HONO, which absorbs in the wavelength range from 300 to 390 nm, leads to the formation of an OH radical and NO [Stockwell and Calvert, 1978; Stutz et al., 2000]:



Because the HONO concentration typically reaches a maximum during the night, especially during sunrise it is an important source for hydroxyl radicals, surpassing other HO<sub>x</sub> sources, such as O<sub>3</sub> or HCHO photolysis [Alicke et al., 2002].

HONO formation mechanisms can be divided into three groups: direct emissions, homogeneous reactions and heterogeneous reactions. The production rate of each source is still unclear. Direct emission can occur from fossil fuel combustion of vehicles, and e.g. contributed to 0.65% of the emitted  $\text{NO}_y$  measured in a traffic tunnel in Germany [Ackermann, 2000]. During the day HONO can be formed in a homogeneous reaction, for example the recombination of the hydroxyl radical OH with NO:



Due to their low reaction rates, homogeneous HONO formation reactions play only a minor role in the atmosphere. Heterogeneous reactions take place at wet surfaces (liquid) and HONO is formed from nitrogen oxides and water [e.g. Veitel, 2002 and References therein]. The majority of the urban formed HONO is suspected to be formed through one of the following reactions [Perner and Platt, 1979; Kessler and Platt, 1984; Platt, 1984]:

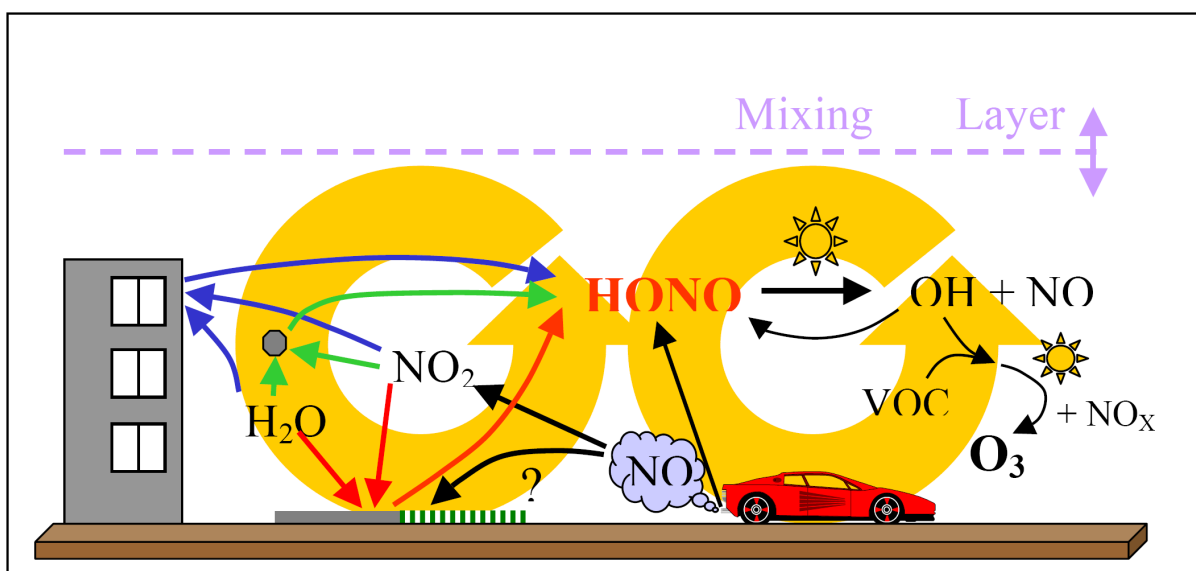
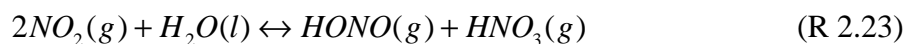


Figure 2-12: The simplified atmospheric chemistry of HONO in urban areas [adapted from Trick, 2004].

Several field observations proved reaction (R 2.22) to be insignificant in cases where low NO levels were observed during the night (or high ozone levels exclude the presence of NO) [e.g. Kessler and Platt, 1984]. This correlates with a number of model studies [e.g. Sakamaki et al., 1983]. The exact mechanism of reaction (R 2.23) is unknown, neither the reaction rate constant nor the nature of the surface, which makes calculations of the OH productions difficult. But reactions of  $\text{NO}_2$  on asphalt or roof tile surfaces are estimated to be sufficiently rapid to explain observations [Trick, 2004].

Besides photolysis the most important destruction mechanism of HONO (few percent) is expected to be the reaction with the OH radical:



The water-soluble acid HONO can also be removed from the atmosphere via wash out by rain (wet deposition), where it contributes to acid rain, or obviously by dry deposition, consisting of agglomeration on aerosols and the ground [Stutz et al., 2002] and chemical reactions. Stutz et al. [2002] also observed HONO formation and deposition on the ground balancing each other. Thus, highest HONO values can be found at the compensation point between both processes. For a grass meadow surface, this compensation point was found at a HONO/NO<sub>2</sub> ratio of  $3 \pm 1$  %. However, deposition of HONO on rough surfaces plays a key role for the HONO gradient measured in the lower PBL [Stutz et al., 2002]. The deposition of HONO is a sink of NO<sub>x</sub> which amount is not exactly known but estimated to be less than 10 % of the total NO<sub>x</sub> deposition (Figure 2-6).

The chemistry of HONO is summarised in Figure 2-12. A review of the HONO processes can be found in Trick [2004].

## ***2.4 Formaldehyde (HCHO)***

Formaldehyde (HCHO or H<sub>2</sub>CO) belongs to the large group of VOCs and is an important high-yield intermediate in the oxidation mechanism of almost every other VOC. It is the most reactive and abundant gas-phase carbonyl compound in the remote and polluted atmosphere. Typical formaldehyde mixing ratios in urban areas are in the order of 1-20 ppb [e.g. Grosjean, 1981; Grosjean et al., 1993] and can reach up to 100 ppb in very polluted areas [e.g. Harris et al., 1989; Grosjean, 1991]. Values of 150 ppb have been measured in the 1960s in the Los Angeles area [Stahl, 1969]. In more remote continental locations and rural areas, mixing ratios of 1-10 ppb have been observed due to input of additional non methane hydrocarbons (NMHCc) by vegetation [e.g. Benning and Wahner, 1998; Harder et al., 1997]. In clean remote air, formaldehyde mixing ratios are between 0.1 and 0.5 ppb [e.g. Platt et al., 1979]. Due to the short lifetime of formaldehyde of few hours, strong spatial and temporal variations arise.

Formaldehyde itself is harmful to human health at elevated concentration levels due to its carcinogenic effect and the irritation of the respiratory tract [WHO, 2000]. Indoor levels are often very high with 25-50 ppb (sometimes even reach up to 280 ppb) due to chemical treatment of furniture, carpets etc. [WHO, 2000]. This is several orders higher than levels in ambient air (see above). Extremely high concentrations of 50 to 100 ppm are also observed in tobacco smoke, which is a major source of indoor formaldehyde levels [WHO, 2000]. Formaldehyde is listed as one of the most hazardous air pollutants [EPA, 2010]. It is only rarely monitored. Thus the real exposure is unclear.

As the generation of formaldehyde (see R 2.25 – R 2.28) also involves the conversion of NO to NO<sub>2</sub>, its concentration represents an indicator for the rate of atmospheric VOC oxidation and thus, the formation of tropospheric ozone. The central role of formaldehyde in the tropospheric photochemistry originates from its radical forming capability. In this regards, the main process is its reaction with OH, NO<sub>3</sub> or Cl and the abstraction of the weakly bound aldehydic hydrogen.

The main sources of formaldehyde are the direct emission by fossil fuel combustion or biomass burning, as well as its production in chemical reactions during the oxidation of

hydrocarbons. It is differentiated between the oxidation of methane ( $\text{CH}_4$ ) and those of Non Methane Hydro Carbons (NMHC):



The chemical reaction can be summarised as follows:



Similar reaction chains as described in R 2.25 – R 2.28 can also be found for other NMHCs. Therefore,  $\text{CH}_4$  can be replaced by a hydro carbon segment RH, which are often followed by further destruction of the hydrocarbons and lead to a HCHO production [Hak, 2006].

According to *Chapter 2.2* (R 2.14 - 2.17), the formation of  $\text{HO}_2$  can lead to a net production of ozone molecules if many hydrocarbons exist. NO will then be oxidised to  $\text{NO}_2$  without depletion of  $\text{O}_3$  and thus increase the ozone concentration. Formaldehyde is therefore a photochemical pollutant.

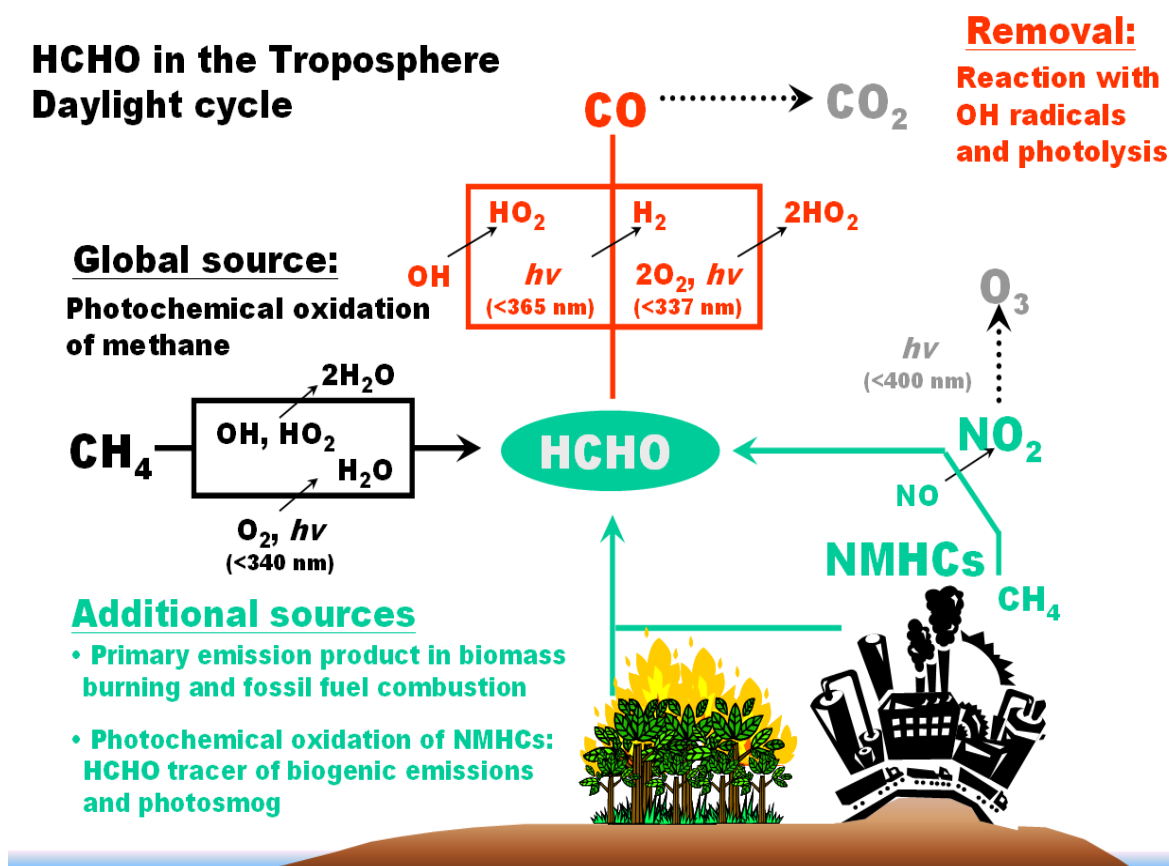


Figure 2-13: Formaldehyde in the atmosphere [Marbach, 2004]<sup>3</sup>.

<sup>3</sup> with corrections, personal communication T.Marbach, 2010.

Formaldehyde is generated by a wide range of VOCs and the individual formation pathways are not delineated here in detail. They are a main precursor of formaldehyde in urban environments, whereas the contribution of biogenic VOC sources can dominate in highly wooded regions, at least during the growing season. In several cases of VOC oxidation, formaldehyde is formed as a secondary product from further degradation of higher carbonyls.

HCHO is mainly removed by three reactions. Two of them are photolysis during the day:



The products created in reaction 2.31 oxidise to HO<sub>2</sub> and CO.



Photolysis is the main sink for formaldehyde, but the reaction which oxidises the hydroxyl radical OH to HO<sub>2</sub> is also important.



An overview of the main HCHO emissions and reactions is given in Figure 2-13.

In the sunlit atmosphere, photolysis and reaction with OH radicals determine the atmospheric residence time of formaldehyde. At night, the removal by wet and dry deposition can be important [e.g. Lowe and Schmidt, 1983]. The lifetime of formaldehyde towards wet and dry deposition is assumed to be in the order of a day [Benning and Wahner, 1998].

Typically, the lifetime during daylight with respect to its two major loss pathways, photolysis (R 2.30 and R 2.31) and reaction with the hydroxyl radical (R 2.34), is in the order of 2-4 hours. Therefore the concentration is mainly not effected by transport and the observed concentration is in steady state between local production and destruction. At night, the lifetime is very long and thus transport becomes important.

## 2.5 Sulphur Dioxide (SO<sub>2</sub>)

Sulphur dioxide is primarily emitted from fossil fuel combustion. Globally about 75 % of the emitted SO<sub>2</sub> has anthropogenic sources; mainly traffic, heating and the industrial production of electricity [Chin and Davis, 1993]. SO<sub>2</sub> is also emitted from asphalt plants [Kuuspalo et al., 1991]. The emissions of SO<sub>2</sub> during asphalt paving are unclear. The most important natural sources are volcanoes which can locally and temporarily create extremely high SO<sub>2</sub> concentrations.

Sulphur dioxide is toxic and is associated with increased respiratory symptoms and diseases like asthma, difficulty in breathing and premature death. Besides NO<sub>2</sub> it is mainly responsible for acid rain.

Various fossil fuels contain different amounts of sulphur. During combustion of these fuels, 90 % or more of the sulphur is reduced to  $\text{SO}_2$  and only a few other compounds are created, such as  $\text{SO}_3$  or sulphate [Finlayson-Pitts and Pitts, 2000]. Thus, the  $\text{SO}_2$  emission can be calculated with relatively high accuracy from the rate of fuel consumption and the percentage of sulphur in the fuel. Due to substantial reductions of sulphur concentration in petrol and heating oil as well as technical improvements in  $\text{SO}_2$  filters, the  $\text{SO}_2$  emissions in Germany have decreased by almost 90 % since the 1990's [Umweltbundesamt, 2005]. In the measurement area of Heidelberg  $\text{SO}_2$  primarily arises from small heating systems which dominate the emission especially in the winter (Figure 2-14). An interesting point is that 24% of the traffic emissions originate from ships. The reasons for this are high sulphur concentrations in shipping diesel and the common lack of  $\text{SO}_2$  filters. This is further investigated in *Chapter 8.15*.

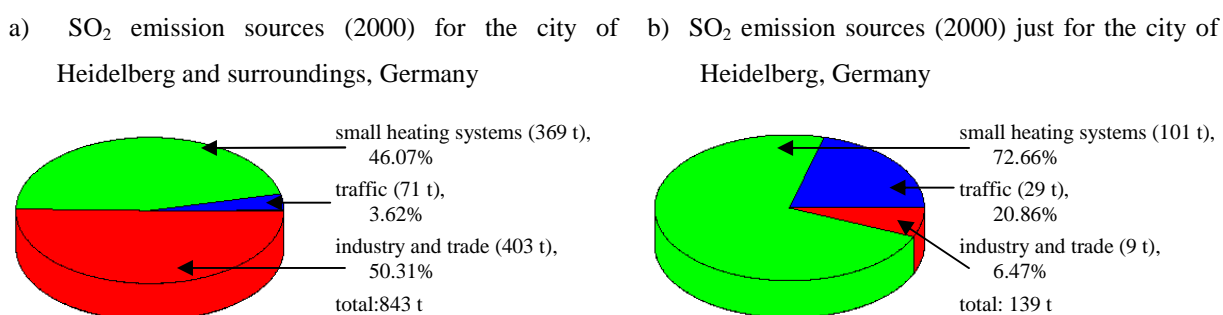


**Figure 2-14: Anthropogenic sources for  $\text{SO}_2$  in Heidelberg, Germany for the year 2000 [Umweltbundesamt, 2000]**

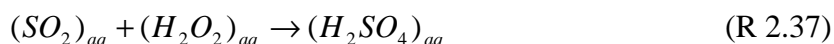
The main sinks of  $\text{SO}_2$  in the troposphere are deposition and oxidation. It has a very high solubility in water. The reaction with a hydroxyl radical forms sulphuric acid ( $\text{H}_2\text{SO}_4$ ):



$\text{HSO}_3$  reacts with oxygen and water to sulphuric acid.



Moreover,  $\text{SO}_2$  can be removed by the oxidation with  $\text{H}_2\text{O}_2$  in solution:



The wet deposition of sulphuric acid is a major sink of  $\text{SO}_2$ . Together with  $\text{HNO}_3$ , it is the main component of acid rain. Dry deposition of sulphur dioxide on the ground, plants or building walls is also important.

## ***2.6 Trace Gas Distributions on Local Scale***

As this work deals with tomographic LP-DOAS measurements in urban areas this chapter concentrates only on local scale trace gas distributions from 1 m up to about 10 km. How distributions actually arise on these scales from chemical and, sometimes even more important, transport processes are discussed.

Apart from direct scientific interest, measurements of trace gas distributions are desirable for research in the following areas:

- Air pollution monitoring.
- Model evaluation and input.
- Emission source and sink strengths.
- Chemical transformation processes.

Although significant progress has been achieved in the last decades in air pollution monitoring and most emissions have been drastically reduced in industrialised countries, large scale environmental problems still arise. The emissions are especially high in regions with extensive industry or high traffic density. Within the EU, air pollution and its monitoring on a national level is regulated by EU and additional national laws. The regulation of the European Air Quality Guideline 96/62/EU and its daughter directives reach down to the municipal level by requiring concentration maps from EU members not only for the state in total, but also for regional conurbations with more than 250.000 inhabitants and heavily polluted micro environments [Schatzmann et al., 2006]. Typically these data is obtained from point measurements (in-situ). The EU directives suggest that those measurements taken at urban background sites should be representative for an area of several km<sup>2</sup> and that those taken at intense traffic or industrial sites are representative for at least 200 m<sup>2</sup> [Truckenmüller et al., 2004]. Applying an obstacle resolving chemical transport model with high spatial resolution (up to 1 m) to a heavily polluted street canyon shows that point measurements at the ground level barely fulfil these criteria even under stationary meteorological conditions [Schlünzen et al. 2003]. Specially resolved measurement techniques would be fundamental for accurate air pollution monitoring. The legislation acknowledges the insufficient state of measurement techniques (typical point measurements) and the high cost of measurement stations by permitting modelled concentration maps for monitoring purposes. The model quality objectives are summarised in Table 2-2.

This brings us to the second point. These models have to be evaluated with measurements. Models in their most complex form have to simulate the emissions, transport and chemical evolution of trace gases and aerosols on different local and global scales. All parts of the model have to be computed with sufficient precision. Calculating transport processes over an even terrain on a mesoscale (~100 km) may be an easy task. However, accurately assessing spatial details, complex terrain and flow patterns on microscales (~100 m) is more of a problem for the model method and for computer power. In urban areas, buildings can e.g. effect the concentration by a factor of two and thus models have to meet rather challenging requirements on these scales [Schatzmann and Leitl, 2002]. The experimental proof, that a

model predicts concentrations with sufficient accuracy, is required. Discrepancies have to be evaluated and traced back to either wrong emission data, incomplete chemical mechanisms, faulty transport calculations or insufficient parametrisation of atmospheric turbulences. Point measurements are in general not suitable due to high spatial and temporal concentration fluctuations, whereas concentration maps with sufficient spatial and temporal quality give information on the location of emission, their transport and concentration variability.

pollutant	quality indicator	model quality objective [%]
SO <sub>2</sub> , NO <sub>2</sub> , NO <sub>x</sub>	hourly mean	50-60
	daily mean	50
	annual mean	30
O <sub>3</sub>	8 h daily maximum	50
	1 h mean	50
Benzene	annual mean	50
CO	8 h mean	50

**Table 2-2: Model quality objectives established by the EU directives 1999/30/EC, 2000/69/EC and 2002/3/EC. The quality objective is defined as the maximum deviation of a measured and a calculated concentration for the given quality indicator.**

Even if chemical dispersion models eventually reach a level of quality where they are allowed to be used for air quality predictions, measurements of concentration distributions are still necessary. One reason is that all models must be initialised with reliable measurement data and boundary conditions. Additionally, models usually have a large amount of free parameters and settings. For transport models, these could e.g. be the grid size, grid spacing, turbulence closure scheme etc. These parameters give the users additional degrees of freedom and thus different users will typically not produce the same results applying the same complex numerical model to the same problem. Within a European project, Evaluation of Modelling Uncertainties (EMU), four experienced user groups predicted the dispersion of dense gas released around a simply shaped building. They applied the same commercially available CFD (computational fluid dynamics) code. The variability between the results of the different modellers was substantial. Differences up to an order of magnitude were reported [Schatzmann and Leitl, 2002 and references therein].

The third mentioned motivation for measurements of spatial trace gas distributions is the uncertainty of emission source strength, which can neither be evaluated by models nor simply by point measurements. These do not have to be necessarily anthropogenic sources, but also natural sources are still unknown in many fields, e.g. halogen oxides in the arctic [e.g. Simpson et al. 2007] or in maritime environments [e.g. Seitz et al. 2010], the allocation of biogenic emissions [e.g. Kesselmeier and Staudt 1999] or exploration of volcanic emission sources [e.g. Louban et al. 2009].

As emission into the atmosphere is always followed by transport, a comprehensive picture of emission source strengths can only be studied by producing a concentration map for the region of emission as well as downwind areas. Sometimes the emission source is known, but

its total emission flux is hard to measure directly under normal conditions (e.g. traffic emissions, air plane emissions at take-off, volcanic emissions).

It is clear that the chemical transformation of reactive species is extremely complex and can only be studied in the laboratory to a limited extent. If the influence of non reproducible factors like precipitation, reactions on different surfaces and the combination of the two is not negligible, the observations have to be made in the real atmosphere. For details on the chemical processes and the current state of science of the measured trace gases see the previous *Chapters 2.1 - 2.5*.

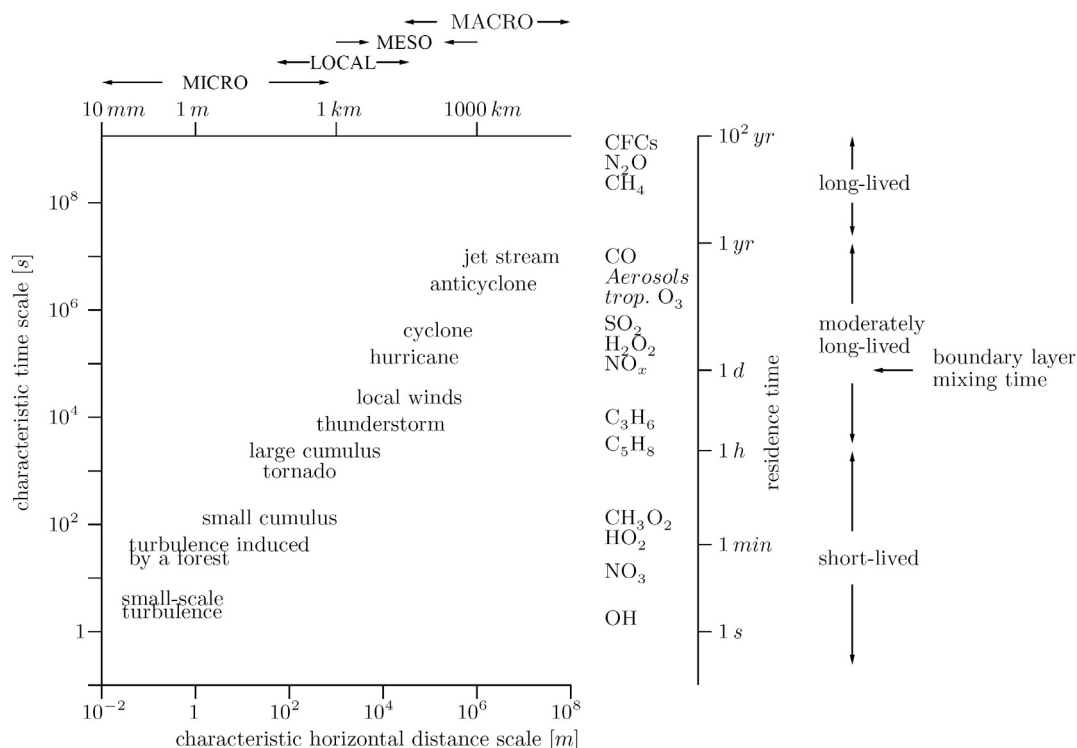


**Figure 2-15: Temporal and spatial scale of turbulent atmospheric processes and lifetime of some species in the atmosphere. Transport of the latter is characterised by spatial scales according to the given turbulent scales. Please be aware that different definitions of Micro, Local, Meso and Macro scale are used in the literature [combined from Stull, 1988; Wayne, 2000].**

The temporal evolution and spatial distribution of trace gases and aerosols are mainly influenced by the temporal and spatial scale of turbulences. Depending on the sources, sinks and lifetime of the component, different scales are of importance (Figure 2-15). Turbulent eddies can be formed thermally by the heating of the atmosphere or mechanically when air moves over a rough surface. Turbulences occur under all circumstances and on the entire time and length scale of atmospheric phenomena (typically ms to years, according cm to thousand kilometres, see Figure 2-15). These scales in time and size should be kept in mind to understand measurements of trace gas distributions.

## 2.7 Atmospheric Dynamics of the Planetary Boundary Layer

The chemical and physical processes in the lower troposphere are strongly influenced by the vertical structure of the atmospheric layers, their diurnal cycle and transport processes.

Primary and secondary trace gases close to the ground are influenced by the metrological processes in the Planetary Boundary Layer (PBL) due to transport and dilution effects. The PBL is defined as the zone of transition between the stationary air masses directly at the earth's surface and the free troposphere which is dominated by the geostrophic wind system. A more precise definition is given in Stull [1988]: "The PBL is the part of the troposphere that is directly influenced by the Earth's surface and responds to surface forcing within a timescale of about an hour or less". Over the land surface, in high pressure regions, the PBL has a well defined vertical structure. The height of the PBL typically extends from below 100 to 1000m and is influenced by various factors and changes with a diurnal cycle. The dynamic processes involve both, the transport of momentum and as well as that of trace gases. Thus characterization of wind speed and direction also specifies the mixing velocities for trace gasses. A brief discussion on the PBL and transport processes is given below. A more comprehensive description of the structure and dynamics of the lower troposphere can be found in Roedel [2000], Stull [1988] and Seinfeld and Pandis [1998].

### 2.7.1 The Structure of the Planetary Boundary Layer

Within the PBL, friction between the air masses moving with the geostrophic flow in the free troposphere increases monotonously with increasing proximity to the ground due to the surface roughness. Thus in the PBL a logarithmic wind speed profile monotonously decreasing towards the ground occurs. The steepness of the logarithmic scale is anti-correlated to the roughness of the ground. The mathematical description of a shear force is based on this friction and thus momentum is exchanged between the two layers moving with different velocities along each other. This process can be described as an exchange of impuls between both layers. If two layers of air move along each other with different velocities, the resulting shear force between the two layers is described by the turbulent and viscous stress tensor  $\tau_{ij}$ , which is defined (for x-y plane) as:

$$\tau_{xy} = -(K + \nu) \cdot \rho \cdot \frac{dv_x}{dz} \quad (\text{Eq. 2.1})$$

$K$  and  $\nu$  characterize the constants of turbulent and laminar diffusion, respectively.  $\rho$  labels the density of the air mass and  $v_x$  the velocity of the horizontal air stream (a time dependence was neglected therein). Considering this relation, the PBL is divided into three sub-layers, defined by the dominating transport regime.

The lowest layer, extending from  $10^{-3}$  to  $10^{-2}$  m above the ground, is called the laminar surface layer as this layer is dominated by laminar viscosity. Thus the transport is dominated by laminar diffusion, which is significantly less effective than turbulent diffusion in the boundary layer and the free atmosphere.

The following layer is called "Surface Layer" (SL) (sometimes also "Prandl" layer) and reaches heights from few meters to 100 m. Within this layer, the major components of the viscous stress tensor  $\tau_{ij}$  feature absolute values of about  $0.1-0.3Nm^{-2}$ . This compares to a variation of  $\tau_{ij}$  with height  $z$  of  $d\tau/dz \approx 10^{-3}Nm^{-3}$  in the same height range. Even though the

gradient  $d\tau/dz$  is at a maximum within this layer, the absolute value of  $d\tau/dz$  is still at least two orders of magnitude smaller than  $\tau_{ij}$  [Roedel, 2000]. Thus, the entire surface layer is characterised by constant turbulent fluxes of momentum, heat and trace gas distribution. During the day, this layer is thin (max. 50 m) and exhibits an overadiabatic temperature gradient (S1 in Figure 2-17). Trace gases emitted into this layer are generally rapidly mixed into the upper air.

The following layer reaches about 1000 m and is called “Mixed Layer” (ML). The absolute value of the wind vector increases to the free tropospheric wind velocities as the friction decreases constantly. The wind direction in this layer is forced by the balance of the friction, the Coriolis and the pressure gradient force. The wind direction turns constantly towards the wind direction in the free troposphere, which is dominated only by the Coriolis and the pressure gradient force. Thus the wind direction turns constantly with increasing height yielding the so called Ekman spiral (hence this layer is sometimes also called the “Ekman layer”).

The height of the PBL depends on the stability of the thermal stratification and the surface roughness. Thermal stratification is stable, when warmer and therefore less dense air masses are situated above colder and denser air masses. Labile stratification is characterised by warmer air situated below colder air. In this labile stratification, the warmer air climbs adiabatically to higher altitudes, while colder air masses descend adiabatically towards the ground until both air parcels have the same potential energy as the surrounding air (including latent and inner heat energy). Consequently, a more effective vertical mixing take place and the PBL extend to higher altitudes. For stable conditions a less effective mixing takes place and thus a lower height extension of the PBL arise.

To investigate if a temperature gradient (warmer air below colder air) would generally yield an effective mixing, the potential energy of the air parcel also has to be considered. An air parcel descending from higher altitudes transforms its potential energy to heat energy while being compressed to the increased pressure of the lower altitude (a process taking place vice versa for the ascending air parcel). To consider this, the potential temperature  $\Theta$  is introduced, which combines both the potential and the thermal energy of the observed air mass:

$$\Theta = T \cdot \left( \frac{p_0}{p} \right)^{\frac{\chi-1}{\chi}} \quad \text{with } \chi = \frac{c_p}{c_v} \quad (\text{Eq. 2.2})$$

$p_0$  indicates the normal pressure,  $T$  the actual temperature,  $c_p$  and  $c_v$  the specific heat of air at a constant pressure and volume, respectively. The virtual potential temperature  $\bar{\Theta}_v$  additionally considers the content of water vapour and liquid water in the air mass [e.g. Stull, 1988]. It is the theoretical potential temperature of dry air that would have the same density as moist air.

Virtual potential temperature profiles are nearly adiabatic in the ML (S1 in Figure 2-17) and thus thermally neutral. This means that any air parcel can be shifted adiabatically to any altitude and features always the same virtual potential energy as the surrounding air mass. An inversion at the top of the ML acts as a lid to the rising thermals, restraining the domain of turbulence.

Rough surfaces (such as tall buildings and trees) or hilly terrain cause a more effective vertical mixing and hence extend the height of the PBL (Figure 2-18). As both are present in the investigation area in Heidelberg, the expected PBL is relatively high with at least few 100 m. Flat surfaces (such as silent water or farmland) cause a thinner PBL. Very rough surfaces can inhibit the establishment of a laminar sub-layer.

Depending on thermal stratification and the surface, the PBL reaches from below 100 m height at night above flat surfaces to more than 1000 m by day and over a strongly structured surface.

### **2.7.2 Diurnal Variations of the Planetary Boundary Layer**

The diurnal cycle of solar radiation directly affects the fluxes from the surface within the lower atmosphere and thus the vertical mixing is directly influenced by solar radiation. This causes a diurnal change of stratification within the PBL, which is shown in Figure 2-16. In daytime, the PBL is assumed as a well mixed layer due to strong turbulences driven by wind shear and convection. Virtual potential temperature profiles are nearly adiabatic in the ML (S1 in Figure 2-17). At nightfall, turbulences in the PBL decrease as only wind shear remains as the driving force. The arising layer of air is often called the “residual layer” or “reservoir layer” (RL) because it initially means that the states and concentrations are the same as those of the recently decayed mixed layer. Most of the trace gas concentrations in the RL stay constant during the night because photo oxidation processes driven by solar irradiation and deposition are not affected here. The RL is neutrally stratified (S2 in Figure 2-17) and does not have direct contact with the ground. Below, a stable boundary layer of sporadic turbulence establishes. In the morning the RL can still exist for a while before it is entrained into the new ML (S4, S5 in Figure 2-17).

During clear, windless nights in the summer, the radiative cooling of the ground often causes the formation of a temperature inversion at ground level. The “stable nocturnal boundary layer” (SBL) arises as soon as the air close to the ground becomes colder than the air above (S2 in Figure 2-17), because the later has a lower density. The extension of the SBL depends on topography and increases during the night (Figure 2-16). The height typically ranges from a few ten meters to 200 m, but can also reach up to 1000 m. The inversion limits the vertical exchange of air masses and thus emitted trace gases (typically emitted close to the ground) accumulate close to the ground with little vertical dispersion. They disperse more rapidly in the horizontal and therefore lead to more spatial homogeneous concentrations. Cloud cover increases the isolation of the ground and thus the intensity of the inversion during the night is reduced and also the heating of the ground during the day. Consequently the ML exhibits slower growth on cloudy days and may even become non-turbulent or neutrally stratified.

Inversions can not only arise during cloud free nights, but also in cold winter days when solar heating is too low to warm up the surface layer. Thus, no mixing occurs and the emitted trace gases are trapped at the surface which can lead to smog events in winter. In warmer seasons the heating will be sufficient to guarantee a good mixing above an urban area.

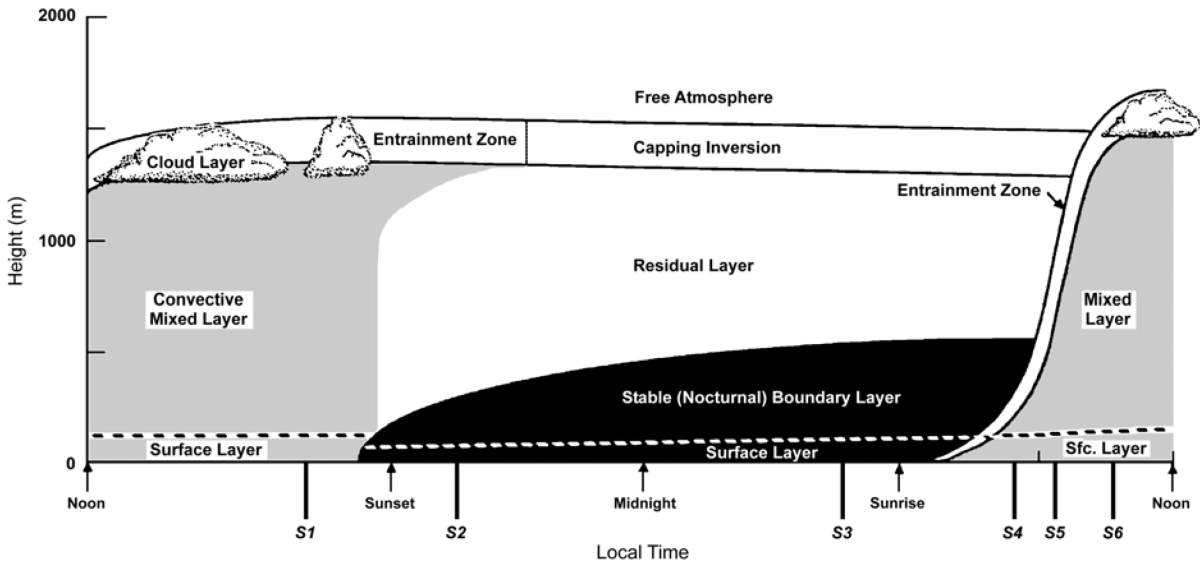


Figure 2-16: Typical diurnal development of the PBL in high pressure regions over the land during the course of the day [Stull, 1988]. Three major layers can be distinguished: a very turbulent mixed layer, a less turbulent residual layer containing former mixed-layer air and a nocturnal stable boundary layer of sporadic turbulence. Vertical structures for the marked times (S1 – S6) are displayed in Figure 2-17.

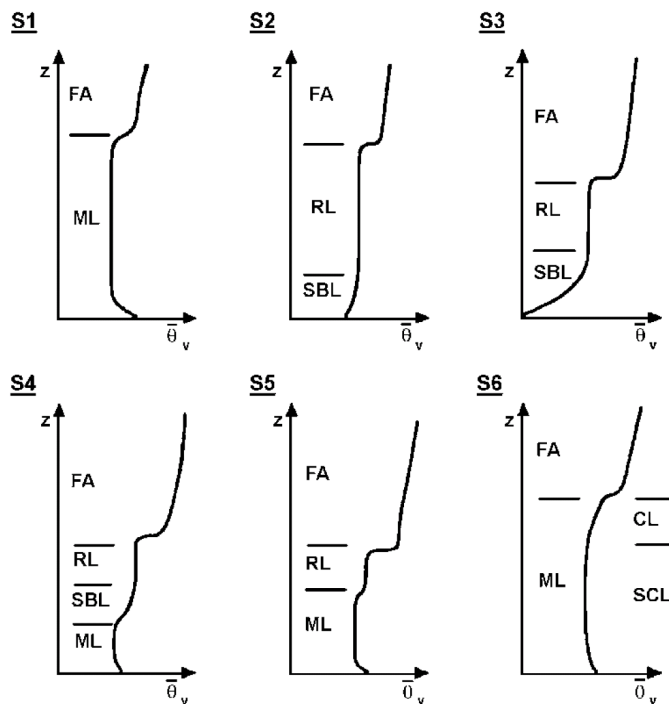


Figure 2-17: Profiles of the mean virtual potential temperature showing the boundary layer evolution during a diurnal cycle at the time markers (S1 – S6) indicated in Figure 2-16 [Stull, 1988]. The labels correspond to the sublayer names introduced in Figure 2-16.

Figure 2-17 presents the vertical profile of virtual potential temperature during a 24-hour period at specific times marked S1-S6 in Figure 2-16. For the identification of the layers of the PBL, the knowledge of virtual potential temperature profile (Figure 2-17) is usually sufficient. This graph directly indicates the dependency of the mixing efficiency on the potential temperature and thus the type of layers. Layers that feature constant virtual potential temperatures over their height range are generally well-mixed. Contrastingly, mixing is hampered when the potential temperatures increase with height.

The stratification of the PBL does not only change within the day but is also influenced by local topography and large-scale atmospheric phenomena such as cyclones. This finally requires the knowledge of the 3-D wind field and the heat flux in the PBL (both at different elevations) for an in-depth analysis of transport mechanisms. However, the assumption of a neutrally stratified PBL is justified to gain an impression of the diffusion constants if detailed meteorological information is not available.

### 2.7.3 Transport Processes in the Planetary Boundary Layer

Since transport processes in the atmosphere apply to transport of impulse and trace gasses, the laws governing the changes of wind speed and direction also specify the mixing velocities for trace gasses. Assuming thermally neutral stratification, and turbulent mixing surpassing laminar mixing, which is well justified in the surface layers, the wind profile may be calculated based on the stress tensor  $\tau_{ij}$  by introducing the friction velocity  $u^*$ :

$$\tau_{xz} = -\rho \cdot (u^*)^2 \quad (\text{Eq. 2.3})$$

Using this definition of the friction velocity, the vertical wind profile  $dv_z/dz$  in a height  $z$  over the ground becomes:

$$\frac{dv_z}{dz} = \frac{1}{\kappa} \cdot \frac{u^*}{z} \quad (\text{Eq. 2.4})$$

with the Karman-constant  $\kappa \approx 0.4$ . In combination with Eq. 2.1 and Eq. 2.3 this yields the turbulent diffusion constant  $K$ :

$$K(z) = u^* \cdot z \cdot \kappa \quad (\text{Eq. 2.5})$$

As friction velocity is almost constant in the surface layer (see above),  $K$  only depends on the height over ground  $z$ . Thus, the flux  $j_i(z, t)$  of both momentums as well as trace gas transport of a species  $i$ , can be described by diffusive transport according to Fick's law:

$$j_i(z, t) = -K(z, t) \cdot \frac{\partial c_i(z, t)}{\partial z} \quad (\text{Eq. 2.6})$$

Based on this relation for vertical transport, the vertical profile of an atmospheric compound can be computed. The difference between the concentrations in two different heights  $z_1 > z_2$  is given by:

$$c(z_j) - c(z_i) = \int_{z_i}^{z_j} \frac{dc(z)}{dz} \cdot dz \quad (\text{Eq. 2.7})$$

Implementing Eq. 2.5 and Eq. 2.6 into this relation yields the logarithmic profile for atmospheric trace gasses:

$$c(z_j) - c(z_i) = -J \cdot \int_{z_i}^{z_j} \frac{1}{K(z)} \cdot dz = -\frac{J}{u^* \cdot \kappa} \cdot \int_{z_i}^{z_j} \frac{1}{z} \cdot dz = -\frac{J}{u^* \cdot \kappa} \cdot \ln\left(\frac{z_j}{z_i}\right) \quad (\text{Eq. 2.8})$$

To obtain typical mixing times for atmospheric trace gasses, the transfer resistance  $R_{ij}$  is defined, characterising the transport time between the heights  $i$  and  $j$ :

$$R_{1,2} = \frac{c(z_j) - c(z_i)}{J} = -\frac{1}{u^* \cdot \kappa} \cdot \ln\left(\frac{z_j}{z_i}\right) \quad (\text{Eq. 2.9})$$

Also the mean flux of trace gasses between two layers can be derived from measured concentration gradients from Eq. 2.8:

$$J = -\frac{c(z_j) - c(z_i)}{\ln(z_j/z_i)} \cdot u^* \cdot \kappa \quad (\text{Eq. 2.10})$$

To solve both equations, the friction or shear velocity is needed. It can be separated between a neutral stratification and a non-neutral stratification. For the neutral stratification, the approximation that the friction velocity is constant with increasing height over ground can be applied [Roedel, 2000] and Eq. 2.4 can be integrated.

$$u^* = v_r \cdot \frac{\kappa}{\ln(z_r/z_0)} \quad (\text{Eq. 2.11})$$

In this approximation, a typical wind speed  $v_r$  at a certain reference height  $h_r$  is required to be measured. The surface roughness is considered by the factor  $z_0$  as the zero level for advection. The combination with equation Eq. 2.3 finally directly yields the turbulent diffusion constant:

$$K(z) = \frac{v_r \cdot \kappa^2}{\ln(z_r/z_0)} \cdot z \quad (\text{Eq. 2.12})$$

This constant increases with height over ground due to the larger eddies which are more effective for the mixing of the PBL and also increase with surface roughness.

To calculate exemplary typical turbulent diffusion coefficients, for a neutral layering, the laminar sublayer can be neglected; an approximation that is valid for the rough surfaces found in cities [Roedel, 2000]. With a wind speed of  $v_r = 3 \text{ m s}^{-1}$  at a height of  $z_r = 30 \text{ m}$  and a surface roughness parameter  $z_0 = 0.5 \text{ m}$  this yields  $K(z) = 0.141 \text{ m}^2 \text{ s}^{-1} \cdot z$ . This value is substantially higher than the laminar diffusion constant [Stull, 1988]. It is evident that turbulent mixing under neutral conditions is very effective as trace gasses may be transported from the lower to the upper border of the layers in a timescale of some minutes.

For non-neutral stratification however, it is absolutely necessary to measure the vertical profiles of wind speed and heat flux to obtain friction velocity. We refer to Roedel [2000] for the retrieval of the turbulent exchange coefficient in this case.

The unmodified  $K(z)$  models are restricted to inert or slowly reacting gases because the effect of chemistry on the vertical flux of a trace gas is not considered. For most trace gases a

modified  $K(z)$  model has to be applied to the analysis, which considers the effects of chemistry and physics of the lower troposphere, as vertical transport of a gas is no longer only a function of its concentration profile, but also of the concentration profiles of other gases. Additionally to the vertical, also horizontal transport (advection) and diffusion of air masses and trace gases occurs. It is driven by the horizontal wind field. For homogeneous distributed emissions, the horizontal diffusion cancels out and only the vertical component has to be considered. For non homogeneous sources like a power plant or even a street, the horizontal diffusion will significantly lower the emitted trace gas concentration especially if strong wind is present. Thus the distribution of air masses and trace gases is a combination of vertical and horizontal diffusion and becomes rather complicated (Figure 2-18).

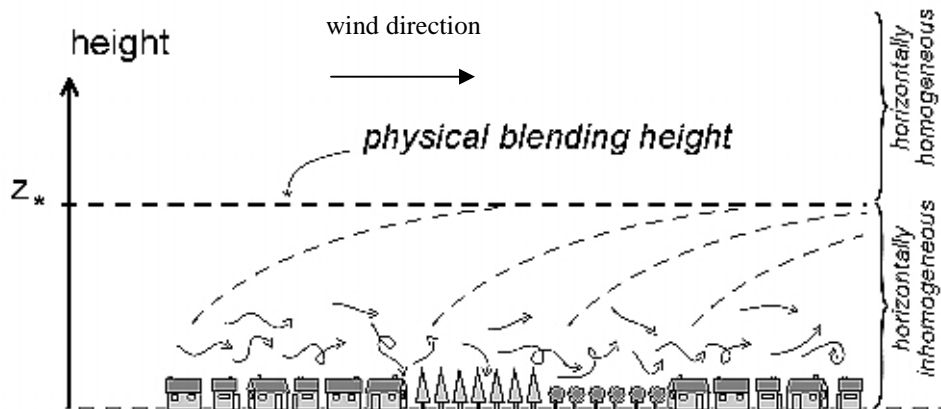


**Figure 2-18: Mixing and diffusion of trace gases in an urban area due to local turbulences and wind [adapted from Schmid, 1997].**

It can be described by the general equation for atmospheric compounds:

$$\frac{\partial C}{\partial t} = \frac{1}{h_{PBL}} [\Phi_P + \Phi_S] - K(z) \cdot \frac{\partial C}{\partial z} + \sum_i P_i - \sum_j L_j - L_s \left[ \frac{1}{h_{PBL}}; K(z) \cdot \frac{\partial C}{\partial z} \right] + Adv \quad (\text{Eq. 2.13})$$

with:

- $C$  mixing ratio near the ground
- $h_{PBL}$  height of the PBL
- $\Phi_P$  primary emission flux
- $\Phi_S$  surface emission flux
- $K(z)$  vertical mass exchange due to eddy diffusion and convection
- $P_i$  chemical production rate from the  $i^{\text{th}}$  pathway
- $L_j$  chemical removal rate from the  $j^{\text{th}}$  pathway
- $L_s$  removal rate from deposition
- $Adv$  advection term forced by horizontal transport

Unfortunately, most of the terms presented by Eq. 2.13 are unknown or only poorly characterized in atmospheric field study campaigns. Especially the vertical diffusion coefficient  $K(z)$  and the boundary layer height have to be measured or at least estimated with sufficient accuracy to characterize the impact of primary and surface emissions as well as chemical production and the removal of a trace gas in the PBL. Thus, the differential equation Eq. 2.13 will generally not be solvable. Tomographic measurements of the horizontal trace

gas distributions give the possibility to quantify the unknown advection parameter. For a continuous emission source of a measured trace gas, the advection can directly be observed. Only the special resolution limits the accuracy. For a non continuous source (single plume emission) additionally the temporal resolution should be sufficient to observe the advection at a typical wind speed. For an urban area of  $4 \times 4 \text{ km}^2$  and a typical wind speed of 3 m/s this corresponds to a minimum temporal resolution of  $\sim 11$  minutes to measure a passing air mass at least twice. Unfortunately such a high temporal resolution could not be achieved with the applied tomographic instrumentation (Chapter 5 and 6). Advections of single plumes can thus only be estimated for much lower wind speeds.

However, this still requires the analytic solution of the equation Eq. 2.13 as the vertical diffusion parameter and the boundary layer height are unknown. This information would be needed to characterise the impact of primary and surface emissions as well as chemical production and removal and thus the lifetime of a trace gas. The micrometeorological parameters with respect to an inert tracer gas can be obtained with the measurement of some tracer data (e.g. radon activity). Unfortunately no such analysis could be applied for the presented tomographic measurements in *Chapter 8*.

Alternatively the advection of a relative inert gas can be used to gain information of the unknown parameters and the distribution can be compared to the gas of interest. As  $\text{SO}_2$  is in first approximation an inert gas, its distribution and thus the advection can be used to analyse chemical process of chemical reactive gases like  $\text{NO}_2$ . To apply this method, both trace gases should be emitted by the same source and background concentrations have to be comparable low. This is a hard to achieve requirement as in urban areas an unknown number of emission sources exists. For the observed distributions the arising  $\text{SO}_2$  events did only feature a low increase in  $\text{NO}_2$ , too low in comparison to the background concentration. Thus transport could be studied for  $\text{SO}_2$  (*Chapter 8.5.1*), but not for the simultaneous arising  $\text{NO}_2$  plume.

### 3 Differential Optical Absorption Spectroscopy (DOAS)

With growing interest in air quality in the second half of the 20<sup>th</sup> century different measurement techniques were developed to analyse their components and concentrations. In the late 70's Platt et al. [1979] introduced the Differential Optical Absorption Spectroscopy (DOAS) for trace gas measurements in the atmosphere. The basic principle is that light typically in the UV and visible wavelength range, passes through the atmosphere where it undergoes absorption processes. The light is collected by a telescope and recorded by a spectrograph-detector system in order to analyse it according to the Lambert-Beer law of light extinction. Broad-band extinction and narrow-band absorption structures appear in the measured spectra. The DOAS method uses only the narrow molecular absorption bands to identify the trace gases as they are characteristic for each species. The absorption strength is used to determine the trace gas concentration. Several trace gases which are of particular importance for atmospheric chemistry can be observed down to ppt levels (e.g. Figure 3-4). For an overview see Platt [1994] and Platt and Stutz [2008]. The compounds NO<sub>2</sub>, SO<sub>2</sub>, O<sub>3</sub>, HONO and HCHO which absorb in the UV spectral range between 280 nm and 360 nm are of special interest for this thesis.

The advantage of spectroscopic methods is that they are non-invasive, in the way of remote sensing. No reactions can occur on surfaces or inlets. This means that the concentrations are not changed and the chemical processes are not influenced during the measurement, what is especially interesting for the determination of reactive compounds. Measurement techniques, where a separated air sample is analysed, are not very precise for such compounds. Additionally the DOAS technique allows simultaneous measurements of several trace gases. Whereas in-situ monitors, typically used for air monitoring worldwide, can only measure one single species with each instrument. The DOAS measurements are made in real time with a relative high time resolution (seconds to minutes). Thus, they are ideal for trace gas monitoring. Another important advantage is that the instrument itself is calibration free. If the absorption structure of a trace gas is once measured in a lab, it can be used for all DOAS instruments. Any instrument degradation does not influence the measured concentration, as the absorption of the molecule along a defined absorption path remains the same. Regular calibrations are therefore redundant.

Nowadays, a large variety of different DOAS instruments exist for different applications. An overview of the DOAS technique and several examples are given in Platt and Stutz [2008] and in *Chapter 3.10*. In general, two groups can be distinguished: depending on the used light source they are called either active or passive systems. Passive systems use natural light sources, for example the sun, the moon or some individual stars. In contrast to active DOAS, passive methods suffer the disadvantage that they rely on scattered sunlight and thus measurements are only possible during daylight. The interpretation of passive measurements requires the accurate modelling of the atmospheric radiative transfer and the use of inversion algorithms to determine the effective light path and thus to retrieve the trace gas concentrations. Therefore, most passive instruments are not ideal for urban trace gas

monitoring where pollutants should be monitored 24 hours with especially a good accuracy close to street level.

For accurate measurements in the boundary layer, active DOAS systems are very popular. They use the light in the visible or ultra violet (UV) spectral range emitted from an artificial light source such as a laser [e.g. Hübler et. al, 1984], LED [Kern, 2005; Sihler et al., 2009], halogen lamp or like mostly used and also applied in this work a xenon arc lamp. The emitted light passes the atmosphere along a well defined path where it undergoes absorption processes. Therefore, in comparison to passive systems, radiative transfer is straight forward. The light is collected by a telescope and recorded by a spectrograph-detector system.

An advantage for many applications is the averaging of the trace gas concentration along the absorption measurement path of a few hundred meters to several kilometres. The determined concentrations are not effected by very local fluctuations. For an area of several hundred meters the observed concentrations are therefore much more representative than an in-situ measurement. However, in-situ monitors allow determining differences in the concentrations at different locations with several independent stations or mobile platforms. Both methods are extensive and expensive, thus they are only rarely applied. A new method to determine such local trace gas variations is the tomographic LP-DOAS approach presented in this thesis. It requires the measurement of average trace gas distributions along several light paths by LP-DOAS. Therefore, this optical method will be discussed in detail in this chapter. Measuring along several independent light paths and using tomographic inversion techniques trace gas distributions can be reconstructed. This method is described in *Chapter 4*. In the used setup the concentrations along 20 light paths could be determined. The instruments and the measurement setup of Heidelberg will be given in *Chapter 5* and *6*, respectively.

### ***3.1 Absorption Spectroscopy***

The principle of absorption spectroscopy is based on the fact that light passing a medium is reduced in its intensity by two effects. First, molecules can enter excited states when irradiated by electromagnetic radiation. There exist electronic, vibrational and rotational excited states, and molecules absorb radiation energy yielding an excited quantum-mechanical state. For different molecules these excited states have different energy levels and therefore the absorption at distinct wavelengths is unique for each molecule. Second, scattering processes reduce the light intensity while passing through a medium. Scattering processes are distinguished between Rayleigh and Mie. Rayleigh scattering occurs on molecules and particles smaller than the light's wavelength (e.g. air molecules and small aerosol particles with spatial dimensions smaller than 0.1  $\mu\text{m}$ ) and is described by the Rayleigh scattering coefficient  $\epsilon_R$ . Scattering on particles larger than the wavelength (e.g. aerosol particles and cloud droplets) is described by the Mie scattering coefficient  $\epsilon_M$ . Both, Rayleigh and Mie scattering, depend on the wavelength  $\lambda$ . Rayleigh scattering is strongly increasing with smaller wavelength with the dependency  $\epsilon_R \propto \lambda^{-4}$  [Hulst, 1957]. Mie scattering has a smaller dependency with  $\epsilon_M \propto \lambda^{-1.3}$  [Hulst, 1957]. Typical Mie and Rayleigh scattering coefficients are given in Table 3-1.

Wavelength $\lambda$ [nm]	Rayleigh scattering cross section $\sigma_R$ [10 <sup>-26</sup> cm <sup>2</sup> ]	Rayleigh scattering coefficient $\epsilon_R$ [10 <sup>-5</sup> cm <sup>-1</sup> ] (at 1 atm, 20°C)	Typical Mie scattering coefficient $\epsilon_M$ [10 <sup>-5</sup> cm <sup>-1</sup> ]	Rayleigh extinction length [km]	Total extinction length $L_E$ [km]	Visibility range* $L_V$ (C=0.02) [km]
300	5.653	15.524	5.8	7.39	5.1	-
400	1.672	4.013	4	24.9	12.5	49
500	0.672	1.612	3	62.1	21.7	85
600	0.317	0.760	2.4	131.6	31.6	123
700	0.170	0.408	1.9	245.4	43.3	169

**Table 3-1: Typical Mie scattering coefficients and calculated Rayleigh scattering coefficients, corresponding extinction lengths and visibility range for a non polluted environment [adapted from Platt and Stutz, 2008]. \* Visibility can be approximated from the contrast of objects and results in approximately 4 times  $L_E$ .**

It can be found that especially Rayleigh scattering strongly increases towards UV. Thus, the total extinction length reduces to about 5 km. This results in low intensities for LP-DOAS measurements along such long absorption paths. The longest applied light path in this thesis was in total 8.4 km for the wavelength range of 285 to 365 nm. More details on Mie and Rayleigh scattering are given in Platt and Stutz [2008] and Roedel [2000].

Although Rayleigh scattering of a molecule is not an absorption process, light scattered out of the light path while passing a medium will normally not reach the detector. Thus the Rayleigh scattering of a molecule can be treated as an absorption process with the scattering cross section  $\sigma_R(\lambda)$  in cm<sup>2</sup>, which is included in the specific absorption cross section  $\sigma(\lambda)$  of a molecule. The absorption of a molecule in an aerosol free medium can be described by the following Lambert-Beer law:

$$dI(\lambda) = I(\lambda) \cdot c(l) \cdot \sigma(\lambda) \cdot dl \quad (\text{Eq. 3.1})$$

The absorption  $dI$  of light is proportional to the length  $dl$  of the light path through the absorbing medium, to the concentration  $c$  of the absorber and to the specific absorption cross section  $\sigma$ .

Considering that different molecules  $i$  with different concentrations  $c_i$  have different absorption cross sections  $\sigma_i$  due to different excited states and including Rayleigh and Mie scattering processes the integration of Eq. 3.1 yields:

$$I(\lambda, L) = I_0(\lambda) \cdot \exp\left(-\int_0^L \left(\epsilon_R(\lambda, l) + \epsilon_M(\lambda, l) + \sum_i \sigma_i(\lambda, p, T) \cdot c_i(l)\right) dl\right) \quad (\text{Eq. 3.2})$$

with  $I(\lambda, L)$ : light intensity after passing through the atmosphere with distance  $L$   
 $I_0(\lambda)$ : light intensity before entering the medium

$\lambda$ :	wavelength
$\varepsilon_R(\lambda, l)$ :	Rayleigh scattering coefficient
$\varepsilon_M(\lambda, l)$ :	Mie scattering coefficient
$\sigma_i(\lambda, p, T)$ :	absorption cross section of the absorber $i$
$c_i(l)$ :	concentration of the absorber $i$
$p$ :	pressure
$T$ :	temperature
$L$ :	total light path length

The absorption of a trace gas  $i$  is characterised by its absorption cross sections  $\sigma_i$ , which depends on the wavelength  $\lambda$ , the temperature  $T$  and the pressure  $p$ . It is quantified by the integrated concentration  $c_i(L)$  of the absorber along the optical path  $L$ . This is also referred to as the column density,  $a_i$ :

$$a_i = \int_0^L c_i(l) dl = \bar{c}_i \cdot L \quad (\text{Eq. 3.3})$$

The measured absorption spectrum is composed of a unique combination of the individual trace gas absorption cross sections. The compounds are identified by their individual absorption cross section (Figure 3-4).

The Lambert-Beer law is the basis for absorption spectroscopy and can directly be applied to chemical and physical studies where scattering is known or can be neglected and the initial intensity  $I_0(\lambda)$  is measurable. This is for example the case for some laboratory studies or instruments with aerosol filters and direct  $I_0$  measurements.

But this classical approach cannot directly be applied to atmospheric measurements for mainly four reasons:

1. Broad-band absorptions arise from continuum bands of the absorbers and from aerosol scattering. It is nearly impossible to distinguish between these two processes. The continuum bands of the individual absorbers feature no characteristic structure, distinction between them is impossible.
2. Stray light from other sources than the initial light source scattered into the light path presents another problem, as it is not considered in the spectrum  $I_0(\lambda)$ . In the case of active LP-DOAS measurements, the main source is typically sunlight scattered into the light path.
3. Typically used artificial light sources for active DOAS (like LP-DOAS) do not only feature a broad-band thermal spectrum defined by Planck's law, but also have spectral structures of a similar bandwidth as trace gas absorption structures. Especially Xenon arc lamps, which are most common, show characteristic emission lines that change both in intensity and spectral shape during the lamp lifetime. Also LED's display often characteristic structures like etalon effects which can interfere with absorption structures [Kern et al., 2006, Sihler et al., 2009].
4. The intensity  $I_0(\lambda)$  which would be received from the light source in the absence of

any atmospheric absorption is difficult to determine. It would involve removing the air from the absorption path and an absolute stable optical system over several kilometres. As turbulences in the air change slightly the light path, no stable intensity can be achieved.

In conclusion, these problems make absolute spectroscopy impossible in the atmosphere. However, DOAS presents a solution to these difficulties.

Next to these basic problems also other points should be considered. Neither the spectral response from spectrograph and detector is ever perfect nor the sensitivity of the detector, which is typically wavelength dependant, and need to be corrected. Photon statistics and detector noise add up to a noise spectrum which is superimposed to the measured spectrum and limit the sensitivity of the measurement and therefore the minimum detectable trace gas concentration (*Chapter 3.6*).

### 3.2 The Principle of DOAS

The key to overcome the problem that broad-band absorption caused by scattering processes in the atmosphere cannot be quantified, the DOAS technique divides the trace gas absorption cross sections into two parts.

$$\sigma(\lambda) = \sigma^b(\lambda) + \sigma'(\lambda) \quad (\text{Eq. 3.4})$$

$\sigma^b$  characterises the broad-band scattering and absorption, while the differential absorption cross section  $\sigma'$  describes the characteristic narrow-band absorption structures of the individual trace gases, varying rapidly with  $\lambda$ . The definition of the threshold between broad-band and narrow-band depends on the width of the absorption bands to be detected and the appearance of other absorption and emission structures, which should be removed from the spectrum.

Using this principle, the exponent in the Lambert-Beer law is separated into two parts; one varying “slowly” with the wavelength and incorporating broad-band absorption and scattering, and the other part featuring a strong dependency on the wavelength due to narrow-band trace gas absorption.

The Lambert-Beer law can now be written as:

$$I(\lambda) = I_0(\lambda) \cdot \exp\left(-\int_0^L \left(\varepsilon_R(\lambda, l) + \varepsilon_M(\lambda, l) + \sum_i \sigma_i^b(\lambda) \cdot c_i(l)\right) dl\right) \cdot \exp\left(-\int_0^L \left(\sum_i \sigma_i'(\lambda) \cdot c_i(l)\right) dl\right) \quad (\text{Eq. 3.5})$$

For the sake of simplicity, the temperature and pressure dependency of the absorption cross sections are omitted, as they play a subordinate role for most absorbers in the boundary layer. The broad-band part of Eq. 3.5 is then merged with the initial light intensity  $I_0(\lambda)$  to form the differential baseline intensity  $I_0'(\lambda)$  simplifying the previous equation to:

$$I_0'(\lambda) = I_0(\lambda) \cdot \exp\left(-\int_0^L \left(\varepsilon_R(\lambda, l) + \varepsilon_M(\lambda, l) + \sum_i \sigma_i^b(\lambda, p, T) \cdot c_i(l)\right) dl\right) \quad (\text{Eq. 3.6})$$

Now also the Lambert Beer law can be simplified to:

$$D'(\lambda) = \ln\left(\frac{I(\lambda)}{I_0'(\lambda)}\right) = -\int_0^L \left(\sum_i \sigma_i'(\lambda) \cdot c_i(l)\right) dl \quad (\text{Eq. 3.7})$$

$D'(\lambda)$  refers to the differential optical density.  $I_0'(\lambda)$  can be obtained in several different ways. In most cases,  $I_0(\lambda)$  is simply used, as it does not differ from  $I_0'(\lambda)$  in narrow-band structure. The differences are all of broad-band nature, thus this will change the absolute value of the quotient but leave the relative depth of narrow-band absorption structures unchanged. In this case additionally the broad-band structures from absorption and scattering have to be removed by dividing the spectrum by a fitted polynomial of appropriate degree and/or applying a high-pass filter to remove all broad-band structures [Stutz and Platt, 1996]. The differential absorption cross sections  $\sigma_i'$ , for all trace gases that feature characteristic structures in the observed wavelength range, have to be computed by applying the same filter algorithm.

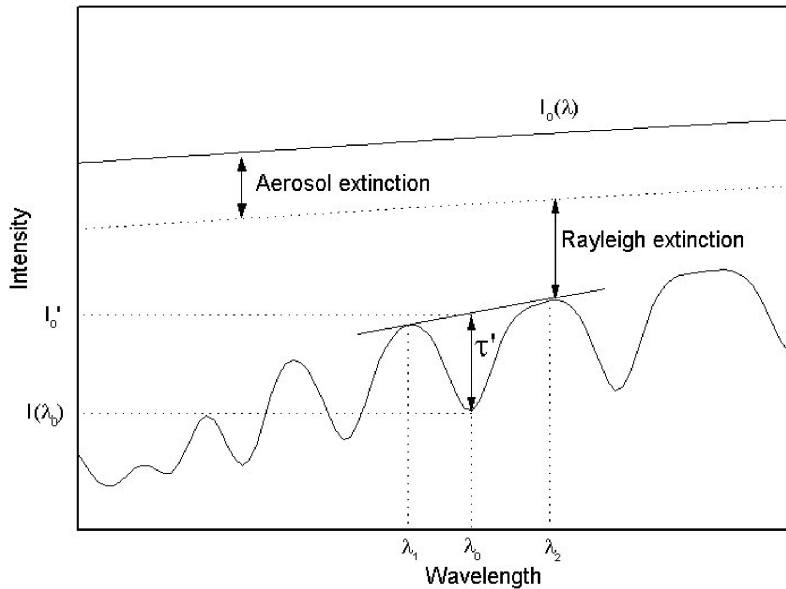


**Figure 3-1: Segmentation of light extinction in the atmosphere. Mie (aerosol) scattering and Rayleigh scattering show broad-band extinction only, while trace gas absorption causes narrow- and broad-band extinction.**

In some cases,  $I_0'(\lambda)$  is also derived from the measured spectrum  $I(\lambda)$  by applying a low-pass filter (e.g. triangular smoothing or Savitzky-Golay smoothing), or by interpolating across the tops of the narrow-band structures in the spectrum, as suggested in Figure 3-1.

The only remaining missing parameter besides the individual concentrations  $c_i$  is the total path length  $L$ . In the case of LP-DOAS, this can accurately be measured by a laser range finder or a GPS. If passive MAX-DOAS measurements are applied, a radiation transport model is necessary to determine the average path of a photon before entering the instrument. The evaluation algorithm can now allocate the different absorption structures and match them

to the corresponding trace gases.

### 3.3 Mathematical Description of a DOAS Spectrum

To obtain atmospheric trace gas concentrations from measured atmospheric absorption spectra, specific instrumental spectral structures, e.g. discretisation of the spectrum during recording, have to be considered within the retrieval process. These corrections depend on the specific configuration of the DOAS instrument and the characteristic of its components. This section follows the discussion by Stutz and Platt [1996].

The principle of a LP-DOAS system for the detection of tropospheric trace gases is sketched in Figure 3-2. The light from a broad-band source with the initial intensity  $I_0(\lambda)$  is transmitted through the atmosphere along a light path  $L$ . Extinction and absorption processes reduce the light intensity as described by Eq. 3.2. At the end of the light path, the transmitted light is spectrally analysed in a spectrograph detector system. In the example of Figure 3-2, for simplicity formaldehyde is assumed to be the only absorber along the light path. Inset (a) describes the spectrum before it enters the spectrograph. At this point, the spectrum is described by an extension of Eq. 3.2, with photon noise  $N(\lambda)$ , which is directly dependent on  $I(\lambda)$ , and a stray light signal  $M(\lambda)$ .

$$I(\lambda, L) = I_0(\lambda) \cdot \exp\left(-\int_0^L \left(\varepsilon_R(\lambda, l) + \varepsilon_M(\lambda, l) + \sum_i \sigma_i(\lambda, p, T) \cdot c_i(l)\right) dl\right) + N(\lambda) + M(\lambda) \quad (\text{Eq. 3.8})$$

The spectrograph and the detector influence the recorded spectrum. Due to the limited resolution of the spectrograph, the resolution degrades to a value of  $\Delta\lambda/\lambda$ , mainly defined by the width of the entrance slit and by the grooves per millimetre on the grating. The spectral resolution for DOAS applications is usually in the range of a few tenths of a nanometre (here approximately 0.4 nm Full Width Half Maximum (FWHM), with the used spectrographs of this thesis approximately 0.5 nm FWHM). Due to this limited resolution the shape of spectrum  $I(\lambda)$  changes (inset (b)). Thus, the natural line widths of the spectrum are not resolved and the spectrum at the detector no longer feature the very narrow-band spectral structures. This process is described mathematically by a convolution of the initial spectrum  $I(\lambda)$  with the instrument function  $H$  to obtain  $I^*(\lambda)$  [Stutz and Platt, 1996].

$$I^*(\lambda) = I(\lambda) * H = \int I(\lambda - \lambda') \cdot H(\lambda') \cdot d\lambda' \quad (\text{Eq. 3.9})$$

Inset (b) of Figure 3-2 represents the spectrum  $I^*(\lambda)$  as it arrives at the detector. Typically,  $H$  is determined by measuring an emission line of an elemental line emission lamp like a mercury lamp.

In a typical DOAS evaluation, high-resolution trace gas absorption cross sections are used as reference spectra and modelled to the measured optical density. These cross sections are measured with high resolution under controlled laboratory conditions. In order to use these references in the evaluation process, they need to be convoluted with the instrument function, as their resolution must be reduced in the same way to that of the DOAS spectrograph.

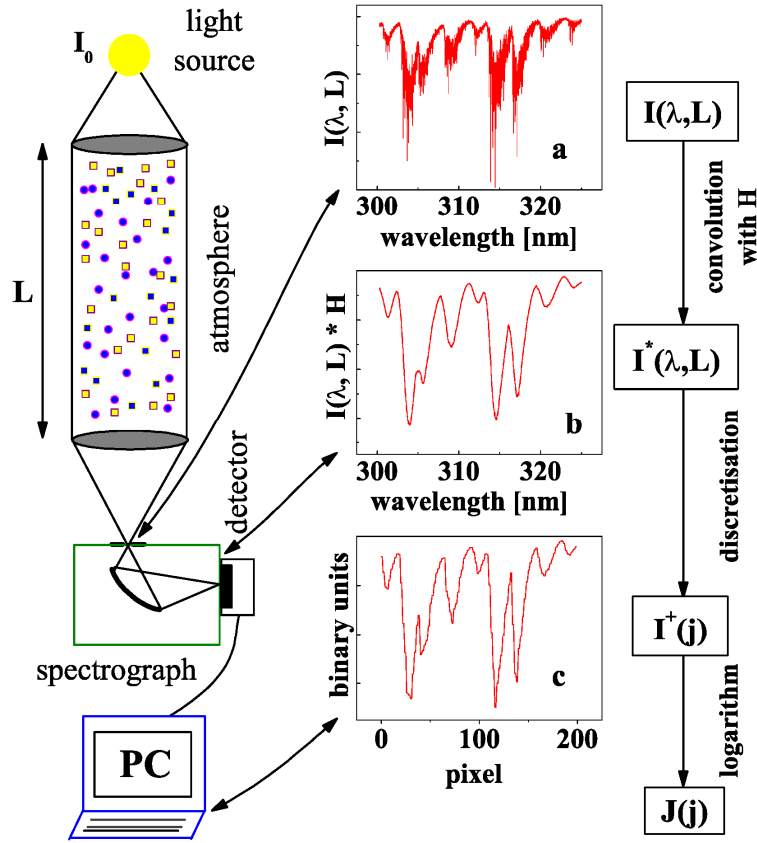


Figure 3-2: Schematic of the basic components and spectral processing steps of an Active Long Path DOAS system. The collimated light undergoes absorption processes on its way through the observed air mass. (a) An example spectrum of this light entering the spectrograph is shown, assuming only formaldehyde (HCHO) to be present in the observed air mass. The absorption spectrum shows the ro-vibronic structure of the HCHO absorption bands. (b) The same spectrum convoluted by the spectrograph’s instrumental function reaches the detector. (c) The spectrum is mapped to discrete pixels by the detector. This spectrum is then stored to the hard-disk of a PC and can be analysed numerically (adapted from Stutz and Platt [1996]).

$$S_i = \sigma_i * H = \int \sigma(\lambda - \lambda') \cdot H(\lambda') \cdot d\lambda' \quad (\text{Eq. 3.10})$$

The detector maps the spectrum of typically some tenth of nanometres onto a discrete number of pixels numbered with  $j$ . Each pixel integrates the intensity in the wavelength interval from  $\lambda(j-1/2)$  to  $\lambda(j+1/2)$ . This discretisation can be expressed by the equation:

$$I^+(j) = \int_{\lambda(j-1/2)}^{\lambda(j+1/2)} I^*(\lambda', L) d\lambda' \quad (\text{Eq. 3.11})$$

Inset (c) in Figure 3-2 represents the spectrum after discrete scanning of the detector unit, digitised and sent to the computer.

In the first order approximation, the wavelength to pixel mapping function  $\Gamma_j$  is a linear function assigning each wavelength to a specific pixel. However, closer examinations show that other orders also contribute to the wavelength to pixel mapping. For this reason, the dispersion function may be described by a polynomial of the order  $q$ .

$$\Gamma_l : \lambda(j) = \sum_{k=0}^q \gamma_k \cdot j^k \quad (\text{Eq. 3.12})$$

The parameter vector  $\gamma_k$  determines the assignment of the pixel  $j$  to the wavelength  $\lambda(j)$ . For most spectrographs a second order polynomial is sufficient to describe the wavelength to pixel mapping.  $\gamma_0$  characterises the placement of the spectrum on the detector.  $\gamma_1$  characterises the linear slope of the dispersion relation. The square and higher dependency of the dispersion relation characterised by  $\gamma_2$  and higher is due to aberration of the spectrograph optic. A spectral shift of the spectrum corresponds to a variation of the parameter  $\gamma_0$  and  $\gamma_1$ , a linear squeeze or stretch to a change of  $\gamma_2$ . In DOAS measurements the change appear mainly as a consequence of varying measurement conditions since the optic is very sensitive for temperature changes. Variations of air pressure, like for airborne measurements, also shift the spectrum on the detector due to a change in the index of refraction of air [e.g. Pfeilsticker and Platt, 1994]. To reduce the effect of temperature changes the spectrograph is typically thermally isolated and temperature stabilized. Nevertheless small changes in the temperature and pressure could arise and should be taken into account in the retrieval process (see *Chapter 7.1*). Due to the physical properties of a spectrograph, the dispersion function  $\Gamma_l$  is a strictly monotonous function in the definition interval, and thus can be inverted, which is important to correct for this shift and squeeze.

The electronics that detect, amplify and digitise the signal also affect the spectrum that is recorded. The quantum yield of each detector pixel is not equal over the whole detector chip and also the dark current and electronic noise can vary. The variation in spectral sensitivity of the detector and transmissivity of the spectrograph is represented by the multiplicative function  $A^+(j)$ .

Analogue to Eq. 3.11 we can also define discrete convoluted absorption cross sections  $S_i^+(j)$ , discrete intensity spectra of the lamp  $I_0^+(j)$ , discrete Rayleigh and Mie scattering summarised as  $R^+(j)$ , discrete stray light  $M^+(j)$  and the term  $N^+(j)$  contributed to detector noise, photon statistic, dark current noise and electronic offset noise which can not be separated from a single spectrum. This leads to the signal measured by the detector:

$$\begin{aligned} I^+(j) &= \left( I_0^+(j) \cdot \exp \left( -R^+(j) - B^+(j) - \sum_i S_i^+(j) \cdot \int_0^L c_i(l) dl \right) + N^+(j) + M^+(j) \right) \cdot A^+(j) \\ &= \left( I_0^{+'}(j) \cdot \exp \left( -\sum_i S_i^{+'}(j) \cdot a_i \right) + N^{+'}(j) + M^{+'}(j) \right) \cdot A^{+'}(j) \end{aligned} \quad (\text{Eq. 3.13})$$

$$\text{with} \quad a_i = \int_0^L c_i(l) dl \quad (\text{Eq. 3.14})$$

The variable  $a_i$  is referred to the column density and is introduced to remove the integral of the concentration over the entire light path, as it cannot be resolved in the evaluation.  $a_i$  is actually measured by the DOAS method. It represents the average concentration along the light path (Eq. 3.3). The variable  $I_0^{+'}$  combines all broad-band absorption  $S_i^{b+}$ , scattering processes  $R^+$ , broad-band absorptions  $B^+$ , the lamp reference spectrum  $I_0^+$  and all the

instrument specific broad-band spectral structures as described in *Chapter 3.2*. This can be achieved by applying a high-pass filter algorithm.

The sum in Eq. 3.13 represents the linear combination of several different absorbers in the atmospheric air mass. In practise, the number of identifiable trace gases with DOAS is limited to those with absorption structures sufficiently strong in the observed wavelength range. As the strength of the absorption varies for different wavelengths for each absorber, only those with absorption structures in the chosen wavelength range should be included in the evaluation process. In the used wavelength range of this thesis the trace gases NO<sub>2</sub>, SO<sub>2</sub>, O<sub>3</sub>, HONO and HCHO display strong absorption structures and were included in the retrieval process (Figure 3-4). The superimposed absorption structures of these absorptions are separated numerically from each other. The evaluation procedure has to evaluate the parameter  $a_i$  and thus the column density taking all atmospheric and instrumental effects into account. This can be solved with least-square methods. Further the error  $\Delta a_i$  of the parameter  $a_i$ , i.e. of the measured slant column, must be derived. This was done from the remaining residual (the remained and not characterised structures) of the spectrum (see *Chapter 3.6*).

### 3.4 Conversion to Concentrations and Mixing Ratios

From the column densities  $a_i$  of species  $i$  the average concentration  $\bar{c}_i$  along the light path with length  $L$  can be calculated by rearranging Eq. 3.3:

$$\bar{c}_i = \frac{a_i}{L} \quad (\text{Eq. 3.15})$$

To calculate mixing ratios from the concentrations, like typically used in environmental science, the ideal gas law is applied. We can obtain the gas density with the equation:

$$\rho_v = \frac{A_v \cdot p}{R \cdot T} \quad (\text{Eq. 3.16})$$

where  $A_v$  represent the Avogadro constant,  $R$  the universal gas constant,  $p$  the pressure and  $T$  the temperature. To account for any change in the air density, the actual pressure and temperature should be used. The average mixing ratios can be calculated from the average concentrations (Eq. 3.15) or directly from the column densities with the equation:

$$\bar{c}_i[\text{ppbv}] = \frac{\bar{c}_i[\text{molec}/\text{cm}^3]}{\rho_v[\text{cm}^3]} \cdot 10^9 = \frac{a_i[\text{molec}/\text{cm}^2]}{\rho_v[\text{cm}^3] \cdot L[\text{cm}]} \cdot 10^9 \quad (\text{Eq. 3.17})$$

The factor  $10^9$  converts to a mixing ratio of parts per billion [ppb].

### 3.5 Evaluation Procedure

The aim of the evaluation is to receive column densities  $a_i$  of the measured trace gases and their error  $\Delta a_i$ . Afterwards both are calculated to concentrations and their error according to Eq. 3.17. But before the evaluation procedure can be performed, some corrections have to be applied to the spectrum [also see Stutz und Platt, 1996; Platt and Stutz, 2008]. Since  $A^+(j)$  is multiplied finally to the Eq. 3.13, it must first be removed by the retrieval algorithm. However this step can be omitted if a spectrum of the initial intensity  $I_0^+(j)$  is also measured by the same spectrograph, as then  $A^+(j)$  is identical to  $I_0^+(j)$  and  $I^+(j)$  and cancels out by the division. If it is not possible to measure  $I_0^+(j)$  and the spectral sensitivity has narrow-band characteristics, it must either be measured in another way or other assumptions like the manufacturers data has to be used which is typically less accurate.

The term  $N^+(j)$  has also to be removed from the equation. Therefore dark current and electronic offset spectra are characterised by recording spectra with the same detector when no light enters the spectrograph. Recording a spectrum with a long integration time (e.g. 100 s) yields the dark current for this time. Recording  $x$  spectra with the shortest possible integration time yields  $x$  times the electronic offset. Now both dark current and electronic offset can be corrected for each measurement spectrum by subtracting it integration time weighted or a scan number weighted spectrum, respectively.

The stray light  $M^+(j)$  for active DOAS measurements mainly arise from solar radiation scattered into the light path. It can also be corrected if a so called background spectrum is recorded with a light source blocked or the light source is switched off. Similar to the dark current spectrum it will be subtracted integration time weighted. But as solar radiation can change relatively fast, e.g. clouds moving in front of the sun, they should be recorded very close to the measurement spectrum.

In the evaluation process the detector noise, changes in offset and dark current, stray light inside the spectrograph and photon statistic are neglected. They play a role in determining the measurement error and detection limit of the individual trace gases (see *Chapter 3.6*). We have to neglect these error sources here as they are not involved in the evaluation process.

After all, recorded spectra are corrected for dark current, offset and background the optical density can be calculated by Eq. 3.7:

$$D^+(j) = \ln\left(\frac{I_0^+(j)}{I^+(j)}\right) = -R^+(j) - B^+(j) - \sum_i S_i^+(j) \cdot a_i \quad (\text{Eq. 3.18})$$

At this point, the individual trace gas column densities can be retrieved. The evaluation procedure is based on a model which describes the physical behaviour of the measured spectra and modelling the measured spectrum as  $F(j)$  which is then fitted to the measured data described in Eq. 3.19.

$$F(j) = P_r(j) + \sum_i S_i'(j) \cdot a_i \quad (\text{Eq. 3.19})$$

The polynomial  $P_r(j)$  of the order  $r$  describes all low frequency structures from the spectral

characteristic like scattering  $R^+(j)$ , broad-band absorption  $B^+(j)$  and  $S_i^{+b}$ , lamp fluctuations in  $I_0^+(j)$  and changes in spectral sensitivity  $A^+(j)$ .

$$P_r(j) = \sum_{k=0}^r n_k \cdot (j - j_c)^k \quad (\text{Eq. 3.20})$$

The parameter  $j_c = n/2$  corresponds to the centre pixel of the spectral region used for the evaluation. The polynomial refers to  $j_c$  to maximize the influence on the nonlinear terms.

The differential trace gas absorption cross sections are represented by  $S_i'$  and must be input by the user. They can either be measured in the laboratory or, as done in this thesis, high resolution cross sections from literature can be used. In the latter, the absorption cross sections must first be convoluted with the instrument function  $H$  which down-samples them to the resolution of the spectrograph (Eq. 3.10). Only then they can be used to be fitted to the recorded spectrum with this instrument. Even if only the differential structures of the absorption cross section is used in the fit, also the complete absorption cross section  $S_i^+$  can be used, as the polynomial  $P_r(j)$  may be used to describe the broad-band part of the cross-section. But this has to be applied carefully, as the cut off frequency for a polynomial and a high-pass filter can be quite different and vary with the chosen evaluation wavelength range. For active DOAS measurements which are typically evaluated over a broad spectral range a polynomial of 3<sup>rd</sup> order is mostly not sufficient to remove all broad-band structures. Furthermore a high-pass filter has to be used in addition.

All DOAS evaluations presented in this thesis are finally evaluated using the software DOASIS developed at the Institute of Environmental Physics, University of Heidelberg [Kraus, 2005].

The fitting routine itself is a combination of the Levenberg-Marquardt Method [Levenberg, 1944; Marquardt, 1963] and a standard non-linear least-squares fit [Albritton et al., 1976; Bevington, 1969]. Both methods minimize  $\chi^2$  between  $F(j)$  and  $D^+(j)$ , by changing the parameter  $a_i$  and  $n_k$  of  $P_r(j)$ , where  $\chi^2$  is defined as:

$$\chi^2 = \sum_{j=0}^n (D^+(j) - F(j))^2 \quad (\text{Eq. 3.21})$$

The procedure starts with a linear fit using some starting values  $a_i$  and  $n_k$ . The resulting parameters  $a_i$  and  $n_k$ , are then used as input data for the following non-linear Levenberg-Marquardt fit. Only one step of this nonlinear fit is performed and the resulting  $a_i$  and  $n_k$  are used as input for the next call of the linear fit. The two fitting procedures are applied alternating and the respective results are used as input for the next call. The fitting procedure is stopped for several breaking conditions for the nonlinear fit. Usually the fit is aborted if the relative changes of  $\chi^2$  in the last step are smaller than a given value (usually  $10^{-6}$ ) and thus the fit has converged. This also happens if a certain number of runs of the fitting procedure is exceeded or if the nonlinear method becomes unstable [Gomer et al., 1993; Stutz and Platt, 1996].

To better match the absorption structures, typically also a slight shift and sometimes also a squeeze in wavelength of the reference cross-section is allowed to better match the absorption structures. When the fit finds the minimum of  $\chi^2$ , the fit coefficient  $a_i$  represents the difference in column density of each individual absorber between the two spectra for  $I_0^+(j)$  and  $I^+(j)$ , what is basically for LP-DOAS measurements the total trace gas column along the measurement absorption path.

For real measurements  $\chi^2$  can never reach zero even if all absorbers in the wavelength range were included in the retrieval. The photon noise and electronic noise would remain. The residual spectrum  $\Psi(j)$  of a DOAS fit, which could not be identified, is defined as the difference between modelled and measured optical density:

$$\Psi(j) = D^+(j) - F(j) \quad (\text{Eq. 3.22})$$

For a good measurement and data analysis the residuum  $\Psi(j)$  only consists of statistical noise, which does not have characteristic spectral structures. For the reliable observation of a trace gas, the residuum should be smaller than the trace gas optical densities. Therefore it is often used to evaluate the quality of a fit, the measurement error and the detection limit for each trace gas (see *Chapter 3.6*)

From the fitting process we receive column densities of the individual absorbers along the light path which allow calculating average concentrations  $\bar{c}_i$  with Eq. 3.15 or mixing ratios  $\bar{c}_i[\text{ppbv}]$  with Eq. 3.17. However, no information about the distributions of the individual trace gases along the light path can be extracted. They can be gained by varying the measured light path what is typically not sufficient for very fast changing distributions like urban areas. The tomographic approach, as presented in this thesis, can be applied by measuring along several light paths simultaneously to retrieve trace gas concentration distributions with high temporal and spatial resolution.

### ***3.6 Measurement Accuracy and Error Estimation***

The errors of the DOAS measurements can be split into systematic (instrumental) and statistical errors. The systematic error describes all errors caused by the recording of the spectra, whereas the statistical error results from statistical processes, like photon noise, and the process of evaluation. An overview of systematic errors is given below.

Beside absolute systematic errors (concentration offsets) the error is defined by the signal to noise ratio in the retrieved spectra. The total noise consists of photon (“shot”) noise  $\sigma_p$ , the optical noise  $\sigma_o$  [Stutz and Platt, 1997] and the instrumental noise  $\sigma_i$ . For good instruments the photon noise  $\sigma_p$  is the limiting factor in the signal to noise ratio. In comparison to the other noise, it is for sure pure statistical, and can be reduced by accumulating more photons. At a certain number of photons the photon noise will be so small that the other noise sources will dominate and the total noise will not further decrease with increasing number of registered photons (or rather photo-electrons). This is the real limit for the best achievable measurement quality of a DOAS measurement. It is important that this number of photons (or number of photoelectrons / scans) is determined for each instrument. The noise tests are shown in

*Chapter 5.3.4.*

Here a short overview of the different noise sources and their mathematical description is given. It is followed by an estimation of the absolute DOAS error of a measurement and details on averaging of data points to increase the signal to noise ratio.

**3.6.1 Systematic Errors**

The most important systematic errors are:

- Uncertainties and errors of the literature cross sections. Depending on the trace gas of interest, the error of the literature cross section is between 1 % and 15 % (e.g. see Table 7-1).
- Stray light in the spectrometer gives a negative offset to the determined concentration. The applied Acton spectrometer (300i and 500i) display only very low stray light (~0.1 %) and thus this error is very small (< 1 %). Additional filters may be applied to further reduce the light of the unused spectral range. Reflections can also produce stray light like reflection at the detector window. All these stray light errors are estimated to be smaller than 3 % [Stutz, 1996].
- For the used configuration additional stray light arise due to the simultaneous measurement of absorption spectra from different light paths with one spectrometer detector unit (see *Chapter 5.3.1*). It could be found that for some extreme configurations with different intensities this can contribute up to 10 % and thus to an error of the same order. For equal light intensities of the different received light paths, this additional stray light is in the order of 1 %.
- The convolution process and differences in the wavelength-pixel mapping can cause errors up to 1-3 % (see *Chapter 3.9*)
- Errors made by the determination of the length of the absorption light path. With the typical applied laser range finders this error is in the order of 0.1 %.
- Errors by the conversion of the concentration to mixing ratios (Eq. 3.17) due to errors in the pressure and temperature. If the simultaneous measured pressure and temperature are used, for typical accuracies their influence is less than 1 %.

**3.6.2 Photon Noise ( $\sigma_p$ )**

The photon noise ( $\sigma_p$ ) is in principle the theoretically achievable accuracy for measurements of electro magnetic radiation. The detected photons (i.e. the photoelectrons) are Poisson distributed. That means there is a randomness of the arrival of each photon and each detection event is independent of each other and independent of the already detected events. The measurement accuracy generally increases with an increased number of detected photons, but is limited by the photon noise ( $\sigma_p$ ), which is equal to the square root of the total amount of measured photons ( $n_p$ ):

$$\sigma_p = \sqrt{n_p} \quad (\text{Eq. 3.23})$$

Thus, if many measurements are done with a certain exposure time  $t_0$  there will be a mean number of photons measured by a single detector element:  $n_p(t_0)$ . The standard deviation of all single measurements is:

$$\sigma_p(t_0) = \sqrt{n_p(t_0)} \quad (\text{Eq. 3.24})$$

The signal to noise ratio therefore is:

$$\left(\frac{S}{N}\right)_{\text{ration}}(t_0) = \frac{n_p(t_0)}{\sigma_p(t_0)} = \frac{n_p(t_0)}{\sqrt{n_p(t_0)}} = \sqrt{n_p(t_0)} \quad (\text{Eq. 3.25})$$

Now instead of using a single channel of the detectors chip and performing a large number of measurements, one can also do only two measurements and use a whole bunch of neighbouring channels (for which the intensity does not change very much) as statistically independent measurements.

To receive the signal to noise ratio of the two spectra  $I_1$  and  $I_2$  they have to be divided channel-wise. This gives a ratio spectrum with values distributed around unity, where all systematic differences between different channels are eliminated and only statistical variation remaining. The observed standard deviation of  $I_1/I_2$  is:

$$\begin{aligned} \sigma_{p, \frac{I_1}{I_2}}(t_0) &= \sqrt{\left(\frac{\sqrt{n_p(t_0)}}{n_p(t_0)}\right)^2 + \left(\frac{\sqrt{n_p(t_0)}}{n_p(t_0)}\right)^2} \\ \sigma_{p, \frac{I_1}{I_2}}(t_0) &= \sqrt{2 \cdot \left(\frac{\sqrt{n_p(t_0)}}{n_p(t_0)}\right)^2} \\ \sigma_{p, \frac{I_1}{I_2}}(t_0) &= \sqrt{\frac{2}{n_p(t_0)}} = \frac{\sqrt{2}}{\sqrt{n_p(t_0)}} = \sqrt{2} \cdot \sigma_p(t_0) \end{aligned} \quad (\text{Eq. 3.26})$$

Thus as a consequence of the channel-wise division of the two spectra, the standard deviation increases by an additional factor of  $\sqrt{2}$  compared to the original relative standard deviation (the original ‘‘signal to noise ratio’’). Plotting the observed  $\sigma_{p, \frac{I_1}{I_2}}(t_0)$  (using the Root Mean Square (RMS) values of the divided spectrum) on a double logarithmic scale, we receive:

$$\log\left(\sigma_{p, \frac{I_1}{I_2}}(t_0)\right) = \log\left(\frac{\sqrt{2}}{\sqrt{n_p(t_0)}}\right) = \frac{1}{2} \cdot \log 2 - \frac{1}{2} \cdot \log n_p \quad (\text{Eq. 3.27})$$

Thus the received straight line will have a slope of  $-1/2$ . To calculate the correct signal to noise ration from the divided spectrum we have to multiply by the factor of  $\sqrt{2}$ . Thus one obtains:

$$\left(\frac{S}{N}\right)_{\text{ration}}(t_0) = \frac{n(t_0)}{\sigma_p(t_0)} = \frac{\sqrt{2}}{\sigma_{p, \frac{I_1}{I_2}}(t_0)} \quad (\text{Eq. 3.28})$$

By increasing scans, and thus observed photons, the photon noise can in principle be reduced unlimited. But in reality from the total noise mainly the photo noise is reduced, and thus at a certain scan number the total noise will not further decrease, as it is then dominated by the instrument noise. It is important to determine at which noise level and after how many scans this level is reached. To perform more scans during a measurement is useless and will only reduce the temporal resolution but not increase the signal quality.

Since for DOAS measurements and data evaluation the noise is displayed in the residuum spectrum, for simplicity, in the noise test we take into account only the standard deviation and not the signal to noise ratio. This makes it easier to compare the achieved values in the noise test with those of measurements. Therefore in *Chapter 5.3.4* only the standard deviation noise is given. As we are in DOAS observations only interested in narrow-band absorption structures, all broad-band variations will be ignored.

### 3.6.3 Optical Noise ( $\sigma_o$ )

Optical noise can arise from all optical components. First of all, the light source can be unstable in the spectral characteristic or intensity. For example a spectral change of the used xenon arc lamp or even a halogen lamp is not necessarily spectrally stable. For the noise test a stable halogen lamp with a stable power supply should be used to exclude any fluctuations arising from this source.

Other optical noise sources are the fibre, which will change its transmittance with different bending. Also other components like mirrors and lenses can be responsible for optical noise if they change the spectrum with time. The spectrograph with the grating can produce optical noise, especially if the fibre will not homogeneously illuminate the grating and the detector of the spectrometer (see *Chapter 5.2.5*). In this case changes in the light distribution can lead to spectral structures. To prevent such inhomogeneous distribution a mode mixer is applied (see *Chapter 5.2.5*). For example a different illumination of the fibre arose in the presented LP-DOAS measurements between shortcut and atmospheric measurement configuration. The shortcut is much closer to the instrument and due to an optimisation of the optical adjustment for far retro reflectors, the reflected light of the shortcut is not homogeneously focused into the fibre. The mode mixer should reduce these effects.

As the noise test is performed with a stable light source and optical set up, it will not determine the optical noise of the measurement. The optical noise can only be determined by comparing the residuum of a measurement to the noise determined in a noise test.

### 3.6.4 Instrument Noise ( $\sigma_i$ )

Instrument noise summarises all noise sources arising associated with the instrument detection and data unit. The main part is electronic noise. In several instruments it is influenced by electro magnetic fields. Thus detector, spectrometer and electronic have to be set on the same ground level. Another noise source is the non linear sensitivity of the detector

with increasing saturation (see *Chapter 5.3.3*).

### 3.6.5 Estimate the Measurement Errors

The statistical error is calculated from the random structures of the residuum of the linear least square fit. The statistical fit error given by the evaluation software DOASIS [Kraus, 2005] depends on the number of channels used for the evaluation. Thus the error decreases with a larger pixel number which can be achieved with a higher spectral resolution or a larger evaluation range. The evaluation range should therefore always be chosen as large as possible in the range where the absorber displays characteristic absorption structures. Additionally, the proportional inverse weighting with the number of absorption band can also be applied, as an absorber is better determined if more characteristic bands are within the evaluation range.

The statistical error may be used to estimate the statistical error of the measurement if the following assumptions are fulfilled [Albritton et al., 1976]:

- the errors of the pixel intensity must have finite variances
- the intensity errors of the individual pixels are independent [Bevington, 1969]
- the systematic error of the pixel intensity is zero

The statistical error in the measured differential optical density is dominated by photon noise and the variation is Poisson-distributed. At the high number of collected photons, however the Poisson distribution can be approximated by a Gaussian distribution with a fixed standard deviation  $\sigma$ . Therefore, the standard deviation of the Gaussian distribution is used for the error of the DOAS intensity. Thus, the statistical errors do have a finite variance and the first assumption is fulfilled.

Unfortunately, the CCD-detector, as well as PDA detectors, used in the DOAS spectrographs often show a cross dependency of several percent between neighbouring individual pixels [Stutz and Platt, 1996]. Sometimes smoothing of spectra is applied to minimize noise effects, which increases the dependency of neighbouring pixels.

Endowments in the pixels or doping errors on the sensor (CCD and PDA) also cause diode sensitivity structures. These can be corrected if known, but the correction is somehow problematic, as the structures can change over time. Therefore, they represent a systematic error.

Thus the residuum of a fitting  $\Psi(j)$  contains not only the statistical error, but all structures that are not explained by the model (also see *Chapter 3.6.3* and *3.6.4*). They are:

- indicate an unknown absorber in the evaluated wavelength range
- originate from a faulty absorption cross section reference
- be caused by the instrument itself (change in emission of the light source, electronics), in which case they normally occur randomly
- arise from different optical systems for  $I_0^+(j)$  and  $I^+(j)$  measurements

Stable residual structures cause systematic errors in the evaluation which cannot be described

by statistical methods. They may be corrected by fitting a typical residual or an average residual of a series of spectra to the measured DOAS spectra as an additional reference. If the unknown residual structures show strong diurnal or seasonal variations they likely arise from unknown absorbers and can therefore be separated from other systematic errors [Veitel, 2002]. However, this method has to be applied carefully, since it will reduce the residuum and thus the measurement error and detection limit as discussed below.

As a result of these problems, the purely statistical fit error provided by the combined linear non-linear least-square fitting procedure, underestimates the true measurement error of a derived concentration. To account for the systemic errors of the fit, a correction factor was introduced by Stutz and Platt [1996]. They performed simulations applying Monte-Carlo methods with artificial absorption spectra containing five identical, Gaussian-shaped absorption lines with FWHM  $\rho$ . These absorption spectra were added to random noise spectra filtered by running mean filters with width  $W$  (smoothing width) and normalized to a standard deviation of 1 %. A DOAS fit was than applied to the spectra to compare the mathematical error, obtained from the fit  $S_{fit}$ , with the known measurement error of  $S_{meas}$  obtained from the simulated experiment. This analysis was repeated for different  $\rho$  and  $W$  values. A correction factor  $C(\rho, W)$  was defined as:

$$C(\rho, W) = \frac{S_{meas}}{S_{fit}} \tag{Eq. 3.29}$$

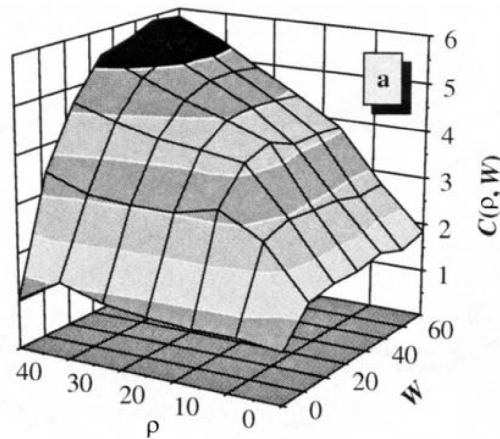


**Figure 3-3: Correction factor  $C(\rho, W)$  as a function of the half width  $\rho$  of absorption bands and the width  $W$  of a running mean filter applied to a random noise spectrum by Monte-Carlo methods. This factor can be used to calculate the measurement error of a DOAS analysis from the statistical fit error. [adapted from Stutz and Platt, 1996]**

The results of this simulation are shown in Figure 3-3. The correction factor  $C(\rho, W)$  increases when the width of the running mean filter with  $W$  approaches the half-width  $\rho$  of the measured absorption line. For broad absorption lines with FWHM above 30 channels, the measurement error  $S_{meas}$  can be up to 6 times larger than the statistical fit error  $S_{fit}$ . This means that a broad filtering  $W$  to reduce spectral noise lead to an increase of the correction factor  $C(\rho, W)$  which results in a compensation of the reduced fit error  $S_{fit}$  due to a less noisy residuum. Additionally, this result also demonstrates that measurement error increases when

the noise structures in the spectrum have a similar spectral width (frequency) as the spectral structures which have been retrieved. The reason is that the application of a filter with width  $W$  to a random noise spectrum will lead to spectral structures which can be similar to absorption structures with several channels width. The width of these structures increases with the increase of filter width and can interfere during the analysis fit. Therefore remaining spectral structures in the residuum will increase the correction factor.

Typically the noise is of a more high frequently nature than the absorption structure. If DOAS evaluations show only high frequency noise structures in the residuum and do not apply any filter result in a correction factor  $C(\rho, W)$  of two. For the measurements conducted in the scope of this thesis a binomial triangular high-pass filter of 1000 iterations was applied which yield in approximately a factor of  $C \approx 3$  for the applied instrument [Mettendorf, 2006]. For more details on the calculation of errors in DOAS measurements see Stutz and Platt [1996] and Platt and Stutz [2008]. Multiplying  $C$  to the statistical error from the least-square fitting procedure yield the  $1 \cdot \sigma$  error which is given for the measurements within this thesis (note:  $\sigma$  represents sigma not the absorption cross section).

### 3.6.6 Averaging Data Points

Averaging data points are applied to many kinds of measurements to improve the data quality by reducing the noise and thus the variability. It is also directly applied to DOAS measurements, by averaging several recorded spectra before applying the evaluation fit (see *Chapter 3.6.4*). Due to averaging of statistical noise the residuum will decrease. After averaging over a number of scans (e.g. 50 - 100 scans for the used CCD cameras), the residuum will no longer decrease by averaging more spectra. At this point the systematic errors dominate the residuum and the best measurement accuracy or the instrument is achieved. Typically in DOAS measurements this is set as the maximum averaged spectral number before an evaluation. Additionally one may think of averaging derived concentrations from several spectra. Such averaging is applicable if the error is only subject to Gaussian error statistics. Then the Gaussian error propagation is applicable to calculate the new measurement error of two averaged data points by:

$$\sigma_{average} = \sqrt{\sigma_1^2 + \sigma_2^2} \quad (\text{Eq. 3.30})$$

Such averaging will lead to smaller measurement errors if applicable. But for DOAS measurements the remaining residual, and thus the measurement error, is not only subject to Gaussian error statistics, but also contain systematic errors e.g. spectral structures with width  $W$ . Thus Gaussian error propagation is generally not applicable and would lead to wrong determined measurement errors and detection limits. If the Gaussian error propagation would be applicable, also the spectra could directly be averaged to reduce the statistical noise and thus improve the measurement error. As this is not the case for the presented measurements it is not applicable.

### 3.7 Detection Limit

The detection limit defines the value above which the concentration of a species is considered to be significantly above the background noise. Thus, the detection is always directly linked to the noise level and no general detection limit exists. It depends on the quality of each measurement if the absorber can be identified. But still a detection limit for a specific noise level can be given. There are two methods to estimate the detection limit of DOAS measurements.

#### a) Detection Limit from Measurement Error

In order to obtain the detection limit for DOAS measurement, statistical considerations are used. Assuming the measurement being subject to Gaussian error statistics, the retrieved measurement error can be used to calculate the detection limit. As the measurement error calculated from the statistical fit error gives the  $1 \cdot \sigma$  range of a measurement, the true measurement value is in this range with a probability of 68 %.

If the DOAS measurement also contains beside statistical errors systematic errors which do not follow Gaussian error statistics, this  $1 \sigma$  range can be used if the error is corrected with the factor  $C$  as described in *Chapter 3.6*. The  $2 \sigma$  confidence interval with a probability to find the measurement true value within 95 %, is obtained by multiplying the error by 2. If the  $2 \sigma$  interval is entirely located above null and thus the determined concentration is larger than the  $2 \sigma$  value than the measurement has a probability of more than 95 % of being above null. Usually, this is considered as significant detection of a certain species. The  $3 \sigma$  confidence interval would give a detection probability of 99.7 %.

#### b) Detection Limit from Fit Residual

If the optical density of the residuum is small compared to the trace gas absorption derived in the fitting procedure, the respective trace gas may certainly be detected. Thus, another method to estimate detection limits of a DOAS instrument is the evaluation of the fit residuum. The assumption is made because a DOAS instrument cannot measure any trace gases whose absorptions structures are smaller than the current fit residual  $\Delta\Psi$ :

$$(S'_{\max} - S'_{\min}) \cdot \bar{c} \cdot L \geq \Delta\Psi \quad (\text{Eq. 3.31})$$

Differences arise in the rating of the absorption structure compared to the residuum. A worst case approximation is using the peak to peak value  $(\Psi_{\max}(j) - \Psi_{\min}(j))$  as  $\Delta\Psi$ . A more realistic approximation uses twice the average deviation from the mean value in the wavelength interval of the considered trace gas absorption band. Since the depth of trace gas absorption structures is a direct function of its differential absorption cross section  $S'$ , its average concentration  $\bar{c}$  and the observed path length  $L$  are the only parameters theoretically limiting the detection limit, beside from the photon noise. The minimum detectable average concentration is therefore:

$$\bar{c}_{\min} = \frac{\Delta\Psi}{(S'_{\max} - S'_{\min}) \cdot L} \quad (\text{Eq. 3.32})$$

### 3.8 Measurable Trace Gases

Depending on the used wavelength range and absorption length, measurements of different trace gases are possible. Figure 3-4 displays only some differential absorption cross sections measurable by DOAS. The typical detection limit for the given trace gases is shown along the right margin, assuming a deviation of the fit residual  $\Delta\Psi$  of  $1 \times 10^{-3}$ , a typical value achieved for active DOAS measurements.

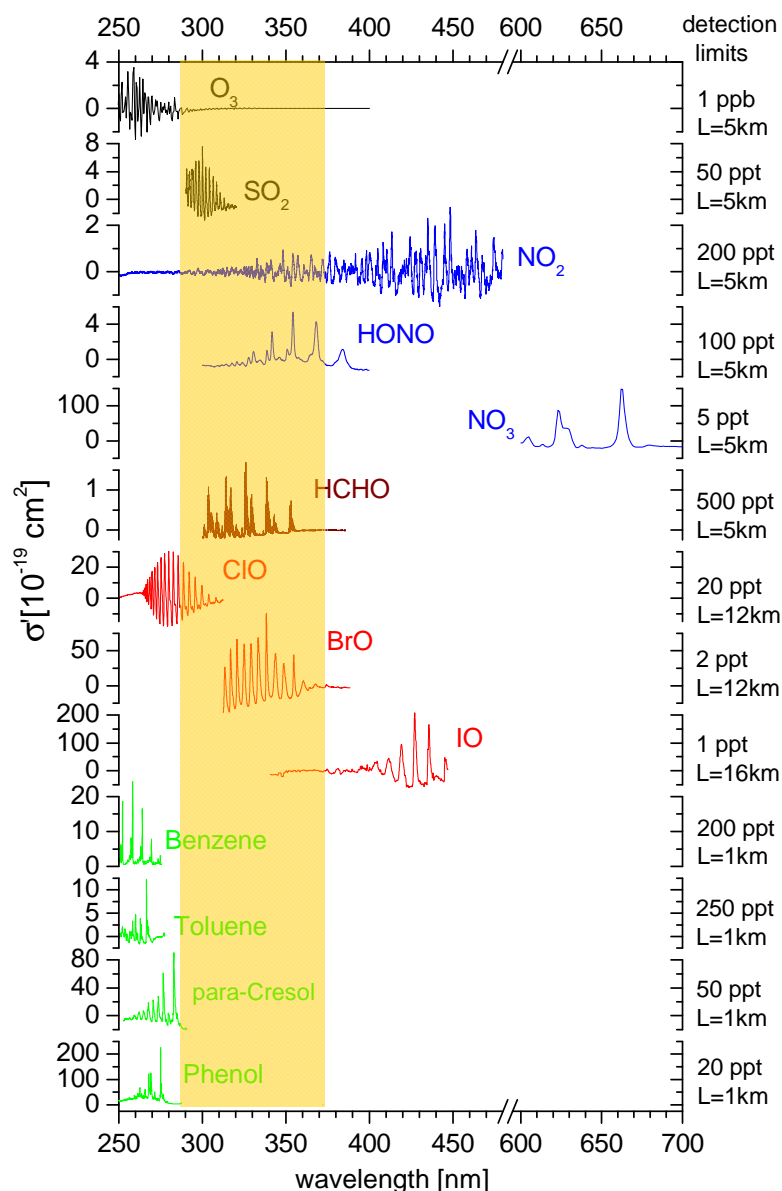


**Figure 3-4: Differential absorption cross sections from some measurable trace gases with DOAS [adapted from Platt und Stutz, 2008]. The differential absorption cross-section  $\sigma'$  is shown as a function of wavelength. The approximated detection limit of the individual species is also given assuming a fit residual deviation  $\Delta\Psi$  of  $1 \times 10^{-3}$  (see Eq. 3.22).**

In fact, new trace gases are still found to which DOAS is sensitive, such as the recent detection of glyoxal (Volkamer et al., 2005a; Volkamer et al., 2005b).

Passive DOAS instruments can observe trace gases absorbing in the visible and UV spectral range down to 300 nm, as the atmosphere does not let pass sun light at smaller wavelengths

due the absorption in the stratospheric ozone layer which protects humanity from deep UV radiation. However, active DOAS instruments can also measure trace gases absorbing below 300 nm if artificial light sources are applied which emit in this spectral range. They can additionally also measure at night.

The measurements of this thesis were performed in the wavelength interval from 285 to 365 nm (highlighted in Figure 3-4), where absorptions of NO<sub>2</sub>, O<sub>3</sub>, SO<sub>2</sub>, HCHO, HONO and O<sub>4</sub> could be verified. These gases (except of O<sub>4</sub>) play a mayor role in urban pollution (see *Chapter 2*). The used absorption cross sections fitted to the measurement spectrum are sketched in Table 7-1.

### 3.9 Spectral Sampling and Aliasing Problems

The detector at the spectrograph maps the continuous wavelength information to discrete numbers of pixels. To obtain a true digital representation of the spectrum, a sufficiently fine spectral sampling is required. The discrete sampling should match the spectral resolution of the dispersing spectrograph. That means that the density of pixels must be sufficient compared to the spectral resolution.

The aliasing problem arises if the number of pixels is too low in comparison to the spectral resolution. In other words, the spectral resolution is too fine for a given detector pixel size. Aliasing problems are well known from many areas of electronic signal evaluation. An example of this effect in spectroscopy is given in Figure 3-5.

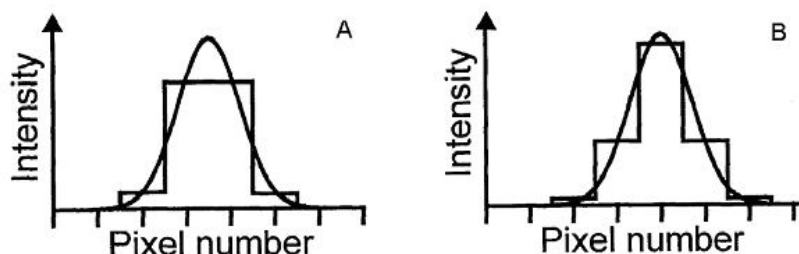


**Figure 3-5:** Aliasing problems occur if the number of pixels is too low in comparison to the spectral resolution of the spectrometer. In this example the line shape of the digitised representation is shown for two different positions. The histogram-like curve in panel A and B is different but describes the same line shape.

In the example the FWHM resolution of the spectrograph corresponds to two pixels. A Gaussian line (A) is shifted by half width of a pixel (B). The digitised representation of the same line shape is drastically different. This is called the aliasing problem or also under-sampling problem.

The Nyquist-Shannon theorem states that the minimal twofold over sampling is sufficient to define the shape of the function. This would allow achieving the best possible use of a given number of pixels. In DOAS however, practical experiences and numerical modelling show that there must be a sufficient large number of pixels for the resolution interval. In practise that means a sufficient large number of pixels compared to the FWHM of the instrumental function.

In order to achieve acceptable errors, a basic guidance is that the spectral width of a detector

pixel should be about 10-20 % of the FWHM of the instrument function [Hofmann et al., 1995; Stutz, 1996; Roscoe et al., 1996; Platt et al., 1997]. This corresponds to 5-10 channels in FWHM of the instrument function.

### ***3.10 Measurement Concepts***

The main two groups of DOAS measurements are “active” DOAS and “passive” DOAS. The first uses artificial light sources, the second natural light sources like the sun, the moon or stars.

Several different active DOAS setups exist. The most common configuration is that of the Long-Path (LP-) DOAS. A telescope sends light through the atmosphere which is then received again by another telescope. If using a reflector this may be the same telescope. The most common setup uses a Newtonian telescope with two adjustable mirrors inside the telescope introduced by Axelsson et al. [1990]. For details see *Chapter 5.1*. Many important findings in atmospheric chemistry are made with such LP-DOAS instruments, for an overview see Platt and Stutz [2008]. A very similar setup is used in this thesis, the Multibeam-LP-DOAS instrument (see *Chapter 5.1*), which allow to measure along several light paths simultaneously with one telescope. Recently, a new LP-DOAS setup was introduced using fibre optics [Merten et al., 2010; Merten, 2008, *Chapter 5.6*]. It allows much simpler setups which can make LP-DOAS measurements more popular and also allow mobile instruments [e.g. Kern et al. 2009, see *Chapter 5.6*]. Fibre-LP-DOAS may also simplify future tomographic setups.

Other active DOAS setups include multi-reflection systems exist such as the White cell [White, 1942; White, 1976]. More recent systems are cavity based setups (CE-DOAS) using very high reflecting mirrors [Fiedler et al., 2003, Platt et al., 2009, Meinen et al., 2010]. They allow in-situ measurements with DOAS. The trace gases detectable with CE-DOAS are continuously increased. At the Institute of Environmental Physics CE-DOAS instruments to measure NO<sub>3</sub> [Meinen et al., 2010], NO<sub>2</sub> [Horbanski, 2010], BrO, O<sub>3</sub>, HCHO and HONO [Hoch, 2010] were developed recently.

Passive DOAS are typically much simpler as they only require a small receiving telescope and no artificial light source. They also observe the absorption of trace gases along the optical path from the natural light source (sun, moon, stars etc.). As the light from the moon or stars is very weak, most passive instruments rely on direct or scattered sunlight. Thus they suffer the disadvantage, in contrast to active DOAS, that measurements are only possible during daylight. Beside scattered sunlight configurations, also direct light configurations can be realised [e.g. Sommer, 2008]. Thus the absorption path is known. Besides the sun during day also the moon or stars may be used in cloud free nights.

Passive DOAS instruments are relatively cheap and flexible. Thus, they are widely used for many kinds of scientific application where a larger set-up is not applicable. Instruments are applied to many different platforms ranging from ground based [e.g. Sinreich et. al, 2005; Lohberger et al., 2004; Louban, 2005; Louban et al. 2009], aeroplane [e.g. Pfeilsticker and Platt, 1994; Heue, 2005], balloons [e.g. Weidner, 2005; Butz et al. 2006], ship [e.g. Martin et

al. 2009] to satellite borne instruments [e.g. Wagner und Platt, 1998; Beirle, 2004].

The most common application measures scattered radiation along several elevation angles and is called Multi Axial (MAX) DOAS [e.g. Hönninger and Platt, 2002]. As the absorption path is unknown, the interpretation of passive measurements requires the accurate modelling of the atmospheric radiative transfer (RTM) and the use of inversion algorithms to determine the effective light path and thus to retrieve the trace gas concentrations [e.g. Friedeburg, 2003; Sinreich et al. 2005; Deutschmann, 2008]. The inversion algorithms rely on assumptions which influence the results. Typically the best achieved vertical resolution is of the order of 100 m close to the ground.

Satellite measurements applying passive DOAS have only a limited spatial and temporal resolution due to few overpasses per day and limited sensitivity to the lower troposphere for areas with low albedo, e.g land, urban areas and water.

Due to all these limitations and required assumptions, most passive instruments are not ideal for urban trace gas monitoring where accurate estimation of the concentration with high temporal and spatial resolution is required. Especially if a strong vertical gradient exists, so that a vertical resolution of 100 m is insufficient, passive instruments can not retrieve the trace gas concentrations at the street level with sufficient accuracy. But due to the small size, cost-benefit ratio and their good detection limit they have many applications like for observations of trace gas profiles, upper troposphere and stratosphere concentrations and monitoring of plumes.

Imaging DOAS (I-DOAS) is a passive measurement technique which measures a whole area by pointing to multitude neighbouring viewing directions in a specified area. A whole viewing field will be scanned. Thus it retrieves a map of slant columns which is a type of a two dimensional measurement [e.g. Louban et al., 2009]. For applications with a well defined emission source (e.g. power plant, volcano), the map visualise the emission plume of trace gases.

In combination with tomographic approaches, the application of MAX- DOAS instruments on airborne platform (AMAX-DOAS) allow to retrieve two dimensional trace gas distributions from multitude measurement directions[Heue et al. 2008] (see *Chapter 4*).

I-DOAS, A-MAX-DOAS and LP-DOAS tomography are the techniques to observe multidimensional trace gas distributions by combining these techniques [Platt et al., 2009a; Pöhler et al., 2008].

## 4 DOAS Tomography

Tomographic retrieval methods can be used to retrieve two- or three-dimensional concentration fields from path integrating measurements along several paths. In the atmosphere knowledge of exact amount and distribution on regional or local scales is necessary to assess the quality of chemical transport models on microscales, quantifying total emissions of sources and distinguishing between them, and also to analyse local exposures of pollutants.

Several studies exist which are dedicated to the remote sensing of indoor gas concentrations and their dispersion by different experimental techniques [e.g. Yost et al., 1994; Drescher et al., 1997; Fischer et al. 2001]. Improvements could be achieved in the time resolution of the measurement procedure and quality of the reconstructed two dimensional (2-D) concentration map.

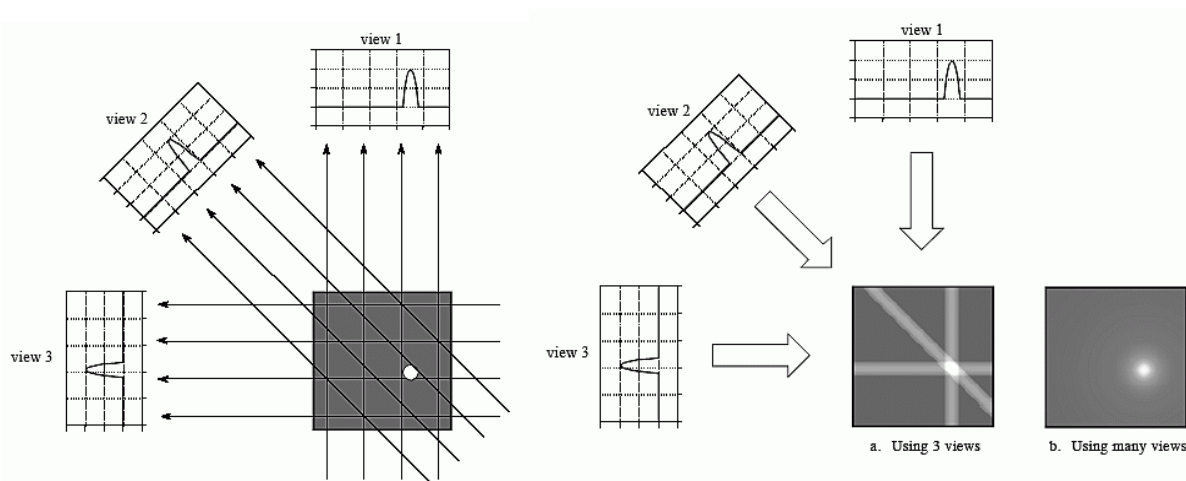


**Figure 4-1: Computer tomography** acquires a set of views (left image) and then reconstructs the corresponding image. Each sample in a view is equal to the sum of the image values along the ray that points to that sample. In this example, the image is a small pillbox surrounded by zeros. While only three views are shown here, a typical CT scan in medical application uses hundreds of views at slightly different angles. A simple reconstruction is a back projection (right image) by taking each view and smearing it along the path from which it was originally acquired. The resulting image is a blurry version of the correct image (a). Applying many viewing directions increases the reconstructed image (b). In computer tomography typical the Radon transformation is applied for the filtered back projection. [adapted from Smith, 2009]

By using several lines of sight in different directions, the difference in concentration can be detected and with mathematical inversion techniques the distribution is retrieved. The method is illustrated in Figure 4-1. A medium of interest is screened with an absorption method by a set of views. The simplest back projection is made by taking each view and smearing it along the path to which it was originally exposed. The resulting image gives an idea of the distribution. The accuracy can be improved by using more viewing directions.

A well known example is the medical tomography (Figure 4-2), seismic tomography (Figure 4-3) and process tomography e.g. in combustion engines.

Different methods can be applied to solve the inverse problem. Most common in tomographic applications with many absorption paths, like computer tomography, are analytical methods where the filtered back projection with a radon transformation is applied. If only a small

number of absorption paths are observed, algebraic inversion methods are preferable which discretize the investigation area. In these cases this gives a better reconstruction of the true two-dimensional absorption.

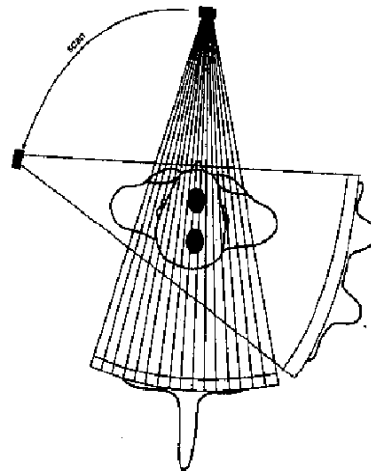


**Figure 4-2: Schematic sketch of a Computerised Tomography (CT) scanning in medicine. The absorption of X-rays is determined for different positions to determine different viscera. The body is subsequently measured in slices.**

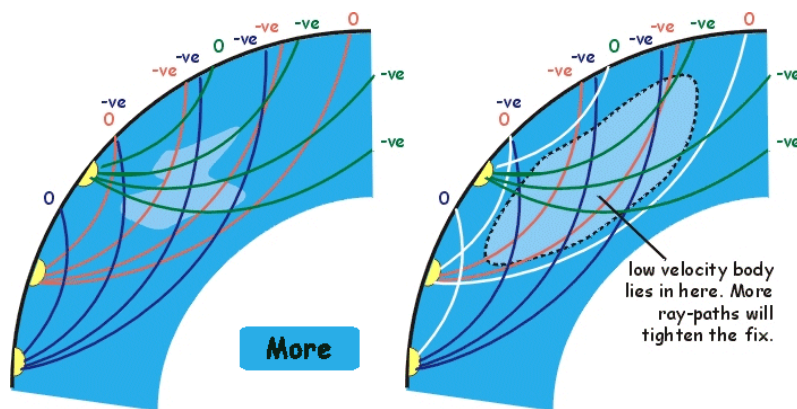


**Figure 4-3: Schematic sketch of seismic computerised tomography in geology. The seismic velocity is measured along different paths to determine different geological layers of the earth.**

In DOAS tomography we have to distinguish between active and passive systems. Passive systems are simple and relatively cheap. One instrument can simply achieve some ten to a few hundred viewing directions, as the telescope can point to any location where it receives scattered or reflected sunlight. If the scanning is fast, a sufficient amount of light paths can be achieved in a short time of few minutes which are applicable for tomographic observations. For the distinct reconstruction of trace gas distributions, at least three instruments are advisable with an optimised geometry [Hartl et al. 2006]. An example for a passive system is the airborne DOAS tomography, measuring scattered sunlight from multiple directions [Heue, 2005; Bruns et al. 2006]. Due to the fast moving platform only one instrument on the plane with different viewing directions is required.

The absorption light path of passive observations has to be calculated by radiative transfer models. In some cases however, accurate radiative transfer can be ignored as an approximation. For example if scattering arise mainly behind the investigating plume like the direct observation of a stack emission. Then, most of the received light has passed the whole plume and the absorption strength can directly be used to derive the plume distribution of

passive measurements from different viewing directions.

For tomographic measurements with the AMAX-DOAS instrument, in a first approximation single scattering and ground reflection can be assumed [Heue, 2005]. Thus total absorption paths are well defined and can be used for tomographic retrievals of the trace gas distribution. But if flight altitudes are high, this simple light path assumption gives significant errors. Then radiative transfer models have to be included for the retrieval of the distributions like shown in Figure 4-5.

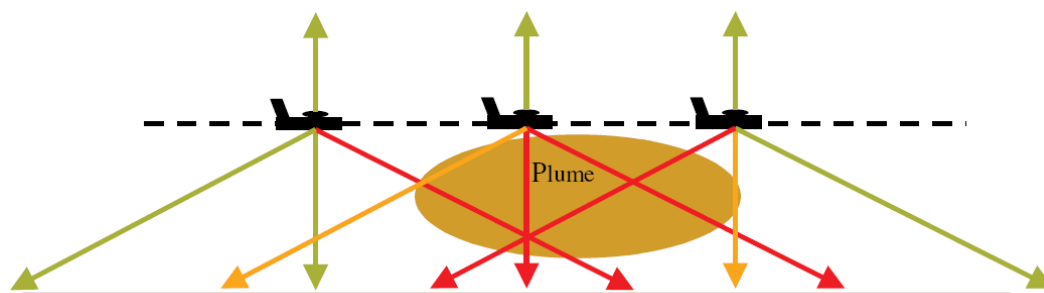


Figure 4-4: Measurement with the AMAX-DOAS instrument above a plume. The colour of the lines indicates the observed slant column. Green stands for no, orange for low and red for high slant column density, respectively [Heue, 2005].

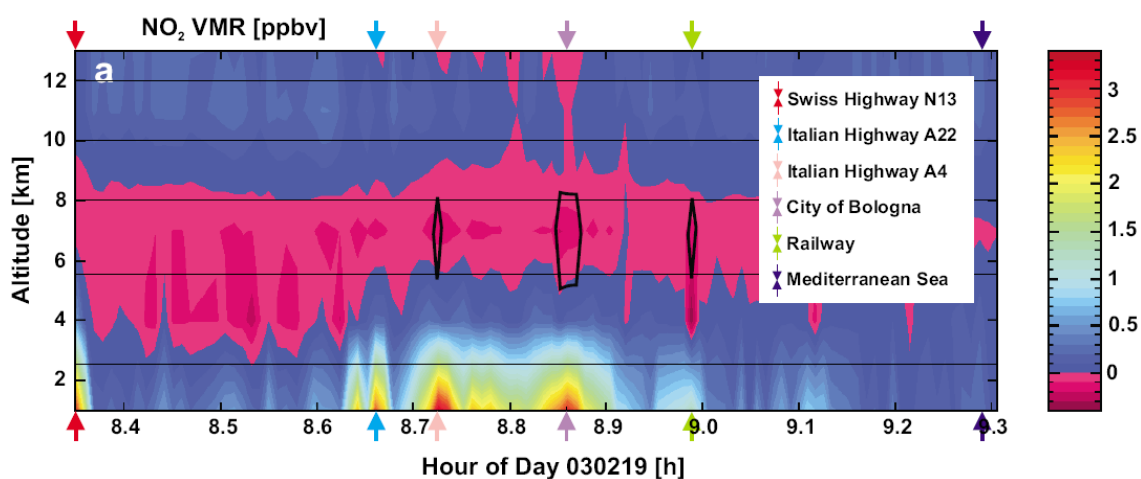


Figure 4-5: Retrieved profiles as a contour plot of a flight with the AMAX-DOAS instrument on February the 19<sup>th</sup> 2003 from Basel, Switzerland to Tozeur, Tunisia. The thin vertical lines indicate the boundaries of the individual layers to be retrieved. The thick lines solid polygons indicate areas of the profile where the profile values added to the error bars are still negative. In other words, the reconstructed concentration is still negative after adding the error [Bruns et al. 2006].

Passive DOAS tomography was also applied for volcanic plumes using several MAX-DOAS instruments [Wright et al, 2008; Johansson et al. 2009]. Both studies used only two scanning passive DOAS instruments. Although this setup is far from ideal, reasonable reconstructions can be achieved by involving additional physical assumptions. For volcanic applications these can be the known emission source at the crater and the assumption of a single Gaussian plume.

Another technique to monitor trace gas distributions with passive DOAS is the Imaging DOAS instrument [e.g. Louban et al., 2009]. It may derive maps of slant column signals, but not the true trace gas distribution. For simple distributions with one plume in the viewing direction like a volcanic plume, or a high way, this can be sufficient to derive information of the distribution. This technique was also applied to airborne measurements [Heue et al, 2008].

Inversion techniques similar to DOAS tomography are also used in other passive DOAS measurements. The best known one is the profile retrieval of trace gases and aerosols in the stratosphere and troposphere by satellite, balloon, airborne or ground based instruments [e.g. Rodgers, 1990; Friedeburg, 2003; Sinreich et al. 2005; Butz et al. 2006, Deutschmann, 2008]. All these retrievals typically use some kind of a-priori. In most cases this is an a priori profile and the a-priori error. The choice of the a-priori and other assumptions is problematic in the degree to which they influence the retrieval. Typically an exponentially decreasing profile is assumed.

For horizontal trace gas distributions in the boundary layer such assumptions can rarely be made, e.g. if strong sources exist (e.g. volcanoes, power plants). In urban areas the combination of a multitude of emission sources, transport and chemical transformation makes the formulation of a useful a-priori for some trace gases virtually impossible. As a consequence retrieval algorithms and parameters should be chosen to be less dependent on a-priori assumptions, e.g. by reducing the number of retrieved parameters, i.e. the spatial resolution.

There are other differences between active and passive tomographic observations worth mentioning: First, it should be considered that although passive DOAS tomography shows good results for some applications, it is not applicable for the determination of trace gas concentration distributions close to the ground as required for an urban area. The reason is that it allows only a limited vertical resolution of about hundred meters at the ground. Thus they do not observe the horizontal distribution at instrument level, but the averaged distribution of the lowest resolved box which may be significantly different. Secondly, passive measurements using scattered sunlight and thus require accurate radiative transport calculations, which strongly depend on the aerosol load. Uncertainties here directly affect the trace gas retrieval through errors in the air mass factors obtained from the radiative transfer modelling. The last point is that most passive tomographic DOAS instruments require sunlight and thus measurements are only possible during daylight.

## ***4.1 Principle of LP-DOAS Tomography***

LP-DOAS has well defined light path. Applying multiple LP-DOAS instruments measuring along a multitude number of light paths, tomographic principles can be applied. LP-DOAS tomography, like computerised tomography, uses the measured column densities to reconstruct the concentration distribution (Figure 4-6). While computerised tomography measures nearly complete projections of the distribution, this is not possible with the LP-DOAS technique. The number of light paths is limited, and so is the reconstruction resolution. The setup of 10 to 50 light paths seems realistic. This rather small number of paths requires special care when designing the observation geometry. A poor geometry leads to a reduction of reconstruction quality of the true distribution. For a given number of light paths the reconstruction generally improves for geometries with increasing number of telescopes [Hartl et al., 2006]. Geometries that give better results for negligible measurement errors and parts of the geometry that are better resolved are also less sensitive to increasing measurement errors [Hartl et al., 2006]. For a realisable number of light paths in an urban area at least three

telescopes are recommended. The discrete reconstruction approach employed in LP-DOAS tomography parameterises the unknown distribution by local piecewise constant or linear functions and solve the resulting discrete linear system by a least square minimum norm principle [Hartl et al., 2006]. This is basically the same principle as used in the linear part of the DOAS fit (*Chapter 3.5*). The main difference is that the latter represents a strongly over-determined system whereas the tomographic reconstructions here tend to be under-determined. Large differences in the reconstruction quality can arise between different geometries. Especially for narrow distributions the reconstruction error crucially depends on the resolution of the reconstruction grid which therefore should be chosen carefully.

In the optimal case, the measurements along the different light paths are performed simultaneously. If concentrations and distributions are constant over a certain time, also successive measurements are possible (e.g. street with relative constant emissions at constant wind). In most cases the absolute concentration and the distribution may change very fast within several minutes, e.g. if concentration plumes arise which are transported by the wind. Successively scanning along all light paths, which require for typical instruments at least few minutes per path, is then not practical and result in artefacts in the reconstruction. Therefore instruments are required which can perform the measurements of all light paths in a short time. The Multi Beam Instrument (MBI) was developed for this purpose and is described in (*Chapter 5*).

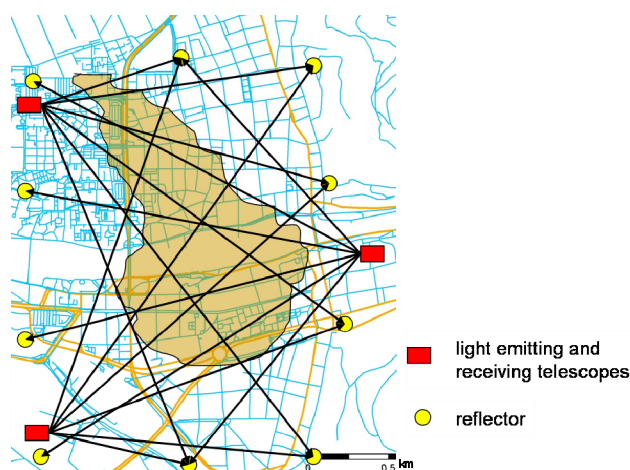


**Figure 4-6: Basic principle of an LP-DOAS tomography setup. Three telescopes measure the absorption column along several absorption light paths to a number of retro reflectors. A concentration distribution is reconstructed applying tomographic inversion techniques.**

First tomographic measurements employing the LP-DOAS technique were carried out to investigate the emission of a motorway [Pundt et al. 2005]. They used two telescopes pointing to two towers with each 8 retro reflector arrays and set up in total 16 light paths (Figure 4-7). Each telescope scanned consecutively eight light paths, four on the same side and 4 crossing the motorway. Measurements along all light paths could be realised within 45 minutes. The  $\text{NO}_2$  concentration field in the vertical plane, perpendicular to motorway direction, was retrieved with a temporal resolution of 4 hours. The inversion was performed with the SIRT method (see *Chapter 4.4*) with a  $4 \times 3$  bilinear interpolation model (200 iterations). The distribution displays the strong concentration increase close to the motor way and the plume propagation downwind. These results were, within all errors, in good agreement with model expectations [Laeppele et al. 2004].

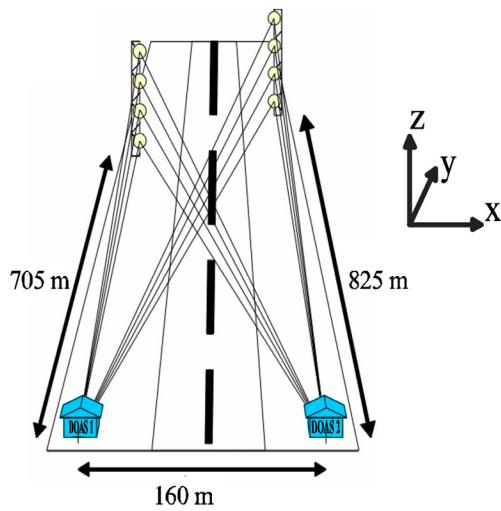


Figure 4-7: Tomographic setup employed for the motorway emission campaign. From each telescope (DOAS 1 and 2) eight light paths are directed towards the eight retro reflector arrays. Altogether eight light paths were located parallel to the motorway, and eight light paths were crossing the motorway. [adapted from Pundt et al., 2005]

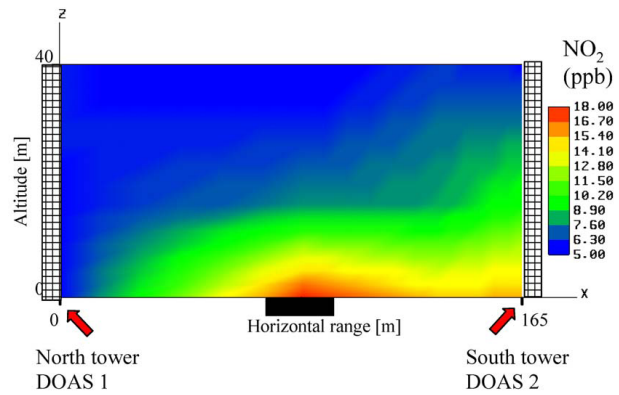


Figure 4-8: 2D reconstruction of the  $\text{NO}_2$  concentration field at right angles to the motorway (between the two towers and the two DOAS instruments) using the SART method (in ppb), 4 h average in the morning on 10 May 2001 (9:00–13:00 CET). Black bar: Location of the motorway, checkered areas: The two towers. [adapted from Pundt et al., 2005]

In an indoor experiment, horizontal LP-DOAS measurements and tomographic reconstructions were tested over an area of  $15 \times 10 \text{ m}^2$  [Mettendorf et al., 2006; Mettendorf, 2005]. 39 light paths crossed this area more or less in a regular geometry which was temporarily filled with one or two  $\text{NO}_2$  cylinders to simulate locally confined concentration fields, e.g. plumes emitted by a point source (Figure 4-9). The cylinders were additionally moved through the test field to simulate transport.

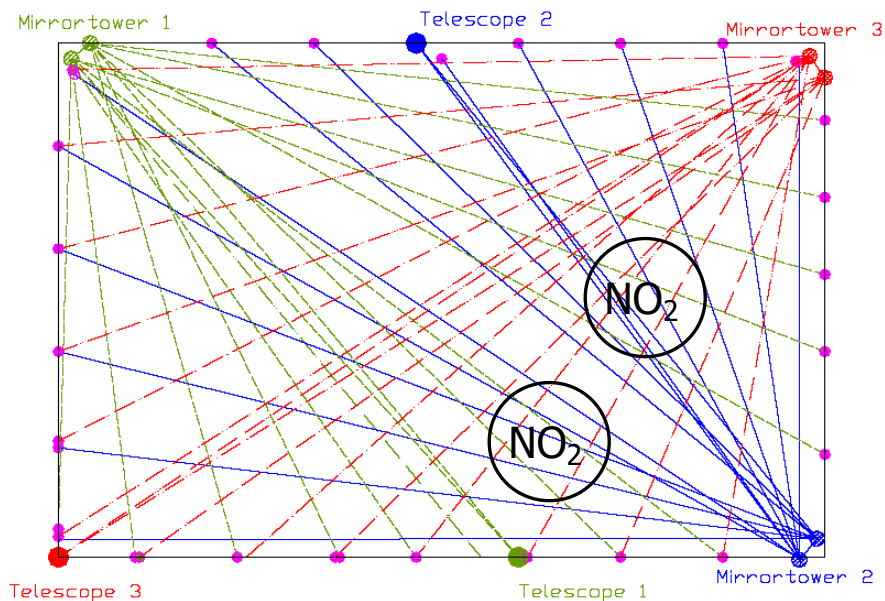
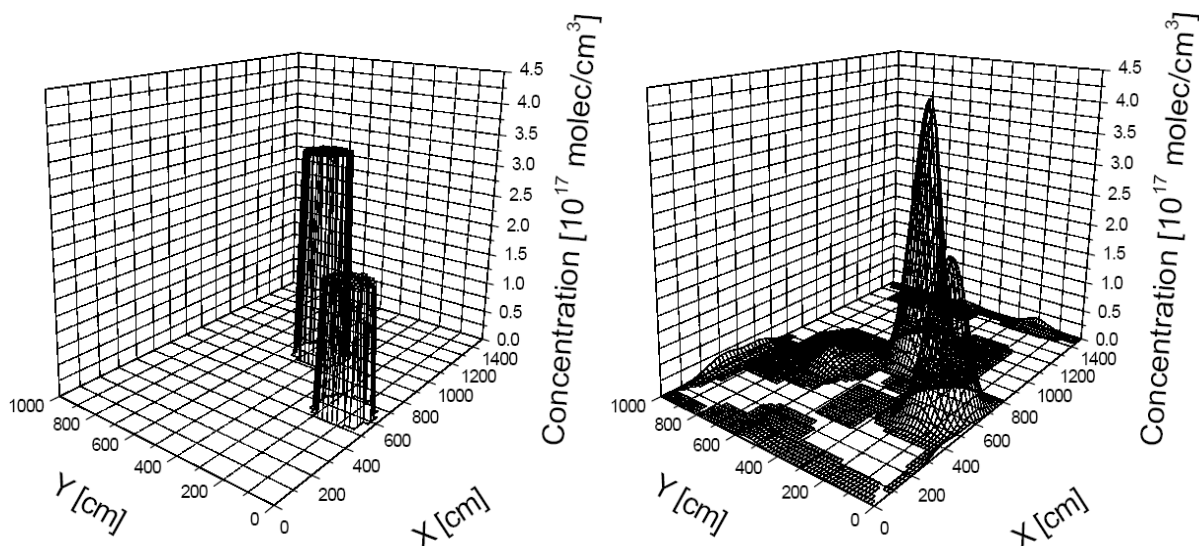


Figure 4-9: Sketch of the measurement setup for the indoor experiment. The light beams emitted and received by the telescopes are redirected and reflected by mirrors and reflectors, respectively. A more or less regular geometry could be achieved. [adapted from Mettendorf et al. 2006]

Bilinear box basis functions were applied (*Chapter 4.2*) as a more or less regular geometry could be realised. Due to their shape and the resolution, the exact shape of the cylinders could not be reproduced. However, the derived distribution from the measurement could very well reflect the artificial distribution (Figure 4-10). The location and concentration of NO<sub>2</sub> could be reconstructed within all errors.



**Figure 4-10: Reconstruction of the concentration distribution. Left: artificial distribution with NO<sub>2</sub> cells. Right: Reconstructed distribution with SIRT on a 12 × 12 grid with bilinear basis function. [adapted from Mettendorf et al. 2006]**

## 4.2 Tomographic Reconstruction

As already stated, tomographic LP- DOAS measurements are different from those in computerised tomography due to the limited number of line integrals. Established tomographic algorithms such as the filtered back projection rely on the measurement of many projections with many paths. These are strongly over-determined system as the number of reconstructed boxes is much smaller than the number of measured light paths. The unknown parameters are the values of the discrete concentration distribution. In contrast to these quasi-continuous inversion methods, LP-DOAS measurements only allow the reconstruction of a small number of parameters. One way of choosing these parameters is to discretise the probed volume so that the unknown parameters are the values of the now discrete concentration distribution. Numerical methods to solve the resulting discrete system of equations will be discussed later in *Chapter 4.4*.

The discretisation in a simple box model which may be achieved by dividing the reconstruction area into boxes with finite size in  $x$  and  $y$  direction, labelled by an index  $j$  (see *Chapter 4.5*, for reconstruction grid of Heidelberg see *Chapter 7.4.1*). For a light path  $i$  crossing box  $j$  the length inside the box is given by  $l_{i,j}$ . If  $c_j$  is the concentration inside the box, the partial column density inside this box will be given by:

$$S_{i,j} = l_{i,j} \cdot c_j \quad (\text{Eq. 4.1})$$

The total column density observed along this path is hence the sum of partial column densities:

$$S_i = \sum_j l_{i,j} \cdot c_j \tag{Eq. 4.2}$$

The length  $l$  is zero for those boxes which are not crossed by light path  $i$ . For all lines of sight and all boxes the length  $l$  can be defined. Eq. 4.2 can be written as a vector equation in the form of:

$$s = L \cdot c \tag{Eq. 4.3}$$

where  $s$  is the vector of the observed column densities,  $L$  is the matrix given by the different light paths in the boxes and  $c$  stands for the concentration in the boxes.

Mathematically, the discretisation described so far corresponds to a representation of the concentration field in terms of piecewise constant, so called, box basis function where the function coefficients are just the box mean concentrations (see Figure 4-11 (a)).

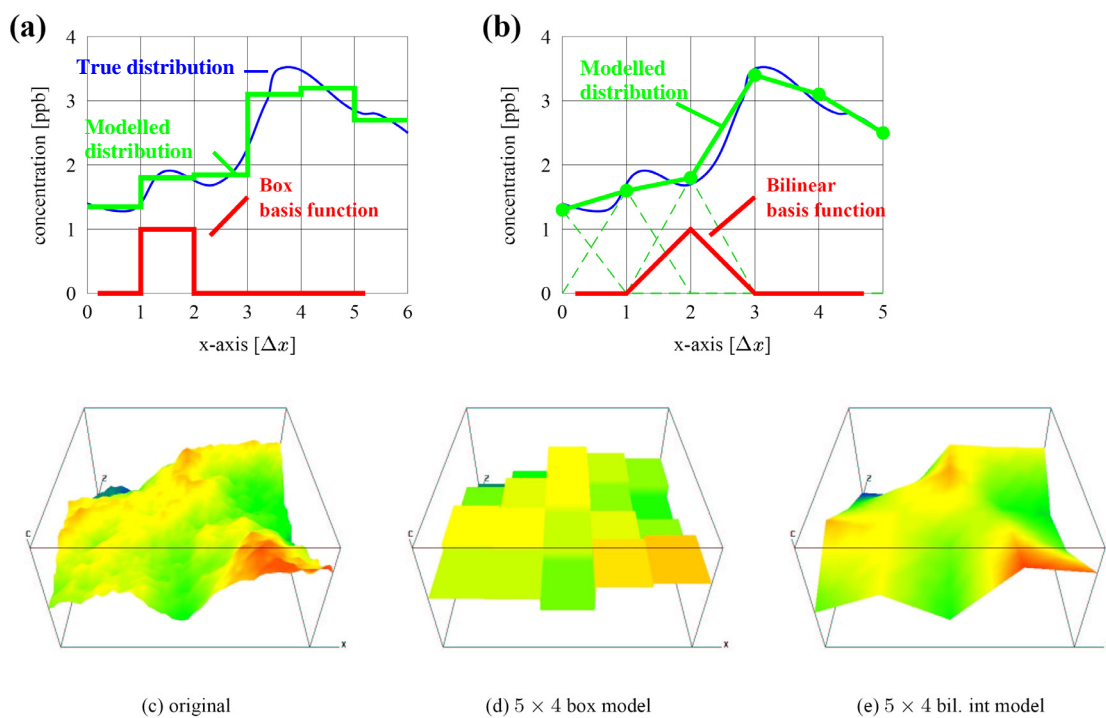


**Figure 4-11: Discretisation models.** The upper two subfigures show a 1-dimensional cross section of a concentration field. In the case of the box model (a) the true concentration field (blue) is approximated by a step function (green), which is constant within each box. For the bilinear interpolation model (b) the basis functions (red) are pyramid shaped. They have a value of one on the affiliated grid point and linearly reach zero on the neighbouring grid points. The resulting model function (green) is continuous and interpolates the values at the lattice points linearly. In subfigures (c), (d) and (e) the discrete modelling of a continuous 2-D function is visualized in colour contour plots: A continuous concentration field (c), its best approximation with the 5x4 box model (d) and the 5x4 bilinear interpolation model (e). [adapted from Laepple et al., 2004].

Other basis functions, like Gaussian or bilinear (Figure 4-11 (b)) [e.g. Inegessonnet al. 1998, Laepple et al., 2004] are possible as well. The latter have pyramid shape with value of one on a grid decreasing linearly to zero on the neighbouring grid point. Thus the resulting overall model function is continuous interpolating bilinearly between lattice points.

It is clear that bilinear basis function can describe a continuous field with peaks better and discretisation errors are reduced. This improves the inversion itself in comparison to the discontinuous box-basis functions [Laeppele et al., 2004]. Therefore they are mostly more appropriate to investigate concentration fields with peaks. In Figure 4-11 (c), (d) and (e), this is demonstrated by modelling a test concentration field using the two types of basis functions.

But significant disadvantages may arise by the use of bilinear box bass functions:

1. The concentration minimum/ maximum can only be located at a reconstruction grid point. Thus not the true location of the local minima/ maxima is observed.
2. For the retrieval more parameters are required, especially for non regular geometries. This is illustrated for two boxes of a reconstruction grid in Figure 4-12 and further described below.

The measurement geometry for Heidelberg (see *Chapter 6.2*) is drawn with lines and the overlaid reconstruction grid. In this example for the box basis function (a), two reconstruction boxes (red) suffice to describe a concentration gradient measured by the two absorption paths (they can even be merged to one) and thus two parameters which have to be determined. For the bilinear box basis function (b) for the same area at least 4 grid points are necessary with 4 unknown parameters. Thus the number of parameters increases and the system becomes under-determined. A modified bilinear discretisation with lower resolution can compensate this effect, but then the reconstruction grid may become less flexible. Therefore box like basis functions might be preferred for such irregular geometries Hartl [2007] and were applied for all final reconstructions of this thesis.

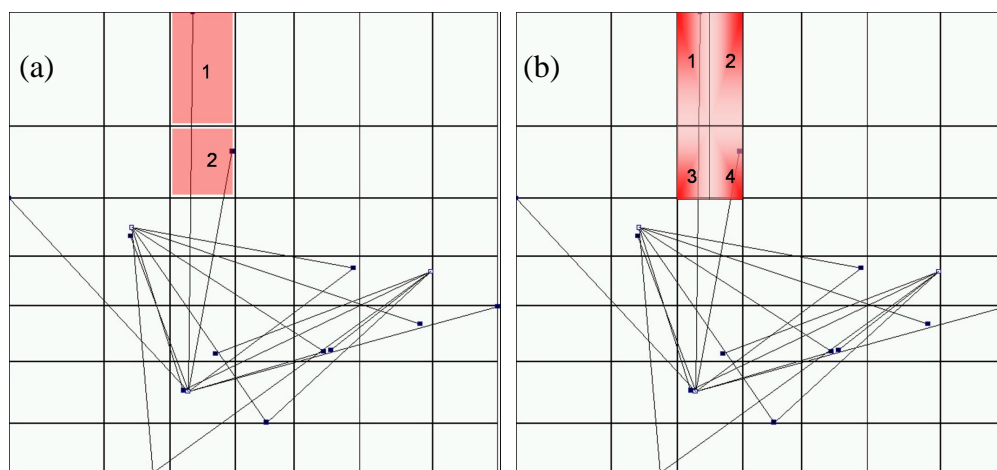


**Figure 4-12: Illustration of the increase of parameters for the bilinear box basis function for irregular geometries. Displayed are the tomographic LP-DOAS light beams (lines) for the measurements in Heidelberg (see Figure 6-6) and a reconstruction grid (Figure 7-12). For this irregular geometry for box like basis functions (a) two parameters have to be derived. For the bilinear basis functions (b), at least four parameters have to be retrieved with the same geometry.**

In the following, the reconstruction method is sketched for the case of box basis functions for simplicity. The case of bilinear reconstruction can be treated in the same way, details can be found in the works of [Laeppele et al., 2004], [Knab, 2003] and [Hartl, 2007].

The objective is to reconstruct the concentration distribution from the observation. Mathematical speaking the matrix equation  $s = L \cdot c$  needs to be solved. If  $L$  could be

inverted, this would be rather simple:  $L^{-1} \cdot s = L^{-1}L \cdot c = c$ . But the problem is ill-posed and cannot be inverted. The main reasons are:

1. A solution does not exist, or
2. A solution exists, but it is not unique
3. A solution exists, but is unstable, e.g. it is very sensitive to small changes of the data.

The first situation arises when the ideally existing true solution is corrupted by measurement errors. The second situation means that the complete solution cannot be inferred from the measurements alone and that further constraints are necessary to choose a particular solution. These two properties of the corresponding system of equations are not special to ill-posed problems, but the third is. It makes the numerically exact solution virtually useless, so that the original problem has to be reformulated to make it stable. This process is called regularisation.

The original ill-posed inverse problem is now restated as least-squares problem to overcome the points 1. and 2. above. This approach is similar to the DOAS analysis fit (see *Chapter 3.5*) where the data residuum is minimised:

$$r^2 = (s - L \cdot c)^T W (s - L \cdot c) = \min! \quad (\text{Eq. 4.4})$$

Weighting is included by the matrix  $W$ . This can be weighting by the measurement error, so that measurements with larger relative error are less weighted than those with smaller errors. For an over-determined problem with more integration paths than boxes, e.g. typical CT, Eq. 4.3 generates the unregularised least-squares solution. For an under-determined problem, e.g. LP-DOAS with relatively few data and thus possibly more boxes than light paths, the same minimisation problem produces the (unregularised) least-squares minimum norm solution [e.g. Hartl, 2006].

At first sight, a choice of the reconstruction grid that leads to an over-determined problem by reducing the number of grid points seems to be best. But it turns out that for the iterative algorithms discussed shortly, the under-determined problem with finer grids can in fact produce better solutions for certain kind of trace gas distributions consisting of local peaks [e.g. Hartl, 2006].

### ***4.3 Iterative Solution of the Least-Square Problem***

Iterative algorithms for least-squares problems have been extensively studied in image processing. The solution is regularised (*Chapter 4.2*, point 3.) by stopping the iteration prematurely before convergence to the exact but unstable solution is reached. We mention some characteristics common to their convergence behaviour when applied to ill-conditioned systems.

#### **Data residuum:**

For the iterative solution  $c^k$ , with  $k$  being the iteration step, the data residual  $r$  is represented by:

$$r = \sqrt{(s - L \cdot c^k)^T W (s - L \cdot c^k)} \quad (\text{Eq. 4.5})$$

Applying the modelled slant column for the iteration step  $k$  as:

$$s_{\text{mod}}^k = L \cdot c_{\text{mod}}^k \quad (\text{Eq. 4.6})$$

the equation can be expressed as:

$$r = \sqrt{\sum_i (s[i] - s_{\text{mod}}^k[i])^2} \quad (\text{Eq. 4.7})$$

with  $i$  being the index of the vector.

The data residuum will typically monotonically decrease during the iteration because the iterative algorithms which are considered here are constructed to reduce  $r$ , see Figure 4-13a). In the consistent under-determined case  $r$  can reach zero.

### Convergence rate

Without any errors  $c_{\text{mod}}^k$  will converge to the exact least-squares solution (or more precisely the least squares-minimum norm solution) with  $c_{\text{mod}}^\infty$  for  $k \rightarrow \infty$ , see Figure 4-13b). The difference between these two vectors  $v$  will decrease with increasing  $k$ . Convergence rates are conveniently analysed with the help of the singular value decomposition.

$$v = \sqrt{(c_{\text{mod}}^\infty - c_{\text{mod}}^k)^T (c_{\text{mod}}^\infty - c_{\text{mod}}^k)} = \sqrt{\sum_i (c_{\text{mod}}^\infty[i] - c_{\text{mod}}^k[i])^2} \quad (\text{Eq. 4.8})$$

### Regularisation

In the presence of errors  $e$ ,  $v_e$  typically shows a behaviour denoted as semi-convergence. In the beginning  $c_{\text{mod}}^k$  approaches the exact solution but deteriorates again for larger iteration numbers, see Figure 4-13c). The solution is regularised by stopping the iteration before this happens – ideally at the optimal iteration number like shown in Figure 7-22.

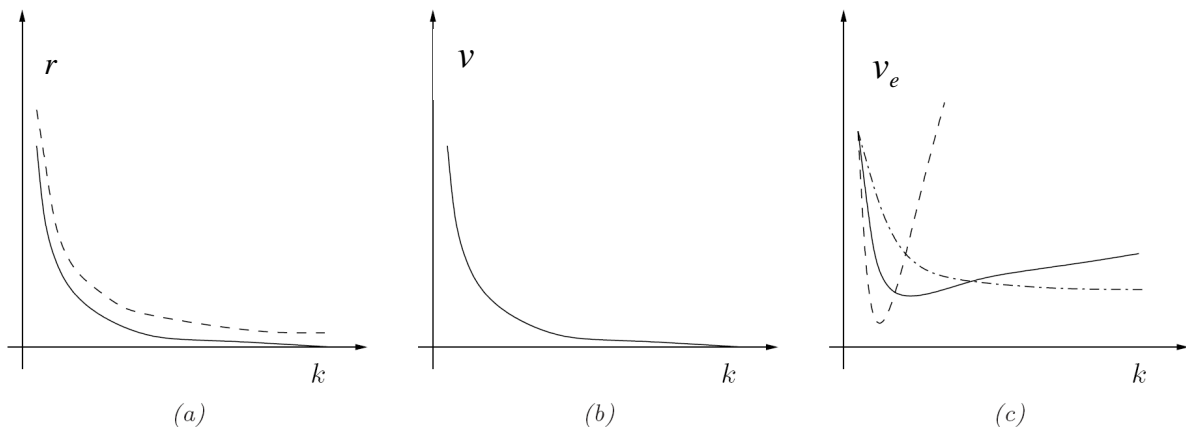


**Figure 4-13:** (a) Data residual versus iteration number  $k$  for the consistent (–) and inconsistent (––) case. (b) Without errors the iterative algorithm converges to the exact (least squares) solution. (c) Typical behaviour of iterative algorithms if errors are present (semiconvergence). The lines in the example correspond to ART algorithm for the solid line (–), CG method (––) and Landweber iteration (–·–) [adapted from Hartl, 2006 with plots from Hansen, 1998].

## 4.4 Algebraic Reconstruction Methods

Iterative projection algorithms converging to least squares solutions of the above kind have been studied extensively in image reconstruction to solve large systems of equations. Three iterative projection algorithms are:

- Algebraic Reconstruction Technique (ART)
- Simultaneous Algebraic Reconstruction Technique (SART)
- Simultaneous Iterative Reconstruction Technique (SIRT)

ART applies corrections of the data residuum sequentially corresponding to the rows in Eq. 4.4 starting with a given  $c_0$ . This technique is reported as best when no noise is present [Hartl et al., 2006]. SART and SIRT apply corrections simultaneously for all rows. They work better when noise is present, but convergence is slower than with sequential methods. The order of the algorithms is  $\text{ART} > \text{SART} > \text{SIRT}$  [Todd and Ramachandran, 1994; Laepple et al. 2004]. With substantial noise, this order of the algorithms is reversed.

The applications of these methods to LP-DOAS tomography is studied by Laepple et al. [2004], Knab [2003], Hartl et al. [2006] and Hartl [2007]. SART weights light paths with the inverse of their length and boxes with the partial light path lengths added up in the boxes. SIRT does not weight boxes whereas light paths get weights inverse to the square of the partial path lengths. The convergence of ART is more involved, but corresponds to SIRT in the consistent case. Favouring better sampled pixels seems to be reasonable, but weighting paths inverse to their length is contradictive to LP-DOAS, where relative measurement errors decrease with increasing absorption path length.

The studies of Hartl et al. [2006], Hartl [2007] conclude that among these three algorithms the best algorithm for horizontal LP-DOAS tomographic measurements is SIRT, which is used in this study. Mathematical details on the iterative reconstruction can be found in these references.

The determination of the optimal iteration steps depends not only on the measurement error but also on the kind of trace gas distribution. Simulations show (*Chapter 7.4.3*) that for the geometry of our measurement, e.g. relative data errors of around 10 % and concentration peaks on a substantial background, the iteration should be stopped after about 20 steps to achieve optimal results.

## 4.5 Measurement Geometry

LP-DOAS tomography measurements are not only limited by the number of possible light paths, as mentioned above, but also in the geometry if performed in an urban area. Large differences in the reconstruction quality could be found between different theoretical geometries [Hartl et al. 2006]. Increasing the number of telescopes for the same number of light paths leads to better reconstruction results, provided that the coverage with light paths can be kept regular and does not decrease. Also the measurement errors have less impact on better geometries, but the sensitivity varies within the area and seems to be weaker for better

resolved regions. For the number of light paths in question these simulations suggest a number of three telescopes to be a good choice. While a fairly optimised geometry with three instruments could be set up in an indoor test experiment [Mettendorf et al., 2006; see Figure 4-9], the light paths in this work were mainly dictated by suitable locations for instruments and reflectors, so that the geometry consisting of 18 paths is far from perfect. This will also apply for other tomographic setups in urban areas. The whole setup is described in *Chapter 6*.

## ***4.6 Reconstruction Grid***

Reconstruction errors and the inaccuracy of reconstructed total amounts of trace gas concentrations can be significantly reduced by choosing an optimal dimension of the reconstruction grid [Hartl et al., 2006]. A grid translation scheme adopted from Verkruyssen and Todd [2004] that averages reconstruction results of several reconstruction grids shifted against each other reduces total reconstruction errors and accidental features of a single reconstruction grid and can therefore help with the a-priori choice of the reconstruction grid. In general it does not lead to better estimation of total amounts of concentration and underestimates peak maxima [Hartl et al., 2006].

In an actual tomographic LP-DOAS setup, the density of light paths will be different for different boxes. Generally it can be assumed that the concentration is better represented in areas with many intersecting light paths. Areas at the edge of the measurement area are likely to be poorer represented and will feature larger errors in the reconstructed concentrations than those in the centre with many intersecting light beams.

Depending on the number of boxes chosen, the reconstruction grid can lead to an over- or under-determined set of equations. Due to the small number of light paths for LP-DOAS tomography it is generally under-determined or (nominally) slightly over-determined. An under-determined grid should be applied with care and be tested with simulation concentration fields.

Simulated reconstructions are not only useful to test geometry and grid, but can also be the best way to determine the choice of the regularisation parameter (here iteration number) if no other criteria for its choice is employed.

The reconstruction grids applied to the measurements in Heidelberg will be discussed in *Chapter 7.4.1*. The simulations for these grids performed with different distributions are presented in *Chapter 7.4.2*.

## ***4.7 Limits of LP-DOAS Tomography***

From the above description of the inversion of trace gas distributions it is clear that only an approximation of the true distribution can be achieved. Additionally, with increasing measurement error, the accuracy of the determined distribution reduces as the inverse problem amplifies the error.

Tomographic LP-DOAS measurements rely on the setup and coverage of the absorption light paths, which will not cover the whole area. Thus the detection of plumes is limited to the realised spatial resolution. That means that a local point source can not be observed if it is

located between measurement paths.

Even if a very local concentration peak is observed with a measurement path, it may not show up in the reconstruction, if the resolution of the reconstruction grid is too low. The highest resolved reconstruction grid possible limits the detection of concentration peaks. Smaller peaks are averaged over the reconstruction box, and can only be determined if the concentration is very high so that the concentration of the box is significantly changed. For the setup in Heidelberg this spatial limitation is discussed in *Chapter 7.4.2* and *7.4.4*.

A good 2-D tomographic LP-DOAS setup should not only display a regular geometry, but also all measurement paths should be at the same height, as the reconstruction assumes that no vertical concentration variation occurs between the paths. If this is not the case any vertical gradient can influence the reconstructed concentration field. In a setup above an urban area, like in this thesis, this requirement can not be completely fulfilled. Systematic errors will arise in the retrieved 2-D horizontal concentration distribution. This can only be overcome by 3-D measurements and retrievals with sufficient number of measurement paths.

Artefacts in the reconstructed trace gas distribution for the applied geometry and reconstruction grid are discussed in *Chapter 7.4.4*.

## 5 Measurement Instruments

For the reconstruction of two dimensional trace gas distributions using LP-DOAS measurements the number of light paths influences the spatial resolution. For a sufficient characterisation of a distribution at least 10 to 20 light paths are required. Conventional LP-DOAS telescopes can only emit and detect one light beam. For the measurements along multiple light paths the whole telescope has to be moved, so that the light beam is aligned to the next retro reflector array. This was done for tomographic measurements in the BAB II campaign [Pundt et al., 2005]. The scanning with these conventional instruments led to a drastically decrease in time resolution. Thus tomography on a reasonable time scale is almost impossible. One solution might be to use a multitude of LP-DOAS instruments, what was unrealistic for the so far used Newton telescopes due to their costs (of purchase), operation demand and size. To solve this problem a Multibeam LP-DOAS instrument (MBI) was developed by Pundt and Mettendorf [2005], which allows the measurement along four light paths simultaneously. By scanning the light beams, measurements can be performed even along more light paths in a short time. When using three of these MBI instruments up to 22 light paths in less than 15 minutes cover the investigation area. *Chapter 5.1* will briefly introduce the LP-DOAS instrument and the differences to the MBI. More details can be found in the work of Mettendorf [2005].

In this thesis these instruments were applied for the first time in an urban area. Due to the high demands for outdoor measurements, several modifications were necessary for reliable long term operation. They are described in the following chapters. The different components of the system and their characterisation are outlined. A new high speed spectrograph shutter was developed for the application in spectroscopy (*Chapter 5.3.2*). An automation of the measurement procedure was implemented with background and shortcut measurements (*Chapter 5.2* and *5.2.4*). The light reflection from retro reflectors is characterised in *Chapter 5.4*. A measurement software was developed for the controlling of the system and performing all required adjustments automatically (*Chapter 5.5*). The application of this setup in Heidelberg and the measurement geometry will be discussed in *Chapter 6*.

With progress in LP-DOAS technology, new instrumentations become available which dramatically reduce the technical demands of a setup. Tomographic measurements with such new LP-DOAS instruments in the future make the setup simpler and cheaper. The main improvements in LP-DOAS technology will be summarised in *Chapter 5.6*. Some of these new instruments which are applicable to new tomographic LP-DOAS measurements are tested and will be discussed in this chapter.

Beside LP-DOAS measurements of trace gases, data from in-situ monitors are used in this thesis. These monitors are introduced in *Chapter 5.7*.

For the investigation of meteorological conditions, data from the meteorological station at the IUP are used and additionally two mobile stations were installed at the two other instrument locations. The characterisation of these stations is presented in *Chapter 5.8*.

## 5.1 The Principle of Long Path-DOAS and Multibeam Instruments (MBI)

The conventional Long Path-DOAS (LP-DOAS) instrument is based on the principle of the telescope of Axelsson et al. [1990] with improvements of Stutz and Platt [1997]. The setup is similar to a Newton telescope. Figure 5-1 shows the sketch of the optical path of such a telescope.

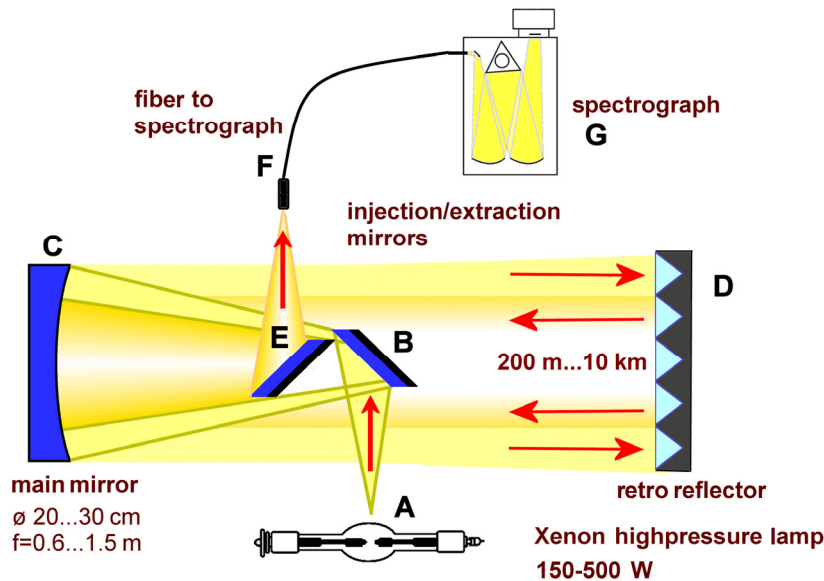


**Figure 5-1:** LP DOAS instrument as introduced by [Axelsson et al., 1990] with emitting and receiving optics in one telescope (A – Xenon lamp, B – in-coupling (injection) mirror, C – spherical main mirror, D – retro reflector array, E – out-coupling (extraction) mirror). [adapted from Merten et al. 2010].

The light from an artificial light source (e.g. high pressure xenon arc lamp) is coupled into the telescope through mirror B, redirected to the spherical main mirror C, and then emitted as almost parallel beam to a retro reflector array D. The light that reaches the reflector is redirected back to the telescope. Due to a small offset in reflection and atmospheric expansion of the light beam, the received light beam at the telescope also covers some parts of the mirror C, which were not illuminated by the light source in the first place. Parts of the light are coupled through mirror E into a fibre and contain the absorption information. This instrument allows only the measurement along one light path. For the observation along several paths, the telescope has to be adjusted to another reflector.

The MBI instrument is a telescope of Axelsson et al. [1990] modified in a way that one telescope is able to emit and receive 4 light beams. This can be achieved by placing 4 light sources close to the point of the original lamp arc place (focal plane of the main mirror C). Then the telescope would emit four parallel light beams with a small angle to each other, all located around the optical axis (Figure 5-2). As using four lamps is unnecessary and not practical, the light of one lamp is redirected by four small “lamp house mirrors” to create four virtual light sources. The angle of the emitting light beam to the optical axis depends mainly on the position of the lamp house mirrors. A simplified sketch of the MBI principle is shown in Figure 5-2 for two light beams. Additional two light beams can be realised by the

separation of the two sketched beams in the image plane and thus in total 4 beams are created. A picture of the lamp house with lamp house mirrors can be found in Figure 5-3.

Like in the telescope from Axelsson et al. [1990], the in-coupling and out-coupling mirrors are positioned inside the telescope. Only a ring of light will reach the main mirror, as the light from each virtual light source redirected from the in-coupling mirror to the main spherical mirror is partly shaded by the out-coupling mirror. Thus, the emitted parallel light beam also features a ring. In practise, the light is slightly focused onto the retro reflector so that a full light beam reaches the reflector.

After reflection at the retro reflector array, the received light has the same angle to the optical axis as the emitted one. Hence each light beam has a different focus and can be coupled into different fibres (Figure 5-7). Due to practical reasons the in- and out-coupling mirrors are rotated by  $90^\circ$ . Thus the in-coupling is performed in the horizontal plane and the out-coupling in the vertical plane of the main optical axis (in the simplified sketch of Figure 5-2 both are in the same plane).

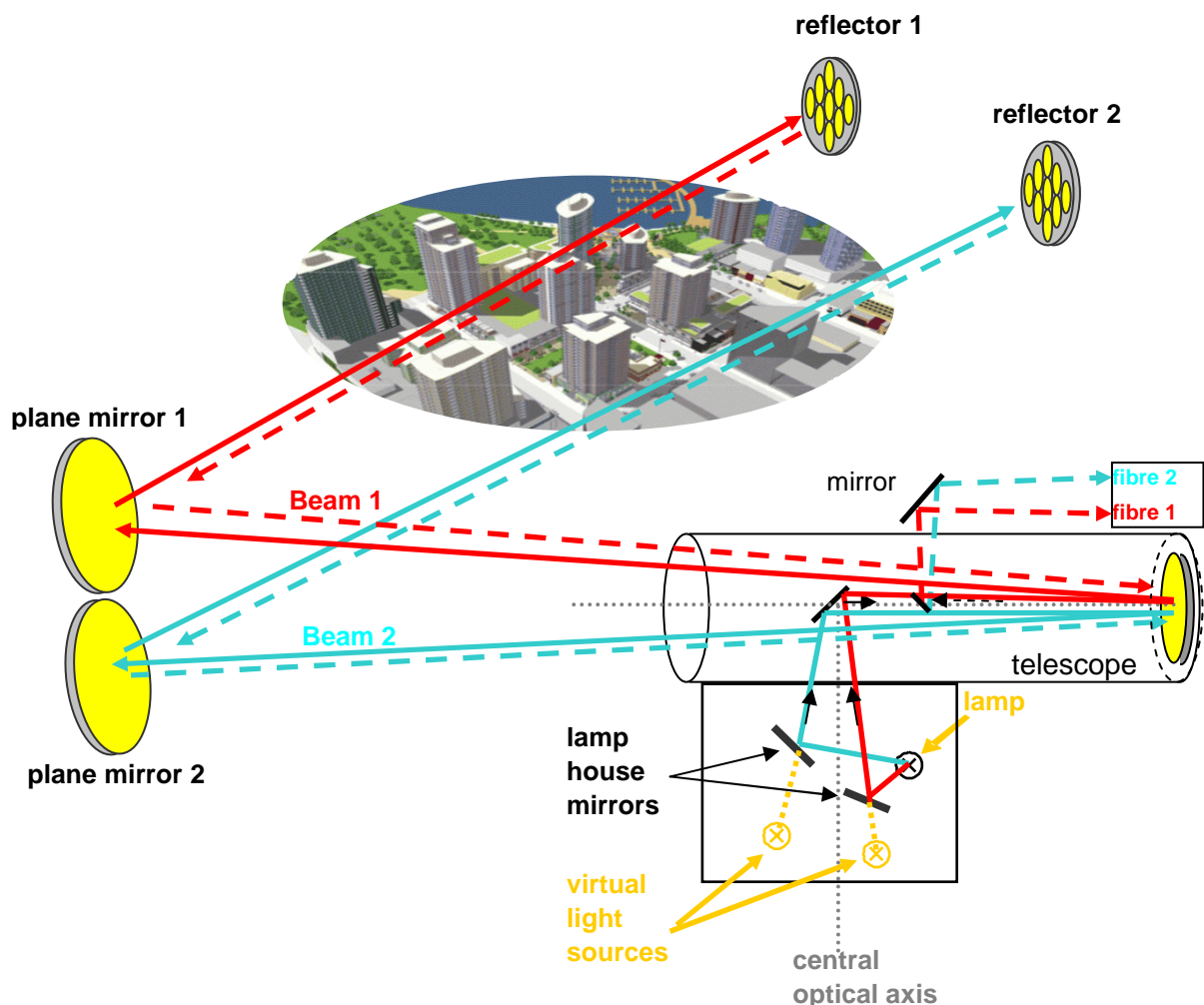
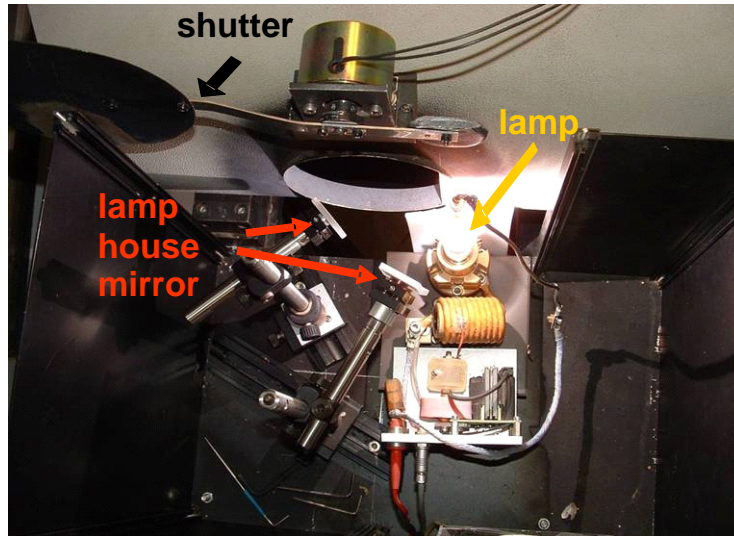
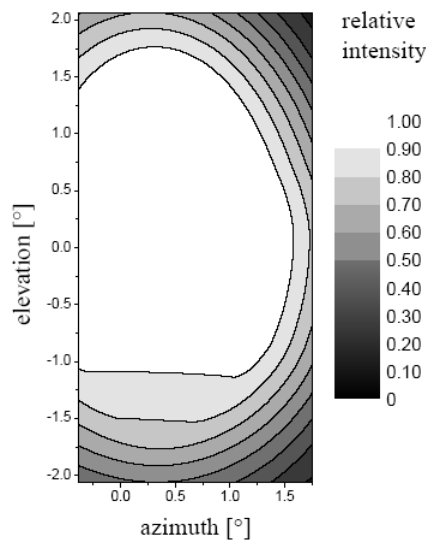


Figure 5-2: Simplified sketch of the MBI principle. Two lamp house mirrors create two virtual light sources which are slightly shifted from the central optical axis. They create two emitting telescope light beams with a small angle to each other. In a distance of at least 15 m the beams are separated from each other and can be redirected to different retro reflectors in the city with two plane mirrors. The reflected light is also redirected over the external mirrors to the telescope and then focused on the fibres.



**Figure 5-3:** Picture of the lamp housing with two lamp house mirrors in the horizontal plane. Additional two mirrors are below the two labelled mirrors. A lamp blocker allows interrupting the light of the lamp to perform background measurements.

As the emitted parallel light beams from the telescope have only small angles to each other, they cannot be adjusted directly along different measurement paths to different retro reflector arrays. The restriction arises from the limitation of the lamp house mirror positions. With larger offset from the central optic axis, the emitted and received light intensity decreases. The loss can be approximated by calculations of lamp radiation and telescope configuration. High losses arise for angles larger than  $1.5^\circ$  [Pundt and Mettendorf, 2005] (see Figure 5-4). Additionally the optical configuration only allows an increase to one horizontal direction (positive azimuth in Figure 5-4), as direct light from the lamp is prevented by a metal plate. This sheet would also block the light from lamp house mirrors with a negative azimuth angle.



**Figure 5-4:** Calculated relative intensity as a function of the “elevation” and “azimuth” angles (the “elevation” is defined as the vertical angle above the horizontal of the optical axis, and the “azimuth” as the angle in horizontal direction from the optical axis). The lamp intensity emission as well as the MBI transmission are accounted. Apertures and mirror size reduce the intensities significantly for larger elevation and azimuth angles. The lamp itself emits in the azimuth direction equal intensities. [adapted from Pundt and Mettendorf, 2005].

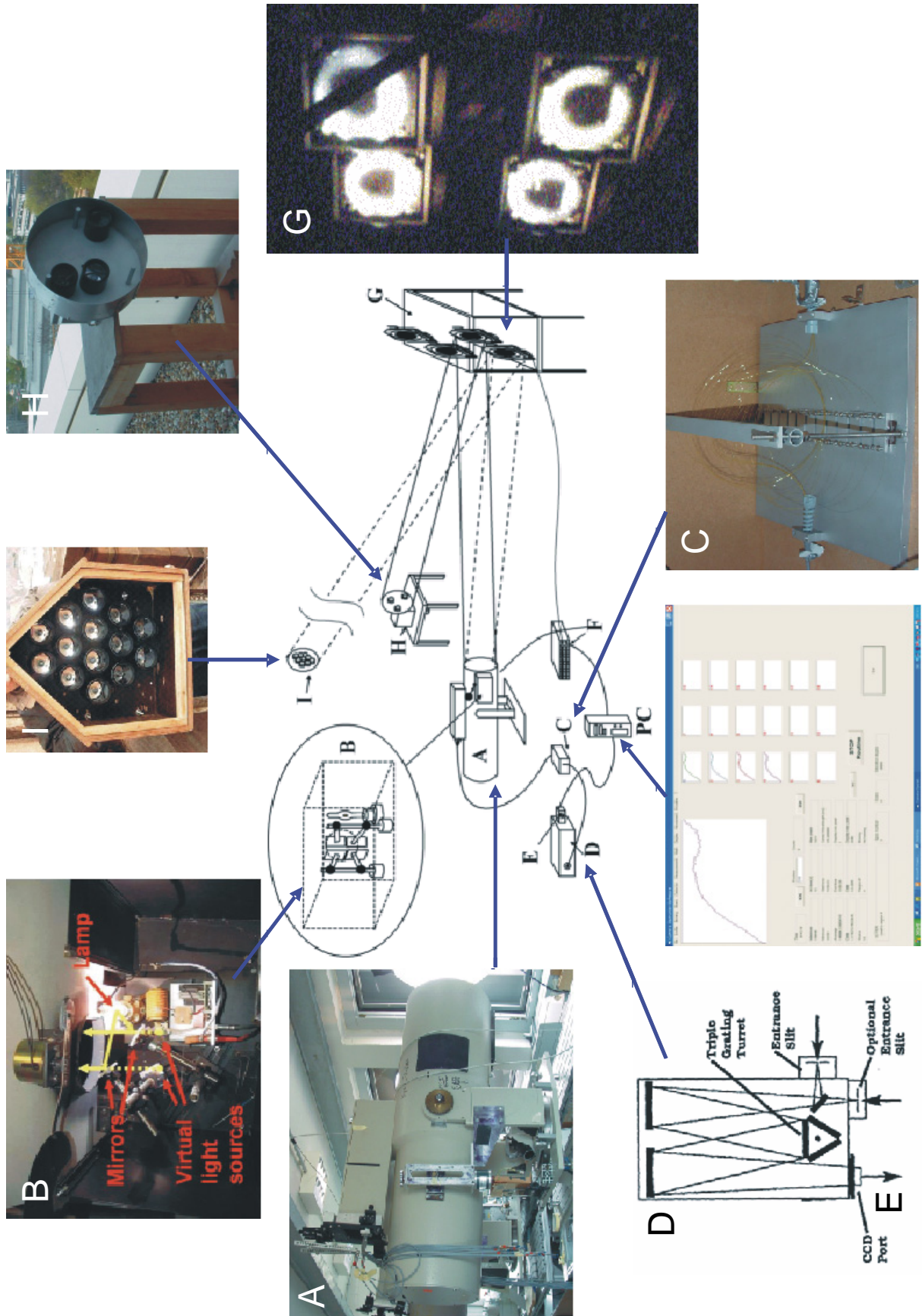


Figure 5-5: Schematic configuration of a MBI setup, consists of a telescope (A), a lamp housing (B), a mode mixer (C), a spectrograph (D) with a CCD camera (E). The stepper motor controller (F) can move the external mirrors (G) to different retro reflector arrays (I). For short cut measurements of the emitted spectra the light can be redirected to a near rotating retro array (H). The distance between telescope (A) and external mirrors (G) is between 15m and 100m.

Thus the light beams emitted by the telescope will have only a slight angle to each other, insufficient to redirect them to different retro reflector arrays directly. Therefore additional external mirrors in a distance of 15 to 100 m in front of the telescope are used (see *Chapter 5.2.2*). They redirect the light beams to the different retro reflector arrays (Figure 5-2). The mirrors are fixed to mirror holders with stepper motors in the horizontal and vertical direction. This gives the possibility to redirect one light beam to multiple retro reflector arrays.

A maximum azimuth angle of 2 degrees can be achieved between two emitted telescope light beams. Pundt and Mettendorf [2005] estimated that with this setup, up six or even nine light beams can be emitted with one telescope. In the framework of this thesis such an adjustment with six light beams was tested, but it proved that this setup is not useful for measurements due to four reasons:

- First, the emitted light beam had a very different intensity (Figure 5-4). But for the measurement of all light beams with one spectrometer (see *Chapter 5.3.1*) the intensities should be similar. For atmospheric measurements this effect can be compensated as some longer absorption paths have a higher light loss. But for the lamp reference measurement with the shortcut system (see *Chapter 5.2.4*) this is not possible.
- Second, the light beam with lowest intensity defines the total measurement time of a sequence to achieve at least a comparable measurement quality. As the light beams at the edge feature very low intensity, the total sampling time increased drastically.
- Third, with increasing elevation angle the lamp house mirrors point on the lamp under a larger elevation angle (not perpendicular anymore). This not only leads to a reduction of intensity (Figure 5-4), but additionally to an increase in broad-band and narrow-band spectral structures arising from xenon emissions. As these structures are not stable with time they lead to larger measurement error.
- Fourth, for most setups on a roof the distance to the external mirrors is limited. The used mirror system requires a separation of at least 50 cm (gap of 20 cm between the light beams). Thus for 6 light beams and an maximal offset of 2°, at least 29 m are required between telescope and external mirrors. This can not be realised on most available locations where the instruments are installed.

An overview of a full MBI setup with images of the applied instruments is given in Figure 5-5. The components are outlined in the following chapters.

## ***5.2 The Multibeam Instrument (MBI) Setup***

For the tomographic measurements in Heidelberg three MBI instruments were applied. Two of the instruments (“Hydra” and “Long”) are commercially manufactured at the Anhui Institute of Optics and Fine Mechanics, Hefei (China) and were already used for different campaigns and an indoor test campaign for the tomographic LP-DOAS technique [e.g. Mettendorf, 2005; Hak, 2006, Mettendorf et al. 2006]. The third telescope (“Cube”) was constructed within this thesis for the tomographic measurements in Heidelberg. The following

chapter will shortly outline the construction of this telescope.

### 5.2.1 The “Cube” MBI Telescope

The “Cube” telescope is a self-construction based on aluminium profiles (ISEL automation) to set up the basic frame and the telescope tube. All optical components like mirrors, fibre, lamp housing and lamp shutter were fixed on the aluminium profile. The profile systems allowed changing the position of any component and thus the easy adjustment in all dimensions. The telescope frame was covered with aluminium plates attached with hinges to allow fast access and painted black to reduce scattered light.

In comparison to standard LP DOAS telescopes the MBI does not need to be permanently adjusted onto the retro reflector. The adjustment is achieved by using motorised external mirrors. But still a horizontal and vertical operation is necessary to align the emitted light beams onto the external mirrors. The horizontal adjustment was achieved with a rotary table between basic frame and telescope. The vertical adjustment is achieved by two extendable front legs attached to the frame with rails.

The properties of the optical components are summarised in Table 5-1

Mirror	size	focal length
Main	Ø 300 mm	1500 mm
in coupling	148 × 128 mm <sup>2</sup>	plane
out coupling	150 × 106 mm <sup>2</sup>	plane
lamp house	20 × 30 mm <sup>2</sup>	plane

**Table 5-1: Size and focal length of the used mirrors in the MBI telescope.**

The received light is guided via 200 µm quartz glass fibres to the spectrometer. The fibres are adjusted to the focal point by using X-Y-Z translation stage. In previous measurements de-adjustment of the fibre position arose. The reason was identified as small vibrations of the telescope which lead to a slow change of the screw position. The problem could be solved by locking the translation stage after adjustment.

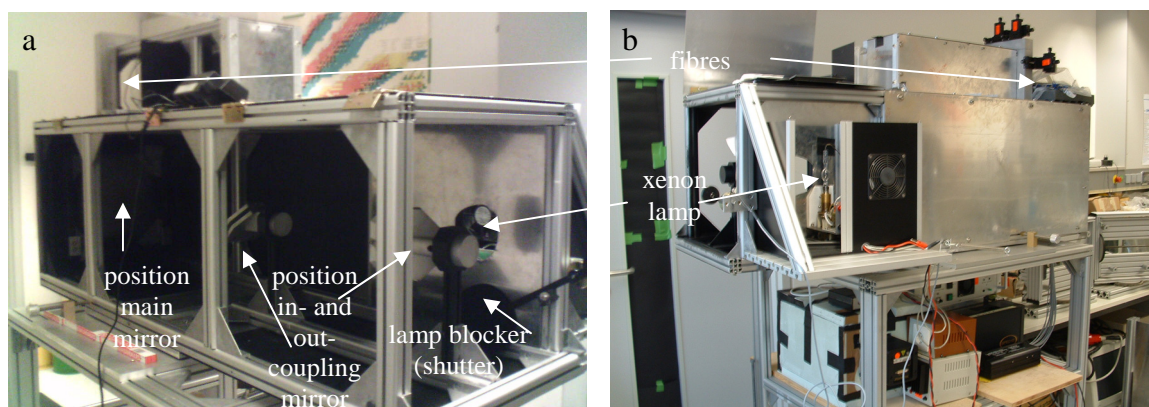


**Figure 5-6: Pictures of the “Cube” MBI during construction. For the frame an ISEL aluminium profiles is used which was than covered with aluminium plates painted black.**

Accurate LP-DOAS measurements require the correction of background light entering the

telescope (mainly sunlight scattered into the light path). Thus separate and automatic measurements of this background spectrum are required. This was achieved by blocking the light with a shutter between lamp house and telescope (see Figure 5-6). The shutter is driven by a rotary magnet and controlled by a TTL controller box.

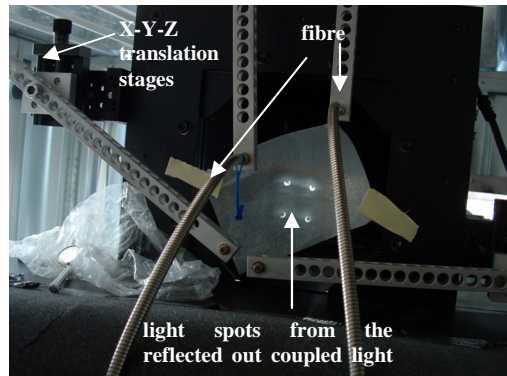


**Figure 5-7:** Picture of the out-coupled light at the fibres before fibres are adjusted to the focal point. On the optical paper (few cm in front of the focal plane) the reflections from the four light beams are visible in form of spots. The adjustment of the fibre is made using X-Y-Z translation stages.

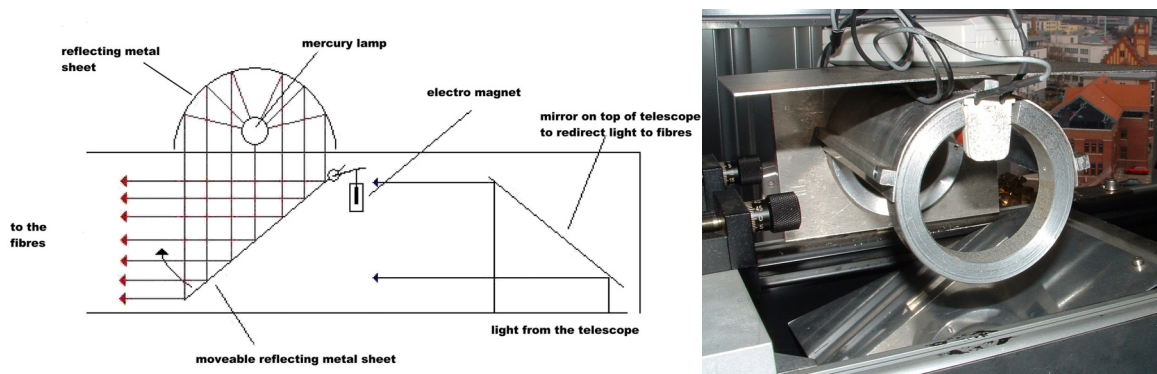


**Figure 5-8:** Sketch of the applied setup for automatic mercury calibration lamp measurements and the picture of the construction at the CUBE telescope. Due to the reflection of the mercury spectrum at the reflecting metal plate, all fibres are equally illuminated.

Additionally during long term observations, measurements of calibration spectra are required, as small changes in temperature and pressure can change the spectral calibration of the spectrometer detector unit. In the applied UV spectral range mercury lamps display several strong emission lines which can be used for the calibration. The installed automatic mercury measurement system provided an equally illumination of all fibres at the same time (Figure 5-8). A polished reflecting aluminium plate was used to reflect the light of the mercury lamp into the fibres. An electromagnet moves the plate into the viewing direction of the fibres and blocks all other light from the telescope.

## 5.2.2 The External Mirrors

The external mirrors redirect the emitted light beams of the telescope to the different retro reflector arrays. They can be placed 15 to 100 m in front of the telescope. As most roofs do not provide sufficient space, the external mirrors can also be placed on a neighbouring roof (like done at the IUP, see *Chapter 6.3.1*). In this chapter the configuration and the properties of the applied external mirrors are presented.

The flat external mirrors have to be larger than the light beam diameter of 30 cm, as the required reflection surface increases with increasing deflection angle. The used mirrors with aluminium coating have a size of  $36 \times 32 \text{ cm}^2$  and a thickness of 4 cm. The thickness is required to guarantee a sufficient flat surface, else additional optical losses due to inaccuracy of the reflection (broadening of the light beam) arise. The surface has a protective layer of  $\text{SiO}_2$  which is UV transparent and water resistant. Thus the mirrors could be exposed to outdoor conditions where rain and dust contaminated the mirror surface. A small roof protected the mirror from most rain. The mirrors were regularly cleaned by rinsing pure water over the reflecting surface. Still degradation in the reflection led to significant loss in light intensity of up to 50 %.

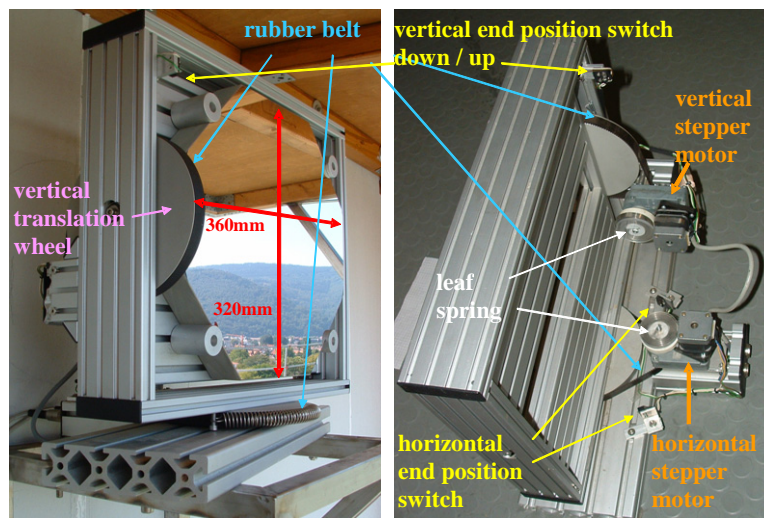


**Figure 5-9: External mirror frame with mirror. The size of each mirror is  $360 \times 320 \text{ mm}^2$ . The frame can be moved  $30^\circ$  horizontally and  $15^\circ$  vertically. 12 of these frames are used for tomographic setup of three MBI.**

The mirrors were placed in a motorised mirror mounting manufactured by “Hoffmann Messtechnik” (HMT) with the following features:

- maximum mirror size:  $365 \times 325 \text{ mm}^2$
- two separate stepper motors for horizontal and vertical moving
- tolerance in horizontal gearing is reduced with a leaf spring, vertical due to the weight of the mirror
- horizontal:  $\pm 30^\circ$  (redirection of light beam  $\pm 60^\circ$ ) with  $\sim 43,000$  motor steps
- vertical:  $\pm 15^\circ$  (redirection of light beam  $\pm 30^\circ$ ) with  $\sim 21,500$  motor steps
- resolution for the light beam position:  $(1.41 \pm 0.01) \times 10^{-3^\circ}$  / motor step (measured experimentally)
- accuracy in the laboratory:  $\pm 1$  motor step
- accuracy in the field: depends on weather conditions, but was  $> 30$  motor steps if strong wind arose
- translation with a rubber belt: 1:50

The stepper motors of these mountings were controlled by a Multistepper Controller from the

same company.

In the first measurements of this thesis it could be demonstrated that these mirror mounts are not suitable for outdoor application if wind arose. As for a setup in an urban area these mirror mounts are installed on a roof, they are permanently exposed to strong winds. A short summary of the technical problems are given and the modifications to make them applicable for outdoor measurements.

### Slack in Mirror Position

The mirror is driven by stepper motors. The movement was transmitted with a rubber belt. The belt moves the mirror just by friction, as the large translation wheel on the mirror mounting has no teeth. With changing temperature the length and precision of this belt changed. In worst case the friction decreased (e.g. belt length increased or rubber indurate) and the mirror rotated below the rubber. Thus, the mirror position was unintentional changed. A fixation of the belt to the large wheel was applied in a way, that in an accidentally case the fixation could brake and no damage to the mechanics and mirror arose. To minimize the slack due to temperature expansion, the tension has to be adjusted regularly. Still problems of the mirror adjustment occurred, as the adjustment could not guarantee a precise positioning of the light beam. The position of the lamp arc on the retro reflector was a smaller problem, as the lamp arc of the applied XBO 500 was relatively large with 0.7 mm in diameter. Mainly the back reflection into the fibre requires a high accuracy, as the fibre diameter is only 200  $\mu\text{m}$ . The slack of the gearing and the belt expansion did not provide sufficient accuracy.

In the following an estimation is made how precise the mirror positioning has to be to receive the transmitted light in the fibre. It is investigated how belt extensions can lead to a loss of reflected light in the fibre and which forces are required for this.

The required specifications for an estimation of the accuracy are the following:

- belt expansion:  $\Delta L_{belt,250N}^{\%} = 0.2 \%$  at  $F_{belt2\%} = 250 \text{ N}$
- free length of the belt between cogwheel and translation wheel:  $L_{belt} > 0.10 \text{ m}$
- diameter translation wheel:  $D_{wheel} = 0.16 \text{ m}$
- telescope focal length:  $f = 1500 \text{ mm}$
- diameter of the fibre:  $D_{fibre} = 200 \mu\text{m}$
- diameter of the lamp arc:  $D_{Lamp} > 700 \mu\text{m}$
- size of the mirror frame:  $D_{Fram} = 0.41 \text{ m}$  (width)
- average retro reflector distance:  $L_{Retro} = 2000 \text{ m}$
- average retro reflector array diameter at 2000 m (7 single reflectors):  $D_{Retro} \sim 0.2 \text{ m}$

The clearance of the transmission is neglected for this estimation, thus perfect mechanical components are assumed. The optical setup of the receiving light is sketched in Figure 5-10, where the telescope is replaced by a lens for simplicity. The fibre only receives the light for a precise adjustment of the external mirror.

The lamp as well as the fibre will display a field of view (FOV) at the retro reflector which size depends on the focal length  $f$  of the telescope and the fibre or lamp diameter  $D$ .

$$\frac{D}{f} = \frac{FOV}{L_R} \quad (\text{Eq. 5.1})$$

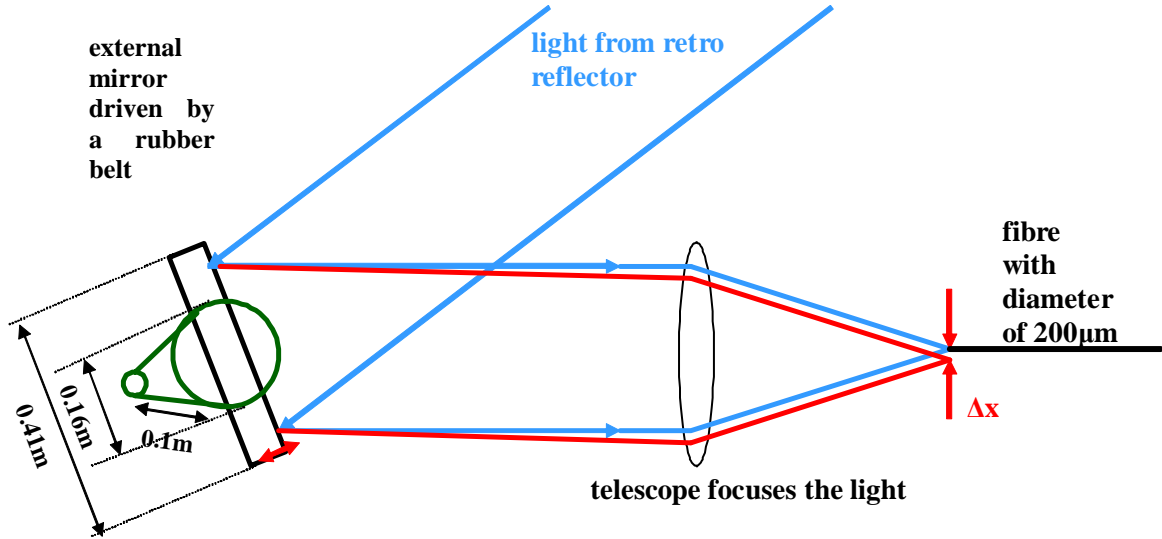


Figure 5-10: Sketch of the misalignment at the fibre by a slightly moved mirror. Drawn is the light path from the retro reflector with reflection over the external mirror (top view) and the focusing on a fibre. The telescope is here replaced by a lens with same properties. A small displacement of the external mirror leads to a loss of light in the receiving fibre.

The field of view of the lamp is accordingly  $0.933\text{ m}$  and is in good agreement to the observed size of  $\sim 1\text{ m}$ . As the diameter of the lamp arc is larger than the fibre diameter, it is sufficient to estimate the accuracy for the fibre. The field of view of the fibre at the retro reflector will be:

$$FOV_{fibre} = \frac{D_{fibre}}{f} \cdot L_{Retro} = 0.266\text{m} \quad (\text{Eq. 5.2})$$

The real field of view is slightly larger as the spherical mirror has spherical aberration and turbulences in the air produce an additional expansion. Still a precise adjustment of the external mirrors to the retro reflector array is required. For this estimation this light beam expansion is ignored. A total loss of light intensity arises if the light beam points next to the reflector what is achieved by a displacement of  $(FOV_{fibre} + D_{Retro})/2$ . This is correlated to an accuracy of the mirror adjustment of:

$$\Delta\alpha = \arctan\left(\frac{FOV_{fibre} + D_{Retro}}{2 \cdot L_{Retro}}\right) = 6.68 \cdot 10^{-3}\text{o} \quad (\text{Eq. 5.3})$$

and thus about 5 motor steps. The change of angle of the mirror is just half of the change of the deflection angle of the light. If we ignore all other clearances of the transmission, the rubber belt expansion at one side ( $\Delta L$ ) can be calculated to achieve this change in angle:

$$\Delta L = \tan\left(\frac{\Delta\alpha}{2}\right) \cdot \frac{D_{Wheel}}{2} = \left(\frac{FOV_{fibre} + D_{Retro}}{4 \cdot L_{Retro}}\right) \cdot \frac{D_{Wheel}}{2} = 1.19 \cdot 10^{-5}\text{m} \quad (\text{Eq. 5.4})$$

If the free expandable part of the rubber belt is  $L_{belt} = 0.10\text{ m}$ , this corresponds to a percentile expansion of:

$$\Delta L\% = \frac{\Delta L}{L_{belt}} \cdot 100 = 1.19 \cdot 10^{-2}\% \quad (\text{Eq. 5.5})$$

The expansion of the belt is nearly linear to the force  $F$ . At  $F_{belt,t2\%} = 250\text{ N}$  the expansion is  $\Delta L\%_{belt,250N} = 0.2\%$ . Then a force  $F$  is necessary to achieve  $\Delta L\%$ :

$$F = \frac{F_{belt,2\%}}{\Delta L\%_{belt,250N}} \cdot \Delta L\% = 14.9\text{ N} \quad (\text{Eq. 5.6})$$

If we consider that the mirror frame acts like a lever, the necessary force at the edge of the frame is reduced to  $F^*$ :

$$F^* = \frac{F}{R_{Frame} / 2} \cdot R_{Wheel} / 2 = 5.83\text{ N} \quad (\text{Eq. 5.7})$$

That means that a small force of  $5.83\text{ N}$  at the edge of the frame result in total loss of received light in the fibre. Wind can easily produce such forces, but for a homogeneous wind field the forces at both sides of the frame cancel out. However at walls and below roofs where the external mirrors are placed turbulences arise and therefore unequal wind forces, which may be stronger than  $5.83\text{ N}$ .

One solution would be to use worm gears or linear stages instead of belts. These gears are very precise and are also self-closing. Thus no forces, e.g. wind, can be transferred to the motor gearing. Unfortunately the reconstruction of all mirror mounts was not possible within this thesis due to the high effort and costs. One mirror mount was modified to demonstrate the better stability of this setup and later also used for a small telescope setup (see *Chapter 5.6*). To improve the measurement stability the fibre was slightly defocused from the focal point. Even if this causes some intensity loss, it improves the measurement stability for low and medium wind speeds. An enhancement of the wind shield around the external mirror mounts also reduced the forces. Continuous measurements could than be realised. During strong winds typically no measurements were possible. A new adjustment of the mirrors was necessary afterwards.

## Stability in Mechanical Components

Not only small forces lead to an extension of the rubber belt and a de-adjustment of the light path, but also the forces to the mechanical components are large. The mechanical mirror construction of HMT could not withstand these forces and several mirror mounts broke. Some details are discussed shortly.

The clearance of the stepper motor gearing is reduced with a leaf spring. The spring fasteners are made of plastic, and could therefore not be tightened up strongly (the plastic did not withstand the large forces) and during cold winter days the plastic broke and the released spring damaged the mechanics. All plastic fasteners were replaced by ones made of aluminium.

The dowel pins connecting cogwheel and motor shaft were not designed for the arising forces. They had to be replaced by thicker and more stable ones.

### **Multistepper Controller**

The stepper motors of the mirrors are controlled by a Multistepper controller from the same company HMT (for up to 12 motors) with a USB connection and an ActiveX interface. Thus the measurement software (*Chapter 5.5*) could perform all necessary adjustments. During the first measurements errors in the motor controller were found. The mirrors moved to completely wrong positions. Extensive tests proved that two main errors arise in the HMT Multistepper controllers. The probability of an error increased if more motors were connected and controlled simultaneously. The occurred errors were:

1. command not performed, also if the controller replay “done” (probability: ~1 of 100)
2. the “Move to Position” command performed wrongly (instead of moving a number of steps, the motor was moved to a random position), (probability: ~1 of 1000)
3. The “Get Motor Position” command result in wrong position (regularity: ~1 of 100)

The reason for the errors was found to be a bug of the micro controller from the HMT Multistepper controller and its hardware communication with the PC. The bug could not be fixed by HMT. To avoid any measurement problems a modified controlling was necessary. To check if a command was performed correctly the software had to check the final position and corrected until the position was reached. The “Move to Position” command was avoided and replaced by relative movements “Move Motor”. Any query to the motor position had to be double checked. Unfortunately these changes result in a drastically increase of time for the mirror adjustment and thus reduced the achieved temporal resolution of the measurement. It is recommended to implement the same changes in any software controlling similar HMT Multistepper controllers.

### **5.2.3 The Controlling of the Instruments**

An overview of the instruments and their connections is displayed in Figure 5-11. For the measurements of absorption spectra, beside a telescope, a spectrograph detector unit is necessary. A mode mixer for the fibres provides an equal illumination of the grating and detector inside the spectrograph. Errors caused by grating irregularities can be reduced [Stutz and Platt, 1997].

For a MBI the components are mainly the same as for a classical LP-DOAS instrument. Measurements of several light beams are performed simultaneously. The light beams are adjusted to different retro reflectors controlling the external mirrors (*Chapter 5.2.2*). A CCD controller performs the read out of the CCD detector and drives the spectrograph shutter. The lamp controller ensures the power supply for the xenon lamp. The TTL controller switches the lamp shutter (light blocker), the mercury lamp and its reflector and the shortcut motor of the lamp reference measurement (*Chapter 5.2.4*).

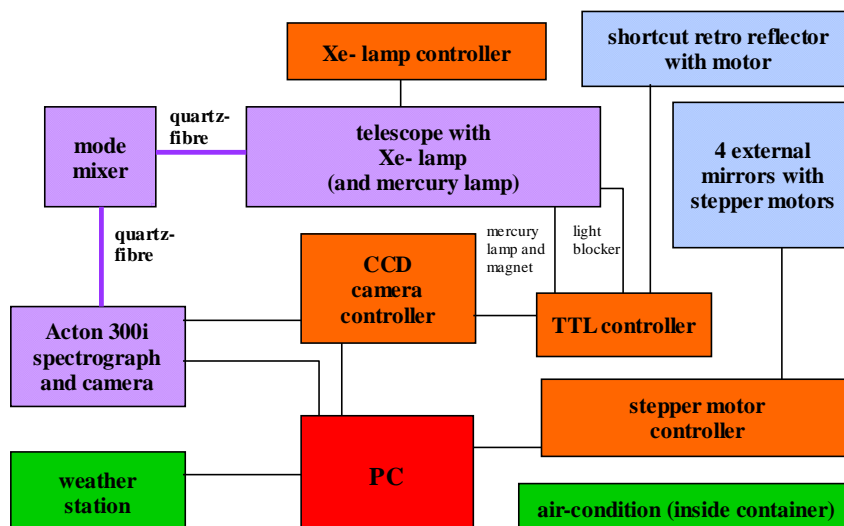


Figure 5-11: Sketch of the instrument connection. The whole system is controlled by a PC. Several electronic devices (highlighted in orange) are used to control the optics and mechanics. The main instrument is the telescope emitting and receiving the light. The used instruments for detection of the spectrum are highlighted in violet. The optical components outside the building (container) are highlighted in blue.

### 5.2.4 Lamp Reference Measurement with a Shortcut System

For the evaluation of atmospheric spectra a reference spectrum of the light source (xenon arc lamp) is necessary (*Chapter 3.2*). To observe this reference spectrum, the emitted light has to be measured almost directly, redirecting the light from the lamp into the fibre without passing the atmosphere. A so-called shortcut system (as the light path is short) is used for these measurements and placed close to the external mirrors. The short absorption path has almost no absorption information in comparison to the measurement along the long light path. The distance to the shortcut reflector is accounted in the evaluation.



Figure 5-12: Shortcut retro reflector at IUP for the measurement of reference spectra. Three retro reflectors are placed at different radii on a rotating disc.

The system consists of three retro reflectors (*Chapter 5.4*) placed on different radii on an aluminium disk. The disk is rotated by an electromotor and thus the whole area of the emitted beam (0.3 m) is covered. Due to the fact that regularly shortcut measurements are necessary, to reduce effects from changing lamp structure, their measurement is automated. This was

achieved by redirecting the emitted light beams with the external mirrors to the shortcut reflector. The motor of the system is started via the TTL controller. Typically the intensity of the shortcut system is much higher than for atmospheric measurements and can yield to over saturation of the detector if the minimum integration time is reached. The intensity was reduced by placing a meshed cloth in front of the single reflectors.

### 5.2.5 Quartz Fibre and Mode Mixer

For the transmission of the received light from the telescope to the spectrograph, an 8 m long quartz fibre with a diameter of 200  $\mu\text{m}$  and an aperture of 0.11 is used (12 fibres per bunch from Loptek, Berlin). This special aperture was chosen as it best fits the aperture of the telescope (with 0.1) and of the used spectrometers. It guarantees best light throughput with lowest stray light in the spectrometer. The fibres are solarisation stabilized and thus withstand UV light below 280 nm. The twelve single fibres are merged to a row configuration at the entrance slit of the spectrometer with one blind fibre between two measurement fibres.

The fibres act directly as slit with a height of 5.75 mm. All fibres illuminate the 2D CCD detector at once. As one MBI has only four receiving light beams, only four of the 12 fibres are used. To reduce the effect of vertical stray light, not neighbouring fibres are selected.

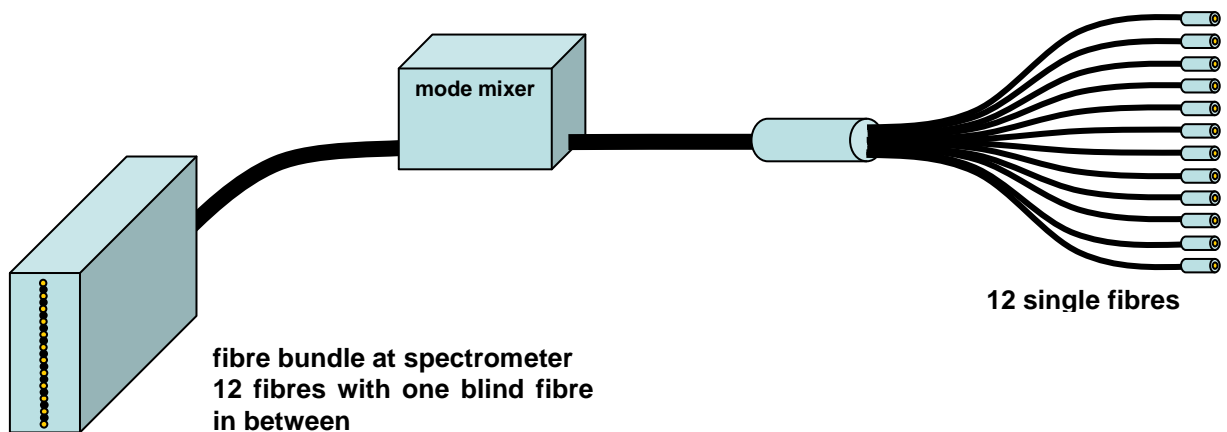


**Figure 5-13:** Sketch of the fibre bundle with 12 single 200  $\mu\text{m}$  fibres which are guided through a mode mixer and afterwards are arranged in a row. Between each measurement fibre one blind fibre is placed. From the 12 fibres only 4 are used with the MBI.

The light coupled into the fibre is kept in the core by internal total reflection which arises due to different refraction indices between core and cladding (Figure 5-14). The difference in refraction index, which is a few percent, defines the critical angle of light which can be accepted by the fibre.

$$\sin \beta = \frac{n_{\text{Cladding}}}{n_{\text{Core}}} \quad (\text{Eq. 5.8})$$

Light in the core below this critical angle will stay within the core and propagate through the fibre. Light with a larger angle will leave the core and is lost. If the light is coupled into the fibre from a medium with refraction index  $n_0 \sim 1$ , the acceptance angle  $\alpha$  is defined:

$$NA = \sin \alpha = \sqrt{n_{\text{Core}}^2 - n_{\text{Cladding}}^2} \quad (\text{Eq. 5.9})$$

The sinus of  $\alpha$  is defined as the numerical aperture ( $NA$ ) of the fibre.  $2 \cdot \alpha$  represents the whole acceptance cone.

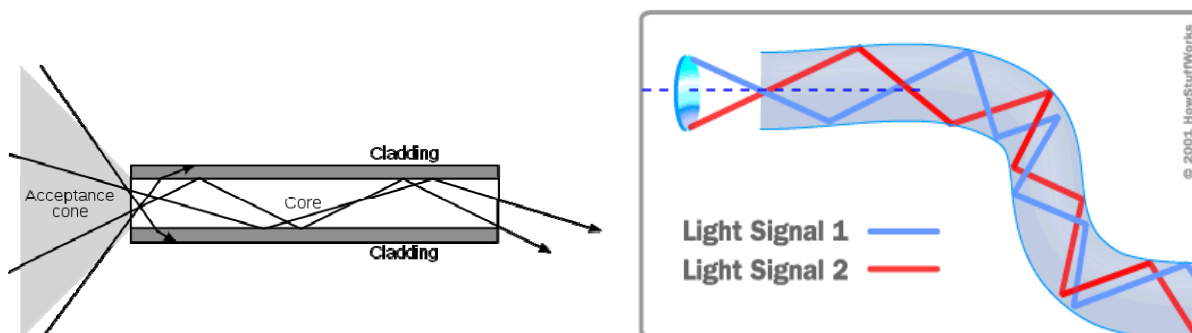


**Figure 5-14: Principle of light transmission in quartz fibres.** A different refraction index between core and cladding will result in a total reflection of light up to the critical angle which defines the acceptance cone (or accepted numerical aperture). The light entering the fibre within this cone will be transmitted along the fibre. Bending the fibre will change the angle of the light inside the fibre and thus the light output can be mixed (reduction of image sharpness).

The fibre is surrounded by a plastic layer to protect it from mechanical forces. As the refractive index of the plastic layer is above the refractive index of the cladding, the light propagation within the cladding is mostly suppressed. The used fibres allow the propagation of many propagation paths or traverse modes in the core and thus called multi mode fibres (MMF).

On the way to the spectrograph the fibres are guided through a mode mixer (Figure 5-15). The mixer should reduce any image information of the received light inside the fibre to achieve a homogeneous illumination of the spectrometer, grating and detector. The application of mode mixers to LP-DOAS observations was investigated by Stutz [1996], who demonstrates that they display much higher transmission than quartz glass diffuser plates and significantly improve the measurement quality. In the mode mixer the fibre was controlled bended by rolling the fibre up and squeezed between two grooved aluminium plates. The light is guided around the edge and due to changes in the angle of light to the fibre-cladding interface the light is dispersed to neighbouring modes (Figure 5-14). The incident angle is not preserved and thus the light is mixed in the fibre and the image sharpness is reduced leading to a homogeneous illumination at the fibre output [Marcuse, 1973].

To achieve good mixing of the used fibres with minimal light loss, the bending and squeezing is adjusted to a position, where the transmitting intensity is reduced by about 10%. This correlates to the lowest achievable residual structures. In this position the force on the fibre is about 2 N. A stronger bending and squeezing leads to new optical structures and should be avoided.

An alternative mode mixing could be achieved by permanent vibrations, e.g. vibrations of a ventilator or the membrane of a speaker which allow different vibration frequencies by applying different acoustic frequencies.

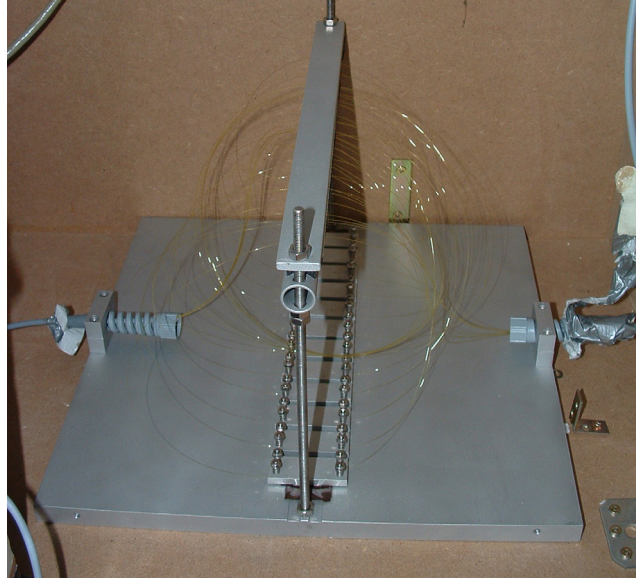


**Figure 5-15: Quartz fibre mode mixer with 12 quartz fibres with diameter of 200 $\mu$ m. Each fibre was banded with a diameter of  $\sim$  20 cm and squeezed and banded between two adjustable aluminium plates with opposite grooves.**

### ***5.3 Spectrograph and Detector***

For the spectral analysis of the received light, the discrete wavelength intervals have to be separately recorded. In spectroscopy nowadays most common is the use of a grating spectrometer in combination with a one or two dimensional detector (e.g. PDA and CCD, respectively). For the tomographic measurements of this thesis we used imaging Czerny Turner spectrographs with 300 mm and 500 mm focal length (*Chapter 5.3.1*) in combination with two dimensional Charge Coupled Device (CCD) detectors (*Chapter 5.3.3*). The spectra of the different fibres are imaged on different areas of the CCD detector and can thus be separated if the read out of the spectrograph and detector is performed in the imaging mode. That means that this spectrograph detector unit measures the spectra of the different fibres at once. For the read out in the imaging mode the light has to be blocked by a shutter during the read out process of the CCD to preserve the spatial resolution. The commercially available and also the installed shutters in the spectrographs have significant problems in terms of lifetime and sometimes also in speed. Thus they are not suitable for long term spectroscopic applications. Within this thesis a simple and cheap electromechanical shutter for imaging spectrometers was developed which meets the needs of imaging spectroscopy with continuous exposure at short integration times. The developed shutter is fast with a total response time of 3 ms to open and 5 ms to close and durable, since the lifetime exceeds 20 million exposures. The shutter is constructed with only a few simple mechanical parts. It can therefore easily be repaired, which reduces the running cost. The construction of the shutter, mechanical properties and the required optical configurations will be described in *Chapter 5.3.2* [Pöhler, 2009]. Furthermore the performance in imaging spectroscopic measurements with short exposure times is demonstrated.

### 5.3.1 Czerny Turner Spectrograph

For the three MBI of this thesis, two different models of imaging spectrographs were used: the Acton 500i and the Acton 300i. They are based on the principle of Czerny and Turner [1930] (Figure 5-16). The 12 receiving fibres are merged together in a vertical row and adjusted to the position where normally the entrance slit is placed. As the diameter of each fibre is only 200  $\mu\text{m}$ , it can directly act as optical boundary and no slit is required. The position of the entrance slit or the fibre is in the focal point of a spherical mirror. Behind the entrance slit position the light passes a mechanical shutter before entering the spectrograph. The

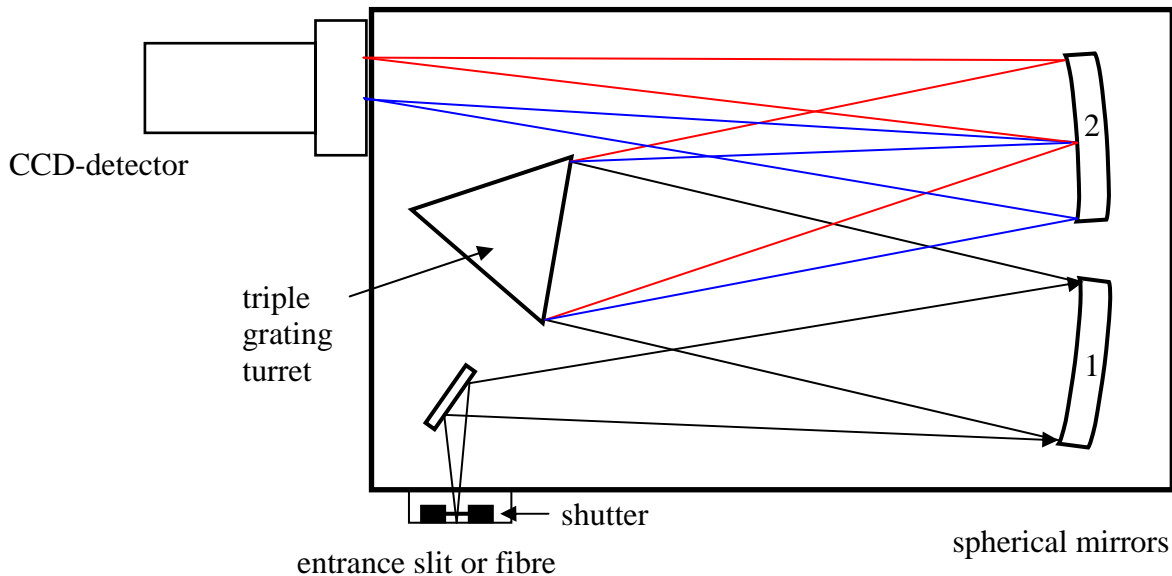


**Figure 5-16: Scheme of the spectrograph (adapted from Acton product information, 2005<sup>4</sup>).**

The first spherical mirror parallelise the light onto the grating. The spectrally dispersed light is then focussed with a second spherical mirror on the CCD detector. The imaging spectrograph has in general the same principle as the basic spectrograph but special care is taken to avoid optical aberrations for better image quality. This allows measuring the different spectra of the different fibres with similar spectral quality.

Two different adjustments of the CCD detector are possible: First, the detector can be set to the position where the wavelength to pixel calibration is nearly linear with highest spectral resolution. Also the instrumental function (thus resolution) will be nearly constant over the spectrum at this adjustment. This is an important advantage for the data analysis, as no assumptions of a changing instrumental function have to be made. But in this adjustment the imaging quality is relatively poor, which means that the dispersion in y direction of the spectrum will change along the chip. Thus, different spectra can only be sufficiently separated if they do not overlap at the end of the recorded spectrum. The used spectrographs Acton 500i and Acton 300i display a sufficient good imaging quality to separate the different spectra if the detector is adjusted to this position (Figure 5-17 and Figure 5-18, respectively). But it is clearly visible that the imaging resolution of the spectrograph with 300 mm focal length (Acton 300i, Figure 5-18) is much lower than that of the one with 500 mm (Acton 500i, Figure 5-17). In this adjustment a maximum of 6 fibres can be sufficiently well be separated

<sup>4</sup> [www.actonresearch.com](http://www.actonresearch.com)

by the Acton 300i. During all measurements of this thesis we adjusted the detector to this position to simplify and improve the data analysis.



**Figure 5-17:** CCD image of lamp spectra measured with four of the 12 fibres with the telescope Long and an Acton 500i spectrograph. The x- axis corresponds to wavelengths and the y- axis to the imaging dimension and thus the different spectra of different fibres. The CCD detector is adjusted to linear wavelength-to-pixel mapping with same wavelength resolution over the whole spectrum. At this position the image properties of the spectrograph are not optimal and at the edges of the spectrum the size of the image (width of the spectrum on the CCD detector) increases slightly.

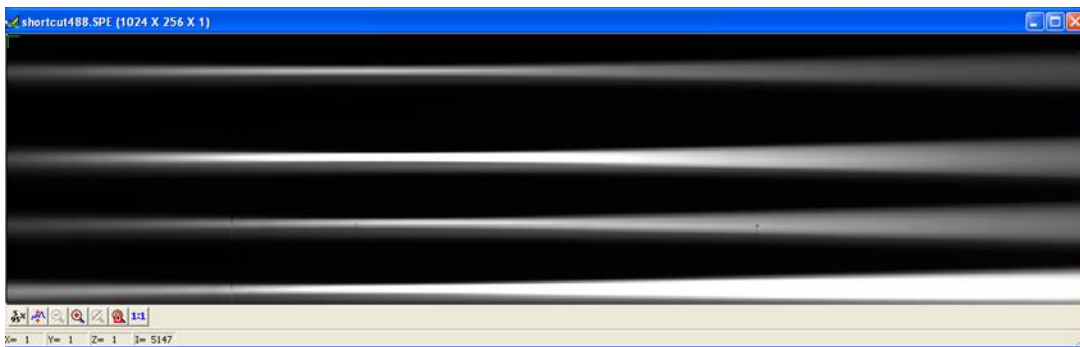


**Figure 5-18:** Similar spectrum to Figure 5-17, but taken with the telescope Cube and an Acton 300i spectrograph. Due to a shorter focal length, the image quality is reduced in comparison to the Acton 500i. The width of the spectrum increases much more to the edges of the recorded spectrum. Four fibres can still be sufficiently well separated.

The second adjustment is optimised to receive a better imaging quality. Therefore the detector needs to be tilted by  $30^\circ$ . In this position the image of each line of sight has a small and constant width, but the spectral resolution changes with the wavelength and thus also the instrumental function. Both effects have to be considered in the data evaluation, which can be complicated, as the real instrument function of each spectral position can not be measured. In some cases a compromise between best imaging and spectral resolution is made by setting the detector to  $15^\circ$ .

The properties of the used spectrographs are summarised in Table 5-2. Three gratings can be selected by a motorised grating turret. During a measurement period the grating and spectral range was not changed, thus the turret motorisation was switched off to avoid any malfunctions. The dispersion, i.e. the relation of the wavelength to the position of the detector,  $d\lambda/dx$  is mainly given by the number of lines per millimetre of the grating,  $g$ :

$$\frac{d\lambda}{dx} = \frac{1}{f \cdot m \cdot g} \quad (\text{Eq. 5.10})$$

$f$  is the focal length of the spectrometer and  $m$  the order of diffraction which is in our case 1.

The used gratings of 600 or 1000 lines / mm for the focal length of 500 or 300 mm, respectively, lead for both configurations to a dispersion of  $\sim 3.3$  nm/mm. With a pixel width of  $13.5 \mu\text{m}$  this corresponds to  $\sim 0.045$  nm/pixel. The spectral resolution of the complete spectrograph detector unit is dominated by the width of the entrance slit. For the used  $200 \mu\text{m}$  fibres we achieve  $\sim 13$  channels corresponding to  $0.59$  nm FWHM. The resolution should be sufficiently small to resolve the observable trace gas absorptions of interest. For most DOAS trace gas measurements a resolution below  $1$  nm is sufficient.

Telescope (Meas. Place)	Hydra (IUP)	Long (SAS)	Cube (HD-Druck)
Company	Roper Scientific		
Spectrograph Type	Acton 500i	Acton 500i	Acton 300i
Focal Length	500 mm	500 mm	300 mm
F/# - number	6.9	6.9	3.1
NA	0.07	0.07	0.12
Gratings [lines/mm]	<b>600</b> ; 900; 1200	<b>600</b> ; 900; 1200	<b>1000</b> , 1200, 1800
Dispersion [nm/mm]	<b>3.0</b> ; 2.0; 1.5	<b>3.0</b> ; 2.0; 1.5	<b>2.9</b> ; 2.4; 1.56
Blazed Wavelength [nm]	<b>300</b> ; 350; ---	<b>300</b> ; 350; ---	---; ---; 250

**Table 5-2: Characteristics of the used spectrographs at different MBI telescopes. Bold numbers indicate the used grating for the tomographic measurements in Heidelberg.**

To increase read out speed, additionally a  $2 \times 2$  binning of detector pixels was applied. Thus the achieved FWHM of the instrument function was reduced to 6.5 pixels. Aliasing (or under sampling) problems were still avoided (see *Chapter 3.9*).

For accurate long term spectroscopic measurements the dispersion of the spectrometer has to be constant (*Chapter 3.3*). Else, spectra are not comparable and the actual calibration is unknown. As the dispersion will change with any small variation in the optical setup, even small temperature changes have to be avoided. Therefore the spectrograph is thermally isolated with 6 cm thick Styrodur plates and temperature stabilised to a temperature above room temperature. We used heating foils on the spectrometer and a PT100 temperature sensor in combination with a linear temperature controller “R1300” of the company “Elotech”. The achieved accuracy was  $\pm 0.1$  °C.

### 5.3.2 Spectrograph Shutter

Spectroscopic measurements are used in many different applications and rely on e.g. Czerny Turner spectrographic configurations [Czerny and Turner, 1930]. Nowadays, imaging spectrometers combined with two dimensional CCD detectors are used widely. If operated in the imaging mode (no full vertical binning), they can resolve a spatial distribution in addition to the spectral distribution and thus measure several different spectra at once [Heue et al., 2008; Poehler et al., 2007; Levelt et al., 2006; Treado and Nelson, 2002]. The read out of a CCD can not be realized at once, instead the stored charges along each line are moved one after the other into the read out register by “clocking” the electrons (except Frame Transfer CCD where the whole chip is moved into a second chip at once) (*Chapter 5.3.3*). In the read out register, the electrons of each pixel are read out successively. Due to the fact that the lines

are transferred on the chip, the detector has to be shaded during the read out procedure. If this is not the case, new photons reach the detector during the read out process and lead to “smearing” of the spatial distribution.

Blocking the light can be realized in different ways, but usually mechanical shutters are used. First developed for applications in photography, they can in general also be used for imaging spectroscopy.

The shutter is often placed in front of the detector, but theoretically any position in the optical path is possible. The best position would be close to the entrance slit of the spectrograph, as the size of the optical beam is smallest there, and only a small baffle is required. Different companies sell optical shutters for spectroscopy. A common model is the Prontor-Magnetic-0 from Prontor-Werk [2007] (belonging to the Zeiss Group), and other shutters often have a similar setup. They consist of up to 5 small shutter plates which move into the light path like an iris, almost symmetrically from the edge to the centre (Figure 5-19). This is useful for most optical camera applications but not necessarily for spectroscopy. It is obvious that the shutter plates have to be connected and driven by several mechanical components transmitting the force. To open the aperture, an electro magnet is used. A return spring closes the shutter. For the mentioned Prontor shutter with this construction a circular aperture of 23 mm is realized with a shortest possible exposure time of 17 ms and a response time of max. 8 ms (manufacturer’s data [Prontor-Werk, 2007]).



**Figure 5-19: Mechanical shutter for optical applications type “Prontor magnetics- 0” from Prontor-Werk [2007]. The shutter opens an aperture of 25 mm. Therefore 5 small shutter plates are moved into the light path like an iris, almost symmetrically from the edge to the centre. On the right, the mechanical components are separated. The shutter is driven by a 5V TTL signal attached to a small electromagnet. The 5 small shutter plates are moved over a driving ring. The lifetime of these shutters is only 1 million movements after which the mechanical components damage and the shutter get stuck.**

The lifetime of these shutters is about 1 million exposures and varies only slightly for different models. The limiting factors are mainly the mechanical parts. This lifetime is not sufficient for imaging spectroscopy applications with continuous measurements at short integration times. This is the case e.g. for Long-Path Differential Optical Absorption Spectroscopy, where the integration time is typically below 1 s. Even when considering read out time, one exposure per second is accomplished on average. This means that the typical lifetime of 1 million exposures, is reached in less than 12 days.

During the first months of measurements in Heidelberg in the framework of this thesis a total of 12 shutters of the type Prontor-Magnetic-0 had to be replaced. Moreover a shutter does not have a fixed lifetime. Instead they start to seize slowly. This led to problems in the measured spectra, because read out with an open shutter leads to over saturation of the CCD and to a

shift of information to other pixels, and thus to other spectra. If, for a measured spectrum with 100 scans, just a few read outs are wrong, the whole spectra can be useless.

Problems with the spectrograph shutter were the main cause of measurement failure during the campaign in 2005 and 2006. Even if the costs could be reduced by not replacing the whole shutter (1200 € by Roper Scientific), instead replacing the moving mechanical components (50 € from Prontor-Werk [2007]) could not solve the problem sufficiently. The main reason was that the replacement of the shutter also required a complete new adjustment for the fibre and thus also a new calibration.

No shutter is commercially available with the required speed, stability and for an acceptable price. An own shutter construction was developed with a similar speed like the Prontor-magnetis-0 shutter (8 ms) but longer lifetime (more exposures before the shutter break).

Increasing the lifetime without additional costs can only be achieved by minimizing the fragile mechanical parts. Therefore, the shutter size is minimized by placing it as close to the entrance slit as possible.

Different options were discussed for the construction. Piezos and galvo drives (incl. additional electronic) are too expensive for spectroscopic applications. An electronic solution could be using two polarizers, distorted by 90 degrees, which can be switched on and off by an electric signal. But such filters are not available for the UV. Applications which require a response time of less than 100 ms, and therefore exposure times of about a second or longer, can use a rotary magnet or lifting magnet with a single shutter plate [e.g. Lohberger et al., 2004]. For several applications, this is not sufficiently fast. Therefore, a different approach was chosen here. An electromagnet is used like a relay but with an extended lever as a shutter plate (Figure 5-20). Using a simple electromagnet was seen as the simplest and cheapest solution. The aim of using an electromagnet like in the shutter Prontor-magnetic-0 was expected to be simple due to the fact that the same shutter signal could be used.

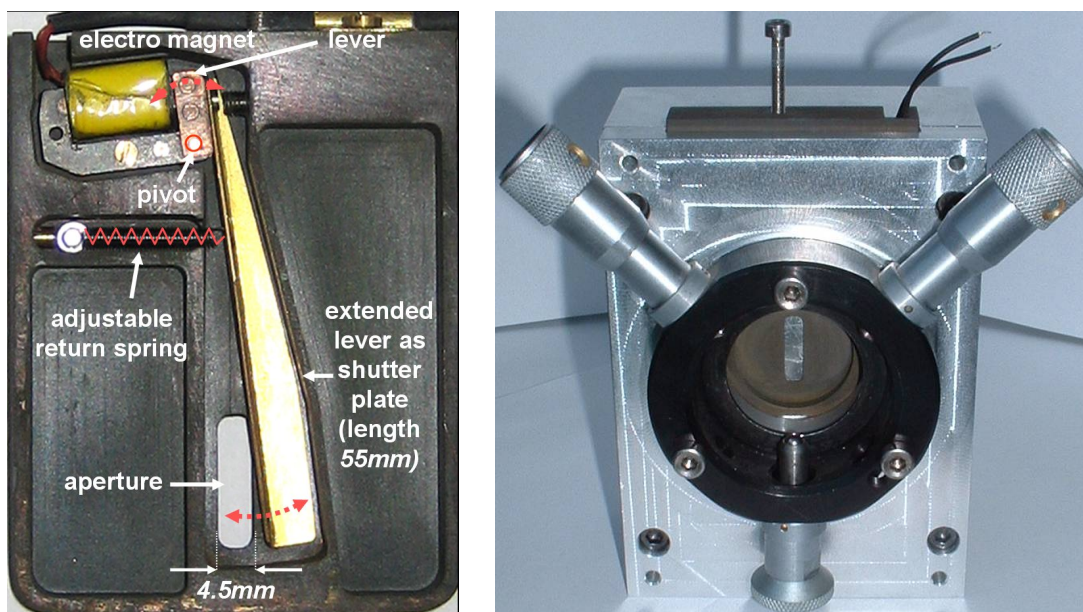


**Figure 5-20: Left: Backside view of the constructed optical shutter in open mode. An extended lever attached to the electromagnet works as the shutter plate which opens and closes the aperture. Red signs are only for illustration purposes. Right: The shutter is placed in an aluminium block outside the spectrograph with adjustments for the optical fibres (front). The shutter is constructed as a slide module which allows removing and checking of the shutter condition without changing the optical setup at the entrance slit**

To calculate the required aperture size, the aperture ratio  $F/\#$  of the spectrograph, the distance to the fibre and the fibre diameter have to be considered. Typical imaging spectrographs have an aperture ratio equal to or larger than the 3.6 of the Shamrock by AndorTechnology [2007]. Therefore a shutter for this spectrograph is sufficient for all others. We could easily realize a setup where the fibre is placed at a distance smaller than  $L_{max} = 15 \text{ mm}$  in front of the shutter. Therefore the shutter aperture width for a  $200 \mu\text{m}$  fibre should be:

$$D_{Shutter} = D_{Fibre} + \frac{L_{max}}{F/\#} = 4.4 \text{ mm} \quad (\text{Eq. 5.11})$$

Thus, the aperture width of the shutter is chosen to be 4.5 mm. The shutter aperture height is less critical in the construction and can easily be modified for different applications. It is useful not to oversize the shutter aperture as this also reduces stray light entering the spectrograph.

The best results could be achieved by using an electromagnet with  $50 \Omega$ , which is typical for optical shutters. Standard relays with much higher resistance display a slower response and are therefore not applicable for this purpose. The lever is extended to 55 mm by a bent stainless steel or copper plate, which has to be especially stable to withstand the forces. The bent steel was therefore heated to release stress. This procedure increased the lifetime significantly. The electromagnet with the extended lever and a return spring are then mounted in a milled copper block and placed behind the entrance slit.

The shutter was controlled via a Princeton Instrument Camera Controller (ST-133), which is the same as used for spectroscopic measurements. The shutter signal from the controller is not a step function, but a 70 V initial voltage which decreases to 3.8 V after 0.1 ms. This reduces the response time of the electromagnet, which is slowed down due to self-induction. The properties of the optical shutter were tested with a light barrier setup consisting of a light emitting diode, a photodiode and an oscilloscope (Figure 5-21).

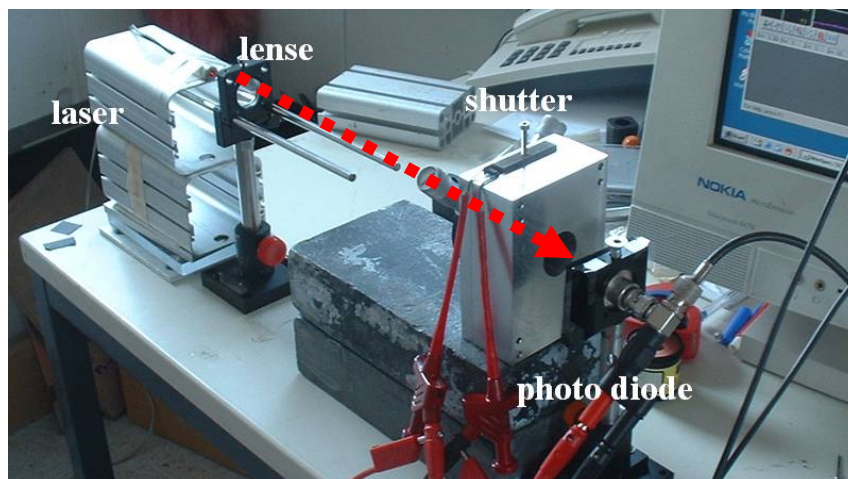


**Figure 5-21:** Light barrier measurement configuration for the determination of shutter response and speed. A laser in combination with a photo detector and the shutter form a light barrier. A lens is used to broaden the light beam to the full size of the shutter. The response time and speed of the shutter are determined by recording the drive voltage and photo diode voltage to a storage oscilloscope.

Compared to the Prontor-Magnetic-0 shutter, the time delay of the mechanical response could be decreased from 6 ms to 1.5 ms and from 7 ms to 3 ms for opening and closing the aperture,

respectively. More relevant is the total response time (time until the aperture is completely opened or closed). This was decreased from 12 ms to 3 ms and from 18 ms to 5 ms for opening and closing, respectively. This effect is mainly due to fewer mechanical parts and a smaller aperture.

The summarised properties of the shutter are:

Open shutter (close electromagnet):	response time:	1.5 ms
	movement:	1.5 ms
	total:	~ 3.0 ms
Close shutter (open electromagnet):	response time:	3.0 ms
	movement:	2.0 ms
	total:	~ 5.0 ms

The achieved lifetime is typically more than 20 million exposures, which means a factor of 20 times higher. The weakest part of the construction is the extended lever. Durability could likely be improved if a different material was used. The measurement of the response time was repeated for a shutter after intensive use in spectroscopy measurements with roughly 100 million exposures. During this time, the shutter plate was exchanged 2 times. The total response time for opening the aperture only increased by about 0.5 ms to 3.5 ms and remained 5 ms for closing it. This shows high performance even after intensive use.

The shutter is placed outside the spectrograph, behind the entrance slit and is constructed as a slide in module, which allows removing and checking of the shutter condition without changing the optical setup at the entrance slit. Replacing broken extended levers was therefore simple and could be done within a few minutes.

Spectroscopic measurements of mercury emission lines were taken to test the shutter performance. The light was coupled through a 200  $\mu\text{m}$  fibre into an Acton 500i spectrograph with 600g/mm grating (80 nm coverage) and 2D CCD Camera Spec-10 2kBUV with a resolution of 1024 $\times$ 256 pixel. The emission lines at 312.57 nm and 313.17 nm were recorded in the imaging mode of the camera (see Figure 5-22). The shutter is closed during readout to prevent the blurring of spatial structures (vertical axis). Readout should start just after the shutter is closed completely, otherwise blurring of spatial structures will occur. The waiting time between the beginning of closing the shutter and beginning of the readout is called shutter compensation time. If no compensation time was applied (Figure 5-22 A, 0 ms) a blurring of about two channels was found.

This correlates well with the maximum expected blurring of 3 channels calculated from CCD readout time and a maximum closing time of 5 ms (this would be the worst case, since 5 ms is the total response time until the shutter closes completely and not the time after which the shutter closes immediately). The measured increase in FWHM image size (measured along the vertical axis) was only 0.4 channels from 7.55 to 7.95, but the full width increased by 2 channels which is an undesirable effect for imaging spectroscopy. For compensation times larger than 4ms (Figure 5-22 B), the spatial size does not further decrease, indicating that the shutter is already completely closed after 4 ms.

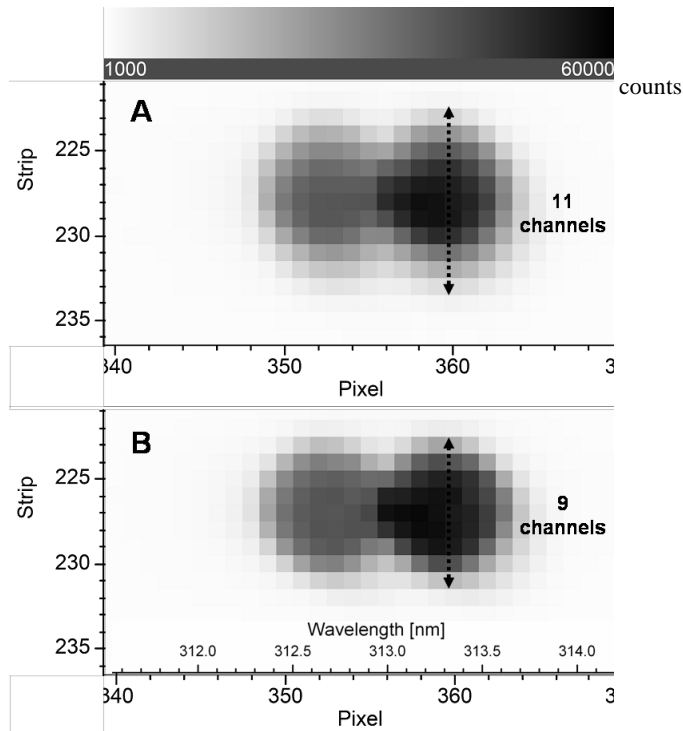


**Figure 5-22: Spectroscopic image of mercury emission lines at 312.57 nm and 313.17 nm (10 exposures each at 10ms integration time) recorded with a 2D CCD Camera (imaging mode) using an Acton 500i spectrograph. After each exposure the shutter is closed before read out to prevent blurring of spatial structures (vertical). Different shutter compensation times were applied with (A) 0 ms and (B) 4 ms. A light blurring can be found for (A), as spatial size increased from 9 (B) to 11 (A) channels. The spatial size does not decrease further for longer shutter compensation times as applied in (B).**

To determine the shortest possible integration time, the intensity was measured at different integration times (Figure 5-23). A linear decreasing intensity was found down to 10 ms. Only for integration times below 10 ms, deviations from the linear behavior were found. This proves that the shutter has only a small inertia and is able to close shortly after opening. The resulting shortest exposure time of 10 ms is shorter than that of commercially available shutters.

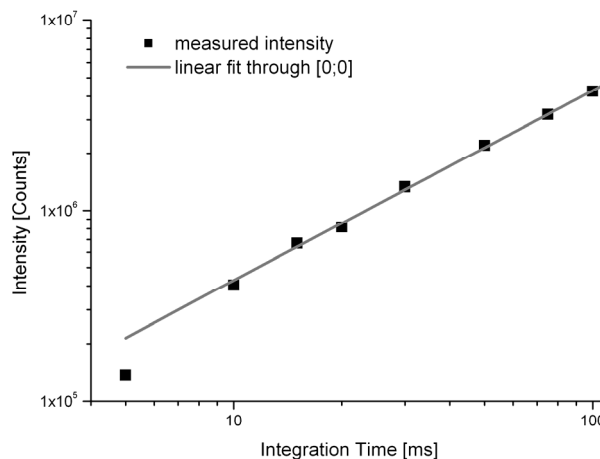


**Figure 5-23: When measuring the intensity at different integration times, a linearity down to 10 ms was observed (shutter compensation time 4ms). The reaction time of the shutter is therefore short enough to allow exposure times down to 10 ms.**

The developed optical shutter for spectroscopy has with at least 20 Million exposures a 20 time longer lifetime than commercially available ones. Thus they full fill the requirements for long term spectroscopic applications like in LP-DOAS. The simple construction using an electromagnet with extended lever makes the shutter very durable, cheap and easy to repair. Due to the smaller aperture, the response time is shorter than for shutters with circular aperture. An overview can be found in Pöhler[2009].

### 5.3.3 CCD Camera (Detector)

As detector a Charge Couple Device (CCD) Spec-10 2kBUV from Roper Scientific with the Chip CCD42-10 from e2V technologies was used for the measurements of this thesis. Most common for LP-DOAS measurements are Photo Diode Array (PDA) detectors. They consist only of one row of photo diodes, thus only one spectrum can be measured at once. The used CCD consists of an array of picture elements (in our case 2048×512 pixels), which convert the incident light into an electronic signal. For the used camera a 2×2 hardware pixel binning is used which sum up 4 pixels to one and reduces the pixel number to 1024×256. The higher resolution was not required and so the readout time could be reduced by a factor of 4. The principle of detection is the same as for a digital camera, the main difference is the way the data is read and digitised.

Before concentrating on the readout of the signal, the principle of light detection will be explained. Each pixel is made of four layers (Figure 5-24), one metal, one isolator ( $\text{SiO}_2$ ), one P- and one N-doped silicon layer. Together they are usually called a MOS (Metal Oxides Silicon) capacitor.

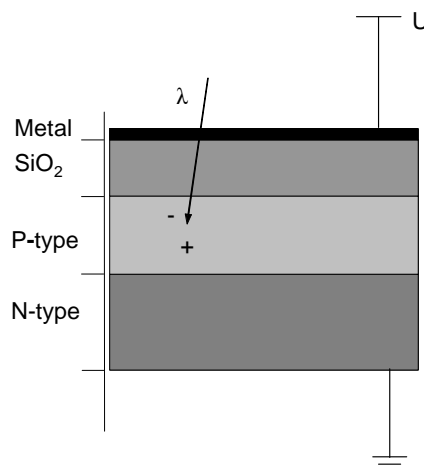


**Figure 5-24: Cross section of a CCD-pixel. The incoming light produces an electron (-) and a hole (+). The hole is refilled by the electrons in the N-type while the electron remains in the P-type until the readout procedure.**

A positive voltage between the N-layer and the metal produces a potential well for electrons in the P-layer. The photoelectrical effect leads to the creation of electron-hole-pairs. Holes and electrons are separated by the potential well. The holes are refilled with electrons from the N-doped silicon, whereas the electrons are stored in the potential well, until they are read out. The number of electrons per time interval is given by the flux of the incident light and the quantum efficiency of the CCD-chip.

$$\eta = \frac{n_{\text{electrons}}}{n_{\text{photons}}} \quad (\text{Eq. 5.12})$$

The quantum efficiency of a detector describes its efficiency for the conversion of photons  $n_{\text{photons}}$  to electrons  $n_{\text{electrons}}$ . Some of the photons are reflected by the chip, other penetrate the chip without the creation of an electron-hole pair. Even if an electron-hole pair is created it can recombine or be absorbed by another process. All these effects cause a typical quantum efficiency well below 1. The achieved quantum efficiency depends on the type of the CCD, its layer, coating etc. and is also dependent on the wavelength. Typical CCD chips have much lower efficiencies in the UV than in the visible wavelength range. The used CCD chip is back illuminated with enhanced UV coating and thus displays almost constant sensitivity over the UV and visible spectral range (Figure 5-25).

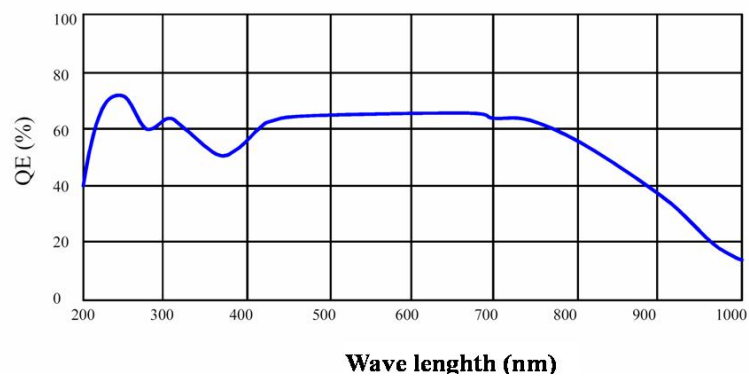


**Figure 5-25: Quantum efficiency of the used back illuminated CCD chip with enhanced UV coating from e2V technologies.**

Additionally to the optical created electron-hole-pairs, some are created by thermal extinction. These electrons are later read out together with the signal. This additional signal is called “dark current” and gives an additional offset to the signal which has to be subtracted. To reduce this effect the CCD is cooled down to  $-40\text{ }^{\circ}\text{C}$ . The dark current is then in the order of 0.1 counts per pixel per second (Figure 7-4).

For data handling the CCD controller adds a defined offset value to each pixel intensity, this is necessary to prevent negative counts (Figure 7-4). For data evaluation the offset needs to be taken into account.

The maximum capacity of the MOS capacitor is called “full well capacity” and is the maximum number of electrons stored by each pixel. For our type of CCD chip this is 100,000 electrons per pixel.

Figure 5-26 shows the principle of the readout procedure. A series of electrodes, installed parallel to the lines, cover the CCD array. The stored charges are moved along the columns by “clocking” the electrodes. All signals are moved simultaneously. The lowest line is transferred into the shift register and all the other lines above move down one line. The shift register has the double capacity of one pixel row, thus the electrons of two rows fit into the readout register at once. The pixels in the shift register are read out one by one and the number of electrons (voltage) are transferred to digital counts by the analogue digital converter (ADC). The shift register has a series of electrodes perpendicular to the lines. If the first pixel is read, the others will move left by one place and then the second pixel will be

read. When the first line is finished, the second line is moved to the shift register. The complete procedure is repeated until the last pixel is read. The applied CCD cameras perform the read out with 1 Mhz. Thus a full readout including the time to shift the register can be performed in 1.4 s. Hardware binning can be applied where several pixels are merged together before the readout. By applying  $2 \times 2$  hardware binning the read out is reduced to 0.48 s. For most measurements within this thesis, this is still longer than the integration time. Thus effectively less than half of the received photons are used for spectroscopic analysis.

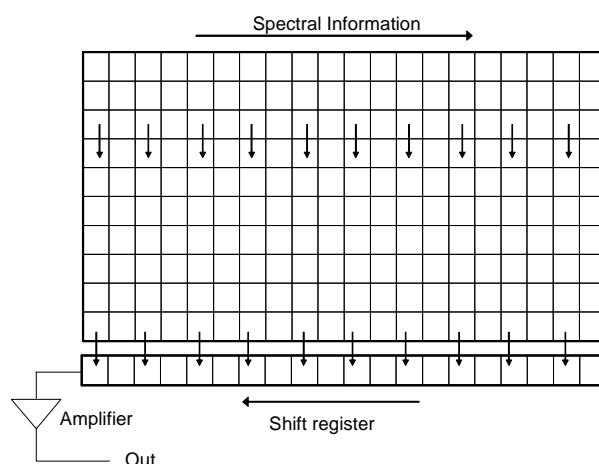


**Figure 5-26: Sketch of the readout procedure. The first line is shifted to the shift register and the others moved up. The shift register is read out via an amplifier and digitised for later analysis.**

Due to the fact that the lines are transferred all together downwards during the readout, the light needs to be blocked with a mechanical shutter during this process (see *Chapter 5.3.2*). Alternatively Frame Transfer CCD's could be used, which have a second readout register and move all data of the chip to this register at once. The data is read out from this second register, while new photons are detected with the first register. But two disadvantages arise: First, during the shift to the second register the data is blurred, as still light reaches the chip. Second, the shortest possible integration time is similar to the read out time (for these CCD's minimum 0.5 s), what is too long for LP-DOAS instrument with integrating times down to view ms.

Depending on the setting of the ADC, the stored electrons are converted to digital counts. For the used cameras  $\sim 100,000$  electrons correspond to 21,000 counts (Figure 5-27). The chip shows a linearity of quantum efficiency up to  $\sim 20,000$  electrons per pixel if no additional amplification is used (Figure 5-27 Left). Increasing the hardware binning of course increases the capacity of the effective pixels as also the effective pixel size increases. In the used arrangement with  $2 \times 2$  hardware binned pixels, the linearity reaches values higher than 60,000 electrons / binned pixel. To ensure that during the measurement the chip is in the linear range, the saturation for one spectrum scan was set to max. 40,000 counts.

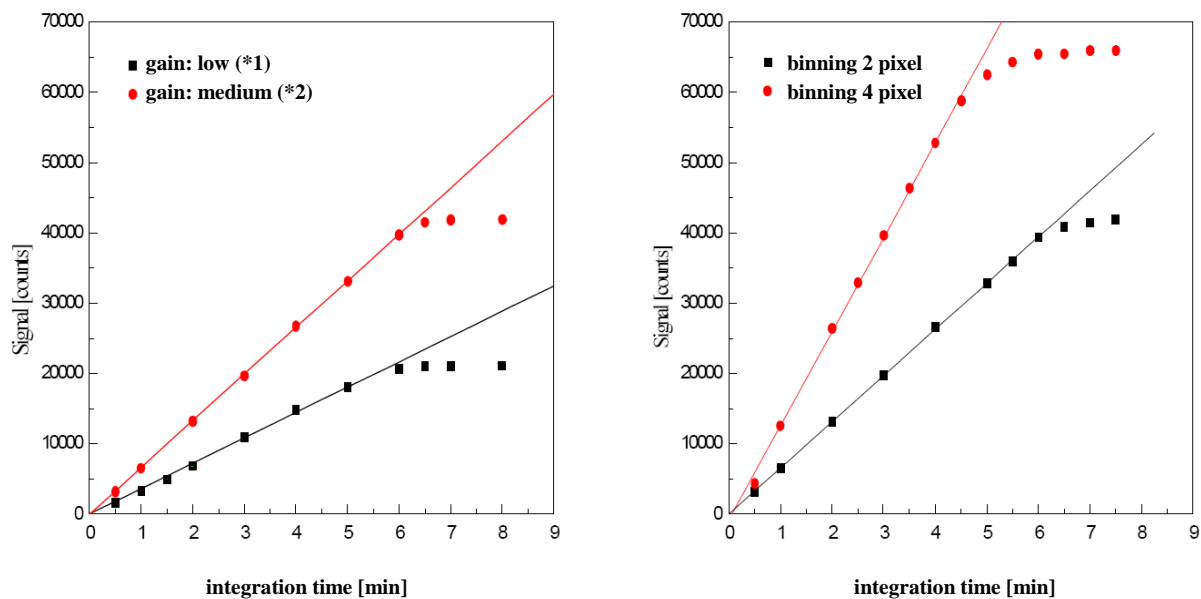


**Figure 5-27: Linearity of the CCD detector measured with constant intensity and variation in integration time. A linear fit to the linear range is included. Left: Linearity for two different gains ( $\times 1$  and  $\times 2$ ). Right: Linearity for different hardware binning settings (pixels merged together before read out) at lowest gain ( $\times 1$ ).**

### 5.3.4 Characterisation of the Measurement Quality (Noise Tests)

The measurement accuracy of a DOAS instrument is in first order limited by the total noise in the spectra (see *Chapter 3.6*). Before an instrument is applied for measurements, extensive noise test should be performed to guarantee optimal performance. Even if such a test can never capture all possible error sources, it can reliably exclude almost all errors arising from the electronic, the spectrograph or the detector.

For good instruments the photon noise  $\sigma_p$  is the limiting factor in the signal to noise ratio. But it has to be tested if this is also the case for the applied instrument. This is done by averaging over a larger number of scans (thus more photons) which should reduce the noise. In most spectroscopic instruments from a certain number of scans onwards the photon noise will be so small that the other noise sources will dominate and the total noise will not further decrease with increasing number of registered photons (or rather photo-electrons). It is important that this number of scans (or number of photoelectrons) is determined for each instrument to determine the best achievable signal to noise ratio. Different noise test are performed and shown below. The basic noise test with increase of integrated photons; does not sufficiently represent the real measurement condition and therefore often lead to an underestimation of the instrumental noise level during the measurement. A method is shown to reduce the instrument noise level. Due to the measurement routine of the MBI this method could unfortunately not be applied to the measurements of this thesis.

#### Setup for Noise Measurements

The light of a stable light source (e.g. halogen lamp) should be homogeneously coupled into the fibre. Therefore, a lens system is not recommended, as it directly images the emitter on the fibre, which can lead to an inhomogeneous illumination of the later and thus arising spectral

structures. Additionally, it is very sensitive to lamp fluctuations. Instead an aluminium diffuser plate (sand blasted aluminium plate) was applied as scattering plate producing a very homogeneous illumination of the fibre (Figure 5-28).

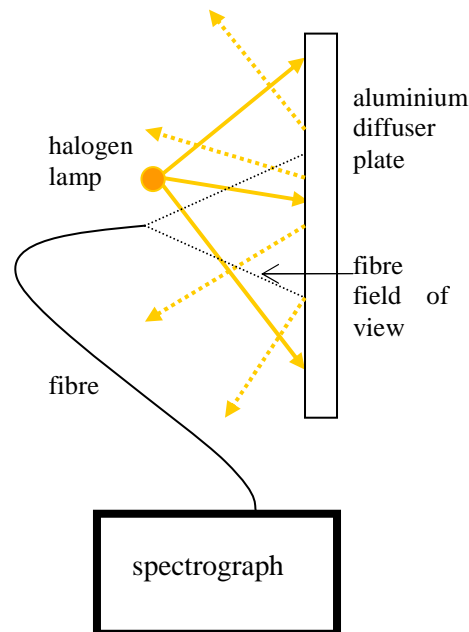


**Figure 5-28: Set up for noise measurements with halogen lamp and aluminium diffuser plate. The diffuser plate guarantees a very homogeneous illumination of the fibre and thus avoids any optical structures.**

### Basic Noise Test with Increasing Scan Numbers

The aim of the noise test is to determine if the quality of the instrument performance under optimal configuration is following the photon noise statistic. The RMS noise of two divided spectra taken with the same exposure time and at the same measurement conditions will be determined with increasing scan number (increasing photons). Theoretically both spectra should only vary in the photon statistics (see *Chapter 3.6.2*).

The channel-wise division and the calculation of the standard deviation was done with DOASIS [Kraus, 2005]. Before the noise calculations could be applied, the spectra were corrected for offset and dark current. A high pass filter with 1000 iterations is applied to the quotient to remove any broad-band structures. Afterwards the logarithm is applied. The displayed results are limited to a spectral range with almost constant intensity. The results of the test are displayed in Figure 5-29 (large dots). The scan numbers of the two spectra were increased by adding more scans for the first spectrum and then averaging the same number of scans for the second spectrum afterwards (“classic”). The data follow the square root dependency until 100 scans ( $\sim 10^8$  photons). For larger scan numbers the instrument noise dominates over the photon noise. For standard measurements this is the best achievable level, and thus no larger scan number is useful.

The theoretic photon noise is calculated from Eq. 4.16 and the photon numbers  $n_p$  are estimated by using the full well capacity, quantum efficiency, measured counts and the *ADC* value:

$$n_p = N_{scans} \cdot \frac{S \cdot C}{ADC \cdot QE} = N_{scans} \cdot 2.0 \cdot 10^6 \frac{\text{photons}}{\text{scan}} \quad (\text{Eq. 5.13})$$

with:

Full Well Capacity:

$$C = 100,000 e^-$$

Corresponding ADC value to C (Figure 5-27):

$$ADC = 21,000 \text{ counts}$$

Quantum Efficiency in the used wavelength range at 400 nm:

$$QE = 60 \%$$

Average signal in the evaluation range for one scan:

$$S = 252,250 \text{ counts}$$

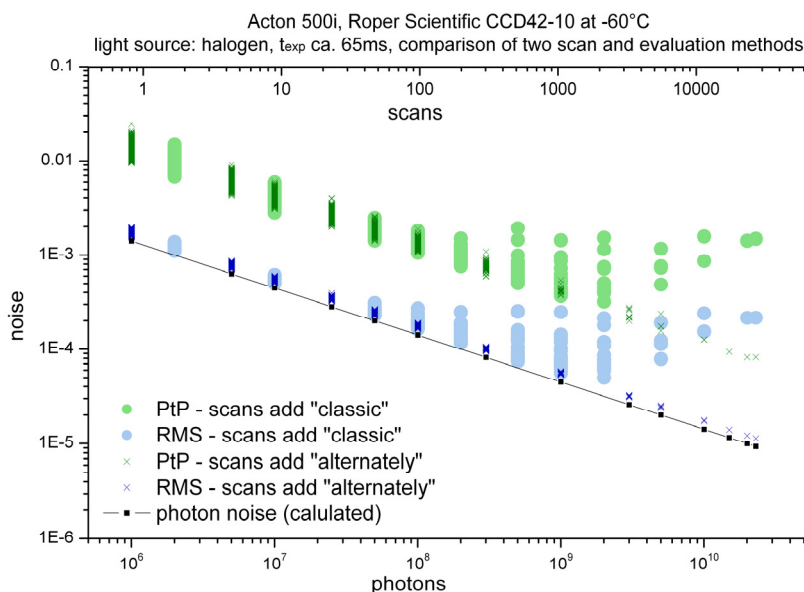


**Figure 5-29: Results of noise tests with Roper Scientific CCD 42-10.** The large dots represent measurements where the scan numbers of the two divided spectra recorded consecutively are increased (“classic”). Blue the Root Mean Square (RMS) values and green the Peak to Peak (PtP) values. The black line indicates the theoretically expected photon noise. If each scan is saved separately and afterwards the scans are alternately added to spectra, the achieved noise is displayed as crosses (“alternately”).

### Noise Test with Varying Time Distance

During the tomographic LP-DOAS measurements the time distance between atmospheric measurement and lamp reference is not only a few seconds, but minutes to hours or even days. The same noise test like above was performed with 50 scans for each spectrum, but the time gap between the two spectra was increased. A slight increase in the noise level by a factor of two was observed within a few hours (Figure 5-30).

As the photo noise does not increase with the time gap, the reason can only arise from an increase of instrument noise. Fortunately the noise stabilised on a still relative low and acceptable level. But to guarantee low noise levels during the measurements, the gap between the lamp reference spectra was reduced to two to three hours. This was only possible with the automation of the lamp reference measurement (see *Chapter 5.2.4*).

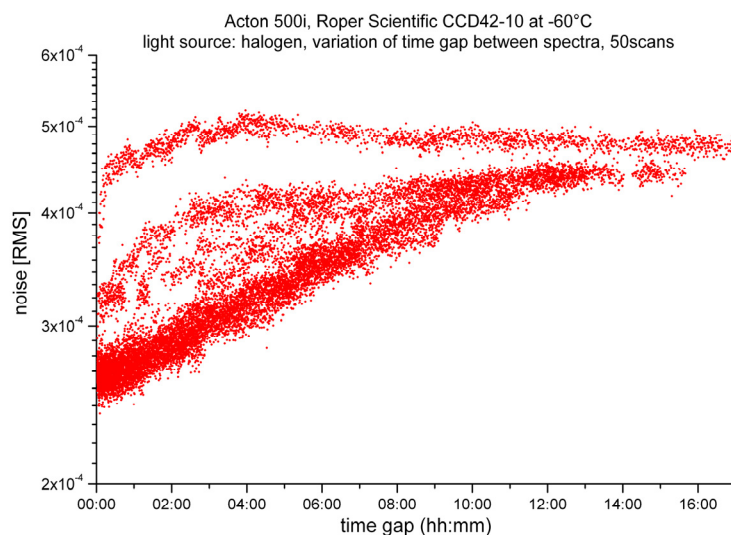


**Figure 5-30: Results of noise tests (RMS) with Roper Scientific CCD 42-10 at 50 scans with increased time gap between the spectra. A slight increase in noise was observed within a view hours. As photon noise does not change with an increase of the time gap, the increase must have its origin in an increased instrument noise.**

### Reducing Noise with Alternately Adding of Spectra

The above noise tests show that the instrument noise increased with time between the two spectra. A similar relation can also be expected for the noise test with large scan numbers. As than also the distance between the centres of the spectra increases with increasing scan number. Thus the increase in instrument noise with scan numbers larger 100 scans in Figure 5-29 may have the same origin. This noise can not be avoided, but its influence can be minimised. The way to reduce the time gap is recording the two spectra as close as possible. The “classical” way of recording spectra by consecutively recording the first spectrum with  $x$  scans and afterwards the second spectrum with  $x$  scans has to be changed. The scans of the two spectra are taken now alternating, what means that the uneven scan numbers are add together to spectrum one and the even scan numbers to spectrum two. Thus the average time gap between the spectra is almost negligible. For example to measure two spectra with ten scans, the first scan is used for spectrum one, the second for spectrum two, the third again for spectrum one and so on until both spectra consist of ten scans. Instrumental variations with time will cancel out and reduce the instrumental noise. Using this measurement method, the noise will follow the theoretic photon noise also if more than 100 scans are added (Figure 5-29, crosses). It can even be observed that the noise never stops decreasing for realistic number of scans, and it seems the noise level can endlessly be reduced by this technique.

For applications where a very low noise level is desirable, it is recommended to apply a similar alternately measurement between reference and absorption spectra. Thus noise levels below  $1 \times 10^{-5}$  can be achieved.

In practice for the tomographic LP-DOAS measurements the alternation can not be applied. The adjustment of the light beams to the shortcut system requires several minutes. Thus only measurements maximum every hour are realistic. But still to implement a kind of alteration, for the data evaluation the last lamp reference spectrum before the atmospheric measurement and additionally the next after this spectrum were used for the data evaluation.

Additional detailed noise test for the Roper Scientific CCD 42-10 detector as well as PDA

detectors can be found in the works of Schubert [2009] and Buxmann [2008].

## 5.4 Retro Reflectors

Retro reflectors are optical elements with the property to reflect back a light beam parallel to the incident direction. This property is independent of the angle between light beam and retro reflector up to a maximum “acceptance” angle. Three reflective faces which are perpendicular to each other form a corner cube. The reflecting faces can be achieved with reflecting surfaces (e.g. mirrors) or through total reflection on the backside of a prism. The light is typically reflected three times, once at each face; before it is send back to the incident direction. The orientation of the picture changes with the reflection (Figure 5-31).

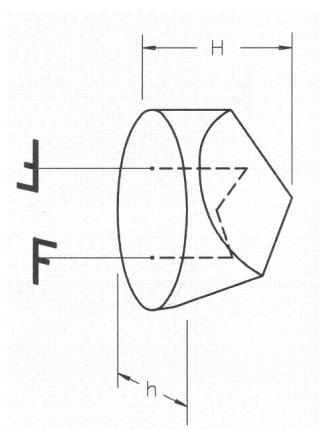


**Figure 5-31: Light path and construction of retro reflector prisms applied to reflect the transmitted light back to the telescope. The scheme displays the change of the picture orientation and the displacement of the incident light with reflection [Linos, 2000].**

The applied reflector arrays consist of single retro reflectors with 62.5 mm diameter. The maximum displacement is accordingly maximum 62.5 mm. The effective reflecting area is smaller (~ 58 to 60 mm), as the reflector backside has to be protected from rain and dust with a housing. In the housing of the used retro reflectors a small bag of desiccants was placed to avoid water condensations. To protect the front side of the reflectors, each array has a small roof.

### 5.4.1 Investigation of Reflectivity with Changing Incident Angle

The optical axis of a retro reflector is perpendicular to the front face and goes through the intersection of all three backside faces, thus it has the same angle to all these faces.

The properties of retro reflector reflections are important to LP-DOAS measurements, especially if the light reaches the reflector at a large angle to its optical axis. Typically the optical axis is adjusted to the light beam. For tomographic measurements many retro reflector arrays are necessary to realise the large amount of light paths. Hence it is of special interest, if the emitted light from different telescopes can use the same reflector array. To quantify this, the “acceptance” angle between the light beam and the optical axis as well as the angle of full width at half maximum (FWHM) intensity has to be determined.

In principal the intensity of the reflection does not depend on the angle to the optical axis. But as the reflective surface seen by the light beam decreases, the intensity will decrease. Due to the geometry of the retro reflector, the reflected light also depends on the rotation angle around the optical axis. If the angle of the light to the optical axis is too large, the critical angle for total reflection is reached at one of the three faces, the light is not reflected back. The same reflection properties can be found by rotating the reflector  $120^\circ$  around the optical axis, thus a  $120^\circ$  symmetry exists.

The dependency of reflectance was firstly presented by [Rityn, 1967] for three different retro reflectors: triple mirror formed out of three flat mirrors, triple prism out of glass and triple prism out of glass with silvered surfaces. In Figure 5-32 the illuminance distribution for the centre of a reflection of a triple mirror is plotted. The reflector alignment is indicated in the centre of Figure 5-33 including the orientation from Figure 5-32 by straight lines. In Figure 5-33 the maximum permissible angle is plotted versus the rotation angle and the angle between light beam and optical retro axis.

For LP-DOAS measurements mostly quartz glass triple prisms are used, which are indicated by the dashed line and highlighted in red. According to Rityn [1967] the “acceptance” angle would be for the  $60^\circ$ ,  $180^\circ$  and  $300^\circ$  rotation  $60^\circ$  to one side and  $20^\circ$  to the opposite side (e.g. straight line in Figure 5-33). This means that the reflection strongly depends on the orientation of the reflector.

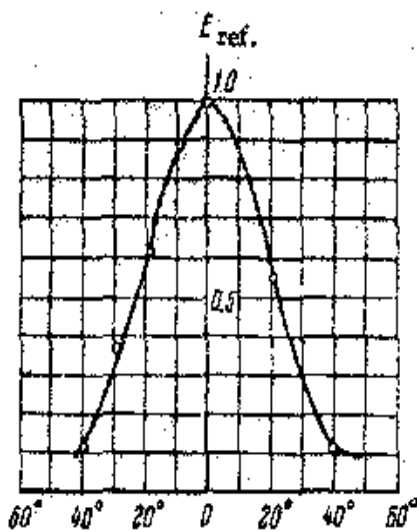


Figure 5-32: Illuminance distribution in the centre of a reflected beam as a function of the angle between the incident rays and the normal to the face of incidence (reflector formed by three flat mirrors) [Rityn, 1967].

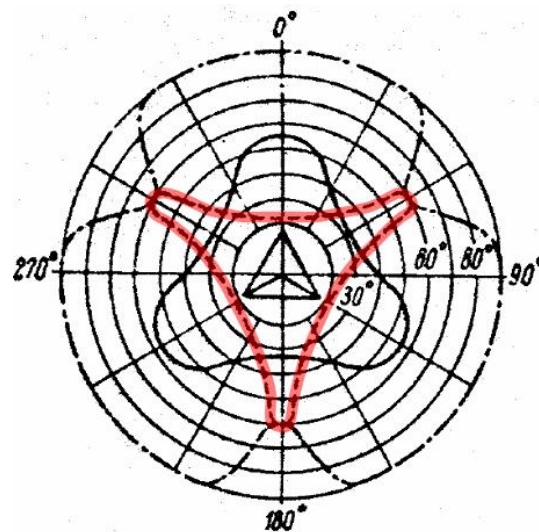


Figure 5-33: Maximum permissible angle at which a corner reflector retains its reflecting properties: — reflector formed by three flat mirrors; - - - - glass reflector with total internal reflection are highlighted red; - · - · - same as above, but with silvered surfaces. [Rityn, 1967].

With an experiment the angle dependency of the reflection was investigated. Two retro reflector arrays were placed at a distance of 1.4 km from the telescope and at 3 m distance to each other (Figure 5-34). One array (7 reflectors) was fixed in a position; the second one (12 reflectors) was rotated in horizontal direction and perpendicular to the incident light. All 12 retro reflectors were set up with the same rotary orientation on the array. Using the MBI one light beam was adjusted to the fixed array and a second to the rotary array. The light spot at

the reflector was much larger than the reflector itself. The intensity reflected back to the telescope was observed for both reflector arrays under different angles at the rotary reflector. The measurements were performed at night to exclude background light with 10 scans each 0.4 s per configuration and by integrating the intensity over the whole wavelength range from 290 nm to 370 nm.

The intensity of the rotary array was divided for each intensity measurement by the intensity of the fixed array to account for different light transmittance of the air during the measurement.



**Figure 5-34: Rotary retro array with 12 quartz glass retro reflectors used for the measurement of the acceptance angle of the reflector. In the background the fixed retro array can be seen from the side. Right: Backside with adjustment of rotational angle and angle between reflector optical axis and incident light beam.**

The performed measurements cover one symmetric cycle of the rotary angle position (Table 5-3). Horizontally the array was moved from  $50^\circ$  (array tilted to the left, clockwise for topview) up to  $130^\circ$  (array was tilted to the right, anticlockwise). The results of the measurement are plotted in Figure 5-35. The intensity distributions display a similar asymmetry for all rotating angles (Figure 5-35). The reason may be an unsymmetrical light intensity of the incident light beam. As the horizontal rotation axis was not directly at the reflector surface, the rotation slightly moves the centre of the reflector to left or right. Thus a larger intensity if rotated to angles  $> 90^\circ$  lead to a longer wing in the reflection curve. As the interest was to investigate the differences of the wings for different rotation angles, this effect does in principle not affect the results.

The measured FWHM are similar for all rotation angles. No strong dependence on the maximum of permissible angle could be found like expected from the study of Rityn [1967]. No strong peaks of permission angle could be determined. The permission angle by Rityn [1967] had to be  $20^\circ$  from the centre for one side at the orientation of  $120^\circ$  and  $180^\circ$ . No such cut offs were observed in the measured intensities. Only the maximum of the distribution seemed to move slightly to the proposed larger permissible angles. If we compare the two contrary situations of  $120^\circ$  and  $180^\circ$  we can see that the intensity dependence is shifted by almost  $10^\circ$ . This feature is small but may indicate the principle described by Rityn [1967]. The characteristic is much smaller than expected. We assume that the intensity is more influenced by the smaller effective area at large angles than at the permissible angle.

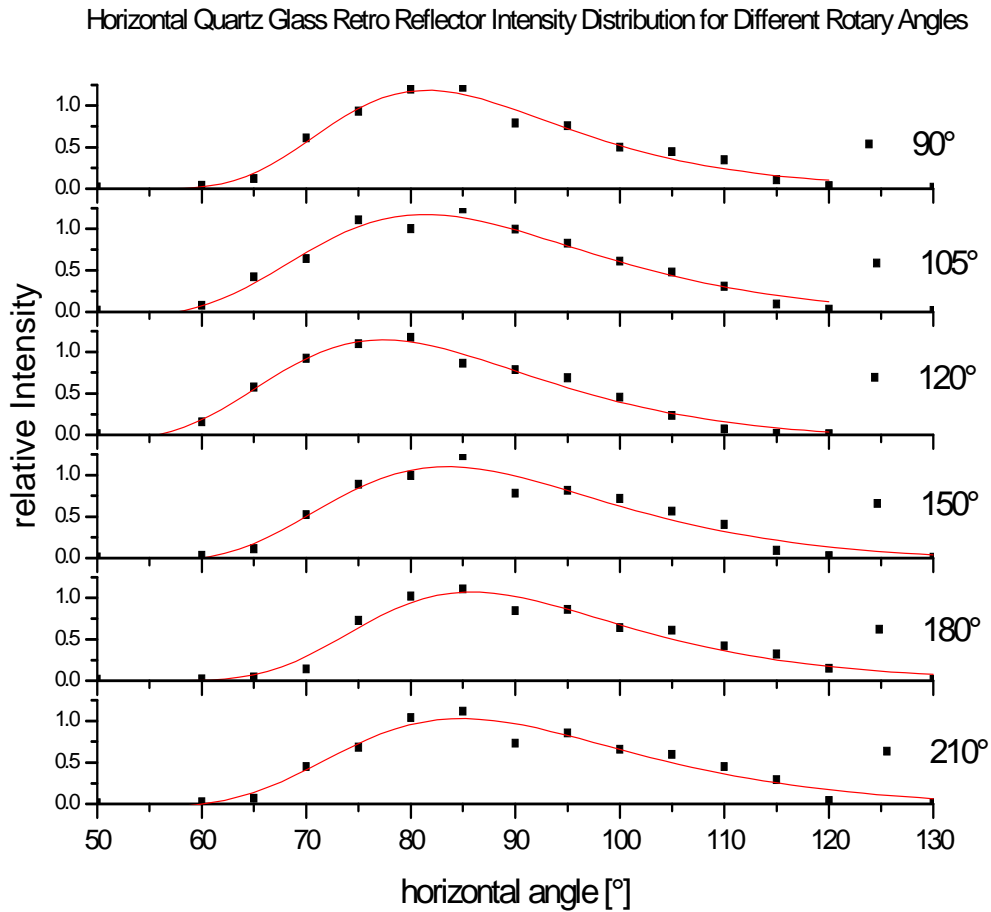


**Figure 5-35: Measurements of the reflected intensity dependence on the reflector orientation. At the reflector array all retro reflectors were orientated to the same direction. The whole retro array was moved horizontally at different rotary angles. The relative intensities are calculated by dividing the intensity with the intensity of a fixed retro reflector next to it.**

	90°	105°	120°	150°	180°	210°
$X_0$	81.6°	81.4°	77.4°	83.5°	85.8°	84.9°
FWHM	31.4°	33.8°	32.8°	33.4°	32.5°	33.9
Max. [°] (experimental)	59.0°	62.0°	59.0°	58.0°	64.0°	66.0°
Max. [°] [Rityn, 1967]	52.0°	50.0°	80.0°	52.0°	80.0°	52.0°

**Table 5-3: Orientations of the retro reflector and measurement results. An entire 120° cycle was covered. The maximum of reflection ( $X_0$ ), FWHM and the maximum permission angle of the experiment are gained from the fit in Figure 5-1. Also the maximum permission angle from Rityn [1967] taken from Figure 5-33 is included.**

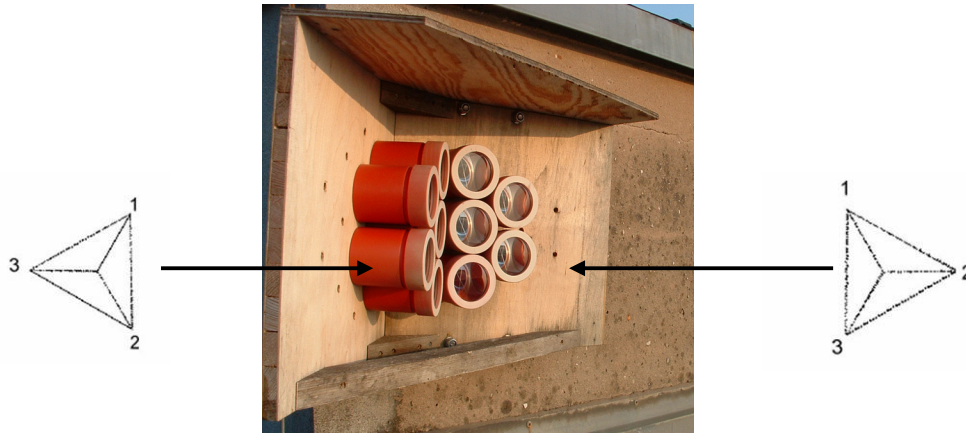


**Figure 5-36: Double retro reflector array installed at the Physical Institute (Philosophenweg) and their rotation orientation.**

As a result of this study we conclude for the tomographic setup of retro reflectors:

1. The rotational angle of the reflector has almost no influence on the reflected intensity as function of the angle between incident rays and the optic axis of the reflector.
2. Using one retro reflector array for two light beams can only be suggested, if the angle between the light beams is less than  $17^\circ$  (HWHM). The rotation of the retro reflectors is unimportant. For larger angles two arrays should be used, each adjusted perpendicular to the light beam.
3. If the angle between the light beams is smaller than  $45^\circ$  (maximum angle for any reflection) and larger than  $17^\circ$  a double array should be applied, where a part of the reflectors is adjusted to one light beam, and the other ones to the second light beam. The reflectors are very close to each other, so light from one light beam can partially also be reflected by the other reflector. The rotation of the retro reflectors should be chosen in such way that one intersection of two faces of the reflector point into the direction of the other light beam. Two of these reflectors are used for tomographic measurements (Figure 5-36).

#### 5.4.2 Comparison of Retro Reflectors of Different Size

The used quartz glass retro reflectors are one of the most expensive parts of a LP-DOAS instrument. The Axellson telescope setup (Figure 5-1) as well as the MBI requires a displacement from the emitted to the received light beam. Part of the displacement is achieved by the retro reflector. Thus large reflectors are typical preferable for these LP-DOAS setups, as they should give higher light throughput. On the other side smaller retro reflectors are much cheaper per reflective surface due to less material and also much lighter (preferable for mobile applications). To investigate the effect of the reflector size, two retro reflector arrays of different single reflector size but similar total reflective surface were compared (Figure 5-37, Table 5-4). The comparison was performed with the Fibre LP-DOAS telescope of the new generation (*Chapter 5.6*), and not with the MBI.

Both retro reflectors were applied at different distances to the instrument, ranging from 7 m to 1550 m. For all configurations similar intensities were achieved for the two arrays. The main reason is that the displacement of the light at the retro reflector is only one component, where displacement occurs. Additional displacements are caused by atmospheric turbulences,

inaccuracy in the surface and the optical components (e.g. spherical mirror) and due to systematic misalignment of the telescope. Thus even other components can compensate this displacement, and also smaller retro reflectors can be applied. Details can be found in the work of [Landwehr, 2010].

It can be concluded, that smaller retro reflectors are similar suitable for LP-DOAS measurements and the same intensities can be achieved with similar reflecting surface.



**Figure 5-37: Left: Retro reflector array with 7 reflectors of ~ 58 mm diameter size. Right: Reflector array with 37 reflectors of 21 mm diameter size. Both arrays have about the same reflective surface.**

	Single effective reflector diameter [mm]	Number of reflectors	Total effective reflector size [cm <sup>2</sup> ]	Weight [kg]	Max. intensity [counts/ms] at 1550 m
A	~ 58	7	165	2.3	460
B	21	37	167	1.4	500

**Table 5-4: Properties of the two compared retro reflector arrays. Measured maximum intensity to the retro reflector position at the Philosophenweg measured with a 200  $\mu$ m fibre bundle.**

## 5.5 Tomographic LP-DOAS Measurement Software

For the tomographic LP-DOAS measurements a software which record the spectra, controls all stepper motors, the TTL controller, the spectrograph as well as the CCD detector was required. The software should also simultaneously process the spectra of the different light paths recorded at once on the CCD chip (Figure 5-17). As no DOAS measurement software could fulfil all these criteria, the new Camera Operation Software (COS) was developed for the operation of the MBI. COS is programmed in Visual Basic, as the camera company provides an interface for this language. The detector readout was performed in the software WinSpec32 (2.5.19.6) from “Roper Scientific” and the data is afterwards transferred to COS. Unfortunately WinSpec32 can only operate stable with the operation system Windows 2000 from Microsoft. The software COS was developed in this thesis to a stage that it allows

continuous tomographic outdoor measurements. All measurement and adjustment processes were automated. The main new implemented tools of the software are listed below. For more details see Pöhler [2008].

- Automatic control of TTL signals for: on/off shortcut motor, in/out lamp shutter; on/off mercury lamp and in/out aluminium reflector for mercury lamp. Implementations in the measurement procedure
- New automatic adjustment routine with improved algorithms which adjust all light paths (all external mirrors) simultaneously on the retro reflectors. Adjustment accuracy could be increased and adjustment time reduced by a factor of 5. For each light path the adjustment parameters can be selected individually (e.g. higher precision for longer light paths)
- Implementation of a fog routine (low visibility) to prevent complete deadadjustment if visibility is too low.
- Automatic search routine to find retro reflector (all mirrors simultaneously). If no signal is received from the retro reflector (light path deadadjusted) a search loop starting from the last known position. This allows measurements also if the external mirrors show large inaccuracies (*Chapter 5.2.2*).
- Automatic measurement of shortcut (lamp reference) spectrum.
- Correction of any malfunction of the HMT Multistep controller (*Chapter 5.2.2*).
- Implementation of a automatic measurement sequence with free selectivity for number of atmospheric measurement scans, background scans and shortcut scans.
- Movement of stepper motors to the final position is optimised. E.g. Movement to the final position always from one side to reduce the effect of motor clearance.
- Save measurement files in a spectral file structure with subfolders similar to DOASIS [Kraus, 2005].

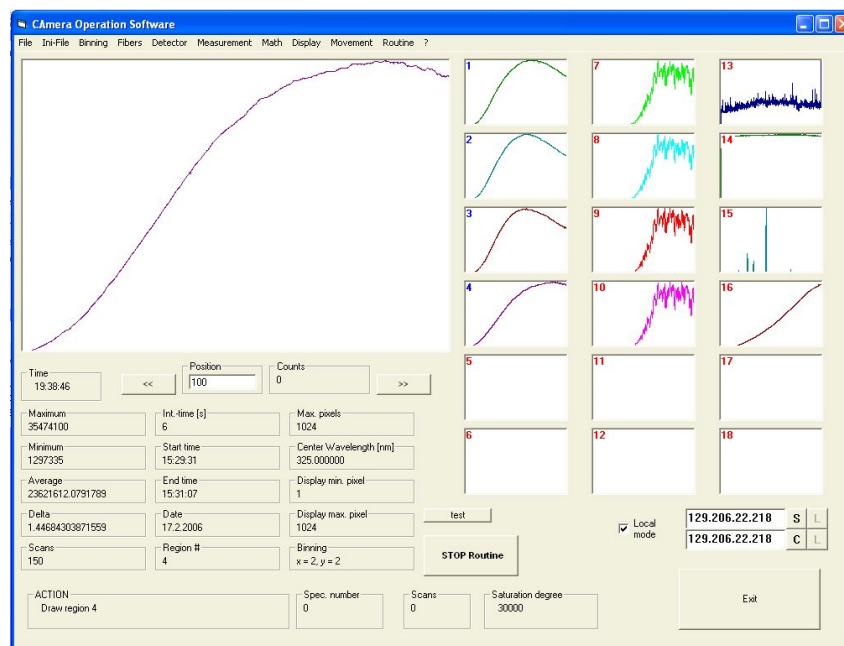


Figure 5-38: Screen view of the measurement software COS (Camera Operation Software).

The spectroscopic DOAS data evaluation was performed with the software DOASIS [Kraus, 2005] (see *Chapter 7.1*).

## 5.6 New Generation of LP-DOAS Instruments

During the last years new LP-DOAS instruments were developed at the Institute of Environmental Physics in Heidelberg, which can also be applied to new tomographic setups. The main new development is the change of the optical system from the Axelsson setup (Figure 5-1) to a fibre setup (Figure 5-39) [Tschritter, 2007, Merten, 2008; Merten et al., 2010; Pöhler et al., 2008], the introduction of LED for LP-DOAS instruments [Kern et al., 2006; Sihler et al., 2009]. Both techniques were extensively tested and applied to LP-DOAS measurements in the last years. For example for long term measurements and monitoring of  $\text{NO}_2$  and other trace gases in Hong Kong. In Spain it was applied for the detection of several air pollutants in a remote sensing site of El Arensillo. Beside the observation of urban pollution the instruments were also successfully applied to measurements of Halogens in marine environment (Mace Head, Ireland) [Seitz et al., 2010] or even Arctic environment (Amundsen Gulf, Arctic) [Pöhler et al. 2010].

Additionally to the innovation of applying special fibre bundles and LED's to LP-DOAS, nowadays compact spectrometers display sufficient quality for urban LP-DOAS trace gas observations. They are simpler to use and display an affordable price (in comparison to the large spectrometers like applied in this thesis). All these innovations start a new era of LP-DOAS instrumentation and also allow simplifying new tomographic LP-DOAS setups. The new system is first described in more detail, before an outlook to a possible simplified tomographic LP-DOAS setup is given.

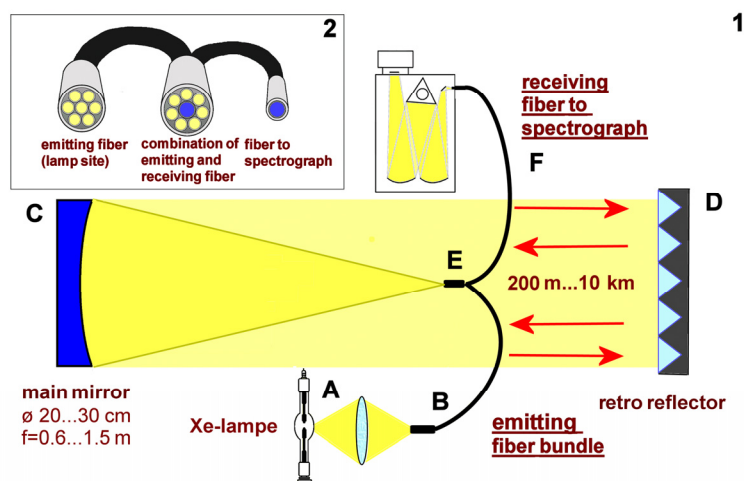


**Figure 5-39: LP-DOAS instrument with fibre optics (1) with emitting and receiving fibres combined in a single bundle. The inset shows the fibre bundle configuration with the ends B, E, F (left to right). [adapted from Merten et al. 2010].**

The Fibre LP-DOAS setup is a large simplification of the telescope, which now only consists of the telescope mirror and the fibre bundle. All other optical components (mirrors) which have to be adjusted in 5 dimensions are redundant. The fibre bundle consists of 7 fibres and radial arranged at the telescope. The fibre at the centre is connected to the spectrometer, the other six to the light source. The light from the light source is transmitted by these six fibres and parallelised by the telescope mirror. The light is similar to other LP-DOAS instruments send to the retro reflector. A part of the reflected light is focused on the central fibre and

guided to the spectrometer. To improve the light throughput, the fibre bundle has to be moved out of the focal point of the telescope mirror (in direction along the optical axis). This can be described as a defocusing of the fibre image at the reflector. An optimum for the received light can be found a few mm from the focal point. More details can be found in Tschritter [2007], Merten [2008], Merten et al. [2010], Müssel [2009] and Landwehr [2010].

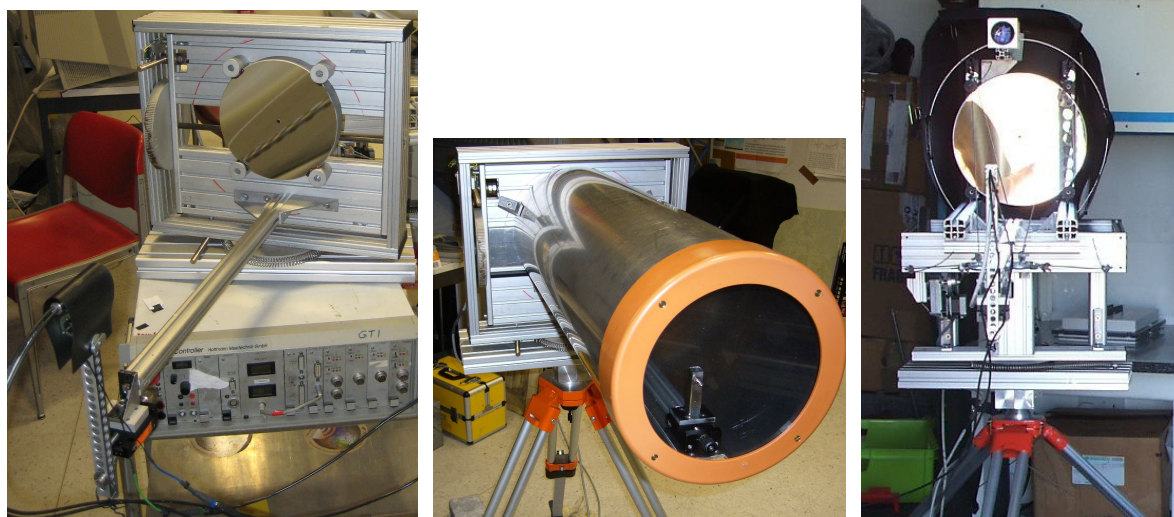


**Figure 5-40:** Left: Small fibre LP-DOAS telescope with  $f = 60$  cm constructed from an external mirror mount. Centre: Similar telescope but with tubing to protect the optic from rain and dust. A window at the front requires the necessary accuracy of the surface not to lose too much light. A quartz glass window has to be used if working in the UV. Right: Reconstructed mirror mount to a  $f = 1.5$  m telescope on a tripod.

The achieved light throughput of the Fibre LP-DOAS is about a factor of 10 higher than for the Axelsson setup Merten [2008]. As additionally the intensity for the MBI is about a factor of 10 lower than the Axelsson setup, the light throughput in comparison to the MBI is a factor of 10 to 100 higher. Thus the other applied components can be less efficient. For example smaller telescopes or light sources with less power. This reduces the cost and demand of such a measurement system.

Another advantage of the Fibre LP-DOAS setup is the simplified lamp reference (shortcut) measurement. It is performed by moving an aluminium diffuser plate to the front of the fibre bundle. Aluminium diffuser plates were applied for the first time in instrument developed in this thesis for the telescopes in Figure 5-40. They are simply sand blasted aluminium, which redirect some emitted light back to the receiving fibre, without passing the atmosphere. Recently performed investigations show that these aluminium diffuser plates display less spectral structures than the before applied quartz glass diffuser glass [Buxmann, 2008]. Also the small size and low weight of the aluminium diffuser plate allows moving it into the light path with a rotary magnet or a lifting magnet. Thus very frequent shortcut measurements are possible, which also allows applying alternating measurement techniques as described in *Chapter 5.3.4*. With these methods lower detection limits are achievable.

The application of LED's to LP-DOAS observations reduces the power consumption, but also allows simpler long term measurements, as the lifetime of LED's are years and not days (like for xenon arc lamps). LED's simplify a LP-DOAS setup, they are relative cheap and display no or only small maintenance demand. High power LED's with few Watts power consumption are nowadays available down to the UV spectral range of 390 nm. UV LED's

down to 240 nm are also available and applicable to LP-DOAS, also if there power is much lower. Each LED covers a spectral range of typically 20 nm. With the combination of several LED's a larger spectral range can be investigated.

Within this thesis these new techniques were applied to the construction of new telescopes. Their application to urban trace gas monitoring and also for tomographic LP-DOAS measurements were investigated. For some of the constructed telescopes, the external mirror mounts from the tomographic LP-DOAS setup were used (*Chapter 5.2.2*) and modified. In the simplest construction the mirror is replaced by a spherical mirror with a focal length of 60 cm and a diameter of 20 cm (Figure 5-40 Left). The fibre is placed on an extended bar and can be adjusted along the optical axis. To avoid reflections at the telescope mirror from the emitting to the receiving fibres, the centre of the mirror is shaded by a black dot. The telescope can be adjusted to a retro reflector simply by the two stepper motors.

The new instruments were applied and tested during several measurement campaigns. One was the application in urban air monitoring, which display similar instrument properties as required for tomographic observations. Therefore, the instrument Figure 5-40 (centre) was applied for NO<sub>2</sub> measurement in a street canyon of Heidelberg [Landwehr, 2010]. Measurements to four retro reflector arrays were performed and the data was applied to determine the vertical NO<sub>2</sub> distribution. The instrument was equipped with a compact spectrometer (QE 65000) from Ocean Opics and a blue Soul B10192 Z-LED. Due to the larger light efficiency of the optical setup, measurements to four reflectors are performed in less than 10 minutes (inclusive adjustment time).

### **5.6.1 Application of New LP-DOAS Instruments for Tomographic Observations**

The above mentioned measurements to several retro reflectors are similar to tomographic observations and demonstrate that with a much simpler and cheaper setup future tomographic observations can be performed. For a full tomographic LP-DOAS setup with this technology basically two configurations are possible which differ in the type of the applied telescopes.

1. The first configuration consists of three to ten of such small full motorised telescopes with 50 - 60 cm focal length and 20 cm in diameter. Each telescope has a waterproof tube and a glass window and can thus placed outside directly on a roof. The measurements to different retro reflectors are performed successively. Due to the large light throughput of the system, measurements to four or more reflectors can be performed in less than ten minutes.
2. The second configuration consists of as many telescopes as light paths. Each telescope is permanently pointing to one reflector (fixed) and thus do not require a full motorisation. The measurement time for each reflector is increased and thus more light is collected in the same time. As no better signal to noise ratio is required, even smaller telescopes with less light throughput can be applied like a  $f = 25$  cm telescope with 10 cm diameter. The telescope will be much smaller and can directly be attached

to a wall or a mast. As still some readjustment of the optic to the reflector is required, this will be performed by adjusting the fibre position perpendicular to the optical axis with motorised translation stages. All other required components for the measurement can be placed with the telescope in one box like sketched in Figure 5-1. The advantage of such a system, also if much more telescopes are required, is the permanent fixation of the instrument to a reflector. Thus measurements without interruptions can be performed, as the telescope is not pointing consecutively to several reflectors. Also the mechanical stability to wind and weather is better, as the telescope is fixed (no external motorisation). This reduced the operation and maintenance demand drastically.

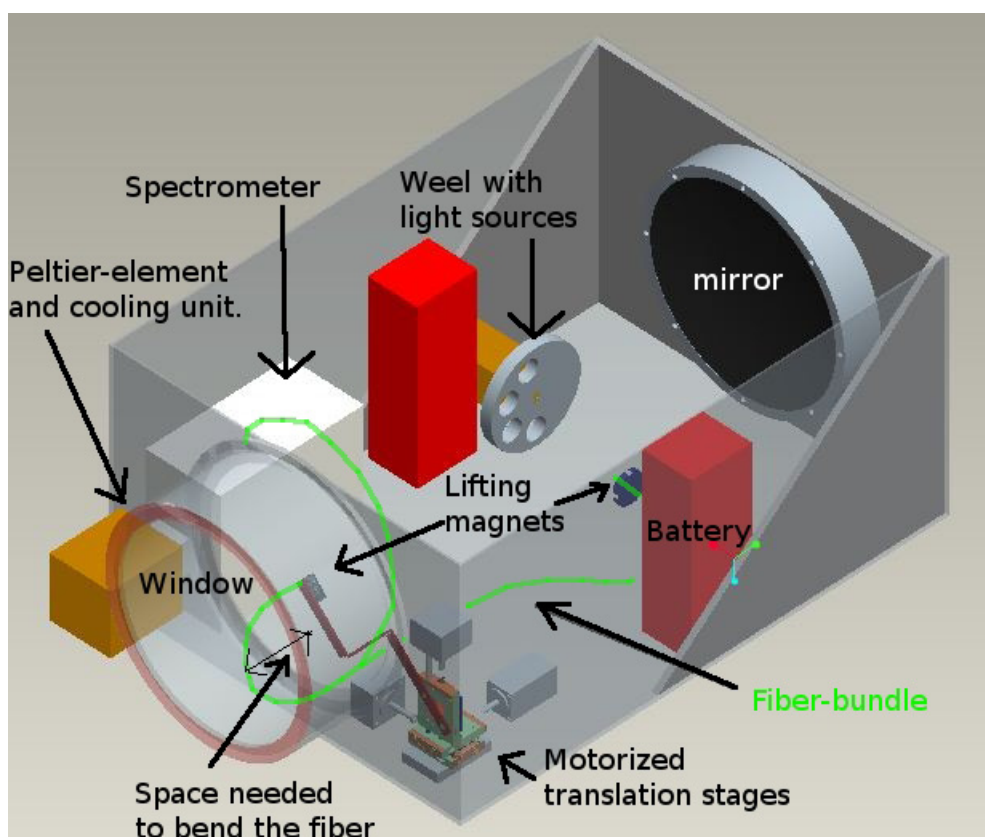


**Figure 5-41:** Sketch of a LP-DOAS instrument with fibre optics and a static orientation to a retro reflector. Beside the telescope also all other components are placed in one box. The precise adjustment on the reflector is performed with motorised translation stages. As light sources LED's are applied. Adapted from Landwehr [2010].

A tomographic setup with such telescopes would be much smaller, and even no laboratory for other components (e.g. PC, spectrometer etc.) is required. Thus more possible locations for the instruments can be found.

For both configurations LED's would be the optimal choice as light sources. The application of blue high power LED would be perfect for the observation of  $\text{NO}_2$ . With additionally UV LED's also  $\text{O}_3$ ,  $\text{SO}_2$ , HCHO, HONO, Benzene and other aromatic compounds can be observed. The different LED's would be combined in the instruments. Compact spectrometers with integrated detectors would be used for the measurement of the spectra. The light source, spectrometers and electronic can be placed in a separate box or together in one housing with the telescopes. Each instrument has an embedded PC and measures completely automatic and

independent. Similar to the tomographic setup of this thesis (*Chapter 6*), about 20 crossing light paths would be applied to the investigation area. As the instrumentation is much smaller and simpler, likely more setup locations can be found. Thus a better tomographic geometry with higher spatial coverage may be realised.

The recorded spectra will be transferred to a data server and evaluated. The tomographic software would automatic determine the actual trace gas distribution.

## **5.7 In situ monitors**

Different in-situ monitors were used in order to compare the results. A chemiluminescence NO / NO<sub>2</sub> and an ozone monitor operate on the institute's roof (IUP in Figure 6-6). The environmental department of the German state of Baden-Württemberg operate a measurement station (LUBW009) in Heidelberg (Figure 6-4) for the trace gases NO, NO<sub>2</sub>, SO<sub>2</sub> and O<sub>3</sub> which are also used in this study for comparison. Details of the measurement instruments are not described in this chapter, but can be found at [Umweltmessung BW, 2006].

### **5.7.1 Chemiluminescence NO / NO<sub>2</sub> monitor**

The used monitor (CLD 770 AL ppt, Eco Physics, Duernten, Switzerland) for NO and NO<sub>2</sub> in-situ measurements at the Institute of Environmental Physics is based on the chemiluminescence method. The data is used to be compared with the concentrations reconstructed from the DOAS tomography at this location in the city. The technique is based on the detection of photons emitted by electronically excited NO<sub>2</sub>\* molecules during a relaxation process (chemiluminescence). The excited NO<sub>2</sub> molecules are produced during the reaction of the ambient NO with ozone (R 2.4 see *Chapter 2.1*) which is generated in the device. The chemiluminescence signal is proportional to the NO concentration in the sampled air. A photomultiplier tube detects the photons. Only about 20 % of the created NO<sub>2</sub> is in the excited state. The main part of the NO<sub>2</sub>\* returns to the ground state without radiation emission due to collisions with other molecules. This process is also known as quenching. In order to enhance the photon yield, the pressure in the reaction chamber is reduced. The measurement of NO<sub>2</sub> can be performed converting NO<sub>2</sub> to NO photolytically, using an UV photo diode. Photolytic converters have the big advantage, in comparison to catalytic converters, to convert almost exclusive NO<sub>2</sub> to NO, and no other nitrogen molecules like NO<sub>3</sub> and HONO. The used photolytic converter (BLC-BWR.SCH, Release 2 from Droplet Measurement Technology, Inc.) was calibrated and displayed an efficiency of 0.34. The photolysis system is followed by chemiluminescence detection of NO as described above. For more information on the use of chemiluminescence for atmospheric measurements see [Navas, 1997].

### **5.7.2 UV- absorption ozone monitor**

Ozone features strong absorption bands in the UV. The ozone monitor uses the absorption at 254 nm emitted from a low pressure mercury discharge lamp. The gas sample flows into a sample cell, passing a valve that alternately guides the flow directly to the cell or via a

selective ozone scrubber in alternations of 10 seconds. The UV light transmitted through the sample cell is detected by an evacuated phototube. The difference in light transmission between the ambient sample and the ozone scrubbed reference sample is directly related to the  $O_3$  concentration through the optical path length and the absorption coefficient of  $O_3$  at 254 nm according to the Lambert Beer law (see Eq. 3.1). Unfortunately the instrument cannot perform absolute measurements, like DOAS, as the light path inside the tube is lengthened due to reflections at the tube walls. The calculation of the ozone concentration is made by using a coefficient periodically determined by calibrations. Conversion of the concentration to mixing ratio units requires the accurate measurement of temperature and pressure in the absorption cell.

## 5.8 Weather stations

Metrological conditions have a large impact on the chemical processes in the atmosphere and influence their concentration and distribution (*Chapter 2*). Thus metrological information is essential for the interpretation of observed trace gas distributions. The present wind field is important to interpret dilution processes. Especially in hilly areas, like the presented measurements in Heidelberg, a strongly varying wind field can exist over the whole measurement area of view  $km^2$ . Thus several weather stations were set up to cover this area.

Besides one professional weather station permanently installed at the Institute of Environmental Physics (IUP) two semi professional radio weather stations MEGA II (WS 2200) were installed on the SAS and Heidelberger Druckmaschinen (HD-Druck) building (Figure 5-42). These weather stations log the data in a logger which can be read out by a PC interface. The main properties are summarised in Table 5-5.

Before these weather stations were set up on their final locations, they were compared to the permanent installed weather station at the IUP building. The comparison was focused on the wind data, thus both wind sensors of the MEGA II station and of the IUP station were set up on the same mast (Figure 5-42) at the IUP building. View days of measurement comparison were performed.

The comparison of wind direction displays good correlation (Figure 5-43). Only a slight offset could be found which may arise due to the setup, as both sensors could only be aligned manually to the same direction. A larger scatter arises during times when only a low wind is present and no clear wind direction exist.

The data of wind speed are less convincing. Also if the observed histories are similar and have the same cycle, the MEGA II station displays higher values than the weather station at the IUP (Figure 5-44). The correlation factor was estimated to 1.6 and for the second MEGA II station to 1.59. The larger scatter can be explained by the lower time resolution of the MEGA II station which only samples one data point every 3 min and average and interpolate these to 5 min values. The IUP station samples every 0.3 s and averages these to 5 min values. Thus scattering is reduced. The reason for the higher values of the MEGA II stations could not be identified. It could not be excluded that also the wind speed at the IUP station is too low, as this station is already in use since several years. A degradation of the wind sensor could have reduced the measured wind speed. As the reason for the different data could not be identified,

all wind data presented in the *Appendix* are not adjusted. Thus all absolute wind speed data should be interpreted with caution.

sensor	accuracy	resolution	sampling	data submission	power supply
wind sensor (direction)	$\pm 5^\circ$	$5^\circ$	3 min	radio communication	solar
wind sensor (speed)	$3\% \pm 0.28 \text{ m/s}$	$0.1 \text{ m/s}$	3 min	radio communication	solar
temperature outside	$\pm 1.0^\circ\text{C}$	$0.1^\circ\text{C}$	3 min	radio communication	solar
relative humidity outside	8 %	1 %	3 min	radio communication	solar
rain	$2\% \pm 1\text{mm}$	$< 0.5 \text{ mm}$	3 min	radio communication	solar
pressure inside	$\pm 1 \text{ hPa}$	$1 \text{ hPa}$	3 min	radio communication	batteries
temperature inside	$\pm 1.0^\circ\text{C}$	$0.1^\circ\text{C}$	3 min	radio communication	batteries
data logger	memory for min. 1.4 days (@ sampling of 2min)		max. 2 min	RS 232	batteries

**Table 5-5: Properties of the MEGA II (WS 2200) weather station applied on the SAS and HD-Druck building. The data is transmitted via radio communication at 433.92 MHz with a maximum range of 100 m (free transmission). The data logger saves the data of min. 1.4 days which can regularly be read out by the PC.**



**Figure 5-42: Left: Mega II weather stations used on the SAS and HD-Druck building. Right: Experimental setup for the comparison of the MEGA II weather station with the permanent weather station at the IUP building.**

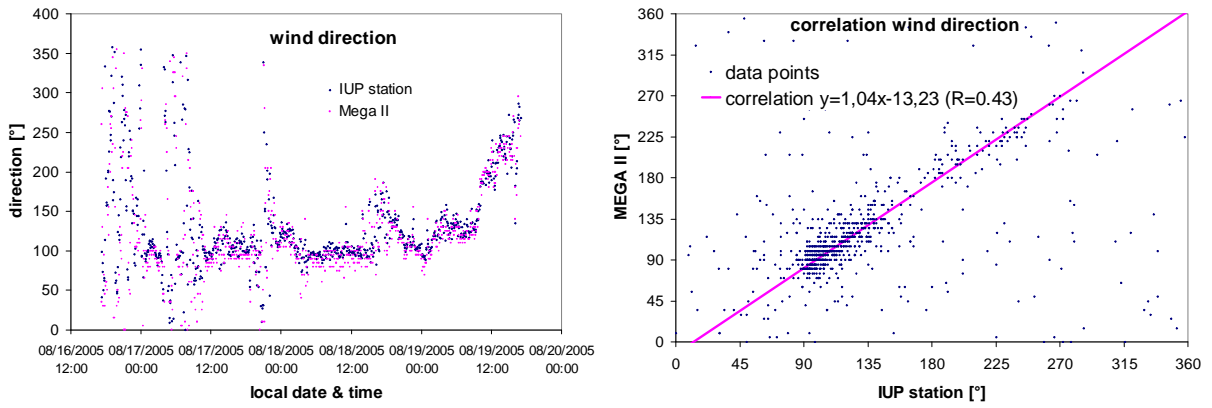


**Figure 5-43: Comparison measurements of wind direction with the weather stations MEGA II (later installed at SAS) and the permanent station at the IUP institute. The data correlate well. The small offset arose from the setup and different sampling times. Data points with larger offset arise from measurements when no or only very low wind was present and thus no exact wind direction was defined.**

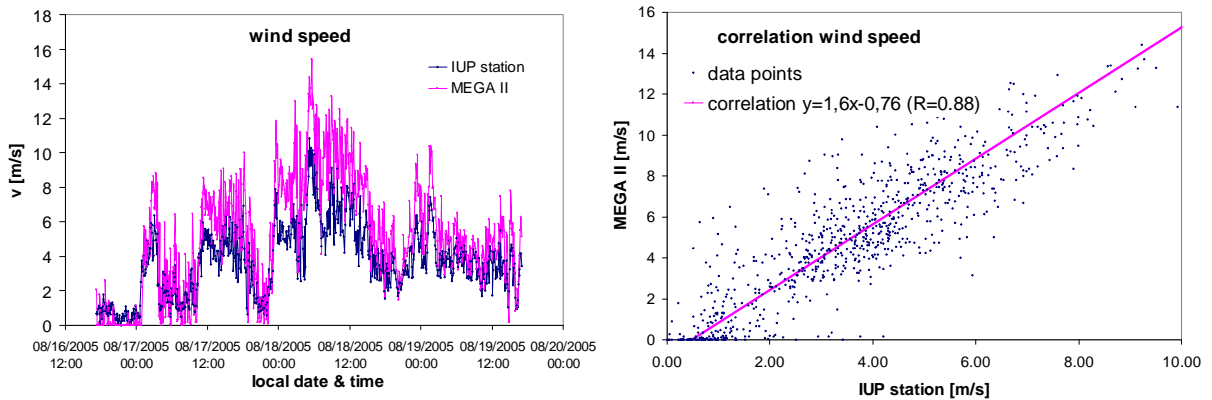


**Figure 5-44: Similar comparison as Figure 5-43 but for wind speed. Both stations show similar history of wind speed, but the data of the MEGA II station are higher by a factor of 1.6 (similar for the second MEGA II station). It could not be solved which weather station display the wrong wind speed.**

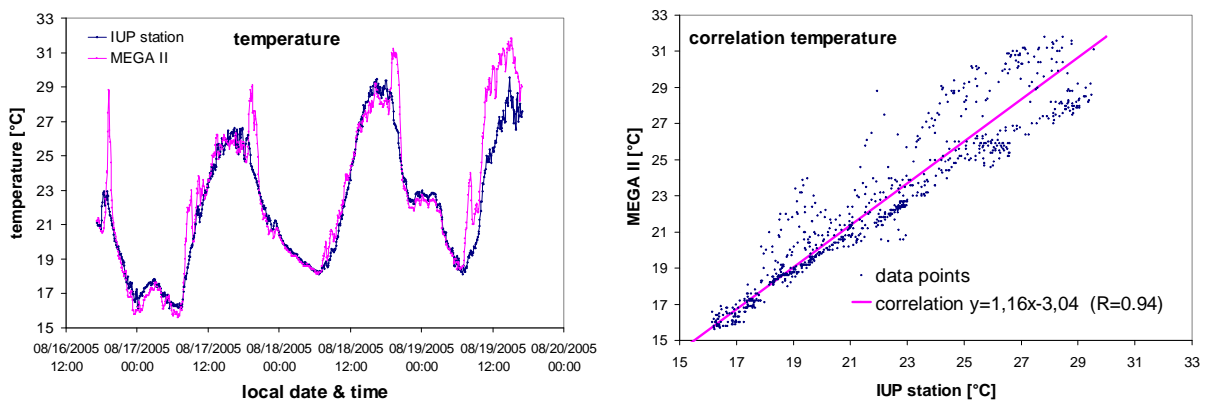


**Figure 5-45: Similar comparison as Figure 5-43 but for temperature. Both stations show similar history of the temperature. The MEGA II sensor could not be shaded perfectly from sunlight and thus especially in the evening sunlight lead to higher observed temperatures.**

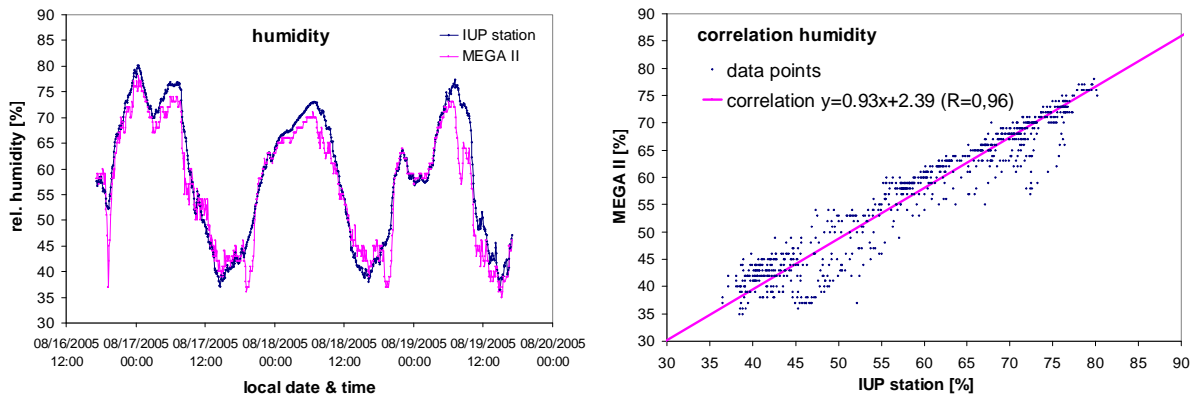


**Figure 5-46: Similar comparison as Figure 5-43 but for humidity. Both stations show similar history of the humidity with slightly lower values of the MEGA II station. The MEGA II sensor could not be shaded perfectly from sunlight, which could be the reason for the slight differences.**

A comparison of temperature and humidity displayed sufficiently good correlation between the different weather stations (Figure 5-45 and Figure 5-46). The pressure sensor was not directly compared. But it is expected that the pressure does not vary significantly over the area of the city, thus the pressure measurements at the later instrument locations can directly be compared (see *Appendix*). They show a slight offset. As both sensors display the absolute pressure (not normalised to sea level), the difference can just arise from calibration differences.

It was concluded that the accuracy of the MEGA II weather station is sufficient to gain information on the weather conditions. Especially the separate wind direction sensor seems to give accurate data. The absolute wind speed data is likely a factor of 1.6 too high, but still important information on the wind field can be gained. The wind speed data between the two MEGA II stations can directly be applied to interpret relative values. To quantify the weather conditions during the tomographic measurements in Heidelberg, the quality of the MEGA II stations are sufficient, especially as the averaging to longer time intervals reduces scattering of the data.

## 6 Heidelberg Tomographic LP-DOAS Setup

In this thesis the tomographic LP-DOAS principle was applied for the first time in order to investigate the horizontal trace gas distribution. The main target was to use this technique in an urban area to investigate its emission sources and arising trace gas distributions. The setup of the instruments and the retro reflectors, which were necessary to achieve the large number of light paths, required an extensive logistic demand. This was one reason why the city of Heidelberg in Germany was chosen, where also the Institute of Environmental Physics (IUP) is located. The size of the city is ideal for this setup, as almost the whole area can be covered. The city displays a characteristic arrangement of streets and areas with different heating systems. Thus a trace gas distribution is expected. No larger industry is located in this area which can dominate the observed trace gas concentration.

This chapter provides information on the measurement location, the geometrical setup, the sites of the instruments and the retro reflectors as well as details about the local setup. A short overview of the setup can also be found in Poehler et al. [2005].

### 6.1 Facts About Heidelberg

The city of Heidelberg is located on the river “Neckar” where it exits the “Odenwald”, a low mountain range, to the Rhine valley at a height of 116 m above sea level. Thus the city is located directly next to the hills, surrounded by the mountain “Königstuhl” with 568 m, “Gaisberg” with 375 m and “Heiligenberg” with 445 m. The city is famous for its castle and the old town located in the Neckar valley (Figure 6-1). The river Neckar flows through the city and divides it into a northern and a southern part.

The urban areas are mainly located in the flat valley (see Figure 6-5). Next to the cities of Mannheim and Ludwigshafen, Heidelberg is one of the three large cities of the densely populated Rhine-Neckar area with a total population of 2.36 million inhabitants. In 2007 about 145,300 inhabitants lived in the city of Heidelberg [Heidelberg, 2009]. This number does not include the American soldiers and their families based in Heidelberg. A territory of 109 km<sup>2</sup> belongs to the city, of which 29.6 % (32.2 km<sup>2</sup>) are populated. The density in the city centre itself is relatively high and the green areas are located in the hills and outside the city. The old town is located at the end of the Neckar valley and the newer territories are more located in the West which is already the beginning of the Rhine valley.

The main economy is the service sector (84%) and to a minor part industry (15.6%). Four universities and a college of higher education are located in the city, which dominate the service sector. 69 % of the employees (52,100) are commuters. They travel daily into the city and contribute significantly to the rush hour traffic. Only 15,650 employees live in Heidelberg and work elsewhere.

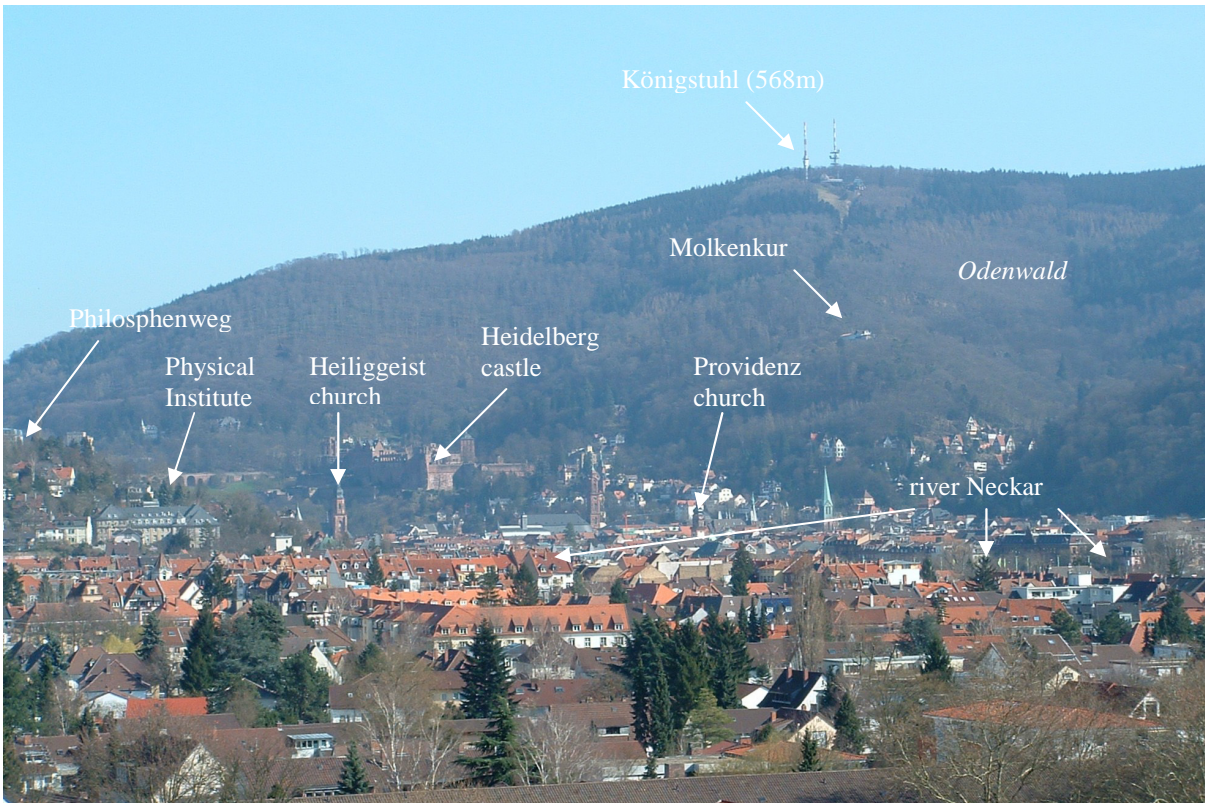


**Figure 6-1:** View from the Institute of Environmental Physics (IUP) to the old town of Heidelberg with its castle and Königstuhl in the background and the beginning of the Neckar valley. Some locations of retro reflectors are highlighted.

### 6.1.1 City Districts

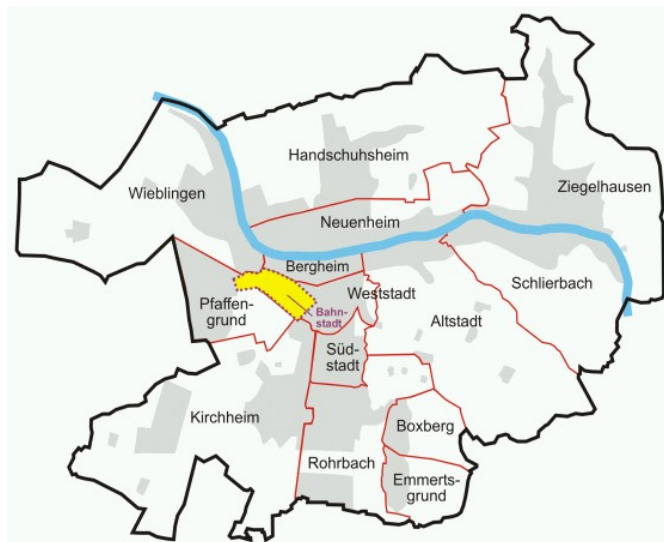


**Figure 6-2:** Map of the city of Heidelberg with its districts. The grey shaded areas indicate populated area. The measurements of this thesis were performed in the territory of the districts “Altstadt” (old town), “Bergheim”, “Neuenheim”, “Handschuhsheim”, “Weststadt” and also in the new developing district “Bahnstadt”, which is a former area of the railway.

The city is divided into 14 districts (Figure 6-2). The old town is mainly located in the Neckar valley, whereas the newer territories next to it are already situated at the beginning of the Rhine valley. The measurements of this thesis include mainly the central territory of the city

with the districts “Altstadt” (old town), “Bergheim”, “Neuenheim”, “Handschuhsheim”, “Weststadt” and also in the new developing district “Bahnstadt”, which is a former area of the railway (Figure 6-2).

The city of Heidelberg has a densely built-up area with a homogeneous development. Only few open areas like plazas and parks can be found in the city. The typical height is about four to five floors with an average of 20 to 30 m (Figure 6-1). As the city was not significantly damaged during the Second World War, most of the old buildings are preserved. Especially the older city districts “Altstadt” (old town), “Bergheim”, “Weststadt” and parts of “Neuenheim” are characterised by buildings built 100 to 200 years ago. Gaps between the buildings were filled with newer buildings of the last century. In the “Altstadt” (old town) several shops, bars, restaurants, offices and university buildings can be found. But still many flats, especially for students, are located in the old town. The districts “Neuenheim” and “Weststadt” are characterised by apartment buildings and few single and smaller buildings. “Bergheim” is a mixed district with university and hospital buildings. Also several offices and apartment buildings can be found there. The West side of “Neuenheim” is a new district with the large new university campus (Figure 6-4). The campus is almost a complete pedestrian area with only few streets. All buildings are also connected to the district heating, thus no heating emissions arise in this area.

### 6.1.2 Transport Sector

The city is located at the old crossing of trading routes, in the North-South direction along the “Odenwald” and in East-West direction along the river Neckar. Today no major trading route is passing the city, but two main roads (B3 and B37) from West to East and North to South are crossing the city on these old roads. About five km West of the city the two highways A5 and A656 can be found which form the “Heidelberger Kreuz”. The highway A656 from Mannheim ends at the West end of the city of Heidelberg. A large portion of the car and lorry traffic is due to transit into and out of the Neckar valley. Due to the location of the city a very inhomogeneous network of roads exists (Figure 6-4). The larger roads are mainly located at the West end in the newer territories. Here the most important traffic junctions and the highest traffic volume cumulate which can be estimated from noise level maps (Figure 6-3). The largest approaching roads to the city come from West or South-West. The most important West to East connections runs along the river Neckar and through “Bergheim”. These roads bypass the old town. All transit traffic into and out of the Neckar valley uses these roads. Two main roads for the North to South connections are located at the two bridges crossing the river Neckar, one in the West and one close to the city centre. This inhomogeneous road network leads to regular traffic jams. The total amount of registered vehicles is 62,000 with 54,200 cars. Thus, 373 cars are registered per 1,000 inhabitants, what is a relatively low value for Germany, where the average is 501 per 1,000 inhabitants. This is due to the high proportion of students which mainly use bicycles and public transport. Heidelberg is connected with the Rhine-Neckar area by an urban railway. Furthermore, the city has access to the international railway system via the city of Mannheim, 20 km away [Heidelberg, 2009]. Also ship transport on the Neckar plays a major role (see *Chapter 8.15*).

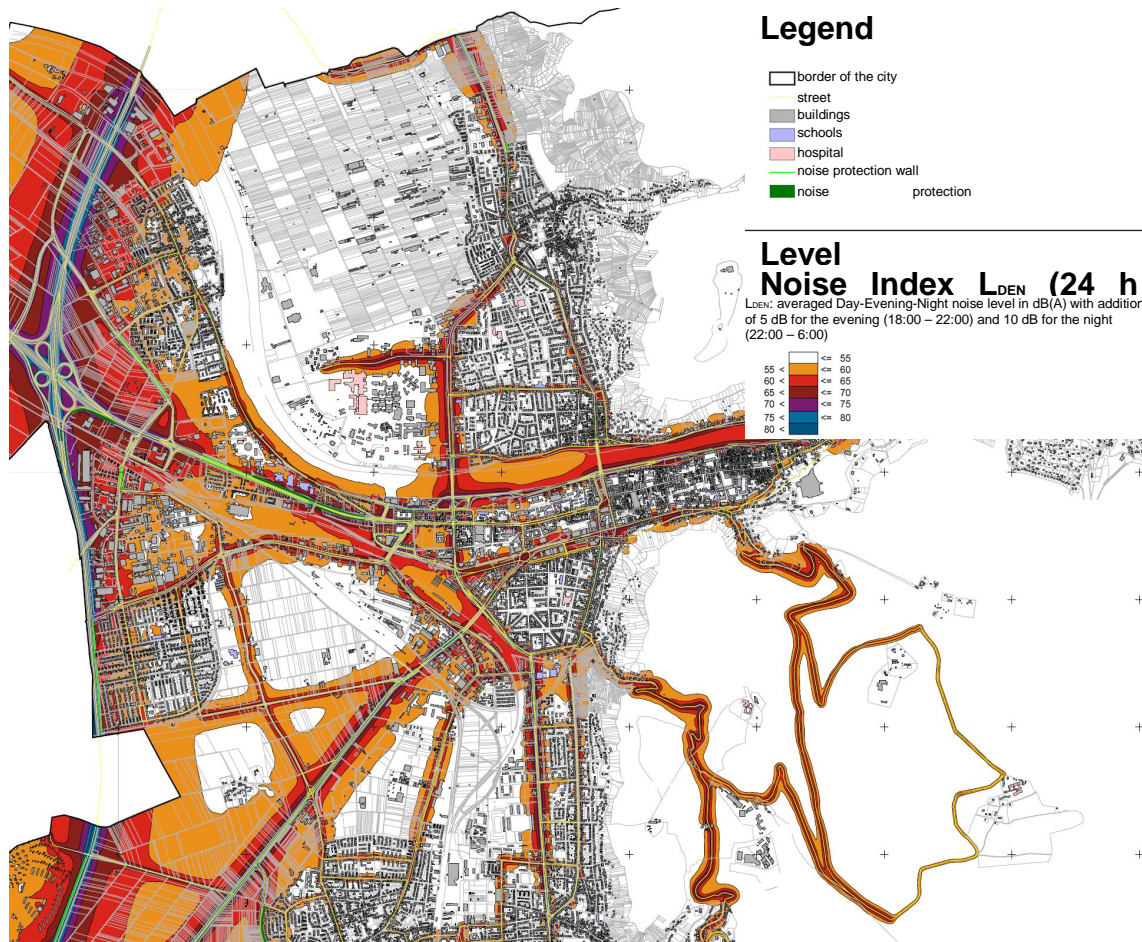


**Figure 6-3: Noise level map (colour code in dimension dB) from streets (no tram nor railway) of Heidelberg for 24 hours dated 2007 according to the EU directive for environmental noise 2002/49/EG. The noise level indicates the traffic volume. However wide roads or roads without buildings (e.g. at the river Neckar) have a larger area of noise propagation, and thus a larger area is marked, but not necessarily a higher traffic load. The emission point of observation is at 4 m height above ground. Only streets with more than 4,000 cars per 24 h are accounted. The noise level in the evening (18:00 – 22:00) has additionally increased by 5dB (due to noise protection regulations), and during the night (22:00-6:00) by 10 dB. [Heidelberg, 2007]**

### 6.1.3 Power Plants and Small Heating Systems

Besides traffic emissions also power plants and small heating systems are of importance. The municipal power plant in the centre of Heidelberg in “Bergheim” is only a standby system and typically not operating. The stack has a height of 60 m. A large power plant can be found north of the university campus in “Neuenheim” (Figure 6-4). It is currently operated by the company RWE and running continuously 24 hours a day on gas to supply electricity, heat and cooling to the university, the cancer research centre, the science park and also the city of Heidelberg. The cogeneration system has a maximum electrical output of 13.5 MW, 162 MW for heating power and 25 MW for cooling. The smaller stack with 60 m is used for the trigeneration plant for power, heat and cooling. The larger stack with 120 m is only used for additional heating power. The power generation and also the emissions are varying and depending on the current power consumption of the customers. They are mainly characterised by the yearly cycle<sup>5</sup>. Details on the real power output during the measurement period could

<sup>5</sup> pers. communication Dietmar Blank, RWE, August 2009

not be provided by RWE. Also if this power plant is outside of the observed area (Figure 6-4), the emissions are clearly visible in the derived concentrations. Unfortunately, due to missing of the real output production data with a temporal resolution of at least a days, no correlation to the concentration can be performed.

Small heating systems can have a significant influence on the emissions. Heidelberg is connected to the district heating system of Mannheim. Especially university buildings and offices are connected to this system. Also many houses in “Bergheim”, “Altstadt”, North and West of “Neuenheim” and partly also “Weststadt” are connected to this district heating system. But especially older buildings have their own small heating system running on gas or even on oil. They can predominantly be found in “Neuenheim” and “Weststadt”.

### 6.1.4 Industry

Industry plays only a minor role in the economy of Heidelberg (15.6 %). But due to meteorological conditions industrial emission may have a significant contribution to the air pollution in the city. The predominant wind directions in Heidelberg are due to the Rhine and Neckar valley from West/East or North/South. Wind from West may transports polluted air from the Rhine valley, especially from the industry centres Mannheim and Ludwigshafen, to the city. In *Chapter 8.11* it is investigated if this pollution considerably contributes to the concentrations in Heidelberg. Other industry areas can be found South of Heidelberg with the companies “Heidelberg Zement” and “Heidelberger Druckmaschinen AG”. The latter has also a smaller exhibition factory in the city of Heidelberg, where one of the instruments was placed (*Chapter 6.3.3*). Wind from the East only transports little pollution from the Neckar valley to the city, as only little industry is located in this area.

### 6.1.5 Spatial Characterisations of Urban Areas

This chapter summarises the most important spatial characteristics in the measurement area of the tomographic measurements. Figure 6-4 shows a colour coded map with different highlighted areas. The colour indicates the dominating building type. On top of the map, the tomographic reconstruction grid I ( $8 \times 8$ , *Chapter 7.4.1*) shows the measurement area. The location of the two power plants is also shown in the map. The RWE power plant in the North is the expected largest emitter of  $\text{NO}_2$  and other trace gases in or close to the measurement area. The locations of the in-situ monitors of the state Baden-Württemberg<sup>6</sup> (LUBW) and at the IUP are indicated with pink dots.

The river Neckar divides the city into a northern and a southern part. The Northern measurement area is dominated by residential areas in the North-East and university and hospitals in the North-West. South of the Neckar a much higher variability can be found. In the East the old town with its historic building is located. Most of its territory is located in the measurement area. West of the old town, in “Bergheim”, a former industry and hospital area is located. Still several hospitals are located there, but from the former industry most of the buildings are reconstructed to residential or office buildings. Also some stores can be found

---

<sup>6</sup> Landesanstalt für Umwelt, Messungen und Naturschutz Baden- Württemberg

there. Beside few left industry also the municipal power plant is located here<sup>7</sup>. The real emission of the left industry is unclear, as it is more composed of several smaller emitters like from printing machines (e.g. Heidelberger Druckmaschinen), a public transport depot (Stadtwerke Heidelberg) and small manufacturing industry.

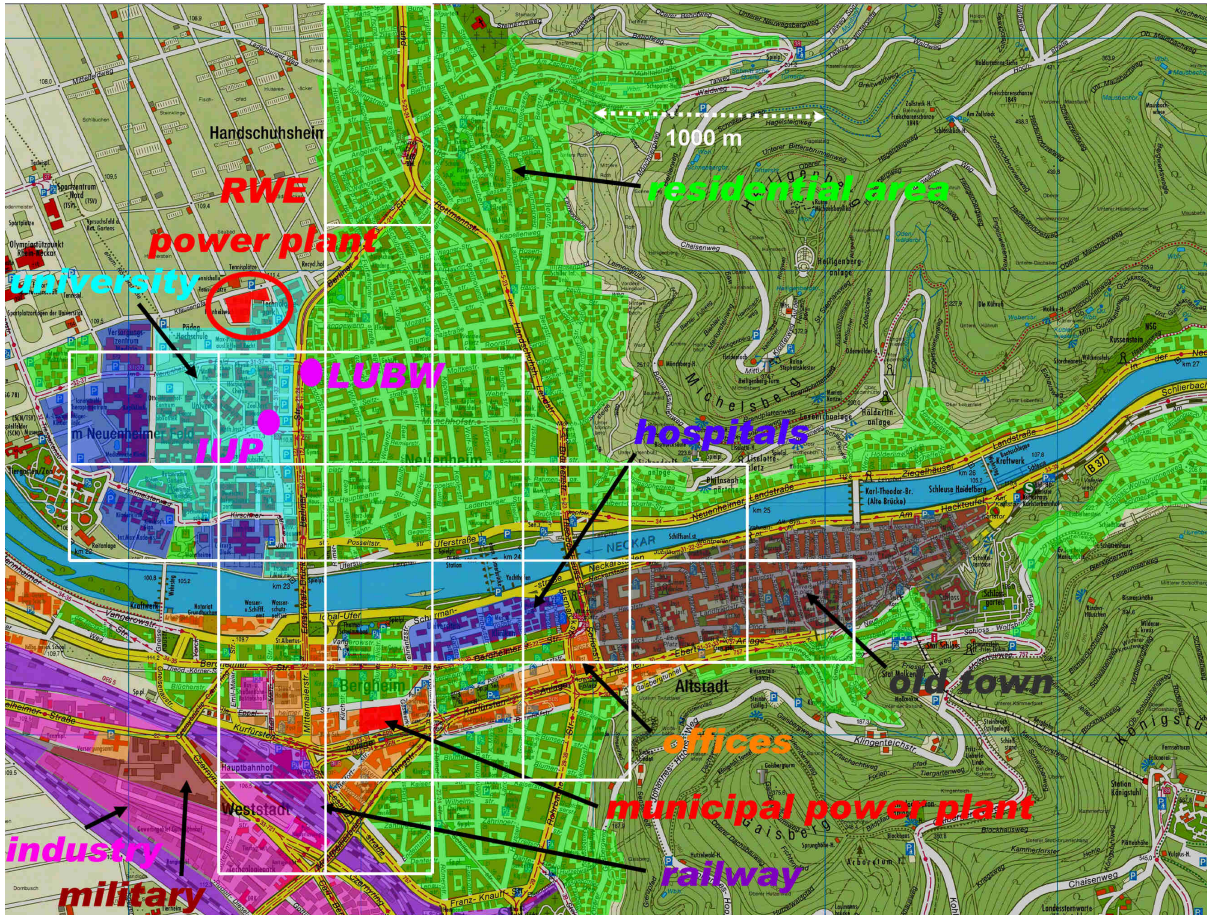


Figure 6-4: Map of Heidelberg with colour coded characterisation of different urban areas. Tomographic reconstruction grid I on top indicated with white lines (see Chapter 7.4.1). In bright green predominantly residential areas, in blue hospitals, in grey the old town, in orange offices and stores, in pink industry, in violet railway, in brown military, in red power plants, streets are left yellow and white. The river Neckar divides the city into a northern and a southern part. For a better contrast view the digital image.

In the South-East parts of the residential area “Weststadt” are covered by the measurements. In South-West the area is dominated by the railway and industrial area. As many trains are electrified and newer diesel engines display much lower emissions, the total emissions are expected to be low. The industrial area does not contain strong emitting industry and should not display strong trace gas concentrations.

The main source of trace gases are expected to arise from traffic. The mayor streets are left yellow in Figure 6-4. The main streets are located in the West and South-West. Two bridges over the river Neckar characterise the main North-South connection. Along the river and further South the main East-West connection can be found.

<sup>7</sup> Stadtwerke Heidelberg AG

## 6.2 Measurement Geometry and Setup

For tomographic investigations a good coverage of the area of interest is necessary. If more light paths are used for the observation, a better resolution in the retrieved trace gas distribution is possible. But the geometry is also important. A homogeneous coverage from independent light paths, e.g. chessboard pattern, would be one of the best solutions [Hartl et al., 2006]. In an urban area this is not possible for several reasons. First, due to different buildings, complicate street network and topography no homogeneous and equal setup is possible. Only few buildings of nearly the same height can be found where instruments or reflectors can be installed in order to realise a direct view between these components. Thus, only an inhomogeneous setup is feasible, but still the best possible homogeneity is tried to be realised. The reconstruction has to deal with the inhomogeneous setup. Second, the amount of instruments would be unrealistically high. As for the current state of the art each instrument is very expensive and requires an own laboratory or container, only few instruments can be applied. Additionally these instruments have high power consumption. This would result in high costs of operation for the application of many instruments.

The Multi Beam Instrument (MBI) (*Chapter 5.1*) was especially developed for tomographic LP-DOAS applications to achieve a large amount of measurement light paths. Each MBI can measure along 4 light paths simultaneously and even along more successively. Thus with three of these MBI a good coverage of an area of few km<sup>2</sup> can be achieved within few minutes of measurement time. But as the light beam origin is always arising at one of the instruments, the light paths are not completely independent from each other and no homogeneous coverage of the investigation area is possible. The number of independent instruments was investigated in detail by Hartl et al. [2006]. The authors demonstrate that the application of at least three independent instruments is recommendet for good tomographic observations.

The setup applied for the tomographic observations of this thesis in Heidelberg uses three MBI instruments located at different locations in the city. The search of possible locations is difficult, as the instrument requires a flat roof with good view to possible retro reflector locations, sufficient space for the whole instrument setup, power supply, a simple access, the approval of the public construction authority, a construction engineer and of course the acceptance of the house owner. Only very few buildings fulfil the technical criteria. The house owners have to be convinced and an allowed construction has to be found with the engineer and the construction authority. For this thesis finally three locations could be found.

The first MBI was set up on the roof of the Institute of Environmental Physics (IUP) and the neighbouring building of zoology. First measurements with this instrument were performed by Rippel [2005]. The second MBI was set up on the roof of the company SAS. Stelzer [2005] performed the first measurements at this location. The third instrument was set up at the company “Heidelberger Druckmaschinen AG” (HD-Druck).

The locations of the three instruments are indicated in the map of Figure 6-5 and Figure 6-6. With the setup and location of the instruments a complete cover of the city was impossible. Thus, the observation territory was focused on the city centre. 20 retro reflector arrays were installed on buildings all over the city to realise in total 20 measurement light paths. They are indicated with arrows in Figure 6-5 and Figure 6-6.

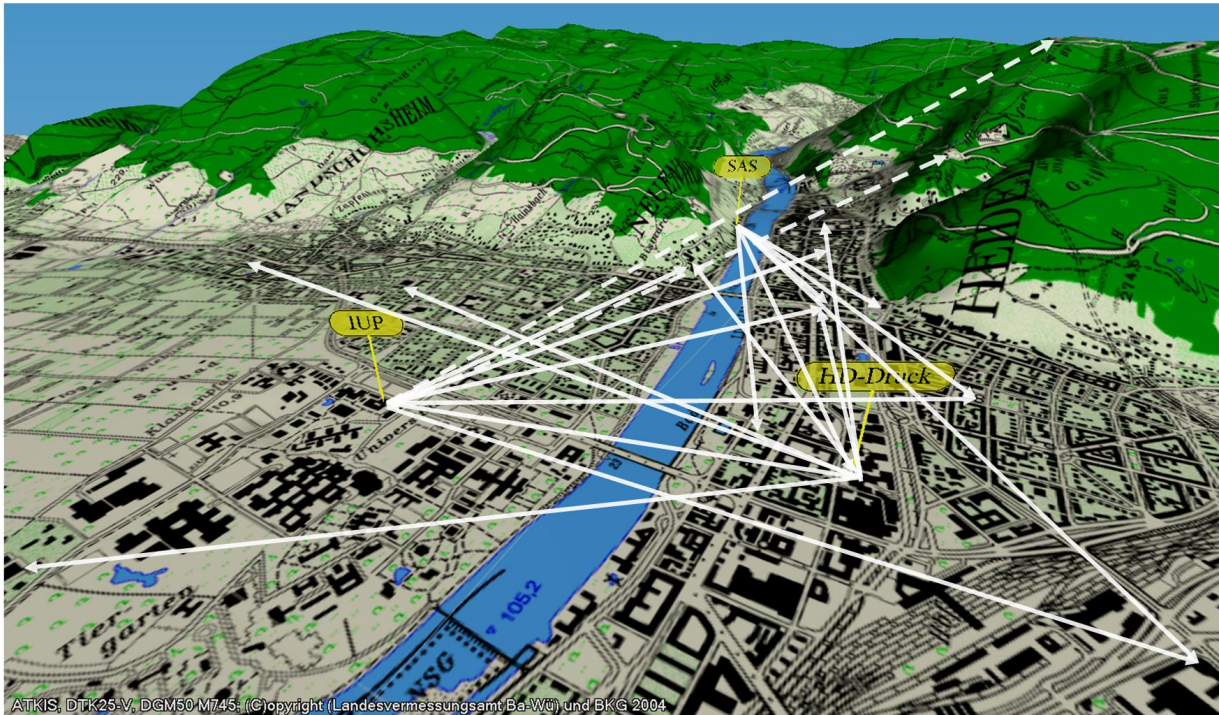


**Figure 6-5: 3-dimensional view of Heidelberg, including the 3 MBI locations (IUP, SAS, HD-Druck) and the measured light paths. Arrows indicate the light paths in the 2-D layer, dashed arrows to retro reflectors in upper layers.**

Locations of the retro reflectors are churches, university buildings, hospitals, apartment buildings, shopping malls, restaurants, office buildings and media towers. For each location a special retro reflector housing was constructed which kept the reflectors protected from rain and fulfil the requirements of the house owners, the public construction authority and safety. For an example of a retro reflector array see Figure 5-36. The details on the retro reflectors installed at these locations are given in the next chapters with the instruments.

The distances from the instruments to the retro reflector arrays are determined with a laser range finder (Riegel Laser Measurement Systems – Lasertape FG21-LR) with accuracy better than 1 m. For absorption paths over 1000 m this error is smaller than 0.1 % of the determined absorption length.

Additionally, where it was possible, the position of the instruments and some reflector arrays were determined with a GPS instrument (Garmin etrex). For the reconstruction of the trace gas distributions not the distance but the coordinates of the positions in a map are necessary. Therefore, the exact positions (Longitude / Latitude) were determined with the GPS data, a high resolution map and the measured distances between instruments and reflectors. They were transformed to an X-Y coordinate system with point of origin at the South-West edge of the investigated area (Figure 6-6). They are displayed in Table 6-1, Table 6-2 and Table 6-3 for each instrument.

It is necessary to mention that such a large setup like done in this thesis requires more than one year. To find possible locations which fulfil the requirements for the setup of instruments and retro reflectors is very time-consuming. The permissions from the house owners, the public construction authority and a construction engineer are extensive and require at least several months. A simpler instrument setup could improve this situation (see *Chapter 5.6*) and

would allow simpler tomographic setups.

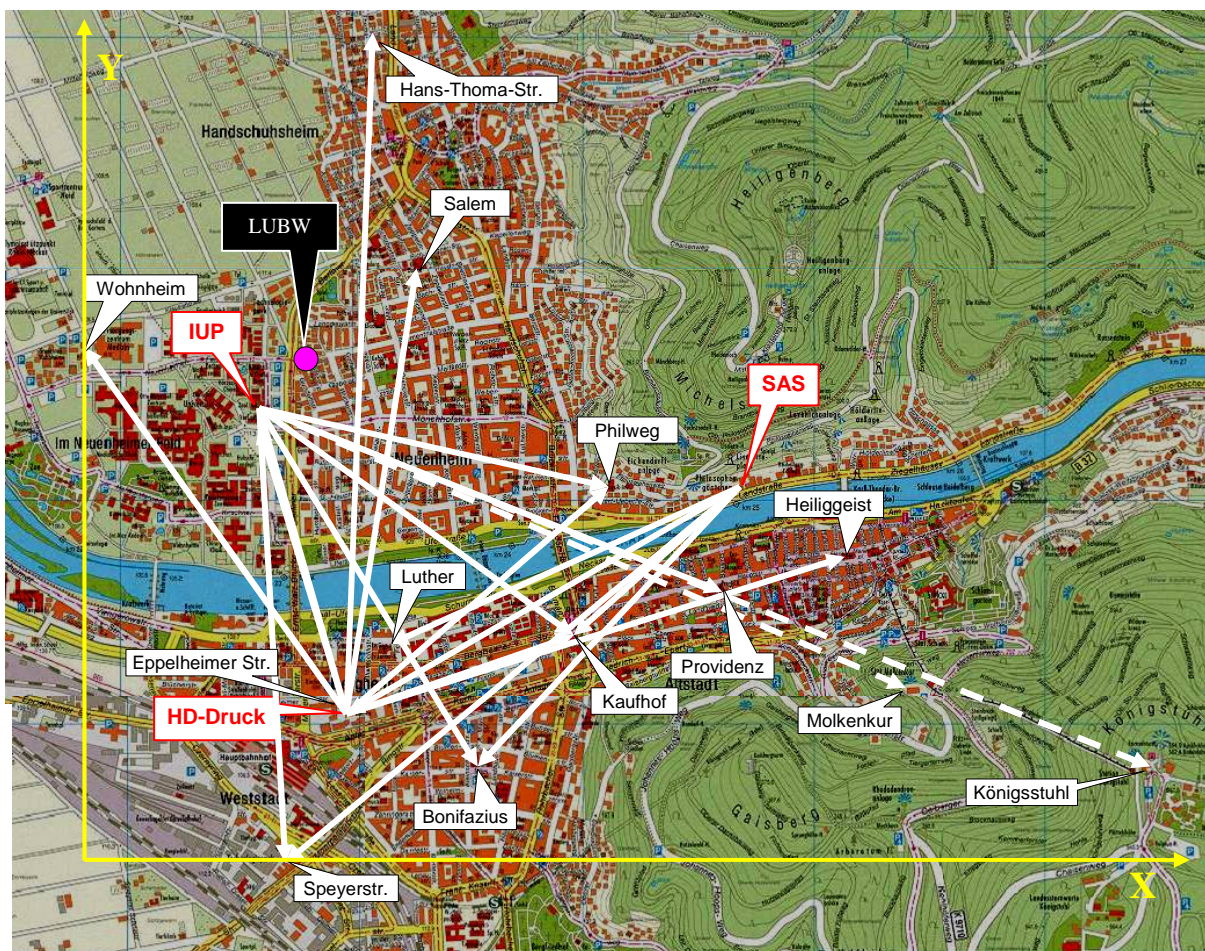


Figure 6-6: Similar plot as Figure 6-5 but as 2-dimensional view. The red names indicate the location of instruments and the black names the locations of retro reflector arrays. Included is the in-situ measurement station LUBW. The yellow arrows indicate the coordinate system used for the reconstruction.

### 6.3 Local Instrument Setup

Here an overview of the MBI setups on the three different buildings which were located at the Institute of Environmental Physics (IUP), SAS and Heidelberger Druckmaschinen (HD-Druck) is given. It is shown how the MBI setups could be realised on these buildings. In the view of these instruments in total 20 retro reflector arrays could be installed on different buildings. The properties of the resulting absorption light paths are summarised for each instrument. The distance between the external mirrors and the retro reflectors and thus the absorption light path, was determined with a laser range finder (Riegler Laser Measurement Systems – Lasertape FG21-LR) with accuracy of 0.1 %.

#### 6.3.1 Institute of Environmental Physics (IUP)

The MBI at the Institute of Environmental Physics was placed in a lab on the 7<sup>th</sup> floor of the

institute and the external mirrors on the roof of the neighbouring Zoology Institute building in 50 m distance. The communication between instrument computer and stepper motor controller (F) of the external mirrors (G) in Figure 5-5 took place via a Bluetooth connection. The instrument was pointing out of an open window (Figure 6-7 left) to the four external mirrors on the zoology building (Figure 6-7 right). The mirrors are protected by a 1.5 m roof from rain and dust. For this setup the telescope Hydra was used (see *Chapter 5.2*).

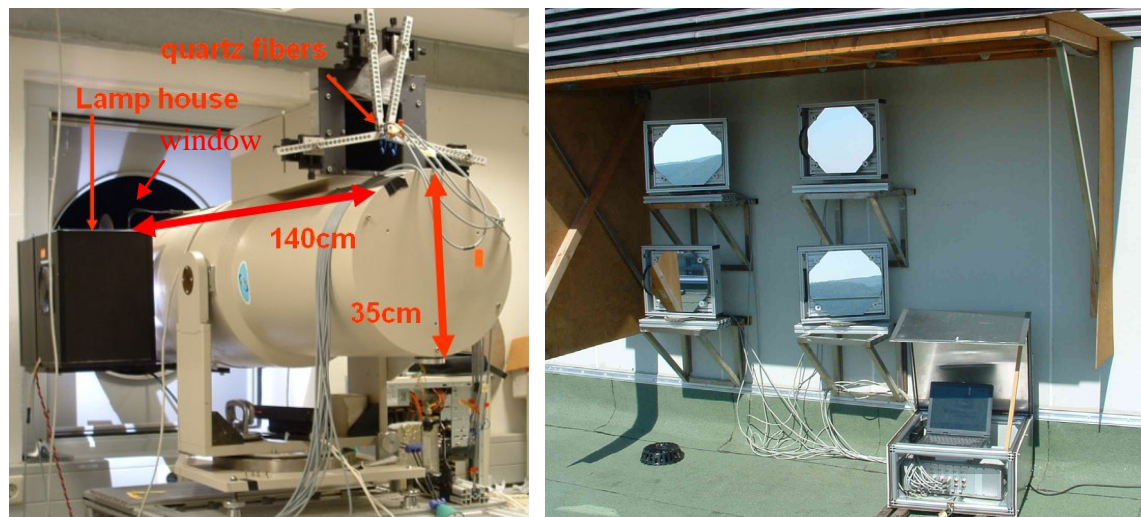


**Figure 6-7:** Left: MBI instrument Hydra at the IUP. Right: External mirrors belong to the IUP instrument on top of the Zoology Institute with Multi Stepper Controller and Notebook. The communication between measurement PC and mirror controller is via Bluetooth connection.

From the roof of the Zoology building a good view to the buildings in the city of Heidelberg can be found. In total eight retro reflector arrays could be installed in the city for this instrument. Six realised measurement light paths are in the horizontal layer. Two reflectors are on the mountain “Königstuhl” and on the half height at the restaurant “Molkenkur”. They allow determining vertical profiles of trace gases above the city (see *Chapter 7.3*). All used retro reflector arrays for this instrument are listed in Table 6-1. The shortcut retro reflector (*Chapter 5.2.4*) was located next to the telescope at the IUP roof. Thus, for shortcut measurements the light was redirected with the external mirrors to this reflector.

The absorption light path is calculated from twice the distance between the external mirrors and the reflector minus the distance between the mirrors and the shortcut system. This is necessary, as the shortcut spectra also contain absorption along the path to the shortcut reflector. This correction gives most accurate concentrations. For the tomographic reconstruction, the X and Y coordinates are used. With the height of the reflector on the “Molkenkur” and “Königstuhl”, vertical profiles for the concentration can be retrieved (*Chapter 7.3*). For real three dimensional reconstructions, more light paths to higher altitudes are required.

The different height of the retro reflector arrays is a problem for the tomographic reconstruction. As the reconstruction has to assume a constant concentration in height, but the vertical gradient can be much larger than the horizontal gradient. Thus, small differences can cause significant errors.

	Number of retro reflectors	Distance [m]	Height above Sea level [m]	Longitude [°]	Latitude [°]	X - coordinate [m]	Y - coordinate [m]
from IUP (external mirrors)			145	8.67466	49.41782	839.6	1983.7
Philweg (Physical Institute)	5	1556	169	8.69565	49.41490	2358.2	1658.7
Providenz (Church)	7	2120	140	8.70194	49.41083	2813.6	1206.0
Kaufhof (Store)	7	1657	145	8.69283	49.40881	2154.4	980.2
Bonifazius (Church)	7	1826	145	8.68742	49.40367	1762.5	408.2
Eppelheimer Str. (HD-Druck Company)	3	1370	152	8.67955	49.40597	1193.4	664.6
Speyerstr. (HD-Druck Company)	10	1983	162	8.67667	49.40000	984.8	0.0
Molkenkur (Restaurant)	17	3064	309	8.71347	49.40694	3647.6	773.1
Königsstuhl (Radio tower)	37	4229	598	8.72847	49.40367	4732.9	408.2
IUP shortcut reflector	3	25	150				

Table 6-1: Characteristics of the retro reflector arrays to which measurements were performed from the IUP instrument. Each array consists of a different number of single reflectors. The distance is measured with a laser range finder. The height is estimated from the tilt of the laser range finder and a map. The street level is about 100 m above Sea level. The coordinates were determined with a GPS instrument or from a high resolution map. They are transformed to X–Y–coordinates used for the tomographic reconstruction. The abbreviations used for the reflectors are indicated in the map of Figure 6-6 and are used throughout this thesis.

### 6.3.2 SAS



Figure 6-8: The setup of the MBI on the roof of the building of the company SAS. The building is directly located at the river Neckar. The instrument was located in a container. The external mirrors could be placed on the same roof, 15 m in front of the telescope.

The second telescope (with the name LONG) was placed on the roof of the building of the company SAS. It is located close to the river Neckar opposite the old town. The telescope and the instruments were placed in a small container with the size of 2×2 m<sup>2</sup>. The container is mounted on long planks which are loaded with several hundred kilograms. Thus, the

container could withstand a storm. To avoid that the vibrations of the container are transferred to the telescope, holes in the container ground plate allowed placing the telescope on the roof. Therefore, no direct mechanical connection between container and telescope existed. A window in the container allowed the direct view from the telescope to the external mirrors. Freezing or overheating in the container was avoided to protect the instruments. Therefore a temperature controller was applied which switched an electrical heater if temperatures dropped below 0°C or an air conditioner if temperature increased above 30°C.

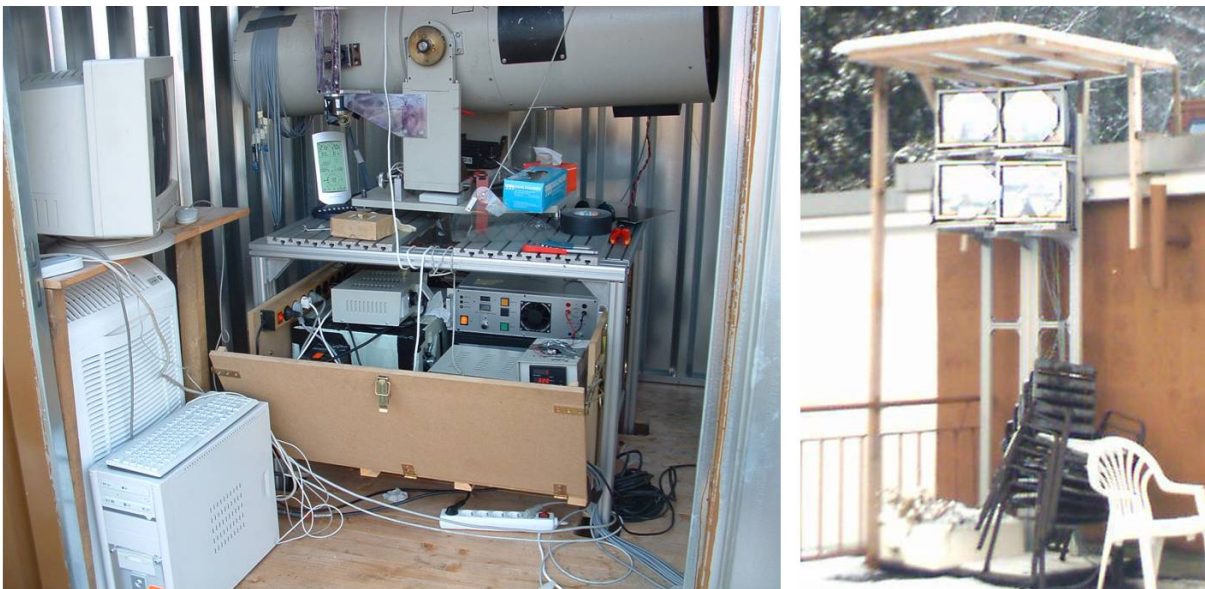


Figure 6-9: Left: Setup of the telescope (LONG) on the building of the company SAS. View inside the container with telescope and instruments. Right: External mirrors attached to the wall with an ITEM aluminium profile. A small roof protects the mirrors from rain.

	Number of retro reflectors	Distance [m]	Height above Sea level [m]	Longitude [°]	Latitude [°]	X - coordinate [m]	Y - coordinate [m]
<b>from SAS (external mirrors)</b>			140	8.70296	49.41462	2887.1	1627.5
<b>Bonifazius (Church)</b>	7	1658	146	8.68742	49.40367	1762.5	408.2
<b>Kaufhof (Mall)</b>	5	928.4	148	8.69350	49.40894	2202.7	995.7
<b>Speyerstr. (HD-Druck Company)</b>	10	2505	162	8.67667	49.40000	984.8	0.0
<b>Eppelheimer Str. (HD-Druck Company)</b>	7	1949	143	8.67954	49.40600	1192.6	667.9
<b>Luther (Church)</b>	7	1617	146	8.68258	49.40867	1412.8	964.8
<b>SAS shortcut reflector</b>	3	5	138				

Table 6-2: Analogue to Table 6-1 for the SAS instrument.

The external four mirrors are attached to a wall 10 m away from the container. This is the shortest possible distance for the instrument, but a larger distance was not possible on the roof of this building. The mirrors were protected from rain with a small roof (Figure 6-9). In case

of stronger winds still large amounts of water reached the mirrors. Thus, they had to be regularly cleaned with distilled water. From the mirrors there is a good view along the Neckar. Measurements to the city centre on the opposite site were not possible, as the distance is too short for sufficient good DOAS measurements.

Finally measurements could be performed towards five reflector arrays which are listed in Table 6-2. The instrument was remote controlled via a LAN network.

Next to the instrument a small weather station WS 2200 (*Chapter 5.8*) was installed to monitor the wind direction, wind speed and other weather parameters.

### 6.3.3 Heidelberger Druckmaschinen AG (HD-Druck)

The third telescope (with the name CUBE) was set up on the roof of the main building of the Heidelberger Druckmaschinen AG (abbreviation HD-Druck). It is located close to the Heidelberg main railway station. Due to regulations of the company and the city authority, in terms of appearance, mounting and safety, strong restrictions for the setup on this roof were made. A compromise had to be found between the requirements for the setup and the regulations. The final setup is displayed in Figure 6-10.

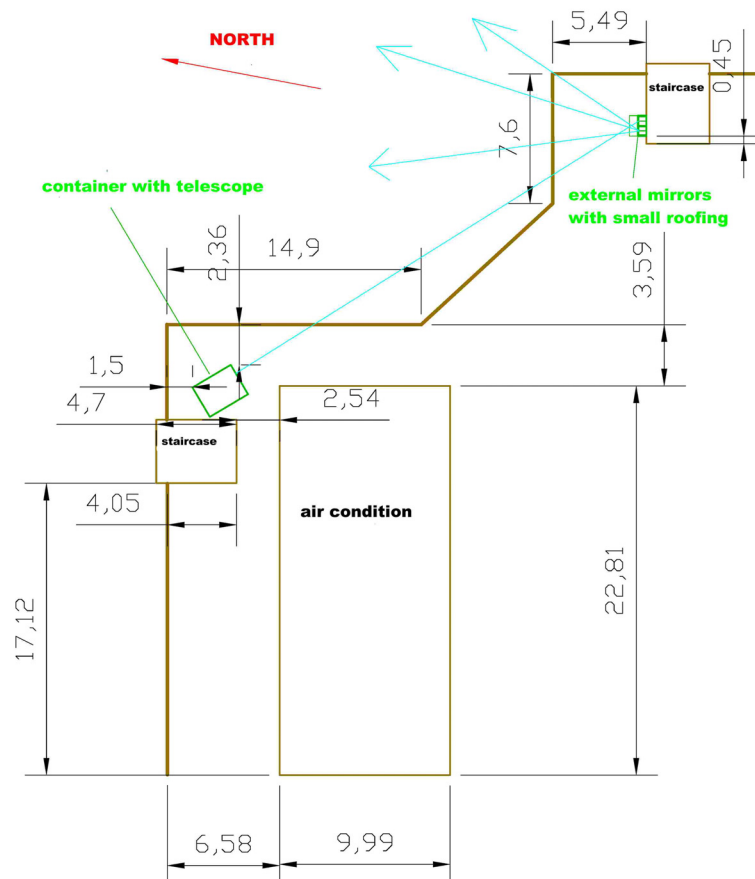


**Figure 6-10:** Sketch of the roof on the HD-Druck building with the MBI setup. The telescope and instruments are located in a container of  $2 \times 2$  m<sup>2</sup> size. The external mirrors are located on a wall of the staircase, 29 m in front of the telescope. The blue lines indicate the light beams.

The telescope and instruments were placed in a container of  $2 \times 2$  m<sup>2</sup> size, similar to the instrument at SAS. The container was also mounted on long planks loaded with several

hundred kilograms to withstand a storm. To avoid that the vibrations of the container are transferred to the telescope, holes in the ground plate of the container allowed placing the telescope on the roof. A window in the container allows the view from the telescope to the external mirrors (Figure 6-12).

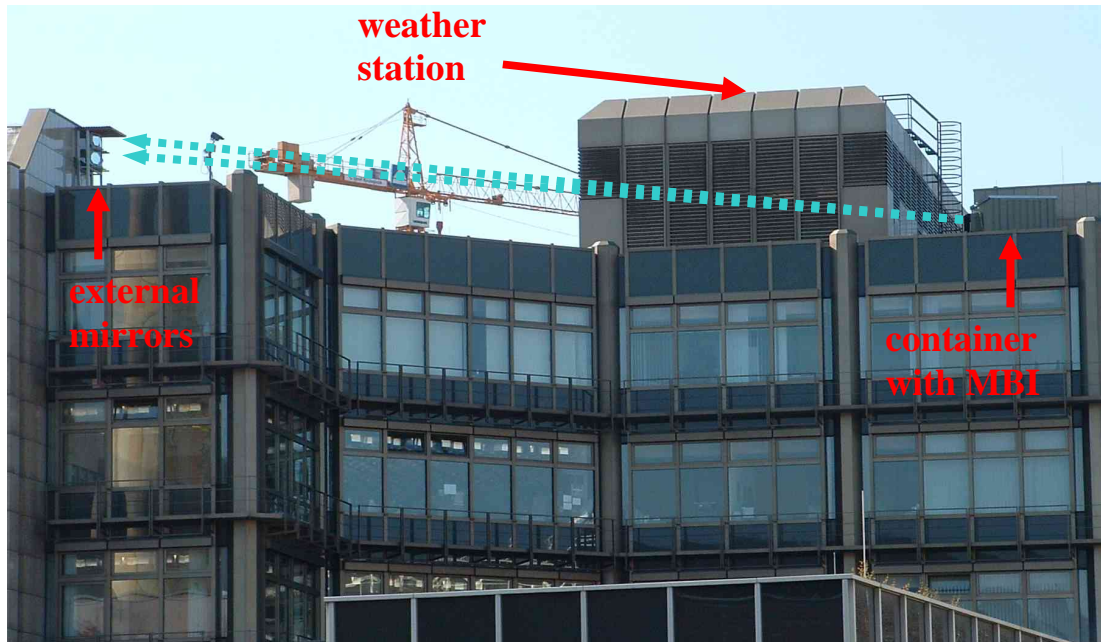


Figure 6-11: View of the Heidelberger Druckmaschinen AG (HD-Druck) building with the MBI setup like sketched in Figure 6-10.



Figure 6-12: MBI setup on the HD-Druck building. Left: Four external mirrors on an ISEL aluminium profile construction with a small roof. The reflected light from the retro reflectors can be seen in the mirrors. The shortcut retro reflector was set up 6 m in front of the external mirrors. The light is redirected to this reflector for the shortcut reference measurement. Right: Multi Beam Instrument inside the container. A window allows the direct view of the light beams to the external mirrors.

To avoid freezing or overheating in the container and to protect the instruments, a temperature controller was applied which switched an electrical heater if temperatures dropped below 0 °C or an air conditioner if temperature increased above 30°C.

The external mirrors were placed on an ISEL aluminium profile which was attached to a wall. A small roof was placed above the mirrors to protect them from rain. The Multi Stepper Controller, placed in the container, drives the mirrors through eight 40 m long data cables.

This setup finally allowed the measurement towards seven different retro reflector arrays. The data of the reflectors is summarised in Table 6-3.

The WS 2200 weather station and all its components were placed on the highest point of the building. The communication with the logging computer was realised via a radio transmitter.

	Number of retro reflectors	Distance [m]	Height above Sea level [m]	Longitude [°]	Latitude [°]	X - coordinate [m]	Y - coordinate [m]
<b>from HD-Druck (external mirrors)</b>			140	8.68000	49.40592	1225.9	659.0
<b>Philweg (Physical Institute)</b>	5	1511	169	8.69565	49.4149	2358.2	1658.7
<b>Heiliggeist (Church)</b>	9	2233	148	8.7093056	49.412083	3346.2	1345.1
<b>Hans-Thoma-Str. (Tower block)</b>	13	3062	161	8.6804167	49.433444	1256.1	3723.0
<b>IUP (Institute)</b>	7	1313	154	8.67454	49.41721	830.9	1915.8
<b>Wohnheim (University hall)</b>	7	1984	157	8.6630556	49.419944	0.0	2220.2
<b>Salem (Hospital)</b>	7	1965	154	8.6841667	49.423361	1527.4	2600.6
<b>Kaufhof (Mall)</b>	4	984	142	8.6928333	49.408806	2154.4	980.2
<b>HD-Druck shortcut reflector</b>	3	3	139				

**Table 6-3: Analogue to Table 6-1 for the HD-Druck instrument.**



## 7 Data Evaluation and Simulations

In this chapter the DOAS data evaluation of the measured spectra in order to receive the averaging concentration along a light path are outlined. To perform the DOAS retrieval of the huge amount of data recorded from 2005 to 2007, an automated evaluation was developed. Different properties of the evaluation are described.

The retrieved average concentrations are proceeded to same time bases. The applied interpolating and averaging is shortly described. The data of the time bases is used to calculate vertical concentration profiles and apply them for the tomographic inversions.

The configuration for the tomographic retrieval is explained in more detail. The arrangements of the reconstruction grids for the realised measurement geometry in Heidelberg are explained. Several simulated distributions are tested with these setup and grids to analyse the tomographic retrieval accuracy. Additionally, simulations were performed to derive the optimum iteration number for the retrieval. The final tomographic reconstructions could be significantly improved in comparison to first data products [Poehler et al., 2007], not only due to an optimisation of the tomographic retrieval but also due to the improvement of the measurements.

Finally, a summary of causes for tomographic artefacts in the derived trace gas distributions are given, which were investigated in this thesis.

### 7.1 DOAS Measurements and Data Evaluation

The DOAS measurements along twenty absorption light paths were performed with three MBI (*Chapter 5.2*). The instruments are controlled with the software COS (*Chapter 5.5*) which also record the required spectra. Besides atmospheric absorption spectra it is also necessary to measure the lamp reference (shortcut), atmospheric background, shortcut background, offset, dark current and mercury spectra. The first five parameters are taken automatically on a regular basis with the measurement routine. Dark current and mercury spectra are nearly constant in time and are taken manually once in a while. The measurement routine is displayed in Figure 7-1 (highlighted in blue). Each MBI telescope could simultaneously measure along up to four light paths at once (see *Chapter 6.2*). To cover more light paths, external mirrors can successively redirect the light beam to different retro reflector arrays. By using two geometries, measurements along eight light paths can be performed for each instrument. If less than eight possible light paths exist, not all mirrors will be moved to a new position for the second geometry. Typically, measurements were performed in both geometries along the light path with the lowest intensity and the spectra added up before evaluation.

The data evaluation was performed with DOASIS (3.2.3505) [Kraus, 2005]. It replaced the data evaluation with WINDOAS [Fayt and Roozental, 2001], used in proceeding works for measurements with the same instrument.

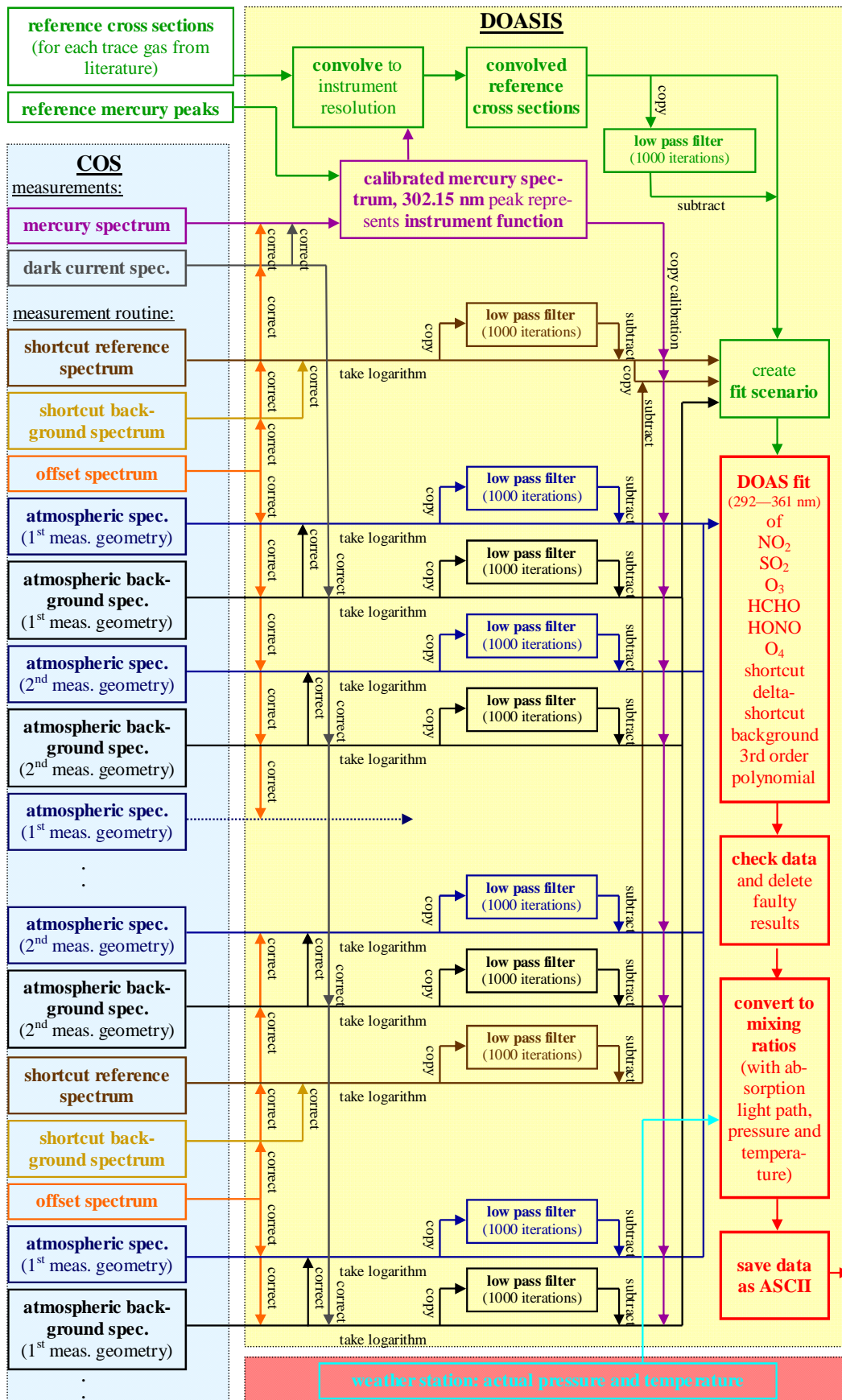


Figure 7-1: Overview of the measured spectra and the data evaluation. Each coloured box indicates a different program. The measurements are made using the program COS (blue). The main evaluation routines are performed in DOASIS (yellow) with a JScript. The treatment of the measurement and reference spectra is outlined. The results are converted to mixing ratios.

DOASIS gives the possibility to use a script language (Jscript) to automate processes of the evaluation. Several new features are introduced within this thesis to the JScript evaluation like the automatic convolution of literature reference absorption spectra, the creation and modification of fit scenarios and the conversion to mixing ratios using the light path as well as actual pressure and temperature from a weather station. This simplifies the data handling and drastically reduced data processing time of the huge amount of measurements over the 20 light paths. In comparison to the WINDOAS evaluation the process and handling time was reduced by up to a factor of 100.

In order to start an analysis several preparation steps are required (Figure 7-1). First, the spectrometer has to be calibrated using a mercury spectrum of known emission lines. Second, the literature absorption cross sections have to be reduced to the resolution of the applied spectrometer. Third, the shortcut spectra ( $I_0$ ) have to be prepared by correcting for offset and background for a shortcut measurement and afterwards the logarithm is taken. Forth, also the measurement spectrum has to be corrected for offset and background for an atmospheric measurement before the logarithm is taken. Additionally, the atmospheric background spectrum is also prepared for the fit to compensate any remaining spectral structures due to changes in this signal. For the evaluation a triangle high pass filter with 1,000 iterations was applied. The filtered reference, shortcut and atmospheric background spectrum are implemented in a fit scenario which contains all properties for a DOAS analysis of a spectrum. The fit is applied to the atmospheric spectrum typically in the wavelength range from 292 to 361 nm.

The absorption cross sections of  $\text{NO}_2$ ,  $\text{SO}_2$ ,  $\text{O}_3$ , HONO, HCHO and  $\text{O}_4$  are included in the fit. The analysis procedure checks the spectrum and the fit for any errors and deletes the data point if necessary. For example if a spectrum display a residuum structure larger than  $1 \times 10^{-3}$  RMS, has too low intensity ( $\sim$  below 5 % of typical saturation), is over-saturated (e.g. due to detector errors or wrong integration time), or spectrograph scattered light changes the concentration significantly. Sufficient good data results are converted to mixing ratios and saved. Details about the spectra, corrections, evaluation preparations and the fit are given in the following sections.

### **7.1.1 Spectrograph Calibration, Mercury Spectrum and Instrument Function**

In order to associate the reference spectra with the measurements, information about the wavelength to pixel mapping is necessary. A good calibration can be achieved by using a known line emitter of very small spectral extension compared to the spectrometer resolution. In the UV this may be achieved by a mercury lamp with several well-known narrow emission peaks. In the measurement wavelength range from 280 nm to 365 nm six strong and distinguishable single peaks can be found (Figure 7-2). Due to the finite size of the spectrograph aperture entrance and the imperfect imaging, the lines are broadened. The spectral resolution is reduced, what is a characteristic property of the instrument. The broadening function is called the instrument transfer function  $H$ . It is determined from the broadening of a very narrow emission line, like a mercury emission line at 302.15 nm, as the width of the line itself is negligible (typically in the order of 10 pm) in comparison to the

instrument resolution. For the applied spectrograph detector unit with the 200  $\mu\text{m}$  fibres the instrument function has a width of about 6.5 channels (with binning  $2\times 2$ ). This corresponds to a width and resolution of about 0.5 nm.

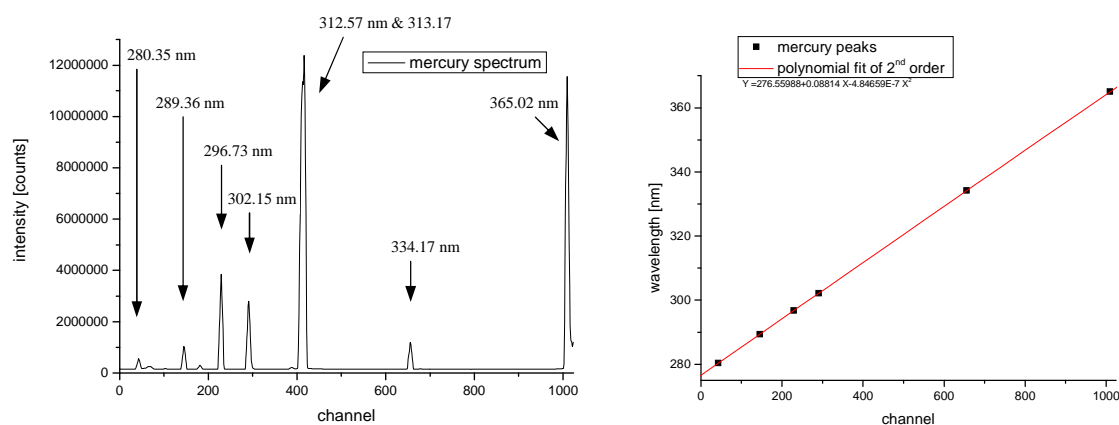


**Figure 7-2: Left: Mercury spectrum of the Acton 500i spectrograph used at the SAS instrument for the fibre 3. The spectrum includes six single mercury peaks in the range from 276 nm to 366 nm. Right: Wavelength to pixel calibration of the same spectrum. The peak centres are determined by fitting a Gaussian function to each single peak and plotted against the reference peak wavelengths (black dots). A polynomial fit of 2<sup>nd</sup> order is used to achieve the calibration function.**

In order to perform the wavelength calibration of the mercury spectrum, each line has to be assigned to a literature wavelength. To determine the centre of a peak, a fit of a Gaussian is applied and the centre of the Gaussian function is used as centre of the line. If an instrument function does not look like a Gaussian function, errors in the determination of the centre of the peak are cancelled out with the convolution (*Chapter 7.1.2*). It is important to mention that the centre of all lines have to be determined in the same way, for calibration to wavelength and for the instrument slit function. The determined channel numbers of the centres are plotted against the reference wavelengths of the emission lines from literature. The wavelength to pixel calibration is achieved with a polynomial fit of 2<sup>nd</sup> order (Figure 7-2). The calibration is almost linear for all applied spectrographs, and the quadratic term of the polynomial is very small ( $< 1.15 \times 10^{-6}$ ). The calibration was copied to the other measured spectra taken with this instrument. If all spectra are wavelength calibrated, the fit procedure may be performed in wavelengths. This is favourable, because the illustration of the fit is directly comparable to other evaluations. To guarantee a relative stable wavelength to pixel mapping, the spectrometer was temperature stabilised (*Chapter 5.3.1*).

Due to slight differences in the fibre position and different spectral properties, each fibre requires its own calibration. If the position of the fibre had to be changed, for example when a spectrograph shutter was replaced (*Chapter 5.3.2*), a new calibration was necessary for all fibres of the instrument.

### 7.1.2 Trace Gas Reference Spectra and Fit Preparation

According to Eq. 3.7 and Eq. 3.13 the trace gas absorption cross sections, or, more accurately, the differential absorption cross sections, are essential for the data evaluation. They can either be measured with the instrument directly by applying absorption cells with the corresponding trace gas or, as done in this thesis, high resolution literature cross sections can be used (Table

7-1). In this case, the absorption cross sections must be transferred to the resolution of the spectrograph detector unit with the applied fibres and entrance slit. This is done by the convolution of the high resolution cross sections with the instrument function  $H$  (see Eq. 3.10).

In order to account for a slight different wavelength calibration of the literature cross sections, the fit algorithm allows a linear shift and squeeze / stretch of the reference spectra when minimising  $\chi^2$  of the fit iteratively. But additional parameters may increase the measurement error. Therefore, the shift and squeeze/stretch is determined and locked for the final evaluation. The determination is performed by evaluating many spectra with a high column density of the respective specie. The retrieved shift and squeeze / stretch are displayed in Table 7-1. By applying these parameters to the literature references, they may all set to the same calibration in the fit evaluation. To compensate any change of the instrument pixel to wavelength mapping due to temperature and pressure change or mechanical shifts, the reference spectra may shift and squeeze / stretch to the measurement spectrum. As all references set to the same wavelength calibration, their shift and squeeze / stretch is linked to reduce the free parameters and thus reduce measurement errors.

Species	Abs. error [%]	Resolution [nm]	Reference	Temperature [K]	Pressure	Shift [nm]	Squeeze [relative]
NO <sub>2</sub>	±2.5 – 4.7 <sup>1</sup>	0.20	Burrows et al., 1998	293	1000 mbar	-0.033	1
O <sub>3</sub>	±3.7 <sup>1</sup>	0.20	Burrows et al. 1999	293	1000 mbar	-0.033	1
SO <sub>2</sub>	±0.1 <sup>1</sup>	0.063	Vandaele et al., 1994	295	1 atm	-0.02	1
HCHO	±5.0	0.025	Meller and Moortgat, 2000	298	1 atm	0	1
HONO	±5.0	0.080	Stutz et al., 2000	298	1 atm	0	1
O <sub>4</sub>	n.s.	0.015	Hermans et al., 1999	room temp.	1 atm	0	0

n.s.: not specified

1 : in the evaluation range

**Table 7-1: Absorption cross sections used for the evaluation of the spectra including estimated shift and squeeze set fix for the references in the final evaluation. The shift and squeeze of all references are linked. The fit is performed in the range from 292 to 361 nm. The given error is the total absorption cross section error. The differential absorption cross section error might be even larger.**

## Comparison of Different NO<sub>2</sub> Absorption Cross Sections

Several different absorption cross sections were compared for the evaluation. The applied references fit best to the observed atmospheric absorptions and result in the lowest residuum and thus in smallest measurement error. This does not include the error of the absorption cross

section itself.

The NO<sub>2</sub> absorption cross section was compared to that of Voigt et al. [2002], Bogumil et al., [2003] and Vandaele et al., [1998]. The differences in the differential absorption cross sections in comparison to the applied reference of Burrows et al. [1998] are in the applied wavelength range: -1.4 %, -3.9 % and -7.4 % respectively. From new comparison measurements of a NO<sub>2</sub> CE-DOAS instrument with precisely known NO<sub>2</sub> concentrations the reference from Vandaele et al. [1998] is most correct for the spectral range around 450 nm [Horbanski, 2010]. A similar difference of -7 % at this wavelength was observed between Voigt et al. [2002] and Vandaele et al. [1998], where a -6 % difference arise in the UV range applied in this thesis. It is expected that the absorption reference from Vandaele et al. [1998] is also more precise for the applied UV spectral range. This would suggest, that all NO<sub>2</sub> results of this thesis should be rescaled by the factor 0.926. As the main focus of the thesis is on concentration differences, which are not affected by a rescaling, it was not applied afterwards.

### **Comparison of Different O<sub>3</sub> Absorption Cross Sections**

The O<sub>3</sub> absorption cross section was compared to Voigt et al., 2001 and Bogumil et al., 2003. The difference in the determined concentration in comparison to the applied reference from Burrows et al., 1999 are in the applied wavelength range  $\pm 0$  % and -3.0% respectively.

### **Comparison of Different SO<sub>2</sub> Absorption Cross Sections**

The SO<sub>2</sub> cross section was compared to the one with higher resolution ( $2 \text{ cm}^{-1} \approx 0.008 \text{ nm}$ ) from Vandaele et al., 1994 and to Bogumil et al., 2003. The two given references from Vandaele et al., 1994 should not give a different concentration. But as the lower resolved absorption cross section was measured several times and averaged, the total absorption cross section error is lower (0.1 % instead of 2.5 %) than for the high resolved. Also the determined concentration is different while the higher resolved absorption cross section gives 5 % higher concentrations. Especially, the lower resolved cross section was applied in this thesis in order to receive more accurate results. Surprisingly the reference from Bogumil et al., 2003 gives higher concentrations of 21 %. The reason for this difference could not be determined.

## **7.1.3 Atmospheric Spectra Measured Along Different Light Paths**

The atmospheric spectrum contains the absorptions in the atmosphere. The light transmitted by the telescope is redirected to a retro reflector array by external mirrors. The reflected light is also redirected over the external mirrors back to the telescope where it is focused on the receiving fibre. The detected light contains the atmospheric absorptions over the light path.

Before a spectrum can be analysed it has to be corrected for offset and background. Afterwards the spectrum is logarithmised, filtered and wavelength calibrated. The spectrum is then provided to the DOAS fit analysis (Figure 7-1).

## **7.1.4 Lamp Reference Spectrum (Shortcut)**

To record a spectrum of the light source  $I_0(\lambda)$  before it passes the atmosphere, a so-called

shortcut system is applied (*Chapter 5.2.4*). This spectrum is called shortcut spectrum, as the absorption path is short (max. few meters) in comparison to the atmospheric spectrum (at least several 100 m). This is achieved by redirecting the light beams to a rotating shortcut retro reflector at close distance (*Chapter 5.2.4*). As the lamp spectrum of the xenon arc lamp changes slowly with time due to degradation of the lamp and intensity fluctuations, a shortcut spectrum at least every few hours should be recorded to achieve good data results. Additionally, the detector noise decreases if the time between measurement and shortcut is shorter (*Chapter 5.3.4*), the regularity of shortcut spectra was increased to at least one per two hours.

The lamp spectrum  $I_0(\lambda)$  is required for the data analysis as it contains the lamp and instrument spectral structures (Eq. 3.13). For the DOAS measurement it is not necessary to record the total  $I_0(\lambda)$  spectrum with the correct radiance. A simple measurement of the spectrum of the light with the shortcut system is sufficient, also if this does not represent the total  $I_0(\lambda)$  intensity.

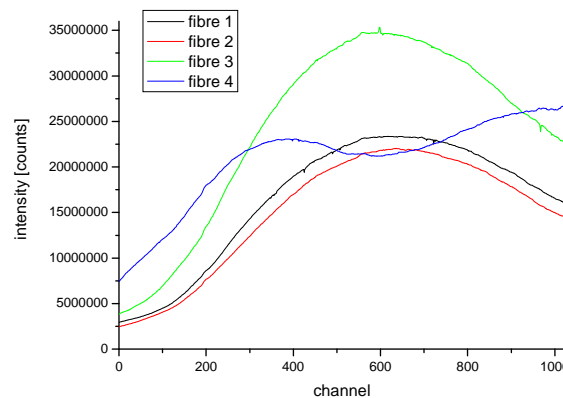


**Figure 7-3: Shortcut reference spectra at the IUP instrument for all four light beams which were measured with four fibres. Each light beam uses different parts of the emitted light from the xenon arc lamp (*Chapter 5.1*). This leads to a different spectral shape of each light beam.**

For the used MBI setup, each emitted light beam of one instrument uses different parts of the light emitted from the xenon arc lamp (*Chapter 5.1*). The reason is the different positions of the lamp house mirrors in relation to the lamp. Thus, each light beam has a different initial spectrum, and even the broad-band structure may be different (Figure 7-3). These emitted spectra are problematic in the evaluation, as they are spectrally unstable in time and contain much stronger narrow-band structures from xenon emissions. The reason is the use of the emitted xenon arc lamp light at an angle different from perpendicular, which are spectrally much more unstable and display a lower intensity. The use of the perpendicular light at different azimuth angles was tested and showed significant improvements in the signal quality.

In order to apply the shortcut spectrum for the evaluation, it has to be corrected for offset and shortcut background. For typical DOAS evaluation, the measured spectrum is divided by the corrected shortcut spectrum. But it is also possible to include the logarithm of the shortcut into the fit procedure. This has several advantages. First, the shortcut spectrum may shift and thus a spectral shift due to temperature variations may be compensated. Second, if the intensity of the xenon lamp structures change, a free fit parameter may compensate this effect.

Third, also more than one shortcut spectrum may be included in the fit procedure. For example if the shortcut, which was taken at closest proximity before the atmospheric spectrum, and the shortcut taken following the atmospheric spectrum are accounted in the fit, changes in the xenon lamp structure are compensated. This is achieved as the second spectrum in the fit is the difference between the two shortcut spectra. Thus, it contains any change in the xenon arc lamp structure. For each measurement spectrum the according shortcut spectra have to be used.

Such an evaluation was implemented for the first time to the evaluation of LP-DOAS spectra. For the presented tomographic LP-DOAS data this drastically improved the data quality, as the error (residuum) was reduced up to a factor of 3 (on average 1.5).

### 7.1.5 Background Corrections

Each measured spectrum of the CCD is overlaid by a background which consists of an electronic offset and dark current. For a CCD chip which is cooled to  $-40.0^{\circ}\text{C}$  the offset display about 50 to 100 times higher intensity than the dark current (for typical integration times below 1 s). The narrow-band structures are comparable, but insignificant for the measurement.

Additionally, to each measured atmospheric or shortcut spectrum, stray light, which arises from other sources than the xenon arc lamp, is collected by the telescope. During the day this is mainly scattered sun light.

#### Offset

The noise of each recorded spectrum can lead to negative values in pixel intensity if the illumination is low. The analogue digital converter (ADC) can not handle these negative values. To avoid this problem, a constant intensity (offset) is added to each signal independently of the integration time and intensity (Figure 7-4 Left). The atmospheric spectra need to be corrected for this artificially added intensity. The offset spectrum is achieved from the measurement of a spectrum without receiving any light (closed spectrograph shutter) with shortest possible integration time (for the used CCD controller 40 ms). 100 scans are added to enhance the signal-to-noise ratio.

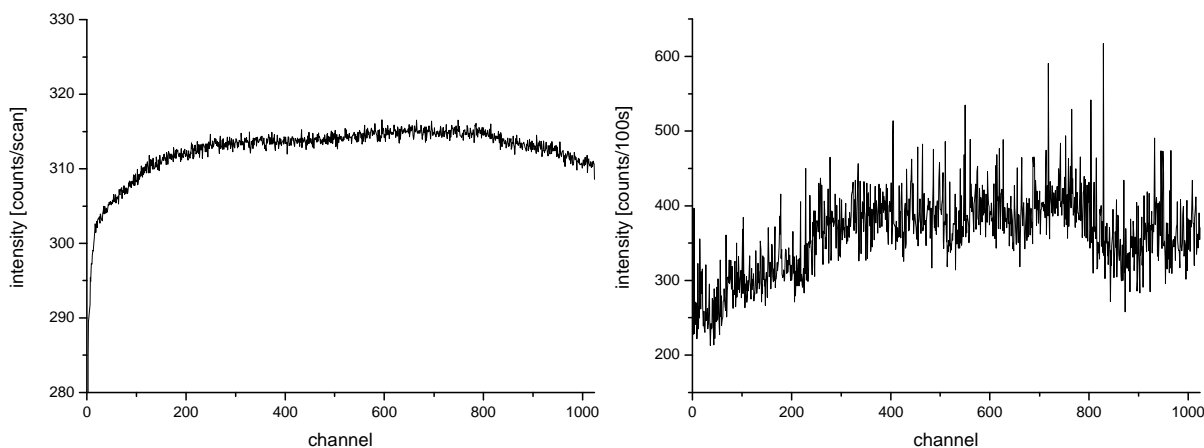


**Figure 7-4:** Left: Example for an offset spectrum which is taken with 100 scans, each with an integration time of 40 ms for the IUP instrument with fibre 1 and averaged 11 lines ( $2 \times 2$  binning). Right: Example for a dark current spectrum of the CCD at  $-40.0^{\circ}\text{C}$  similar taken with one scan and duration of 100 seconds.

For the correction of offset for each measured spectrum, the number of scans needs to be considered.

$$I_{Okor}(n) = I(n) - \frac{Scans_{I-Spec}}{Scans_{O-Spec}} \cdot O(n) \quad (\text{Eq. 7.1})$$

with:  $I_{Okor}$  offset corrected spectrum  
 $I(n)$  measured not offset corrected spectrum  
 $O(n)$  offset spectrum  
 $n$  channel number

The offset of the applied detectors (Spec-10 2kBUV from Roper Scientific) is adjusted within the detector controller. It was found that the resistance value of this potentiometer is strongly temperature dependent. Thus a change in the laboratory temperature changes the offset signal. As the instrument were placed in an open laboratory (IUP) or in open containers (SAS and HD-Druck), the temperature change during a day was large even if air conditioning and heaters were applied. The resulted change in offset signal was of the order of 10 % during a day and even more for a period of several weeks. To reduce effects due to changes in the offset, it was measured regularly (several times a day) within the measurement routine. The closest offset in time was always used to correct the measured spectra.

## Dark Current

From the thermally oscillation in the silicon crystal of the CCD detector, charge carriers are created even without light. The signal is called dark current. The amount of free charge carriers depends on the temperature and the position (pixel) on the chip and is linear to the integration time. Therefore, the CCD chip is cooled and stabilised to a temperature of -40.0 °C. To characterise the dark current, a spectrum with long integration (100 seconds) should be measured if no light reaches the detector.

Before applying a dark current correction to a measurement spectrum, the dark current spectrum  $D(n)$  has to be corrected for the offset. Due to the integration time dependence of the dark current intensity, integration times have to be taken into account for the correction.

$$I_{Dkor}(n) = I_{Okor}(n) - \frac{Int.time_{I-Spec}}{Int.time_{D-Spec}} \cdot D_{Okor}(n) \quad (\text{Eq. 7.2})$$

with:  $I_{Dkor}$  dark current corrected spectrum  
 $I(n)$  measured offset corrected, not dark current corrected spectrum  
 $D_{Okor}(n)$  dark current spectrum, offset corrected  
 $n$  channel number

In general, all spectra have to be corrected for dark current. But as also background spectra are recorded after each atmospheric or shortcut spectrum, which also contain the dark current, only the spectra for which no background is recorded have to be corrected (e.g. mercury spectrum).

## Background Spectrum (Scattered Light)

The MBI telescope emits and receives the light from a xenon arc lamp. But additionally light from other sources is scattered into the light path and enters the telescope. This gives a so called background intensity. Xenon arc lamp light and background are recorded together by the instrument and spectra have to be corrected for this background before evaluation. During daylight, it contains mainly scattered sun light and the background spectrum is characterised by the Fraunhofer lines, which have their origin in the sun atmosphere. The spectrum changes slowly with time according to the position of the sun, clouds and fog. The emitted light of the sun is in first approximation similar to that of a blackbody. Only the absorption processes in the solar as well as terrestrial atmosphere are responsible for characteristic absorption lines. Most Fraunhofer spectral structures are different to the observed tropospheric absorptions, and almost no spectral interferences arise. But if these spectral structures are not entirely removed from the measured spectrum, the error increases and the determined concentration may have an offset. It is important to mention that the background is typically different for different light paths, as it depends for example on the solar azimuth angle, clouds, fog, particles, absorption path length and the background around the reflector (e.g. building, trees, mountain, sky). Additionally, the intensity may change quickly if the cloud cover changes or due to variations in the optical setup (variation in the position of the external mirrors). Therefore, for each measured atmospheric or shortcut spectra a background spectrum should be recorded before or directly afterwards. It was found that the correction of shortcut background, which was ignored in earlier studies, may reduce the residuum by 30 %. Shortcut background measurement were therefore implemented in the measurement routine and in the evaluation process (Figure 7-1). In order to record the background spectrum, a light blocker (*Chapter 5.2.1*) shades the light from the xenon arc lamp and a spectrum with 10 seconds is recorded.

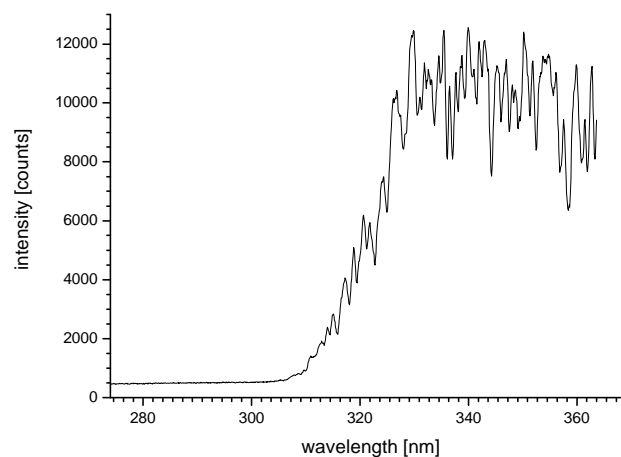


**Figure 7-5:** An example for a background spectrum taken with one scan and a duration of 10 seconds on February the 17th 2006 15:15 by the IUP instrument in the direction of the reflector at Speyerstr.

The recorded background spectrum also contains the dark current and is similarly proportional to the integration time. Thus, their correction has to account for the different integration time in comparison to the measurement spectra like done for the dark current (Eq. 6.2 ). If a spectrum is corrected for background, it does not require to be corrected for dark current. This has also the advantage that any change in the dark current signal is covered in the actual background spectrum. Before a background correction can be applied, the

background spectrum has to be corrected for offset.

Even if the measurement spectra were corrected for background with a spectrum directly recorded afterwards, regular slight background structures remained in the evaluation spectrum. This may be explained by variations in the light path adjustment due to vibrations at the external mirrors (see *Chapter 5.2.2*). Thus, the field of view of the telescope changes slightly and therefore also the background intensity. To account for these variations, the background spectrum is additionally included in the evaluation procedure to remove remaining spectral structures. Therefore, the spectrum is corrected for dark current, logarithmised and the same filter is applied like for the measured spectra. No shift and squeeze is allowed for this background spectrum in the evaluation.

### 7.1.6 High Pass Filter

To eliminate broad-band absorption structures and broad-band xenon arc lamp structures from the spectra, a binomial high pass filter with 1,000 iterations (triangle, width one) is applied. The filter is applied after the spectra are corrected for offset, background and the logarithm is taken and thus the spectra are in optical density (see Eq. 3.7). From definition the high pass filter is the spectrum without the low pass filtered spectrum of the same iteration number (Figure 7-1). The high pass filter in the software DOASIS is defined in intensity and thus as the spectrum divided by the low pass filtered spectrum with the same iteration number. Mathematically this is identical. In practice however, differences may arise, when using discretized variables with a limit number of decimals. Numerical limitations may appear. To avoid such problems a method is introduced which uses a high pass filter in the optical density space by subtracting the low pass filtered spectrum. This is illustrated in Figure 7-6. The reference spectra can now be treated with the same filter, as they are already in optical density.

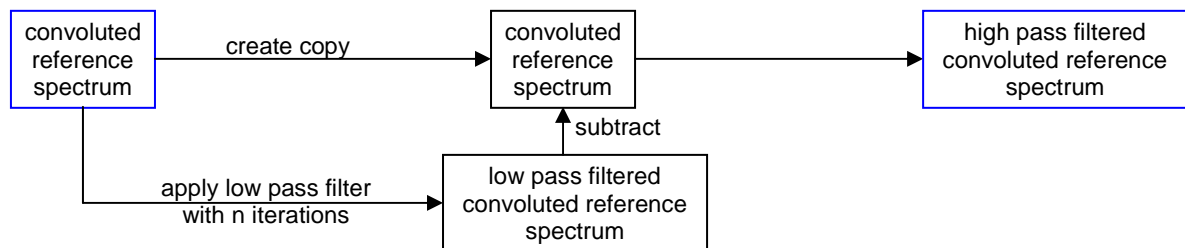


**Figure 7-6:** Schematic of new procedure to apply a high pass filter to the reference spectra. The same procedure can also be used for the logarithmised measurement and shortcut spectra.

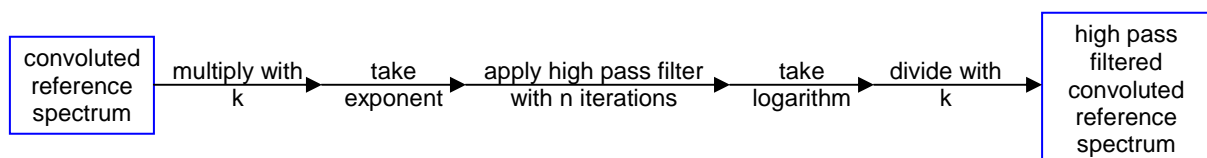


**Figure 7-7:** Schematic of old procedure to apply a high pass filter to the reference spectra. With a wrong chosen  $k$  factor the high pass filtered spectrum will feature significant errors as shown in Figure 7-8.

This procedure avoids problems of earlier evaluations shortly described and illustrated in Figure 7-7. First the exponential is taken from the references. Then the DOASIS high pass

filter is applied, defined by dividing the spectrum by the low pass filtered spectrum, and afterwards the logarithm is taken. Due to the numerical limitations in the DOASIS software this does not give any output. Therefore, the absorption cross section was multiplied with a factor  $k$ , before the exponential is taken. Afterwards the factor  $k$  is divided.

$$I_{HP}(\lambda) = \frac{1}{k} \cdot \ln(HPF(\exp(k \cdot I(\lambda)))) \quad (\text{Eq. 7.3})$$

This factor  $k$  has to be chosen with care and depends on the absorption cross section. Only the right selected factor  $k$  gives correct results like shown in Figure 7-8 for the  $\text{SO}_2$  absorption cross section.

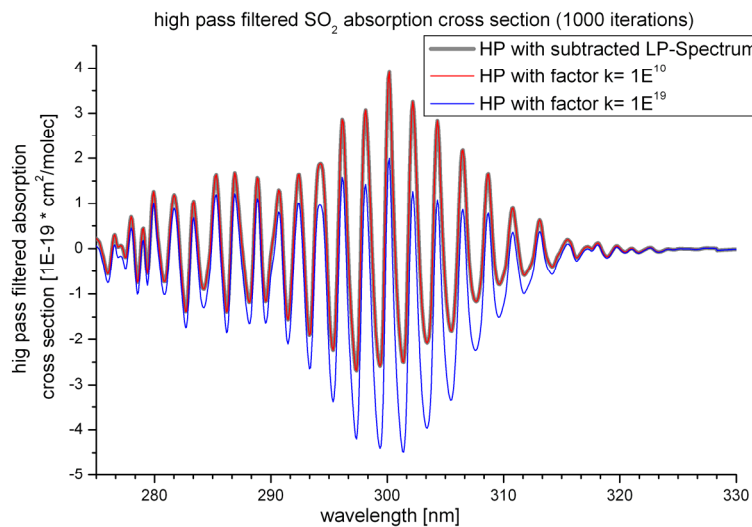


**Figure 7-8: High pass filtered  $\text{SO}_2$  absorption cross sections with 1,000 iterations.** Two methods are applied with the software DOASIS: First, where the low passed filtered spectrum (1,000 iterations) is subtracted from the spectrum (gray). Second, where the cross section is multiplied with  $k$ , the exponential is taken, the high pass filter is applied (1,000 iterations), the logarithm is taken and the spectrum is divided by  $k$ . The factor  $k$  has to be applied to avoid numerical problems in the software. The correct factor  $k$  has to be found for each absorption cross section, else large errors can arise. This may be difficult. The new introduced method (first) always gives the correct result.

The application of a high pass filter has several advantages. First, the cut-off frequency between narrow- and broad-band absorptions is well defined. This is not the case for a polynomial, where very different cut off frequencies can arise within the same evaluation and change with varying the evaluation wavelength range. Second, also broad-band structures like broad-band waves, e.g. arising from the xenon arc lamp, can be removed. Third, broad-band absorption structures from the optical components, which can have characteristic shapes, are removed. These points lead to the most important advantage, that a much broader wavelength range can be applied for the evaluation. This means, the fit may be performed over a larger wavelength range, e.g. 70 nm instead of 10 to 20 nm. This has the big advantage that much more absorption lines are used at once for the determination of the trace gas, and thus the measurement error is much smaller. Furthermore, if the residuum increases slightly with increasing wavelength range, the measurement error will typically decrease if more absorption lines are used in the evaluation. This is already included in the derived measurement errors of DOASIS, where the error is weighted opposite to the number of fitted channels.

Evaluation tests were performed with different high pass filter iterations. Increasing the filter iterations (thus reducing the applied low pass filter), can also remove useable absorption structures. Reducing the filter iterations, let pass more broad-band structures, but can lead to remaining broad-band lamp and optical structures. The optimum was found to be the applied 1,000 iterations for the spectral dispersion of 80 nm to 1024 channels. This corresponds to a filter full width half maximum of 4.6 nm for a single peak. For a different dispersion the filter has to be adapted.

A low pass filter was not applied to the data, even if this led to a smoothing of the spectra. In a mathematic correct way this would not result in an improvement of the measurement error, even if the residuum decreases. The reason is that after a low pass filter the pixels are not independent of each other and thus a correction factor has to be used which exactly compensates the reduction in the given measurement error (*Chapter 3.6*).

### 7.1.7 DOAS Fit with DOASIS

After the preparation of the spectra the fit can be performed using the fit parameters from Table 7-1. A typical fit is performed from channel 200 to 900 of the CCD chip which is related to the wavelength range from 292 nm to 361 nm, depending on the calibration of the spectrograph and fibre.

Additionally to the cross sections of NO<sub>2</sub>, SO<sub>2</sub>, HCHO, HONO, O<sub>3</sub> and O<sub>4</sub>, the shortcut spectrum (SC spectrum), a spectrum containing the difference between two shortcut spectra (DeltaSC) the background spectrum (BG Fit) and a polynomial of the 3<sup>rd</sup> order are fitted to the spectrum.

Because of the optical setup, additional spectral structures can arise due to (a) the different optical properties of the atmospheric measurement setup in comparison to the shortcut setup, what may result in a different xenon arc lamp spectrum and (b) from fluctuations in the lamp spectrum with time. The first one is almost constant with time, but can be different for each light beam. The quality of the evaluated spectra may be increased by fitting a generated lamp structure to compensate such optical structures. This was not necessary for the evaluation of the spectra, as no narrow-band lamp structures remained with the improved evaluation with fitting of the logarithmic of the shortcut spectrum. Broad-band lamp structures only remain for some light beam configurations. They are removed by additionally fitting the characteristic broad-band structure. It is created from averaging the residual spectra of a whole elevation sequence and applying a low pass filter of 500 iterations. Thus, the spectrum only contains broad-band structures.

Changes in the spectrum of the light source can additionally lead to strong residual structures. Typically, they are narrow-band and occur in the same wavelength range randomly during the lifetime of the lamp. The older the lamp the higher is the fluctuation of the lamp spectrum. Therefore, the lamp must be exchanged before its lifetime ends. The applied xenon arc lamps are therefore changed at least every 2 months.

If necessary also regions are excluded from the fit which contain bad pixels on the CCD chip. They occur if a pixel in the used area of the CCD chip does not work or has no linear quantum efficiency.

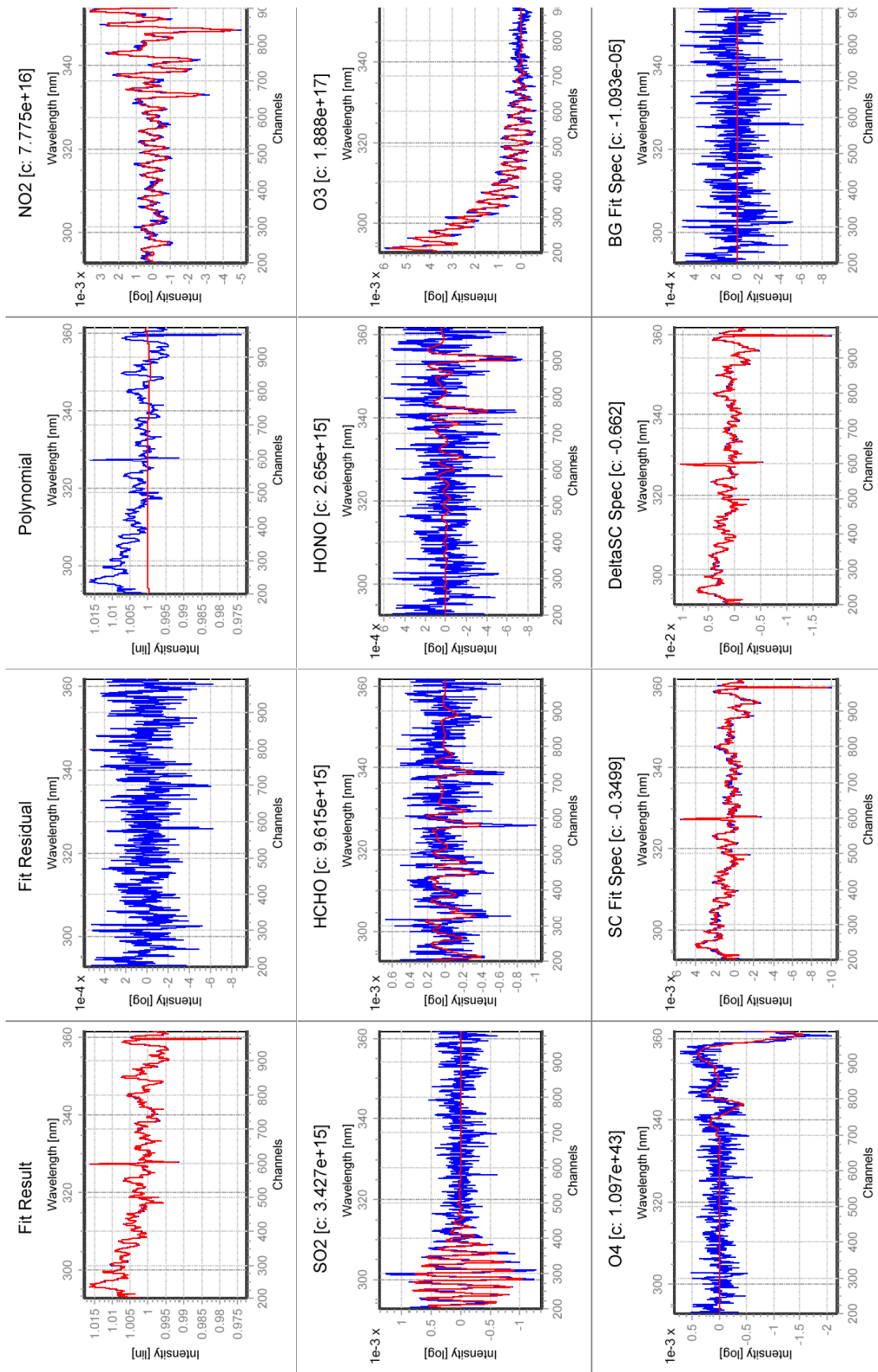


Figure 7-9: Example of an LP-DOAS evaluation in DOASIS. The fit is for a spectrum taken at the IUP to the retro reflector at HDSpeyer on September 22<sup>nd</sup> 2006 06:40 (red lines: fit result; blue lines: fit result + residuum; for the Polynomial – blue line: atmospheric spectra). The fit is performed from channel 200 (293 nm) to channel 990 (353 nm).

The measurement error and detection limit are determined as described in *Chapter 3.6 and 3.7*. The Mathematical fit error was multiplied with the factor  $C = 3$  to retrieve the measurement error  $1 \sigma$ . As detection limit always the  $2 \sigma$  confidence interval is given.

An example fit of a spectrum is displayed in Figure 7-9 with the obtained concentrations of:

	S (column density) [molecules/ cm*cm]	fit error $\Delta S$ [+/- molecules/ cm*cm]	c (mixing ratio) [ppbv]	measurement error $\Delta c$ [+/- ppbv]	detection limit [ppbv]
NO2	7.77E+16	6.39E+14	7.97	0.20	0.39
SO2	3.43E+15	1.01E+14	0.35	0.03	0.06
HCHO	9.62E+15	5.80E+14	0.99	0.18	0.36
HONO	2.65E+15	1.96E+14	0.27	0.06	0.12
O3	1.89E+17	4.09E+15	19.36	1.26	2.51
O4	1.10E+43	5.20E+41	1.12E+27	1.60E+26	3.19E+26
residuum (peak to peak)	1.40E-03		residuum (root mean square)	1.98E-04	

**Table 7-2: Obtained concentrations for the fit of Figure 7-9. The absorption path is 3896 m. The average concentrations are calculated by using Eq. 3.17.**

The derived slant column densities are converted to mixing ratios using Eq. 3.17 with the temperature and pressure measured with the IUP weather station at the same time and the total absorption paths (see Table 6-1 - Table 6-3) The distance between the instrument and the shortcut retro reflector was subtracted from the total absorption path as it also contains absorptions along this path.

The data were converted to mixing ratios, also if the tomographic retrieval requires slant column densities, as they can also be directly analysed and different average concentrations between the paths directly show where concentration maxima arise.

## 7.2 Interpolating and Averaging of Measurement Data

### 7.2.1 Averaging to Time Bases

The different measurements of trace gases along the 20 light paths, as well as the weather data and the in-situ monitor data is not measured absolutely simultaneously. The trace gas data of the three MBI are not synchronised. The different integration and adjustment time would also make a synchronisation difficult. All three instruments measured iteratively along two geometric setups. Due to the time for the mirror movement and adjustment only about half of the time can be used for the measurement. The background scan additionally reduces the used integration time. Thus only about two minutes remain within ten minutes for the measurement along one retro reflector and the measurement can never be performed simultaneously. This leads to a temporal spacing between the data. For further analysis in the tomographic retrieval as well as the vertical profile, the data have to be interpolated and averaged to the same time bases.

Interpolating and averaging is a difficult task if the data is not taken continuously like done with the MBI. Data can only be interpolated between the measured points, if the change

between the data points is approximately linear. For continuous emission sources, what can be assumed for an urban area, the change arise slowly within one hour, thus the observed concentrations can be interpolated over a gap of up to about an hour. As for most observed trace gases only one to two concentrations peaks arise during a day even longer interpolation times are acceptable. Especially if the data afterwards is averaged to time bases of several hours, small errors average out due to longer interpolation times. For very short events, like a passing plume, the interpolation may lead to errors in the derived distributions. Only a continuous measurement system could avoid them. A correct interpolation has to take into account that the measurement is not performed instantaneously but over an integration time and the determined concentration represent the average over the integration time period. The principle is displayed in Figure 7-10. After the linear interpolation between these data points, the achieved continuously concentration can be averaged to time base.

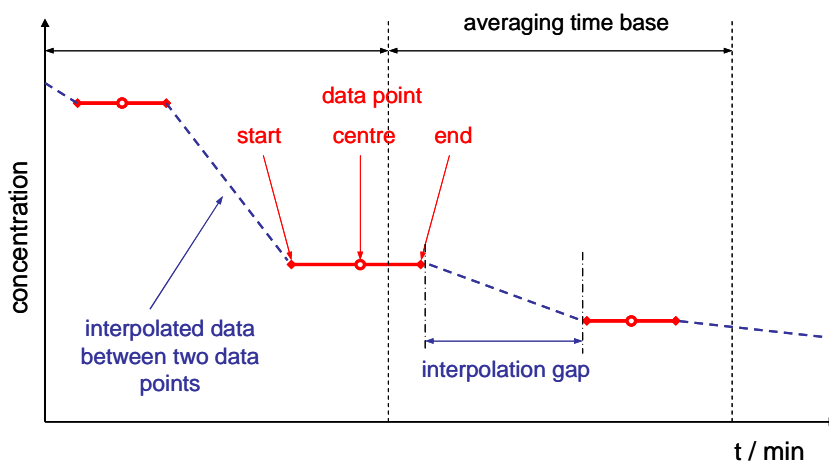


**Figure 7-10: Principle of the applied averaging of measurement data to time bases. The gaps between end and next start time of measurements are linearly interpolated before the mean value of a time base is derived.**

Each time base average over the interpolated values within the defined base. The time base should have at least a duration that one to two measurements are taken within one slot. As one full measurement cycle of all three MBI along the 20 light paths took about 10 minutes, the shortest applicable time base is 15 minutes.

All measurement data, including metrological, is averaged to the time bases shown in Table 7-3. An averaged value for a time base is only determined if at least half of the slot is represented by measurement and interpolated data.

	averaged time base [hh:mm]	max. interpolation gap [hh:mm]
1	00:15	1:00
2	1:00	1:00
3	3:00	2:00
4	24:00	6:00

**Table 7-3: Applied interpolating and averaging parameters to derive measurement data with equal time bases.**

## 7.2.2 Averaging to Daily, Weekly and Annual Cycles

Additionally to the averaging of the data to time bases also the averaging to special conditions (time or situation) are of interest for the analysis. The main cycles for urban trace gases are:

- Daily cycle: All data of a measurement period, typically one month, averaged to a mean daily cycle. The applied averaging takes the mean concentrations for all measurements observed in a one hour time base independent of the day. Thus, an averaged daily cycle is received. Different week days are ignored here.
- Weekly cycle: Similar to the daily cycle averages for each day of the week was performed. The received value represents the typical concentration for the day of the week and allows analysing the weekly cycle.
- Annual cycle: To analyse the yearly cycle all data of a month of the year are averaged to one value. Additionally also the monthly average for each year are calculated.

The averaging of the data to the cycles was performed with a programmed software in Jscript. In order to guarantee an equal weighting of the different time bases, not the measured data are used for this averaging, but the already averaged data to one hour time bases. The reason is that the original data is recorded with different time resolution, e.g. due to different weather conditions. Thus, periods with better visibility, and consequently with more data for the same time period, would have a larger contribution to the averaged data than other periods. The use of the averaged data guarantees that all one hour bases are equally weighted. An additional interpolation is not necessary.

## 7.3 Retrieval of Trace Gas Profiles from LP-DOAS Data

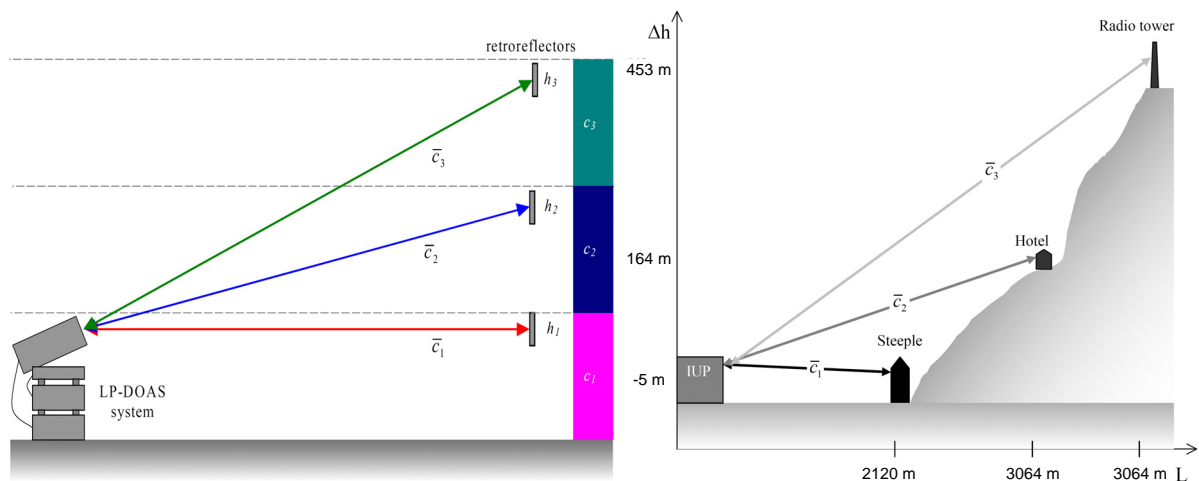


**Figure 7-11: Left: Retrieval from vertical profiles from LP-DOAS measurements on multiple light paths. The mean concentrations  $\bar{c}_1, \bar{c}_2, \bar{c}_3$  are interpolated and averaged concentrations of the LP-DOAS measurements. They are computed to the mean concentrations  $c_1, c_2, c_3$  in the layers defined by the reflector heights  $h_1, h_2, h_3$ . Right: Light paths for the vertical profile measurements in Heidelberg. The distance and the height are indicated in respect to the external mirrors of the IUP instrument (see Chapter 6.3.1). [modified graphic from Veitel, 2002]**

To derive vertical concentration gradients LP-DOAS measurement to retro reflectors at different heights were performed simultaneously to the tomographic observations (Figure

7-11). For the retrieval of the concentration at different heights above ground a plane-parallel model with fixed layer heights was applied [Veitel, 2002]. The model simply divides the boundary layer into layers with limits defined by the retro reflector heights. The model assumes that the vertical concentration gradient is constant or linearly decreasing or increasing in each layer. The mean concentration of each layer  $c_i$  can be calculated from the mean concentration  $\bar{c}_i$  measured over the light paths. In practice the mean interpolated and averaged measurement data to a time base are used (*Chapter 7.2*). The concentration in the lowermost layer is directly the concentration of the light path:

$$c_1 = \bar{c}_1 \quad (\text{Eq. 7.4})$$

For the following light paths, the measured concentrations are assumed to be composed of the mean concentrations in the layers passed to / from the retro reflector. The concentrations are added up and weighted by the height of the respective layer. Thus we receive for a setup of  $m$  light paths / layers:

$$c_i = \frac{1}{h_i} \cdot \sum_{i=1}^m \bar{c}_i \cdot (h_i - h_{i-1}) \quad (\text{Eq. 7.5})$$

By solving this system of equations, the mean concentration in the layer can be derived. For each layer it results in a simplified equation, where only the mean concentration and the reflector heights of the current and the previous light path are required:

$$c_i = \frac{\bar{c}_i \cdot h_i - \bar{c}_{i-1} \cdot h_{i-1}}{h_i - h_{i-1}} \quad (\text{Eq. 7.6})$$

The errors of the mean concentrations  $c_i$  can be calculated neglecting the errors of the reflector heights as these are determined with high precision:

$$\Delta c_i = \sqrt{\left( \frac{\Delta \bar{c}_i \cdot h_i}{h_i - h_{i-1}} \right)^2 + \left( \frac{\Delta \bar{c}_{i-1} \cdot h_{i-1}}{h_i - h_{i-1}} \right)^2} \quad (\text{Eq. 7.7})$$

The simplified plane-parallel model can be applied to the data even if temporal and spatial variations exist. The reasons are that duration of the measurement is in the range of 1 to 3 minutes and thus gives a good averaging over short temporal fluctuations. Additionally, the LP-DOAS measurements always represent an average value over a large air mass, as long as absorption paths of at least several hundred meters are applied. Spatial as well as temporal fluctuations are averaged out and the determined concentration represents a spatial average. Even if still spatial and temporal variations exist, like presented in *Chapter 8* of this thesis, they are on a much smaller scale than the typical vertical gradients. Thus, the additional error is rather small.

From the measurement setup the vertical profile can be divided into 3 boxes (Figure 7-11). Box 1 represents the horizontal concentration at the measurement height of 40 to 45 m above street level what corresponds to 140 to 145 m above sea level. The concentration is determined from the concentrations to the Providenz church. The concentration of Box 2 is

representative for the height of 45 to 209 m with a box centre of 127 m. This corresponds to sea level heights of 145 to 309 m and a centre height of 237 m. The concentration of Box 2 is determined from the measurement to the reflector at Molkenkur. Box 3 represents the concentration from 209 to 498 m and the box centre at 353.5 m. This corresponds to a sea level height of 309 to 598 m with centre height of 453.5 m.

## 7.4 Tomographic Inversion

For the tomographic inversion of the trace gas distribution the software TOMOLAB developed by T. Laepple with modifications by A. Hartl was used. Several recent investigations on the theory of tomographic LP-DOAS reconstructions [Hartl et al., 2006; Hartl, 2007] are implemented in the updated software. The measurement geometry, the observed trace gas concentrations and the reconstruction grid are required as an input. The reconstruction methods ART and SIRT can be selected, where, following the findings in Hartl et al. [2006] (*Chapter 4.4*), SIRT is chosen here. The algorithm was used with a fix number of iterations for each trace gas with a box discretisation (both explained in *Chapter 4.2*).

The software was modified to allow reconstructions with the performed for the given measurement setup. Also several bugs were fixed. The main new points are:

- Irregular and non rectangular investigation areas can be investigated. Reconstruction boxes without crossing light beam are excluded from the reconstruction.
- Retrieval with a variable number of measured light paths. Thus, also distributions can be reconstructed if not all measurement paths give useable results. This is a prerequisite for the reconstruction of longer time series because regularly one of the measurement light path failed.
- For different numbers of measured light paths, different reconstruction grids can be used. Thus, a lower resolution grid can be applied if less measurement data exists.
- The number of iterations can be changed with the grid.
- The reconstruction may be performed from mixing ratios (ppbv) observed along the light paths. The dimensions of retrieved distributions is then also in mixing ratios.

All tomographic retrievals of this thesis do not apply a weighting before the fit, i.e. the unweighted least-squares-squares problem was solved. Applying weights equal to the measurement error as described by Eq. 4.4 had a negligible impact on the reconstructed concentrations (less than 0.01 % change in retrieved concentrations).

In the following chapters tomographic retrievals are shown for simulated distributions for the measurement setup in Heidelberg. It is demonstrated how the retrieval parameters like reconstruction grid and iteration number are optimised. The aim is to reduce errors and artefact in the retrieved distributions. Artefacts are a misrepresentation of the true distribution which can arise due to a variety of phenomena. They can be caused by the geometry, measurement errors, systematic errors or from the retrieval algorithm. Therefore also systematic errors of the measurements are discussed.

### 7.4.1 Reconstruction Grid

As described in *Chapter 6.2*, the light path setup for Heidelberg was irregular and from a theoretic point of view far from perfect. This is inevitable in urban areas, where sometimes only few instrument and retro reflector locations can be found. The irregular geometry and coverage makes a suitable discretisation rather challenging. Additionally, the number of measured light paths varies due to technical complications of this involved setup. For example a light beam may loose the focus on a retro reflector. Or low visibility can decrease the intensity to an extent that makes retrieval of column densities impossible, especially on the long absorption light paths. Finally data is skipped for tomographic reconstruction if the measurement is not considered accurate enough (spectral residuum too high). As a result of all this, the measurement geometry changed. For good measurement periods this arose only once a day or week. At difficult metrological conditions the geometry changed often even one an hour.

Suitable reconstruction grids for the different measurement geometries have to be found. It is demonstrated by Hartl [2007], that the retrieval error can significantly be reduced with an optimised reconstruction grid for different geometries. Different grids were tested for the tomographic setup of Heidelberg with simulated and measured distributions. The finally chosen grids displayed lowest artefacts in the reconstruction and best resolution to the investigation area. They are shortly described.

The measurement geometries were divided into 4 groups, each assigning an individual reconstruction grid. Grid I is for geometries with at least 17 out of 18 measurement paths, grid II between 14 and 16, grid III between 11 and 13 and grid IV between 8 and 10 (Figure 7-12 - Figure 7-15). The grids for fewer measurement paths feature a lower spatial resolution and thus also the number of reconstruction boxes decreases. Additionally, if all measured paths crossing a box failed, the according box is excluded from the retrieval and the box number and investigation area is reduced. Both changes guarantee that the ratio between reconstruction boxes and measured paths remain nearly constant and thus the retrieval could display similar accuracy. An overview of the reconstruction grids is given in Table 7-4. The grid I with the highest resolution has in total 24 reconstruction boxes (Figure 7-12). The minimum number of light paths for a tomographic reconstruction is set to 8.

no. of light paths	reconstruction grid	resolution $x \times y$ (box border lines)	no. boxes (max.)
17 – 18	I	$8 \times 8$	24
14 – 16	II	$8 \times 7$	20
11 - 13	III	$7 \times 7$	17
8 - 10	IX	$6 \times 6$	13

**Table 7-4: Properties of the applied reconstruction grids for the tomographic inversion used in this thesis. These grids are displayed in Figure 7-12 - Figure 7-15.**

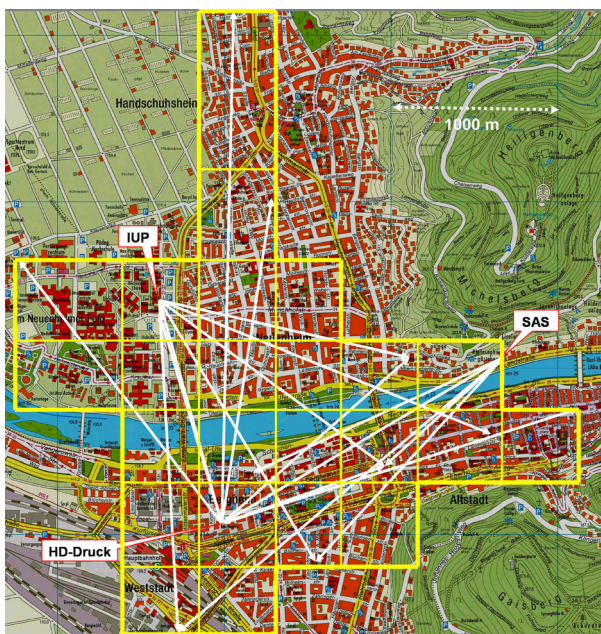


**Figure 7-12: Reconstruction grid I (8×8) (yellow lines) for measurements in Heidelberg with 24 boxes used for inversion with box basis functions. The white arrows indicate measured LP-DOAS absorption paths. This grid is only applied to the retrieval if at least 17 out of 18 measured absorption paths give usable results.**

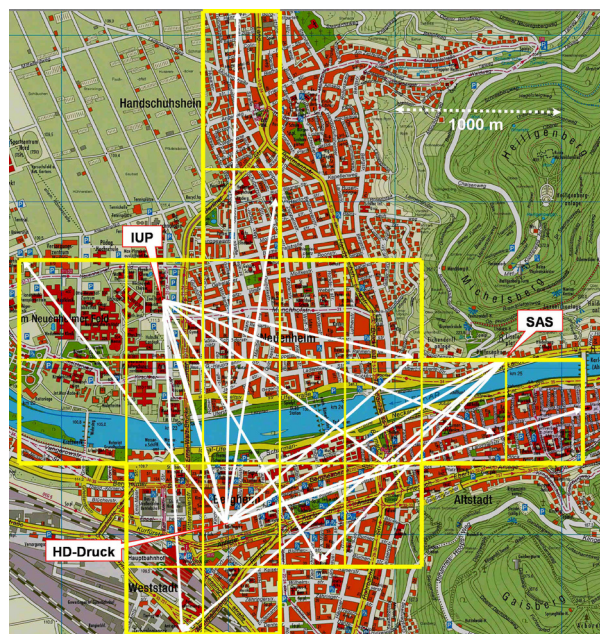


**Figure 7-13: Reconstruction grid II (8×7) with 20 boxes similar to Figure 7-12. This grid is applied if between 14 and 16 out of 18 light paths give usable results.**

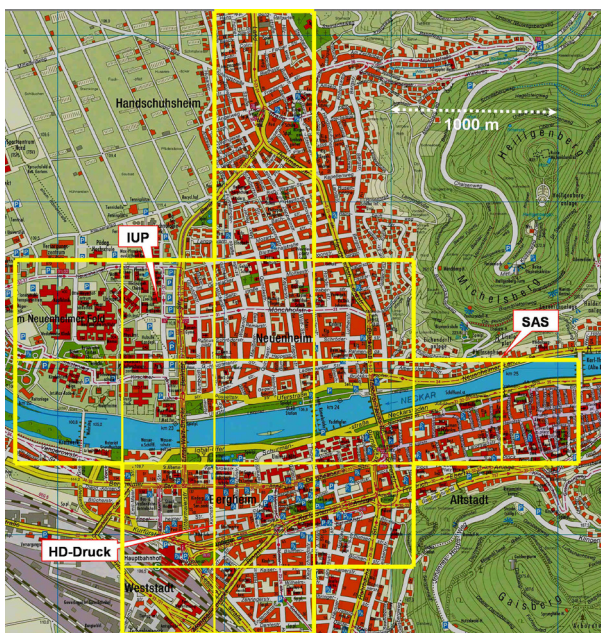


**Figure 7-14: Reconstruction grid III (7×7) with 17 boxes similar to Figure 7-12. This grid is applied if between 11 and 13 out of 18 light paths give usable results.**

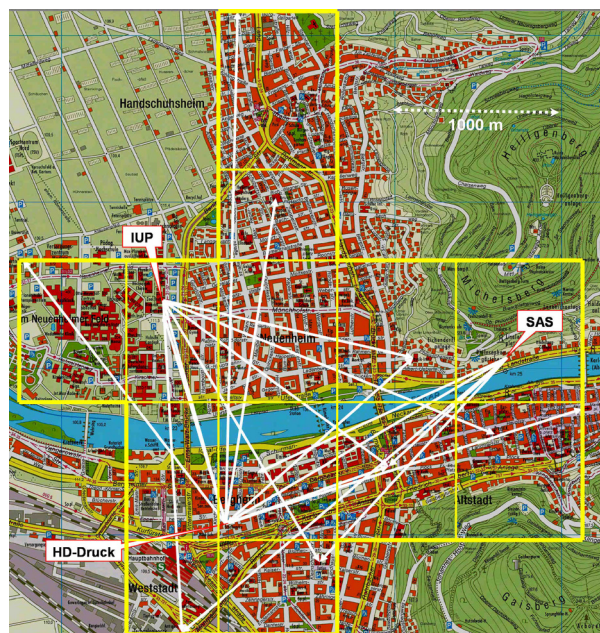


**Figure 7-15: Reconstruction grid IV (6×6) with 13 boxes similar to Figure 7-12. This grid is applied if between 8 and 10 out of 18 light paths give usable results.**

The grid I to IV are arranged to represent expected concentration distributions, e.g. separate boxes at the river Neckar. Concentrations are expected to be lower there due to missing emission sources or temporally higher due to ship emissions. Main streets like the

Bismarkplatz in the city centre or the traffic loaded bridges over the Neckar are covered within one box.

Urban areas with less are set to separate boxes in order to represent the concentration there as well as possible (e.g. “Neuenheim” in the North, “Im Neuenheimer Feld” in the West or “Altstadt” in the East (see Figure 6-4)). If streets would also be included in the same reconstruction box, the derived concentration would be a mixture from both areas, which makes it difficult to distinguish the main sources.

## 7.4.2 Reconstruction of Simulated Trace Gas Distributions

This chapter presents simulation results for reconstruction of various synthetic 2 dimensional trace gas distributions. Simple simulation fields contain single or multiple points like concentration peaks which can be described by Gaussian plume or puff models. The emitted trace gases are distributed by transport and turbulent diffusion. Line sources, like streets, are expressed by Gaussian plumes with different FWHM for the dimension. These simulations are used to quantify the quality of the tomographic measurement setup and reconstruction of such single plumes with the applied grids of Table 7-4.

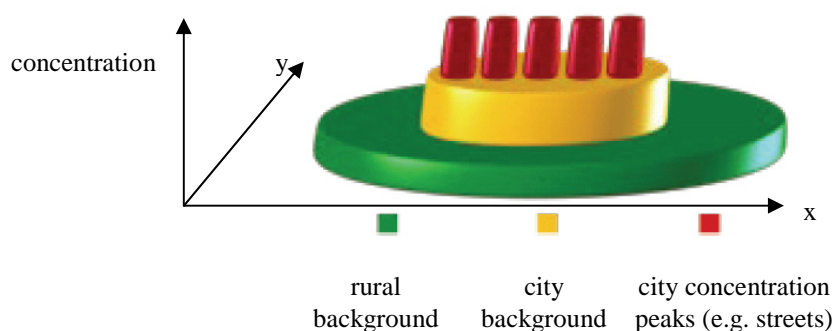


**Figure 7-16: Sketch of trace gas concentration distributions in urban areas with different urban areas [Umweltbundesamt, 2010]. This type of distributions is used for the generation of artificial distributions in this chapter.**

However, the assumption that the trace gas occurs only as a concentration puff is unrealistic for most observed species in urban areas. Dominant background concentrations are produced by emission sources present over a large area (e.g. traffic, small heating systems) or formed in chemical reactions on a larger scale (*Chapter 2*). Overall, urban trace gas distributions relevant for this work can be characterised as depicted in Figure 7-16: A general (rural) background concentration with an increased urban concentration in the city (city background). On top of this combined background, concentration peaks close to emission sources (e.g. main streets) arise. Different simulation fields were created for the investigation area following this scheme, assuming different main sources like emissions from traffic hot spots or ship emissions from the river Neckar. These fields were also used to determine suitable reconstruction grids presented in *Chapter 7.4.1*. Here only results with these grids are discussed.

For the reconstruction of the simulated measurements of these synthetic concentration fields only boxes containing at least one partial light path are taken into account and displayed.

Other areas are displayed by white areas. Measurement errors are ignored here; their influence is studied in *Chapter 7.4.3*. SIRT was run with an iteration number of 100 and a starting value for the box concentrations obtained from averaging over all mean path integrated concentrations.

### Distributions without Background Concentration

Figure 7-17 shows simulated distribution consisting of two distinct Gaussians placed more or less randomly such that the broader left hand peak lies only partly inside the grid while the narrower right hand one is in the centre of the monitored area. Both concentration peaks can be found in all simulated reconstructions. The peak positions can be reproduced reliably within the resolution of the reconstruction grid. Peak size increases due to the lower resolution. At least in this particular example a higher resolved grid results in a more accurate reconstruction of both peak locations and maximum concentrations.

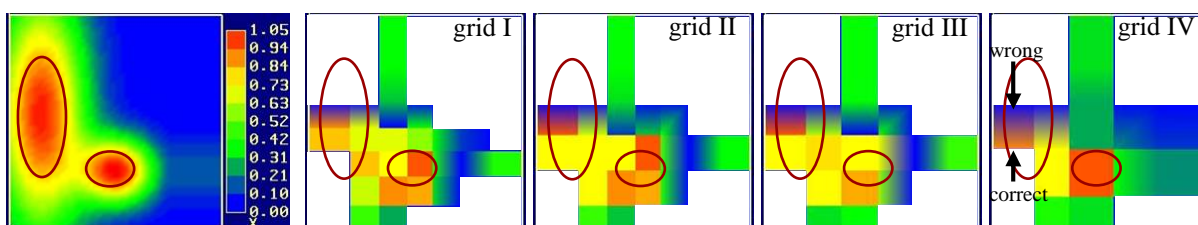


**Figure 7-17:** Colour coded 2-D simulated trace gas distribution with two Gaussian peaks at random location and without additional background. Peaks highlighted in dark red. Left: True concentration field. Right: Reconstructed distribution with grids I to IV (for details see main text). Same colour scale for all plots. A bug in the graphic software (not from reconstruction) is responsible for changes of concentration within boundary boxes. Here the highest displayed concentration is the valid value like highlighted for grid IV, for one box.

It can also be observed that areas outside the peaks show too high concentrations. The higher resolution (grid I) displays the highest concentration. The reason for this artefact is impact of the a-priori in this under-determined system. Especially the boundary boxes are poorly determined by the few light beams. Thus they may remain at or close to the a-priori value. As for the lower resolution (grid IV) the system is better determined and this artefact becomes smaller.

Still this simulation indicates that the setup and reconstruction scheme considered here can reproduce single Gaussian peaks. However, the zero background concentration might be retrieved less accurately.

### Distributions with Background Concentration

Now simulations with distributions on a non-negligible background are investigated. For urban scenarios, these are more realistically, even if the peak concentration may be very different in comparison to the background level. Different locations, sizes and ratios of peak to background concentrations are studied in the following.

#### *NO<sub>2</sub> Point Emissions from Traffic Hot Spots*

The first concentration distribution consists of two peaks rising about 20 % above the background (Figure 7-18). The peak locations correspond roughly to a large crossroad close to the main station, and a main road connecting the East and West of the city. The peak to

background ratio of 20 % is a realistic assumption for a  $\text{NO}_2$  concentration at 30 to 40 m height above ground. The reconstructed distribution of this concentration field correctly reproduces both the peak locations and the negative gradient towards the borders of the monitored area. The background values as well as its distribution are well captured for all grids. The peak concentrations are relative precisely determined. Artefacts arise of the order of  $< 10\%$  and are not reduced for the lower resolution grids.

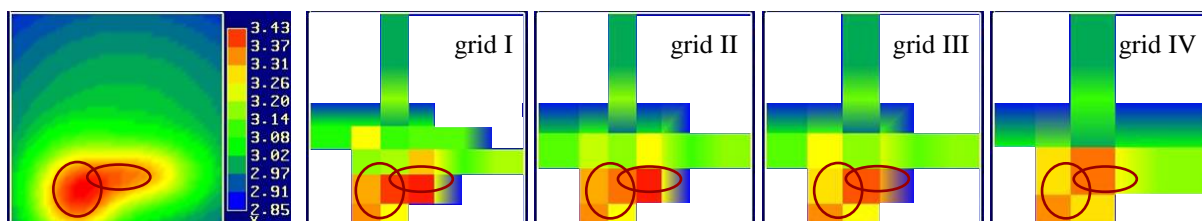


**Figure 7-18:** Colour coded 2-D simulated trace gas distribution with two Gaussian peaks on a background concentration. Peaks highlighted in dark red. Left: True concentration field. The concentration peaks are located at a main junction and heavy traffic street. The peaks are close to each other and almost merged. Right: Reconstructed distribution with grids I to IV (for details see main text). Same colour scale for all plots. A bug in the graphic software (not from reconstruction) is responsible for changes of concentration within boundary boxes. Here the highest displayed concentration is the valid value like shown in Figure 7-17.

### $\text{SO}_2$ from Ship Emission

The second artificial concentration distribution is a highly distorted Gaussian peak on a low background (Figure 7-19) to simulate a local ship emission. A low background concentration in comparison to the direct emission is realistic for  $\text{SO}_2$ , as its background concentrations in Europe nowadays typically are lower than 3 ppb. If wind speed is low, the emission forms a very local plume which is here approximated by a distorted Gaussian peak (here 100 m FWHM). The width is much smaller than the resolution of the reconstruction grid (450 m).

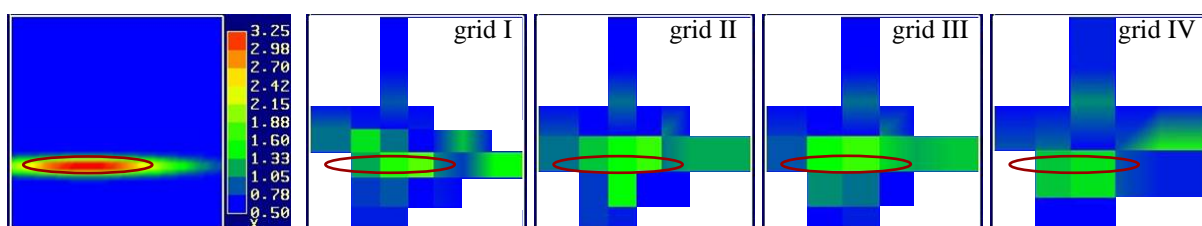


**Figure 7-19:** Colour coded 2-D simulated trace gas distribution of a distorted Gaussian peak with large extension in x and small in y direction to illustrate a local ship emission at the river Neckar with low background concentration. Peak highlighted in dark red. Left: True concentration field. Right: Reconstructed distribution with grids I to IV (for details see main text). Same colour scale for all plots. A bug in the graphic software (not from reconstruction) is responsible for changes of concentration within boundary boxes. Here the highest displayed concentration is the valid value like shown in Figure 7-17.

While enhanced concentrations around the true location of the plume can be found in the reconstructions for all grids, the actual peak value is underestimated due to the relatively large box size compared to the peak extension. Areas outside the true peak location display in the reconstruction often enhanced values. For this example, a finer grid gives a better estimate of both the peak location and its value.

Although the distribution of such a local ship emission cannot be exactly reproduced, especially in the term of the peak concentration, the reconstructed distribution can localise the concentration peak.

### Several Concentration Peaks

The following simulated concentration fields are the most realistic, but also the most complex ones considered in this work. They consist of two (different) background distributions and several concentration peaks of different size and magnitude (Figure 7-20) in correspondence to Figure 7-16: A constant background (rural background) plus an additional background (city background) which has slightly higher concentration in the city centre than in the suburbs plus Gaussian peaks to mimic various point sources that might occur in the city. In the first simulation field (a), the two strongest peaks were set to two main traffic junctions of the city. A third squeezed concentration peak was arranged along a heavy frequented main road. The fourth peak is smaller with lower maximum concentration and represents a local ship emission.

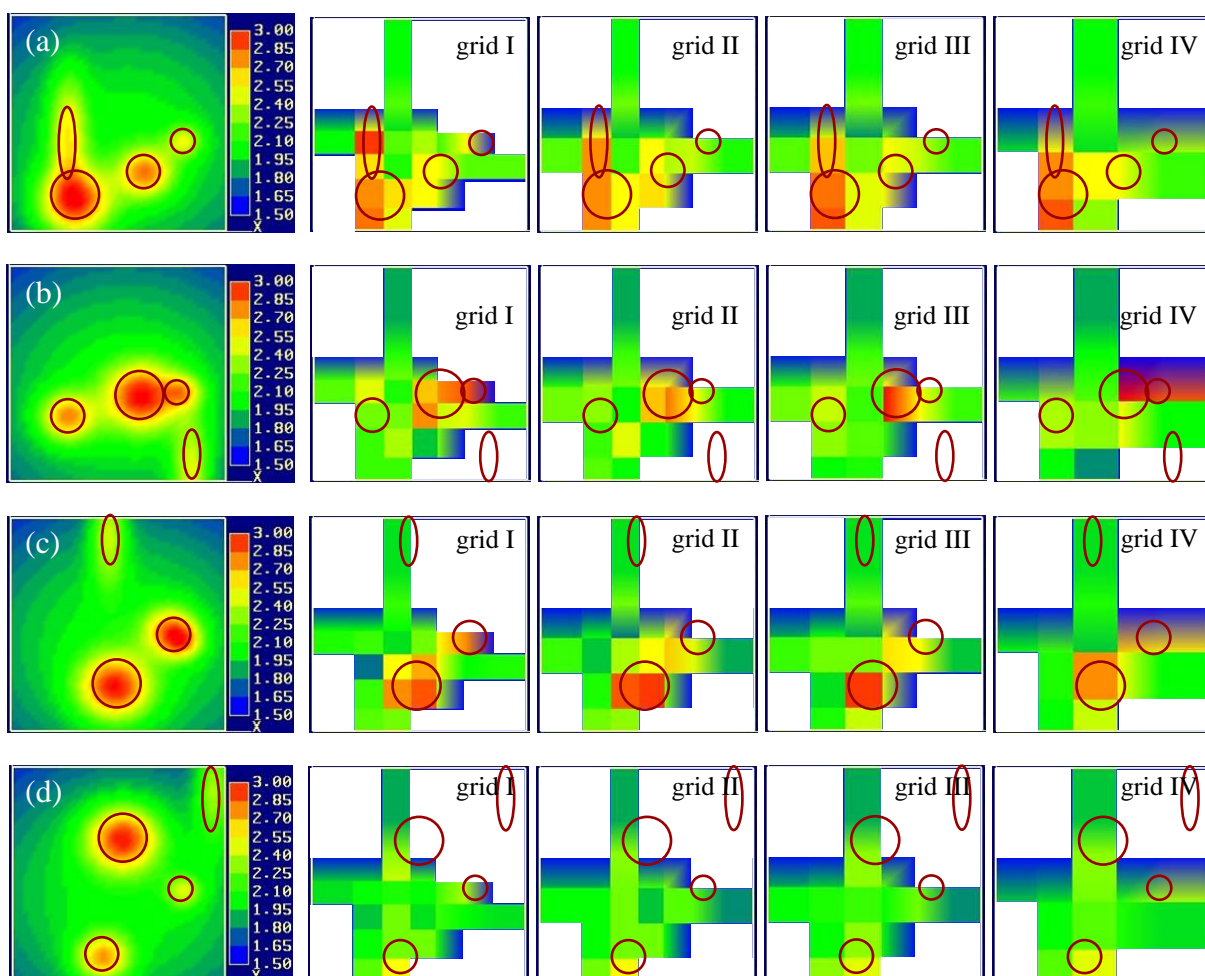


**Figure 7-20:** Colour coded 2-D simulated trace gas distributions with four Gaussian peaks on a background concentration. (a)-(d) represent different locations of the peaks. Peaks highlighted in dark red. Left: True concentration field. Right: Reconstructed distribution with grids I to IV (for details see main text). Same colour scale for all plots. A bug in the graphic software (not from reconstruction) is responsible for changes of concentration within boundary boxes. Here the highest displayed concentration is the valid value like shown in Figure 7-17.

The reconstructed distributions of this field (a) contain the main features for all grids. All four peaks can be found only for the highest resolution (grid I). Even the smallest peak in the East is reconstructed. This grid also displays the best spatial reproduction of the true distribution. The concentration of the largest and strongest peak is reproduced by all grids with high accuracy (concentration error < 10%). Overestimated concentrations arise predominantly in

grid I with highest resolution ( $\sim 10\%$ ). Such an artefact appears in the North-East. These relatively small errors are the price one has to pay for the gain in spatial information.

The following simulation fields in Figure 7-20 ((b) – (d)) are a random variations of the peak locations of field (a). For (b) and (c) the large concentration peak is well represented in the reconstructions. Again, higher resolution gives better localisation and a better representation of the peak concentration. Weak concentration errors (under- or over-estimated concentrations) are found in the finest grid ( $< 10\%$ ) where also small shifts of the true peak location (e.g. in the West) are found. The grid with lower resolution does not contain these errors, but leads to less accurate spatial features in the reconstruction, especially if peaks happen to fall between to boxes (as in the East in the fields of (b) and (c)) and the concentration is thus smeared over more than one box.

The last example Figure 7-20 (d) demonstrates a distribution which is insufficiently reconstructed. The main concentration peak in the North cannot be reproduced by any of the reconstruction grids corresponding to a concentration error of  $\sim 20\%$ . The likely reason is that only one light beam is measuring this peak. In this case, the achieved information of the measurement is not sufficient to reconstruct the true distribution. This was confirmed by analysis of the linear independence of the two boxes in the North using the Singular Value Decomposition. It revealed that concentration differences between the two boxes can only be poorly reconstructed<sup>8</sup>.

The narrower concentration peaks in the above distributions are not always well reconstructed. Especially the grids with lower spatial resolution (grid III and IV) cannot capture these peaks. Additionally their reconstruction depends on the location in the measurement field. In most cases the peaks can be localised with errors in concentration of about  $\sim 15\%$  (for grid I). But if a peak is not detected by any light path, it naturally will not show up in the reconstruction.

The background concentration is in all cases well reconstructed. No errors or artefacts are found. The retrieved concentration equals the simulated concentration with accuracy better than  $5\%$ .

### Very Localised Peaks

Turning now to the extreme case of very localised emissions in the form of very narrow peaks, it is by now clear that they can only be insufficiently captured by the measurement. Depending on their location it is possible that several light beams detect the increased concentration. An example of such a distribution is displayed in Figure 7-21(a).

Here a strong plume is assumed close to the light beams of the HD-Druck instrument (Chapter 6.3.3). Because the reconstruction grid is much coarser than the plume size, these peaks cannot be reconstructed. But as the light beams still measure the increased concentration, the reconstruction process will try to put the enhanced concentration somewhere into the grid. Thus, very deceptive errors in the reconstructed distribution can arise as pointed out in the figure (by arrows). Depending on the distribution errors emerge for different reconstruction grids at different locations. Due to the larger box size for lower resolved grids larger areas are affected.

<sup>8</sup> A. Hartl, personal communication

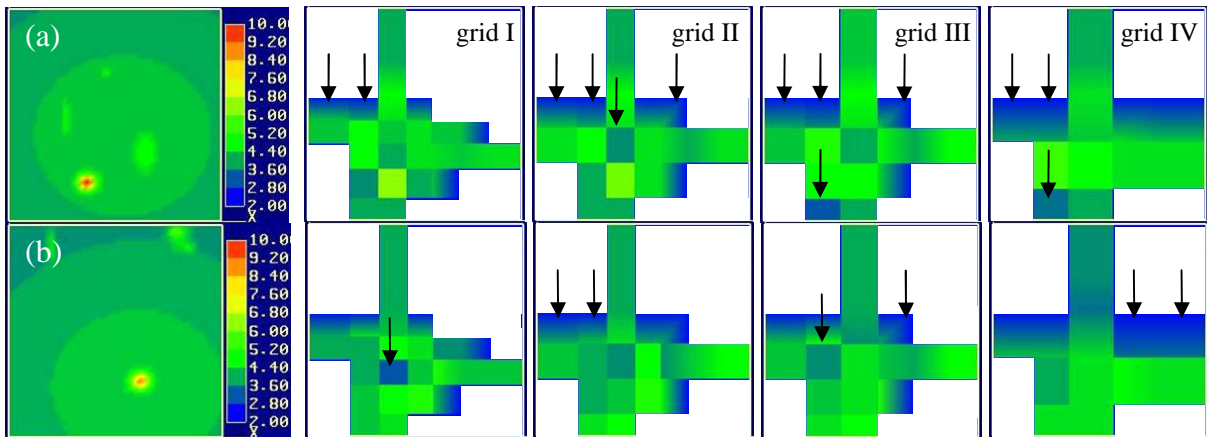


Figure 7-21: Colour coded 2-D simulated trace gas distribution with four very local Gaussian peaks on a background concentration. Left: Assumed concentration field with one strong plume. Upper row position is located to HD-Druck instrument. Right: reconstructed trace gas distribution with different applied grids and 100 iteration steps. The concentration peaks are too local to be captured by the measurement and tomographic reconstruction. As the resolution of the reconstruction grid is too small in comparison to the plumes, artefacts arise (marked with arrows). A bug in the graphic software (not from reconstruction) is responsible for changes of concentration within boundary boxes. Here the highest displayed concentration is the valid value like shown in Figure 7-17.

## Conclusions on Simulated Trace Gas Distributions

The above simulations demonstrate that the measurement geometry and a reasonably chosen reconstruction grid are well suited to retrieve most trace gas distributions with a size comparable to the grid size with fair accuracy. Especially reconstructions for the most likely case of substantial background concentration can reproduce both background and peak concentrations accurately. Artefacts occur if the background concentration is low in comparison to the peak concentration. The reason is of course the influence of the a priori in the form of the iteration start vector for the discrete box concentrations for these effectively under-determined least-squares problems. Choosing the average concentration of all light paths as iteration start will work the better, the more the true distribution resembles a constant concentration field, i.e. an uniform background. For trace gases with known negligible total background, a zero concentration field should be chosen as iteration start.

The above simulations also clearly show that with increasing resolution of the reconstruction grid the true distribution is better localised and peak values better derived. But the probability of reconstruction errors and artefacts increases, as the least-squares problem becomes more and more under-determined. Not shown here is how grids with higher resolution than grid I lead to even much higher errors. On the other hand, the gain of information on both peak values and spatial features demonstrated in the reconstructions above justifies the risk of introducing minor artefacts in higher resolved grids. This risk can be reduced by empirically determining an optimal grid through simulated reconstructions as demonstrated here and can be also applied to measurement geometries with smaller numbers of light paths (Table 7-4). Additional examples for reconstruction errors for real measurements will be presented in *Chapter 7.4.4*.

### 7.4.3 Determination of the Optimal Iteration Number

As discussed in *Chapter 4.4*, the algebraic reconstruction method SIRT employed throughout

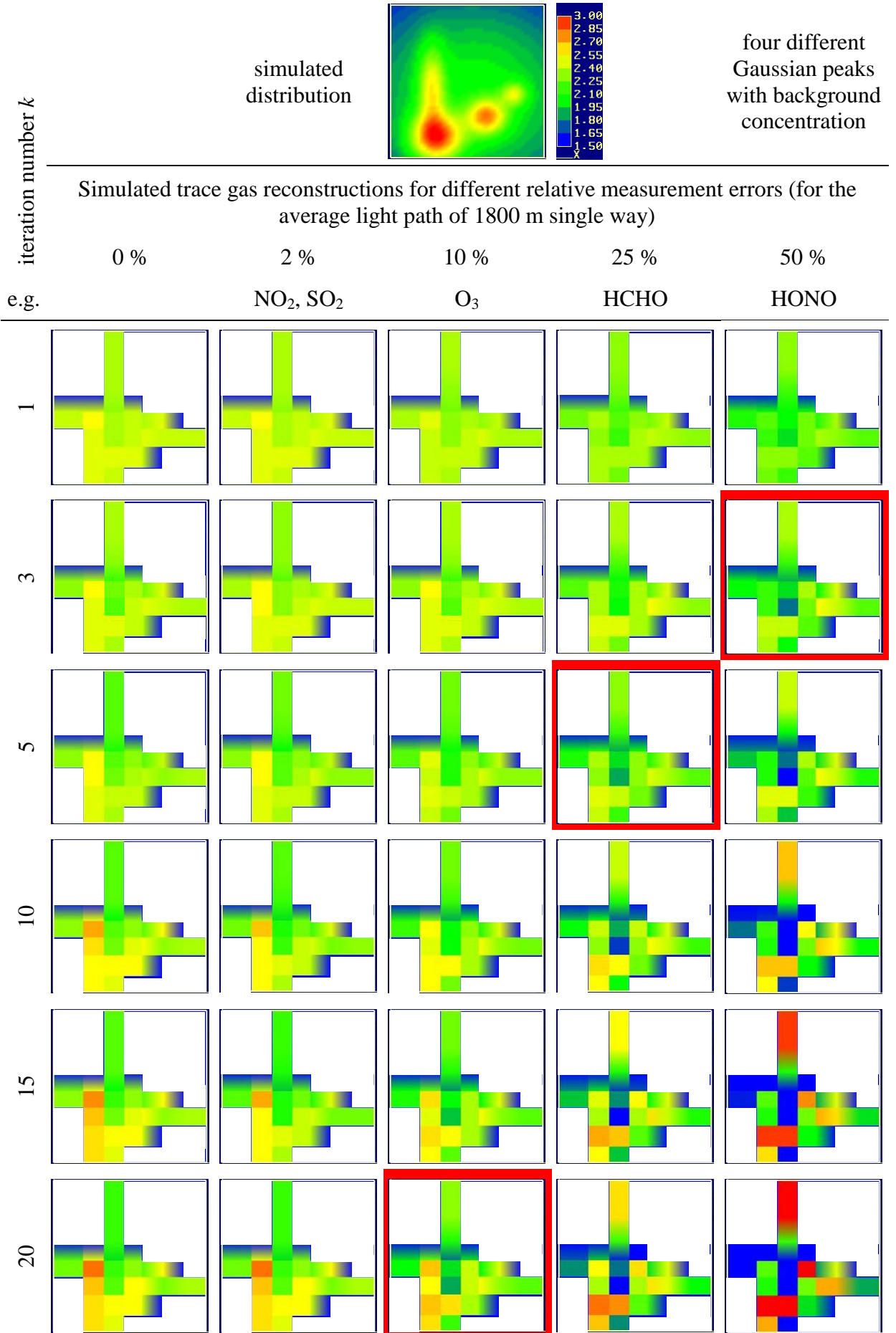
this thesis solves the pure least-squares problem Eq. 4.4 iteratively. To account for the ill-posedness of this problem arising from the underlying LP-DOAS remote sensing measurement, a regularisation scheme is introduced by stopping the iteration prematurely (so called iterative regularisation).

The choice of the regularisation parameter, i.e. iteration number, depends for a given experimental setup and trace gas scenario on the measurement error. Here, again, an empirical approach is chosen to find optimal values for the iteration number by applying different error levels to simulated measurements. Systematic errors are not included, as their magnitude is largely unknown. Systematic errors can be an offset in the concentration of an instrument or systematic concentration differences due to different heights of the measurement light paths in the presence of a vertical concentration gradient. Systematic errors of this kind will be discussed in *Chapter 7.4.4*. In order to simulate data with statistical errors, a relative random error was added to the modelled column of all light paths. As in practice an LP-DOAS measurement error of the column does not change with the absorption light path, different relative errors occur for same measurement accuracy. The error variance was therefore investigated for the average absorption light path length of 1800 m (single path) and then applied to all other light paths. Thus, in the following, an error of 10% means a relative error of 10% for the light path of 1800 m, but in fact a smaller relative error for longer absorption paths and a larger one for shorter paths is applied. For the investigation of different relative errors (columns in Figure 7-22), the same derived statistical error for each light path was scaled before added to the column density.

The results of this sensitivity study are summarised in Figure 7-22. If no measurement error is applied (first column), the reconstruction improves with increasing iteration number in agreement with what was stated in *Chapter 4.3*. For smaller iteration numbers (stronger regularisation) absolute values as well as the peak location are less accurate. A very good reconstruction can be found for 50 iterations and more. With higher iteration numbers only very small or even no improvements can be found.

If measurement errors are taken into account, artefacts and errors arise in the reconstruction at large iteration numbers (weak regularisation). With increasing measurement errors also artefacts increase if the iteration number is kept constant. The location of reconstruction errors and artefacts is similar for the different measurement errors, as they follow the same statistic. The optimum result of this empirical evaluation is a compromise of regularisation between reconstructing the characteristics of the distribution sufficiently and letting artefacts not become too large. In Figure 7-22 reconstructions for the optimum iteration number are highlighted in red. This optimum iteration number decreases with increasing measurement error, i.e. regularisation has to become stronger to achieve optimal results. Therefore a smaller iteration number is applied to measurement data with larger measurement error.

The iteration numbers found this way agree well with the results by Hartl [2007], who estimated an optimum iteration number of 15 – 20 for a distribution with several concentration peaks on a dominating background and relative measurement error of about 10 %. It shows that the different measurement geometry and reconstruction grid does not have a significant influence on the optimum iteration number.



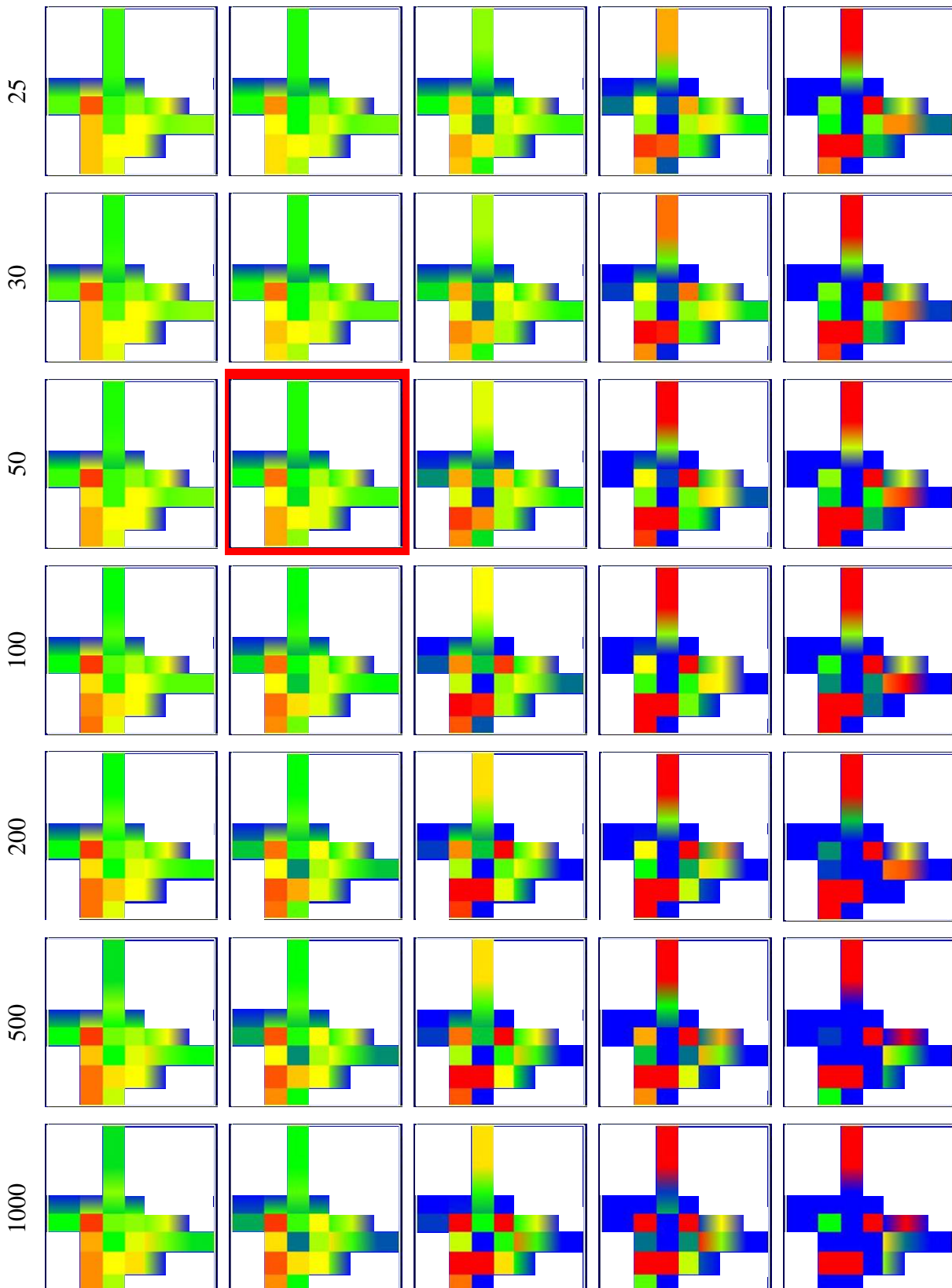


Figure 7-22: Colour coded 2-D simulated trace gas distribution (top) and reconstructed distributions for different relative measurement errors and iteration numbers (counting starts with 0). Grid I was applied. Areas outside the grid are displayed as white areas. Optimum iteration number for the reconstruction is defined by most accurate retrieval of the true distribution with only small artefacts. With increasing measurement errors, the reconstruction error increases and the optimum iteration number decreases (highlighted in red). A bug in the graphic software (not from reconstruction) is responsible for changes of concentration within boundary boxes. Here the highest displayed concentration is the valid value.

To relate the optimal iteration numbers just found to actual LP-DOAS measurements, their absolute measurement errors have to be converted to relative ones. A main feature of LP-DOAS measurements is that the absolute error does not change with the absolute concentration. Thus the relative error is different for different concentrations. A typical concentration value is chosen here to determine the typical relative error of a DOAS measurement. These values are used to estimate the optimum iteration number according to Table 7-5 and used for all retrievals of this trace gas.

	NO <sub>2</sub>	SO <sub>2</sub>	O <sub>3</sub>	HCHO	HONO
typical concentration [ppb]	10 - 40	1 - 10	10 - 80	1 - 4	0 - 1.5
average absolute error for 1800 m absorption path (single way)	0.03	0.025	1.0	0.25	0.3
typical relative error	~ 2 %	~ 2%	~ 10 %	~ 25 %	~ 50 %
applied optimum iteration number	50	50	20	5	3
estimated reconstruction accuracy (without systematic errors)	~ 10 %	~ 10 %	~ 20 %	~ 30 %	~ 50 %

**Table 7-5: Typical concentrations and errors for LP-DOAS measurements along a 1800 m absorption path (single way) used to determine a typical relative measurement error. With this relative error the optimum iteration number is estimated from simulations in Figure 7-22. The derived value does not apply to additional systematic errors.**

This estimation does not account that the DOAS measurement errors can be a dominated statistical error which would decrease if averaging over several data points within a time base (*Chapter 3.6.6*). As the DOAS measurement error of the data in this thesis are dominated by systematic errors which do not decrease with averaging over several data points (*Chapter 3.6* and *5.3.4*), such considerations are not applied here.

Apart from pure random errors considered so far, additional systematic errors can emerge which vary for different instruments and measurement paths (see *Chapter 7.4.4*). These errors significantly deteriorate the reconstruction quality and are responsible for artefacts. Simulations performed (not shown here) with such systematic errors show that neither reduction of the iteration number nor the spatial resolution (larger boxes) can significantly lower their influence on the results. The optimum iteration number and grid are similar to those with only random noise.

#### 7.4.4 Artefacts in the Tomographic Reconstruction

Within this work different sources for artefacts in the tomographic reconstruction have been identified and investigated. They are given by the DOAS measurement error, systematic measurement errors, the limited tomographic setup (geometry) and the reconstruction algorithm. The influence of the DOAS measurement error was discussed in *Chapter 7.4.3*. The influence of systematic errors is difficult to estimate, as they are unknown. The most typical systematic error sources for the setup here are:

1. Offsets in signal between different instruments. They can be caused by the use of different spectrometers (e.g. Acton 300 and Acton 500) with different dispersion and instrumental functions (*Chapter 5.3*). This error is estimated to be smaller than 3% (*Chapter 3.6*).
2. Offset in signal between different light paths of one and the same instrument due to stray light in the spectrometer. This occurs if the light of one light beam is very weak in comparison to the other, so that the scattered light in the spectrometer from other light beams is significant (*Chapter 5.3.1*). This can cause large concentration offsets of up to 10 %.
3. Stray light due to imperfect optical components like dust and dirt on optical filters in the spectrometer can be responsible for additional signal offsets. Even if optical filters are used to reduce stray light (from other spectral ranges), it could be observed that dust and dirt on these filters also responsible for additional stray light due to scattering of up to 20 %.
4. Malfunction of an instrument can cause significant concentration errors, as is the case e.g. for defects of the spectrograph shutter (*Chapter 5.3.2*) or detector electronics. Electronic errors due to a detector malfunction occurred at the SAS instrument from Nov. 2006 to March 2007 where detector saturation changed randomly and led to over-saturated spectra. Therefore the derived concentrations are underestimated. Even if a filter is applied to remove such data points, it cannot be excluded that wrong measurement data result in errors in the retrieved distributions.

While instrumental errors can in principle be avoided by optimised instrumentation, flaws in the reconstruction arise from limited measurement geometry cannot be corrected. The most important shortcomings of our geometry are (apart from the necessarily limited number of light paths):

5. Instruments and reflectors are not at the same height and therefore the light paths do not lie in a plane. Usually large vertical concentration gradients can be found in the urban boundary layer, so that light paths even at slightly different heights record concentration differences which are not caused by horizontal concentration variations.

In this thesis, simultaneously to the 2-D horizontal tomographic, also vertical profile measurements were carried out. The concentration gradients (*Chapter 8.10*) obtained this way were used to estimate the influence of vertical variations on the total observed light path variations. The gradient depends on the trace gas and its concentration and ranges typically from -1 %/m to + 1 %/m height. In the setup of this thesis, the reflector height varies by 30 m (see *Chapter 6.3*). The average measurement height varies by 15m due to the inclined paths. Thus the vertical gradient can cause concentration variations of up to 15 % which in the tomographic retrieval process are wrongly interpreted as horizontal concentration differences. Although these vertical gradients did not show up in a systematic way in the reconstructed distributions, they are certainly affecting their accuracy.

6. If plumes display a much smaller distribution than the measured and the

reconstruction resolution they may only insufficiently be resolved. E.g. If the light paths directly cross a very local plume of an emission source like a heating exhaust, or if an instrument is located next to an emission source, the observed signal is not representative for the corresponding box of the grid - a light path close by but outside the emission plume would detect a very different signal. The resolution of the reconstruction grid is too low to resolve these gradients causing additional errors in the reconstruction.

In an urban experiment it is likely that several light beams pass through the emission plume of a chimney. Their actual number may be unknown and therefore the influence on the reconstructed concentration field is unclear. If the emission strength is low and the plume size very small, its influence on the observed concentration is small and the reconstructed distribution is not affected. But larger plumes with high concentrations can have a significant influence. One of these sources could be identified at the instrument located at HD-Druck (*Chapter 6.3.3*). The light beams passed through the exhaust of the air ventilation and the air conditioning of the large office building of Heidelberger-Druckmaschinen. Furthermore, it could not be excluded that an exhibition of printing machines inside the building produced significant amounts of trace gases as they were directly blown to the light beams by the air ventilation. Additionally, the municipal energy supplier has its main premises with a power plant on the neighbouring territory. Even if the main power plant was not operating during the measurements, other industrial facilities may have caused an increase in concentration. All these emission sources add up to a local concentration peak. If this plume is small in comparison to the reconstruction boxes, it cannot be resolved and leads to errors in the derived distribution.

Simulations of artefacts due to an under-sampling are shown in Figure 7-21. Errors in the distribution arise because the trace gas distribution cannot be resolved with the reconstruction grid. Reconstructed boxes show lower concentrations than the original distribution. The reconstruction procedure moves the signal to different boxes. The error is reduced for a finer reconstruction grid.

In the following, some examples for the influence of the reconstruction grid on the retrieval are given for real measurements. In general it cannot be assumed that a finer grid causes less errors just because of its higher spatial resolution as the least-squares problem also becomes more under-determined. The influence of the parametrisation was discussed in *Chapter 7.4.1*. Here the influence on measurement data is demonstrated in Figure 7-23. Significant differences in the retrieved distributions are found for different grids.

The derived distributions of  $\text{NO}_2$  and  $\text{O}_3$  are characterised by strong spatial gradients for the lower resolution (b, c). These are very unlikely as the gradients are too large and  $\text{O}_3$  does not display a spatial anti-correlation to  $\text{NO}_2$  (locations of errors are highlighted). Furthermore,  $\text{NO}_2$  peaks are observed in low traffic areas. The distributions obtained from a finer grid (a) in this case display smaller gradients with a homogeneous background concentration and small peaks on top. These distributions appear to be more likely.

Finer grids leading to under-determined least-squares problems can equally result in wrong pictures of trace gas distribution as illustrated in Figure 7-24. For the case of HCHO a peak emerges in the South-West (a) which is not present for other grids (b, c). The large gradient to

the neighbouring pixels makes it appear very unlikely as no local HCHO is present in this area. In the same example of Figure 7-24, also a strong variation of the SO<sub>2</sub> concentration can be found. The location and concentration of these SO<sub>2</sub> peaks are different for different grids.

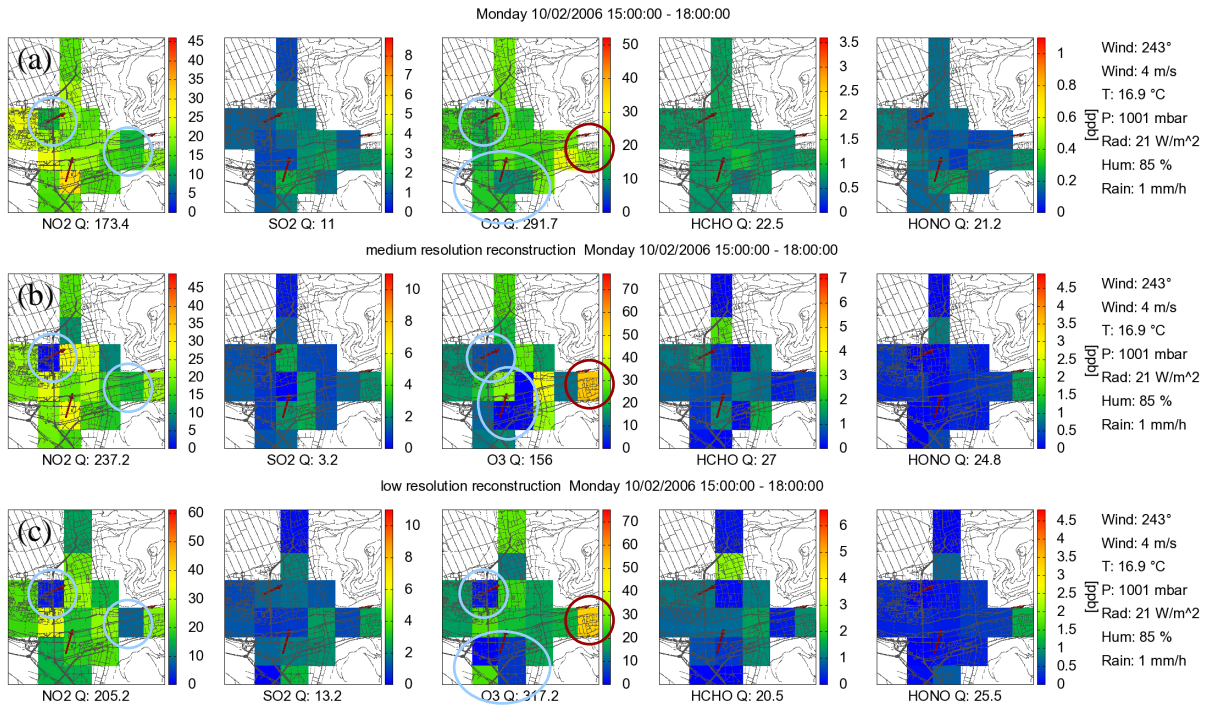


**Figure 7-23:** Example of reconstruction errors for a grid of lower spatial resolution. Shown are reconstructions of the same data with different reconstruction grids ((a) grid I, (b) grid II, (c) grid III). In this example especially the distributions for NO<sub>2</sub> and O<sub>3</sub> are wrong for the lower resolutions. Locations of errors are highlighted. Both do not show a spatial anti-correlation e.g. low concentration in North- West at the IUP. The ozone concentration is also unlikely to be zero in areas without high NO<sub>2</sub> and to be varying on few 100 m by 50 ppb. Mind the different colour scales.

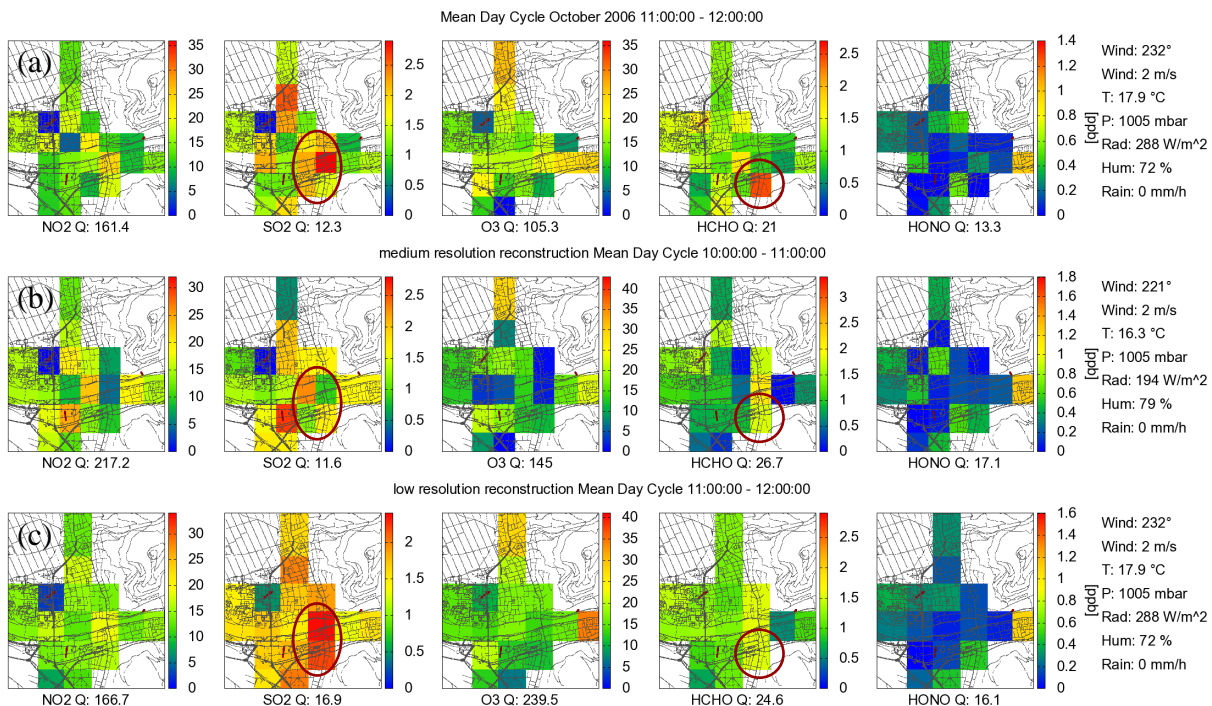


**Figure 7-24:** Example for the influence of the reconstruction grid on the retrieved concentration field (extreme case). An artefact of high HCHO concentration (South-East) can be removed by reducing the resolution of the grid. The SO<sub>2</sub> distribution strongly varies with the resolution of the grid. These discrepancies are mainly caused by how the peaks fall into the boxes. Mind the different colour scales.

7. Different choices of reconstruction grids can cause significantly different results (Table 7-5). The grid and other parameters of the reconstruction process should be optimised for the given setup as described in *Chapter 7.4.1* and *7.4.3*.

### 7.4.5 Quality Measure for Tomographic Retrieval

The most basic quality measure for any inverse problem is the data residuum according to Eq. 4.4). Its actual value also depends on the number of light paths, their absorption length and the signal. For the performed measurements the number of light paths changed and therefore the residua are not comparable for different reconstructions. To reduce the dependency of the residuum on the number of light paths and allow a better comparison between retrieved distributions for different geometries, the following quality measure  $Q$  is introduced:

$$Q = \frac{r \cdot \sqrt{n}}{\sum_{i=0}^n L_i} \quad (\text{Eq. 7.8})$$

Here  $n$  is the number of light paths used for the reconstruction,  $L_i$  the absorption path length of ray  $i$  and  $r$  the data residuum in Eq. 4.4. This quality factor representing the data residuum has the units of a concentration and depends on the absolute concentration. The derived  $Q$  factor for each derived distribution is indicated below the image like in Figure 7-23 and Figure 7-24.

## 7.5 Plotting Trace Gas Distributions

To display the 2-D concentration maps of the city, colour coded contour plots are used in the following (where the x and y-axis contain the horizontal coordinates and the concentration values are represented by different colours). The display of such graphics can be realised with various graphical software programmes, but here it was also required to plot irregular grid data (as the reconstruction grid is irregular), bilinear as well as box basis functions, to include a background image of the city and to allow automated plotting of time series of all observed trace gases. Additionally, the metrological data is included in the maps.

The software Gnuplot was automated for the plotting of time series with a Jscript program. It converts the output from the tomographic reconstruction to a Gnuplot format and writes a Gnuplot script for the plotting of the data. The colour scale of the concentration can be set manually or choosing the full scale of a defined data set. Normally the highest colour corresponds to the maximum concentration for the whole time series (typically one month). Therefore, the concentration of each individual distributions usually does not exploit the full colour scale. This was done to make reconstructed distributions of one time series directly comparable. Additionally, the meteorological data from the weather station at the IUP is included. The wind direction and speed from the weather stations at IUP, SAS and HD-Druck (*Chapter 5.8*) are indicated in the map with arrows starting at the measurement location. A Heidelberg street map is overlaid on top of the trace gas distributions to give better orientation (Figure 7-25). The concentration maps are exported as gif images, which can also be

displayed in an animation.



**Figure 7-25: Heidelberg street map of the investigation area (blue and yellow lines) which shows the same part of the city like the maps in Figure 7-12. Drawn in green the measurement geometry and in red the reconstruction grid I.**

## 8 Tomographic Measurement Results

This chapter discusses the results from tomographic and LP-DOAS observations for the trace gas concentrations of  $\text{NO}_2$ ,  $\text{SO}_2$ ,  $\text{O}_3$ , HCHO and HONO. Tomographic LP-DOAS measurements could be performed in Heidelberg from September 2005 to February 2006 and from September 2006 to March 2007. Additional measurements of one instrument placed at the IUP were performed from June 2007 to September 2007. It is one of the largest scientific LP-DOAS time series observed in an urban area like Heidelberg. Due to the amount of data and the focus of this thesis on the retrieved trace gas distributions, only few LP-DOAS results are analysed here. In the *Appendix* a part of the time series are shown, that the reader has the possibility to study the observed trace gas concentrations. All measurement data can be found in a digital form on the attached data DVD (*Chapter 8.16*). This chapter focuses on the derived trace gas distributions.

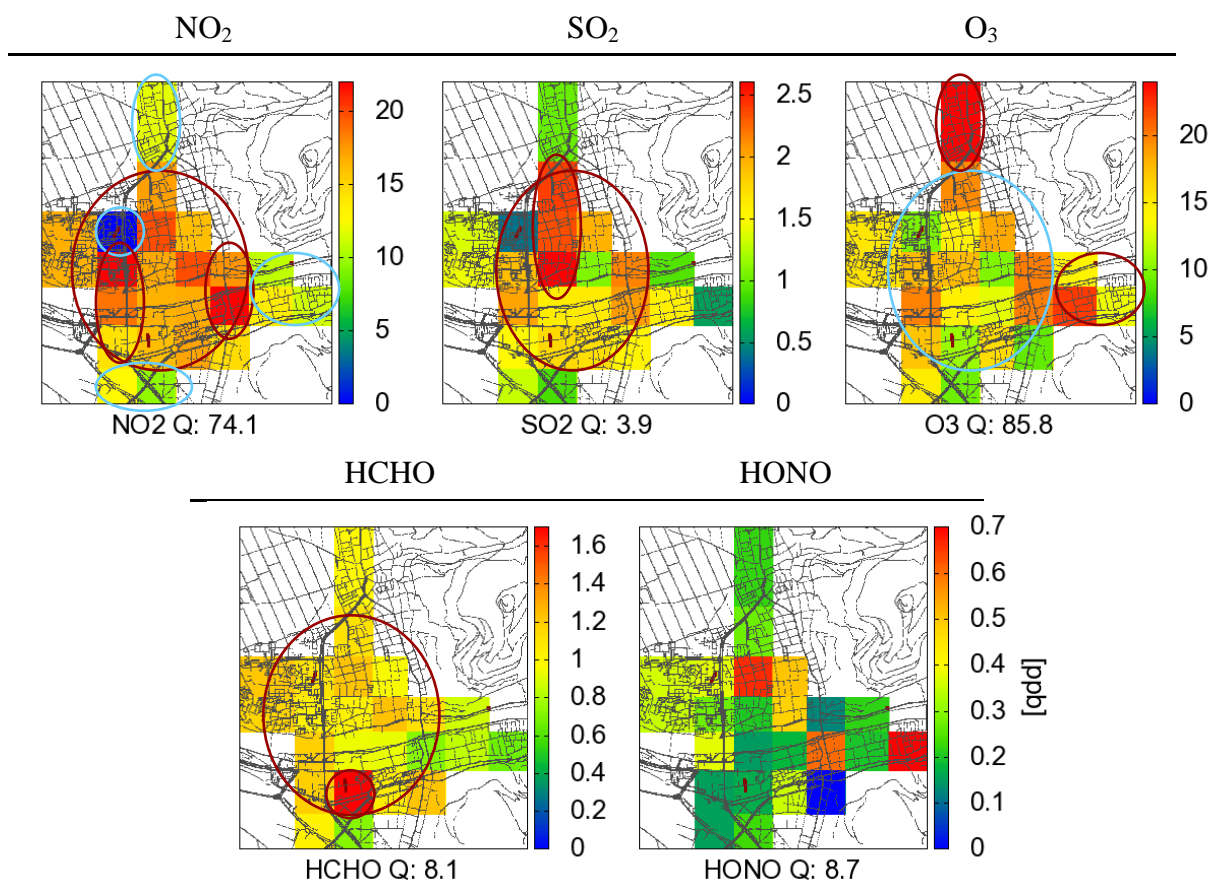


**Figure 8-1:** Trace gas distribution averaged for the whole measurement period. Main spatial features are highlighted with maxima in dark red and minima in light blue.  $\text{NO}_2$  maxima arose close to main streets. The  $\text{SO}_2$  peak in the North may be due to the RWE power plant.  $\text{O}_3$  is depleted in the city due to high  $\text{NO}_2$  levels. High levels are found at the city border. HCHO shows a broad increase with a local maximum at HD-Druck. Lower levels are found in the East in the Old Town. Averaged HONO concentrations are below the measurement accuracy. Thus the distributions are not reliable.

Tomographic reconstructions of all five trace gas distributions could be performed for periods when all three MBI LP-DOAS instruments were running. The improved analysis (*Chapter 7*) gave the possibility to retrieve trace gas distributions also for varying measurement

geometries as not all light paths were continuously measuring. Thus, continuous time series of retrieved trace gas distributions could be determined with time scales of several weeks. Some of these results are selected and presented to demonstrate the potential of the tomographic LP-DOAS technique.

The derived trace gas distributions have a maximum temporal resolution of 15 minutes. Data with lower temporal resolution is achieved by averaging over more DOAS data points before using them for the tomographic retrieval of the trace gas distributions. Depending on the investigation, different resolutions are preferable. For a short concentration event, a high temporal resolution is required. For the investigation of the change of the concentration over the day, a resolution of one to three hours is better suited. If differences over a year are of interest even daily or monthly averages are favourable. Therefore, the shown data is of different temporal resolution. If the same feature is observed in different resolutions, due to space limitations, here the lowest resolution is shown. The same time series with higher temporal resolution can be found on the data DVD (*Chapter 8.16*).

Beside the analysis of time series, influences of different parameters like wind direction and time dependencies for daily and weekly cycle are studied for trace gas distributions.

The averaged trace gas distributions of all measurements are displayed in Figure 8-1. As most measurements were performed in winter months, these distributions are mainly representative for this time of year. NO<sub>2</sub> displayed highest concentrations in the centre (highlighted in dark red) and lower in the North, East and South. Highest concentrations were located at the two main roads crossing the river Neckar (highlighted), where high traffic volume arose regularly. Lowest concentrations are in areas with less traffic in the urban area in the North, the pedestrian area in the city centre in the East and in the railway area in the South. A measurement and reconstruction artefact in combination with a local concentration minimum is responsible for the underestimated concentration at the IUP (highlighted in light blue) and will be discussed in more detail in *Chapter 8.2.4*. O<sub>3</sub> displayed, in contrast to NO<sub>2</sub>, lowest concentrations in the centre and highest concentrations at the city border in the North and East. NO<sub>x</sub> emissions in the city were responsible for the O<sub>3</sub> depletion their. SO<sub>2</sub> features higher concentrations in the centre, like NO<sub>2</sub>, but a maximum in the North close to the RWE power plant. HCHO distributions were relatively homogeneous with a maximum in the South at the HD-Druck instrument. The averaged HONO concentrations are very low and below the measurement accuracy. Thus, the derived distribution does not display a reliable distribution here. A more detailed analysis of the distributions, the sources and the correlations is given in the following sections.

The distributions of the retrieved trace gases in this chapter are always shown in one graphic to allow an easy intercomparison. In Figure 8-3 a labelled distribution is shown. The derived trace gas distributions are plotted with an overlaid street map to give better orientation (*Chapter 7.5*). Wind direction and speed observed with the three meteorological stations (*Chapter 5.8*) are indicated with brown arrows in the map. Other meteorological data is plotted next to the images. The concentration is displayed as colour coded map with the concentration scale right of each image in the dimension ppb. The quality measure (Q) indicates the retrieval accuracy (*Chapter 7.4.5*) derived from the reconstruction residuum. The value depends on the trace gas concentration. An increase at same concentrations indicates a

lower accuracy of the reconstruction.

All retrieved distributions for the whole measurement period can be found on the attached data DVD (see *Chapter 8.16*).

The analysis of these results demonstrates that tomographic LP-DOAS measurements in an urban area can provide measured trace gas distributions which can be used for monitoring and studying chemical and transport processes. Locations of concentration maxima and minima were observed for the different trace gases. Also temporally emitted or passing plumes could be observed. Therefore, these data is suited to identify local sources and study chemical processes. The derived distributions were correlated to known emission sources and the influence on the absolute concentration and spatial distribution on meteorological parameters is studied as well.

The data can also be used to compare or validate chemical transport models (*Chapter 2.6*), to improve the knowledge of transport and chemical processes and to increase the prediction accuracy.

Most chemical transport models work with a grid size of several km<sup>2</sup>. This is of course too low to determine trace gas variations on a scale of an urban area like the city of Heidelberg. The increase in spatial resolution to one km<sup>2</sup> or even to m<sup>2</sup> range is rather complicated and extensive as physical processes of local emissions, transport and mixing have to be taken into account. Thus, such high resolution models are rarely applied. For the German Federal state Baden-Württemberg and the city of Heidelberg chemical model results are produced by the Karlsruhe Institute of Technology with a resolution of 2.8 × 2.8 km<sup>2</sup><sup>9</sup>. Model calculations are performed for special events and not in general. A continuous model study for the Rhine valley including Heidelberg is performed by the Atmo-rhenA<sup>10</sup> study. The resolution of this model is 4 × 4 km<sup>2</sup>. Both models use the in-situ measurement data of the LUBW station (see Figure 6-4) as input data for the local concentration. This means, that the according model pixel, where the in-situ monitor station is located, is set to this concentration. It is obvious that models with such a coarse resolution cannot be compared to the tomographic measurement results where the whole investigation area fits almost in one model pixel. The distribution of the Karlsruher model discretisation was compared to the tomographic measurement area of this thesis. The model covers almost the whole tomographic measurement area in one pixel. Only few 100 m in the North, South and East are in neighbouring pixels. As even the central model pixel is set to the in-situ measurement data from the LUBW, the results would just give a correlation to the in-situ data. A correlation to these models is therefore useless. A finer model would be required. It is planned to reduce the resolution of the Karlsruher model to 1 × 1 km<sup>2</sup> for projects in the future<sup>9</sup>. Thus a comparison cannot be performed within this thesis.

## ***8.1 An Exemplary Day with High Trace Gas Concentrations***

In this chapter the derived one hour averaged trace gas distributions dated 01/22/2007 are used as an example to demonstrate results and possibilities of the tomographic measurement system.

---

<sup>9</sup> Personal communication Bernhard Vogel, Karlsruhe Institute of Technology, January 2008.

<sup>10</sup> [www.atmo-rhena.net](http://www.atmo-rhena.net)

01/22/2007

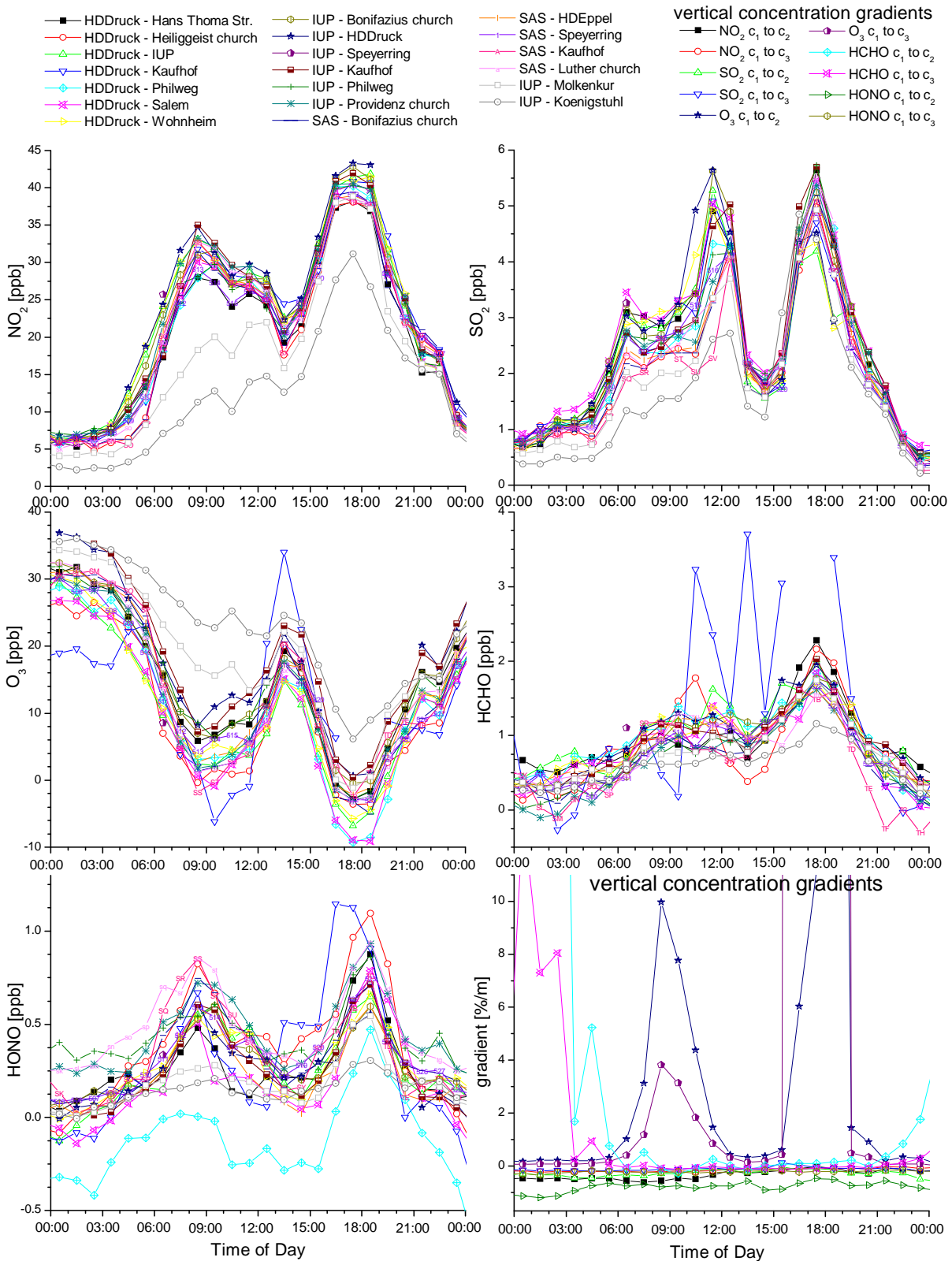


**Figure 8-2: One hour averaged concentrations of the different LP-DOAS light paths on the 01/22/2007. These data is used to derive the distributions in Figure 8-3. Very short light paths (e.g. HDDruck-Kaufhof) had larger relative errors and thus featured much more scattering of data. Light paths to higher altitudes (Molkenkur and Koenigstuhl) displayed very different concentrations and thus indicate a very strong vertical gradient. The gradient is retrieved from the determined concentration at different altitudes for box c1 (instrument height) to c3 (below Koenigstuhl) (*Chapter 7.3*). If the concentration became zero close to the ground the gradient reached very large values.**

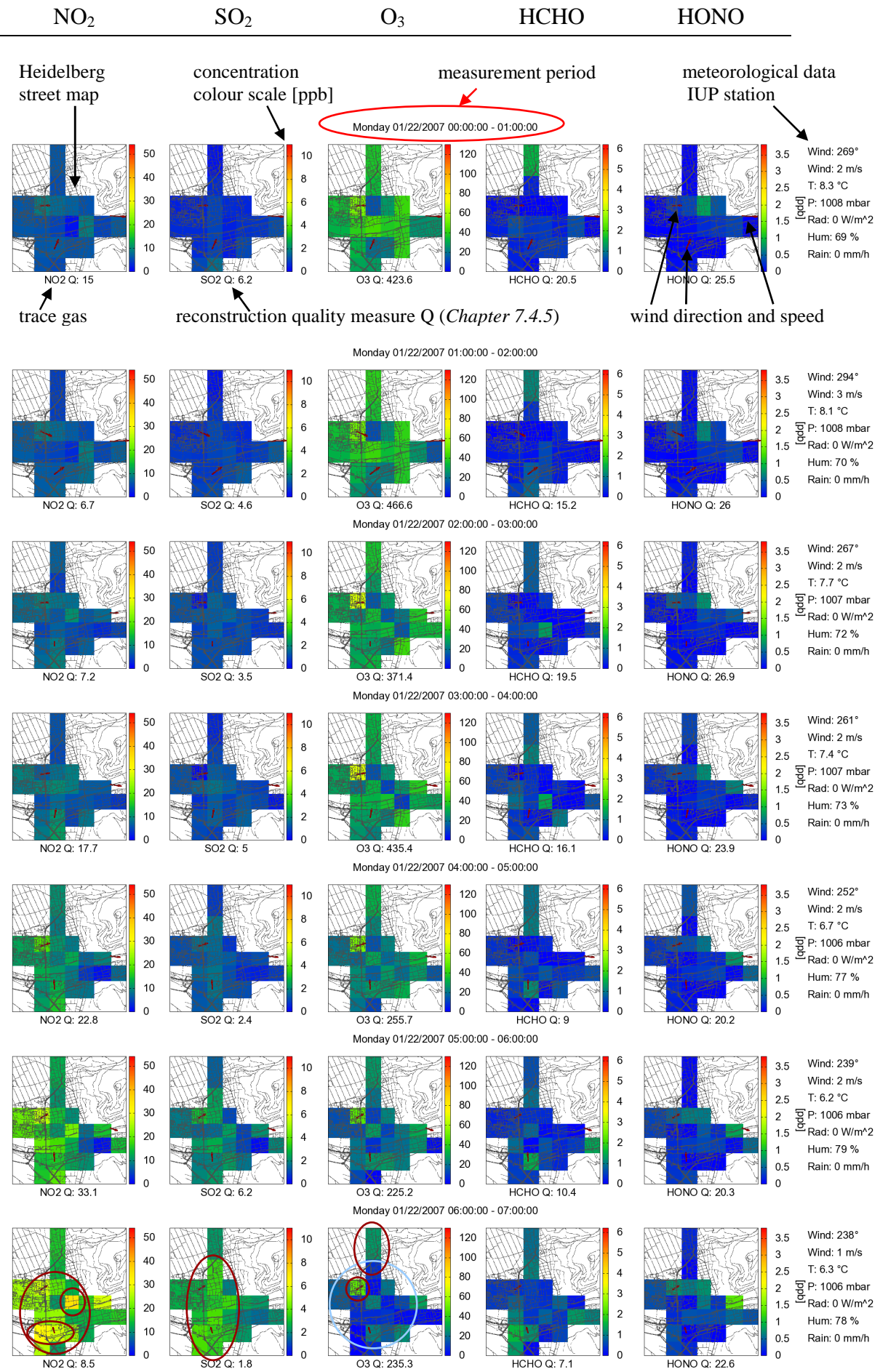
The selected working day was characterised by high variable trace gas concentrations at low wind speeds which suppressed the turbulent mixing. Additionally, relatively low temperatures (6 to 8.5 °C) and low solar radiation led to an inversion situation with stable PBL. Emitted trace gases were trapped and a strong vertical gradient arose.

The observed trace gas concentrations are displayed in Figure 8-2. Concentrations along the different light paths displayed similar diurnal cycle. Variations between the measurements were much smaller and characterised the spatial variability used for the tomographic inversion. Due to the stable PBL a much larger variability is observed for the light paths to higher altitudes (Molkenkur, Koenigstuhl). The calculated gradients (calculated according *Chapter 7.3*) displayed a very strong concentration change for NO<sub>2</sub> and HONO with decreased concentrations with altitude. O<sub>3</sub> featured a strongly increasing concentration. Due to completely depletion of O<sub>3</sub> at the ground, the values of the gradient became very large. The strong gradients may influence the derived distributions, as the light paths are not all in one perfect layer.

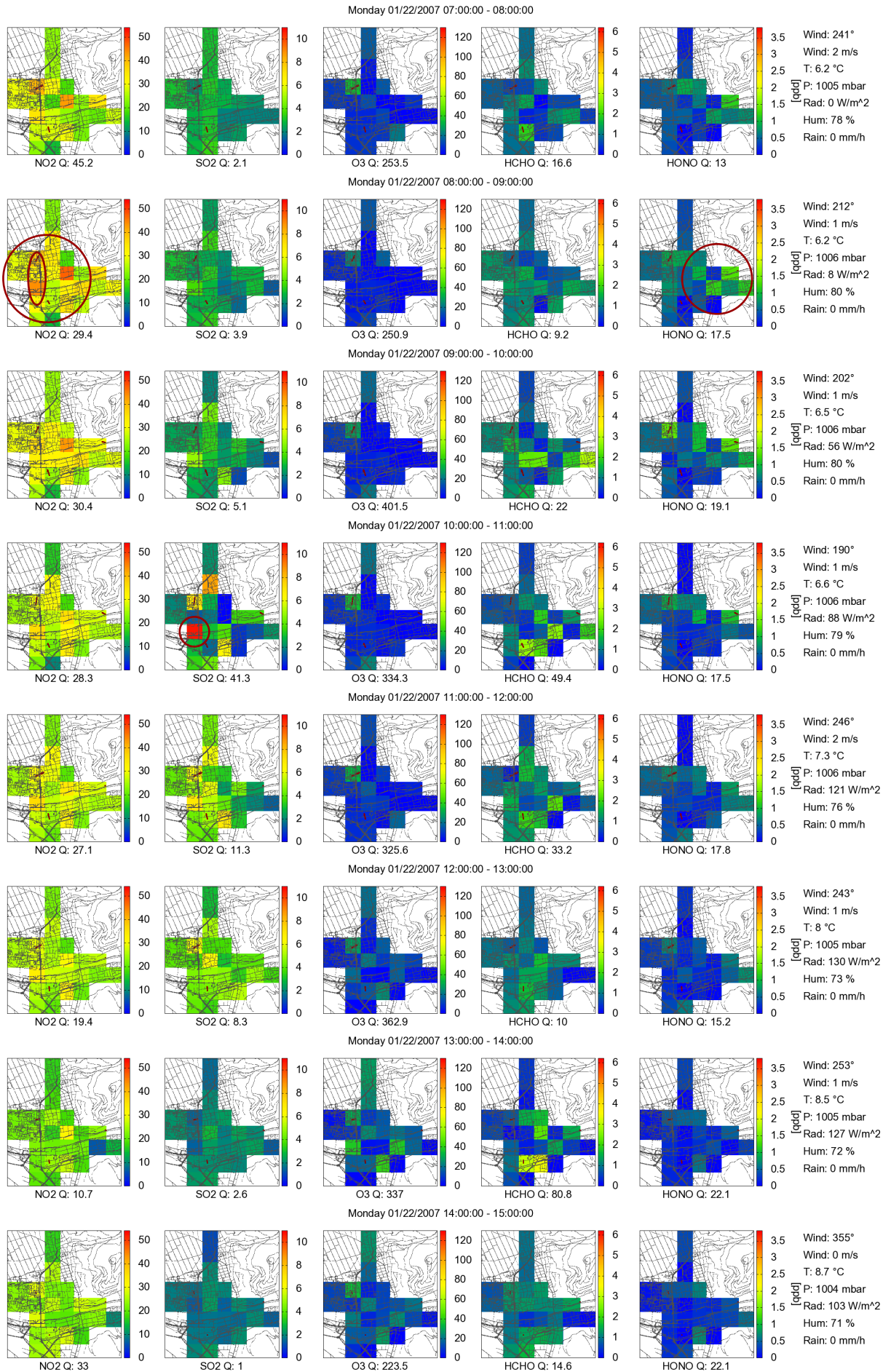
For trace gas concentrations with larger measurement error (HONO, HCHO) especially for very short light paths (e.g. HDDruck-Kaufhof) strong scattering was found, as they were characterised by very high relative errors. These runaway values may produce wrong distributions for these trace gases.

The derived trace gas distributions from the one hour averaged data are displayed in Figure 8-3. Beside a strong concentration change over the day, also the distribution changed, as the suppressed mixing localise the concentrations to the emission sources. These results are shortly discussed. Details on the chemical processes and analysis of the distributions are studied in more detail later in this chapter.

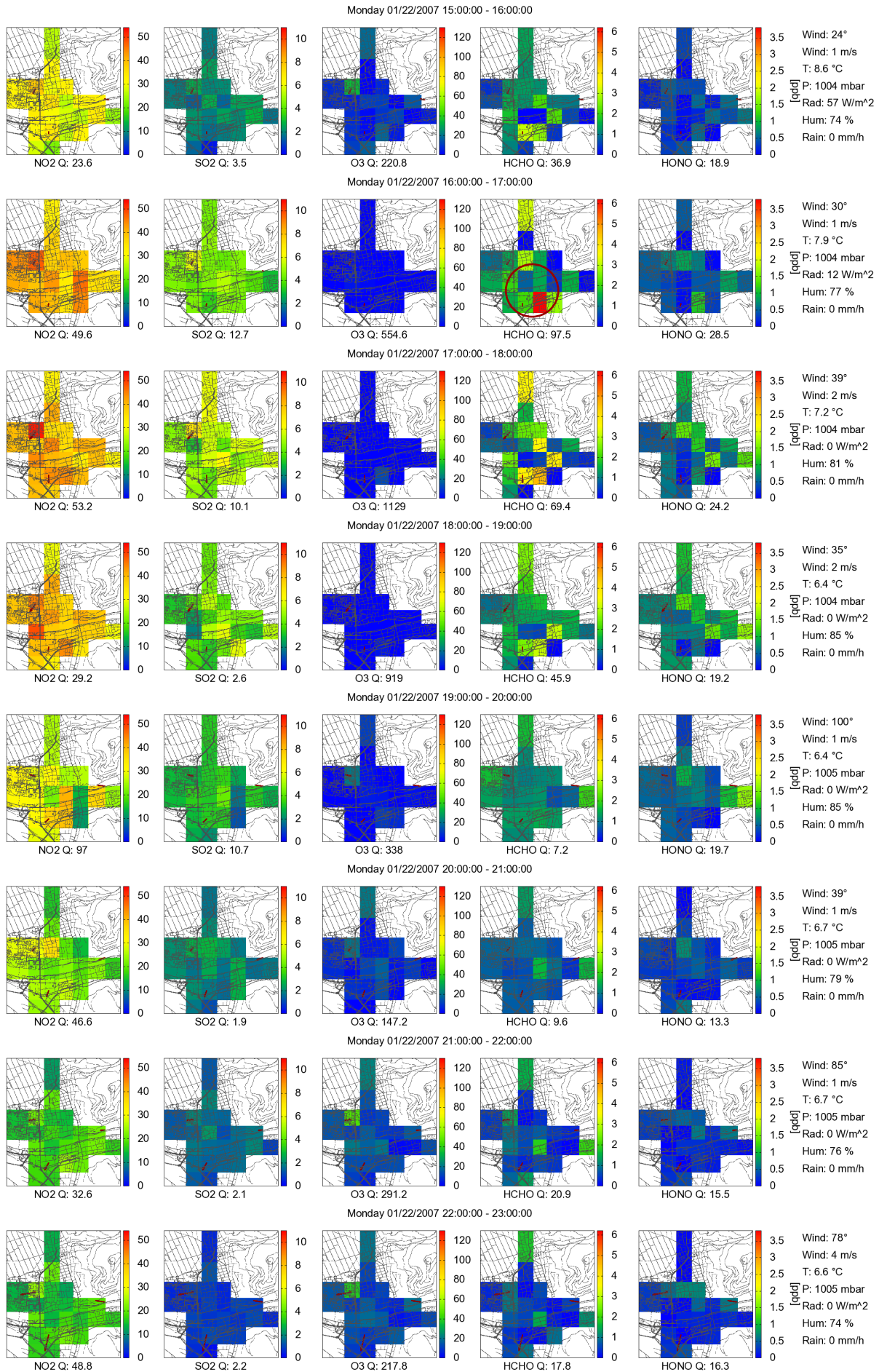
In the night trace gas concentrations of NO<sub>2</sub>, SO<sub>2</sub>, HCHO and HONO were low and ozone was at background levels of 30 ppb. In general only very small spatial variability emerged. For ozone this was most likely due to mixing with ozone rich background air. Mixing can be more effective at different locations because of topography and different height of buildings. The variability in HCHO and HONO arose most likely due to measurement and reconstruction errors as the concentrations are below the detection limit. A first increase in NO<sub>2</sub> and SO<sub>2</sub> concentration shows up after 4:00 and 5:00, respectively. The emissions may be due to small heating systems or first traffic. Increased concentrations were located in the centre and in the East and South of the investigation area, where large residential areas are located (see Figure 6-4). But also transported pollution from the highway and main streets westerly of the city may contribute to these increased levels, as the low wind was blowing from this direction. With the beginning of the rush hour after 7:00 NO<sub>2</sub>, SO<sub>2</sub>, HCHO and HONO concentrations increased quickly. A strong spatial variability can be found for NO<sub>2</sub>. Highest concentrations arose at the main streets in the West and close to the Neckar, where also many streets are located. Ozone directly decreased with increasing NO<sub>2</sub>, as combustion engines emit ~ 90 % of the NO<sub>x</sub> as NO which reacts with O<sub>3</sub> to form NO<sub>2</sub> (see *Chapter 2.1*). Ozone first decreased at the same locations where highest NO<sub>2</sub> concentrations were found and reached there values of 0 ppb. Small areas in the North, South and East outside the main traffic routes still displayed some ozone. SO<sub>2</sub> maxima were located more to the West, but without a strong variability.



# TOMOGRAPHIC MEASUREMENT RESULTS



CHAPTER 8



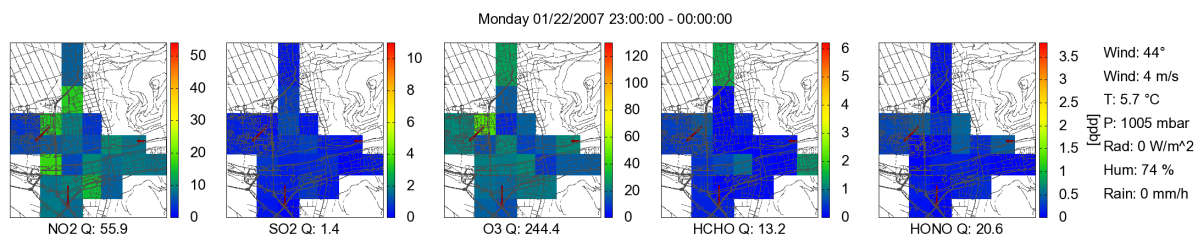


**Figure 8-3: One hour averaged time series of reconstructed trace gas distributions dated 01/22/2007. This working day was characterised by high trace gas concentrations and low wind speeds which guarantee the occurrence of strong spatial variations. Main spatial features are highlighted with maxima in dark red and minima in light blue. Q – quality measure of the reconstruction. High values indicate a larger reconstruction residuum. Increased NO<sub>2</sub> levels are found during the morning and evening rush hour at the main streets in the West and over the river Neckar. O<sub>3</sub> was spatial anti-correlated to the NO<sub>2</sub> and reached 0 ppb in the centre of the observation area. HONO concentrations increased downwind of maximum NO<sub>2</sub> levels before and after sunset. SO<sub>2</sub> increase in the morning and afternoon is shifted in time to NO<sub>2</sub> and arose from another source than traffic.**

Distributions of HCHO displayed no spatial characteristics. A small enhancement in HONO was found in the morning hours in the East and North-East. It was spatially not correlated to NO<sub>2</sub>, and thus not directly emitted by the same source. But the maximum was downwind from the highest NO<sub>2</sub> concentration in the centre and West of the investigation area indicating the later formation of HONO.

Between 8:00 and 10:00 NO<sub>2</sub> reached a maximum. O<sub>3</sub> was then completely destroyed in the entire investigation area. After 10:00 a SO<sub>2</sub> increase arose with a peak in the West located at the Neckar. The high Q value indicates that the reconstruction could not correctly reproduce the distribution. This does not mean the reconstruction is absolutely wrong or SO<sub>2</sub> was measured wrong, as the accuracy for this trace gas was relatively high. An interpretation is that the measured SO<sub>2</sub> distribution does not fit to the reconstruction what can be caused by a plume of smaller size than the reconstruction box size or a strong temporal variation. The SO<sub>2</sub> could be emitted from a ship. Between 11:00 and 13:00 SO<sub>2</sub> increased with homogeneous distribution. Due to the temporal shift in the NO<sub>2</sub> and SO<sub>2</sub> peak concentrations and the different spatial variability, SO<sub>2</sub> did not emerge from traffic emissions.

After 13:00 the NO<sub>2</sub> and SO<sub>2</sub> concentrations decreased and the ozone level could slightly recover due to photolysis of NO<sub>2</sub> to form NO and ozone. After 15:00 the NO<sub>2</sub> concentrations again increased due to the afternoon rush hour. SO<sub>2</sub> increased later and without any strong spatial variation, again indicating that its main source did not emerge from traffic. But NO<sub>2</sub> also featured lower spatial variation than in the morning. Still highest concentrations were found in the West at the largest streets, but differences are lower. O<sub>3</sub> was again completely destroyed. This of course influenced the NO<sub>2</sub> concentration, as the emitted NO can only form NO<sub>2</sub> if it is mixed with ozone rich air masses. Thus, NO<sub>2</sub> was not directly formed at the source but after the mixture with ozone and a relative homogeneous distribution established. In the same time period between 15:00 and 19:00 HCHO displayed a concentration increase and a strong spatial variation. But at the same time the Q value increased, and as the measurement error is larger for this species, it can indicate most likely combined measurement error and reconstruction artefact. They are most likely caused by the scattering of the concentrations for short light paths. Thus, this distribution is not representative. HONO levels increased after 17:00 when solar radiation reached zero and NO<sub>2</sub> levels were high. The maximum is again found downwind from the NO<sub>2</sub> maximum.

In the last hours of the day the  $\text{NO}_2$  and  $\text{SO}_2$  concentrations decreased due to lower emissions and mixing with clean air masses.  $\text{O}_3$  increased again as the clean air masses contained higher ozone concentrations. First the concentration recovered at the city border where mixture was highest. Over the night the other areas also reached almost background concentration. HCHO and HONO also decreased in the evening.

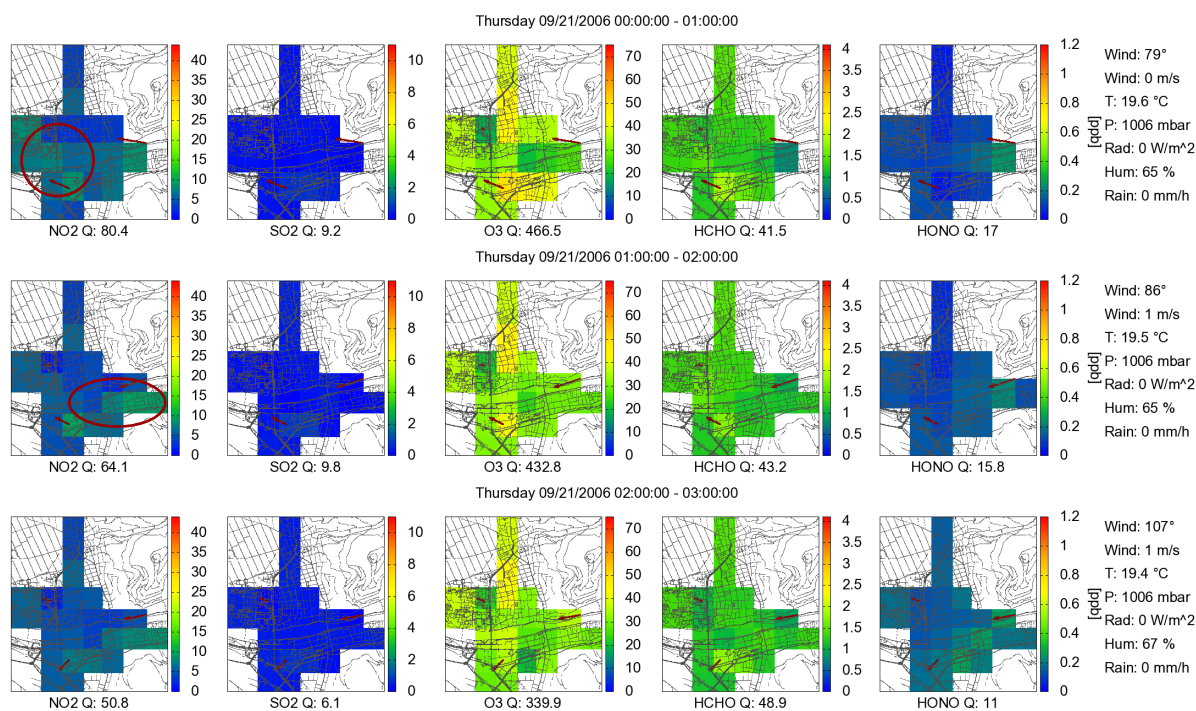
## 8.2 $\text{NO}_2$ and $\text{O}_3$ Distributions

The  $\text{NO}_2$  emissions in Heidelberg are dominated by anthropogenic sources of the transport sector and power plants. The arising concentrations are dominated by traffic volume and production of heat, cooling and electricity, but also by meteorological and chemical composition. A few examples are given below in order to demonstrate the ability of the tomographic setup for  $\text{NO}_2$  and  $\text{O}_3$  observations and the identifications of emission sources. Also the chemical daily cycle is studied.

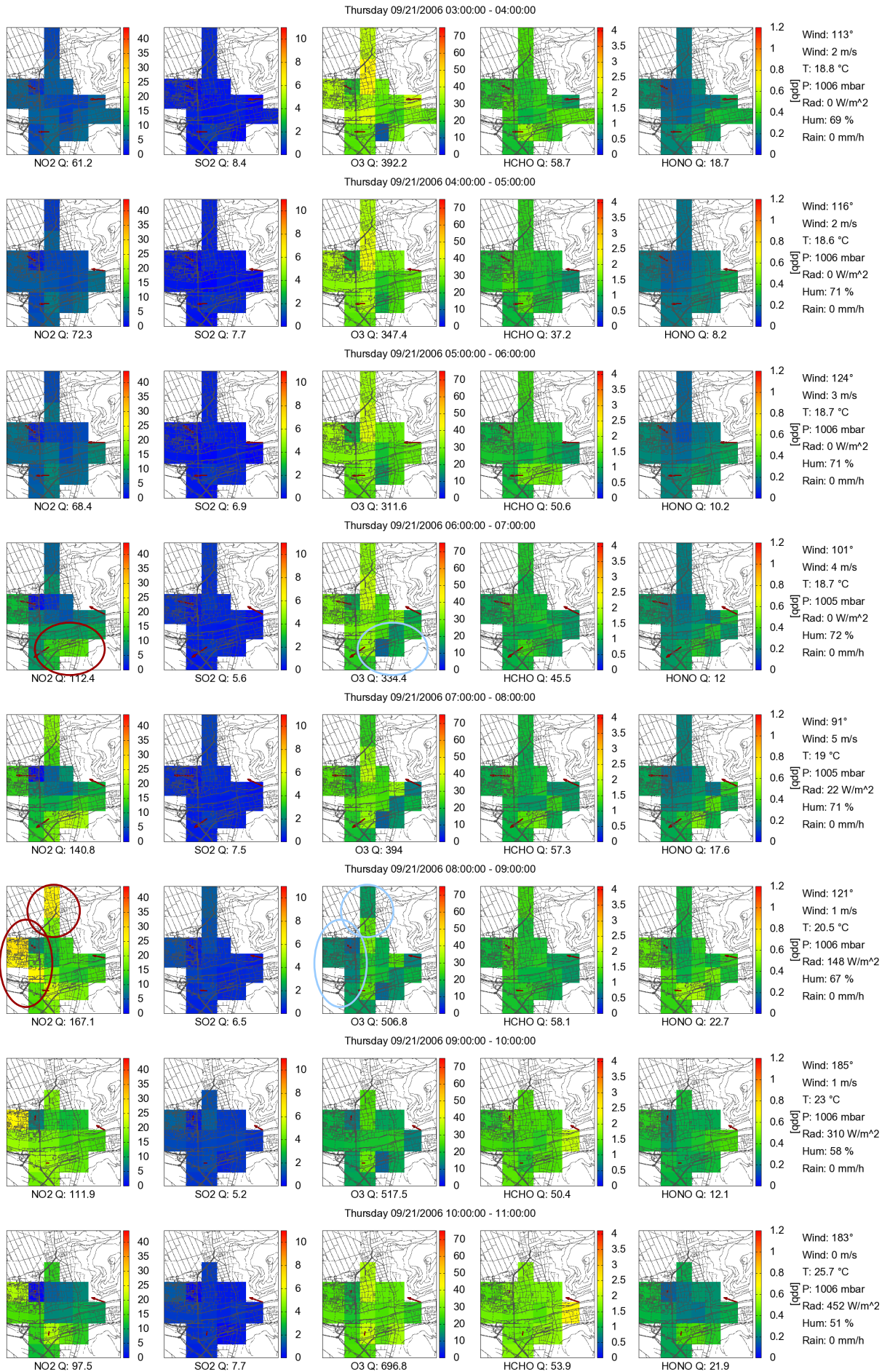
### 8.2.1 $\text{NO}_2$ Cycle at High $\text{O}_3$ Concentrations

According to *Chapter 2.1* the  $\text{NO}_2$  and  $\text{O}_3$  concentrations are linked, as NO can oxidise with  $\text{O}_3$  to  $\text{NO}_2$  and  $\text{O}_2$ . Additionally,  $\text{NO}_2$  is photolysed to NO and O which quickly form  $\text{O}_3$ . If there is sufficient  $\text{O}_3$ , the emitted NO can react to  $\text{NO}_2$ . The so-called Leighton ratio is formed (see *Chapter 2.1.2*).

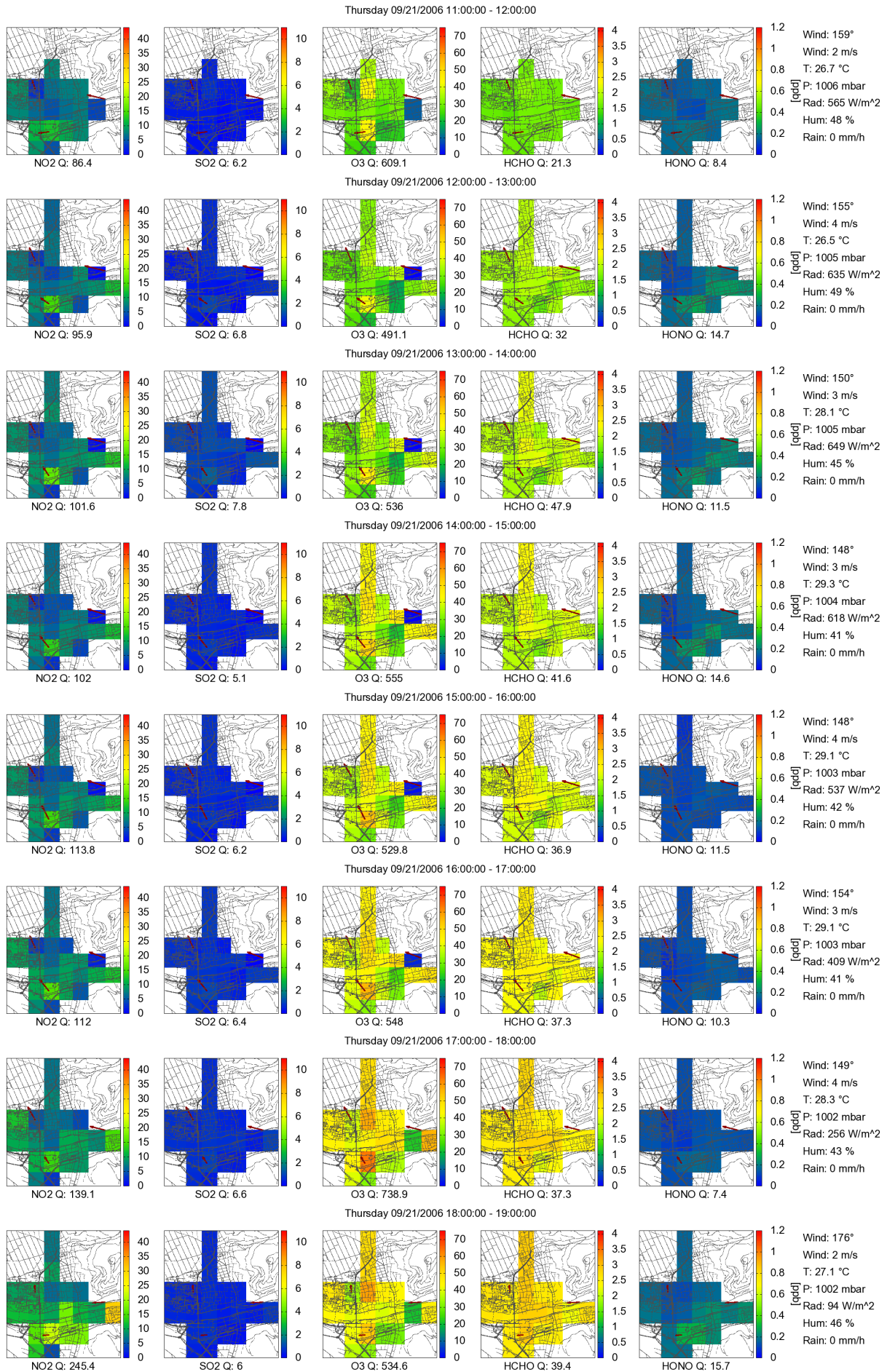
In Figure 8-4 the one hour averaged trace gas distributions of a warm and sunny September week day are plotted. During this day temperatures increased to 30 °C at noon. The wind was blowing at low wind speeds of 2 – 3 m/s from easterly or southerly directions.



# TOMOGRAPHIC MEASUREMENT RESULTS



# CHAPTER 8



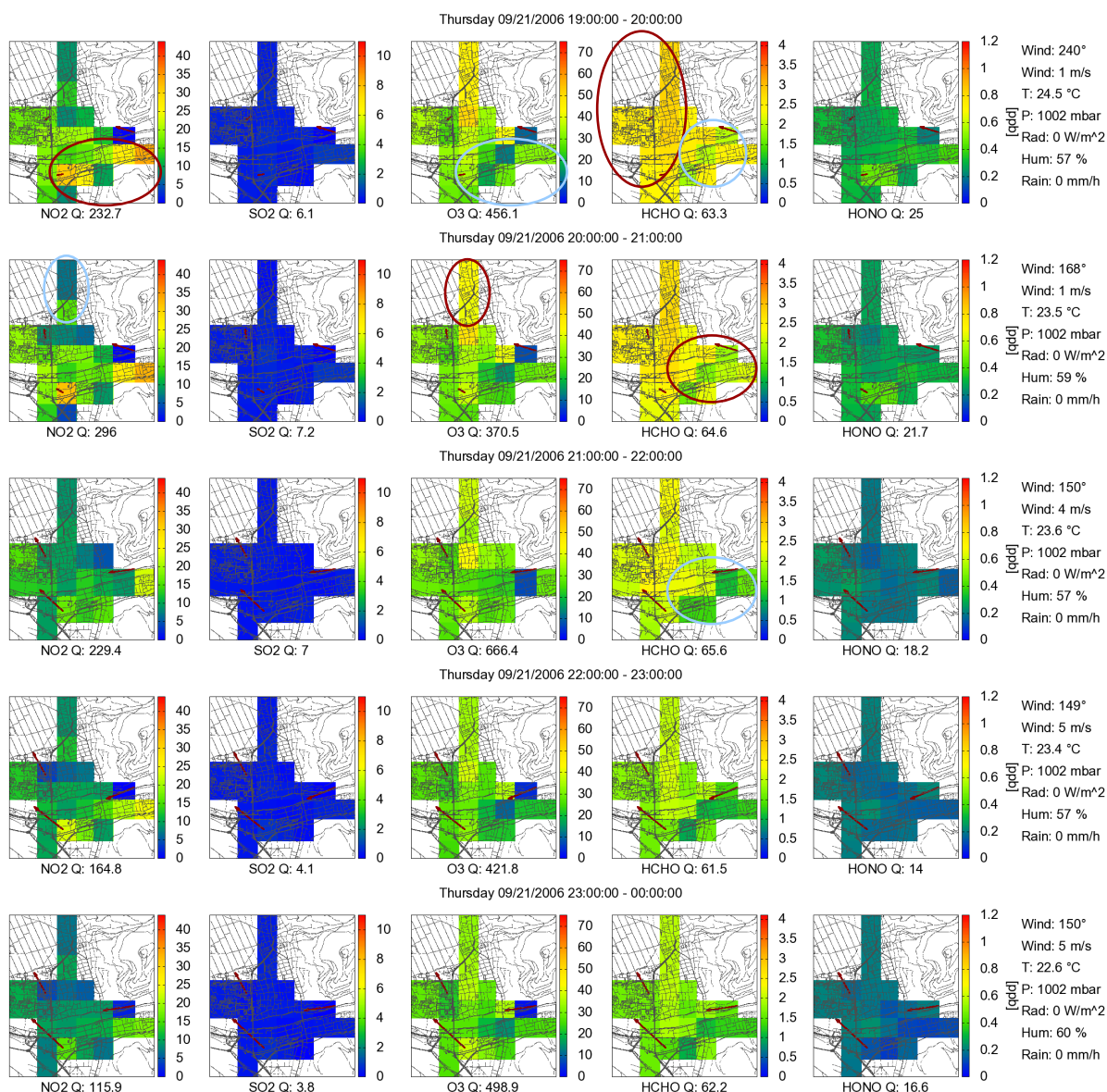


**Figure 8-4: One hour averaged time series of reconstructed trace gas distributions for a full week day at high ozone levels. A clear anti-correlation of NO<sub>2</sub> to O<sub>3</sub> can be found, with highest NO<sub>2</sub> concentrations during rush hour located at the main streets. Main spatial features are highlighted with maxima in dark red and minima in light blue. For labelling see Figure 8-3. NO<sub>2</sub> is dominated by the traffic emissions during rush hour with anti-correlated O<sub>3</sub> levels. During the day O<sub>3</sub> and HCHO increases due to photochemical production. Clean air masses brought lower levels in the South-East.**

In the night the distribution featured low NO<sub>2</sub> concentrations. Slightly increased levels can still be found until 2:00 close to the main streets in the West and along the streets from East to West at the river. Ozone levels were high in the night. From 6:00 until 11:00, strongly increased NO<sub>2</sub> levels were observed due to the morning rush hour. The concentrations first increased in the South-East and later in the West and North-West. The concentration peak was expected to be shifted to these areas due to the arising wind field from East / South. Ozone concentrations dropped with increasing NO<sub>2</sub>, with lowest values where the highest NO<sub>2</sub> concentrations arose. With increased NO<sub>2</sub> in the morning, HONO did also increase until 9:00. Later HONO concentrations dropped with increasing solar radiation due to photolysis. It is interesting that the HONO distribution featured much lower characteristics than the NO<sub>2</sub> distribution. This is discussed in more detail in *Chapter 8.3.5*.

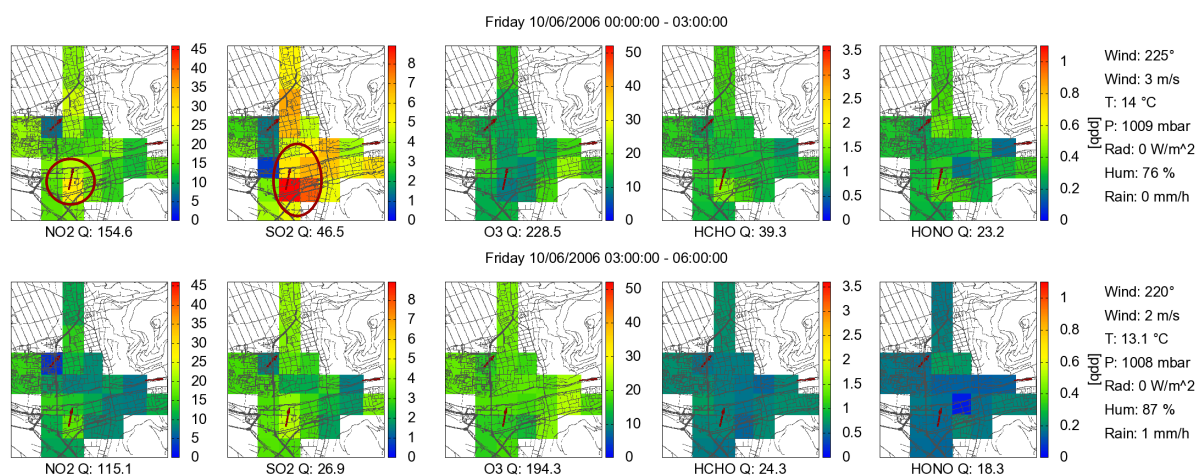
NO<sub>2</sub> concentrations reached a local minimum around noon / early afternoon with simultaneous increase in O<sub>3</sub> as the NO<sub>2</sub> was photolysed to form ozone. Ozone reached a daily maximum in the afternoon when high NO<sub>x</sub> emissions from the evening rush hour (*Chapter 8.13*) were combined with high solar radiation. There were probably sufficient OH radicals, at this warm and sunny late summer day, which could be converted to HO<sub>2</sub> from emitted VOCs. With HO<sub>2</sub> the NO could be converted to NO<sub>2</sub> without the destruction of O<sub>3</sub> (*Chapter 2.2*). This means that the photolysis of NO<sub>2</sub> increased the O<sub>3</sub> concentration during the day and photochemical smog increased.

The highest evening NO<sub>2</sub> concentration arose after 19:00. This is later than the start of the evening rush hour (see *Chapter 8.13*) as at this time the solar radiation was sufficiently high to reduce the lifetime of NO<sub>2</sub> by photolysis. With decreasing solar radiation NO<sub>2</sub> increased and ozone decreased. In the South-East, where the highest increase in NO<sub>2</sub> was observed, ozone displayed the lowest values. In the North, where NO<sub>2</sub> remained low, no reduction in ozone was seen. The data shows that HONO featured a second maximum after sunset in the late afternoon after 19:00, which again does not display a strong spatial variability like NO<sub>2</sub>.

No spatial distributed SO<sub>2</sub> was observed for this day. HCHO displayed a strong diurnal cycle with a maximum in the early afternoon at 18:00, typically for a photochemical pollutant on a sunny clear-sky day. The homogeneous distribution and missing spatial correlation to NO<sub>2</sub> indicate that the observed HCHO was not directly emitted by combustion engines, but rather created photochemically due to emissions of VOCs (*Chapter 2.4*).

## 8.2.2 NO<sub>2</sub> Cycle at Medium O<sub>3</sub> Concentrations

During the year, high ozone concentrations, as for the presented day in *Chapter 8.2.1*, typically arise at sunny and warm summer days. For most days of the year ozone levels are lower and may even be 0 ppb. At colder and less sunny days, the photochemical ozone formation of H<sub>2</sub>O, formed by VOCs from OH radicals, is low. The day shown in Figure 8-5 displayed ozone levels from 0 to 40 ppb.



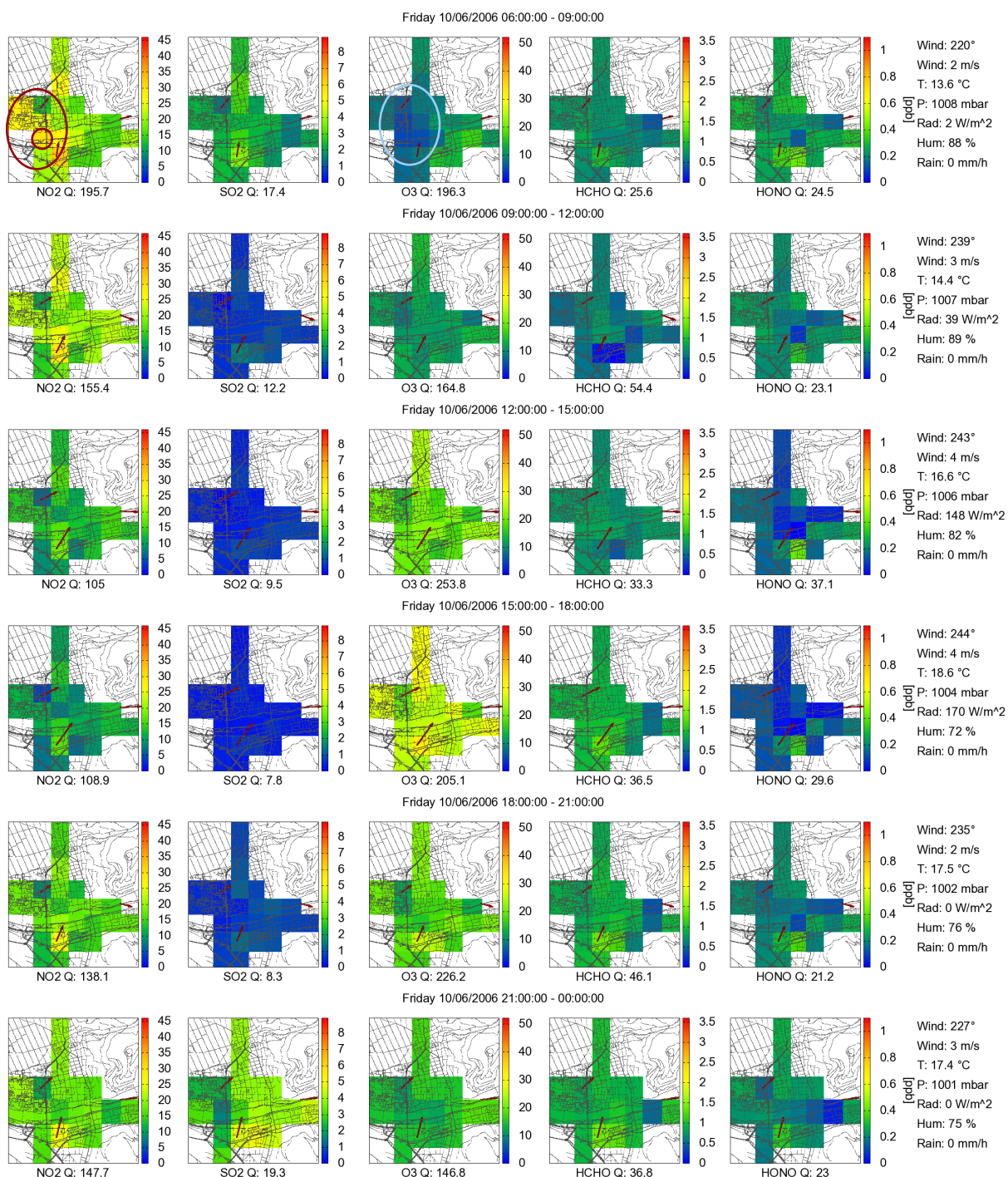


**Figure 8-5: Three hour averaged time series of reconstructed trace gas distributions for a full week day at average ozone levels. Main spatial features are highlighted with maxima in dark red and minima in light blue. For labelling see Figure 8-3. In the night high and local SO<sub>2</sub> and NO<sub>2</sub> plume was observed. During the day NO<sub>2</sub> concentrations increased due to traffic at the main streets in the West. Ozone was partly completely destroyed. SO<sub>2</sub> displayed no correlation to NO<sub>2</sub> during the day.**

With lower NO<sub>2</sub> concentrations during the night, ozone reached a small maximum. With the morning rush hour after 6:00, ozone decreased locally to 0 ppb in the West. At the same location NO<sub>2</sub> featured highest concentrations. It can be correlated to the main streets and especially to the westerly bridge over the river Neckar where most of the rush hour traffic passes (see Figure 6-4). The ozone depletion led to a limited formation of NO<sub>2</sub> from emitted NO. Ozone reached a maximum in the afternoon and NO<sub>2</sub> a smaller concentration peak in the evening. HONO concentrations were low, as NO<sub>2</sub> was lower this day. Contrary to warm

sunny days, HCHO displayed much lower concentrations with only a weak diurnal cycle. For the displayed period a strong SO<sub>2</sub> emission could be observed in the night. The concentration was disturbed by the wind to the North and North-East. A weak correlation to NO<sub>2</sub> could be found, but as the SO<sub>2</sub> did not increase with the rush hour NO<sub>2</sub>, it has a different origin. Further discussions on the SO<sub>2</sub> source are presented in *Chapter 8.5*.

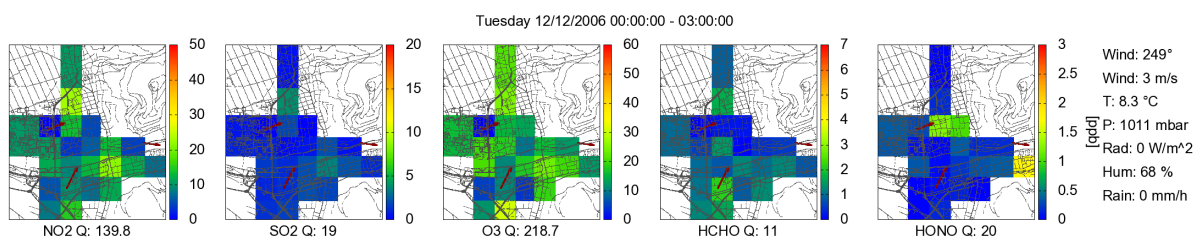
### 8.2.3 NO<sub>2</sub> Cycle at Low O<sub>3</sub> Concentrations

During winter days with low solar radiation ozone regularly reaches concentrations of 0 ppb as the emitted NO oxidises with depletion of ozone to NO<sub>2</sub>. If no ozone is left, the reaction with NO is interrupted. The diurnal cycle of the trace gases of a December day with low solar radiation is shown in Figure 8-6.

Increased ozone levels were found in the night when the air masses mixed with fresh air with a typical background ozone concentration of a few ten ppb. With the beginning of the rush hour, NO<sub>2</sub> concentrations increased and ozone concentrations dropped quickly to zero. NO<sub>2</sub> and ozone are spatially anti-correlated in the morning hours with lowest ozone concentrations close to the main streets in the West of the city (see Figure 6-4). NO<sub>2</sub> featured a much higher spatial variability than in the examples with higher ozone concentrations (*Chapter 8.2.1 and 8.2.2*). As more than 90 % of the NO<sub>x</sub> emissions are NO (see *Chapter 2.1*), the local mixture with ozone rich air masses may create NO<sub>2</sub> concentration maxima. Such local increase in mixing can arise due to the ruff surface and locally different turbulences (see *Chapter 2.7.3*). This also explains why the concentration peaks of NO<sub>2</sub> arose in the North-East downwind from the main emission sources in the West and South-West, as the emitted NO first had to mix with ozone rich air masses. The NO<sub>2</sub> peak in the North is expected to have its origin in the RWE power plant emissions, as this is providing the heating energy for the university (see *Chapter 6.1.3*). The emissions were transported with the westerly wind into the investigated area. As the emissions arose at a height of 60 and 120 m and located at the city border in the direction from where the wind was blowing, more of the emitted NO could react with ozone to NO<sub>2</sub> and thus dominate the concentration in this area.

SO<sub>2</sub> concentrations were low during this period. Slightly increased levels were found in the North where also NO<sub>2</sub> featured a maximum. It may have also its origin in the RWE power plant.

HCHO and HONO displayed only very low concentrations during the presented day. Increased HONO concentrations were found downwind in the North-East and East and later in the West. Especially in the evening hours HONO increased when solar radiation was zero and high NO<sub>2</sub> arose.



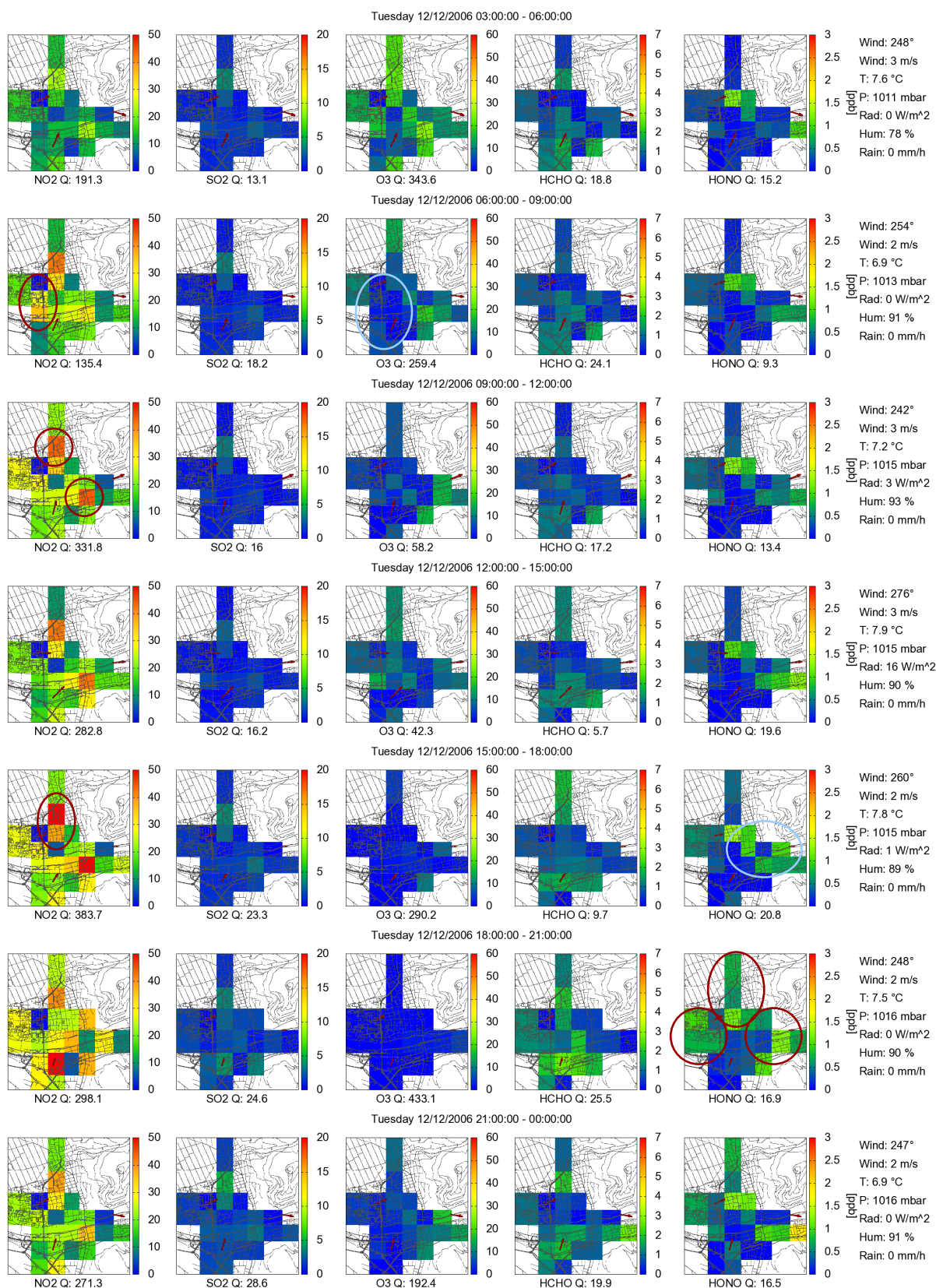


**Figure 8-6: Three hour averaged time series of reconstructed trace gas distributions for a full week day at average ozone levels. Main spatial features are highlighted with maxima in dark red and minima in light blue. For labelling see Figure 8-3. Strong spatial variations of NO<sub>2</sub> arose when O<sub>3</sub> levels were low. In the morning they quickly depleted. HONO showed increased levels downwind of the NO<sub>2</sub> maxima.**

## 8.2.4 Local NO<sub>2</sub> Concentration Minimum at IUP

In many reconstructed distributions (e.g. Figure 8-4 - Figure 8-6) a local NO<sub>2</sub> concentration minimum, which is often close to zero, was observed at the IUP instrument (location see Figure 6-4). This locally low concentration emerged mainly in the period from September 2006 to December 2006. Possible reasons are a systematic measurement error, the measurement geometry, a reconstruction artefact, a local concentration minimum due to higher local mixing of air masses or a combination of these factors. A systematic measurement error could arise from a malfunction of the instrument which may lead to a wrong concentration by few percent. This may be insignificant for absolute concentrations but leads to tomographic reconstruction errors which accumulate in one reconstruction box close to the instrument. For the given period systematic errors may be caused due to a contaminated optical filter in the spectrometer which increased stray light. Also electronic components like the detector or ADC may be responsible. After a removal of the filter and a restart of the system slightly higher concentrations were observed. The locally low concentrations disappear in the retrieved distributions from January 2007 on.

From systematic measurement errors reconstruction artefact may emerge in the distributions. As all affected light beams of a instrument crossing the box at the instrument, the concentration offset will be placed by the retrieval in this box.

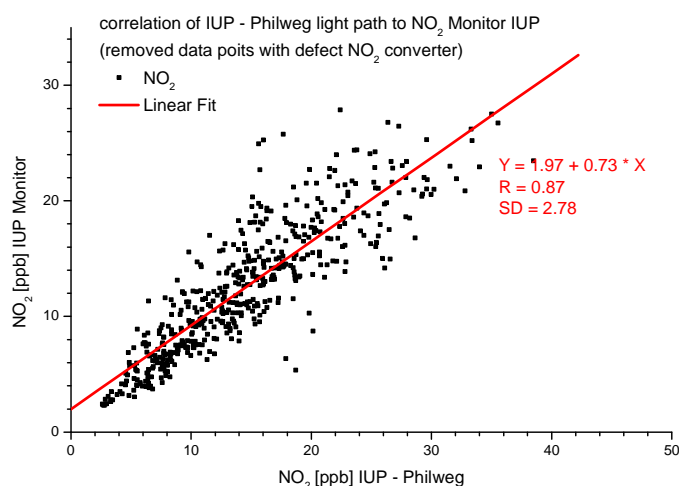


**Figure 8-7: Correlation of in-situ NO<sub>2</sub> measurements at the IUP with LP-DOAS NO<sub>2</sub> measured between IUP and Philweg for the whole measurement period (one hour averaged data). Measurement data with defect NO<sub>2</sub> blue ray converter were removed. The in-situ monitor observes much lower concentrations than the LP-DOAS light path indicating locally lower concentrations.**

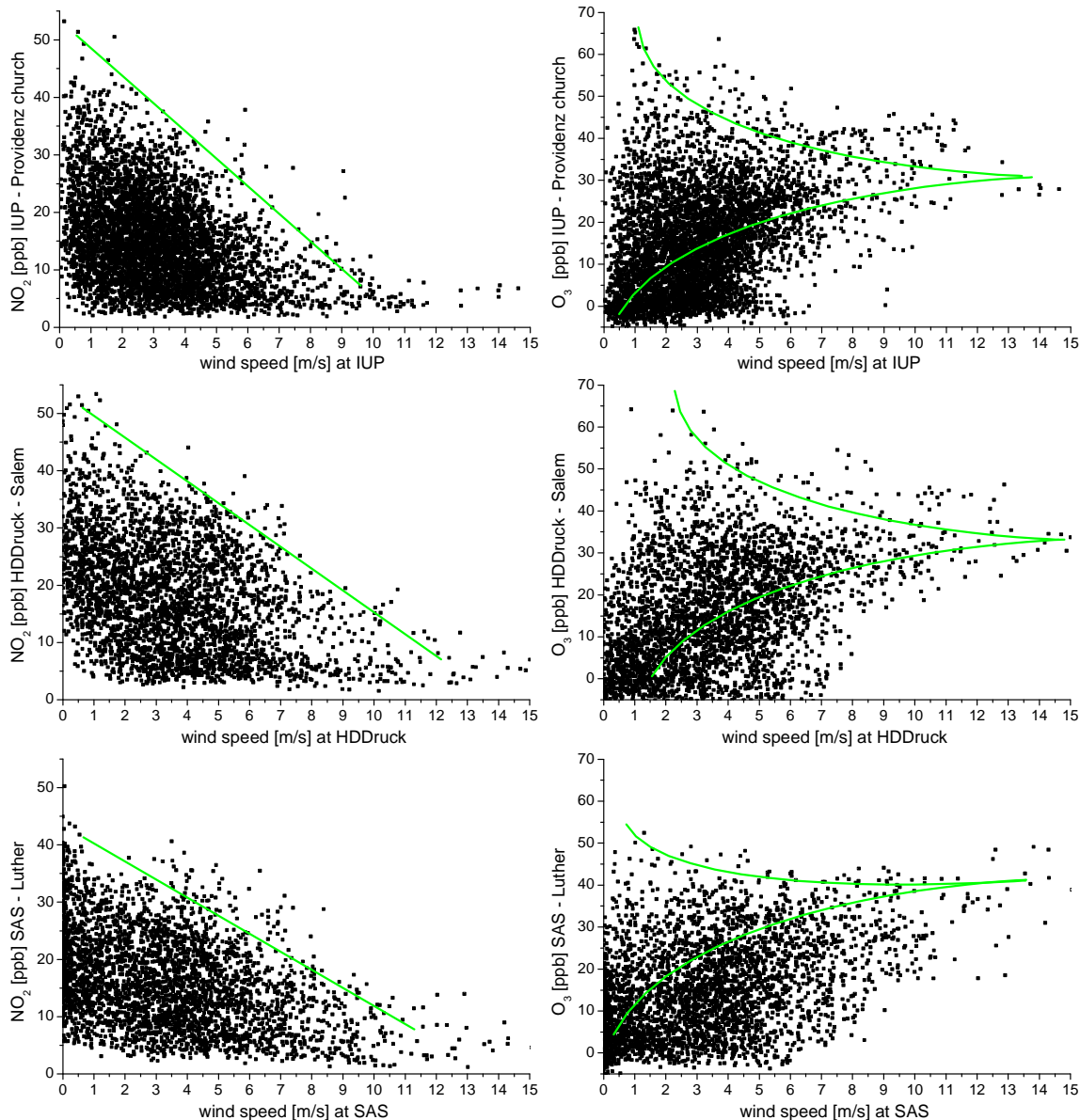
Additionally, it should be investigated if the locally lower concentration is a true distribution. By comparison of measured LP-DOAS NO<sub>2</sub> concentration versus an in-situ NO / NO<sub>2</sub> monitor at the IUP (Figure 8-7) such a local lower concentration was confirmed. A large scatter between the data sets could be found since LP-DOAS averages over a long light path and the in-situ monitor provided concentrations on site which were much more affected by local variations. Additionally, the NO<sub>2</sub> monitor data displayed a much lower concentration. Even if it could not be excluded that the lower concentration values arose due to measurement errors of the in-situ monitor, as the last calibration was performed before the measurement campaign in 2005, the data showed a local concentration minimum. The reason might be the local mixing of clean air on this sampling site. As only low emissions should appear in the

area of the university campus in the “Neuenheimer Feld”, where the IUP is located, and the high university building amplifies turbulences, this may be the reason for locally lower NO<sub>2</sub> concentrations. It should be considered that the retrieved concentration in the box may be correct for the part of the box where the light paths are crossing, but not for the rest of the box (see Figure 7-12). It is therefore an artefact of the measurement geometry. This means that the derived values are not representative for the whole reconstructed box and should not be used to interpret concentrations e.g. in comparison to neighbouring boxes or to in-situ measurement data in the same box.

### **8.2.5 Influence of High Wind Speeds on NO<sub>2</sub> and O<sub>3</sub> Concentrations and Distributions**

With increasing wind turbulences and local mixing of air masses increased (according to *Chapter 2.7*) and resulted to homogeneous trace gas distributions (Figure 8-10). Simultaneously, the trace gases were mixed with “clean” background air. This led to a decrease of NO<sub>2</sub> and also ozone levels converged to background concentrations. Figure 8-8 display the correlation of NO<sub>2</sub> and ozone with wind speed for three selected measurement light paths. Depending on the path and the wind sensor slight differences arose. In general it can be stated that the maximum NO<sub>2</sub> concentration decreased almost linear with increasing wind speed. Above 10 m/s the concentrations reached background level of 5 ppb. This indicates that the maximum emission and formation of NO<sub>2</sub> was relatively constant and the mixing due to wind defines the concentrations. The relation between ozone concentrations and wind speed depended on the pollution situation. In winter when ozone is depleted due to NO emissions, the concentration increased with wind speed to the background value of ~ 30 to 40 ppb. In summer-smog situations with increased ozone levels, the O<sub>3</sub> concentration was reduced and similar converged to the background concentration.

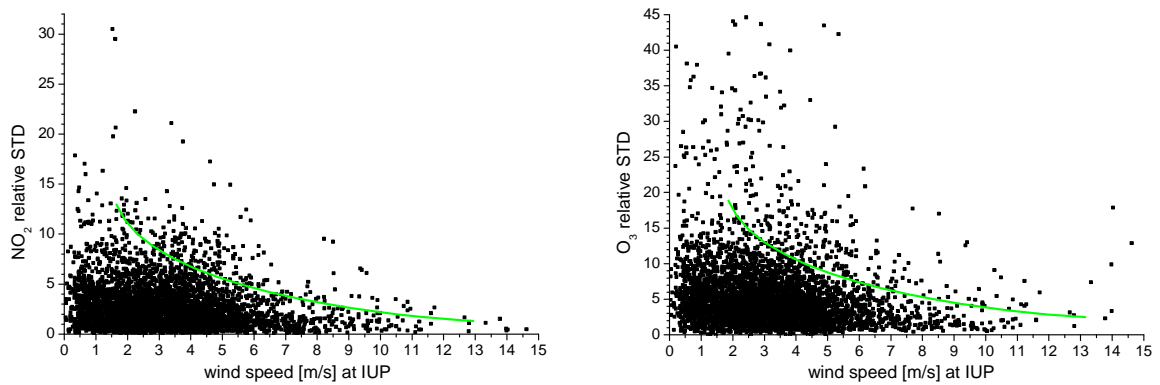
The derived distributions at high wind speeds are characterised by homogeneous distributions of trace gas concentrations. This was investigated by studying the standard deviation (STD) of the derived trace gas distribution. To remove the influence of the absolute concentration, a relative STD is used which divides the STD value by the mean concentration of the distribution. This also removes the influence of reduced concentrations at increasing wind speed and display the pure spatial variation. The relative STD strongly decreases for NO<sub>2</sub> and O<sub>3</sub> with increasing wind speed (Figure 8-9). Clearly the stronger turbulences cause the higher mixing and thus a reduction in spatial distribution. Although the highest values may arise from measurement errors and reconstruction artefacts, an exponential like decay in the relative STD can be found. At wind speeds above 6 m/s the spatial variability is mainly suppressed. The absolute values of the relative STD are similar for NO<sub>2</sub> and O<sub>3</sub> as they are chemically directly linked.



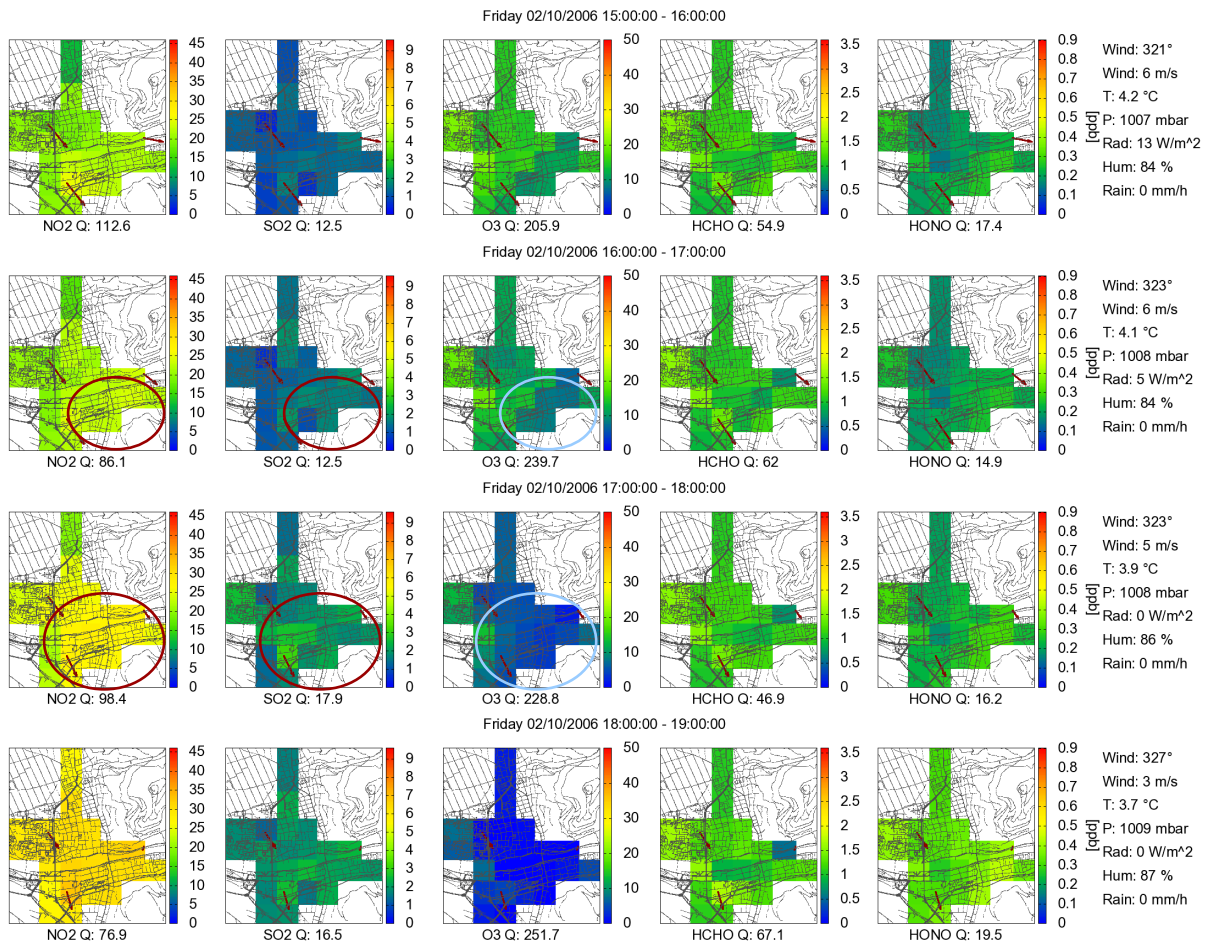
**Figure 8-8: Correlation of NO<sub>2</sub> (left column) and O<sub>3</sub> (right column) with wind speed for three selected light paths (1 hour averaged data). First row displays measurements from IUP to Providenz church versus wind speed at IUP, second row for measurements from HD-Druck to Salem versus wind speed at HD-Druck and third row for measurements from SAS to Luther church versus wind speed at SAS. Green lines indicate the trend of the concentrations versus wind speed. NO<sub>2</sub> maximum concentrations quickly decrease with increasing wind. At 10 m/s background levels are reached. For O<sub>3</sub> the change in concentration depends on the pollution situation. In both cases the concentrations converge to the background level of 30 to 40 ppb.**

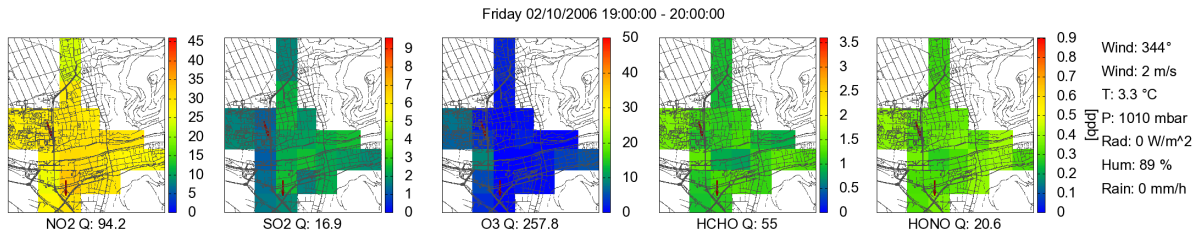
An example of a distribution at high wind speed is shown in Figure 8-10. Additionally to the observation of the homogeneous distribution, the mixing with new air masses can be studied in this example. Here the strong north-westerly winds transported the NO<sub>2</sub> and also low SO<sub>2</sub> emissions to South-East, where the highest concentrations were observed. Simultaneously, ozone depleted in the same area where NO<sub>2</sub> displayed highest concentrations. The wind brought cleaner air into the investigation area and caused low NO<sub>2</sub> as well as SO<sub>2</sub> and high O<sub>3</sub> concentration in the North-West. With decreasing wind speed after 18:00, these characteristic distributions disappeared as less clean air was brought into the investigation area. As at the same time NO<sub>2</sub> and SO<sub>2</sub> emissions increased, due to the evening rush hour, the distributions featured enhanced concentration levels in the whole investigation area. O<sub>3</sub> levels were then

depleted all over the city. The wind was still too high to observe any significant spatial variation in the distributions.



**Figure 8-9: Correlation of relative STD of derived trace gas distributions for NO<sub>2</sub> (left) and O<sub>3</sub> (right) with wind speed. The relative STD is the STD value of the distribution divided by the mean value and represents the variability of the concentration in the investigation area. The relative STD decreases significantly with increasing wind speed. Highest values may have arose from reconstruction artefacts.**

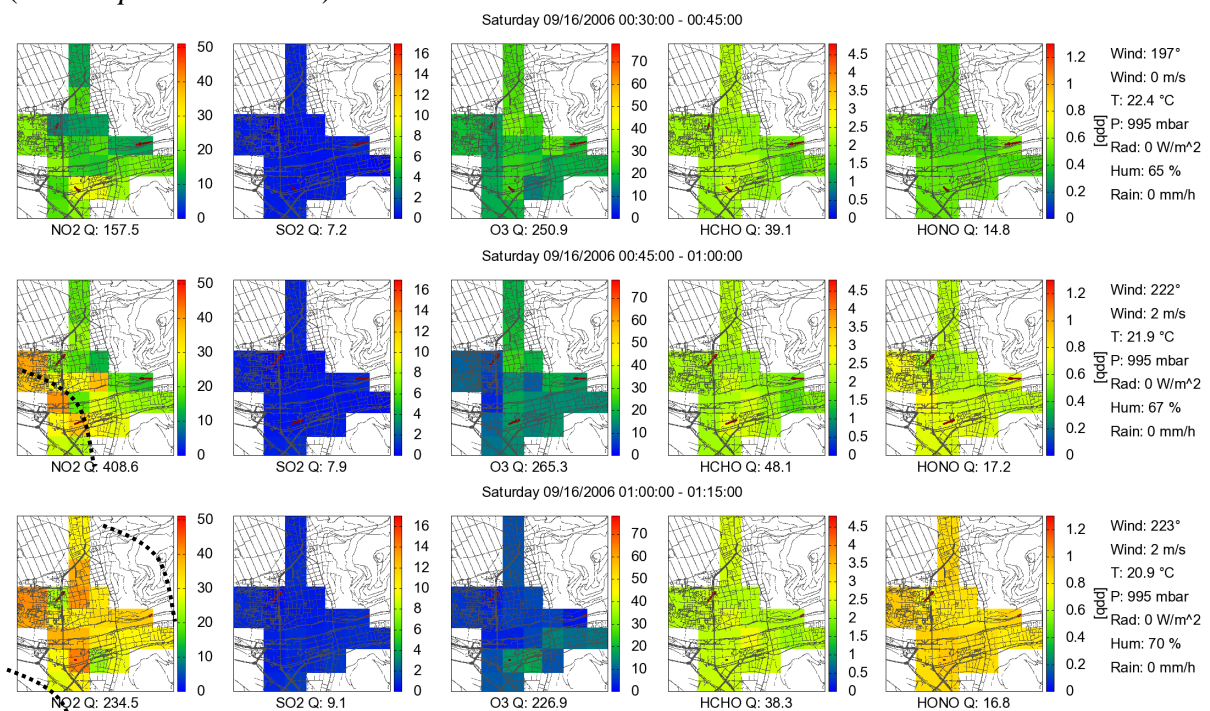




**Figure 8-10: One hour averaged time series of reconstructed trace gas distributions during strong winds. Main spatial features are highlighted with maxima in dark red and minima in light blue. For labelling see Figure 8-3. Much lower concentrations emerged as high wind increased the mixing with clean background air. Increased concentrations are found downwind in the South-East.**

### 8.2.6 Passing NO<sub>2</sub> Plumes

The investigations of NO<sub>2</sub> plumes transported to Heidelberg are difficult, as in most cases they cannot be separated from the locally arising emission. Additionally, at typical wind speeds above 2 m/s a passing plume cannot sufficiently be observed with a time resolution of 15 minutes in the investigation area of 4 × 4 km. The event in Figure 8-11 was characterised by low south-westerly winds with about 1 m/s. The plume arrived in Heidelberg at night when local NO<sub>2</sub> emission sources only emit very low values and no interference arose. The plume was clearly observed with the retrieved distributions. It passed the observation area within one hour on a distance of about 3.5 km. Through the measured wind speed the plume size was calculated to about 1 km. Ozone decreased simultaneously with the NO<sub>2</sub> plume while HCHO and HONO increased. The O<sub>3</sub> depletion to 0 ppb indicates that the plume was likely recently emitted and still not mixed up with ozone rich background air. The assumption of a recent emitted plume correlates with the small plume size and the high variability of the NO<sub>2</sub> distribution. The HCHO and HONO distributions displayed much lower spatial variability and also their concentration did not decrease directly after the plume passed the measurement site, but rather remained constant for a while. This supports that they are formed indirectly (see *Chapter 8.3 and 8.4*).



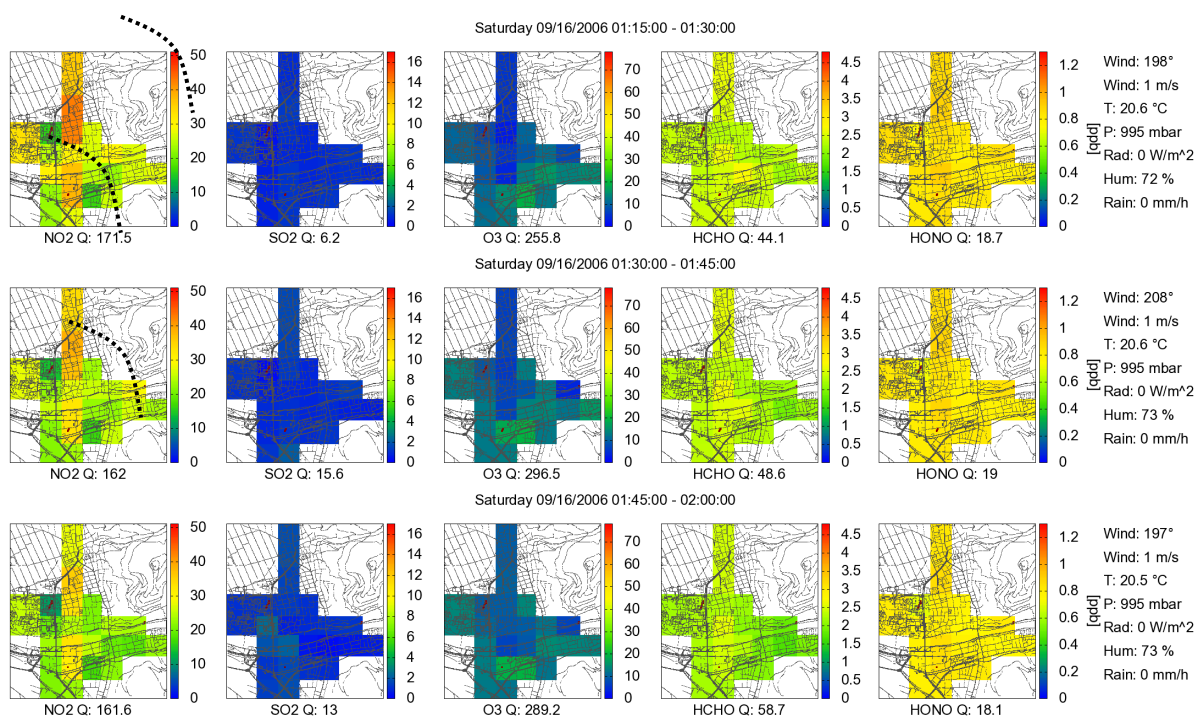


**Figure 8-11: 15 minutes averaged time series of reconstructed trace gas distributions during a passing NO<sub>2</sub> plume which is clearly observed in the distributions. The plume had approximately a size of 1 km. The front and end of the plume is highlighted. For labelling see Figure 8-3.**

### 8.3 Nitrous Acid (HONO) Distributions

Nitrous acid plays a major role in atmospheric chemistry especially in polluted areas. It is only rarely studied and the reaction mechanisms are still not well known (see *Chapter 2.3*). Therefore the observation of spatial HONO distributions in correlation to the other trace gases can help to understand the chemical processes involved. As HONO can be emitted directly or formed by heterogeneous reaction from NO<sub>2</sub>, different spatial distributions arise for these two sources.

The retrieval of spatial HONO distributions for the measurements in Heidelberg is difficult, as the concentrations are low and most of the time below the detection limit. A typical measurement error for typical concentrations of 1 ppb is still of the order of 50 %. To reduce the influence of reconstruction artefacts, only 3 iterations for the tomographic reconstruction were applied resulting in a reconstruction error of about 50 % (see Table 7-5). Still the derived distributions contain sufficient information to study the chemical processes.

The previous distributions in Figure 8-4 to Figure 8-6 and Figure 8-10 to Figure 8-11 display the occurrence of HONO at darkness if high NO<sub>2</sub> levels arose, but no spatial correlation to NO<sub>2</sub> concentration maxima were observed. High HONO concentrations were preliminarily found at stable stratified PBL with ineffective mixing when it could accumulate close to the ground. The correlation to NO<sub>2</sub> and properties of the HONO distribution are discussed. It can be shown that HONO is formed by heterogeneous reactions and not directly emitted by the same source where NO<sub>2</sub> arose.

### 8.3.1 Influence of Solar Radiation, Temperature and Wind Speed

HONO is photolysed by wavelengths below 390 nm. After sunrise the concentrations are reduced below the detection limit and only increase again after sunset (Figure 8-12, left). Also a weak correlation to temperature is observed with maximum HONO concentrations around 5 °C. Low temperatures support the formation of a stable PBL with lower vertical mixing and thus the accumulation of HONO. At even lower temperatures the heterogeneous formation on wet surfaces is limited due to absence of liquid water.

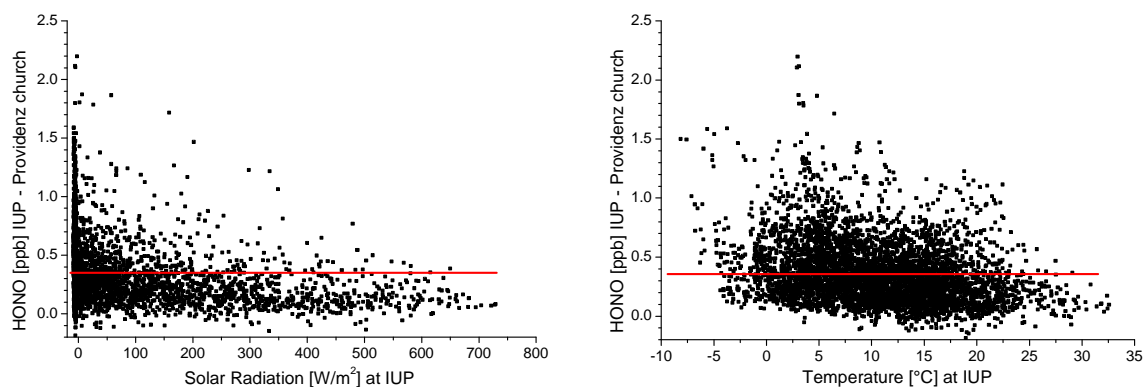


**Figure 8-12:** Correlation of HONO to solar radiation (left) and temperature (right) measured along one selected light path from IUP to Providenz church. Red line indicates average detection limit. HONO is quickly reduced by the occurrence of sunlight due to photolysis. Thus high concentrations are found in darkness or at very low solar radiation. Temperature plays a role for the stability of the PBL. Stable conditions can typically be found at low temperatures and led to increasing HONO concentrations.

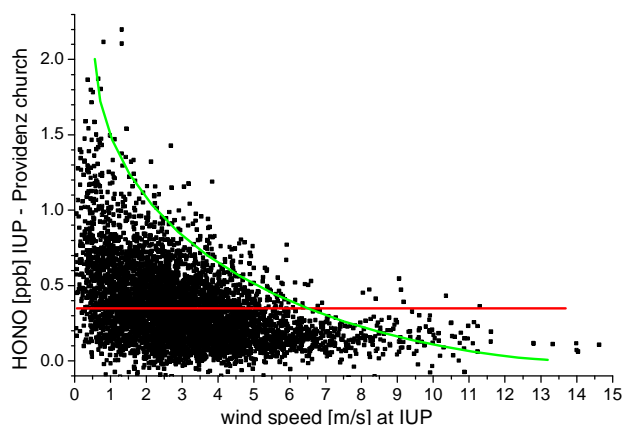


**Figure 8-13:** Correlation of HONO with wind speed (one hour averaged data) for measurements from IUP to Providenz church versus wind speed at IUP. Red line indicates average detection limit. Green line shows the strong decrease of HONO concentration with wind speed which is much stronger than for NO<sub>2</sub>.

The requirement of stable PBL conditions is supported by the correlation of HONO concentrations to wind speed (Figure 8-13). With strong wind turbulent mixing increased and stable PBL conditions are disturbed. Thus, not only the concentrations decrease due to the mixture with clean air masses like for NO<sub>2</sub> levels, but also due to the lower formation rates. A much stronger dependency for the correlation between wind speed and concentrations were observed (Figure 8-8) than for NO<sub>2</sub> and O<sub>3</sub> (*Chapter 8.2.5*) and thus indicating that this reduction is not a pure mixing effect of air masses. It can be speculated if the heterogeneous

reactions require stable PBL and a low mixing to be most effective.

### 8.3.2 HONO to NO<sub>2</sub> Correlation

The HONO concentration is linked to NO<sub>2</sub> concentration for the direct emission and for the heterogeneous formation on wet surfaces. In the first case, any direct emission of HONO from a combustion engine will also emit NO<sub>x</sub> and thus increase the NO<sub>2</sub> concentration close to the source as reaction with O<sub>3</sub> is fast (*Chapter 2.1.2*). The spatial distributions of HONO should thus be similar to these of NO<sub>2</sub>. In the second case when HONO is formed by heterogeneous reactions on surfaces the emitted NO<sub>2</sub> is first mixed up and diluted. HONO is formed only after the NO<sub>2</sub> get in contact with potential reaction surfaces and thus typically downwind of the emission sources. Thus, the spatial characteristic is lower or at least different to that of NO<sub>2</sub> as the HONO formation arise after the mixing.

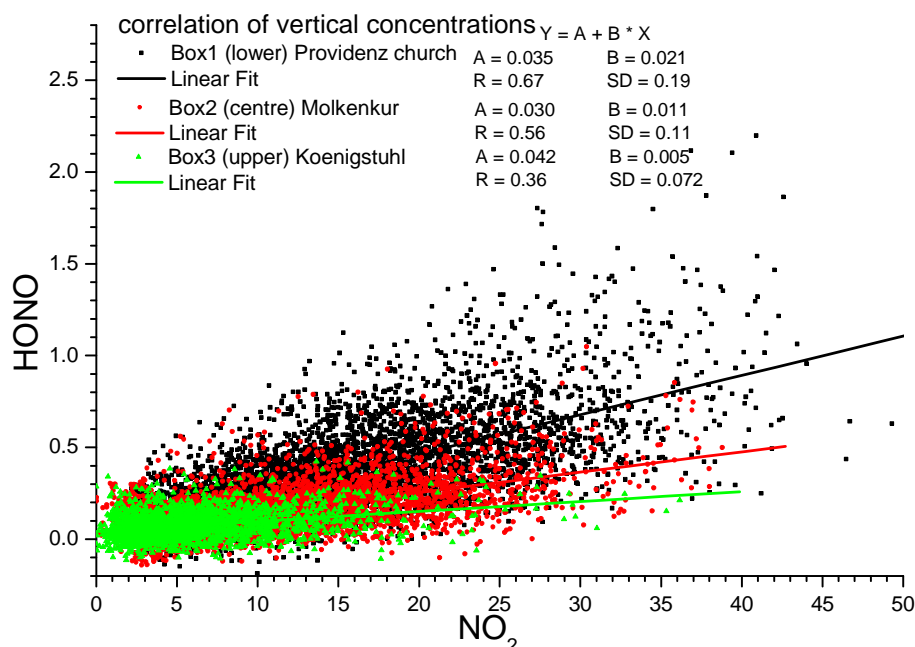


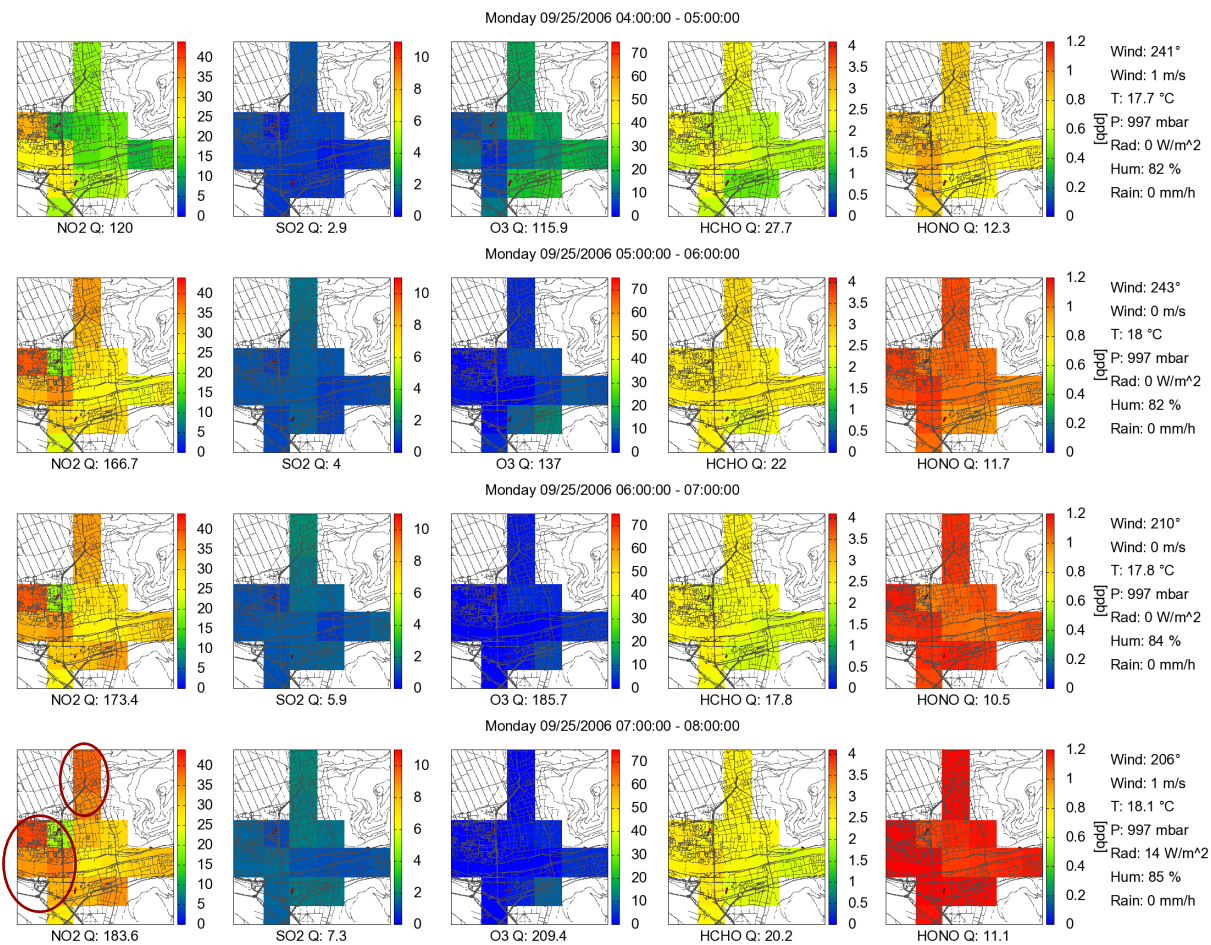
**Figure 8-14:** Correlation between HONO and NO<sub>2</sub> for the different heights derived from the profile retrieval (see *Chapter 7.3*). Linear fits indicate the correlation factor. A higher correlation is observed close to the ground indicating a stronger vertical gradient for HONO. This suggests the HONO formation close to the ground.

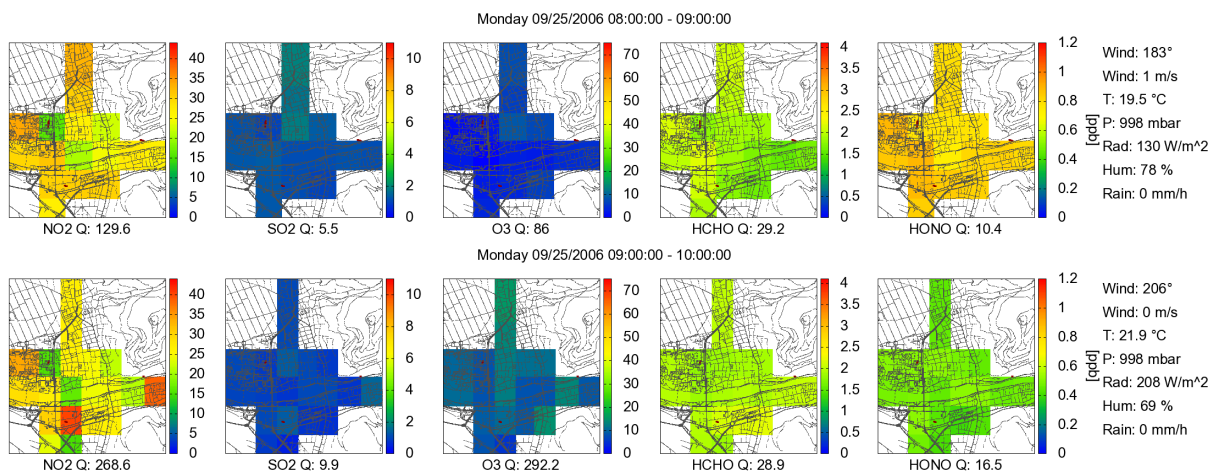
The correlation between measured HONO and NO<sub>2</sub> concentrations for different heights is illustrated in Figure 8-14. The vertical concentration profile is derived from LP-DOAS measurement light paths at different heights (see *Chapter 7.3*). The correlation displays a large scatter as also other factors like solar radiation play a major role for the observed HONO concentration. A clear correlation was observed for the box closest to the ground. With increasing height the correlation quickly decreases what implies a steeper gradient for HONO than for NO<sub>2</sub>. This approves the formation at the ground by heterogeneous reactions and not the emission like NO<sub>2</sub>. The results agree well with similar measurements from Veitel [2002], who also found a steeper gradient for HONO and preferable high HONO concentrations in

darkness at stable atmospheric conditions with high NO<sub>2</sub> levels. A higher correlation of NO<sub>2</sub> and HONO is especially determined for situations with a stable stratified PBL featuring ineffective vertical mixing.

### 8.3.3 HONO Distributions at Sunrise

With increasing emission of NO<sub>2</sub> in the morning before sunrise, also HONO concentrations increased. The emission in the night arose due to the early morning traffic, but also from emissions from power plants and small heating systems. An example of such a cycle is presented in Figure 8-15. With increasing NO<sub>2</sub> concentration also HONO increased. Highest NO<sub>2</sub> concentrations were located in the West and North, where also HONO featured a slight local maximum, but in general it shows a much lower spatial distribution. The missing spatial correlation to NO<sub>2</sub> indicates that both trace gases were not emitted or directly formed at the same source. This supports the theory of heterogeneous formation of HONO on surfaces which occurs slowly after NO<sub>2</sub> is mixed in the air. Mainly the overall NO<sub>2</sub> concentrations are responsible for the HONO formation and local concentration peaks are of minor importance. The other observed trace gases display no correlation to the observed HONO levels. With sunrise at 7:15, the maximum HONO concentration is observed, as simultaneously also NO<sub>2</sub> features highest concentrations in darkness. With increasing solar radiation HONO is reduced and characterised by a very homogeneous distribution.

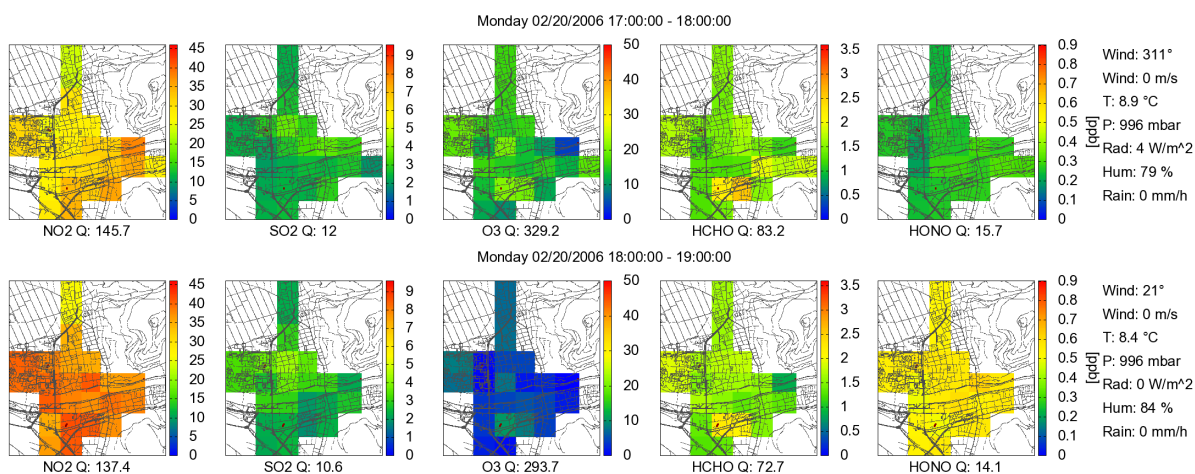




**Figure 8-15: One hour averaged time series of reconstructed trace gas distributions in the morning with correlated HONO to NO<sub>2</sub> concentrations before sunrise. NO<sub>2</sub> and HONO show up different distributions whereby the latter has no spatial characteristic. After sunrise HONO is photolysed and concentrations decrease. Main spatial features are highlighted with maxima in dark red. For labelling see Figure 8-3.**

### 8.3.4 HONO Distributions at Sunset

Increased HONO levels are observed after sunset as reduced solar radiation led to a reduction of HONO photolysis. An example is given in (Figure 8-16) where sunset was at 17:05. HONO concentrations did not increase immediately indicating a slower formation process and exclude the direct emission of HONO by the same source where NO<sub>2</sub> is emitted and quickly formed by the reaction of NO with ozone. This example even shows that the NO<sub>2</sub> maximum and the HONO maximum are shifted by about one hour, as the maxima can be found between 18:00 to 19:00 and 19:00 to 20:00, respectively. A similar shift of about one hour can be observed from the mean daily cycle (see *Chapter 8.7*). Again different spatial variations between NO<sub>2</sub> and HONO are clearly visible. Where the NO<sub>2</sub> maximum was located in the centre with lower concentrations in the North and South-West, HONO displayed a much smaller spatial variability. The small fluctuations arose mainly due to measurement errors.



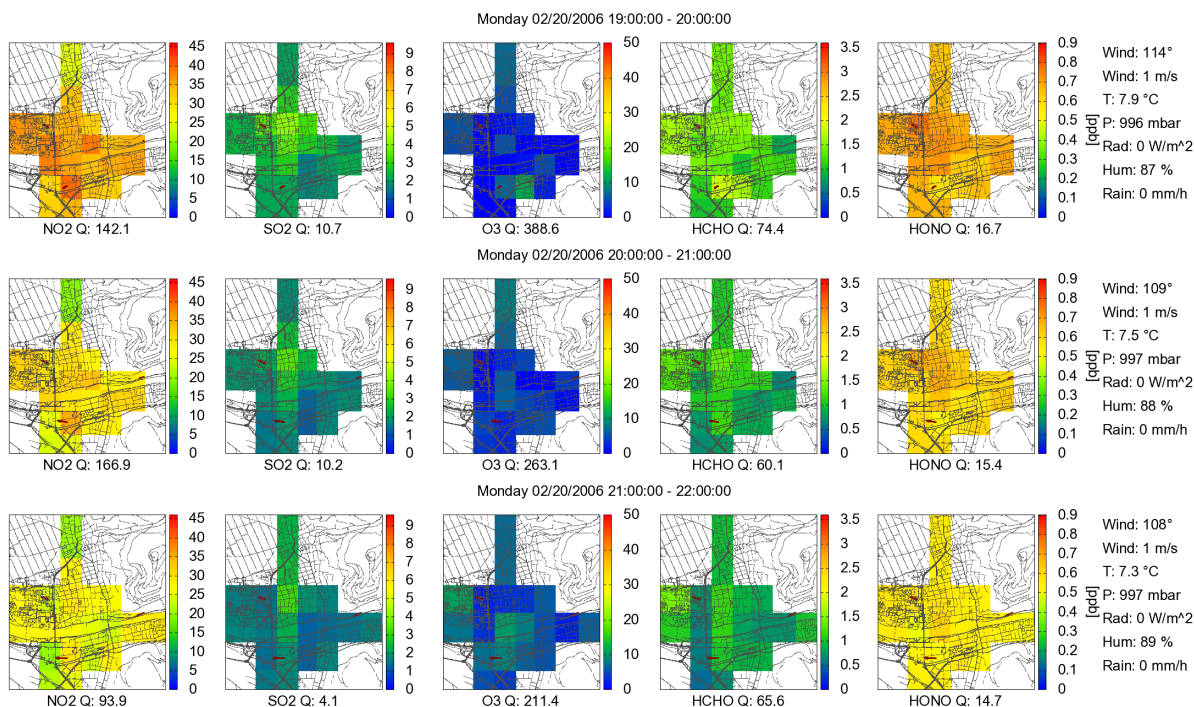


**Figure 8-16:** One hour averaged time series of reconstructed trace gas distributions during HONO formation after sunset. Concentrations increased after sunset due to high NO<sub>2</sub> levels and low photolysis. The concentrations are reduced in the late evening after NO<sub>2</sub> decreased. No spatial characteristic was found. For labelling see Figure 8-3.

### 8.3.5 Characterisation of HONO Distributions

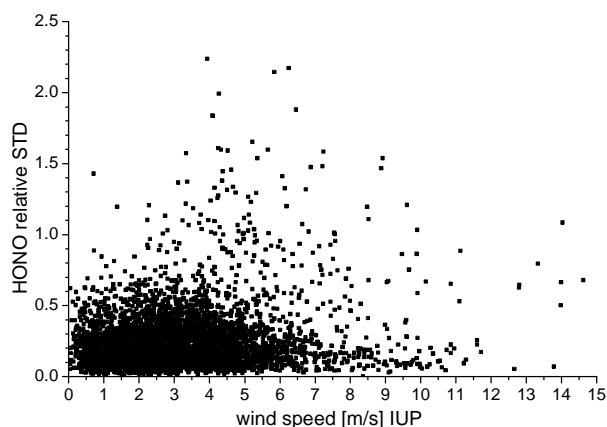


**Figure 8-17:** Correlation of relative STD of derived trace gas distributions for HONO with wind speed. The relative STD is the STD value of the distribution divided by the mean value. The low relative STD values indicate a low spatial variability. A weak correlation with wind speed is observed, as the distributions are already homogeneously distributed at low wind speeds.

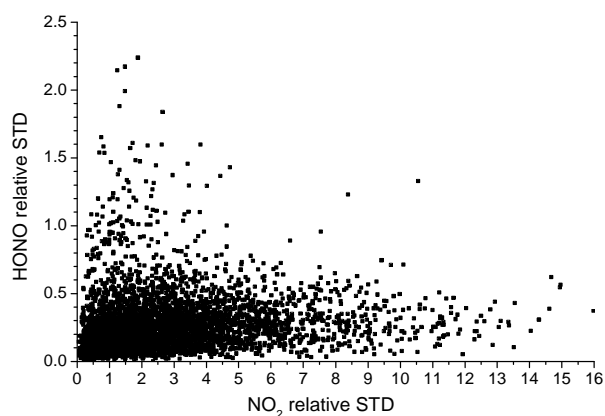


**Figure 8-18:** Correlation of NO<sub>2</sub> and HONO relative STD. NO<sub>2</sub> displayed much higher relative STD than HONO and also no correlation arose. If strong spatial variability of NO<sub>2</sub> was found, HONO still featured a homogeneous distribution. Thus both are not emitted by the same sources.

The derived HONO distributions show only very weak spatial characteristics (Figure 8-17). The relative STD shows values typically below 1 and thus one order of magnitude smaller than those for NO<sub>2</sub> and O<sub>3</sub> distributions. It has to be taken into account that due to the relative large measurement errors a smaller iteration number was applied for the tomographic

reconstruction, what can explain a reduced spatial variability for HONO due to up to 50 % reconstruction error (see *Chapter 7.4.3*). Still, most of the difference cannot be explained by the retrieval and was a real characteristic of the concentration distribution. It can be stated that the HONO distributions showed only a very low spatial variability. The concentrations increased and decreased homogeneously over the investigation area. The distribution is different to NO<sub>2</sub> (Figure 8-18) and thus the observed HONO was not emitted by the same source where NO<sub>2</sub> emission or formation arose. It confirms the assumption of heterogeneous HONO formation at the surface.

## 8.4 Formaldehyde (HCHO) Distributions

Formaldehyde can be directly emitted by fossil fuel combustion or formed by the oxidation of hydrocarbons. Due to the large group of hydrocarbons, several sources arise in urban areas which are difficult to differentiate. Distributions of formaldehyde (HCHO) were already shown in the previous chapters with increased concentrations in the Figure 8-3, Figure 8-4 and Figure 8-15. The HCHO distributions can provide new information on the formation processes and therefore improve our knowledge. Maximum concentrations arose in the afternoon which is typical for a photochemically created pollutant. Increased concentrations arose during warm and sunny clear-sky days. The observed concentrations display a strong correlation to ambient temperature, wind speed and also slight correlations to other observed trace. These results are shown in the following sections.

### 8.4.1 Influence of Solar Radiation, Temperature and Wind Speed

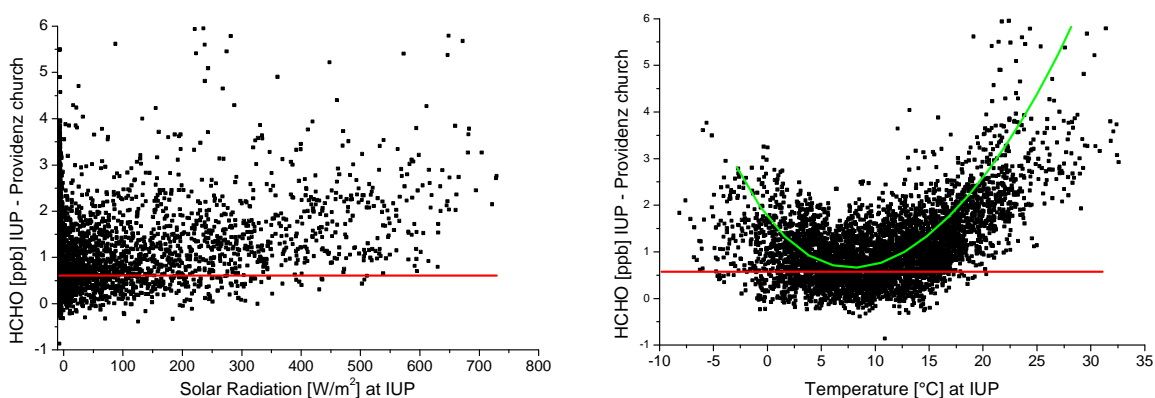


**Figure 8-19:** Correlation of HCHO to solar radiation (left) and ambient temperature (right) measured along one selected light path from IUP to Providenz church. Red line indicates the average detection limit. Even if HCHO is a photochemical pollutant it displays only a weak correlation to solar radiation, as it is also destroyed by photolysis. The correlation to temperature shows a clear minimum between 5 to 10 °C. Green line indicates the averaged concentration behaviour.

The correlation of HCHO to solar radiation is low although if it is a photochemical pollutant (Figure 8-19). The reason is photolysis during the day. Thus, the maximum was detected in the late afternoon before sunset. The correlation with temperature indicates a maximum for high temperatures typical for sunny clear-sky days which are favourable for high OH concentrations to oxidise VOCs (see *Chapter 2.2*). The determined concentrations decrease to

a minimum at 5 to 10 °C. For lower temperatures the concentration increased again. The values below 0 °C typically arose in the night. The concentration peaks can be found in the measurement time series e.g. January and February 2006 (see *Appendix 12.5* and *12.6*). It is clear that HCHO cannot be destroyed in the night by photolysis or hydroxyl radicals, which are not present during the night. The lifetime of formaldehyde towards wet and dry deposition is assumed to be in the order of a day (see *Chapter 2.4*) and thus unimportant for the occurrence of this concentration increase.

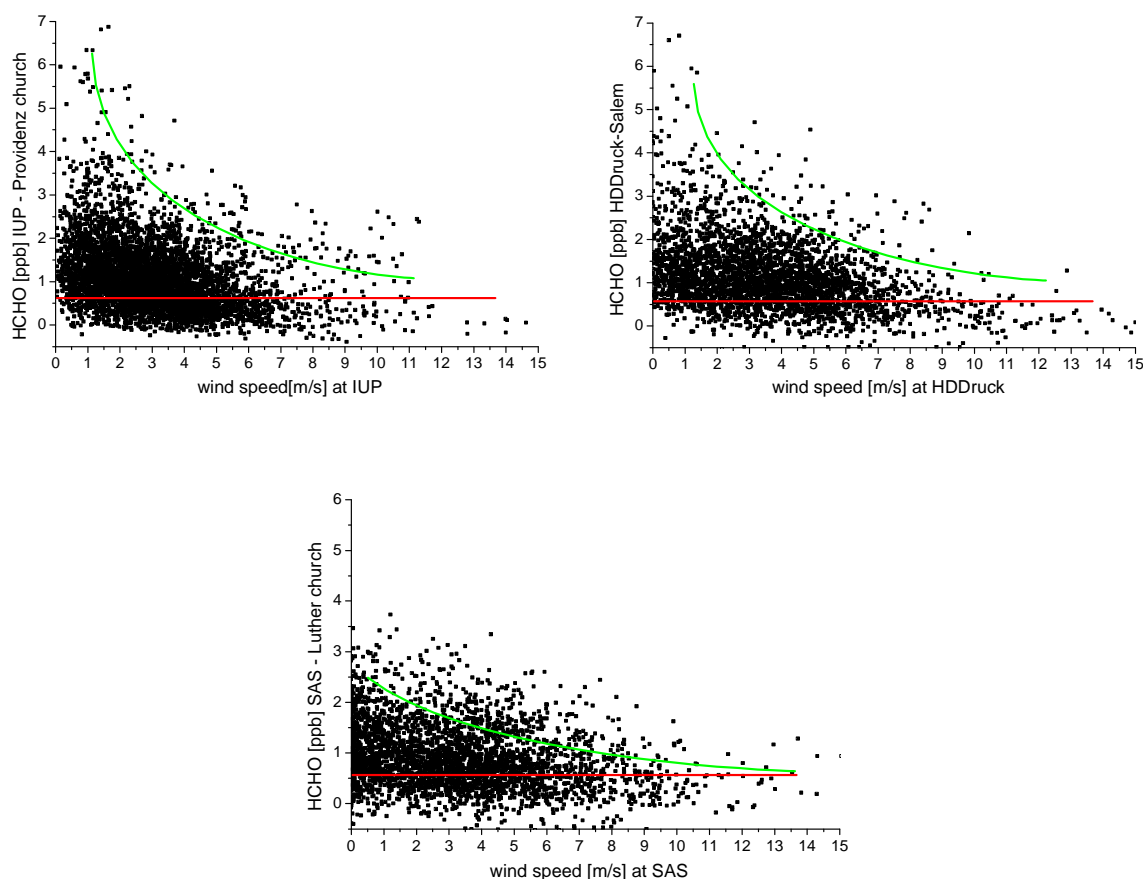


**Figure 8-20: Correlation of HCHO with wind speed for three selected light paths (one hour averaged data). First plot displays measurements from IUP to Providenz church versus wind speed at IUP, second row for measurements from HD-Druck to Salem versus wind speed at HD-Druck and third row for measurements from SAS to Luther church versus wind speed at SAS. Red lines show the average detection limit. Green line indicates the maximum concentration behaviour with wind speed. Concentrations strongly decrease with increasing wind but display different characteristic for various light paths due to different local concentrations.**

During the night the photochemical formation cannot contribute to the HCHO concentration. Thus the source can only be fossil fuel combustion and the direct emission of HCHO. The increase to colder temperatures arises due to a more stable PBL and reduction of PBL height. Thus the directly emitted HCHO are trapped close to the ground and result in a concentration increase compared to warmer days. Also emissions from heating are higher at colder temperatures and may lead to increased emissions.

A strong correlation of HCHO concentration to wind speed was observed (Figure 8-20). High concentrations above 5 ppb only arose at wind speeds below 3 m/s. The observed concentrations decreased with higher wind speeds, but still values up to 3 ppb are found as

photochemical formation mechanisms are less influenced if sufficient precursors exist. This would be the case for HCHO formation from methane. For directly emitted HCHO and emitted non-methane hydrocarbons (NMHC), which form HCHO by photochemical oxidation, the increased mixing at higher wind speed reduces effectively the observed HCHO concentration. Different dependencies are observed for different light paths, as local variations exist. The light path from SAS to Luther church (Figure 8-20 last plot) displays a lower correlation, as maximum HCHO concentrations are lower. The measurements here are in the East of the investigation area and were mainly located over the river Neckar, where fewer sources are expected.

### 8.4.2 HCHO Correlation to NO<sub>2</sub> and O<sub>3</sub>

Formaldehyde displays a correlation to NO<sub>2</sub> as it is also emitted by fossil fuel combustion like NO and NO<sub>2</sub> (Figure 8-21). The correlation is not that pronounced, as also other formation processes exist and HCHO is photolysed at high solar radiation. Opposite to HONO no difference in the correlation for different altitudes can be observed. The HCHO from fossil fuel combustion is directly emitted with NO and NO<sub>2</sub> by undergoing the same mixing processes. The lifetime of HCHO and NO<sub>2</sub> are both in the order of few hours and thus the relative ratio does not change significantly with altitude. Thus, NO<sub>2</sub> and HCHO display the same vertical gradient.

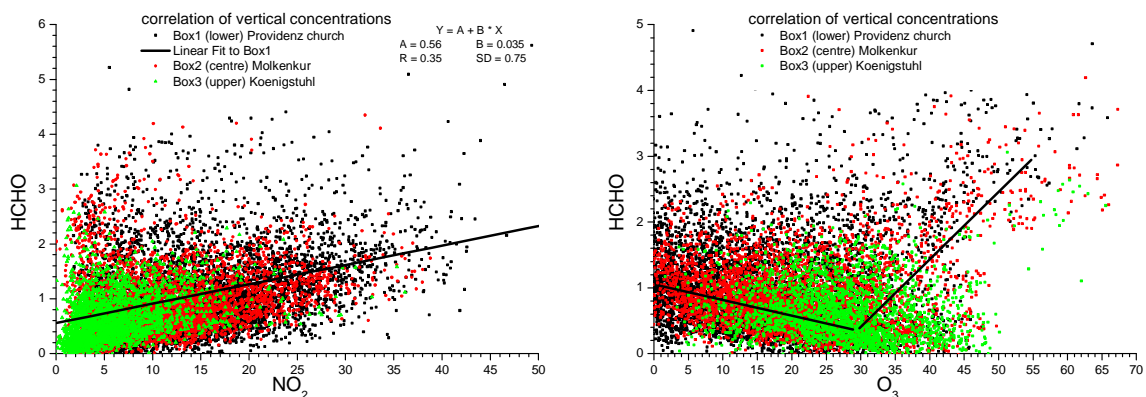


**Figure 8-21: Correlation of HCHO with NO<sub>2</sub> (left) and O<sub>3</sub> (right) for the different heights derived from the profile retrieval (see *Chapter 7.3*). Correlation does not vary for different altitudes. A clear correlation with NO<sub>2</sub> is observed as both are emitted by the same sources, but no difference for the different altitudes. Correlation with O<sub>3</sub> depends on the arising pollution situation.**

The correlation with ozone displays a more complex relation. It is directly linked to two different states dependent on the pollution situation. For ozone depletion events at low solar radiation anti-correlation could be observed. These events arose at stable PBL during cold winter days where typically emitted NO and NO<sub>2</sub> emissions are trapped close to the surface and O<sub>3</sub> is destroyed by NO. The simultaneously emitted HCHO is also trapped and concentration increased. During warm and sunny days increased concentrations of hydroxyl radicals (OH) led to increased oxidation of VOCs and thus to an increase of ozone, the summer smog. HCHO also increased as it is formed as a secondary product from the oxidation of the VOCs. This led to the positive correlation of ozone and HCHO above O<sub>3</sub> levels of 30 ppb. Thus, HCHO can also be used as a tracer for photo smog.

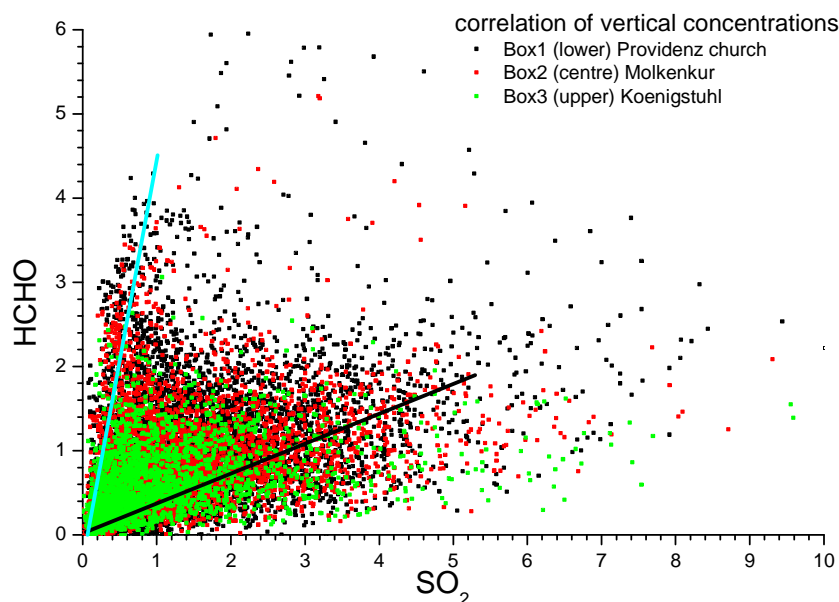


**Figure 8-22: Correlation of HCHO with SO<sub>2</sub> for the different heights derived from the profile retrieval (see Chapter 7.3). Two correlations can be found with a strong correlation for low SO<sub>2</sub> levels (light blue) which is mainly found for the lower layers and a weaker correlation for high SO<sub>2</sub> levels (black). The differences are discussed in the main text.**

Also a correlation to SO<sub>2</sub> was observed. An example of a time series where HCHO increased with SO<sub>2</sub> is shown in Figure 8-41. The correlation of all data is shown in Figure 8-22, where two situations are observed. The first very strong correlation arose for low SO<sub>2</sub> concentrations and predominant for data points from Box 1 and 2 and thus close to the ground. They can be assigned to days with high temperatures and high photochemical activity. The correlation has most likely no chemical reason, but as both concentrations depend on wind speed they may display a simultaneous increase. The second correlation arose for high SO<sub>2</sub> concentrations and can be found for all altitudes. Even for situation with stable PBL, the HCHO concentrations increase at higher altitude with SO<sub>2</sub> increase. SO<sub>2</sub> has its origin at these stable PBL conditions due to direct emission into these higher layers by stacks from power plants and industrial facilities. Thus, HCHO was likely emitted by the same sources.

### 8.4.3 HCHO Daily Cycle

A characteristic daily cycle of HCHO arises especially from the formation of NMHCs during photo smog situations. Such a full daily cycle is shown in Figure 8-4. Low values arose in the night and morning hours. In the afternoon the concentrations increased simultaneously to O<sub>3</sub>, indicating that HCHO is involved in the photochemical pollution and formation of O<sub>3</sub>. The HCHO and distribution was relatively homogeneous. The relative STD at 18:00 to 19:00 had a value of 0.18 in comparison to NO<sub>2</sub> and O<sub>3</sub> with 11.3 and 10.4 respectively. Lower concentrations were found in the East from where the wind was blowing. Thus, the reduction can be interpreted as a mixing with cleaner air. An increase arose in the centre of the investigation area and downwind, thus after the oxidation of NMHCs and mixing of air masses.

Another example of such high HCHO photochemical formation is shown in Figure 8-23. It was a sunny clear sky Sunday, when direct emissions are low as indirectly displayed by low

NO<sub>2</sub> concentrations. HCHO increase emerged due to photochemical oxidation of Methane and NMHCs and was strongly correlated to maximum concentrations of O<sub>3</sub>. Both increased over the day and reached a maximum in the afternoon between 15:00 and 18:00. The HCHO concentrations reached 3 to 4 ppb, when O<sub>3</sub> reached locally 70 ppb. After sunset the concentrations decreased. The spatial variability was much lower for HCHO with 0.19 relative STD and 14.27 for O<sub>3</sub>.

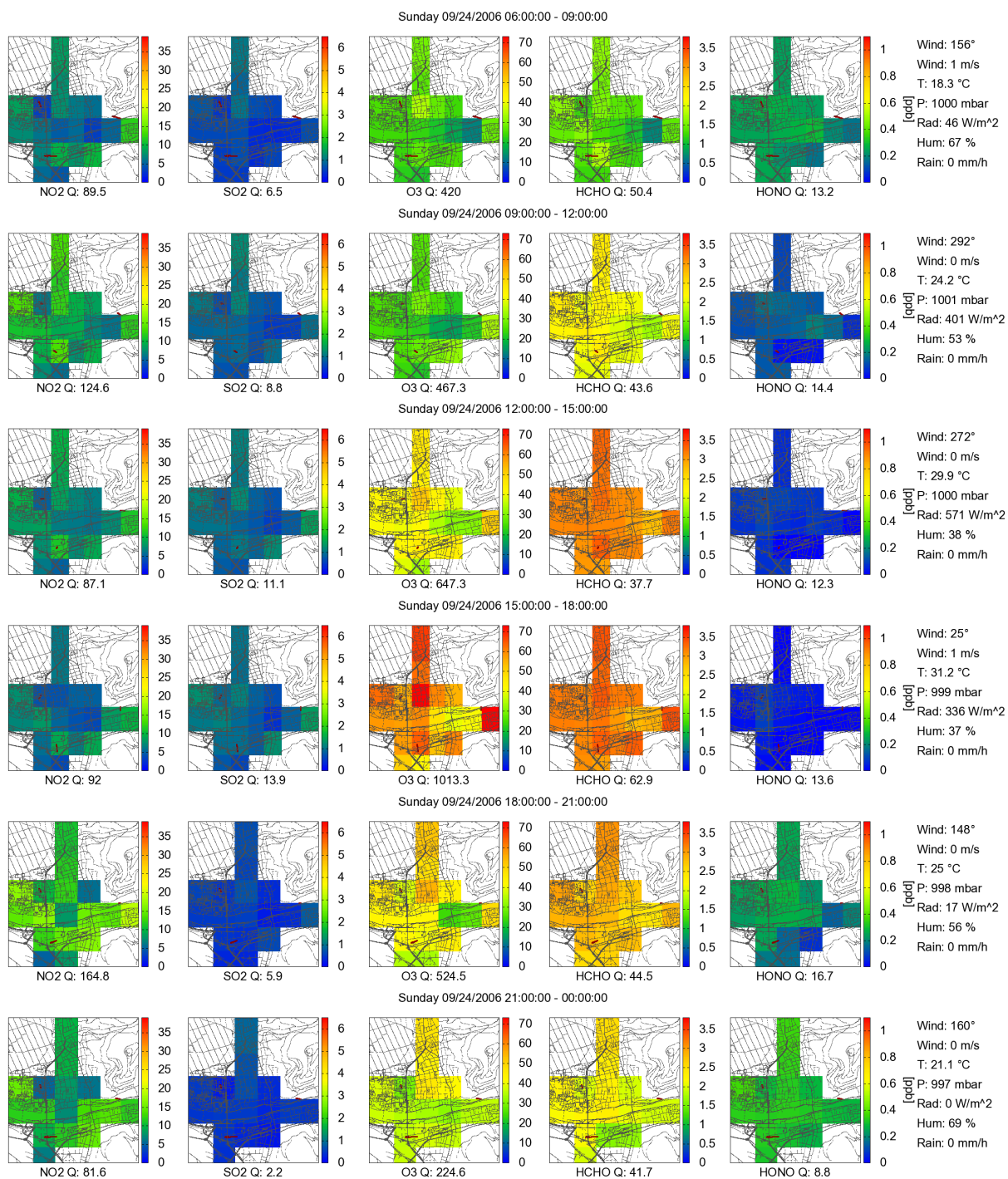
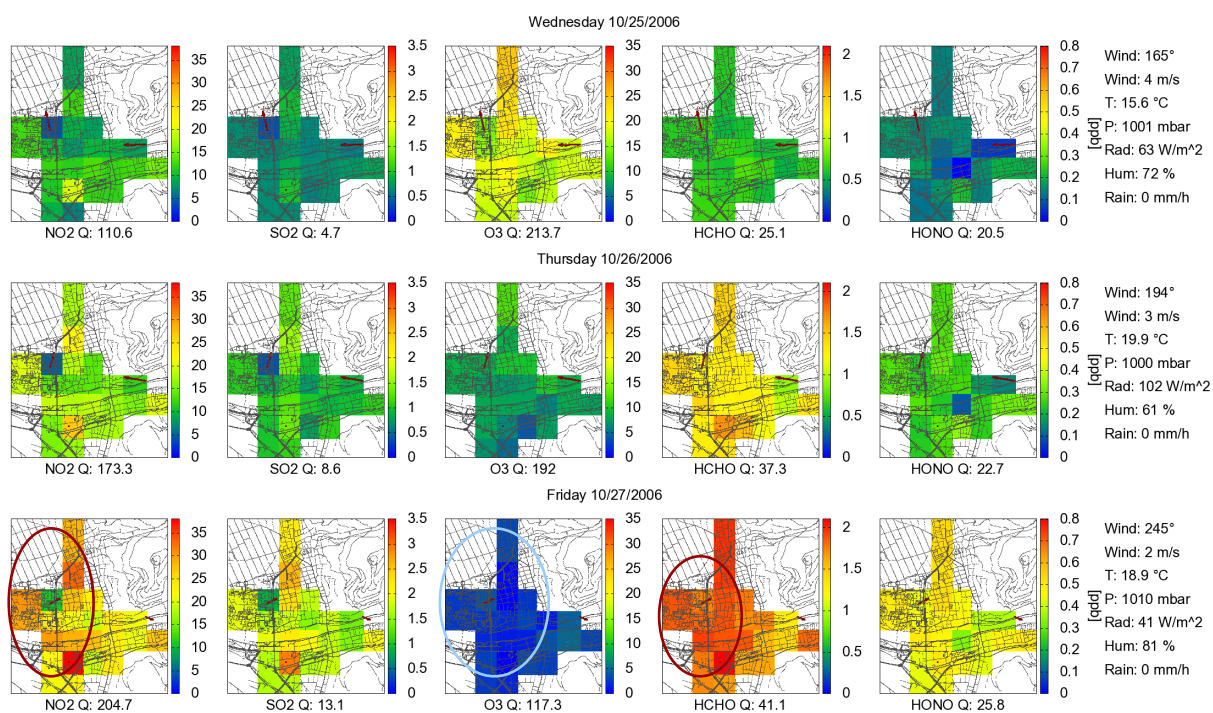


Figure 8-23: Three hour averaged time series of reconstructed trace gas distributions at photochemical production of HCHO during a warm sunny clear-sky Sunday. The maximum showed up in the afternoon when photochemical production from VOC was high. For labelling see Figure 8-3.

### 8.4.4 Variation of HCHO due to Direct Emissions

Also directly emitted HCHO from fossil fuel combustion displayed a characteristic daily cycle as the emissions are characterised by the rush hours and other periodic cycles like heating. These cycles are correlated to  $\text{NO}_2$ . Similar to variations in  $\text{NO}_2$  concentrations due to changes in meteorological characteristics with a change in PBL, wind direction or occurrence of single emission plumes, absolute concentrations for different days vary significantly even if comparable emissions appeared. An example of five consecutive days in October 2007 is shown in Figure 8-24, where the averaged distributions of each day are plotted. A strong variation between the days in the concentrations of  $\text{NO}_2$  and also HCHO can be observed. On the first day low levels were present. They increased till the third day. This day was characterised by very high  $\text{NO}_2$ , HCHO and HONO concentrations. Ozone was almost completely destroyed due to strong NO emissions. At these meteorological conditions HCHO could not arise from photochemical production of NMHCs and Methane, but rather due to direct emissions of fossil fuel combustion. If photochemical production were possible, also ozone levels would be increased. A weak spatial correlation for  $\text{NO}_2$ ,  $\text{O}_3$  and HCHO was visible, but with much lower characteristic for HCHO than for  $\text{NO}_2$ . The relative STD values were 0.26 and 3.5 for HCHO and  $\text{NO}_2$  respectively. The spatial variability of direct emitted HCHO was already higher than for photochemical produced HCHO during photo smog situations, but still much lower than that of  $\text{NO}_2$ .

With reduced emissions of the following two days which are indicated by reduced  $\text{NO}_2$  concentrations, also HCHO and HONO concentrations decreased.  $\text{O}_3$  again increased to background levels.



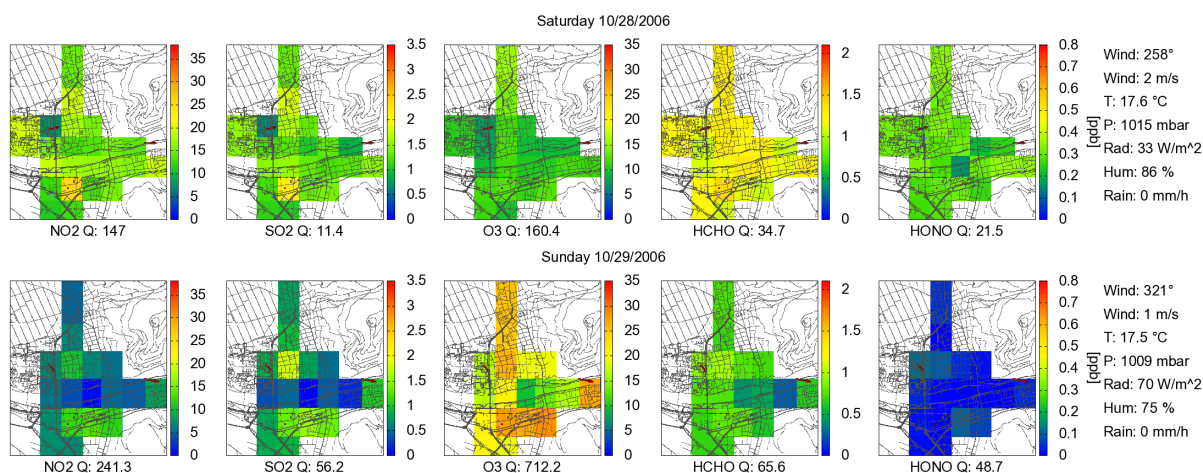


**Figure 8-24: Daily averaged time series of reconstructed trace gas distributions with strong change in concentrations from day to day with highest concentrations on Friday (opposite for ozone). For days with increased NO<sub>2</sub> also SO<sub>2</sub>, HCHO and HONO featured increased concentrations and ozone was depleted. Main spatial features are highlighted with maxima in dark red and minima in light blue. For labelling see Figure 8-3.**

### 8.4.5 Characterisation of HCHO Distributions

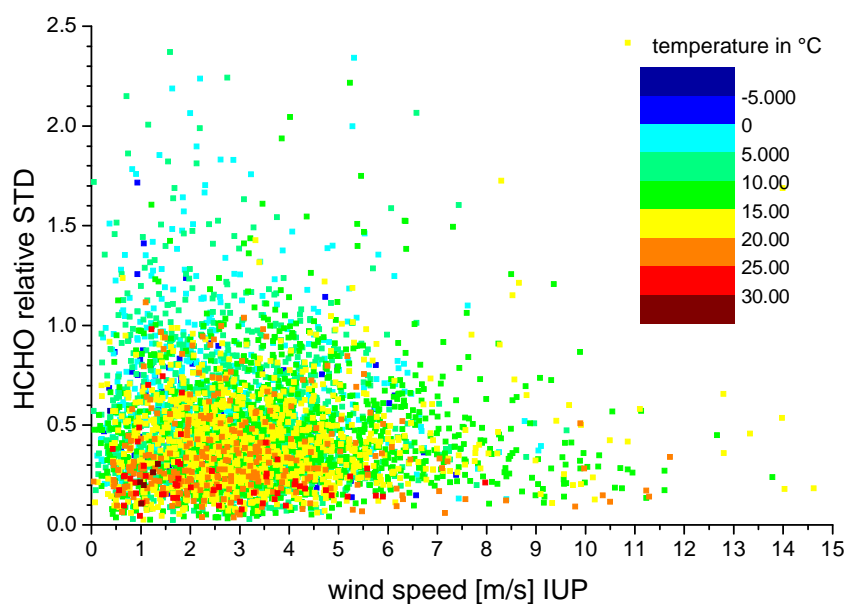


**Figure 8-25: Correlation of relative STD of derived trace gas distributions for HCHO with wind speed and colour coded ambient temperature. The relative STD is the STD value of the distribution divided by the mean value. The low relative STD values indicate a low spatial variability. A correlation with wind speed is observed. At high temperatures (orange and red colour, values for high temperatures plotted on top of lower temperatures), indicating high photochemical activity, mostly very low relative STD value are observed which indicate a low spatial variability. Higher relative STD arose at low temperatures, if direct emissions were dominating.**

The shown distributions of HCHO display a low spatial variability with low relative STD values (Figure 8-25). The lowest values were observed for photochemical produced HCHO during warm and sunny days. The production arose in the mixed atmosphere and was only to a small part directly localised at VOC emission sources. Thus, the HCHO concentration was in these cases homogeneously distributed. They are displayed in Figure 8-25 by values at high temperatures (orange and red colour coding), situations which are typically correlated to high

photochemical production. The relative STD values were below 0.2 and thus smaller than the average of 0.5. The higher variability was observed for direct emitted HCHO correlated to NO<sub>2</sub>. But the variability was much lower than for NO<sub>2</sub> (see Figure 8-9). The lower applied iteration number in the tomographic retrieval (see *Chapter 7.4.3*) could be responsible for up to 30 % lower determined variability, due to 30 % reconstruction error. Still this error cannot explain the large difference and chemical characteristics must be responsible. The differences may establish as the combustion of different fossil fuels had different emission ratios of NO<sub>2</sub>/HCHO and led to different distribution characteristics.

The change of relative STD of HCHO with wind speed (Figure 8-25) displays a similar characteristic like that of NO<sub>2</sub> and O<sub>3</sub> (Figure 8-9). Therefore, it can be stated that the concentration is similar mixed up with increasing wind speeds. This mainly affects directly emitted HCHO from fossil fuel combustion, as the photochemical produced HCHO already displayed lower spatial variability.

## 8.5 SO<sub>2</sub> Distributions

The observed SO<sub>2</sub> concentrations were relatively low in Heidelberg during the measurement period. The time series were dominated by irregular short events with duration of typically less than an hour which featured concentrations about ten times higher than typically background levels in Heidelberg of 1 to 3 ppb. Most of these events arose during the night and exclude periodic emission sources like rush hour traffic. The peaks displayed concentrations of up to 25 ppb and show sometimes strong spatial variability with localisation of the plume to one or only few pixels in the derived trace gas distributions. This correlates to plume sizes of less than 1 km<sup>2</sup>. The origin of the emissions remained unclear although the presented tomographic results give hints on the sources. SO<sub>2</sub> is a slow reacting trace gas (lifetimes of several days) it can be seen as constant for the residence time in the measurement area. Therefore, it may simply be used to demonstrate the ability of these tomographic measurements to observe concentration plumes. No chemical reactions have to be considered. The plumes which showed up for a very short period can only clearly be observed in the trace gas reconstructions with 15 minute temporal resolution as typically wind above 1 m/s led to a fast transport and changes in spatial distribution. Typically in one hour averaged data the information on plume location and maximum concentration is lost due to averaging over different distribution situations and just the general concentration increase remains in the observed trace gas distributions.

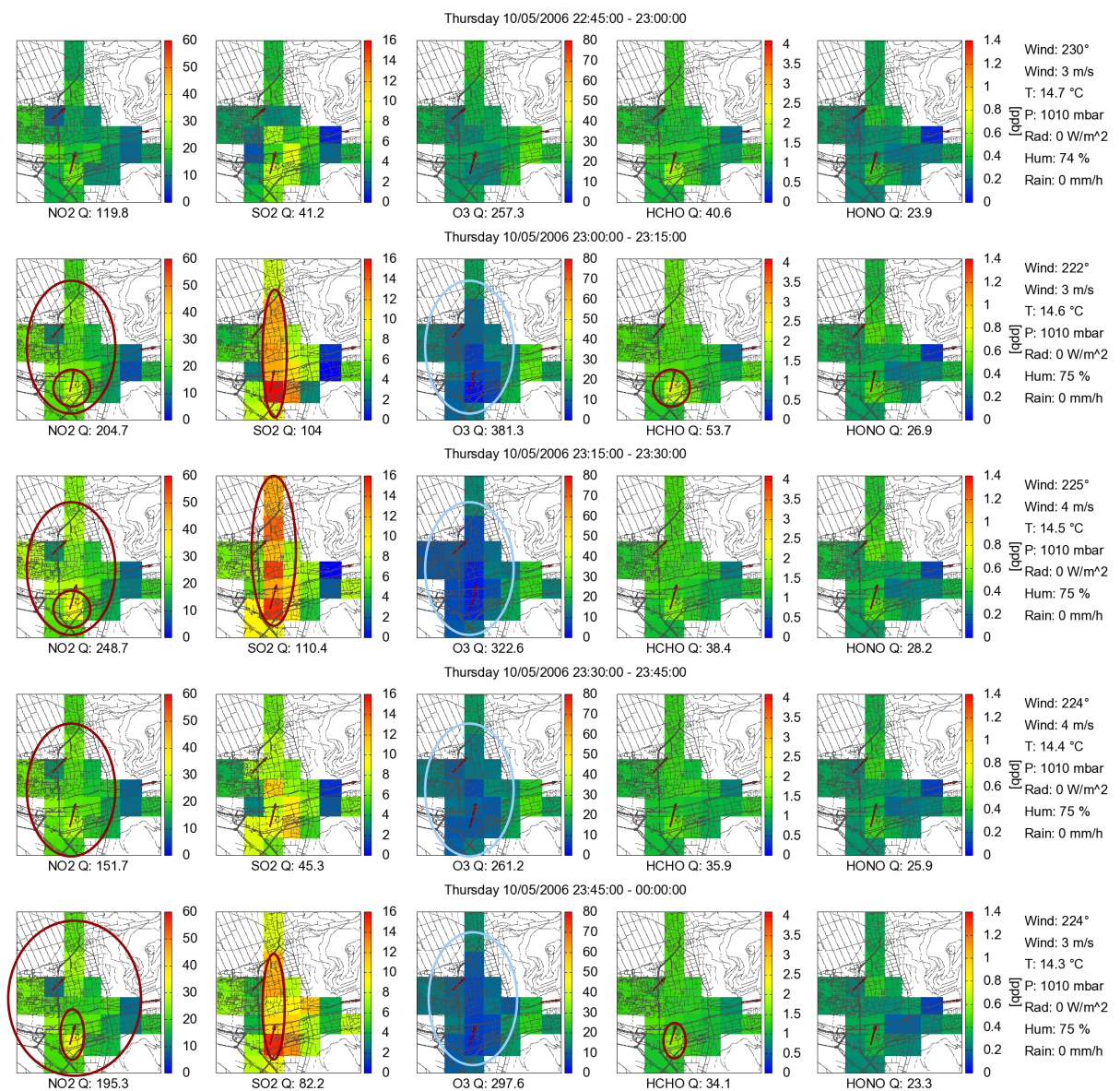
In Figure 8-5 an example for a local SO<sub>2</sub> plume is already given, which was observed in the night. During this emission event the SO<sub>2</sub> concentration increased over several hours. The peak was located in the area of the HD-Druck close to the municipal power plant, which was not operating at this time (see Figure 6-4). It is expected that SO<sub>2</sub> emissions could still emerge, e.g. due to maintenance or other work at this power plant. In-situ measurements of SO<sub>2</sub> at the LUBW station in the North (see Figure 6-4) located at a street did not display this high SO<sub>2</sub> concentration. It is expected that the emitted plume was not mixed down to the street level.

The SO<sub>2</sub> concentrations from traffic and small heating systems are an order of magnitude smaller. An example is shown in *Chapter 8.5.2*. Emission data state that 24 % of arising SO<sub>2</sub>

in Heidelberg originates from ships on the river Neckar (see *Chapter 2.5*). This could not be confirmed by the measurements. Neither the arising SO<sub>2</sub> plumes located at the Neckar nor SO<sub>2</sub> concentrations correlate to the ship density. These results are discussed in detail in *Chapter 8.15*.

### 8.5.1 SO<sub>2</sub> Plume Emissions

The time series of Figure 8-26 displays an event with two consecutive arising SO<sub>2</sub> emission plumes. Similar to the plume displayed in Figure 8-5, it was located in the area of the HD-Druck instrument and had its origin most likely at the municipal power plant. However, the provided data from the power plant does not state any operation during this day but may arise from maintenance works.



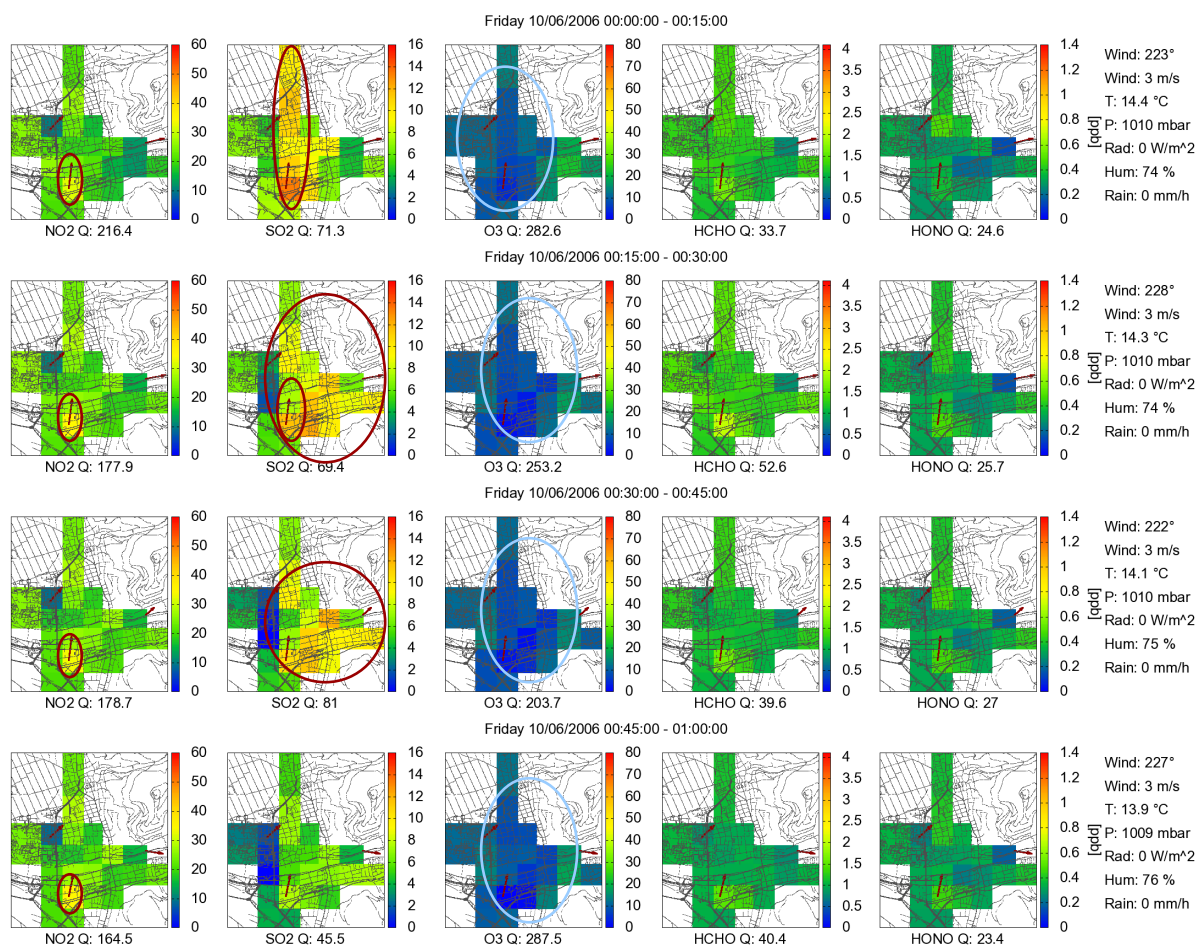


**Figure 8-26: 15 minutes time series of reconstructed trace gas distributions during a SO<sub>2</sub> plume event where at the same time also a strong NO<sub>2</sub> increase and O<sub>3</sub> reduction could be observed. Main spatial features are highlighted with maxima in dark red and minima in light blue. For labelling see Figure 8-3. The source of the emissions was located in the area of the municipal power plant in the South with peak concentrations up to 16 ppb. Three distinct emissions are observed which were disturbed with the wind to the North.**

The first emission plume was observed at 23:00. Due to southerly winds with 3 m/s the concentration was dispersed to the North and a long SO<sub>2</sub> plume arose at 23:15. The determined concentration variations inside the plume with three maxima may arise from systematic errors, as not all light paths measured simultaneously. The fast moving plume could thus create such artefacts in the reconstructed distributions which can be avoided with a continuously measuring instrument without changing light paths. Simultaneously to SO<sub>2</sub> also NO<sub>2</sub> concentrations increased and ozone decreased. A small increase in HCHO and HONO was also observed. All emissions had the same origin. It is interesting, that the NO<sub>2</sub> plume was less spatially concentrated than the SO<sub>2</sub> plume. First of all this is due to the much higher background concentration of NO<sub>2</sub>. Second, ozone is quickly destroyed at the emission source what limits the formation of NO<sub>2</sub>. Only if the emitted NO was mixed up with ozone rich air masses, NO<sub>2</sub> would be formed. Thus the observed NO<sub>2</sub> plume has a larger size. After the emissions reduced at 23:30, a second plume emerged at 23:45. The SO<sub>2</sub> concentrations afterwards slowly decreased whereas NO<sub>2</sub> remained high and also ozone was still locally depleted. This indicates that the emission source was further operating and SO<sub>2</sub> was a single emission e.g. due to a restart of the system. Slightly easterly wind direction led to a dispersion of the emission plume to the North-East.

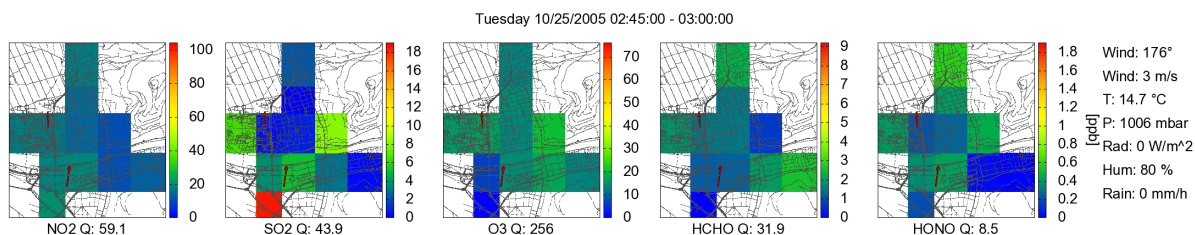
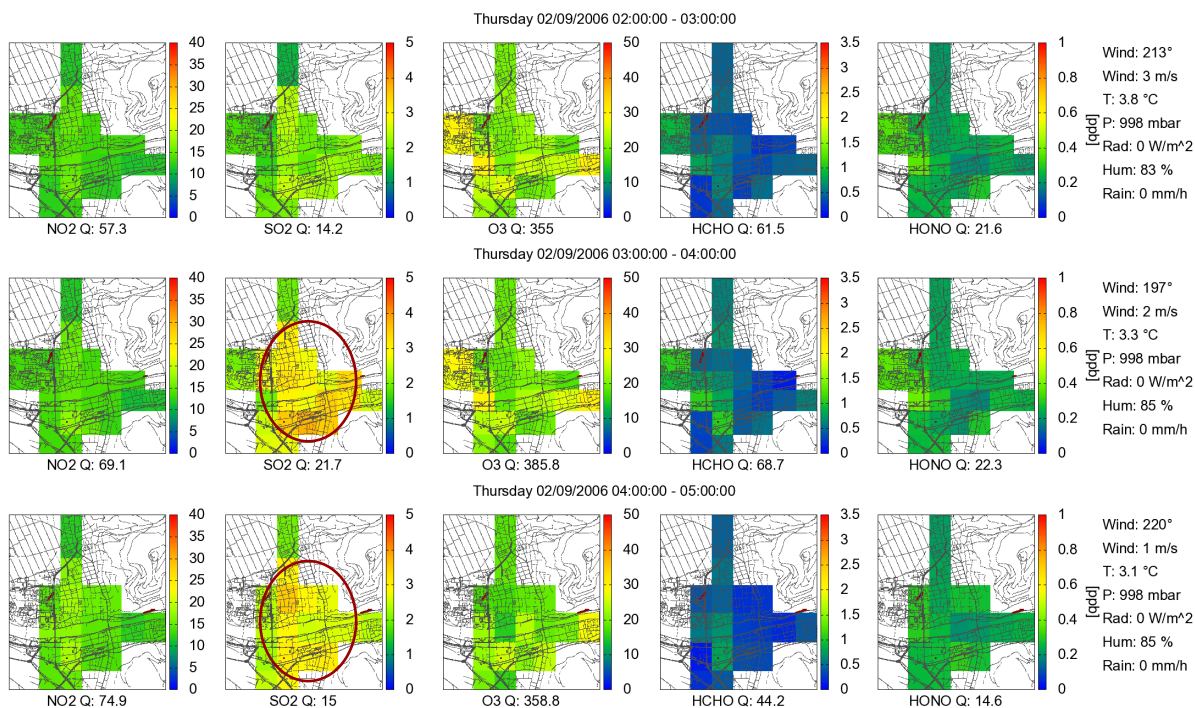


Figure 8-27: Reconstruction of a SO<sub>2</sub> plume in the South-West where no increase with other concentrations was found. For labelling see Figure 8-3.

Not all observed SO<sub>2</sub> emission plumes had its origin at the location of the example in Figure 8-26. In Figure 8-27 a different location of an emitted SO<sub>2</sub> plume is displayed. Here it could be localised to the South-West. It might arise from the industry area or the railway. In this case no correlation to other trace gases was seen.

### 8.5.2 SO<sub>2</sub> from Heating and Traffic

SO<sub>2</sub> emissions in Heidelberg also appear from traffic and small heating systems. The determined concentrations are typically lower than those of the observed events in *Chapter 8.5.1* as the petrol is desulphurised and the gas mainly used for heating should also contain very low sulphur concentrations. Large residential areas are connected to the district heating system and should not display any emissions of trace gases. Unfortunately it was not possible to receive any information on the use of oil for heating which contains higher sulphur concentrations. However, a weak correlation of observed SO<sub>2</sub> concentrations to heating periods was observed if the concentration scale of SO<sub>2</sub> was enlarged. An example is given in Figure 8-28.



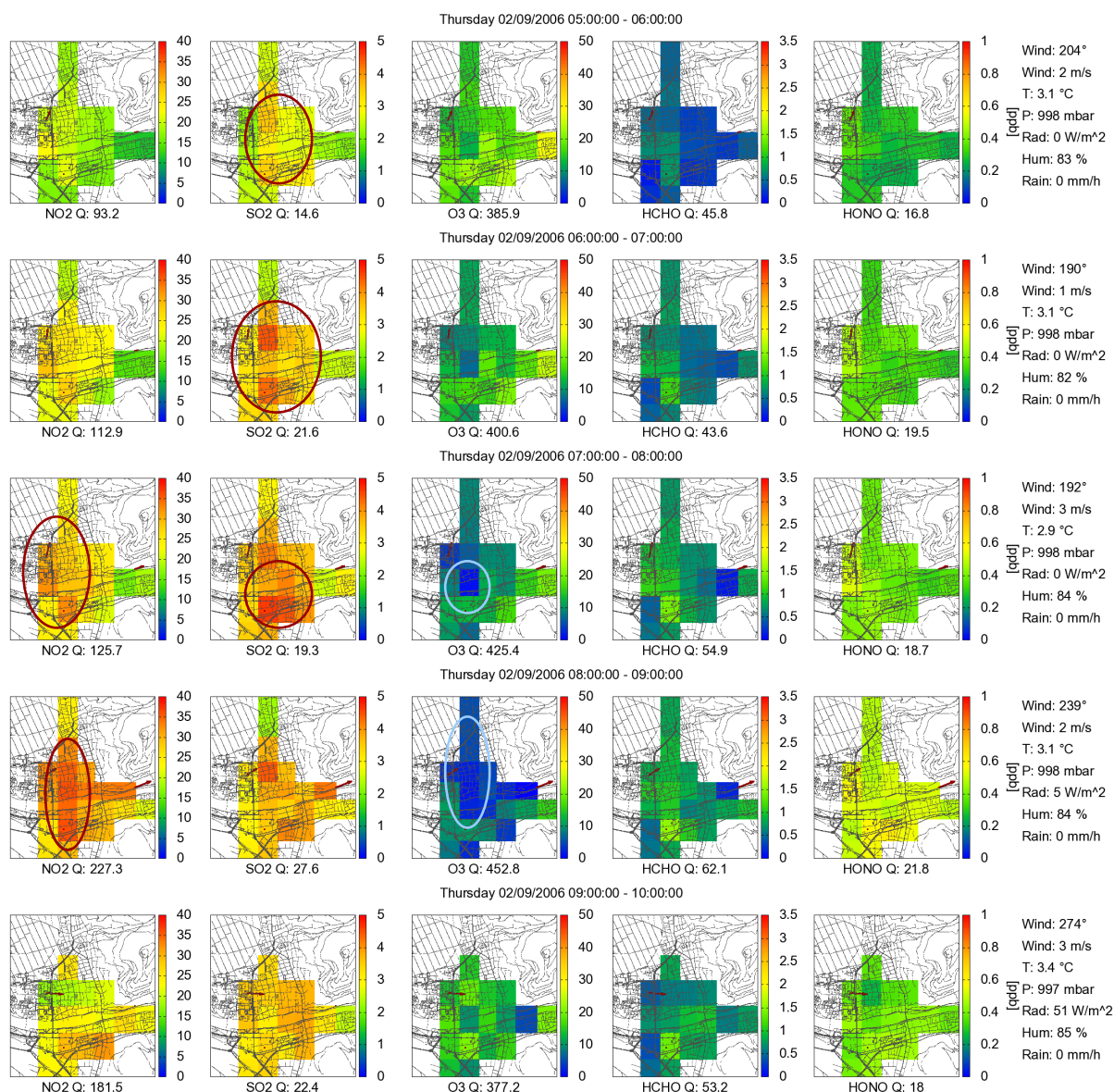


**Figure 8-28:** One hour averaged time series of reconstructed trace gas distributions with enhanced SO<sub>2</sub> concentration due to heating and traffic emissions. Concentrations are much lower than for the dominating SO<sub>2</sub> peaks in the time series. First SO<sub>2</sub> increase was after 3:00 indicating domestic heating. A second strong increase was after 6:00. A shift between SO<sub>2</sub> peak and NO<sub>2</sub> peak illustrates different sources. Main spatial features are highlighted with maxima in dark red and minima in light blue. For labelling see Figure 8-3.

The SO<sub>2</sub> concentration increased after 3:00 mainly in the older residential areas of the old town, “Weststadt”, “Bergheim” and “Neuenheim”. The pixels in the South from where the air mass was coming during this day displayed enhanced but lower concentrations. Thus, it can be excluded that the SO<sub>2</sub> was transported to the measurement site. No strong correlation to the other trace gases was observed and thus the SO<sub>2</sub> sources must displayed a low NO<sub>x</sub> emission. A second SO<sub>2</sub> peak was observed between 7:00 and 8:00. NO<sub>2</sub> increased after 6:00 with the beginning of the rush hour and reached a maximum between 8:00 and 9:00. The NO<sub>2</sub> concentration peak was located further in the West. They are emitted mainly at the main streets in the West and South-West and diluted due to the south-westerly wind over the city. It is unlikely that the second SO<sub>2</sub> peak arose due to traffic emissions as the different distributions do not support this assumption. The much lower SO<sub>2</sub> concentrations on warmer

days also exclude traffic emissions to be a significant source for the enhanced  $\text{SO}_2$ . Simultaneously with  $\text{NO}_2$ , ozone decreased and HCHO and HONO increased.

The timing of the  $\text{SO}_2$  concentration peaks can be explained by the expected heating periods. Especially oil heating systems are of interest here. In the early morning the heating is switched on to heat up the warm water reservoir and start to heat up the residences for the morning. This led to the first peak after 3:00. After the residents woke up and had a shower, new cold water was heated again. Additionally the houses were still heated in the early morning. Thus, a second emission peak arose between 6:00 and 9:00. Afterwards the people took the car to work. This is responsible for the rush hour  $\text{NO}_2$  peak shifted by about an hour to the previous  $\text{SO}_2$  peak. Only low  $\text{SO}_2$  concentrations were observed in the afternoon and in the evening which may also appeared from heating.

### 8.5.3 $\text{SO}_2$ Transported to Heidelberg

Most of the  $\text{SO}_2$  peak events do not display any spatial characteristic and must have its origin in sources at larger distances to the observation site. Thus, the air mass is already well mixed up and no strong spatial variations could be found. An example of such a passing plume is given in Figure 8-29. The plume was transported to the measurement site by the south-westerly wind direction. No strong concentration peak was observed, but the front of the plume is identified and drawn as dashed line. The areas in front of the plume in the North and the East displayed still lower concentrations. Some artefacts might emerge due to the consecutive measurement of the light paths.

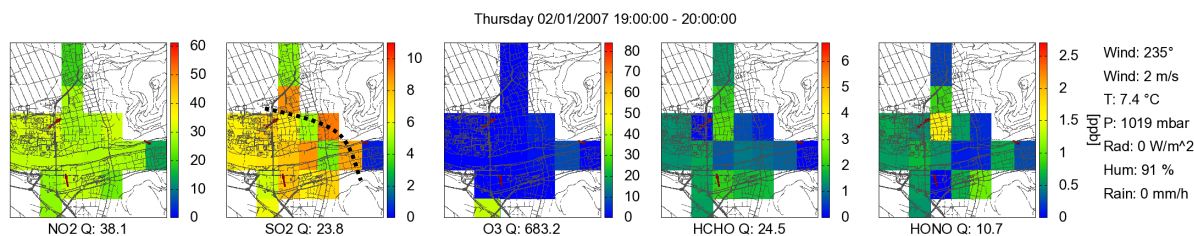


**Figure 8-29:  $\text{SO}_2$  trace gas distributions for a transported plume. The dashed line indicates the  $\text{SO}_2$  plume front. Spatial variations in the plume arise from the consecutive measurements along the different light paths. For labelling see Figure 8-3.**

### 8.5.4 Influence of High Wind Speeds on $\text{SO}_2$ Concentration and Distributions

Similar to the other trace gases, also the  $\text{SO}_2$  concentration is influenced by high wind speed and mixing of air masses. Maximum concentrations of up to 17 ppb could be observed. Maximum observed concentrations decrease with increasing wind and reach at 10 m/s levels around 0 ppb. But as the irregular high  $\text{SO}_2$  emissions of different concentration appeared without systematic, also the correlation with wind speed is less pronounced (Figure 8-30). This is contrary to  $\text{NO}_2$  where the maximum emissions are constant, as the sources are not changing too much. For  $\text{SO}_2$  strong variations in the emission exist. Therefore, also lower concentrations can be observed with increasing wind, but if strong emissions arise at high wind speeds they can still be responsible for significant  $\text{SO}_2$  increase. De facto it depends on

how strong the SO<sub>2</sub> emission is. Still

The derived relative STD values for SO<sub>2</sub> distributions (Figure 8-31) display high spatial variations with typical values of up to 5. This is still much lower than for NO<sub>2</sub> and O<sub>3</sub>. The reason is that if a localised SO<sub>2</sub> plume arose, it was typically only one plume, only few pixels were affected and the STD value only slightly increased due to these few pixels. A relative peak to peak value would be a better value to characterise such SO<sub>2</sub> plumes. In the case of NO<sub>2</sub> and O<sub>3</sub> a complicated distribution with several maxima and minima were observed resulting in a much higher relative STD. As most of the time only low SO<sub>2</sub> concentrations were observed, the general distribution was relatively homogeneous with relative STD values below five.

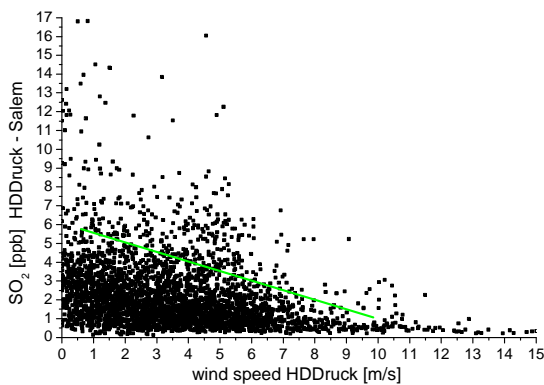


**Figure 8-30:** Correlation of SO<sub>2</sub> (measured from HDDruck to Salem) with wind speed at HD-Druck (one hour averaged data). A similar strong dependency as for NO<sub>2</sub> is observed, but with more scattering due to strong plume events.

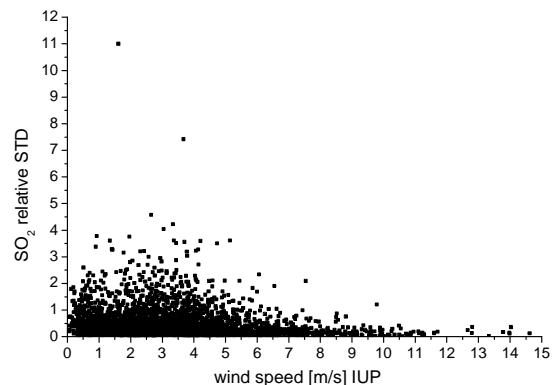


**Figure 8-31:** Correlation of relative STD of derived trace gas distributions for SO<sub>2</sub> with wind speed. The relative STD is the STD value of the distribution divided by the mean value. Much lower values than for NO<sub>2</sub> indicate a lower variability. A correlation with wind speed is observed but weaker than for NO<sub>2</sub>, as lower variability is found for low wind situations.

## 8.6 Trace Gas Concentrations During Fireworks



**Figure 8-32:** Picture of the Heidelberg castle illumination with fireworks.

During the first measurements in Heidelberg, an important event took place in the city, the Heidelberg castle illumination on the 3<sup>rd</sup> September 2005. This is a show with an illuminated castle remembering the burning of the castle in 1693. The show ended with large fireworks between 22:30 and 22:45. This chapter will analyse the observed trace gas concentrations during this fireworks.

On 3<sup>rd</sup> September, the instrument at the IUP performed measurements along 7 light paths. Two of them were directed to retro reflectors at higher altitude. One to the top of the mountain Koenigstuhl and the second located on half way up at the Molkenkur. The other five light paths (Philweg, Providenz church, Bonifazius church, HDDruck, Speyerring) covered the city area. During this day a strong easterly wind arose with maximum wind speeds of 10 m/s in the late evening and thus during the fireworks.

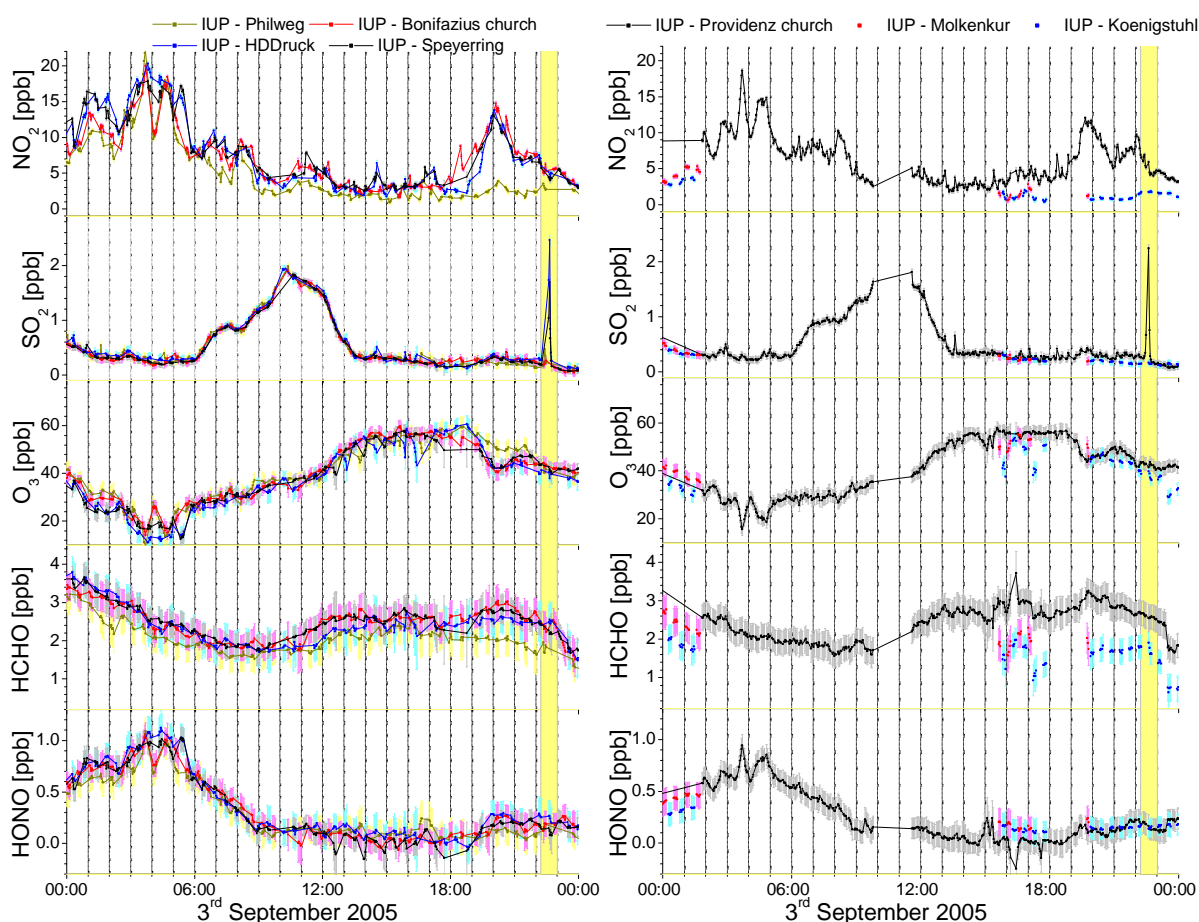


**Figure 8-33: Observed trace gas concentrations during the fireworks of the Heidelberg castle illumination on the 3<sup>rd</sup> September 2005. A short increase in SO<sub>2</sub> was observed on light paths pointing to the city. Concentrations decrease quickly afterwards to background values.**

The observed trace gas concentrations for this day are displayed in Figure 8-33 with the time frame of the fireworks highlighted in yellow. A strong and short increase in SO<sub>2</sub> was observed for the light paths pointing to the city centre and measuring the disturbed plume (to Providenz church, HDDruck and Speyerring, see Figure 6-6). The other light paths as well as the one to Molkenkur did not show an SO<sub>2</sub> increase (no measurements to Koenigstuhl due to low visibility). All other trace gases were not affected and remain at the same concentration level. The determined average SO<sub>2</sub> concentration over a light path of 2.7 ppb is relatively low.

Similar concentrations arose on typical days (see same plot Figure 8-33). Much higher concentrations with up to 20 ppb were observed during strong SO<sub>2</sub> events. But if accounting that the plume of the fireworks is small and thus only a small part of the light path measures these emitted trace gases, the concentration in the plume can be estimated to be much higher. If only 10 % are in the light beam, the concentration in the plume is ten times higher and thus up to 27 ppb. Still the total influences of these fireworks on local trace gas concentrations were very low. Only few minutes later the concentrations reach the previous level. Due to the strong wind a quick mixing and transport of the trace gases arose so that the plume was fast outside the observation area.

## 8.7 Mean Daily Cycle

In order to analyse photochemical processes and periodical emission events, the averaging of the measurement data to mean daily cycles provides new insights, as single events are averaged out. Thus, the pure periodic cycle remains. Data products for the averaged daily cycle are produced for each month (see Data DVD *Chapter 8.16*) and for the whole measurement period (Figure 8-34). As tomographic measurements were performed in autumn, winter and spring, and not in summer, the average over all data does not represent the real average daily cycle of a whole year but more of the winter period. A change in the cycle over the year can be found due to change of emission sources and change of solar radiation and thus different photochemical activity and stability of PBL.

The averaged data displayed in Figure 8-34 are characterised by a very strong daily cycle for all trace gases. The determined concentration differences between the light paths are much smaller, but systematic. For the different trace gases, different light paths display enhanced values. The average diurnal cycle of solar radiation for the same measurement period is displayed in Figure 8-35. The derived trace gas distributions for the mean daily cycle are plotted in Figure 8-36. The results are shortly discussed.

NO<sub>2</sub> concentrations are characterised by two distinct maxima which have their origin in the morning and the evening rush hour. The evening rush hour starts at 16:00 but the maximum is observed only between 18:00 to 19:00, as photolysis of NO<sub>2</sub> during the day reduces the concentration in the afternoon. Thus, the maximum arises if solar radiation is reduced as reflected in the mean diurnal cycle of solar radiation for the same measurement period in Figure 8-35. As emissions are smaller during the night, the concentrations decrease until the next morning rush hour e.g. due to conversion to water soluble species (HNO<sub>3</sub>) and mixture with clean background air (see *Chapter 2.1.3*). The distributions show that NO<sub>2</sub> mainly increases for the peak concentrations in the centre of the observation area (highlighted 7:00 – 8:00 and 9:00 – 10:00). The boxes in the North, East and South display lower values. Also the West features slightly lower concentrations. Thus, the commuter traffic on the approaching roads to the city did not increase the concentrations at the city border significantly in comparison to the high loaded roads in the city.

mean daily cycle

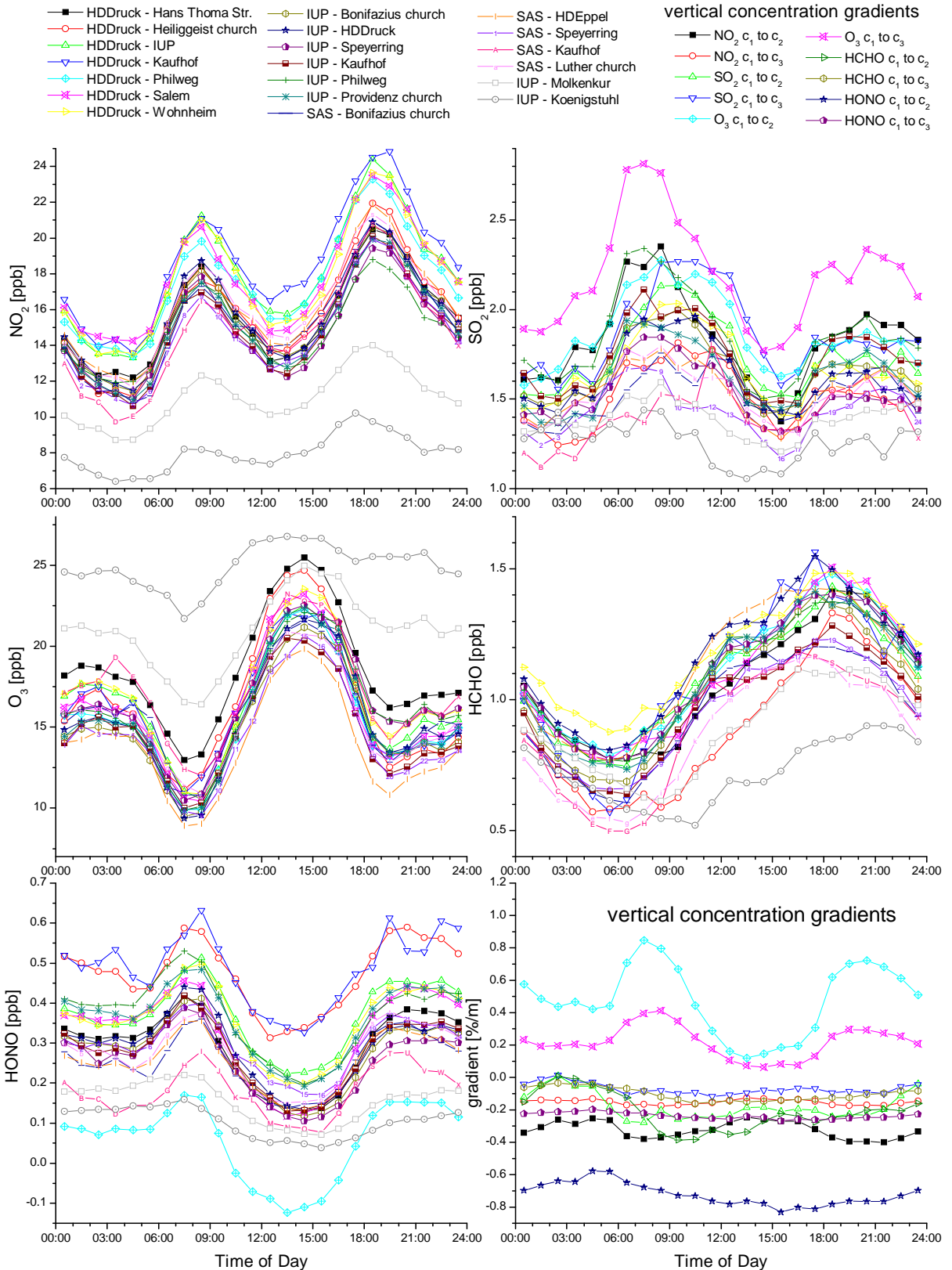
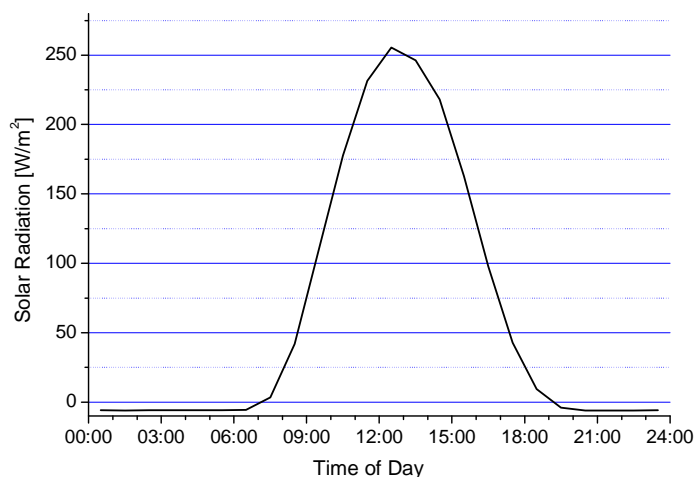


Figure 8-34: Daily averaged cycle of all LP-DOAS data of the measurement period. Vertical concentration gradients are observed from the profile retrieval. Light paths to higher altitudes (Molkenkur and Koenigstuhl) displayed very different concentrations and thus very strong vertical gradients arose. The gradient is retrieved from the determined concentration at different altitudes for box  $c_1$  (instrument height) to  $c_3$  (below Koenigstuhl) (Chapter 7.3). Positive gradients imply increasing concentration with altitude and negative decreasing. For details on the trace gas cycles see main text.



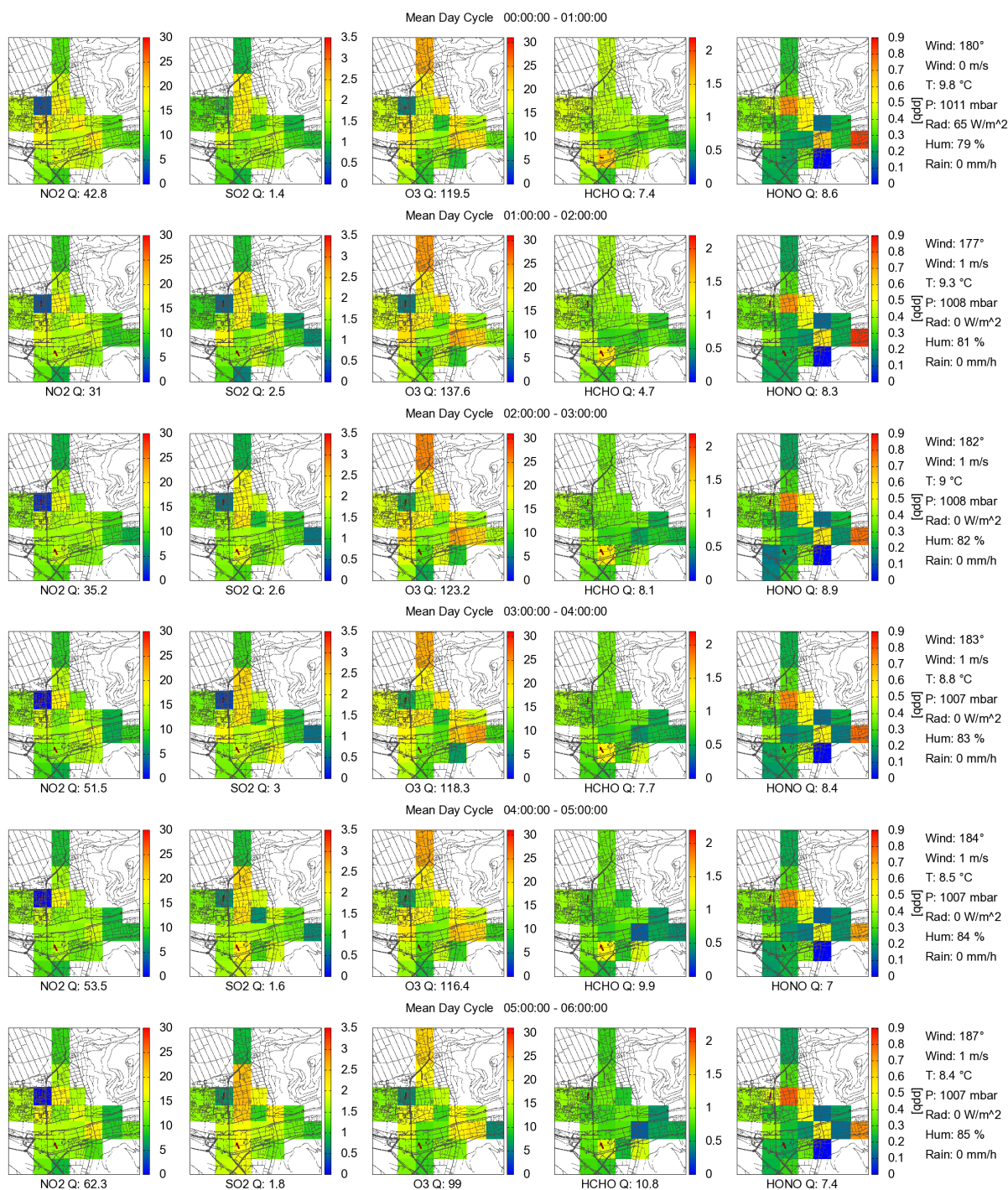
**Figure 8-35: Mean daily cycle of solar radiation for the whole measurement period of tomographic observations.**

A box with very low concentration arose at the IUP due to an artefact from the measurement (see *Chapter 8.2.4*). Peak concentrations were located at the main streets for the North South connection in the West and East were bridges cross the river Neckar (highlighted for 8:00 – 9:00). The high traffic load at the bridges and neighbouring streets led to the local concentration maximum.

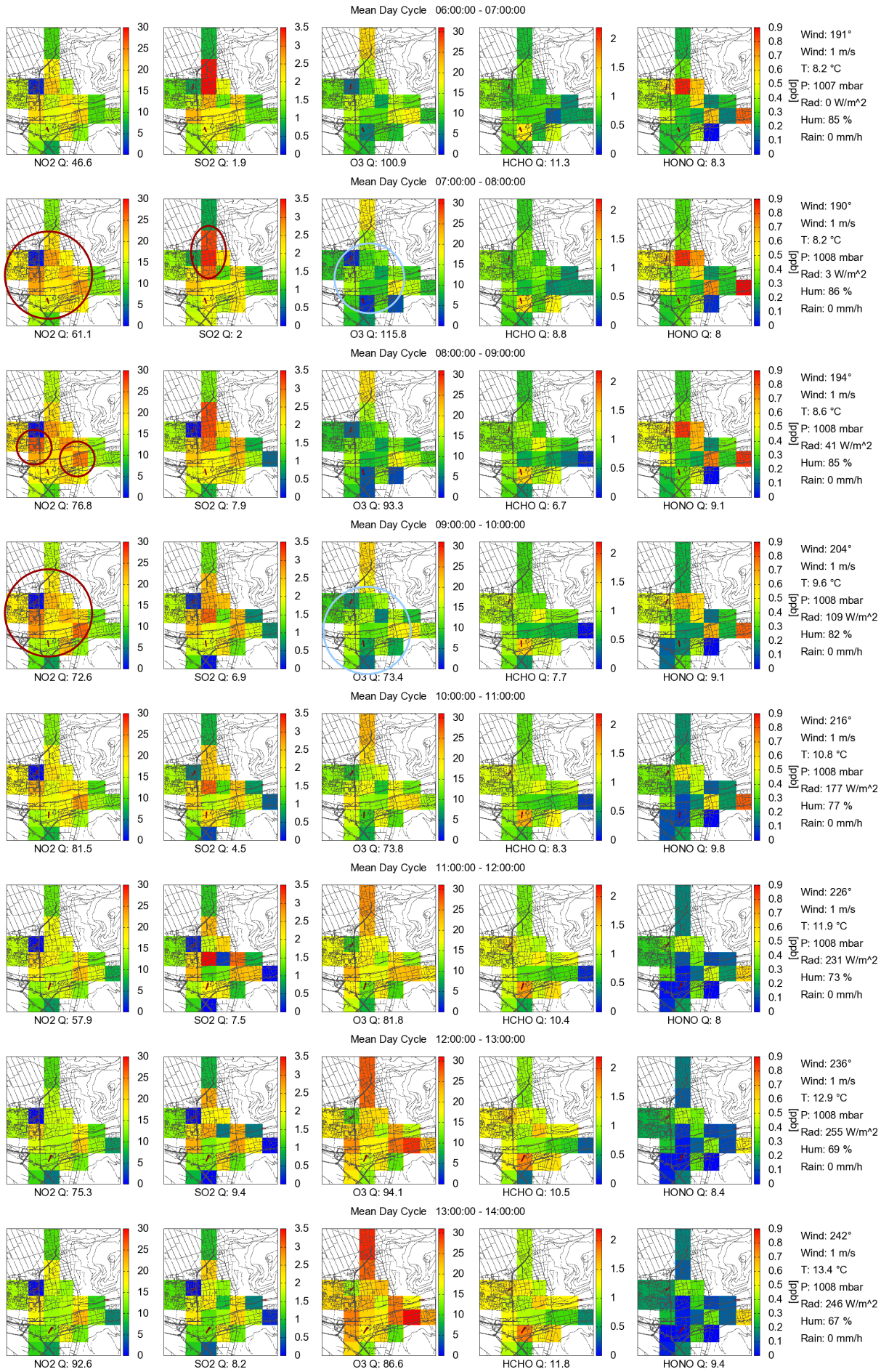
For the evening concentration peaks similar spatial distributions appeared. The concentrations are typically higher in the evening than in the morning peak, as emissions accumulate as NO over the day and converted with O<sub>3</sub> to NO<sub>2</sub> after sunset. As also the evening rush hour is often after sunset, even higher concentrations emerged. O<sub>3</sub> displayed the opposite cycle in concentration and spatial distribution. A concentration minimum arose in the morning due to destruction from the reaction of emitted NO from the morning rush hour to NO<sub>2</sub>. Concerning the distributions, the reduction arose in the centre of the investigation area. Opposite to the distributions of single days, this was not exactly at the same location where the highest NO<sub>2</sub> concentration was observed. The averaging over all days with different concentration distributions for cold and dark as well as warm and sunny days may have removed the detailed spatial distribution. During the day the ozone concentration rose with increase in solar radiation due to photolysis of NO<sub>2</sub> to NO and formation of O<sub>3</sub>. NO can form NO<sub>2</sub> again if HO<sub>2</sub> exists from oxidation of OH due to VOCs in a sunny and warm atmosphere. Because of the different lifetimes of NO<sub>x</sub> and VOCs and also new emissions of NO in the centre of the investigation area, the ozone maxima arose downwind and thus at the border of the city in the North and East (highlighted for 14:00 – 15:00). The evening rush hour with emitted NO<sub>x</sub> and VOCs shifted the concentration maximum by two hours to about 14:30. With sunset a second small minimum show up in O<sub>3</sub> concentrations. In the night the concentrations decreased and reached background values again. At the same time the distributions also displayed slightly higher values at the city border.

The daily cycle of HONO featured a correlation to NO<sub>2</sub>, but the maxima were shifted to periods before and after sunrise and sunset respectively when NO<sub>2</sub> still emerged in sufficient concentrations. During the day much lower HONO values were observed due to photolysis. The spatial distribution of HONO is less characteristic than that of NO<sub>2</sub>. Some concentration peaks showed up which can neither be correlated to sources nor to peaks of single days. These artefacts may have arisen from data averaging.

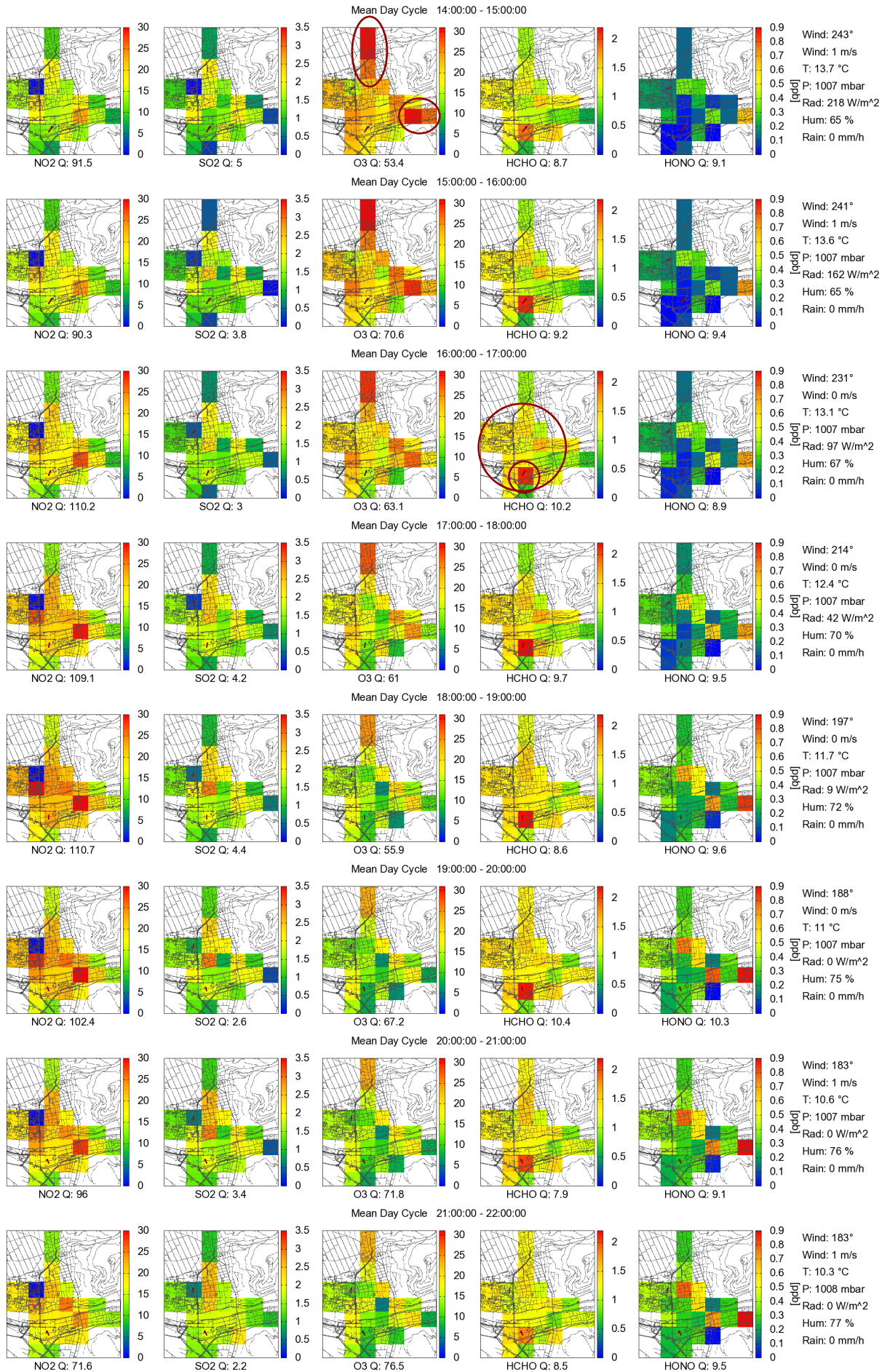
HCHO had a clear maximum in the late afternoon and a clear minimum before sunrise. The direct emission by fossil fuel combustion led to increased values in the morning and evening. The cycle of NO<sub>2</sub> can be used as indication of direct emissions. The photochemical oxidation of NMHCs at sunlight led to a maximum during the day. As HCHO is also photolytically destroyed, the maximum was shifted to evening hours when still emission and production arose, but solar radiation was reduced. The long lifetime of HCHO during the night led to only slowly reduction of concentrations due to mixing of air masses. The spatial distributions displayed only a small spatial characteristic. The increased concentration arose in the centre of the investigation area (highlighted for 16:00 to 17:00). A concentration peak at the HD-Druck instrument (see Figure 6-4) may indicate a regular local emission.



# CHAPTER 8



# TOMOGRAPHIC MEASUREMENT RESULTS



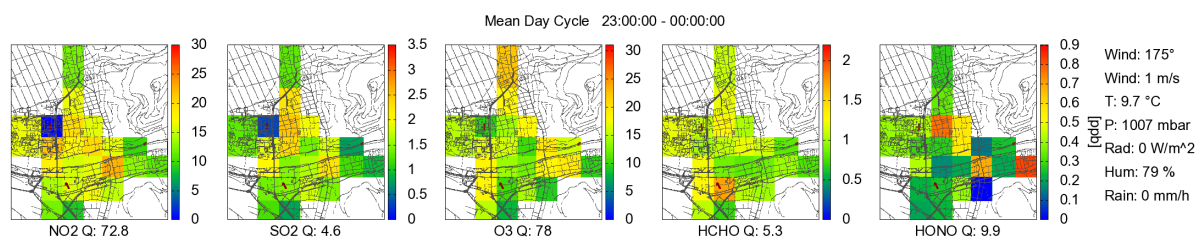


**Figure 8-36: One hour averaged mean daily cycle of reconstructed trace gas distributions of all tomographic measurements. Main spatial features are highlighted with maxima in dark red and minima in light blue. For labelling see Figure 8-3. Distributions feature a characteristic distribution with the mean daily cycle. For details on the distributions see main text.**

SO<sub>2</sub> also features a daily cycle. The mean values for the different light paths show a very strong variation. The point is that SO<sub>2</sub> concentrations are dominated by single strong concentration events and only to a minor extent caused by regular local emissions. Averaging over several very different single SO<sub>2</sub> events gives a non homogeneous time series. The mean daily cycle displays a maximum in the morning with enhanced values up to the early afternoon and a second small peak in the late afternoon. They are due to power plant, small heating systems and traffic emissions. The spatial distributions show up a low characteristic, as the observed SO<sub>2</sub> peaks were very different. One clear peak could be observed in the North (highlighted for 7:00 – 8:00). This enhancement had its origin in the RWE power plant close by (see Figure 6-4, Chapter 8.14).

## 8.8 Mean Weekly Cycle

The weekly cycle in trace gas concentrations displays the change of anthropogenic emissions and its influence on atmospheric chemistry. As solar radiation is the same for working days and weekend, photochemical processes are only influenced by emitted pollutants. Figure 8-37 shows the mean weekly cycle of all LP-DOAS measurement data. For all trace gases a dependency on the day of the week is observed. The corresponding trace gas reconstructions are displayed in Figure 8-38. As the measurements were performed in the months from September to March, the weekly cycle is representative for this period and not for the summer. The weekly cycles are changing over the year as changes in the meteorology, photochemistry and emission sources arose. An additional example for a warm September is shown in the *Appendix 12.7*.

First of all, the averaged weekly cycle of the whole period is discussed. It showed minimum emissions on Sundays, due to a minimum of NO<sub>2</sub> concentrations and a maximum of O<sub>3</sub>. NO<sub>2</sub> levels increase on Monday and rise until Friday as more and more emitted trace gases accumulate. On Saturday reduced emissions led to a concentration reduction. Accordingly O<sub>3</sub> decreased from Monday to Friday where it reached the minimum and on Saturday concentrations increase again.

mean weekly cycle

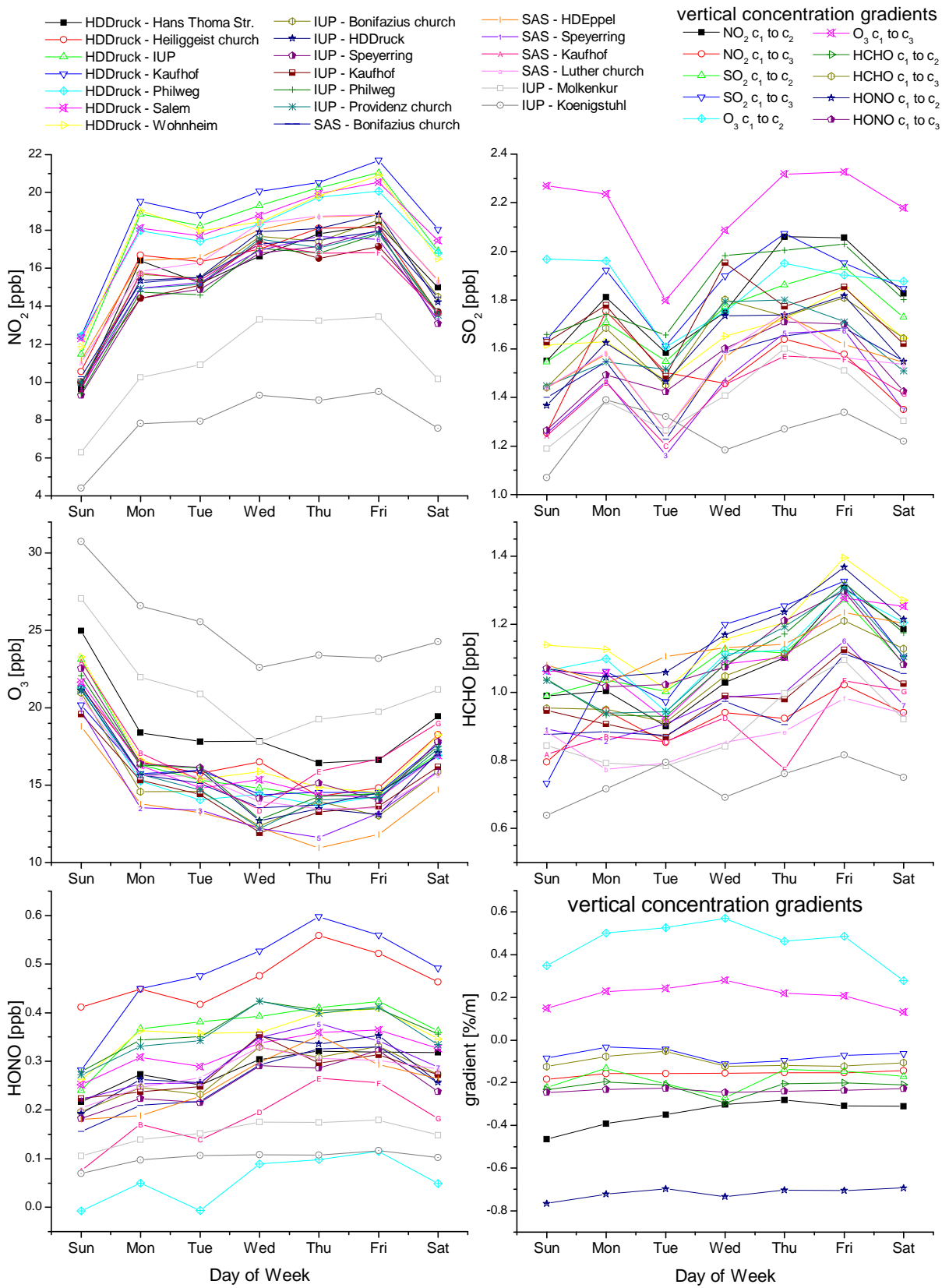


**Figure 8-37:** Weekly averaged cycle of all LP-DOAS data for the whole measurement period. Vertical concentration gradients are observed from the profile retrieval. Light paths to higher altitudes (Molkenkur and Koenigstuhl) displayed very different concentrations and thus very strong vertical gradients arose. The gradient is retrieved from the determined concentration at different altitudes for box c1 (instrument height) to c3 (below Koenigstuhl) (Chapter 7.3). Positive gradients imply increasing concentration with altitude and negative decreasing. For details on the trace gas cycles see main text.

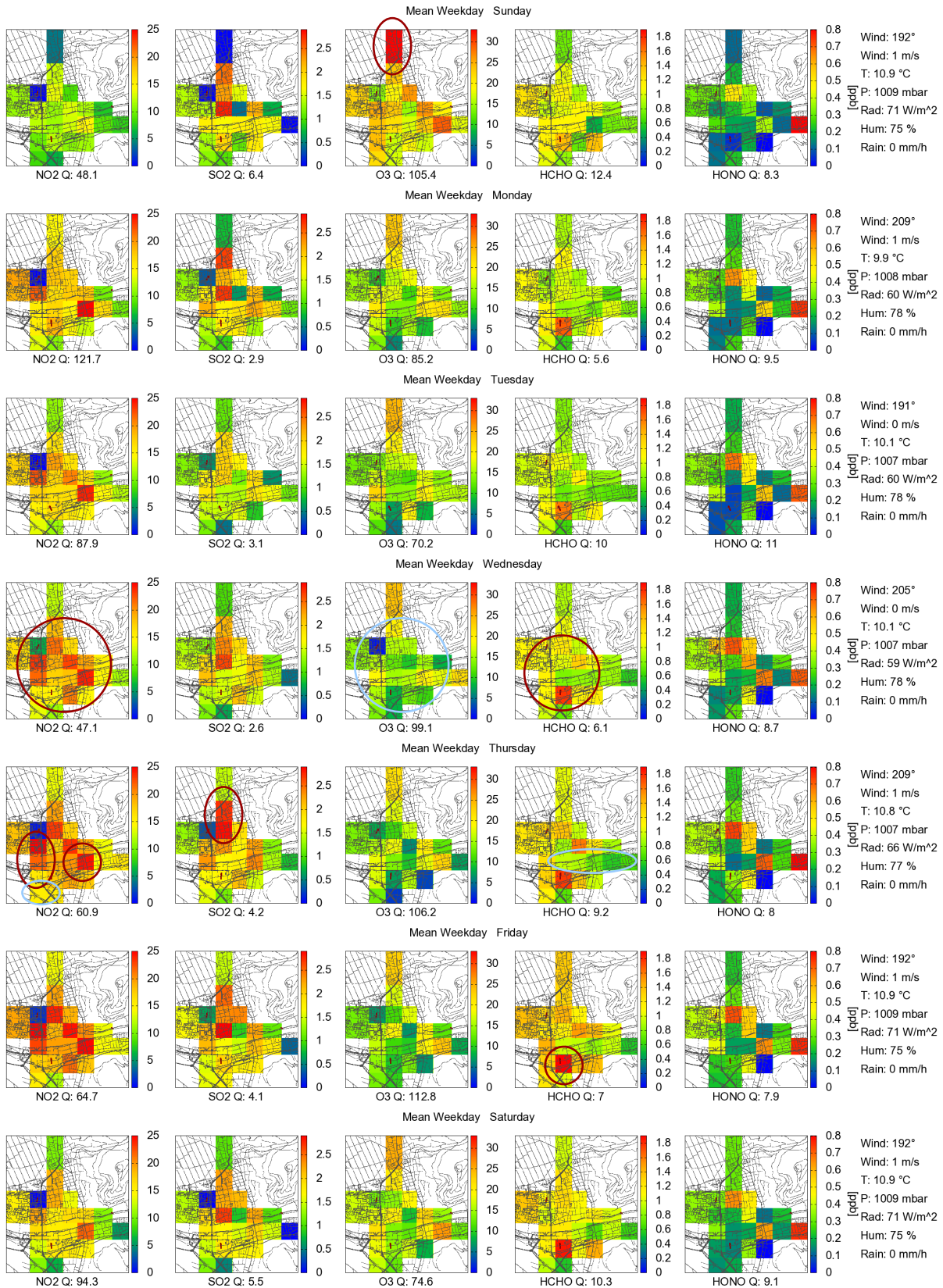


**Figure 8-38: Mean weekly cycle of reconstructed trace gas distributions of all data. Main spatial features are highlighted with maxima in dark red and minima in light blue. For labelling see Figure 8-3. Concentrations are characterised by the weekly behaviour of residence. Week days display high emissions due to increased traffic and industry activity. Weekends are characterised by low emissions. For details on the distributions see main text.**

The derived distributions display the same pattern as for the time series. Highest NO<sub>2</sub> values arise in the centre and lowest in the North and East (highlighted for Wednesday). The local maxima are located to the main streets over the Neckar (highlighted for Thursday). The minimum in the South in the area of the railway can also be clearly identified even if it is located close to the city centre. Ozone displays the opposite distribution with lowest values in the centre and highest at the border. The maximum can be located to the North, the area furthest from the city centre.

The observed weekly cycle of NO<sub>2</sub> and O<sub>3</sub> correlate well with the characteristic routines of German residents in service dominated industries like present in Heidelberg (*Chapter 6.1*). They work during the week, and not at weekends. On Saturday still many people use the car to travel to the city. On Sunday much lower traffic arises and thus also emissions are reduced. As Heidelberg has only little industry which works on a 24 hour basis, no or only low industry emissions are present on the weekend.

HONO displays a similar cycle as NO<sub>2</sub>, as it is mainly formed by heterogeneous reactions from NO<sub>2</sub>. As this reaction does not occur immediately, the rise in HONO levels at the beginning of the week is slower than that of NO<sub>2</sub>. The distributions of HONO do not give much information. The relative variances of the averaged data was too small and below the measurement accuracy. The HCHO weekly cycle display maximum concentrations on Friday. Even if this is in correlation to NO<sub>2</sub>, the weekly cycle does not display a clear minimum during the weekend nor an increase on Monday. Thus on average, directly emitted HCHO does not dominate the weekly cycle. This is the case for the accumulation of emitted VOCs which lead to photochemical production of HCHO during warm and sunny days. The distribution shows that the enhancement is located in the West (highlighted for Wednesday), but without direct correlation to the NO<sub>2</sub> distribution. A concentration minimum showed up along the river Neckar and in the Old Town in the East (highlighted for Thursday). A locally increase can be seen close to the HD-Druck instrument (highlighted for Friday) and might be due to emissions from the printing exposition or the municipal power plant.

SO<sub>2</sub> displays a concentration minimum on Tuesday. The reason remains unclear, but may arise from regular procedure in a power plant or other industry. As it is shown that high SO<sub>2</sub> concentrations are transported from the South to the city and may arise from industry emissions (Heidelberger Zement, *Chapter 8.11*), working routines influence the absolute emissions. It is speculated that on Tuesdays a regular interruption of the production due to maintenance etc. is responsible for the reduction. The spatial distribution displays a concentration maximum in the North close to the RWE power plant (highlighted on Thursday).

The weekly cycles for a warm September day in 2006 feature different characteristics (*Appendix 12.7*). Photochemical activity is higher than for the absolute mean values which are mainly winter data. But as only 2.5 weeks of measurement were performed in September 2006 the averaged values still contain a meteorological change. Monday and Tuesday are colder and display more stable PBL than the other week days.

## 8.9 Mean Annual Cycle

The annual cycle displays the change in emissions, photochemistry and meteorology during the year. Winter days are characterised by cold temperatures and often a stable PBL, whereas in summer photochemistry is very active. No tomographic summer measurements could be performed, but summer data were included for the IUP instrument to complete the annual time series. Only data is missing for April and May. All data is used in order to give the yearly cycle overview in Figure 8-39. For periods of tomographic measurements the retrieved distributions are displayed in Figure 8-40.

Photochemistry and stability of the PBL dominate the variation in concentration.  $\text{NO}_2$  and  $\text{SO}_2$  displayed the highest concentrations in winter when often a stable PBL arose and emissions were trapped. The lowest concentrations arose in summer when the PBL is instable, emissions from heating are much lower and also photolysis converted  $\text{NO}_2$  to  $\text{NO}$  during the day. The spatially highest concentrations of  $\text{NO}_2$  were always located in the centre of the investigation area with maxima at the main streets (highlighted for March and December) or in the North close to the RWE power plant (highlighted for November and December). The latter did also show increased  $\text{SO}_2$  levels.

$\text{O}_3$  shows the opposite annual trend. In winter it was destroyed and due to the stable PBL air masses not mixed with background  $\text{O}_3$  concentrations. In summer photosmog was responsible for highest  $\text{O}_3$  levels. Spatially the lowest concentration in winter was located in the centre of the investigation area where  $\text{NO}_2$  is highest (highlighted for December). Maxima arose at the city border, especially in the North. This was also the case for warm sunny months where  $\text{O}_3$  was formed photochemically (highlighted March). Due to the different lifetimes of  $\text{NO}_x$  and VOCs, the  $\text{O}_3$  maximum was located typically downwind, or at least outside the emission area (see *Chapter 2.2*).

The HONO cycle was correlated to  $\text{NO}_2$ . Due to lower  $\text{NO}_2$  concentrations in summer, also HONO formation and thus concentrations were lower. Additionally, the unstable PBL increased the air mass mixing and reduced HONO levels. The spatial distributions did not contain useful characteristics as averaged concentration differences between the light paths were much smaller than the measurement accuracy. Thus, no reliable reconstruction of the distribution was possible with these mean values.

HCHO displayed the highest concentrations in summer when it was created by photochemical oxidation of NMHCs. The maxima are located in the centre and in the North (highlighted for September).

mean annual cycle

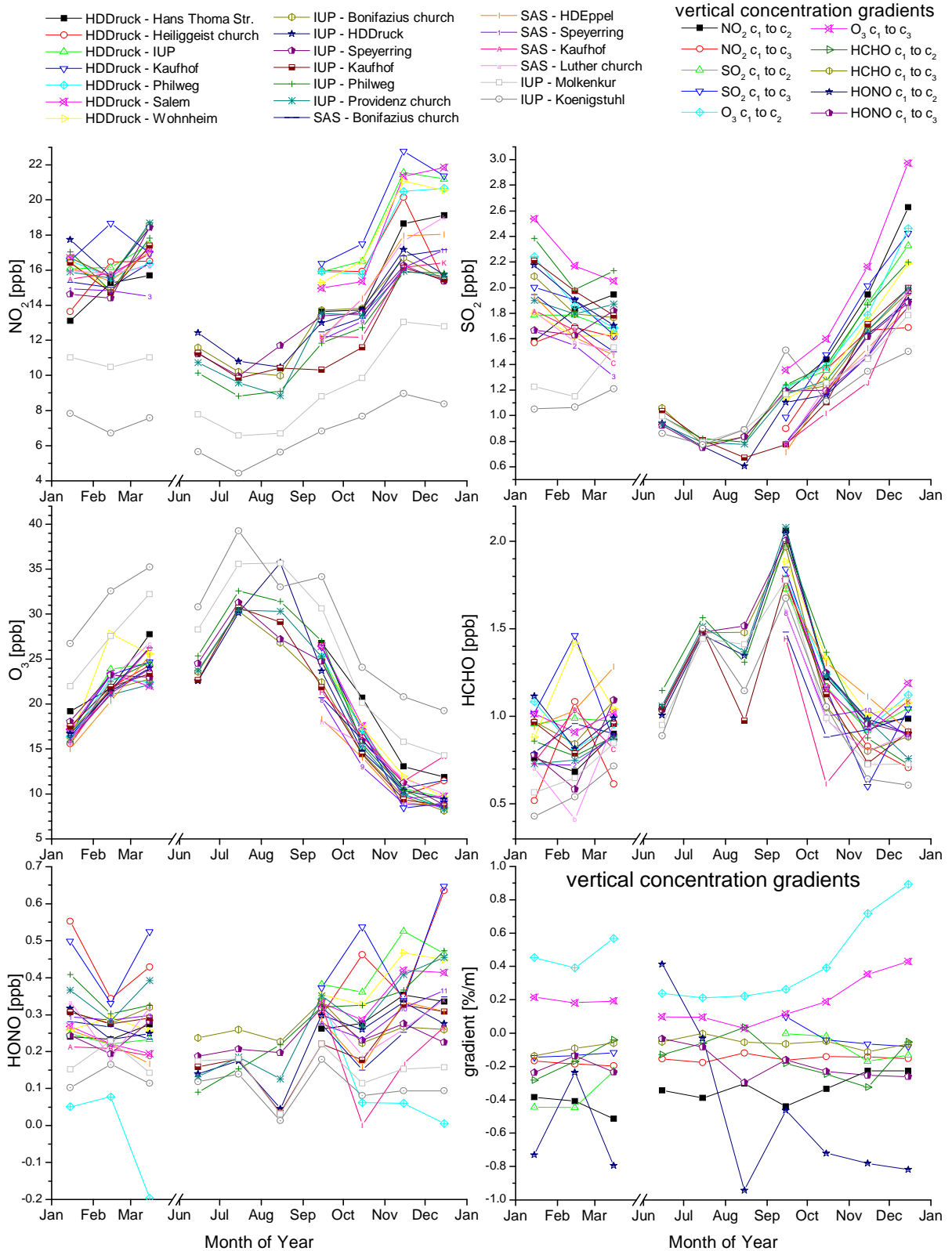


**Figure 8-39: Annual averaged cycle of all LP-DOAS data for the whole measurement period (September 2005 to February 2006, September 2006 to March 2007 and June 2007 to August 2007). Vertical concentration gradients are observed from the profile retrieval. Light paths to higher altitudes (Molkenkur and Koenigstuhl) displayed very different concentrations and thus very strong vertical gradients arose. The gradient is retrieved from the determined concentration at different altitudes for box c1 (instrument height) to c3 (below Koenigstuhl) (*Chapter 7.3*). Positive gradients imply increasing concentration with altitude and negative decreasing. For details on the trace gas cycles see main text.**

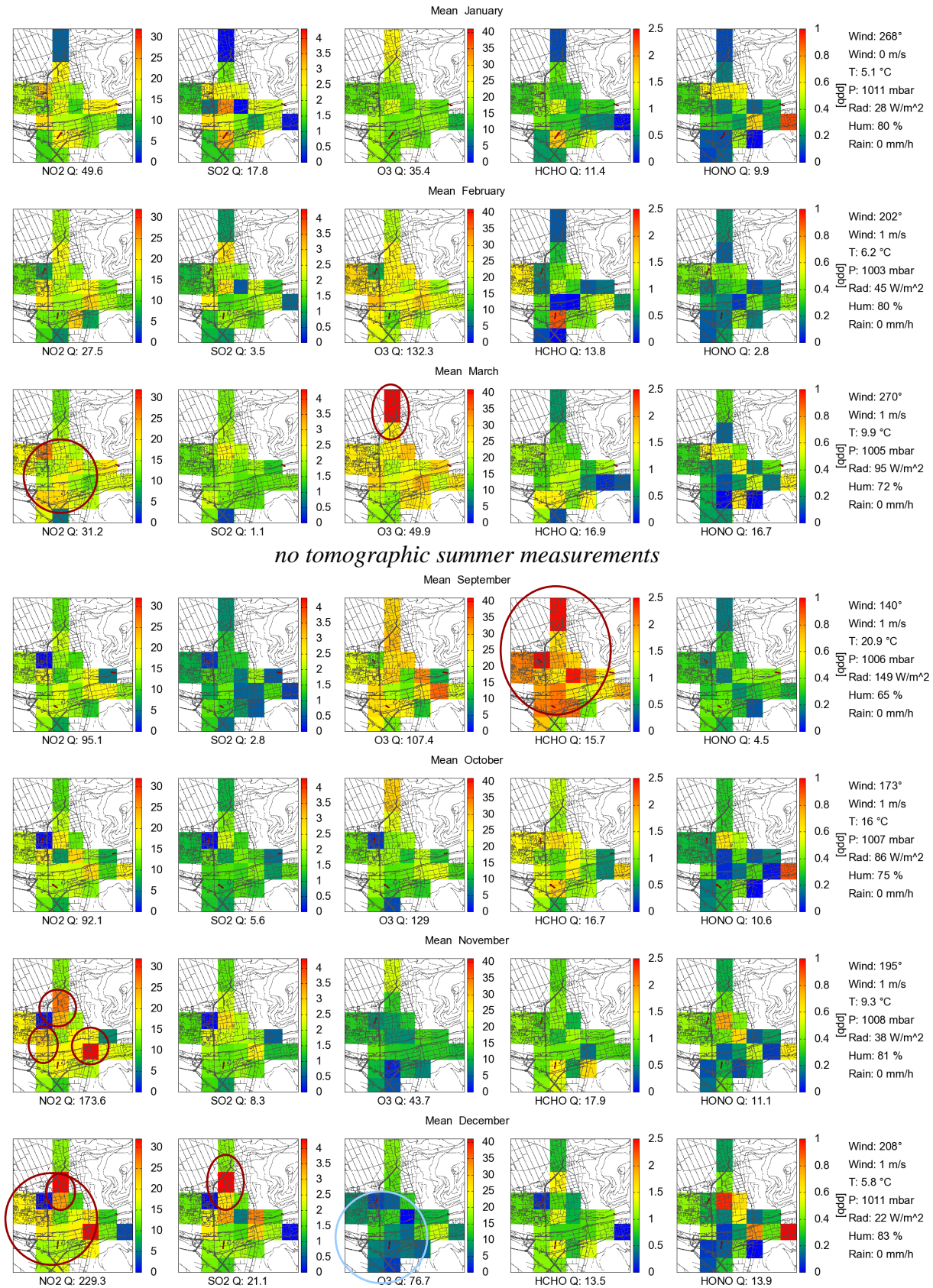


**Figure 8-40: Mean annual cycle of reconstructed trace gas distributions of all data. Main spatial features are highlighted with maxima in dark red and minima in light blue. For labelling see Figure 8-3. Strong variations for the different months are found for the absolute concentration and the distribution as also the emission sources are changing. For details on the distributions see main text.**

## 8.10 Trace Gas Profiles

The profiles of the different trace gases are derived from the measurements of absorption light paths to different altitudes according to *Chapter 7.3*. They represent the concentrations at different altitudes divided in three boxes:  $c_1$  40 to 45 m,  $c_2$  45 to 209 m and  $c_3$  209 to 498 m above ground. The derived trace gas profiles for January 2007 are displayed in Figure 8-41. All other profiles are found in digital form on the Data DVD (*Chapter 8.16*).

The derived profiles are used in order to determine the vertical concentration gradient, a marker for the change in concentration per m in height. The profile is therefore linear interpolated between the box centres. This is only a rough estimation, but sufficient to indicate concentration variances with height.

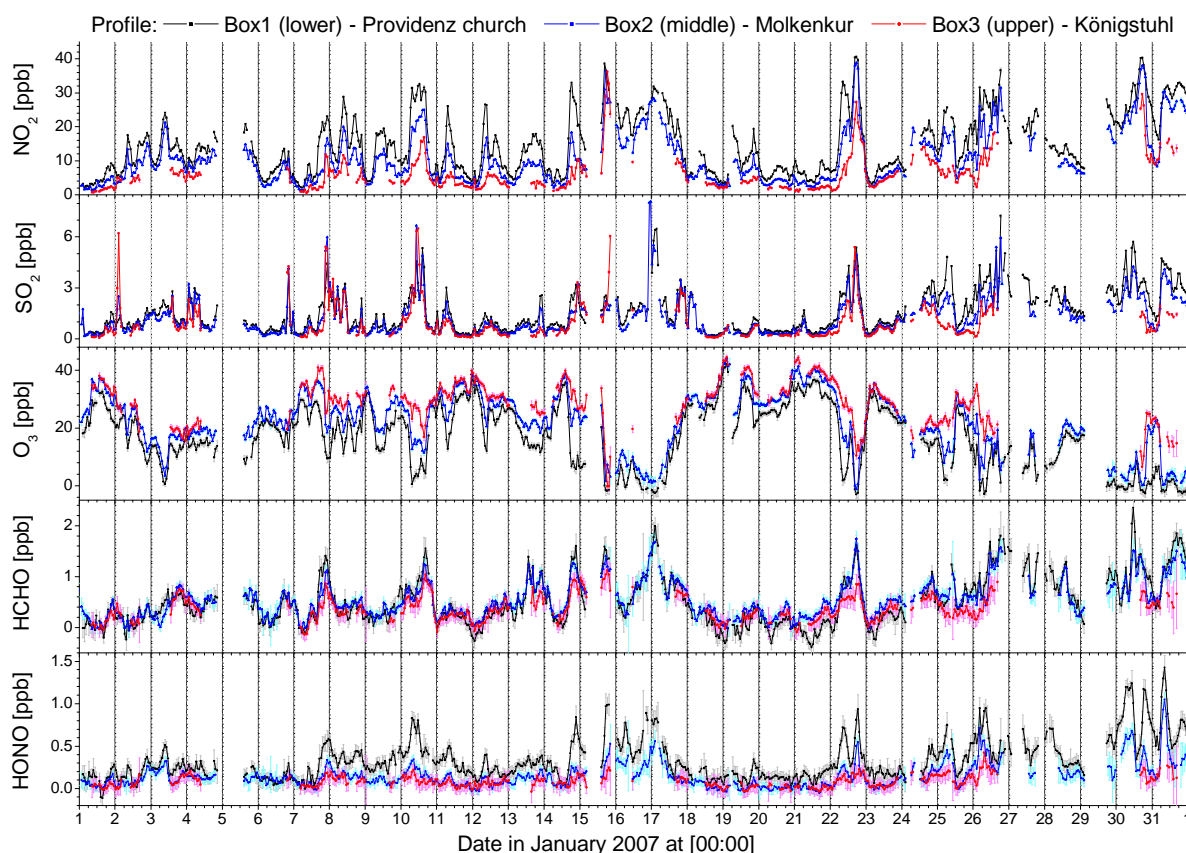


**Figure 8-41: Retrieved vertical trace gas profiles for January 2007. Concentrations are determined for three different boxes defined in *Chapter 7.3*. Stable PBL conditions lead to strong gradients and thus accumulation of emitted pollutants at the ground. Trace gases formed at the ground (HONO) display the strongest gradient. Depletion of  $O_3$  at the  $NO_x$  emission source at the ground led to increasing concentrations with altitude. If pollutants are emitted into higher altitudes (e.g. a stack) the higher altitude displays higher concentrations like for  $SO_2$ .**

During cold winter days at low wind speeds a stable PBL forms. Thus air masses and emitted trace gases are trapped close to the ground and result in high concentrations in the city. Higher layers are decoupled from urban emissions and will feature much lower concentrations. A strong vertical concentration gradient can arise like shown in Figure 8-41 for several days. Strong variations in  $NO_2$  concentration were present for the three altitudes in the period from 8<sup>th</sup> to 15<sup>th</sup> January. Emitted trace gases like  $NO_x$  are trapped and result in high  $NO_2$  and low  $O_3$  concentrations at the ground (Box 1) and a strong decrease to higher altitudes (Box 2 and

Box 3). HONO even features a much stronger gradient as it is expected to be formed heterogeneously on surfaces and thus localised close to the ground. SO<sub>2</sub> displays only a low gradient, as the main sources are not localised to the street level. Often even higher concentrations arose at higher altitudes. This correlate with the tomographic results in *Chapter 8.5* and *8.11*, where the main sources were estimated to be power plants and industry (Heidelberg Zement), both emit SO<sub>2</sub> with a stack directly to higher altitudes. In winter HCHO also featured only a small vertical gradient. The HCHO may also be directly emitted by the same sources like SO<sub>2</sub>. In summer when HCHO is photochemical formed by the oxidation of NMHCs, an even lower gradient was observed.

The averaged trace gas profiles of the whole measurement period are displayed in Figure 8-44, where they are additionally separated for different wind directions. Strongest gradients are also found here for NO<sub>2</sub>, O<sub>3</sub> and HONO. Lower gradients arose for HCHO and SO<sub>2</sub>. Additionally the gradient for SO<sub>2</sub> strongly depended on the wind direction.

Besides the analysis of concentration gradients of the trace gases they were applied to study their influence on the derived horizontal tomographic concentration distribution due to the imperfect instrument setup. The tomographic retrieval assumes that the concentrations of the horizontal light path are not influenced by a vertical gradient. But as the tomographic measurements of 18 light paths were performed at slightly different heights due to different instrument positions and also different heights of the retro reflectors, systematic gradients can lead to systematic concentration differences and thus reconstruction artefacts. Examples of such derived vertical concentration gradients are given in Figure 8-34, Figure 8-37 and Figure 8-39. Typical values range from a positive gradient for O<sub>3</sub> of up to 1 %/m down to -1 %/m for HONO. The derived trace gas distributions were checked for the influence of the vertical concentration gradients. Therefore, spatial locations of very high and low retro reflectors were chosen which should be influenced most by the vertical gradient (see Table 6-1 - Table 6-3). Locations with lower reflectors should display higher concentrations of NO<sub>2</sub>, HONO and HCHO and lower for O<sub>3</sub>. The opposite way should be the case for higher reflectors. Even if gradients were up to 1 %/m, there influence could not directly be found in the reconstruction and no systematic correlation arose. This does not imply that these gradients do not influence the derived distributions, but it was concluded that no direct visible artefacts arose.

### ***8.11 Influence of Wind Direction on trace gas Concentrations and Distributions***

Wind influences the observed concentrations in mainly two ways. First, wind leads to turbulent mixing of air masses and thus a reduction of concentrations. If no wind is present and a stable PBL is formed, the emissions are trapped and pollutants increase. Second, transport of trace gases arise out of the city, but also other trace gases can be brought into the city. In order to study the concentrations and distributions for different wind directions, the measurement data was averaged according to the current wind directions observed at the IUP weather station. Wind directions are divided into North (315° to 45°), East (45° to 135°), South (135° to 225°) and West (225° to 315°). Situations with wind speeds below 2 m/s were accounted as calm. Averaging of measurement data was performed for the whole data set and

also separate for each month. Trace gas distributions were created for the different wind situations (Figure 8-42). For calm wind, the average wind speed for the same period as tomographic data was below 0.5 m/s, for the other directions 3 – 4 m/s.

Highest concentrations of NO<sub>2</sub>, SO<sub>2</sub>, HCHO and HONO are found during calm wind situations (Table 8-1). This clearly shows that emissions from sources in the city dominate the observed trace gas concentrations. Transport of pollutants from other sources like the industry in Mannheim and Ludwigshafen plays a minor role.

wind direction	NO <sub>2</sub> [ppb]	SO <sub>2</sub> [ppb]	O <sub>3</sub> [ppb]	HCHO [ppb]	HONO [ppb]
calm (< 2 m/s)	18.4	1.80	11.8	1.31	0.43
North	11.6	1.12	23.1	0.59	0.19
East	10.7	1.20	23.2	1.25	0.22
South	15.5	1.56	13.9	1.09	0.31
West	14.1	1.48	18.4	0.77	0.24

**Table 8-1: Mean concentration for the whole investigation area at different wind directions (Figure 8-42) used from the IUP meteorological station. Calm wind is defined by wind speeds below 2 m/s. Significant higher NO<sub>2</sub>, SO<sub>2</sub>, HCHO and HONO concentrations arose at calm wind. A slight increase is found for southerly and westerly winds in comparison to northerly and easterly.**

Northerly and easterly winds display lowest concentrations for NO<sub>2</sub>, SO<sub>2</sub> and HONO, where concentrations are almost two times smaller than for calm wind situations. For wind from South and West also increased concentrations are observed, but still significantly below values for calm wind. Ozone displayed opposite highest concentrations for northerly and easterly winds with twice the concentration at calm situations. For southerly and westerly winds the concentration is also significantly reduced. HCHO displayed higher concentrations for easterly winds. The reason remains unclear. A possible explanation could be that warm measurement months (e.g. September 2006) often displayed easterly winds. Thus, warm and sunny days with high HCHO levels, due to photochemical oxidation of NMHCs, led to an increase of HCHO concentration for this wind direction.

For calm wind situations almost the whole measurement area displayed enhanced NO<sub>2</sub> values with maxima of 25 ppb. Only in the North at the city border and in the East in the Old Town lower concentrations down to 10 ppb were observed. SO<sub>2</sub> displayed a strong maximum close to the RWE power plant with an increase by 2 to 3 ppb. The emissions from the RWE stack can descent and reach the measurement altitude at low wind situations. O<sub>3</sub> was depleted according to the high NO<sub>2</sub> concentrations locally down to 0 ppb. In the North a maximum with 22 ppb is observed. HCHO showed high concentrations all over the measurement area with a slight local maximum at the HD-Druck instrument. This may arise from emissions from the printing exposition emissions there. In general HONO also displayed enhanced concentrations but with a maximum in the North also close to the RWE power plant. As the low mean concentrations were at the detection limit, this feature may arise from artefacts.

The derived trace gas distributions for the different wind directions displayed much lower concentrations with a homogeneous pattern. Turbulent mixing averages most spatial variability. Only few properties can still be observed.

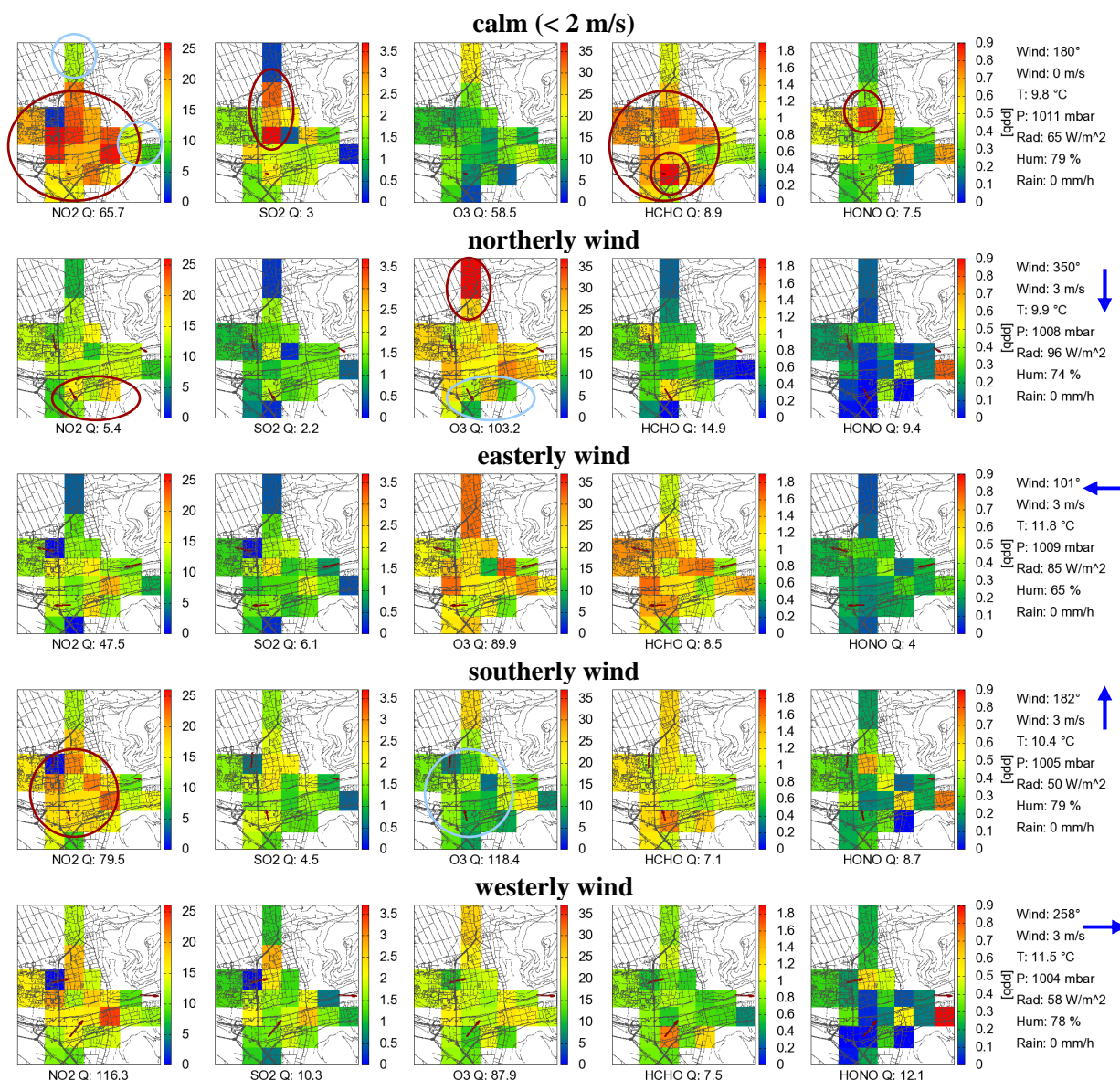


**Figure 8-42: Reconstructed trace gas distributions for different wind directions of all data. For the averaging of data the wind measurements at the IUP weather station were used. First row displays results for calm situations, if wind was below 2 m/s and the following rows reflect northerly, easterly, southerly and westerly wind. The averaged wind data is drawn in the map for all three weather stations. Main spatial features are highlighted with maxima in dark red and minima in light blue. For labelling see Figure 8-3. Highest concentrations of NO<sub>2</sub>, SO<sub>2</sub>, HCHO and HONO were at calm wind situations. A slight increase in NO<sub>2</sub>, SO<sub>2</sub> and HONO can be found for southerly and westerly wind.**

For northerly wind, low NO<sub>2</sub> concentrations were found. A small increase arose in the South due to accumulation of emissions, where also the O<sub>3</sub> minimum was located. The low NO<sub>2</sub> concentrations also resulted in a low HONO level. HCHO concentrations were also very low. For easterly wind except from HCHO similar low concentrations were found for the different trace gases.

Southerly winds displayed higher NO<sub>2</sub> and lower O<sub>3</sub> concentrations. South of the measurement area some city districts are located. In case of southerly wind, emissions of these areas can be blown to the measurement area. Additionally, industry located in the South may contribute to the increase. The largest emitter there is Heidelberg Zement in Leimen. An increase in SO<sub>2</sub> also indicates some additional emission sources in the South.

Westerly winds also displayed enhanced concentrations of NO<sub>2</sub> and SO<sub>2</sub>. NO<sub>2</sub> might be

transported to Heidelberg from the highway or even from the industrial centres in Mannheim and Ludwigshafen.  $\text{SO}_2$  might also arise from industry emissions.

Strong changes in trace gas concentrations between situations with and without wind are especially observed for winter months, where a stable PBL is formed if it is calm. In Figure 8-43 the distributions for January 2007 are displayed.

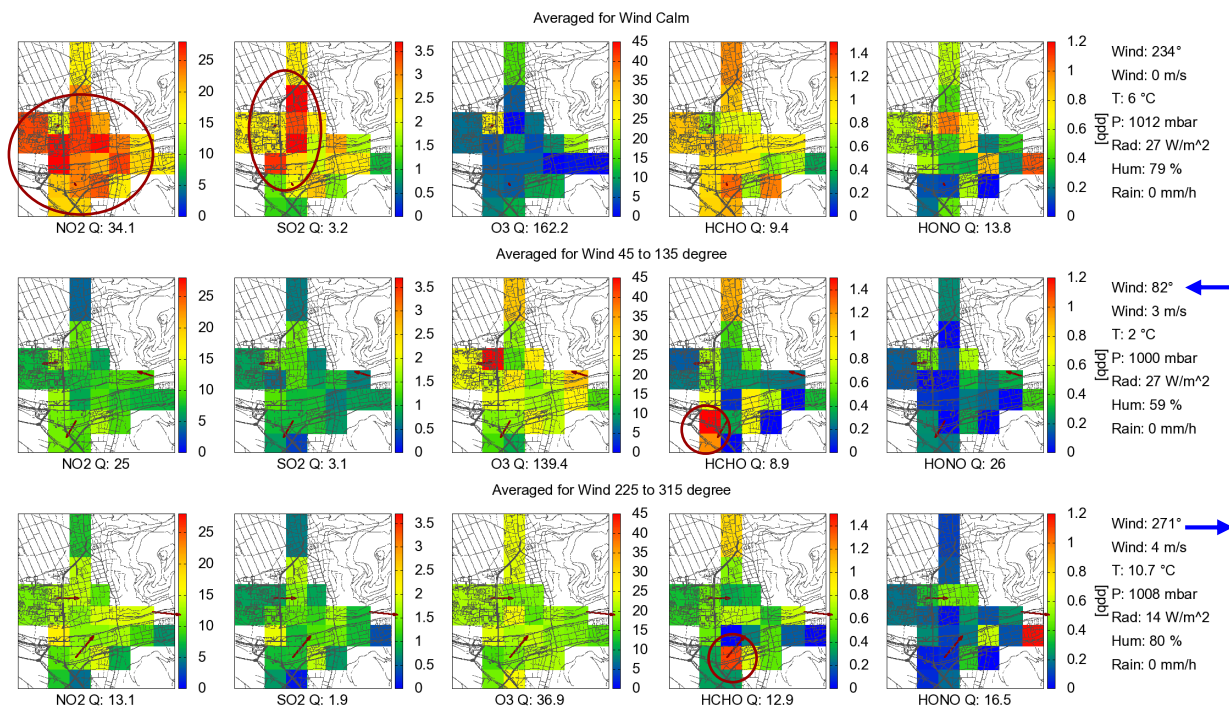


**Figure 8-43: Reconstructed trace gas distributions for no wind (< 2 m/s), easterly and westerly wind for January 2007. For the averaging of data the wind measurements at the IUP weather station were used. Main spatial features are highlighted with maxima in dark red and minima in light blue. For labelling see Figure 8-3. High concentrations of  $\text{NO}_2$ ,  $\text{SO}_2$ , HCHO and HONO with strong spatial variability are only found for calm wind situations when a stable PBL could be formed.**

The high concentrations from calm periods could not be found for easterly or westerly wind directions. Concentrations are slightly higher for westerly winds indicating the influence of an additional emission source as stated above. It is interesting to mention that a small maximum in HCHO, located at the HD-Druck instrument (highlighted), moves its maximum depending on the wind direction. For easterly winds it is located further in the West and opposite for westerly winds. This confirms the assumption of a local HCHO emission may be from the printing exposition.

In order to study the impact of external emission sources, the derived trace gas profiles for different wind directions were used. The results are displayed in Figure 8-44. For the lowest altitude ( $c_1$ ), where also the tomographic reconstructions were performed, like in the observed distributions in Figure 8-42, the highest concentrations were found for calm wind situations. The opposite is valid for  $\text{O}_3$ . Lowest concentrations for  $\text{NO}_2$ ,  $\text{SO}_2$  and HONO arise for northerly and easterly winds. Higher concentrations arise for southerly and westerly winds due to impact from industry and the highway.  $\text{O}_3$  displays the opposite pattern. HCHO featured the maximum for easterly and southerly winds.  $\text{NO}_2$ ,  $\text{O}_3$ , and HONO display the same concentration profile for all wind directions or if no wind arose.

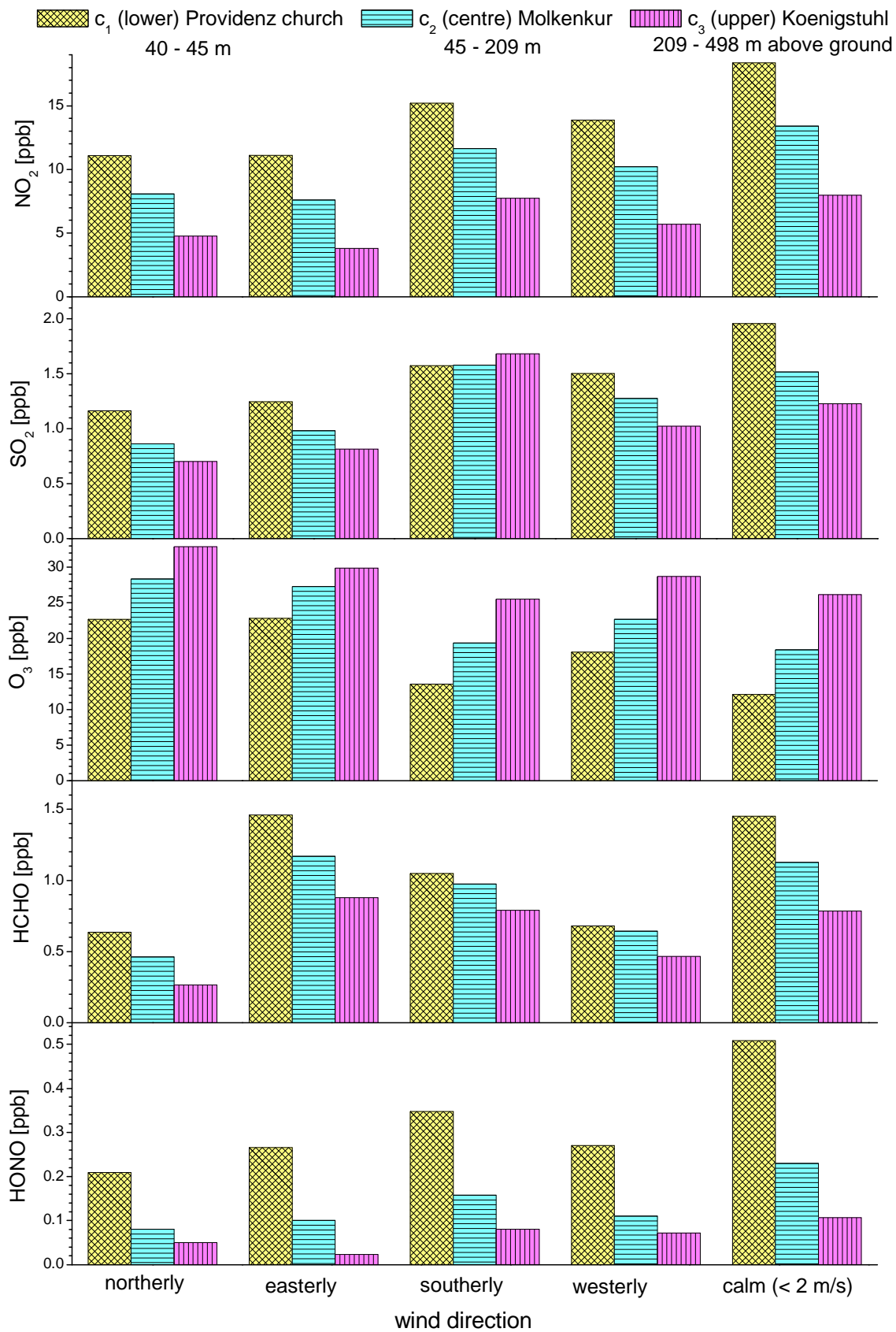


**Figure 8-44:** Trace gas concentration profiles for different wind directions derived according to *Chapter 7.3*. Highest accumulation of pollutants arose for calm situations. Northerly and easterly winds displayed lowest concentrations for NO<sub>2</sub>, SO<sub>2</sub> and HONO. But differences for different altitudes arose. For southerly winds SO<sub>2</sub> displayed highest concentrations at higher altitudes, else in the lowest altitude. HCHO concentration and profile also changed strongly with wind direction.

SO<sub>2</sub> had different characteristics where highest concentrations could be observed for c<sub>3</sub> and c<sub>2</sub> at southerly winds. The concentrations in these layers are even higher than for no wind situations. The concentration gradient was inverted with highest concentrations at higher altitudes. This indicates that a major SO<sub>2</sub> source was located in the South and directly emitted into higher altitudes like an emission stack. Two emitters can be responsible. First, the municipal power plant within the tomographic investigation area (see Figure 6-4) and second, the Heidelberg Zement manufactory in Leimen, 7 km south of the city centre. The first one does not operate most of the time and is therefore unlikely to be responsible for this increase. The stack from the Heidelberger Zement production facility continuously emits trace gases and thus also likely SO<sub>2</sub>.

### ***8.12 Comparison with In-Situ Monitors***

The comparison of the retrieved trace gas distributions with local measurements is important to prove the accuracy of tomographic results. The derived local concentrations from the tomographic measurements should correlate with local measurements. Measurements of in-situ monitors and thus point measurements can be used for comparison. But it has to be considered, that these measurements do not necessarily represent the concentration of an area of few 100 m by 100 m like a reconstruction box of the tomographic retrieval. Strong spatial variances of the concentration can already arise on these scales. The retrieved concentration from tomographic observations represents the average for the box. Thus, in-situ and tomographic results can vary significantly. Additionally, the monitors should be located at the same height of the tomographic measurements. This is of course difficult, as the tomographic setup is located about 30 to 50 m above street level, and typical atmospheric measurement stations are located at street level. The same is true for the LUBW measurement station at Berliner Strasse, close to the IUP (see Figure 6-4). They measure NO, NO<sub>2</sub>, O<sub>3</sub>, SO<sub>2</sub> (until 2006) and PM10. Concentrations are much more influenced by direct emissions of vehicles. The strong vertical gradient leads to significant concentration variations. The location of this station is covered by the reconstruction grid, but in fact this box is only poorly determined as only the light beam from the IUP instrument crosses this box further in the South (see Figure 7-12). Due to all these facts, it was not expected to receive a one to one correlation between both data sets, but the trend should be similar over time.

In order to compare tomographic measurement results, additionally, in-situ monitors of O<sub>3</sub> and NO<sub>2</sub> were operated at the IUP roof. The monitors were located at the same height as the tomographic measurements. But due to the location of the IUP on the campus without emission sources the concentration may not be representative. Unfortunately, both monitors did not optimally operate during the campaign. The monitors could not be calibrated. Old calibration data from 2005 was applied. The NO<sub>2</sub> converter of the NO<sub>2</sub> monitor had a failure in December 2006 and continued to run only with a much smaller conversion than calibrated. This error was only observed after the campaign. Thus, only part of the data could be used. The O<sub>3</sub> monitor had also some problems. Several times malfunctions arose in winter 2005/06. After a complete maintenance of all compounds in summer 2006, the monitor continued to run again without problems, but the data showed that a complete offset in the concentration arose, as the lowest observed concentration was 6 ppb, even if other measurements observed 0

ppb. Therefore, the comparison to these monitors is difficult as it is not clear, if they display a reliable concentration.

Besides problems of the in-situ monitors also errors in the tomographic data results have to be considered like reconstruction artefacts. If systematic errors arise at one location, the results can still be correct for other areas. Especially reconstruction boxes at the border of the reconstruction field or with only few crossing light beams are affected. Indications for systematic reconstruction errors could be found for the reconstruction box at the IUP (*Chapter 8.2.4*) where both in-situ measurement stations are located. A comparison makes only sense during periods when these errors did not emerge. Alternatively, the neighbouring box located at the same street can be used. Both methods were applied.

### 8.12.1 Comparison for NO<sub>2</sub>

In Figure 8-45 and Figure 8-47 time series of NO<sub>2</sub> data of both in-situ monitors and the derived tomographic NO<sub>2</sub> concentrations are plotted. Data is included from the monitor, tomographically retrieved concentrations at the same location, in the neighbouring Berliner Strasse and in the city centre (Bismark Platz). All time series display the same characteristics. Differences are observed in the minima and maxima. The concentrations from tomographic measurements often feature higher levels. This can also be found in the correlation plot of Figure 8-46 and Figure 8-48.

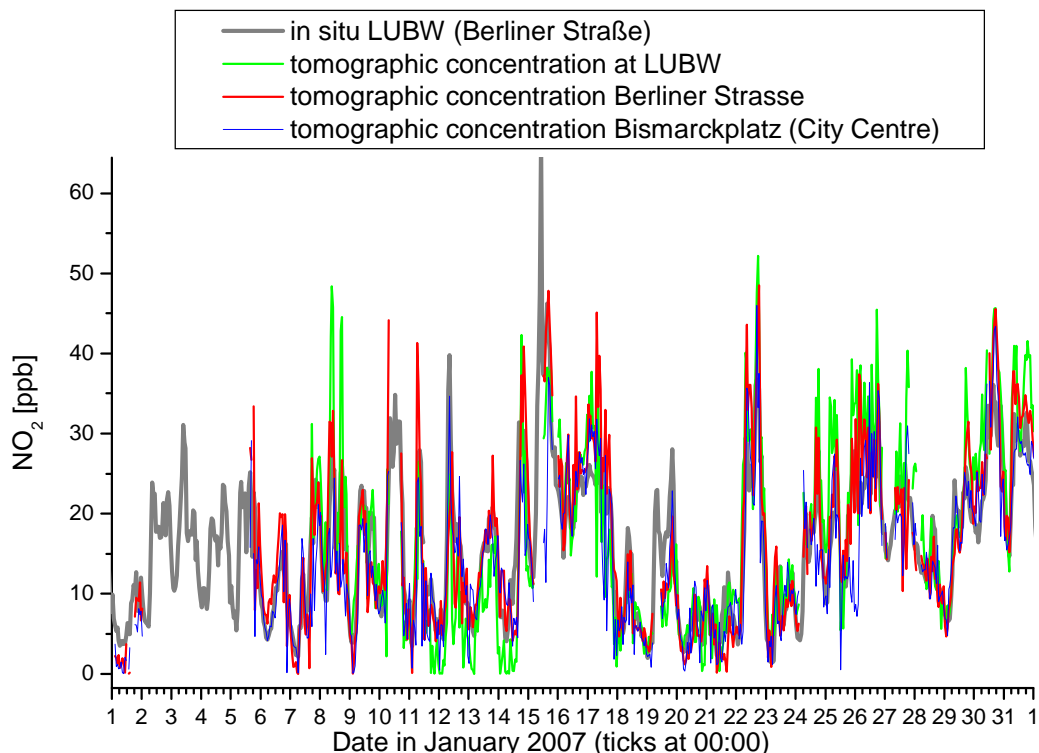


**Figure 8-45:** Time series of NO<sub>2</sub> in-situ measurements at the IUP and tomographic concentrations at the same location, the next box called Berliner Strasse and the city centre for February 2006. The time series show good agreement. The retrieved concentration at the LUBW is problematic due to arising tomographic artefacts. The data agree better with the neighbouring pixel of the Berliner Strasse. In the maxima, the in-situ monitor observes lower concentrations.

A good correlation for the LUBW in-situ monitor can be found in Figure 8-46 up to concentrations of 30 ppb. For higher levels the in-situ monitor displays lower concentrations. For January lower concentrations are expected at high levels close to the street level. Especially in winter, the NO emissions quickly deplete all O<sub>3</sub>. At high emissions, the NO may not completely be converted to NO<sub>2</sub> and only after the air is mixed with ozone rich air masses at higher altitudes it is formed. Thus, a slight increasing concentration arises up to few ten meters height.

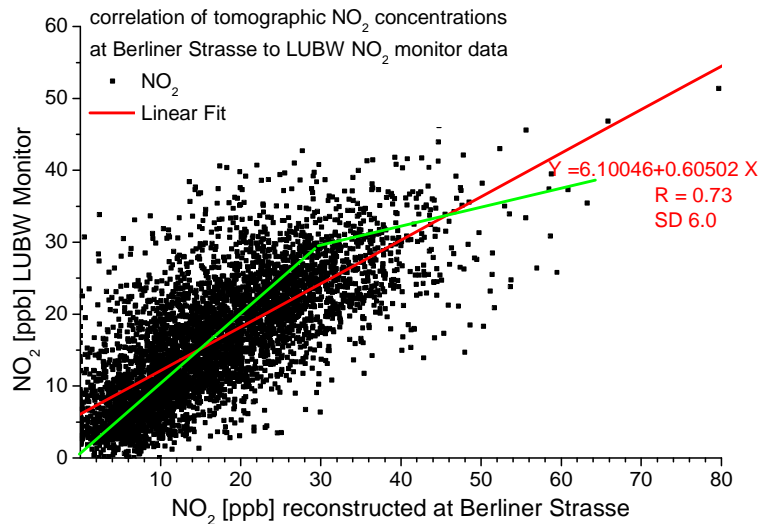


**Figure 8-46: Correlation of in-situ NO<sub>2</sub> data from LUBW with tomographic NO<sub>2</sub> at Berliner Strasse. The green line indicates the correlation up to 30 ppb and with smaller correlation factor for higher concentrations.**

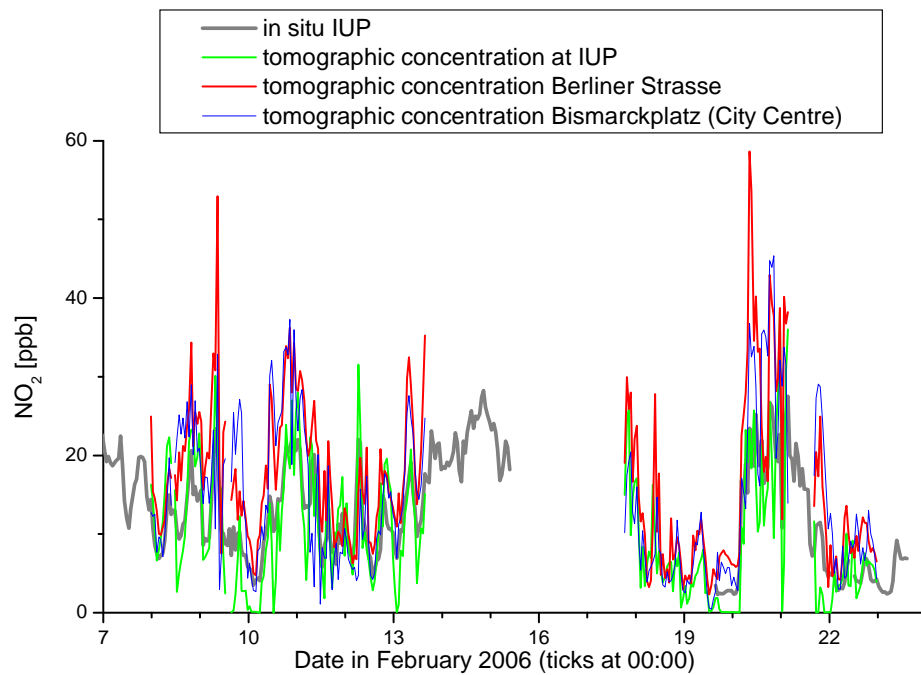


**Figure 8-47: Time series of NO<sub>2</sub> in-situ measurements of the LUBW and tomographic concentrations at the same location, the next box called Berliner Strasse and the city centre for January 2007. Time series show similar characteristic but with significant differences. They may be caused by the non representative location of this in-situ monitor.**

The comparison with the IUP in-situ monitor gives sufficiently good correlation (Figure 8-47, Figure 8-48), even if the concentrations are different which can arise due to the location of the in-situ monitor or a change in the calibration of the monitor.

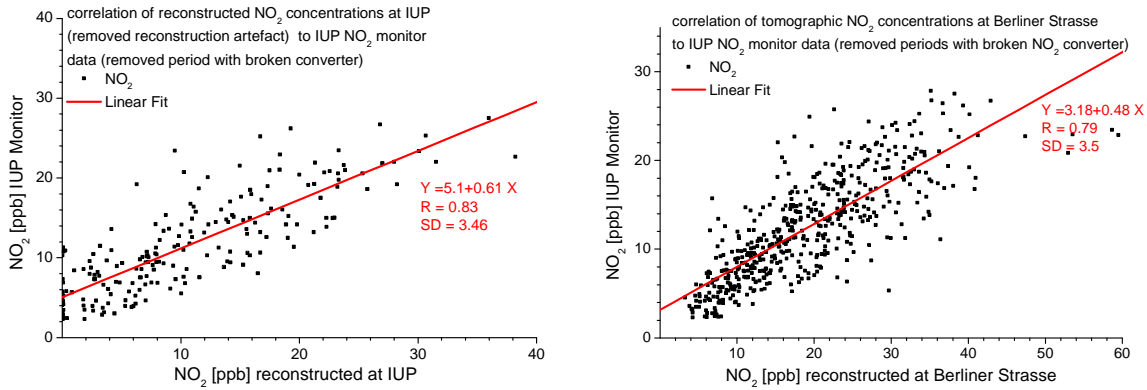


**Figure 8-48:** Correlation of in-situ NO<sub>2</sub> data from IUP with tomographic NO<sub>2</sub> at the IUP (left) with removed data of tomographic artefacts and to neighbouring Berliner Strasse (right). Data with broken NO<sub>2</sub> converter is removed. A sufficient good correlation was found but with very different concentrations. They may be caused by the in-situ monitor sampling site or from a change in the monitor calibration.

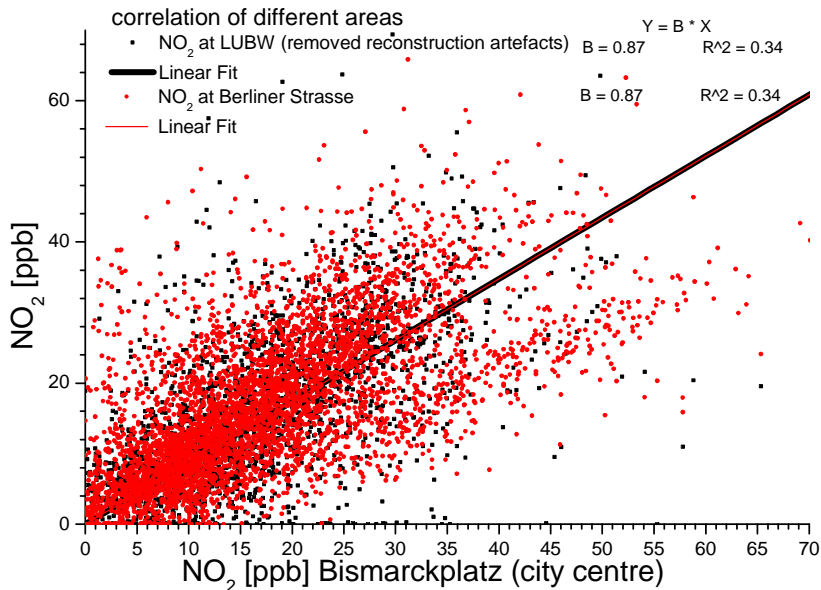


**Figure 8-49:** Correlation of retrieved tomographic trace gas concentration of NO<sub>2</sub> for Bismarckplatz in comparison to the LUBW (black) and to the Berliner Strasse (red). Both data sets have the same correlation. The concentrations at the LUBW and Berliner Strasse where the LUBW in-situ monitors are located are about 15 % lower than in the city centre.

A comparison of the concentration derived from the tomographic measurements for the city centre (Bismarckplatz), the location of the LUBW environmental measurement station or Berliner Strasse shows that the concentrations in the city centre observed from the tomographic measurements are higher by on average 15 % (Figure 8-49). The peak concentrations can even be up to two times higher. However, the derived concentrations at the Berliner Strasse are also one of the highest in the observed area. Still it can be concluded that the monitored concentrations might not be representative for the city. For environmental monitoring reasons, measurements in the city centre would be necessary. Strong emission

events may not be observed correctly. If especially in the city centre the concentrations are higher where many people can be found, dangerous exposures arise with risks for public health. This comparison of local concentration differences shows how important it is to monitor the real concentration distribution.

### 8.12.2 Comparison for O<sub>3</sub>

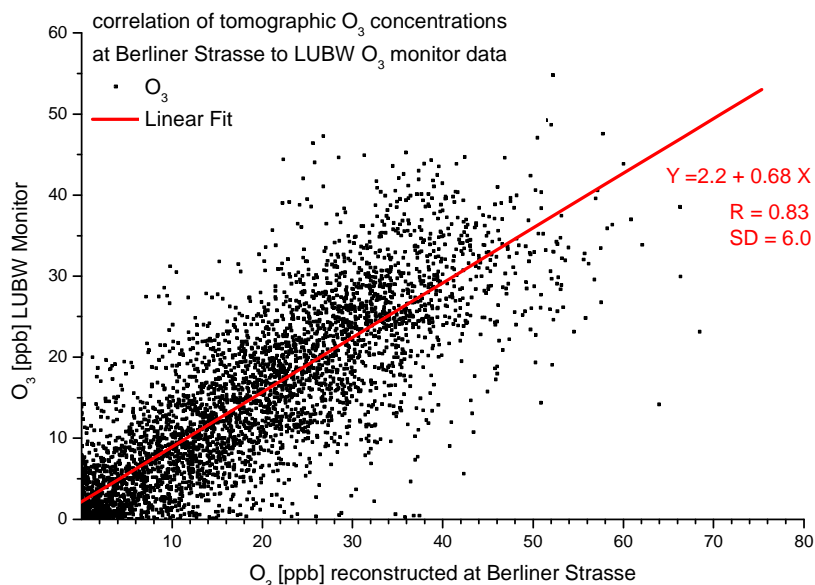


**Figure 8-50: Correlation of retrieved tomographic trace gas concentration of O<sub>3</sub> for Berliner Strasse in comparison to the LUBW.**

The correlation for tomographical retrieved O<sub>3</sub> to the LUBW in-situ monitor data displays the same concentration variations (not shown here). A good correlation is derived with higher concentrations of the tomographic retrieved values than the in-situ data (Figure 8-50). This is similar to NO<sub>2</sub>. So both, NO<sub>2</sub> and O<sub>3</sub> concentrations increased from street level to 45 m measurement height of the tomography. They may arise from the higher measurement location where a higher photo activity in summer takes place and better mixing with ozone rich air masses in winter occur when O<sub>3</sub> concentrations are depleted at street level. Thus both trace gases will increase with height.

### 8.12.3 Comparison for SO<sub>2</sub>

The correlation for SO<sub>2</sub> with the LUBW in-situ monitor displayed a different characteristic (Figure 8-51). A good correlation was found for low concentrations. For high concentrations the in-situ monitor at street level shows lower values. These are transported SO<sub>2</sub> plumes or emitted SO<sub>2</sub> at higher altitudes which do not reach the street level where the monitor was located.

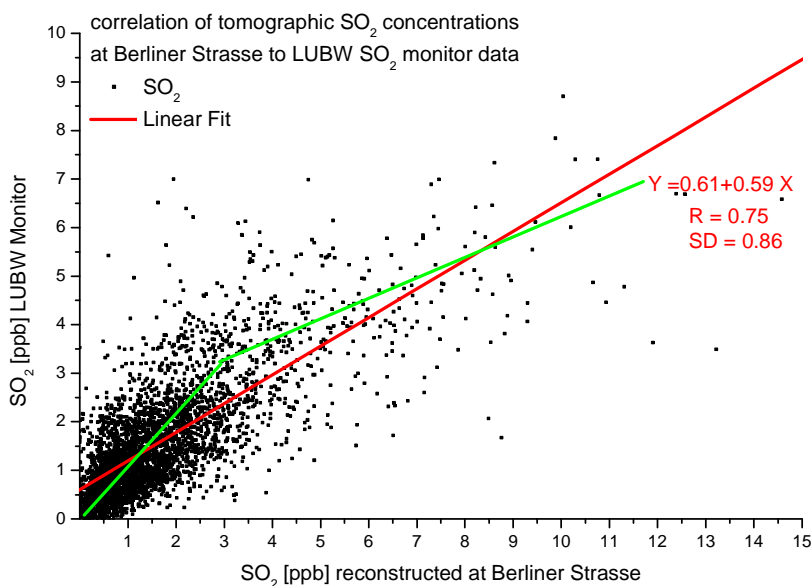


**Figure 8-51: Correlation of retrieved tomographic trace gas concentration of SO<sub>2</sub> for Berliner Strasse in comparison to the LUBW. The correlation displays two stages (green curve). One to one correlation for low concentrations due to sources close to the ground and much lower correlation for plumes with high concentrations transported to the city. The later are not mixed down to street level and the monitor observed lower concentrations.**

### 8.13 Comparison to Vehicle Measurements

Traffic is the main source of pollutants in Heidelberg. The influence of traffic emissions on trace gas distributions were discussed with the presented results. A direct comparison to the traffic load could give a clear correlation. In many streets so called induction loops can register the traffic load. Unfortunately, these data are not logged due to technical reasons. The city gains information on the traffic volume by manual counting of the cars for a special location for one day. Due to the effort, such counting is performed rarely. They were not realised when tomographic measurements were performed in Heidelberg. Thus, no direct correlation can be made.

Here a quantitative comparison is done between traffic load data for 23<sup>rd</sup> October 2007 at the crossing of Bergheimer Strasse and Mittermaier Strasse [Schlothauer and Wauer, 2009], close to the bridge passing the river Neckar in the West (see Figure 6-4). They were compared with tomographic averaged daily cycle data of NO<sub>2</sub> retrieved for the same crossing (Figure 8-52). The maxima of traffic load and trace gas concentration correlates very well. A small shift of the concentration peak to an earlier time for the morning and a later time for the evening rush hour arose due to photolysis of NO<sub>2</sub> during the day. The traffic emissions are the main source for the observed NO<sub>2</sub> daily cycle at this location.

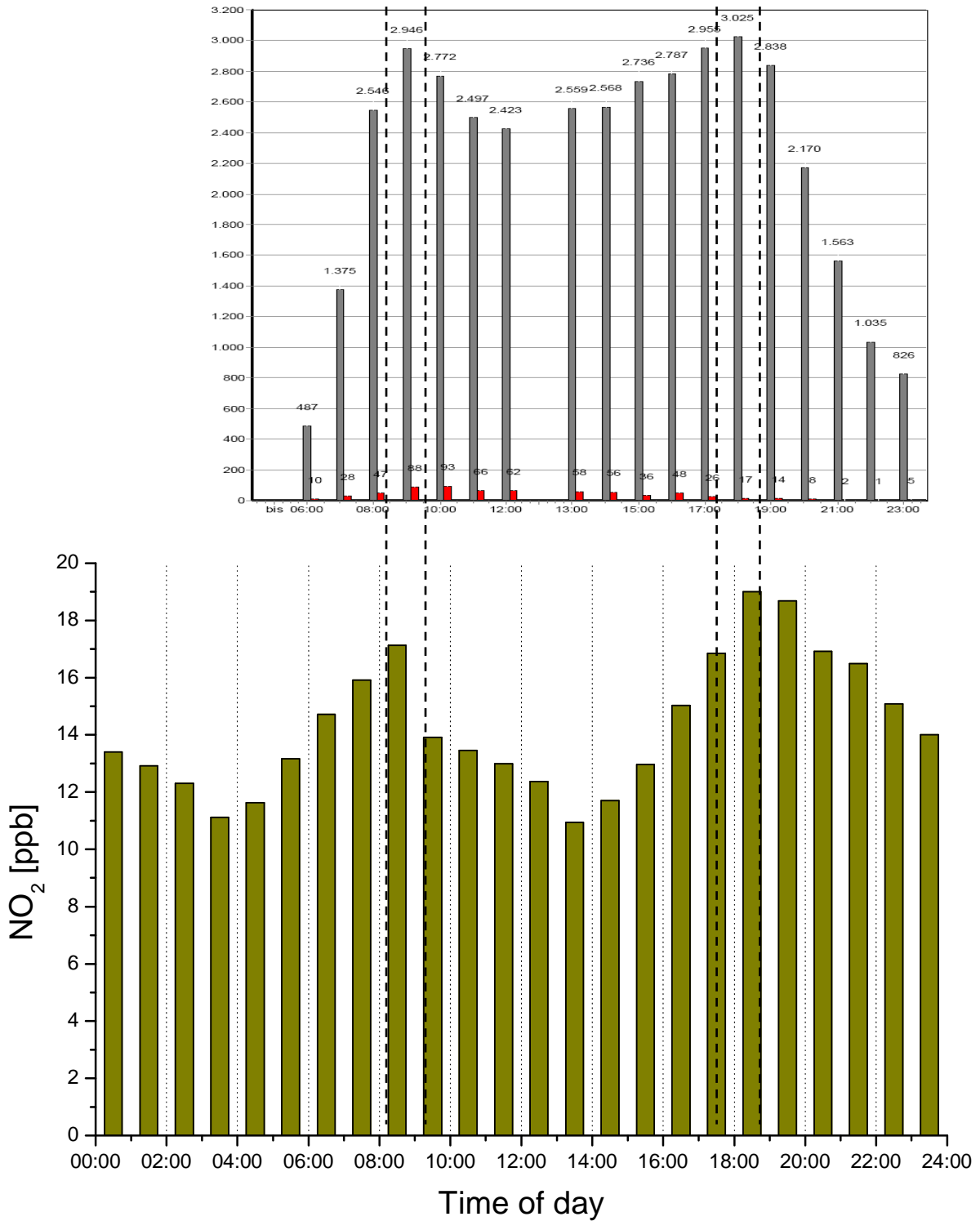


Figure 8-52: Traffic load data at the crossing of Bergheimer Strasse with Mittermaier Strasse on 23<sup>rd</sup> October 2007 (upper plot). Cars are in grey and trucks are in red. Tomographic trace gas concentration of NO<sub>2</sub> at the same location averaged for the whole measurement period (2005 – 2007). Plots are shifted and stretched/ squeezed so that data for the same hour is plotted on top of each other. Maxima arise at the same times but slightly shifted to periods with lower solar radiation (early morning and late evening) due to NO<sub>2</sub> photolysis at sunlight.

### 8.14 Comparison to Power Plant Emissions

Emissions of power plants are a major source of trace gases. The two power plants in

Heidelberg are highlighted in Figure 6-4. Their influence was shown in the retrieved trace gas distributions in *Chapter 8.2.2*, *8.2.3* and *8.11*. They increased locally the NO<sub>2</sub> concentration by 10 to 20 ppb and for SO<sub>2</sub> by up to 2 to 3 ppb.

The municipal power plant close to the city centre is only a stand-by system. From the received time tables of operation it was proven that almost no operation occurred during tomographic measurements. Only on 24<sup>th</sup> January and 9<sup>th</sup> February 2006 measurements were performed when the power plant was operating for a short time. But as the system was running at very low power and only for few hours, no correlation was found in the observed concentrations. Concentration peaks were observed for the location of this power plant during other times as presented in *Chapter 8.5.1*. At this time the power plant was not operating for power production, but maybe maintenance work and test runs were responsible for the emissions. This could not be proven as details on such maintenance works could not be received.

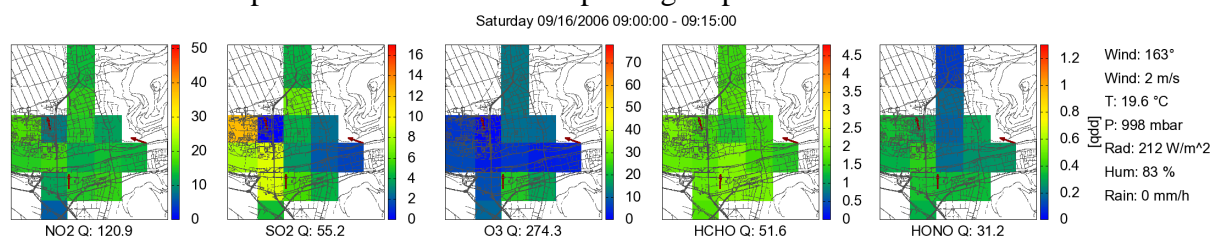
The largest power plant in the city is operated by RWE in the North of the city and about 200 outside of the investigation area (Figure 6-4). This power plant runs continuously, but with a different load depending on the request of heating, cooling and electricity. The strong emissions are still visible in many distributions as shown in *Chapter 8.2.3* and *8.11*. The emissions are mostly not observed as they are emitted over high stacks. Only if inversions arise and the emitted trace gases settle down, concentration increases arose. RWE did not provide data on the operation and gas consumption. Thus, unfortunately a correlation of these data with observed trace gas concentrations was not possible.

## 8.15 Comparison to Ship Emissions

Emissions from freight and passenger ship traffic on the river Neckar should be responsible for 10 % of NO<sub>x</sub> and 20 % of SO<sub>2</sub> emissions in Heidelberg [Umweltbundesamt, 2000]. NO<sub>x</sub> emissions are too low to significant increase locally observed NO<sub>2</sub> concentrations at the Neckar in comparison to other emission sources. SO<sub>2</sub> should be observable, as no other strong emitters can be found in the area of the Neckar.

In the derived tomographic trace gas distributions only rarely concentration peaks are observed along the river. An example is shown in Figure 8-53, where for a short time a local SO<sub>2</sub> plume arose. Two ships were passing this area at this time.

In order to get the real influence of ship emissions, the observed trace gas concentrations on the Neckar are compared with the amount of passing ships.



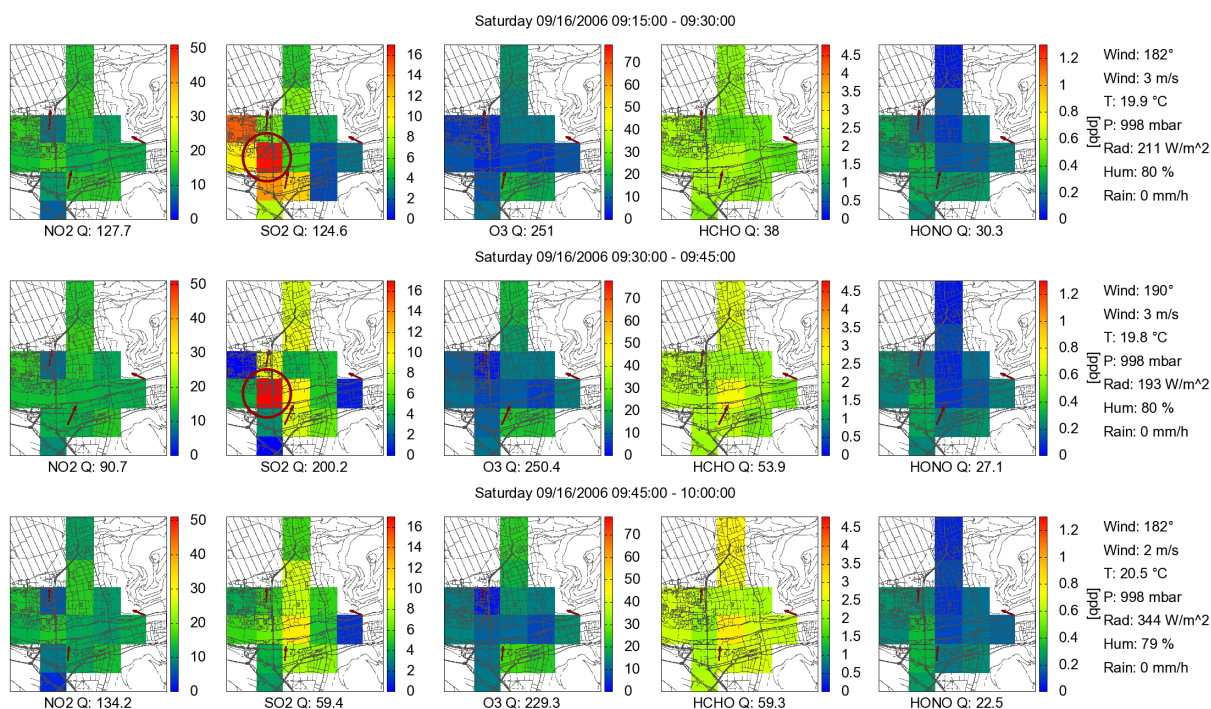


**Figure 8-53: Trace gas distributions with SO<sub>2</sub> concentration peak which may arise from ship emissions on the Neckar. Main spatial features are highlighted with maxima in dark red and minima in light blue. For labelling see Figure 8-3.**

Ship traffic data is taken from the hand written Heidelberg canal lock book<sup>11</sup>. The canal lock is located easterly of the city and thus outside of the investigation area. The log book contains the amount and time when a ship was passing the canal lock. The times of the canal lock were corrected for the investigation area as follows, in order to obtain the real passing time of the ships. The times for ships going upstream (easterly direction) was subtracted by 10 minutes before entering the canal lock and for ships going downstream (westerly direction) 10 minutes are added after they left the canal lock. This corresponds about to the time the ships passed the investigation area. The data was manually written from the paper log book to a data file for the months February, September and October 2006. A time resolution of one hour was applied. The amount of passing ships per hour is plotted in Figure 8-54. The ships are differentiated by freight ships, passenger ships and other. They are all added up as “all ships”. Passenger ships sometimes do not pass the city but just go to the landing stage close to the old town and at the border of the tomographic observation area. Thus, errors of the real passed amount of ships may arise. Additionally, one of the passenger ships is a solar boat, which runs on solar energy and so does not emit any trace gases. The log book of the canal lock does not separate different engines and thus this cannot be accounted in these data. Best correlation with trace gas concentrations are expected for freight ships, as they have much stronger engines and often use cheaper diesel which produce more pollutants. Freight ships always pass the whole investigation area.

For the comparison to the derived trace gas concentrations, all concentrations along the river are averaged. This should give a better determination of the enhanced concentration. The correlations for NO<sub>2</sub> and SO<sub>2</sub> are plotted in Figure 8-55.

<sup>11</sup> provided by the water and shipping authority Heidelberg, Rüdiger Englert, August 2009.

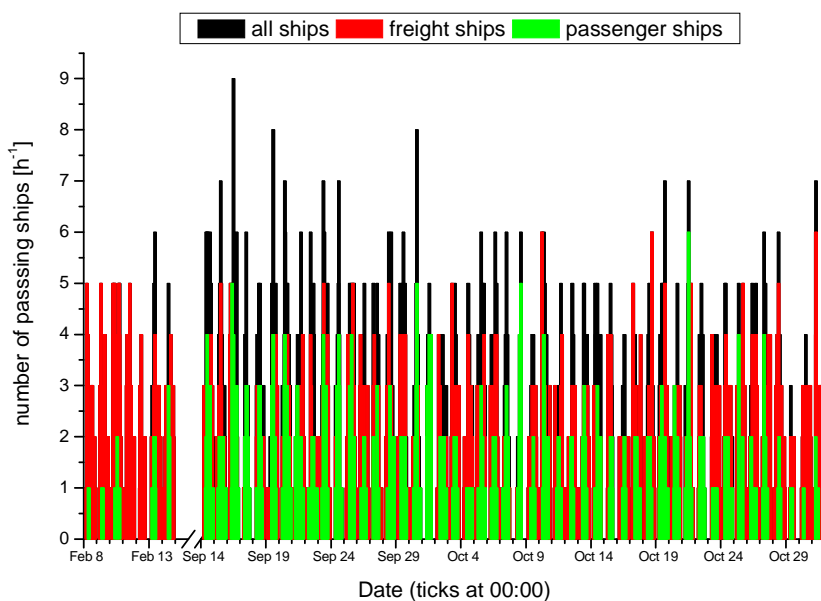


**Figure 8-54: Number of passing ships in Heidelberg for 2006 derived from the passing of the lock Heidelberg, East of the investigation area.**

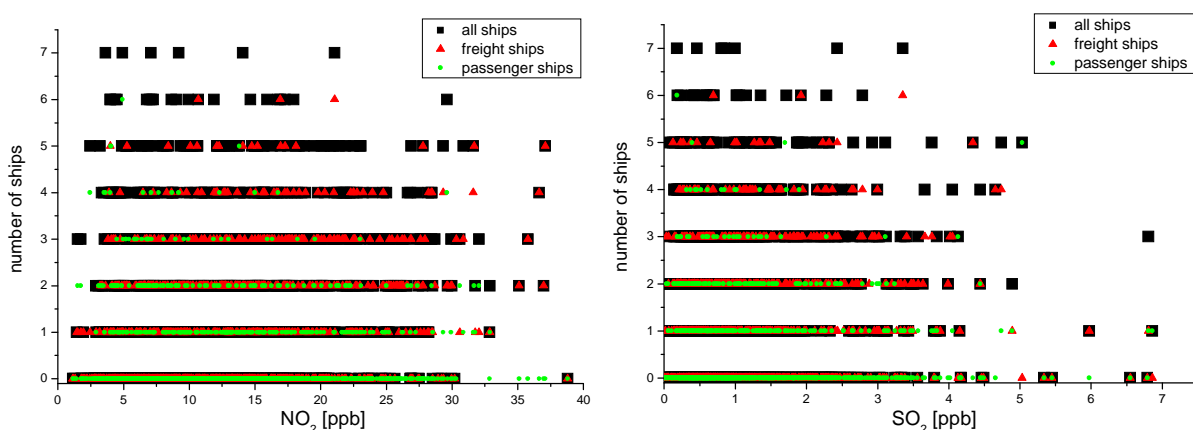


**Figure 8-55: Correlation of ship traffic with trace gas concentrations along the river Neckar for NO<sub>2</sub> (left) and SO<sub>2</sub> (right). No direct correlation was observed. Observed concentrations are thus not directly influenced by ship emissions.**

No correlation could be observed between the number of passing ships and observed trace gas concentrations neither for NO<sub>2</sub> nor for SO<sub>2</sub>. Highest concentrations are even observed if only few or no ship pass the city. Two conclusions can be made. First, ships are less responsible for emitted trace gases in Heidelberg than stated in the report of Umweltbundesamt [2000]. This can be due to an improvement of ship engines and cleaner ship diesel. Second, increased emissions do not arise from all ships, but from few ships running with old engines and dirty diesel. Thus, only these single ships emit large amounts of trace gases and no general correlation between ship number and trace gas concentration arises.

## 8.16 Long Term Measurement Data and Data DVD

Tomographic LP-DOAS measurements were performed from summer 2005 to spring 2007 and data is available for September 2005 to February 2006 and September 2006 to March 2007. Not for all periods all instruments were running due to several malfunctions. Therefore

tomographic trace gas distributions are only produced for periods with sufficient data. Nevertheless, the LP-DOAS measurements of the trace gas concentrations present a unique long term overview of trace gas concentrations in Heidelberg. Additionally, the instrument at the IUP could be started again in summer 2007 to receive some summer concentrations. Thus, the complete long term measurement data contain concentration of trace gases for all seasons. All these results cannot be discussed here but are provided in the *Appendix* and on the Data DVD. In the *Appendix* for each month the observed concentrations for four light paths are shown for the whole period.

Summer measurements display higher O<sub>3</sub> concentrations up to 100 ppb. NO<sub>2</sub> is lower due to higher photolysis. Also HCHO features higher concentrations up to 7 ppb as it is produced as photochemical smog. Thus, in summer highest concentrations of O<sub>3</sub> and HCHO arose simultaneously. An analysis of the yearly change was given in *Chapter 8.9*.

Due to the large amount of measurement data and derived trace gas concentrations, only some of them could be shown in this printed version of the thesis. The whole data set can be found on the attached data DVD. They include the plots for:

- meteorological data of the three weather stations at IUP, SAS and HD-Druck (e.g. see *Appendix*)
- in-situ trace gas concentrations from LUBW and IUP (e.g. see *Appendix*)
- observed trace gas concentrations of the 20 different light paths at full temporal resolution (e.g. see *Appendix 12.11*)
- 1 hour averaged trace gas concentrations of the 20 different light paths (e.g. see Figure 8-2)
- derived vertical profiles of the trace gases (e.g. see Figure 8-41)
- derived vertical gradients of the trace gases (e.g. see Figure 8-34 lower right plot)
- daily cycles of trace gas concentrations for each month (e.g. see Figure 8-34)
- weekly cycles of trace gas concentrations for each month (e.g. see Figure 8-37)
- tomographic trace gas distributions for a temporal resolution of 15 minutes, 1 hour, 3 hours, 24 hours and one month (e.g. see Figure 8-2)
- tomographic trace gas distributions for the mean daily cycle and weekly cycle for each month (e.g. see Figure 8-36 and Figure 8-38)
- tomographic trace gas distributions for different wind directions for each month (e.g. see Figure 8-42)

On the DVD the data is separated in folders with the corresponding year and month of the measurements in the form “YYYY\_MM”. The subfolder “Plots” contains all plots of meteorological and measurement data as well as the derived vertical profiles for the according month. The subfolder “TomographicDistributions” contains all derived trace gas distribution with different temporal resolution as well as for the different cycles of the according month. They can be found in the according labelled subfolders. The images of the distributions are in GIF format.



## 9 Conclusions and Outlook

Tomographic observations using 18 LP-DOAS measurements were successfully performed in order to observe horizontal two dimensional trace gas distributions. They demonstrate that tomographic LP-DOAS is capable of observing trace gas distributions in the ambient atmosphere and therefore can revolutionise the local scale chemistry observations and modelling. The measurements were conducted in Heidelberg (Germany) and covering an urban area of a few km<sup>2</sup>. It focused on the distributions of the trace gases NO<sub>2</sub>, SO<sub>2</sub>, O<sub>3</sub>, HCHO and HONO. These trace gases are known to play a major role in the chemistry of the polluted atmosphere. In this concluding chapter the most important results are summarised. The Conclusions are divided into three parts: instrumentation and developments, measurement setup and data retrieval, and finally observations of trace gas distributions.

### *9.1 Instrumentation and Developments*

Tomographic LP-DOAS observations require a large amount of independent absorption light paths (at least 10 to 20) which should be measured within few minutes, as trace gas concentrations can change quickly in time and space. Conventional scanning LP-DOAS instruments were not able to cover the entire area of investigation and perform measurements along several light paths within the desired temporal resolution. To overcome this shortcoming, three Multi Beam Instruments (MBI) were applied in this thesis. Each of them could perform simultaneous LP-DOAS measurements along four light paths and more by consecutively scanning (*Chapter 5.1*). Thus, each instrument could cover 8 light paths within less than ten minutes, what is sufficient for the observation of typical distributions in urban areas where continuous local emissions dominate. The stable operation of this rather involved and sensitive setup in the open atmosphere at all weather conditions turned out to be difficult. Mechanical instabilities and failures led to regular measurement interruptions. The simultaneous observation of different spectra with one spectrometer was identified as problematic for the required accuracy of these measurements. Several improvements were applied to the system in order to guarantee a better stability, higher quality of the measured spectra and to perform long term observations. Three major improvements were: First, the external mirrors which redirect the light beams to different retro reflectors, were reconstructed and stabilised in order to improve their accuracy and stability (*Chapter 5.2.2*). Second, a high speed spectrograph shutter was developed, featuring a 20 times higher durability and a three times shorter response time than commercially available alternatives (*Chapter 5.3.2*). Third, fully automated measurement routines were implemented. This included the automation of background and lamp reference measurements (*Chapter 5.2 and 5.2.4*). Also, an automatic optimisation of optical alignment was established (*Chapter 5.5*).

In the future, novel LP-DOAS instruments (*Chapter 5.6*), may be used as an alternative to MBI instruments. They are based on three main developments: The use of an optical fibre bundle to couple light in and out of the telescope, the application of high power or UV LEDs and the application of compact spectrometers. The light throughput of these systems is about

an order of 10 to 100 higher than for the MBI. This and the much simpler setup make their application for future LP-DOAS tomography attractive. Two possible configurations are proposed:

- First, with at least three scanning instruments, different light paths are observed in rapid succession. Due to the high light throughput, the measurement time along each light path can be kept short in comparison to the conventional LP-DOAS or MBI setup and full coverage may be achieved within a few minutes.
- Second, a tomographic setup may be achieved by means of downsized telescopes. Thanks to the high light output of fibre optic LP-DOAS instruments, considerably smaller telescopes with less light throughput may be applied. This would allow set up a larger number, e.g. 20, of such smaller telescopes, each measuring along a fixed light path. Scanning is then not required, thus reducing experimental expenses. Each telescope would measure the spectrum independently with a compact spectrometer. If an instrument fails, the other instruments would not be affected. Such a fixed setup would have the capability to monitor rapidly moving plumes, as no temporal shift due to scanning would occur.

Passive DOAS tomographic setups are another alternative for the retrieval of trace gas distributions during daylight. In order to achieve a high spatial resolution close to the ground Topographic Target light scattering (ToTal) DOAS setups [Frins et al., 2006] may have the potential to provide a sufficient number of light paths in a feasible manner.

## ***9.2 Measurement Setup and Data Evaluation***

A complete tomographic measurement setup consisting of three MBI instruments and 20 retro reflector arrays was realised in Heidelberg. Due to local restrictions, the setup was complex and the light path geometry irregular and required special treatment for the tomographic reconstruction. The three MBIs and their respective external mirrors were located on different buildings about 2 km from each other (*Chapter 6.2*). Additionally, 20 retro reflector arrays were installed on various buildings in the city. The 18 light paths in the horizontal and two in the vertical plane cover an area of  $4 \times 4 \text{ km}^2$ . Tomographic measurements with this setup were performed from September 2005 to February 2006 and from September 2006 to March 2007. For the instrument at the IUP, additional measurements were performed between June 2007 and September 2007.

An automatic evaluation procedure for the extensive data set was developed with the DOAS method (*Chapter 3 and 7.1*). Optimisation of the data evaluation reduced the measurement error by more than a factor of 3 and thus allowed reliable results for weak absorbers like HCHO and HONO in addition to  $\text{NO}_2$ ,  $\text{SO}_2$  and  $\text{O}_3$ . The improved measurement setup and data evaluation allowed data output of two dimensional trace gas maps with a time resolution of 15 minutes and less.

The reconstruction parameters were optimised for the applied setup using simulations (*Chapter 7.4*). Before measurement data was treated with the tomographic reconstruction algorithm using the SIRT method. Due to the irregular measurement geometry, box basis functions had to be used. Different reconstruction grids were tested in model studies (*Chapter*

7.4.1). The best achievable discretisation consisted of 24 reconstruction boxes of the entire investigation area. Simulations with different artificial trace gas fields showed that reasonable reconstructions could be achieved for concentration distributions consisting of a homogeneous background with superimposed peaks of a spatial extent of at least few hundred meters, comparable to the reconstruction box size (*Chapter 7.4.2*). These distributions are reasonable for urban areas. If simulated concentration peaks were smaller than the resolution of the reconstruction grid or if peak concentrations were very high in comparison to the background concentration, significant reconstruction errors emerged. Optimal iteration numbers for the reconstruction of the different trace gases were determined in simulations and applied to the measurement data. They vary for the different measurement errors from 3 to 50. The tomographic reconstruction was automated for time series, where different reconstruction grids were applied for a variable number of measurement light paths. This allowed evaluating the entire data set even if de-adjustments or malfunctions of single light paths occurred.

### ***9.3 Observations of Trace Gas Distributions***

Continuous trace gas distributions for the investigation area were successfully determined for several periods of weeks to months. Additionally systematic averaged periods like daily and weekly cycles were investigated. Some selected events and distributions are presented in *Chapter 8*. All data is provided as a digital supplement of this thesis (*Chapter 8.16*).

In general, the distributions were characterised by strong spatial variability for NO<sub>2</sub>, SO<sub>2</sub> and O<sub>3</sub> and relatively low variability for HCHO and HONO. Retrieved profile measurements (*Chapter 8.10*) suggest that concentrations of emitted trace gases decreased with altitude. Ozone displayed an opposite gradient with significantly lower values at the ground. All trace gases featured a clear daily cycle, with much stronger concentration variability over the day than found in the spatial distributions.

A strong anti-correlation to wind speed was also found. Observed peak concentrations for NO<sub>2</sub> and SO<sub>2</sub> decreased with increasing wind speed linearly up to 10 m/s and reached background values of 5 ppb and 0.5 ppb, respectively. The obtained background value of O<sub>3</sub> was 30 to 40 ppb at the same wind speed. HCHO and HONO were characterised by an even stronger dependency on wind speed with an exponential like decrease of the maximum observed concentrations. The investigation for different wind directions showed that concentrations at no wind (< 2 m/s) were almost two times higher (half the concentration for O<sub>3</sub>) than for occurring wind with on average 3 to 4 m/s (*Chapter 8.11*). Therefore, it can be concluded that most pollutants have their origin in local emissions and are not transported to the city. While lowest concentrations of NO<sub>2</sub>, SO<sub>2</sub> and HONO coincided with northerly and easterly winds, these trace gases show slight enhancements for southerly and westerly winds. This suggests that for these wind directions industrial emissions in the South of Heidelberg (most probably Heidelberg Zement) and from the cities Mannheim and Ludwigshafen in the West or traffic induced emissions from highways in this area were transported to the city. Especially, SO<sub>2</sub> increased significantly for southerly winds. The concentrations in the layer between 209 and 498 m above ground rose from 1.2 ppb (calm) to 1.7 ppb and led to an inversion of the vertical gradient. This supports the assumption of a stack directly emitting

high SO<sub>2</sub> levels into higher altitudes south of Heidelberg.

With increasing wind also the spatial variability of the observed trace gases decreased (*Chapter 8.11*). Besides the enhanced mixing with background air, turbulence also increases directly over rough surfaces like city buildings and additionally increased the mixing process with ambient air. Thus, concentrations dropped to background levels. Strongest spatial variability of NO<sub>2</sub>, SO<sub>2</sub> and O<sub>3</sub> was found for calm wind where concentrations typically vary by 25 ppb, 3.5 ppb and 25 ppb, respectively, in the observation area. Only very weak variability was observed when wind increased above 2 m/s. As HCHO and HONO displayed relatively homogeneous spatial distributions, no such strong influence of the wind speed was observed.

Time series with 15 minutes temporal resolution were used to study transport processes like the passing of pollution plumes. Numerous SO<sub>2</sub> plumes with peak concentrations of typically 10 ppb were identified. They transported SO<sub>2</sub> from South or South-West to the investigation area (*Chapter 8.5*). Also, several locally emitted SO<sub>2</sub> plumes could be identified with peak concentrations of up to 20 ppb. They were traced back to the area around the municipal power plant in the city which was not operating at the same time. Thus emissions may be due to maintenance work. NO<sub>2</sub> plumes could not be identified during daytime, as typical concentrations of up to 50 ppb in the city were too high to distinguish a superposed plume. During night, when concentrations were lower, several NO<sub>2</sub> plumes could be observed with peak concentrations up to 50 ppb (*Chapter 8.2.6*). No correlation of ship traffic on the river Neckar to local increases in SO<sub>2</sub> and NO<sub>2</sub> was found (*Chapter 8.15*). This proves that their influence on the local pollution is lower than so far stated in the emission inventories of the municipality.

Derived time series of daily, weekly and annual cycles were used to study pollution. NO<sub>2</sub> and O<sub>3</sub> concentrations were studied for different meteorological conditions (*Chapter 8.2*). A distinct diurnal cycle was observed with a maximum of NO<sub>2</sub> with 25 ppb in the early morning and late afternoon when high traffic load arose during rush hour and photolysis was low. The highest NO<sub>2</sub> concentrations of about 50 ppb were localised to the centre of the investigation area, especially where the main streets are located in the West, over the river Neckar and at the city centre (Bismarkplatz). Lowest concentrations arose at the city border in the North, West and East where the "Old Town" is located in the Neckar valley. This clearly shows that traffic emissions are the major source of increased NO<sub>2</sub> concentrations. Emissions from the RWE power plant in the North-West were observed during winter. Locally NO<sub>2</sub> concentrations were increased by 10 to 20 ppb (*Chapter 8.14*). On average, the highest concentrations were located at the city centre (Bismarkplatz) and were about 15 % higher than in the area of Berliner Strasse in the North-West, where the environmental monitoring station of the government (LUBW) is located (*Chapter 8.12.1*). Thus it can be stated, that the provided concentrations underestimate the concentrations in the city. The distribution of O<sub>3</sub> was characteristically anti-correlated to NO<sub>2</sub>. O<sub>3</sub> was regularly depleted in winter, especially in areas where high NO<sub>2</sub> concentrations were detected. The maximum concentration was reached between 14:00 and 15:00 with on average concentrations of 25 ppb. During warm and

sunny days concentrations of up to 70 ppb and located at the city border were observed, where  $\text{NO}_x$  emissions were low and photochemical  $\text{O}_3$  formation due to VOCs was high.

As expected HONO concentrations (*Chapter 8.3*) featured a concentration peak of a maximum of 2 ppb before sunrise and after sunset when  $\text{NO}_2$  levels were high and HONO photolysis low. The distributions had distinctly less spatial variability than  $\text{NO}_2$ . This suggests that HONO was not directly emitted by a source identical to the  $\text{NO}_x$  source but is rather a secondary emission product. Also a growing ratio of  $\text{NO}_2$  to HONO with increasing height was identified. Both findings support the assumption that it was formed by heterogeneous reactions of  $\text{NO}_2$  on wet surfaces (*Chapter 8.3.5*).

HCHO concentrations indicated direct emissions from fossil fuel combustion as well as the production from photochemical oxidation of VOCs during warm and sunny days (*Chapter 8.4*). The distributions were characterised by little spatial variation especially during warm days where HCHO is expected to be produced photochemically from VOCs and reached a maximum of typically 3 to 4 ppb (*Chapter 8.4.5*). Directly emitted HCHO concentrations were lower and reached about 2 ppb.

The observations of concentration fields of averaged daily and weekly cycles showed the dominant influence of anthropogenic emissions on local concentrations. The highest  $\text{NO}_2$ ,  $\text{SO}_2$ , HCHO and HONO (lowest for  $\text{O}_3$  in winter) levels were observed in the city centre and close to main streets and power plants during the day and especially for working days. The old town with its pedestrian area was characterised by lower concentrations. Emitted levels were much lower on weekends.  $\text{SO}_2$  was an exception, it showed a minimum on Tuesdays and Sundays and was proposed to be linked to industry activity. The investigation of the yearly cycle shows that  $\text{NO}_2$  and  $\text{SO}_2$  concentrations were lowest in summer with an average of 10 ppb and 0.8 ppb, respectively (monthly average) (*Chapter 8.9*). In winter they increased to 22 ppb and 3.0 ppb. Ozone and HCHO were highest in summer with up to 35 ppb and 2.0 ppb, respectively, due to photochemical formation. In winter, they reached 10 ppb and 1.0 ppb, respectively. HONO did not show a strong yearly cycle and had an average concentration of 0.3 ppb.

## ***9.4 Final Remarks***

Spatially resolved measurements of two and three dimensional trace gas distributions may revolutionise the field of atmospheric chemistry observations in the troposphere [Platt et al., 2009a]. Other spatial measurement techniques, like observations from satellite, cannot provide time series with resolutions in a range of few 100 m. Even chemical transport models are still not sufficiently accurate to determine trace gas distributions on these scales.

This thesis demonstrates that the tomographic LP-DOAS technique provides such two dimensional trace gas distributions of investigation areas of a few 100 m to km's. The high sensitivity and achievable resolution close to the ground make it ideal to investigate urban areas where strong sources and local gradients exist.

Potential applications are air quality monitoring, investigation of emission sources, the studying of chemical and transport processes and the validation and improvement of chemical transport models. Besides urban air pollution, measurements of the trace gas distributions are

also of interest in areas where the exact sources and their distributions are unknown, like halogen emissions from algae beds or sea ice. In all these fields tomographic LP-DOAS observations may significantly improve our level of scientific understanding. The development of new and simplified instruments will enable applying this technique to future investigation areas.

## 10 References

- Ackermann, R., *Auswirkungen von Kraftfahrzeugemissionen in der urbanen Atmosphäre*, PhD thesis, Institut of Environmental Physics, Heidelberg, **2000**.
- Albritton, D. L., Schmeltekopf, A. L. and Zare, R. N., *An introduction to the least-squares fitting of spectroscopic data*, Molecular Spectroscopy: Modern Research, edited by R. K. Narahari and M. W. Weldon, Academic, Orlando, Florida, **1976**.
- Alicke, B., Platt, U. and Stutz, J., *Impact of nitrous acid photolysis on the total hydroxyl radical budget during the limitation of oxidant production/ Pianura Padana Produzione di Ozono study in Milan*, J. Geophys. Res. 107, 8196, **2002**.
- Andor Technology, Shamrock SR-163i/SR-163, 7 Millennium Way, Belfast, BT12 7AL, Northern Ireland, **2007**.
- Atkinson, R., Baulch, D.L., Cox, R.A., Crowley, J.N., Hampson, R.F., Hynes, R.G., Jenkin, M.E., Rossi, M.J. and Troe, J., *Evaluated kinetic and photochemical data for OX, HOX, NOX and SOX*, Atmos. Chem. Phys., 4, 1461-1738, **2004**.
- Atkinson, R., Winer, A.M. and Pitts, J.N.Jr., *Estimation of night-time N<sub>2</sub>O<sub>5</sub> concentrations from ambient NO<sub>2</sub> and NO<sub>3</sub> radical concentrations and the role of N<sub>2</sub>O<sub>5</sub> in night-time chemistry*, Atmos. Environ., 20, 331-339, **1986**.
- Axelsson, H., Galle, B., Gustavsson, K., Regnarsson, P. and Rudin, M., *A transmitting/receiving telescope for DOAS-measurements using retroreflector technique*, Dig. Top. Meet. Opt. Remote Sens. Atmos., OSA, 4, 641-644, **1990**.
- Baumüller, J. and Kapp, R., *Die Luft in Stuttgart*, Amt für Umweltschutz, Abteilung Stadtklimatologie, (<http://www.stadtklima.de/Stuttgart/s-luft/zusammensetzung.htm>), **2000**.
- Beirle, S., *Estimating source strength and lifetime of Nitrogen Oxides from satellite data*, PhD thesis, Institut of Environmental Physics, Heidelberg, **2004**.
- Beirle, S., Platt, U. and Wagner, T., *European Space Agency Homepage Results from Heidelberg* ([http://www.esa.int/esaEO/SEM340NKPZD\\_index\\_0.html](http://www.esa.int/esaEO/SEM340NKPZD_index_0.html)), **2004**.
- Beirle, S., Platt, U., Wenig, M. and Wagner, T., *Weekly cycle of NO<sub>2</sub> by GOME measurements: A signature of anthropogenic sources*, Atmos. Chem. Phys., 3, 2225–2232, **2003**.
- Benning, L. and Wahner, A., *Measurement of atmospheric formaldehyde (HCHO) and acetaldehyde (CH<sub>3</sub>CHO) during POPCORN 1994 using 2,4-DNPH coated silica cartridges*, J. Atmos. Chem., 31, 105-117, **1998**.
- Bevington, P. R., *Data reduction and error analysis for the physical sciences*, New York, **1969**.
- Bogumil, K., Orphal, J., Homann, T., Voigt, S., Spietz, P., Fleischmann, O. C., Vogel, A., Hartmann, M., Bovensmann, H., Frerick, J. and Burrows, J. P., *Measurements of molecular absorption spectra with the SCIAMACHY pre-flight model: Instrument characterization and reference data for atmospheric remote sensing in the 230-2380 nm region*, J. Photochem. Photobiol. A.: Photochem, 157, 167-184, **2003**.
- Bruns, M., Bruns, Buehler, S. A., Burrows, J. P., Richter, A., Rozanov, A., Wang, P., Heue, K.-P., Platt, U., Pundt, I. and Wagner, T., *NO<sub>2</sub> Profile retrieval using airborne multi*

- axis UV-visible skylight absorption measurements over central Europe*, Atmos. Chem. Phys., 6, 3049-3058, **2006**.
- Burrows, J. P., Dehn, A., Deters, B., Himmelmann, S., Richter, A., Voigt, S. and Orphal, J., *Atmospheric remote-sensing reference data from GOME: 1. Temperature-dependent absorption cross sections of NO<sub>2</sub> in the 231–794 nm range*, J Quant Spectrosc Radiat Transfer, 60, 1025–1031, **1998**.
- Burrows, J. P., Richter, A., Dehn, A., Deters, B., Himmelmann, S., Voigt, S. and Orphal, J., et al., *Atmospheric remote-sensing reference data from GOME: 2. Temperature-dependent absorption cross sections of O<sub>3</sub> in the 231–794 nm range*, J Quant Spectrosc Radiat Transfer, 61, 509–517, **1999**.
- Butz, A, Bösch, H., Camy-Peyret, C., Chipperfield, M., Dorf, M., Dufour, G., Grunow, K., Jeseck, P., Köhl, S., Payan, S., Pepin, I., Pukite, J., Rozanov, A., von Savigny, C., Sioris, C., Wagner, T., Weidner, F., and Pfeilsticker, K., *Inter-comparison of stratospheric O<sub>3</sub> and NO<sub>2</sub> abundances retrieved from balloon borne direct sun observations and Envisat/SCIAMACHY limb measurements*, Atmos. Chem. Phys., 6, 1293-1314, **2006**.
- Buxmann, J., *Optimierte Langpfad- DOAS Messungen von BrO und ClO an der irischen Westküste*, Diploma thesis, University of Heidelberg, Germany, **2008**.
- Chin, M. and Davis, D.D, *Global sources and sinks of OCS and CS<sub>2</sub> and their distribution*, Global Biogeochem. Cycl. 7, p. 321–337, **1993**.
- Crutzen, P.J., *The influence of nitrogen oxides on the atmospheric ozone content*, Quart. J. Roy. Met. Soc. 96, 320-325, **1970**.
- Czerny, M. and Turner, A. F., *Über den Astigmatismus bei Spiegelspektrometern*, Z. Phys., 61, 792 - 797, **1930**.
- Dentener, F.J., and Crutzen, P.J., *Reaction of N<sub>2</sub>O<sub>5</sub> on tropospheric aerosols: impact on the global distributions of NO<sub>x</sub>, O<sub>3</sub> and OH*, J. Geophys. Res., 98, 7149-7163, **1993**.
- Deutschmann, T., *Atmospheric radiative transfer modelling using Monte Carlo methods*, Diploma thesis, University of Heidelberg, **2008**.
- Drescher, A. C., Park, D. Y., Yost, M. G., Gadgil, A. J., Levine, S. P. and Nazaroff, W. W., *Stationary and time-dependent indoor tracer-gas concentration profiles measured by OP-FTIR remote sensing and SBFM-computed tomography*, Atmos. Environ., 31, 727–740, **1997**.
- EPA, *National Air Quality – Status and Trends trough 2007*, **2007**.
- EPA, *Original list of hazardous air pollutants*, U.S. Environmental Protection Agency, <http://www.epa.gov/ttn/atw/188polls.html>, **2010**.
- Fayt, C. and Roozendael, M.: *FaWin DOAS 2.1 software user manual*. IASB/BIRA Uccle Belgium, **2001**.
- Fiedler, S.E., Hese, A. and Ruth, A.A., *Incoherent broad-band cavity-enhanced absorption spectroscopy*, Chem. Phys. Lett. 371, 284-294, **2003**.
- Finlayson-Pitts, B. J. and Pitts, J. N. ,*Chemistry of the upper and lower atmosphere: Theory, experiments and applications*, San Diego: Academic Press, **2000**.
- Fischer, M. L., Price, P. N., Thatcher, T. L., Schwalbe, C. A., Craig, M. J., Wood, E. E., Sextro, R. G., and Gadgil, A. J., *Rapid mea-Fig. 12. As Fig. 11 for the information*

- content. surements and mapping of tracer gas concentrations in a large indoor space*, Atmos. Environ., 35, 2837–2844, **2001**.
- Fishman, J. and Crutzen, P., *The origin of ozone in the troposphere*, Nature 274, p. 855–858, **1978**.
- Friedeburg, C. von, *Derivation of Trace Gas Information combining Differential Optical Absorption Spectroscopy with Radiative Transfer Modelling*, PhD thesis, Institut of Environmental Physics, Heidelberg, **2003**.
- Frins, E., Bobrowski, N., Platt, U. and Wagner, T., *Tomographic MAX-DOAS observations of sun illuminated targets: a new technique providing well defined absorption paths in the boundary layer*. Applied Optics 45, 6227-6240, **2006**.
- Gomer, T., Brauers, T., Heintz, F., Stutz, J. and Platt, U., *MFC user manual, version 1.98*, inhouse publication, Institut für Umweltphysik, University of Heidelberg, Germany, **1993**.
- Grosjean, D., *Ambient levels of formaldehyde, acetaldehyde and formic acid in Southern California: Results of a one-year base-line study*, Environ. Sci. Technol., 25, 710-715, **1991**.
- Grosjean, E., Williams, H., Grosjean, D., *Ambient levels of formaldehyde and acetaldehyde in Atlanta, Georgia*, Journal of the Air Waste Management Association, 43, 467-474, **1993**.
- Haagen-Smit, A., Darley, E., Zaitlin, M., Hull, H. and Noble, W., *Investigations on injury of plants from air pollution in the los angeles area*, Plant Physiol., 27: 18-34, **1952**.
- Hak, C., *Variability of Formaldehyde in the polluted planetary boundary layer – Measurements in the Milano metropolitan area, Italy (Po basin)*, PhD Thesis, Universität Karlsruhe, Karlsruhe, **2006**.
- Hammeed, S. and Dignon, J., *Global emissions of nitrogen and sulphur oxides in fossil fuel combustion*, Air Waste Management Association, 42: 159-163, **1992**.
- Hansen, P. C., *Rank-deficient and discrete ill-posed problems*, Siam, Philadelphia, **1998**.
- Harder, J. W., Fried, A., Sewell, S. and Henry, B., *Comparison of tunable diode laser and long-path ultraviolet/visible spectroscopic measurements of ambient formaldehyde concentrations during the 1993 OH Photochemistry Experiment*, J. Geophys. Res., 102 (D5), 6267- 6282, **1997**.
- Harris, G.W., Mackay, G. I., Iguchi, T., Mayne, L. K. and Schiff, H. I., *Measurements of formaldehyde in the troposphere by Tuneable Diode Laser Absorption Spectroscopy*, J. Atmos. Chem., 8, 119-137, **1989**.
- Hartl, A., Song, B. C. and Pundt, I., *2D Reconstruction of Atmospheric Concentration Peaks from Horizontal Long Path DOAS Tomographic Measurements: Parametrisation and Geometry within a Discrete Approach*, Atmos. Chem. Phys., 6, 847-861, **2006**.
- Hartl, A., *Tomographic Reconstruction of 2-D Atmospheric Trace Gas Distributions from Active DOAS Measurements*, PhD thesis, Institut of Environmental Physics, Heidelberg, **2007**.
- Heidelberg, *Jahresgang der Ozon-Konzentration 2008*, City of Heidelberg, <http://www.heidelberg.de/servlet/PB/menu/1199055/index.html>, **2009d**.
- Heidelberg, *Jahresgang der Stickstoffdioxid-Konzentration 2008*, City of Heidelberg, <http://www.heidelberg.de/servlet/PB/menu/1199055/index.html>, **2009b**.

- Heidelberg, *Jahresmaximal- und –mittelwerte der Ozon-Immisionen an der Mesststation Berliner Straße seit 1990*, City of Heidelberg, <http://www.heidelberg.de/servlet/PB/menu/1199055/index.html>, **2009c**.
- Heidelberg, *Jahresmaximal- und –mittelwerte der Stickstoffdioxid-Immisionen an der Mesststation Berliner Straße seit 1990*, City of Heidelberg, <http://www.heidelberg.de/servlet/PB/menu/1199055/index.html>, **2009a**.
- Heidelberg, *Lärmkartierung Heidelberg 2007*, Stadt Heidelberg, Amt für Umweltschutz, **2007**.
- Heidelberg, *Online city information board*, [http://www.heidelberg.de/servlet/PB/menu/1025663\\_11/index.html](http://www.heidelberg.de/servlet/PB/menu/1025663_11/index.html), **2009**.
- Hermans, C., Vandaele, A. C., Carleer, M., Fally, S., Colin, R., Jenouvrier, A., Coquart, B. and Mérienne, M. F., *Absorption-cross sections of atmospheric constituents: NO<sub>2</sub>, O<sub>2</sub> and H<sub>2</sub>O*, Environ. Sci. and Pollut. Res., 6(3), 151-158, **1999**.
- Heue, K. P., *Airborne Multi AXis DOAS instrument and measurements of two-dimensional tropospheric trace gas distributions*, PhD thesis, Institut of Environmental Physics, Heidelberg, **2005**.
- Heue, K.-P., Wagner, T., Broccardo, S., Walter, D., Piketh, S., Ross, K. and Platt, U., *Direct observation of two dimensional trace gas distribution with an airborne Imaging DOAS instrument*, Atmos. Chem. Phys., 8, 6707-6717, **2008**.
- Hoch, D., *Resonator Verstärkte Differentielle Optische Absorption Spektroskopie: Labormessungen von BrO, HCHO, HONO und O<sub>3</sub>*, diploma thesis, Institut of Environmental Physics, Heidelberg, **2010**.
- Hofmann, D., Bonasoni, P., De Maziere, M., Evangelisti, F., Giovanelli, G., Goldman, A., Goutail, F., Harder, J., Jakoubek, R., Johnston, P., Kerr, J., McElroy, T., McKenzie, R., Mount, G., Platt, U., Pommereau, J.-P., Sarkissian, A., Simon, P., Solomon, S., Stutz, J., Thomas, A., Van Roosendael, M. and Wu, E., *Intercomparison of UV/visible spectrometers for measurement of stratospheric NO<sub>2</sub> for the network for the detection of stratospheric change*, J. Geophys. Res. 100, 16765-16791, **1995**.
- Hönninger, G. and Platt, U., *Observations of BrO and its vertical distribution during surface ozone depletion at Alert*, Atm. Env., 36, 2481 – 2489, **2002**.
- Horbanski, M., *A Compact Resonator Based Instrument for DOAS Measurements of Ambient Nitrogen Dioxide*, Diploma thesis, Institut für Umweltphysik, Heidelberg, **2010**.
- Hoshino, M., Ogata, T., Akimoto, H., Inoue, G., Sakamaki, F. and Okuda, M., *Gas Phase Reactions of N<sub>2</sub>O<sub>5</sub> with Propylene*, Chemistry Letters, Chem. Soc. of Japan, 1367-1370, **1978**.
- Hübner, G., Perner, D., Platt, U. and Ehalt, D.H., *Groundlevel OH, Radical concentration: New measurement by optical absorption*, J. Geophys. Res., 89, 1309-1319, **1984**.
- Hulst, H.C.v.d., *Light scattering by small particles*, Wiley, New York, 1957.
- Inegesson, L.C., Alpher, B., Chen, H., Edwards, A. W., Fehmers, G.C., Fuchs, J. C., Giannella, R., Grill, R. D., Lauro-Taroni, L. and Romanelli, M., *Soft x-ray tomography during ELMs and impurity injection set*, Nuclear Fusion, 38, **1998**.
- IPCC, International Panel on Climate Change, *Third Assessment Report*, **2001**.
- Johansson, M., Galle, B., Rivera, C. and Zhang, Y., *Tomographic reconstruction of gas plumes using scanning DOAS*, Bull Volcanol, 71, 1169-1178, **2009**.

- Junkermann, W., Platt, U. and Volz-Thomas, A., *A photoelectric detector for the measurement of photolysis frequencies of ozone and other atmospheric molecules*. J. Atmos. Chem. 8, 203-227, **1989**.
- Kern, C., Sihler, H., Vogel, L., Rivera, C., Herrera, M. and Platt, U., *Halogen oxide measurements at Masaya volcano, Nicaragua using Active Long Path Differential Optical Absorption Spectroscopy*, Bull. Volcanol. 71, 659–670, DOI 10.1007/s00445-008-0252-8, **2009**.
- Kern, C., Trick S., Rippel B. and Platt U., *Applicability of light-emitting diodes as light sources for active DOAS measurements*, Appl. Opt. 45, 2077-2088, **2006**.
- Kesselmeier, J.K. and Staudt, M., *Biogenic volatile organic compounds (VOC): An overview on emission, physiology and ecology*, J. Atmos. Chem., 33 (1), 23 – 88, **1999**.
- Kessler, C. and Platt, U., *Nitrous acid in polluted air masses: Sources and formation pathways*. Proceeding on the 3<sup>rd</sup> European Symposium on PhysicoChemical Behaviour of Atmospheric Pollutants, Varese, Italia, 10-12 Apr., pp. 412-422, D.Reidel, Norwell, Mass, **1984**.
- Kiehl, J.T. and Trenberth, K.E., *Earth's Annual Global Mean Energy Budget*, Bulletin of the American Meteorological Society 78 (2): 197–208, **1997**.
- Knab, V., *Basic theory on DOAS tomography, Reconstruction of 2D trace gas distributions by discrete linear inversion techniques*, Diploma thesis, Institut of Environmental Physics, Heidelberg, **2003**.
- Kraus, S., *DOASIS A Framework Design for DOAS*. PhD thesis, University of Mannheim, Mannheim, Germany, **2005**.
- Kuusalo, K., Alander, T., Raunemaa, T. and Noponen, M., *Reduction of SO<sub>2</sub> emissions in asphalt plants*, Journal of Aerosol Science, 22, Supplement 1, p 471 - 473, **1991**.
- Laepple, T., Knab, V., Mettendorf, K. U. and Pundt, I., *Longpath DOAS tomography on a motorway exhaust plume: Numerical studies and application to data from BABII campaign*, Atmos. Chem. Phys., 4, 1323-1342, **2004**.
- Landwehr, S., *Design eines kompakten Lang Pfad DOAS Messgerätes basierend auf Faser Optik*, Diploma Thesis, Institute of Environmental Physics, University of Heidelberg, Heidelberg, **2010**.
- Lee, D. S., Köhler, E., Grobler, F., Rohrer, F., Sausen, R., Gallardo-Klenner, L., Olivier, J., Dentener, F. and Bouwman, A., *Estimates of global NO<sub>x</sub> emissions and their uncertainties*, Atmospheric Environment, Vol. 31(12), 1735–1749., **1997**.
- Leighton, P., *Photochemistry of air pollution*, Academic Press, New York, **1961**.
- Levelt, P.F., van den Oord, G.H.J., Dobber, M.R., Mslkki, A., Visser, H., de Vries, J., Stammes, P., Lundell, J. and Saari, H., *The ozone monitoring instrument*, IEEE Trans. Geo. Rem. Sens. 44, 1093-1101, **2006**.
- Levenberg, K., *A method for the solution of certain non-linear problems in least squares*, Quart. Appl. Math, 2, 164 - 168, **1944**.
- Linos GmbH, Linos Photonics Katalog. **2000**.
- Logan, J., *Nitrogen oxides in the troposphere: global and regional budgets*, J. of Geophys. Res., Vol. 88(C15), 10785–10807, **1983**.
- Lohberger, F., Hönninger, G. and Platt, U., *Ground-Based Imaging Differential Optical Absorption Spectroscopy of Atmospheric Gases*, Appl. Optics **43**, 4711-4717, **2004**.

- Louban, I, Bobrowski N, Rouwet D., Inguaggiato S. and Platt U., *Imaging DOAS for Volcanological Applications*, *Bulletin of Volcanology*, Doi: 10.1007/s00445-008-0262-6, **2009**.
- Louban, I, *Zweidimensionale Spektroskopische Aufnahmen von Spurenstoff-Verteilungen*, diploma thesis, Institut of Environmental Physics, Heidelberg, **2005**.
- Lowe, D. C. and Schmidt, U., *Formaldehyde (HCHO) measurements in the nonurban atmosphere*, *J. Geophys. Res.*, 88 (C15), 10 844-10 858, **1983**.
- Marbach, T. , Beirle, S., Platt, U. and Wagner, T., *Identifcation of tropospheric emission sources from satellite observations: Synergistic use of trace gas measurements of formaldehyde (HCHO), and nitrogen dioxide (NO<sub>2</sub>)*, *Proceedings of the ENVISAT & ERS Symposium*, **2004**.
- Marcuse, D, *Coupled Mode Theory of Round Optical Fibres*, *Bell Syst. Tech J.*, 52, 817-842, **1973**.
- Marquardt, D. W., *An algorithm for least squares estimation of non-linear parameters*, *J. Soc. Indust. Appl. Math.*, 11, 431 - 441, **1963**.
- Martin, M., Pöhler, D., Seitz, K., Sinreich, R. and Platt, U., *BrO measurements over the Eastern North-Atlantic*, *Atmos. Chem. Phys.*, 9, 9545-9554, **2009**.
- Meinen, J., Thieser, J., Platt, U. and Leisner, T., *Using a high finesse optical resonator to provide a long light path for differential optical absorption spectroscopy: CE-DOAS*, *Atmos. Chem. Phys.* 10, 3901–3914, **2010**.
- Meller, R. ; Moortgat, G.K.: *Temperature dependence of the absorption cross sections of formaldehyde between 223 and 323 K in the wavelength range 225-375 nm*. In: *JGR*, S. 7089–7101, **2000**.
- Mentel, T., Bleilebens, D. and Wahner, A., *A Study of Nighttime Nitrogen Oxide Oxidation in a Large Reaction Chamber - the Fate of NO<sub>2</sub> N<sub>2</sub>O<sub>5</sub> HNO<sub>3</sub>, and O<sub>3</sub> at Different humidities*, *Atmos. Environ.*, 30 (23), 4007 - 4020, **1996**.
- Merten, A., *Neues Design von Langpfad-DOAS-Instrumenten basierend auf Faseroptiken und Anwendungen der Untersuchung der urbanen Atmosphäre*, PhD thesis, Institut of Environmental Physics, Heidelberg, **2008**.
- Merten, A., Tschritter, J. and Platt, U., *New Design of DOAS-Long-path Telescopes based on fiber optics*, submitted to *Applied Optics*, **2010**.
- Mettendorf, K. U., *Aufbau und Einsatz eines Multibeam Instrumentes zur DOAS tomographischen Messung zweidimensionaler Konzentrationsverteilungen*, PhD thesis, Institut of Environmental Physics, Heidelberg, **2005**.
- Mettendorf, K. U., Hartl, A. and Pundt, I., *An indoor test campaign of the tomography long path differential optical absorption spectroscopy technique*, *J. Environ. Monit.*, 8, 1–9, **2006**.
- Morris, E.D., and Niki, H., *Reaction of the nitrate radical with acetaldehyde and propylene*, *J. Phys. Chem.*, 78, 1337-1338, **1974**.
- Müller, J. F., *Geographical distribution and seasona variation of surface emissions and deposition velocities of atmospheric trace gases*, *J. Geophys. Res.* 97, 3787 – 3804, **1992**.
- Müssel, W., *Bestimmung optischer Eigenschaften des Faser-Langpfad-DOAS*, Miniforschungsbericht, Institut of Environmental Physics, Heidelberg, **2009**.

- Navas S., M.J., Jimenez M., A.M. and Alfonso, G.G., *Determination of Nitrogen Compounds By Chemiluminescence*, Atmospheric Environment, 31, Num. 21., p. 3603-3608, **1997**.
- Nielsen, T., Plinegaard, K., Egelov, A.H., Granby, K., Hummelshoj, P., Jensen, N.O. and Skov, H., *Atmospheric nitrogen compounds: occurrence, composition and deposition*, Sci. Total. Environ., 189/190, 459-465, **1996**.
- Perner, D. and Platt, U., *Detection of nitrous acid in the atmosphere by differential optical absorption*, Geophys. Res. Lett. 6, 917-920, **1979**.
- Pfeilsticker, K. and Platt, U., *Airborne measurements during Arctic stratospheric experiment: Observations of O<sub>3</sub> and NO<sub>2</sub>*, Geophys. Res. Lett., 21, 1375-1378, **1994**.
- Platt, U. and Perner, D., *Measurements of Atmospheric Trace Gases by Long Path Differential UV/visible Absorption spectroscopy*, Optical and Laser Remote Sensing, edited by Killinger, D.K. and Mooradian, A., pp. 95-105, Springer Verlag, New York, **1983**.
- Platt, U. and Stutz, J., *Differential Optical Absorption Spectroscopy: Principles and Applications, Physics of Earth and Space Environments*, ISBN 978-3-540-21193-8. Springer-Verlag Berlin Heidelberg, **2008**.
- Platt, U., *Differential Optical Absorption Spectroscopy (DOAS), Monitoring by Spectroscopic Techniques*, M. W. Sigrist, J. Wiley, New York, **1994**.
- Platt, U., Heue K.-P. and Pöhler D., *Two- and Three dimensional Observation of Trace Gas and Aerosol Distributions*, in: Kim Y.J., Platt U., Gu M.B., Iwahashi H. (Eds.), Atmospheric and Biological Environmental Monitoring, XIX, Proc. 7th Internatl. Symp. Advanced Environmental Monitoring, Hawaii 2008, Springer, Heidelberg, ISBN: 978-1-4020-9673-0, pages 3-11, **2009a**.
- Platt, U., Marquard, L., Wagner, T., and Perner, D., *Corrections for zenith scattered light DOAS*, Geophys. Res. Lett., 24, 1759-1762, **1997**.
- Platt, U., Meinen, J., Pöhler, D., Leisner, T., *Broadband Cavity Enhanced Differential Optical Absorption Spectroscopy (CE-DOAS) - Applicability and Corrections*, Atm. Meas. Tech. 2, 713-723, **2009**.
- Platt, U., Perner, D. and Pätz, H.W., *Simultaneous measurement of atmospheric CH<sub>2</sub>O, O<sub>3</sub> and NO<sub>2</sub> by differential optical absorption*, J. Geophys. Res., 84 (C10), 6329-6335, **1979**.
- Platt, U., Perner, D., Harris, G.W., Winer, A.M. and Pitts, J.N., *Observations of nitrous acid in an urban atmosphere by differential optical absorption spectroscopy*, Nature 285, 312-314, **1980**.
- Platt, U., *The origin of nitrous acid in the atmosphere*, W. Jäschke, (ed.) NATO ASI-series, Springer Verlag, Heidelberg, pp. 299-319, **1986**.
- Poehler, D., Hartl, A. and Platt, U., *Tomographic LP-DOAS measurements of 2D trace gas distributions above the city of Heidelberg, Germany*, Proceedings of the 6th International Conference on Urban Air Quality, March 27-29 2007, Limassol, Cyprus, UAQ2007 publication, **2007**.
- Poehler, D., Rippel, B., Stelzer, A., Mettendorf, K.U., Hartl, A., Platt, U. and Pundt, I., *Instrumental setup and measurement configuration for 2D-tomographic DOAS measurements of trace gas distributions over an area of a view square km*, Proceedings of the 31st International Symposium of Remote Sensing of the Environment, June 20-24 2005, St.Petersburg, Russia, ISPRS-publication, **2005**.

- Pöhler D., *Fast and durable electromechanical shutter for imaging spectrometers*, Rev. Sci. Instrum. 80, 036104; doi: 10.1063/1.3103628, **2009**.
- Pöhler, D., *Fast and durable electromechanical shutter for imaging spectrometers*, Rev. Sci. Instrum. 80, 036104; doi: 10.1063/1.3103628, **2009**.
- Pöhler, D., *Installations- und Messanleitung zu LP-DOAS mit der „Camera Operating Software“ – COS für Roper Scientific CCD's*, University of Heidelberg, **2008**.
- Pöhler, D., Platt, U., Merten, A., Sihler, H. and Tschritter, J., *Neue Entwicklungen zur (multidimensionalen) Messung der Luftqualität mit DOAS (New developments in (multidimensional) pollution monitoring by DOAS)*, Neue Entwicklungen der Messung und Beurteilung der Luftqualität, VDI-Bericht 2040: 291-295, **2008**.
- Pöhler, D., Vogel L., Frieß U. and Platt U., *Observation of Halogen Species in the Amundsen Gulf, Arctic, by Active Long-Path Differential Optical Absorption Spectroscopy*, Proc. National Acad. of Sciences, **2010**.
- Pöhler, D., Vogel L., Frieß U. and Platt U., *Observation of Halogen Species in the Amundsen Gulf, Arctic, by Active Long-Path Differential Optical Absorption Spectroscopy*, Proc. National Acad. of Sciences, **2010**.
- Prontor-Werk Alfred Gauthier GmbH, Carl Zeiss Group, Gauthierstraße 56, 75323 Bad Wildbad, Germany, SN: 141016-6020-000, **2007**.
- Pundt, I. and Mettendorf, K. U., *The Multibeam long path differential optical absorption spectroscopy instrument: A device for simultaneous measurements along multiple light paths*, Appl. Opt., 44 (23), 4985-4994, **2005**.
- Pundt, I., Mettendorf, K.U., Laepple, T., Knab, V., Xie, P., Lösch, J., Friedeburg, C.v., Platt, U. and Wagner, T., *Measurements of trace gas distributions using Long-path DOAS-Tomography during the motorway campaign BABII: expermeintal setup and result for NO<sub>2</sub>*, Atmos. Environ. 39, 967-975, **2005**.
- Rippel, B., *Vorarbeiten zu tomographischen Langzeit-Spurenstoffmessungen in Heidelberg*, Diploma thesis, Institute of Environmental Physics, Heidelberg, **2005**.
- Rityn, N.E., *Optics of Corner Cube Reflectors*, Sov. J. Opt. Technol. 34, 198, **1967**.
- RNZ, Rhein-Neckar Zeitung, *Wenn der Himmel geröntgt wird, Physik-Doktorand misst purengaskonzentrationen mit Lichtstrahlen – Reflektoren im ganzen Stadtgebiet*, Heidelberg, Newspaper from 31.12.2006.
- Rodgers, C. D., *The Characterization and Error Analysis of Profiles Retrieved from Remote Sounding Measurements*, J. Geophys. Res., 95, p5587-5595, **1990**.
- Roedel, W., *Physik unserer Umwelt: Die Atmosphäre*, Springer Verlag, Berlin Heidelberg New York, **1994**.
- Roscoe, H. K., Fish, D. J. and Jones, R. L., *Interpolation errors in UV-visible spectroscopy for stratospheric sensing: implications for sensitivity, spectral resolution, and spectral range*, Appl. Opt. 35, 427-432, **1996**.
- Russell, A.G., Winner, D.A., Herley, R.A., McCue, K.F. and Cass, G.R., *Mathematical moedlling and control of the dry deposition flux of nitrogen-containing air pollutants*, Environ. Sci. Technol., 27, 2772-2782, **1993**.
- Sakamaki, F., Hatakeyama, S. and Akimoto, H., *Formation of nitrous acid and nitric oxide in the heterogeneous dark reaction of nitrogen dioxide and water vapor in a smog chamber*, Int. J. Chem. Kinet. XV, 1013-1029, **1983**.

- Schatzmann, M. and Leitl, B., *Validation and application of obstacle-resolving urban dispersion models*, Atmos. Environ., 36, 4811 – 4821, **2002**.
- Schatzmann, M., Bächlin, W., Emeis, S., Kühlwein, J., Leitl, B., Müller, W. J., Schäfer, K. and Schlünzen, H., *Development and validation of tools for the implementation of European air quality policy in Germany (Project VALIUM)*, Atmos. Chem. Phys., 6, 3077 – 3083, **2006**.
- Schlothauer and Wauer, *Anmerkungen zur Verkehrszählung K 113 23.10.2007*, provided by the city Administration of Heidelberg, **2009**.
- Schlünzen, K.H., Hinneburg, D., Knoth, O., Lambrecht, M., Leitl, B., Lopez, S., Lüpkes, C., Pankus, H., Renner, E., Schatzmann, M., Schoenemeyer, T., Trepte, S., and Wolke, R., *Flow and transport in the obstacle layer – First results of the microscale model MITRAS*, J. Atmos. Chem., 44, 113 – 130, **2003**.
- Schmid, H. P., *Experimental design for flux measurements: matching scales of observations and fluxes*, Agricultural and Forest Meteorology, 87, 2 – 3, **1997**.
- Schubert, A., *Messungen von spektralen Signaturen in an Oberflächen reflektiertem Licht*, Staatsexamen thesis, University of Heidelberg, Germany, **2009**.
- Seinfeld, J. H. and Pandis, S.N., *Atmospheric chemistry and physics: From air pollution to climate change*, John Wiley & Sons Inc., New York Chichester Weinheim Brisbane Singapore Toronto, **1998**.
- Seitz, K., Buxmann J., Pöhler D., Sommer T., Tschritter J., Neary T., O’Dowd C. and Platt U., *The spatial distribution of reactive iodine species IO from simultaneous active and passive DOAS observations*, Atmos. Chem. Phys. 10, 2117-2128, **2010**.
- Sihler, H., Kern C., Pöhler D. and Platt U., *Applying light-emitting diodes with narrow-band emission features in differential spectroscopy*, Optics Letters 34 (23), 3716-3718, **2009**.
- Sillman, S., Logan, J.A. and Wofsy, S.C., *The Sensitivity of Ozone to Nitrogen Oxides and Hydrocarbons in Regional Ozone Episodes*, J. Geophys. Res. 95, D2 1837-1851, **1990**.
- Simpson W. R, Glasow, R. von, Riedel, K., Anderson, P., Ariya, P., Bottenheim, J., Burrows, J., Carpenter, L. J., Frieß, U., Goodsite, M. E., Heard, D., Hutterli, M., Jacobi, H.-W., Kaleschke, L., Neff, B., Plane, J., Platt, U., Richter, A., Roscoe, H., Sander, R., Shepson, P., Sodeau, J., Steffen, A., Wagner, T and Wolff, E., *Halogens and their role in polar boundary-layer ozone depletion*, Atmos. Chem. Phys., 7, 4375-4418, **2007**.
- Sinreich, R., Frieß, U., Wagner, T. and Platt, U., *Multi Axis differential optical absorption Spectroscopy (MAX-DOAS) of gas and aerosol distributions*, Faraday Discuss., 130,1-12, **2005**.
- Smith, S.W., *The Scientist and Engineer's Guide to Digital Signal Processing*, online book's website at: [www.DSPguide.com](http://www.DSPguide.com), **2009**.
- Sommer, T., *Direct sun light measurements of volcanic plumes using differential optical absorption spectroscopy*. Diploma thesis, University of Heidelberg, **2008**.
- Stahl, Q. R., *Air pollution aspects of aldehydes*, Scott Research Laboratories, NTIS Report PB 188081, **1969**.
- Stelzer, A., *Tomographische Spurengasmessungen in Heidelberg*, Diploma thesis, Institute of Environmental Physics, Heidelberg, **2005**.

- Stockwell, R.W. and Calvert, J.G., *The near ultraviolet absorption spectrum of gaseous HONO and N<sub>2</sub>O<sub>3</sub>*, J. Photochem. 8, 193-203, **1978**.
- Stull, R. B., *An Introduction to Boundary Layer Meteorology*, Kluwer Acad. Publ., Dordrecht, Boston, London, **1988**.
- Stutz J., Alicke, B. and Neftel, A., *Nitrous acid formation in the urban atmosphere: Gradient measurements of NO<sub>2</sub> and HONO over grass in Milan, Italy*, J. Geophys. Res., 107, **2002**.
- Stutz, J. and Platt U., *Numerical analysis and estimation of the statistical error of differential optical absorption spectroscopy measurements with least-squares methods*, Appl. Opt., 35 (30), 6041-53, **1996**.
- Stutz, J. and Platt, U., *Improving long-path differential optical absorption spectroscopy (DOAS) with a quartz-fiber mode-mixer*, Appl. Opt., 36, 1105 – 1115, **1997**.
- Stutz, J., Kim, E.S., Platt, U., Bruno, P., Perrino, C., Febo, A., *UV-visible absorption cross-section of nitrous acid*, J. Geophys. Res. 105, 14585-14592, **2000**.
- Stutz, J., *Messung der Konzentration troposphärischer Spurenstoffe mittels Differentieller-Optischer-Absorptionsspektroskopie: Eine neue Generation von Geräten und Algorithmen*, PhD Thesis, Institute of Environmental Physics, Heidelberg, **1996**.
- Todd, L. and Ramachandran, G., *Evaluation of algorithms for tomographic reconstruction of chemical concentrations in indoor air*, Am. Ind. Hyg. Assoc. J., 55, 403–416, **1994**.
- Treado, P. J. and Nelson, M. P., *Handbook of Vibrational Spectroscopy*; J. M. Chalmers, P. R. Griffiths, Wiley, New York; 1429-1459, **2002**.
- Trick, S., *Formation of nitrous acid on urban surfaces, A physical-chemical perspective*, PhD Thesis, Institute of Environmental Physics, Heidelberg, **2004**.
- Truckenmüller, A., Grawe, D., and Schlünzen, K. H., *A model system for the assessment of ambient air quality conforming to EC directives*, Meteorol. Zeitschrift, 13 (5), 387 – 3949, **2004**.
- Tschritter, J., *Entwicklung einer DOAS Optik der 3. Generation und ein vergleich mit herkömmlichen Systemen*, Diploma thesis, University of Heidelberg, Germany, **2007**.
- Umweltbundesamt, *Auswertung der Luftbelastungssituation 2009*, Umweltbundesamt Fachgebiet II 4.2 „Beurteilung der Luftqualität“, **2010**.
- Umweltbundesamt, *Hintergrundinformation: Sommersmog*, Umweltbundesamt, **2005**.
- Umweltbundesamt, *Luftbelastung Deutschland 2008 (vorläufige Auswertung)*, from <http://www.umweltbundesamt.de/luft/schadstoffe/luftbelastung.htm>, **2009**.
- Umweltbundesamt, *NO<sub>2</sub>- und SO<sub>2</sub>- Emissionsdaten für Deutschland* **2000**.
- Umweltbundesamt, *Report to the air quality in Germany*, **2005**.
- Umweltbundesamt, *Statistic of NO<sub>2</sub> between 2000 and 2005*, from <http://www.env-it.de/umweltbundesamt/luftdaten/documents.fwd>, **2006**.
- Umweltmessung, Landesanstalt für Umwelt, *Messungen und Naturschutz Baden-Württemberg (LUBW)*, <http://www.lubw.baden-wuerttemberg.de>, **2006**.
- UniSpiegel, University Heidelberg, *Wenn der Himmel geröntgt wird, Physik-Doktorand misst purengaskonzentrationen mit Lichtstrahlen – Reflektoren im ganzen Stadtgebiet, January, Heidelberg, 2007*.

- Vandaele, A.C., Hermans, C., Simon, P.C., Carleer, M., Colins, R., Fally, S., Mérienne, M.F., Jenouvrier, A. and Coquart, B., *Measurements of the NO<sub>2</sub> absorption cross-sections from 42000 cm<sup>-1</sup> to 10000 cm<sup>-1</sup> (238-1000 nm) at 220 K and 294 K*, J. Quant. Spectrosc. Radiat. Transfer 59, 171-184, **1998**.
- Vandaele, A.C.; Simon, T.C.; Goilmont, J.M.; Carleer, C.M.; R.Colin: *SO<sub>2</sub> Absorption Cross Section Measurement in the UV using Fourier Transform Spectrometer*. In: J. Geophys. Res. 99, S. 25599–25605, **1994**.
- Veitel, H., *Vertical Profiles of NO<sub>2</sub> and HONO in the boundary layer*, PhD Thesis, Institute of Environmental Physics, Heidelberg, **2002**.
- Voigt, S. ; Orphal, J. ; Bogumil, K. ; Burrows, J. P., The temperature dependence (203-293 K) of the absorption cross sections of O<sub>3</sub> in the 230-850 nm region measured by Fouriertransform spectroscopy, J. Photochem.and Photobiol. A, 143, 1-9, **2001**.
- Voigt, S., Orphal, J. and Burrows, J. P., *The temperature- and pressure-dependence of the absorption cross-sections of NO<sub>2</sub> in the 250-800 nm region measured by Fouriertransform spectroscopy*, J. Photochem. and Photobiol., A, 149, 1-7, **2002**.
- Volkamer, R., Molina, L. T., Molina, M. J., Shirley, T., Brune, W. H., *DOAS measurement of Glyoxal as a new marker for fast VOC chemistry in urban air*, Geophys Res Lett 32: L08806, **2005a**.
- Volkamer, R., Spietz, P., Burrows, J.P. and Platt, U., *High-resolution absorption cross-section of Glyoxal in the UV/vis and IR spectral ranges*, J Photoch Photobio A: Chemistry 172:35 – 46, **2005b**.
- Wagner, T. and U. Platt, *Satellite mapping of enhanced BrO concentrations in the troposphere*, Nature, 395, 486-490, **1998**.
- Wayne, R. P., *Chemistry of Atmospheres: An Introduction to the Chemistry of the Atmospheres of Earth, the Planets, and their Satellites*, Oxford University Press, 3rd edition, **2000**.
- Weidner, F., *Development and Application of a Versatile Balloon-Borne DOAS Instrument for Skylight Radiance and Atmospheric Trace Gas Measurements*, Dissertation, Institut of Environmental Physics, Heidelberg, **2005**.
- White, J. U., *Long optical paths of large aperture*, J Opt Soc Am, 32:285-288, **1942**.
- White, J. U., *Very long optical paths in air*, J Opt Soc Am, 66:411-416, **1976**.
- WHO - World Health Organisation, *Air quality guidelines for Europe - Second edition*, WHO Regional Publications, European Series, No. 91, WHO Copenhagen, **2000**.
- Winner, A.M. and Biermann, H.W., *Long Pathlength Differential Optical Absorption Spectroscopy (DOAS) Measurements of Gaseous HONO, NO<sub>2</sub> and HCHO in the California South Coast Air Basin*, Research On Chemical Intermediates, 20 (3-5), 423-445, **1994**.
- Wright, T. E., Burton, M. R., Pyle, D. M. and Caltabiano, T., *Scanning tomography of SO<sub>2</sub> distribution in a volcanic gas plume*. Geophys Res Lett 35:L17811, **2008**.
- Yost, M. G., Gadgil, A. J., Drescher, A. C., Zhou, Y., Simonds, M. A., Levine, S. P., Nazaroff, W. and Saisan, P.: *Imaging indoor tracer-gas concentrations with computed tomography: experimental results with a remote sensing FTIR system*, Am. Ind. Hyg. Ass. J., 55, 395–402, **1994**.

CHAPTER 10

Zel'dovich, Y.B., Raizer, Y.P., *Rates of relaxation processes in gases (8/9), Physics of Shock Waves and High-Temperature Hydrodynamic Phenomena 1*, 374–382, **1967**.

# 11 Acknowledgements & Danksagung

Das diese Arbeit zustande gekommen ist habe ich zahlreichen Personen zu verdanken, denen ich allen auf diesem Weg danken möchte. Insbesondere möchte ich folgende Personen erwähnen:

Ganz besonders möchte ich mich bei Ulrich Platt bedanken für die Möglichkeit in seiner Arbeitsgruppe diese Doktorarbeit auf diesem Gebiet durchzuführen. Vielen Dank für die große Unterstützung und die zahlreichen Ideen, von denen noch nicht alle hier realisiert werden konnten. Vor allem möchte ich mich für die Freiheiten und Möglichkeiten bedanken die es mir ermöglichten auch auf anderen interessanten Themengebieten aktiv zu arbeiten und zu forschen. Ich hoffe auf noch zahlreiche Jahre gemeinsamer Arbeit.

Besten Dank an Thomas Wagner der diese Arbeit immer unterstützte und nicht nur motivierte, sondern auch viele hilfreiche Ideen beisteuerte. Außerdem hat er sich bereit erklärt diese Arbeit zu begutachten. Vielen Dank dafür.

Der ehemaligen DOAS Tomographie Gruppe unter der Leitung von Irene Pundt für das anbieten dieser Arbeit. Ohne das Tomographie Projekt hätte es diese Arbeit nie gegeben.

Ganz besonderer Dank gilt Andreas Hartl der mit mir über die Jahre an den tomographischen Inversionen gearbeitet hatte um sowohl die zahlreichen Softwarefehler zu beheben, als auch die Rekonstruktion zu verbessern. Ohne seine zum großen Teil freiwillige Arbeit, wäre es nicht zu diesen Ergebnissen gekommen.

Den Zahlreichen Firmen und Unterstützern des Projektes sei gedankt, die es kostenfrei ermöglichten die Messgeräte und Reflektoren in Heidelberg zu installieren. Dabei sei besonders „Heidelberger Druckmaschinen“ (insbesondere Herr Brandenburger und Frau Stichert) und „SAS Deutschland“ (insbesondere Frau Richter und Herr Dennert) zu danken, die es mir ermöglichten die großen Teleskope mit all ihren Geräten auf deren Gebäuden zu installieren sowie mir Zugang für regelmäßige Wartungsarbeiten und Kontrollen gewährten. Danke auch für die Übernahme der Betriebskosten (Strom). Allen Kolleginnen und Kollegen vielen Dank die beim Auf- und Abbau der Geräte geholfen hatten.

Den folgenden Kirchen, Firmen, Einrichtungen, Organisationen und Gemeinschaften seien gedankt für die Ermöglichung der Installation der Retro Reflektoren an deren Gebäude (alphabetisch sortiert): Galleria Kaufhof (Bismakplatz 1), Heidelberger Druckmaschinen AG, Heidelberger Hausverwaltung Hans-Thoma-Str. 72, Heiliggeistkirche, Hotel-Restaurant Molkenkur, Luthergemeinde, Heidelberg Physikalisches Institut, Providenzkirche, Krankenhaus Salem, St. Bonifazius Kirche, Studentenwerk & Studentenwohnheim INF 683, SWR Königstuhl.

Ein großes Dankeschön an die Arbeitsgruppe für die Unterstützung und die gemeinsame Arbeit und inspirationen in den letzten Jahren. Besonderer Dank an André Merten, Bernhard

Rippel, Bing Chao, Christoph Kern, Claudia Hak, Holger Sihler, Ilia Louban, Jens Tschritter, Joelle Buxmann, Katja Seitz, Klaus-Peter Heue, Leif Vogel, Maria Martin, Robert Holla, Roman Sinnreich und Thomas Lehmann.

Allen vielen Dank die diese Arbeit korrigiert und viele Anregungen beigesteuert haben: Alexandre de Aguinaga, Andreas Hartl, Christoph Kern, Holger Sihler, Jens Tschritter, Joelle Buxmann, Katja Seitz, Klaus-Peter Heue, Martin Horbanski, Nicole Bobrowski, Johannes Zielke und Robert Holla.

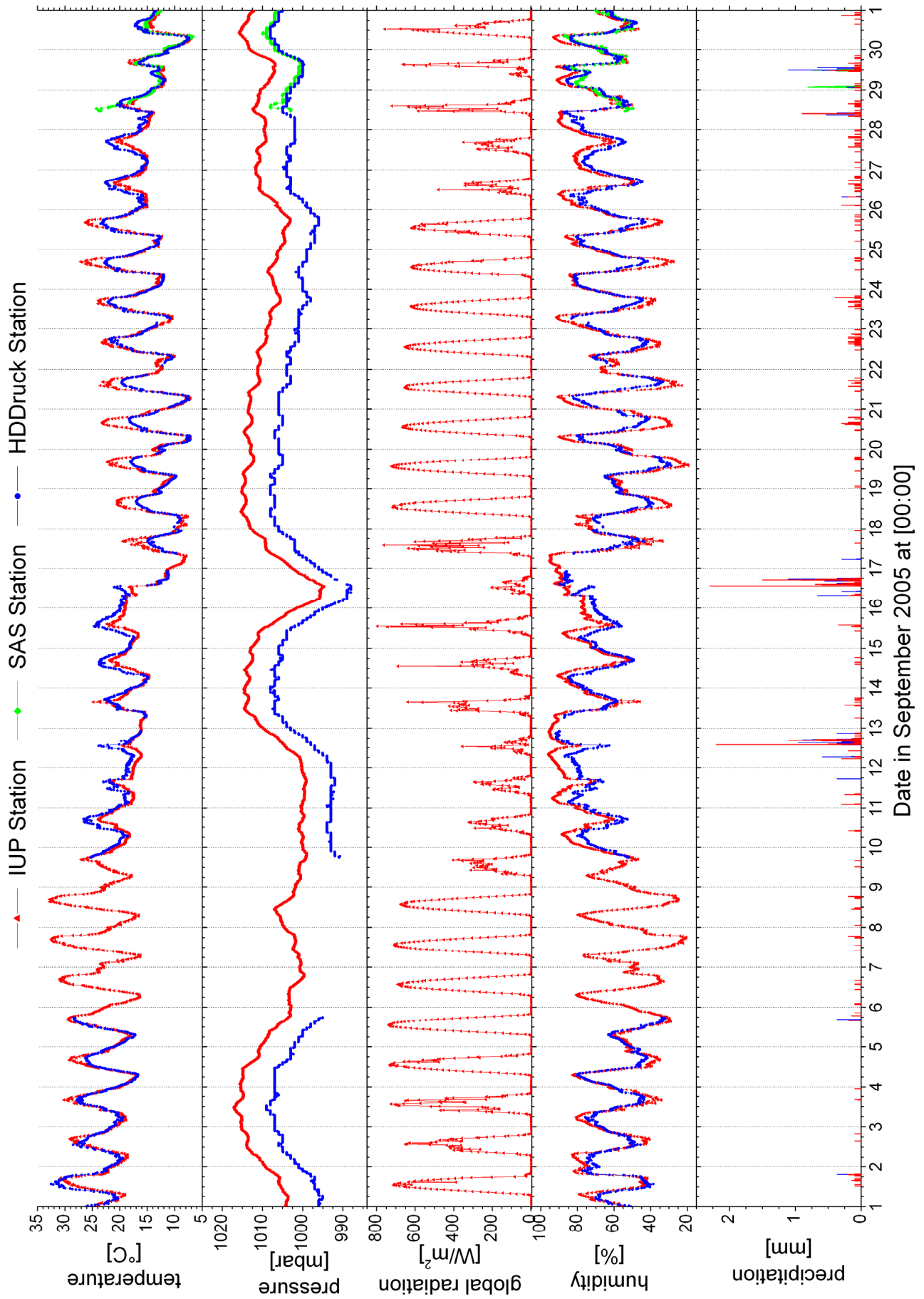
Ein Großes Dankeschön an die IUP Werkstatt für die Konstruktion der vielen Bauteile.

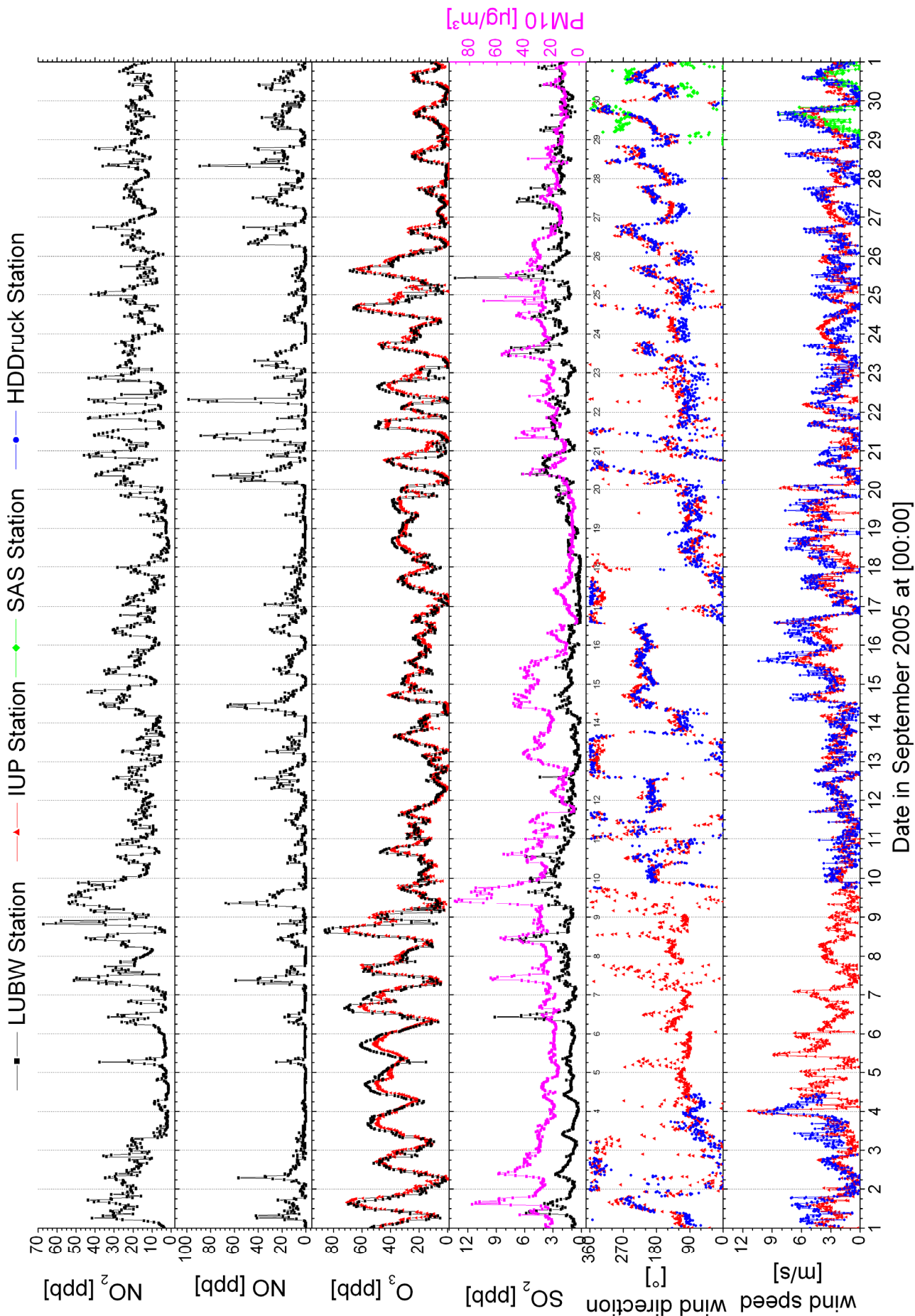
Zum Schluss noch der wichtigste Dank an meine Familie und Freunde die mich über die vielen Jahre so unterstützt haben das ich so weit geschafft habe. Am meisten meiner Frau Julia, die mich über die vielen Jahre so sehr unterstützt hatte und es erduldet wenn ich wieder Nächte und Wochenenden an den Geräten arbeitete. Ohne diese Unterstützung, vor allem seit der Geburt unseres Sohnes Fabio, wäre die Arbeit wohl nicht so vollendet worden. Ich bin Dir so dankbar und freue mich auf die weiteren gemeinsamen Jahre.

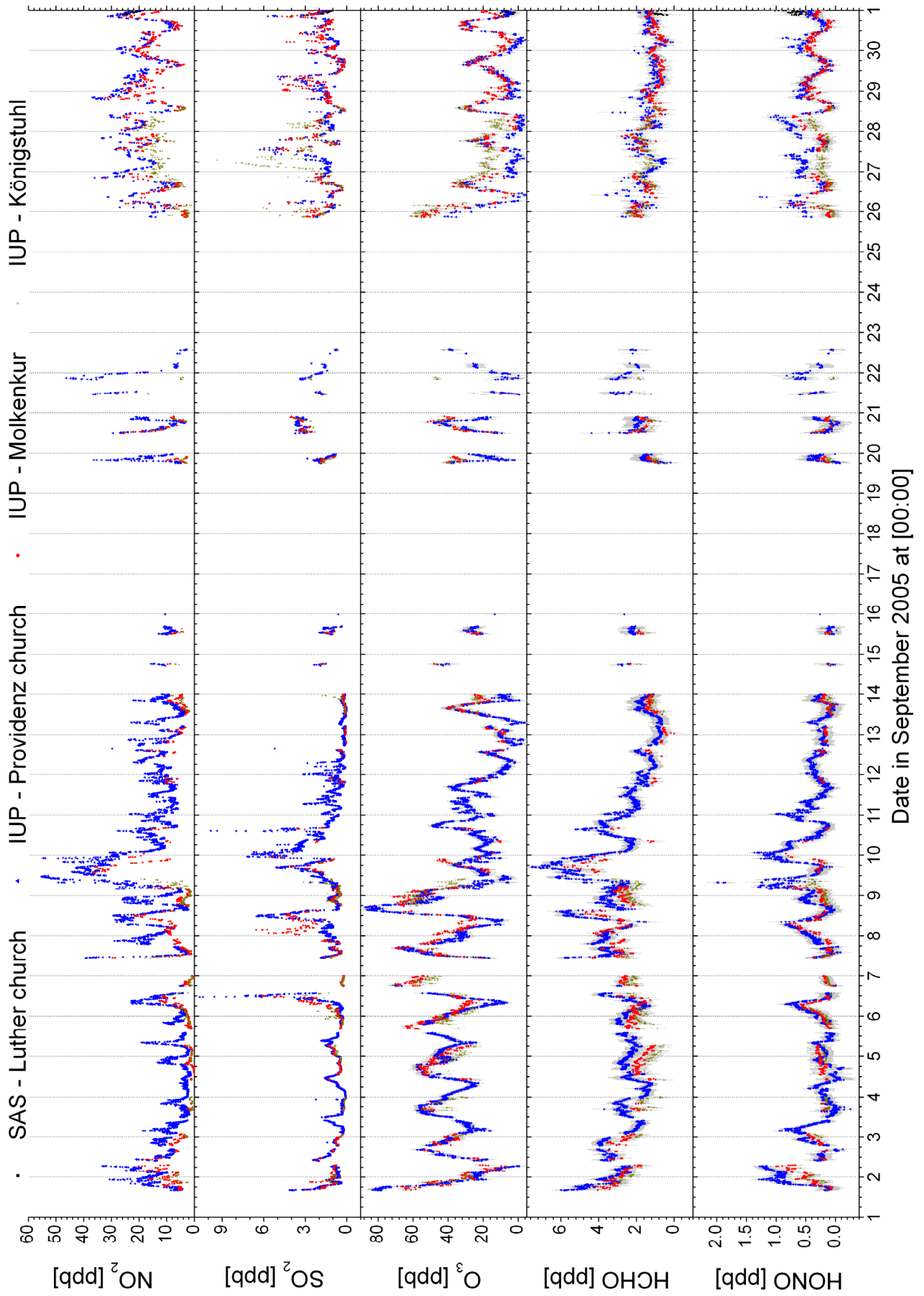
## 12 Appendix

For each month here are the following data shown from metrological stations, in-situ monitors and some LP-DOAS measurements (full time resolution). For January 2007 all available time series are plotted as an example. They can be found for the other months on the supplemented data DVD (*Chapter 8.16*).

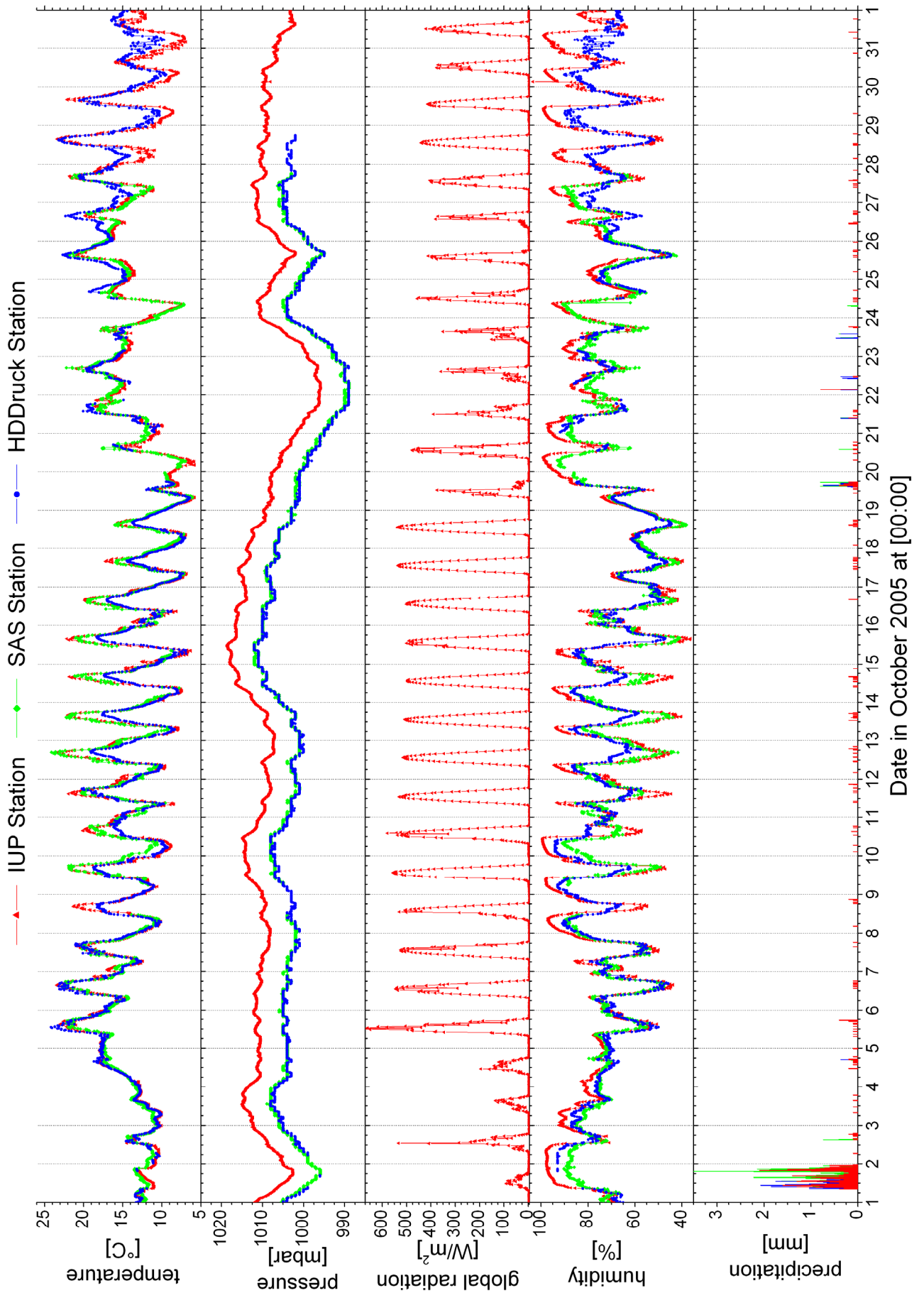
12.1 Data September 2005 (selected plots)

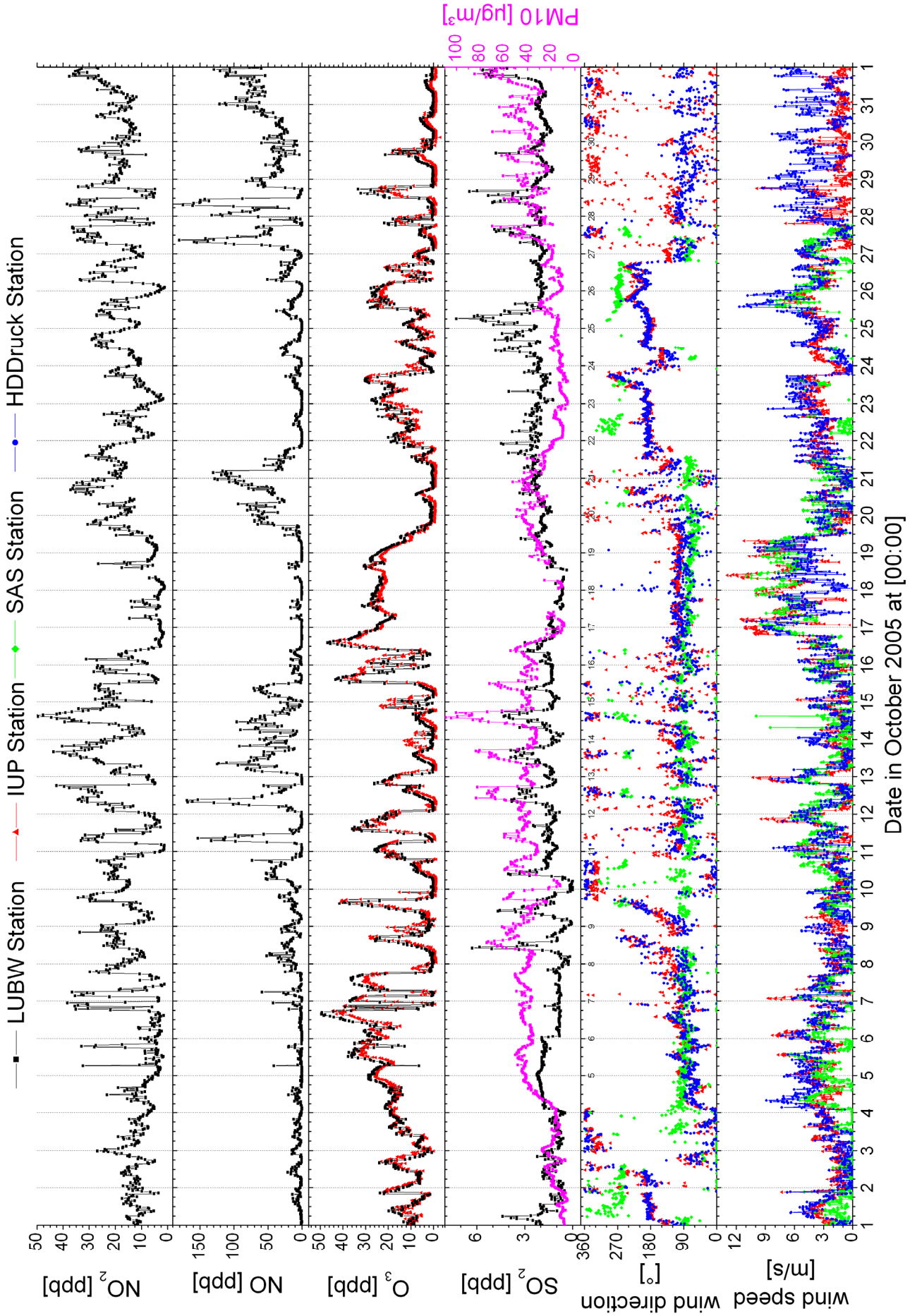


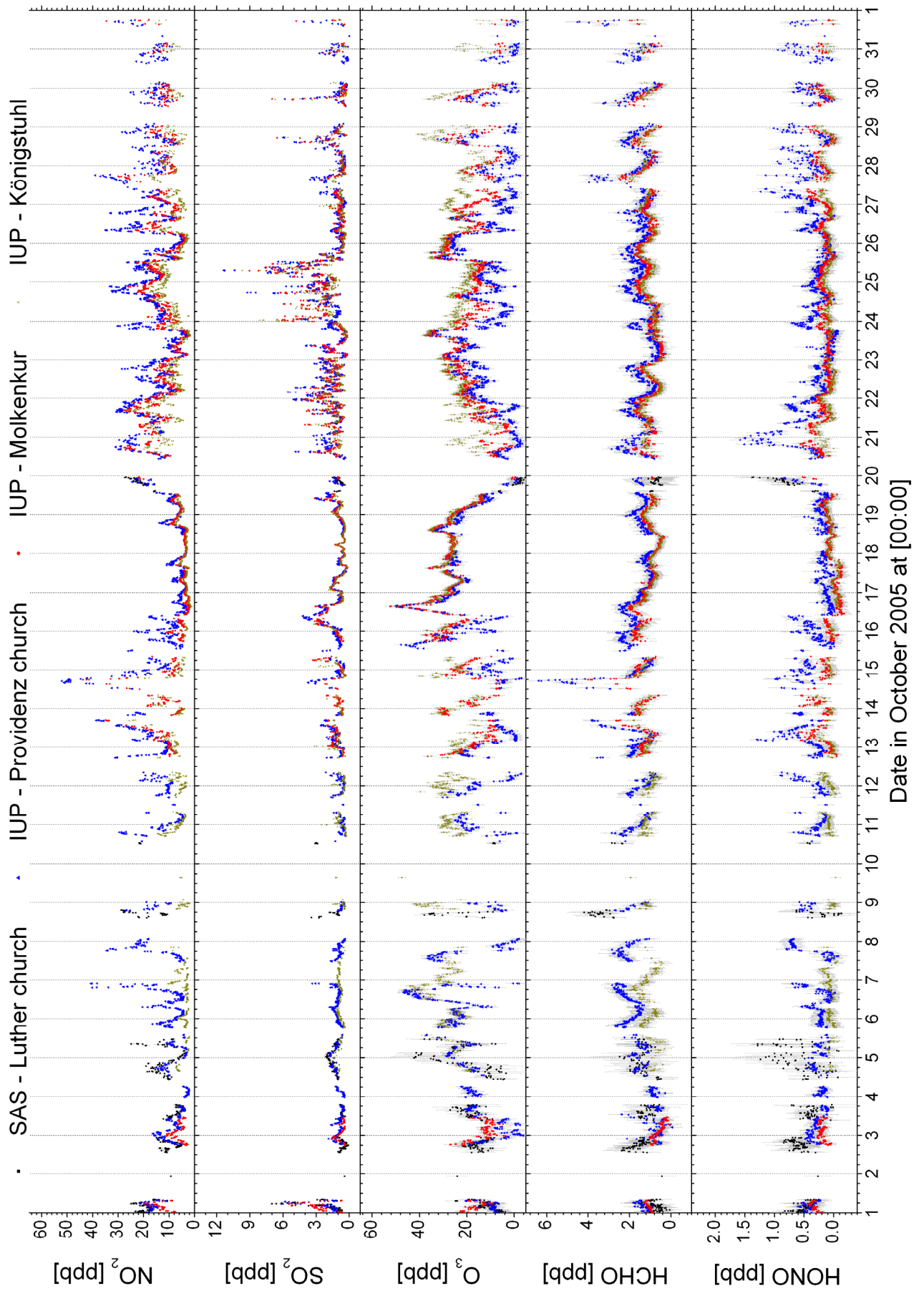




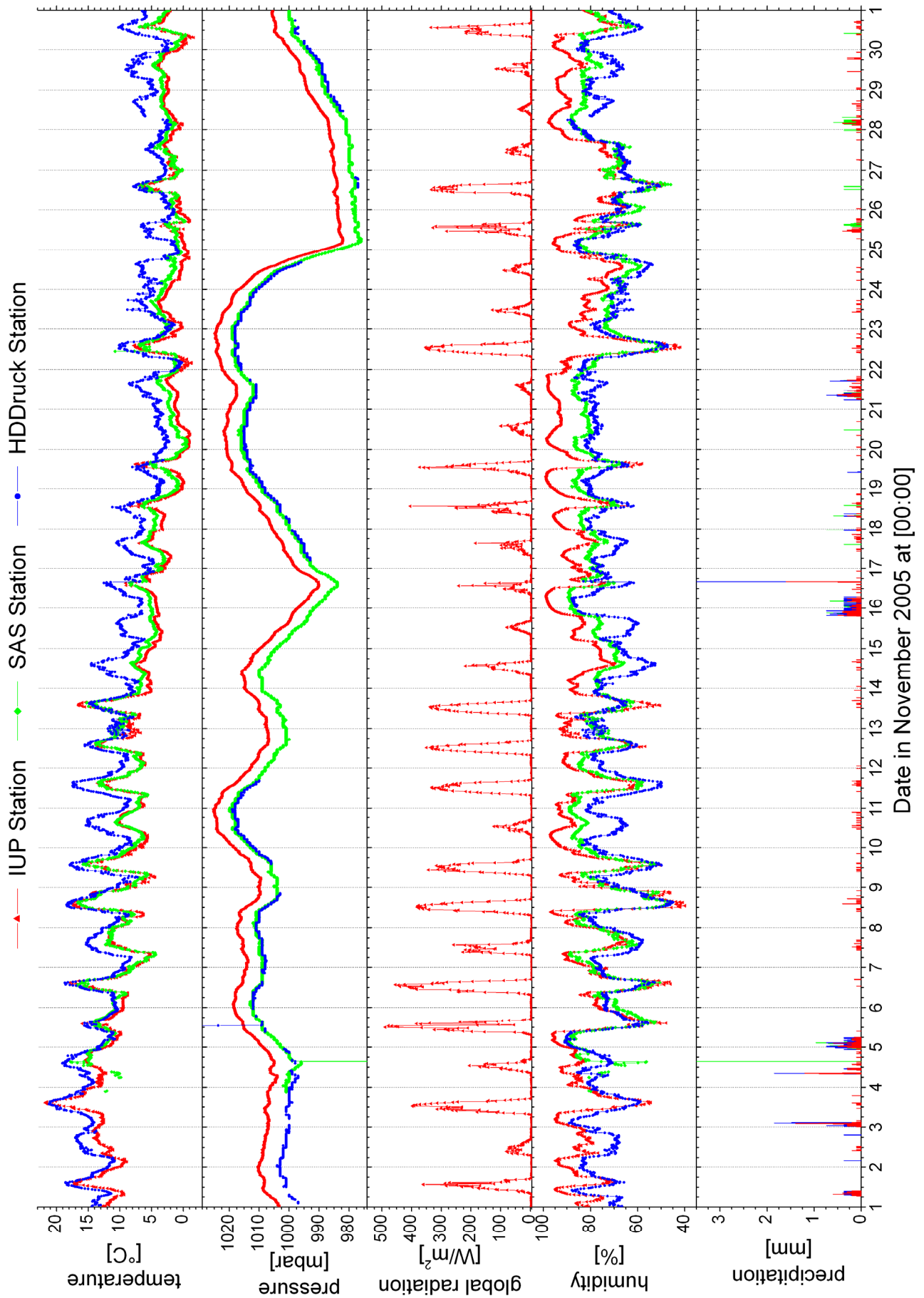
12.2 Data October 2005 (selected plots)

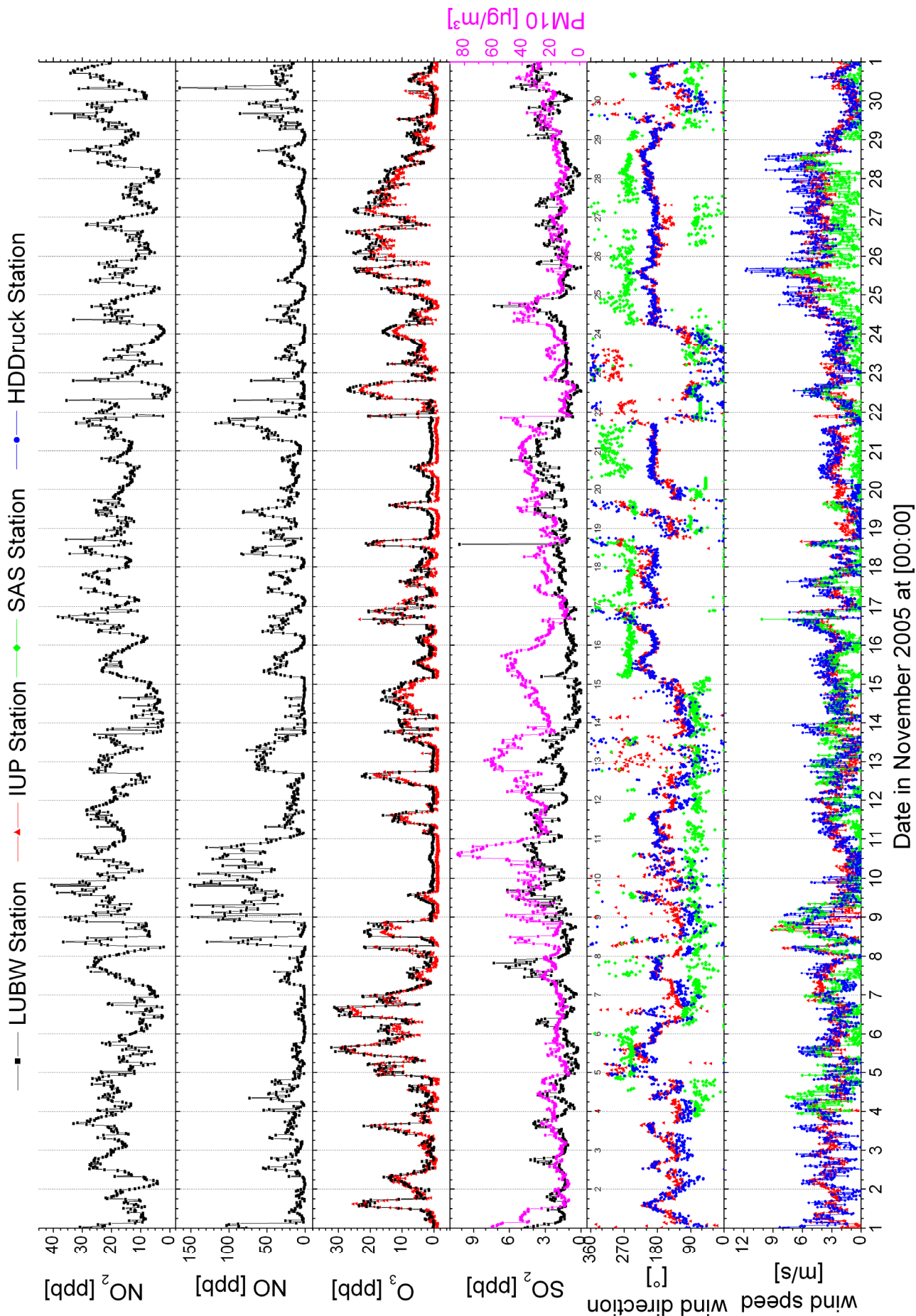


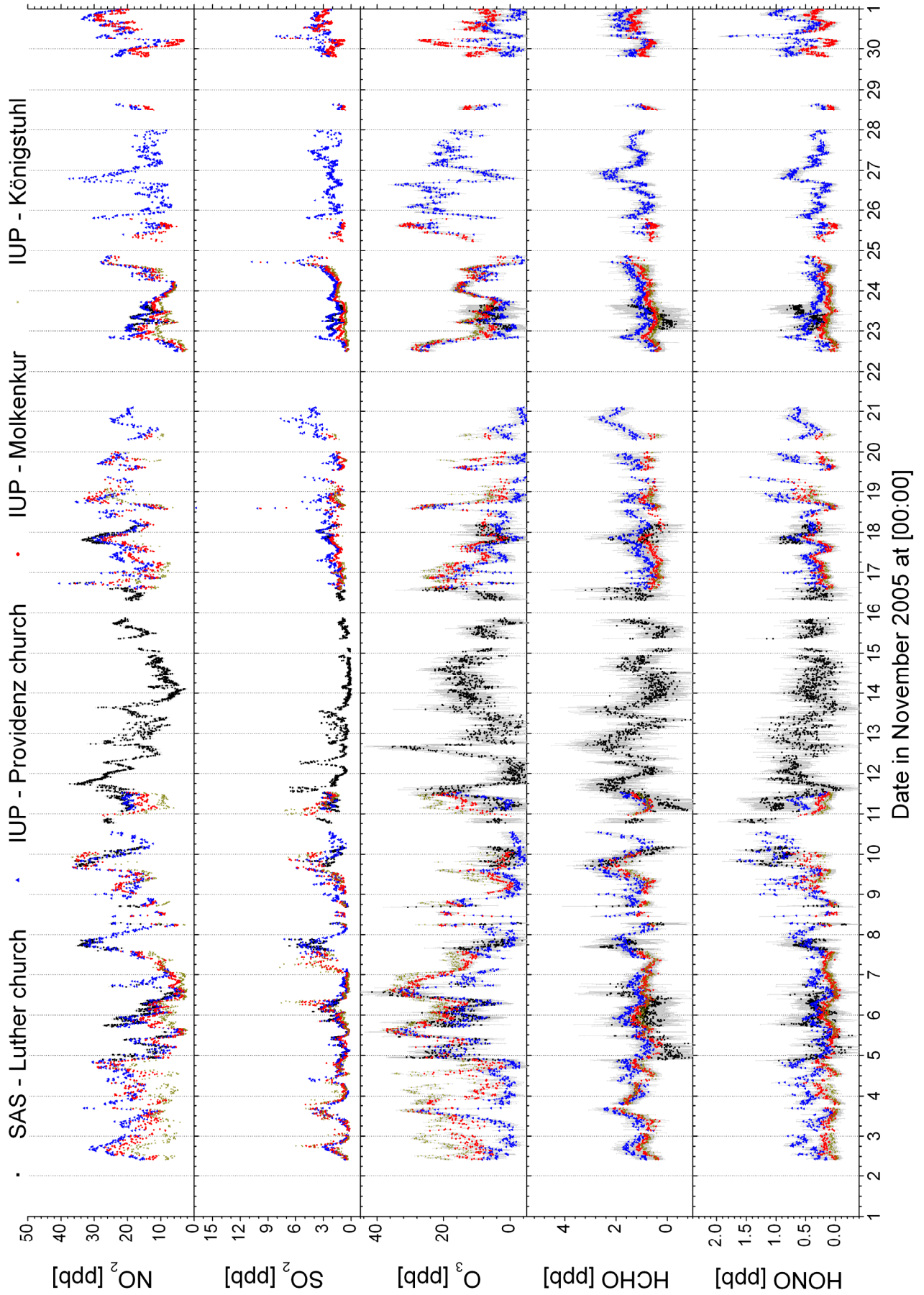




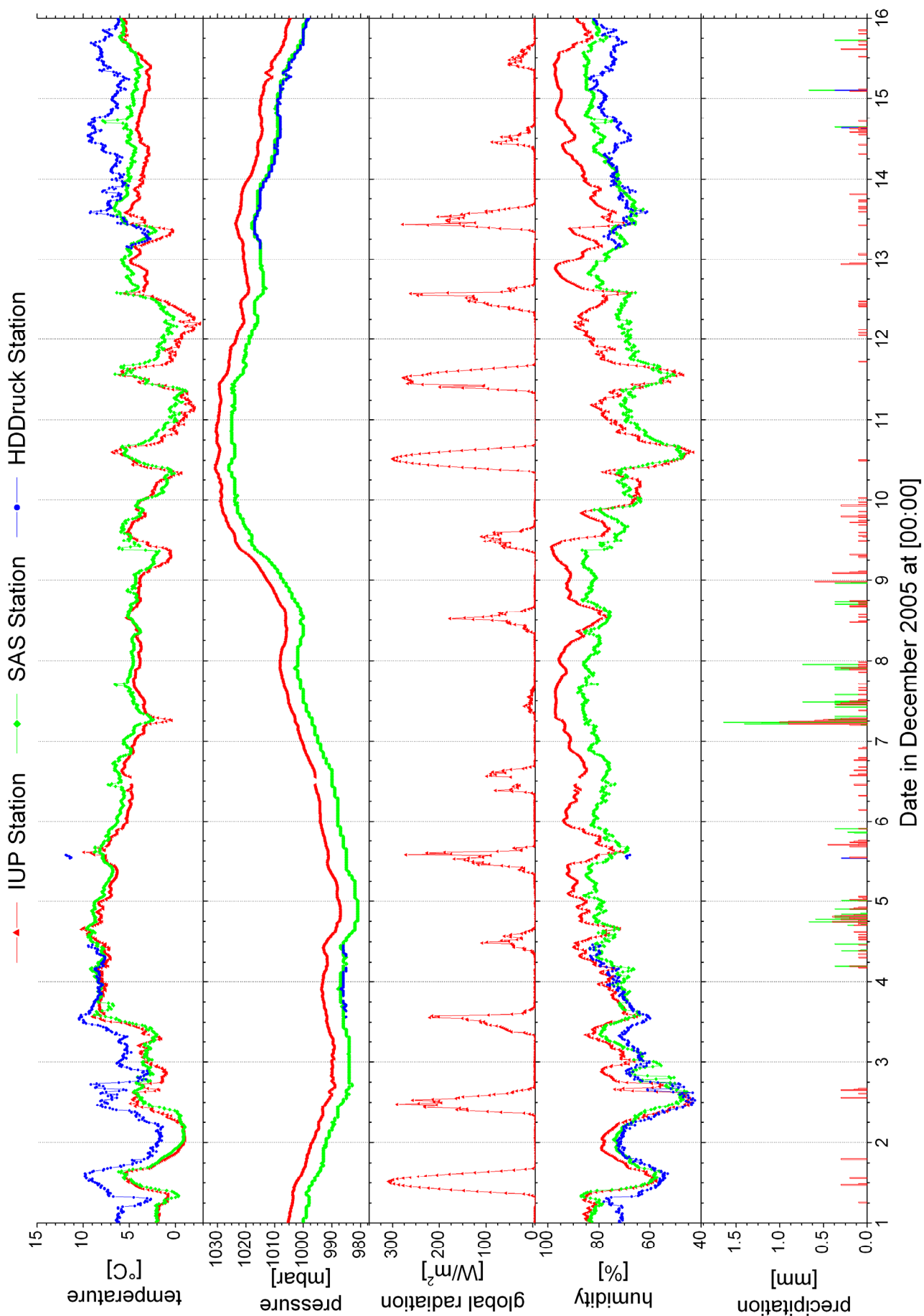
12.3 Data November 2005 (selected plots)

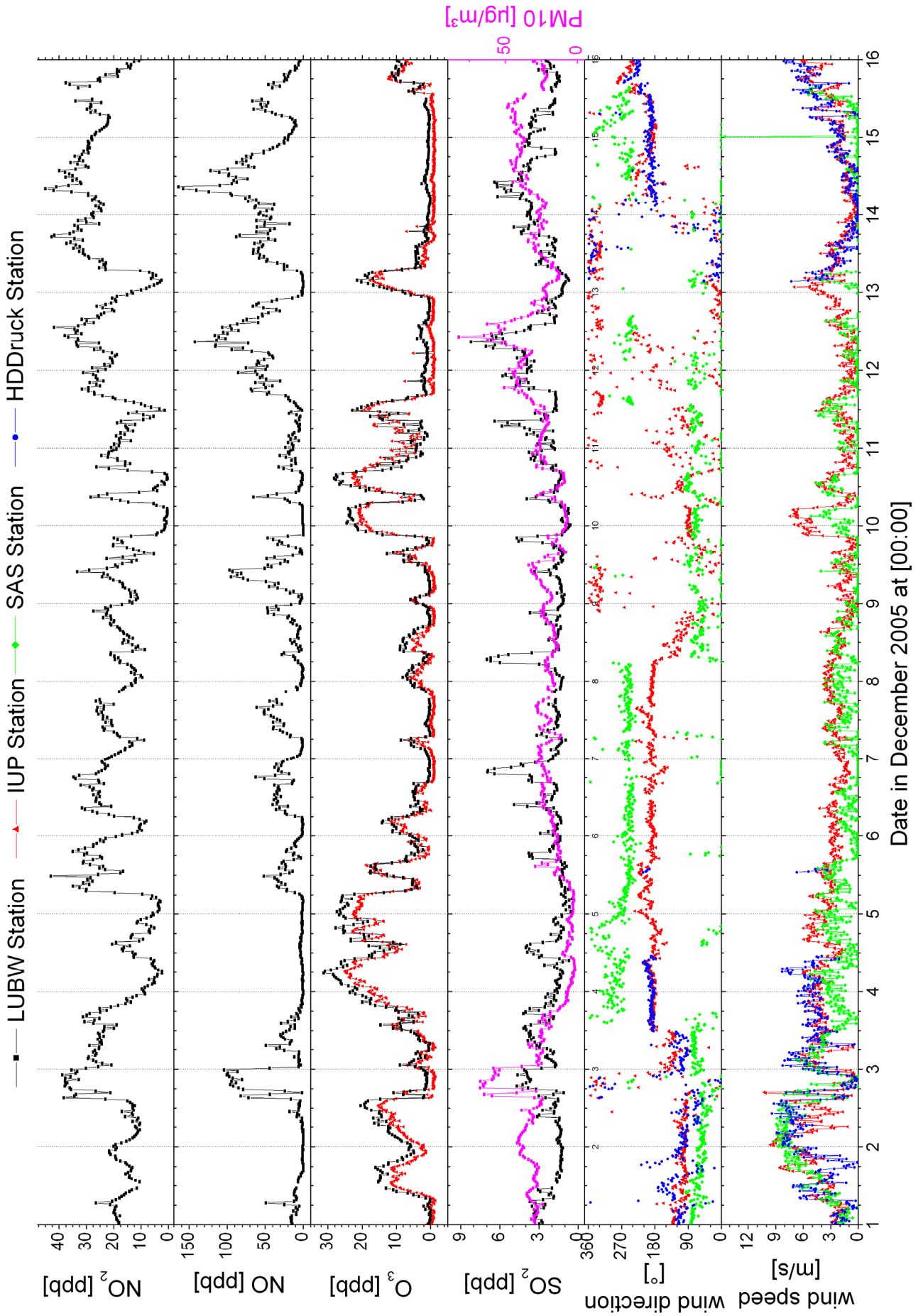


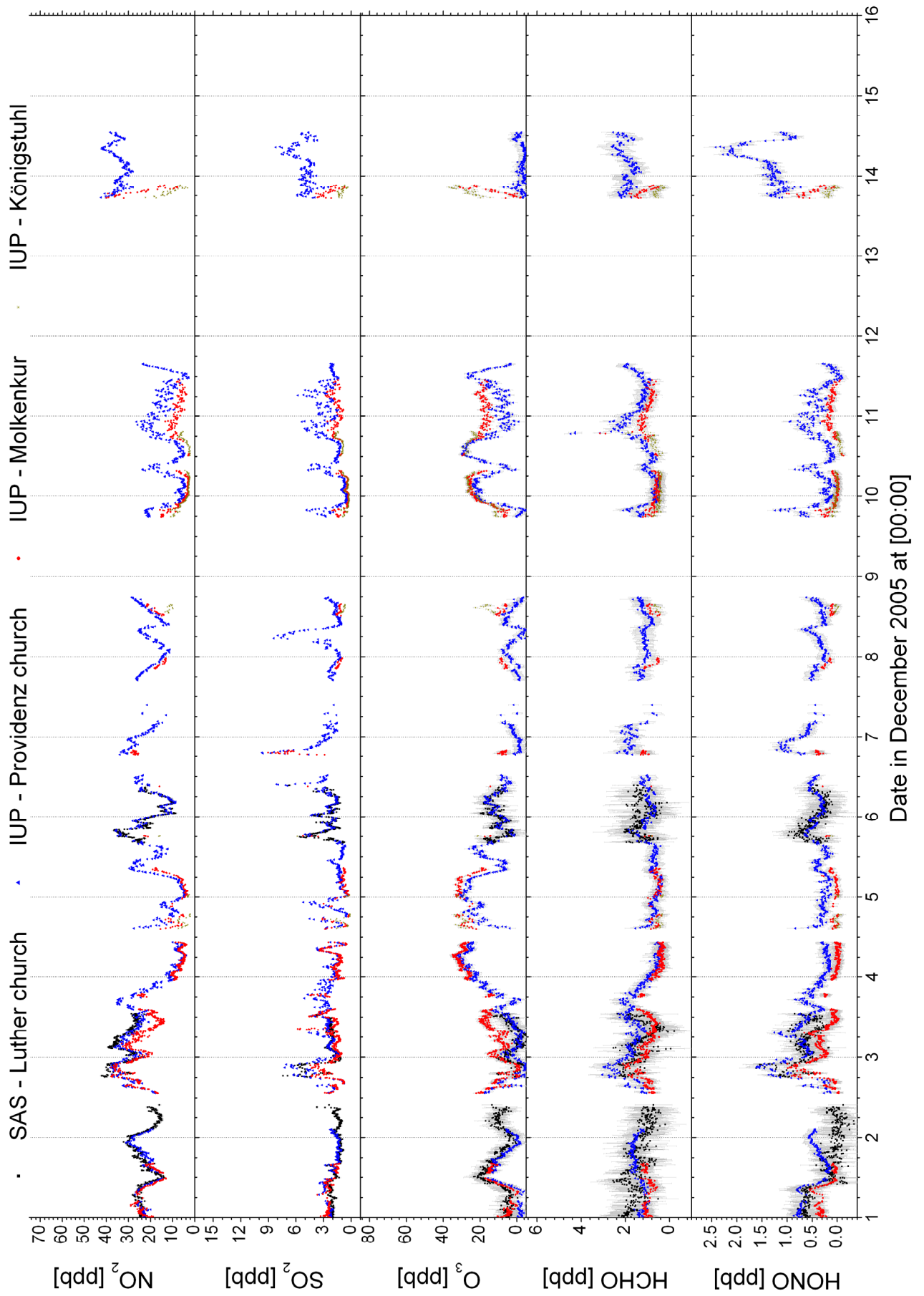




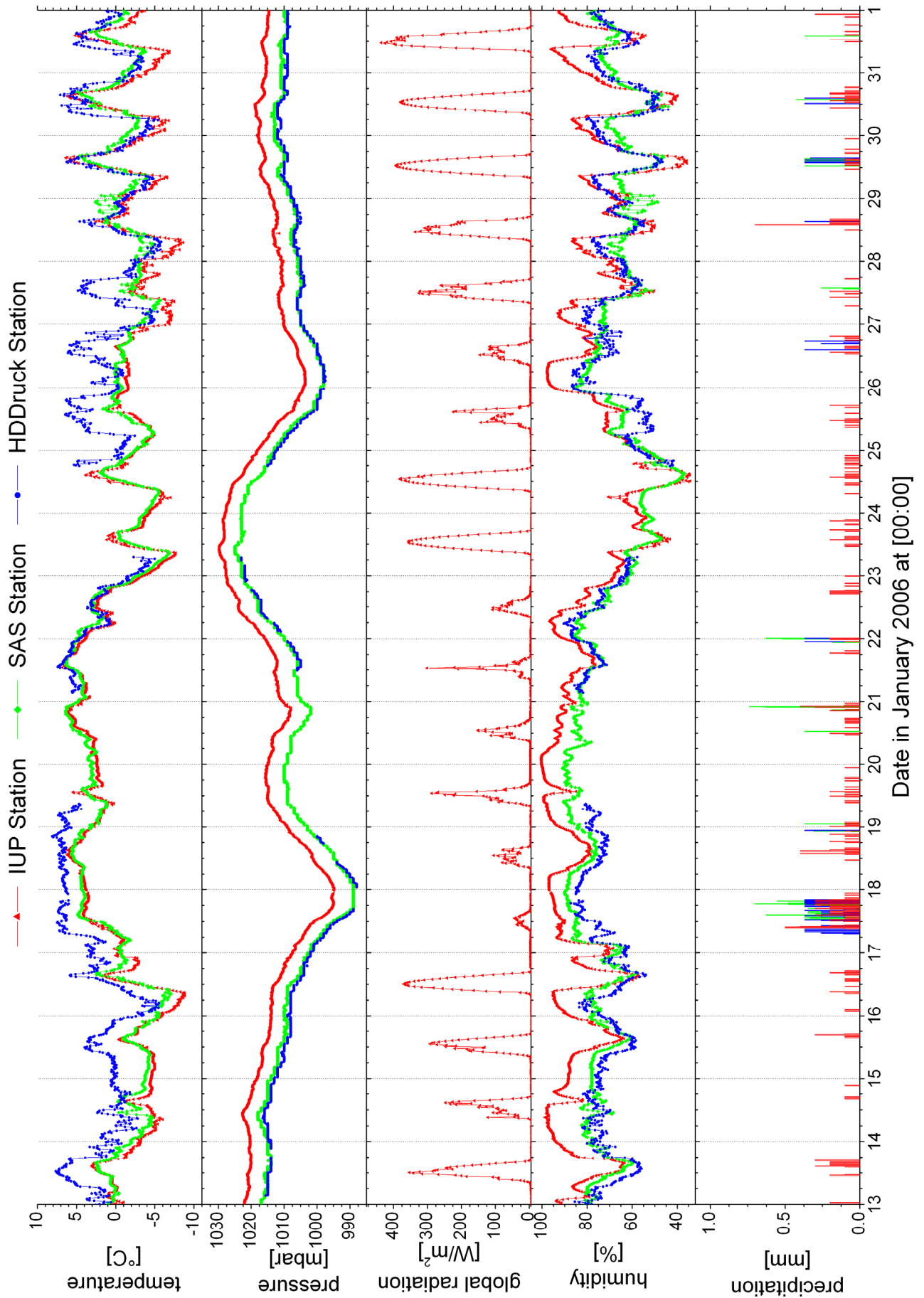
12.4 Data December 2005 (selected plots)

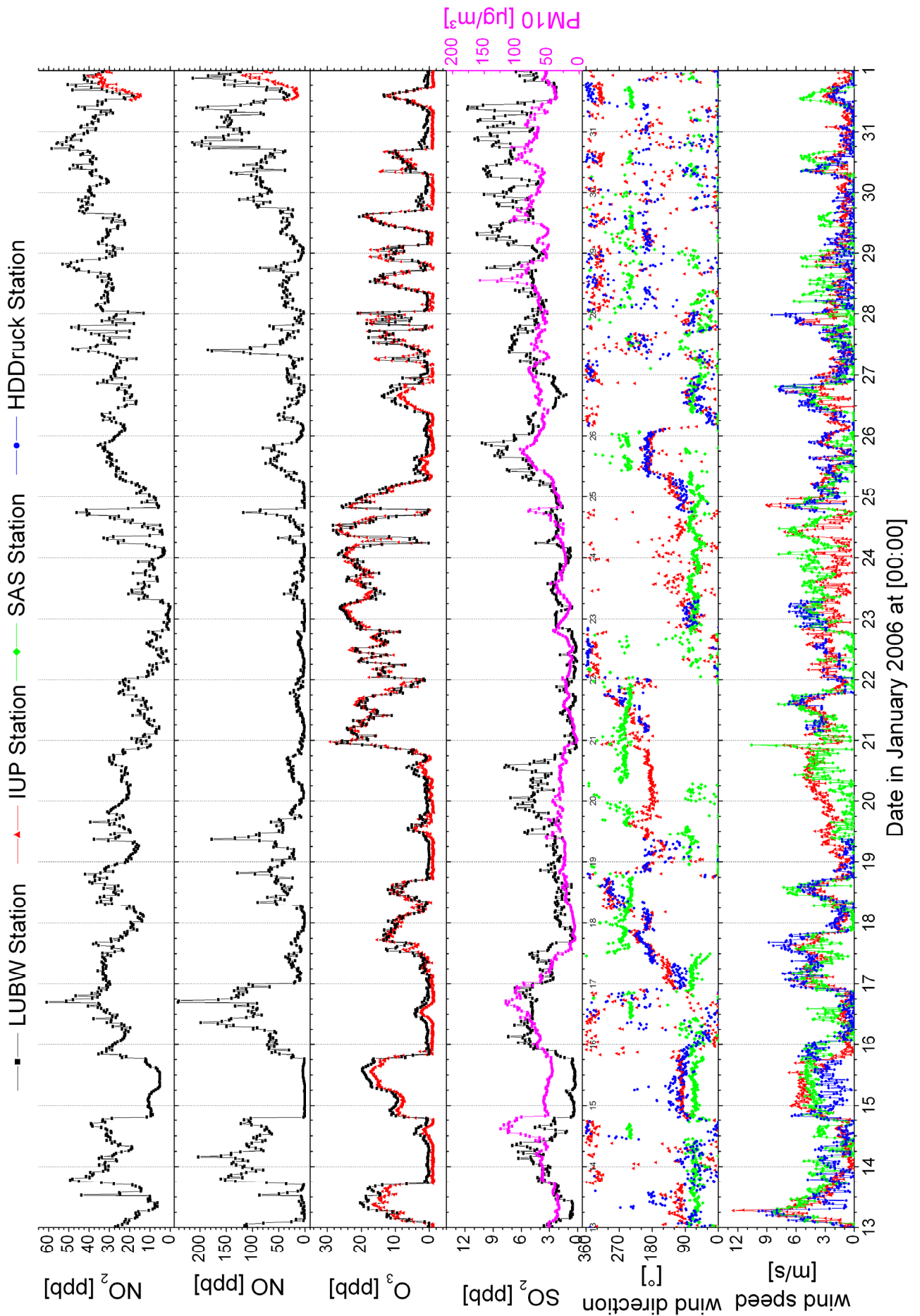


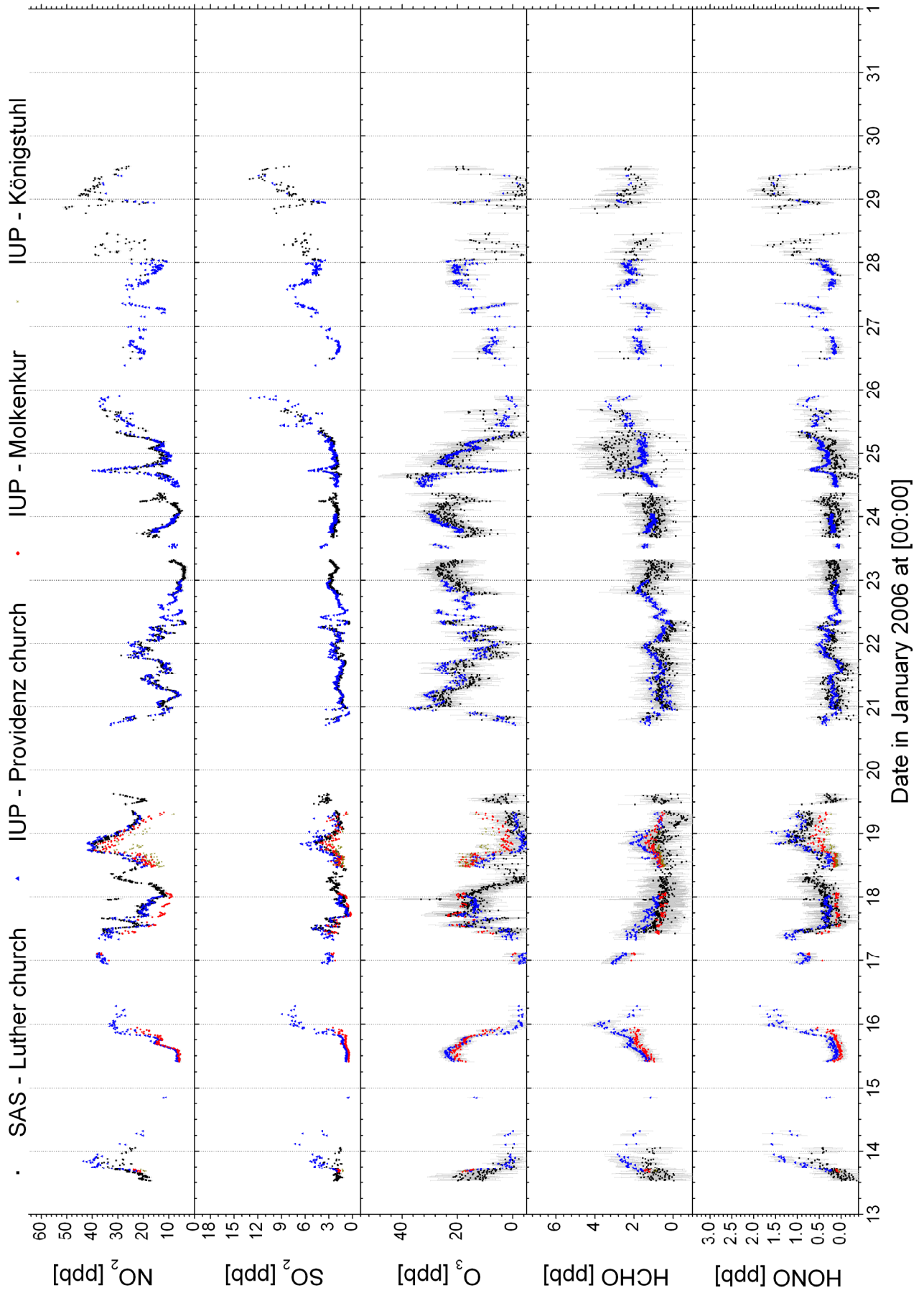




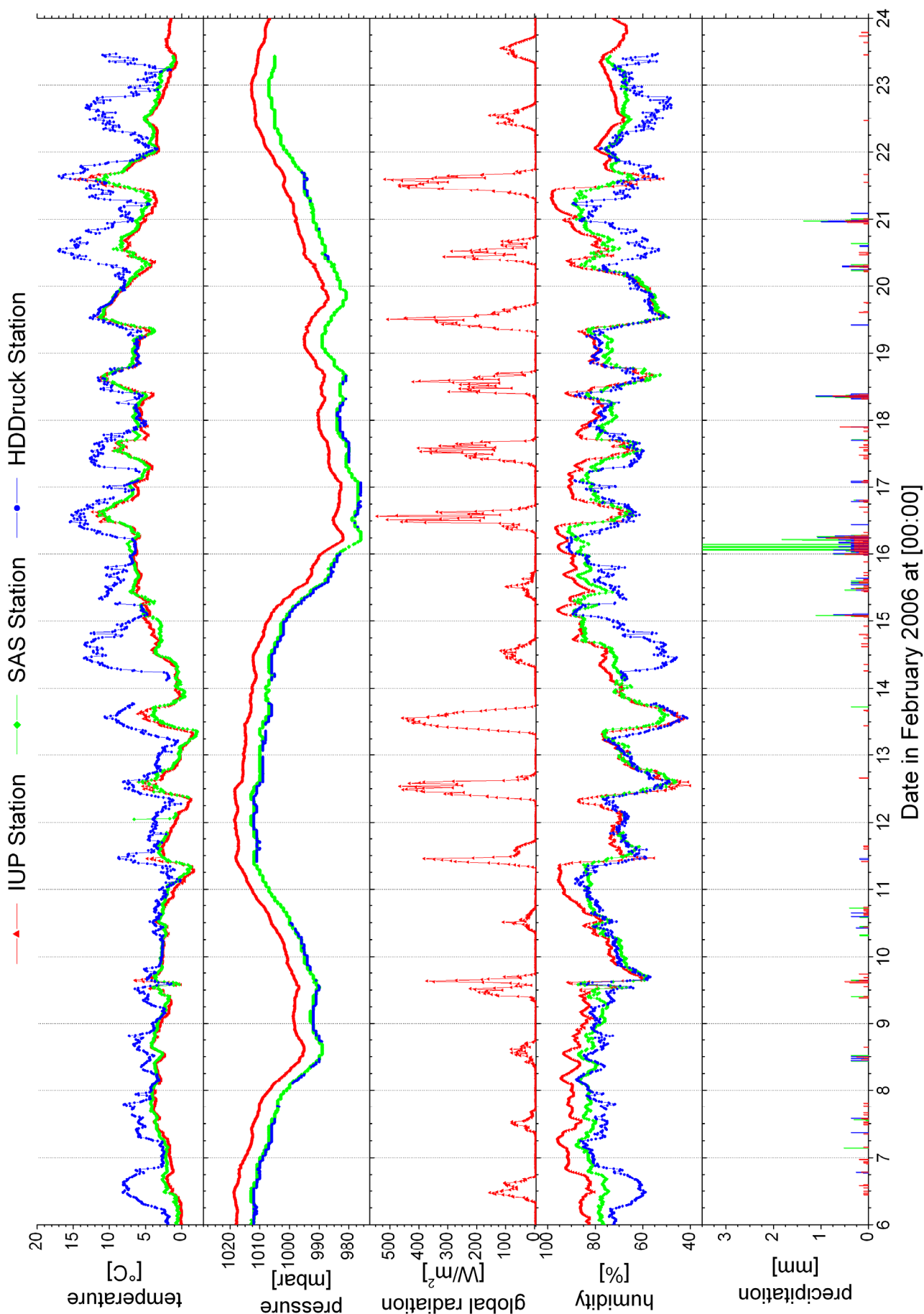
*12.5 Data January 2006 (selected plots)*

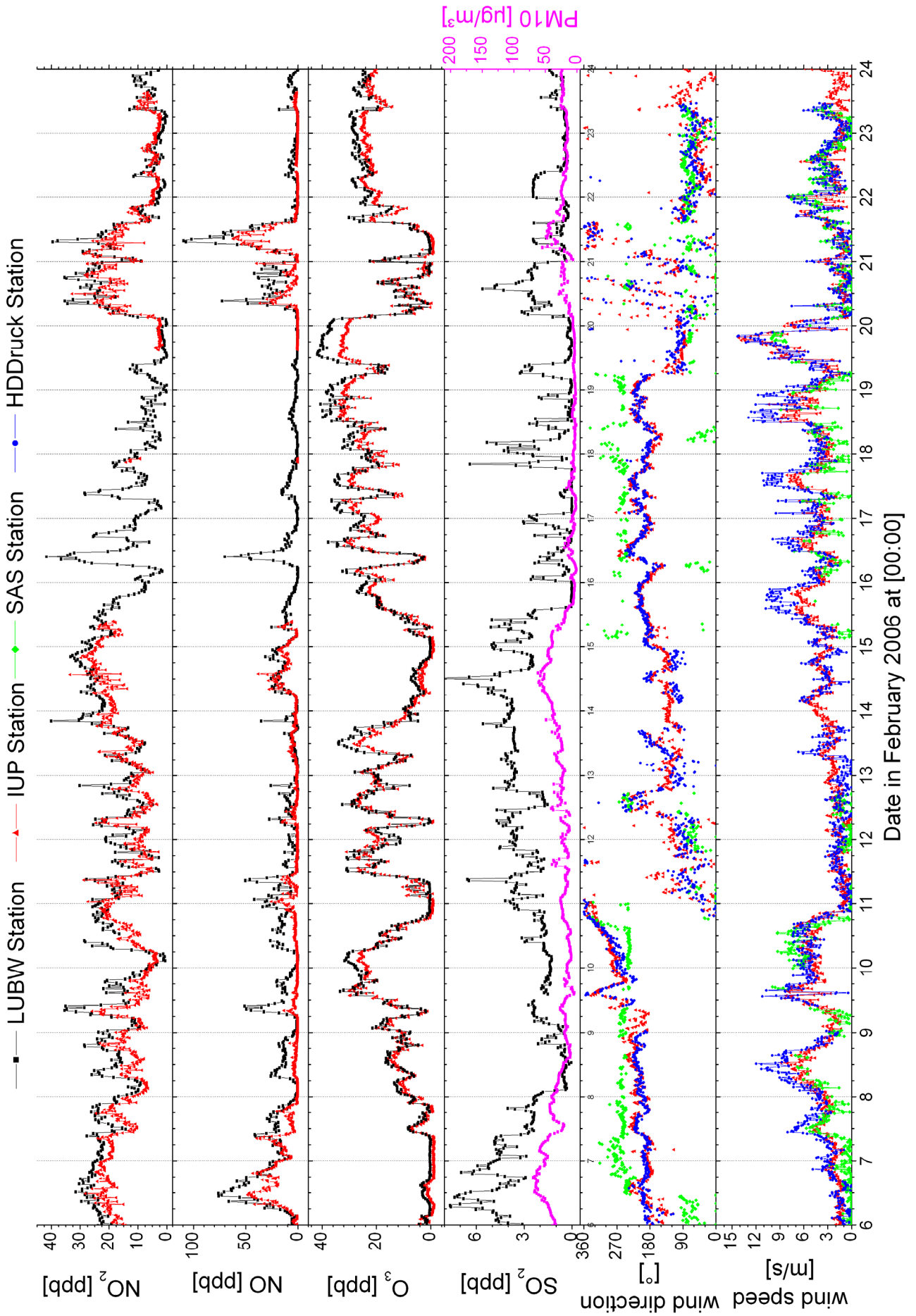


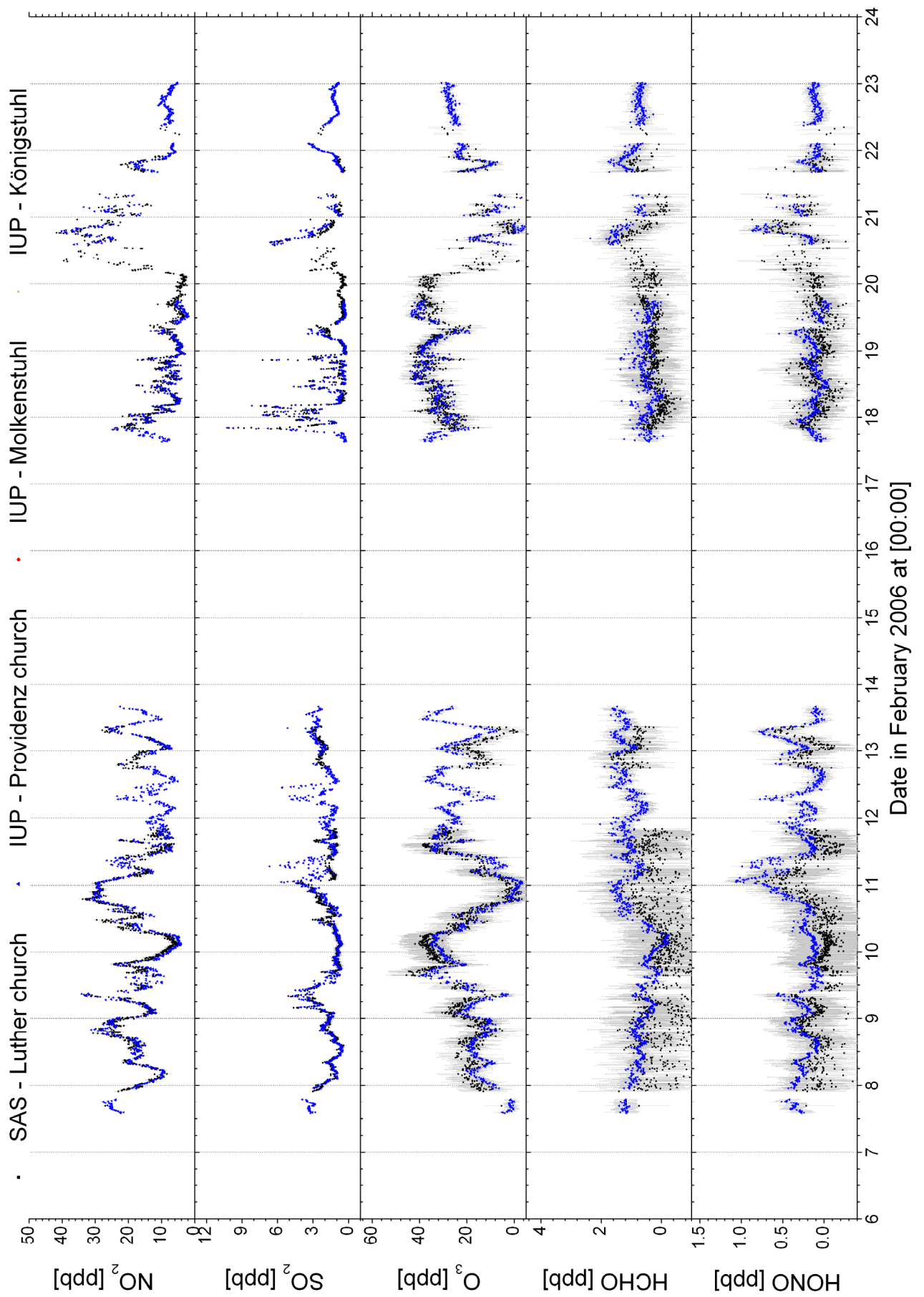




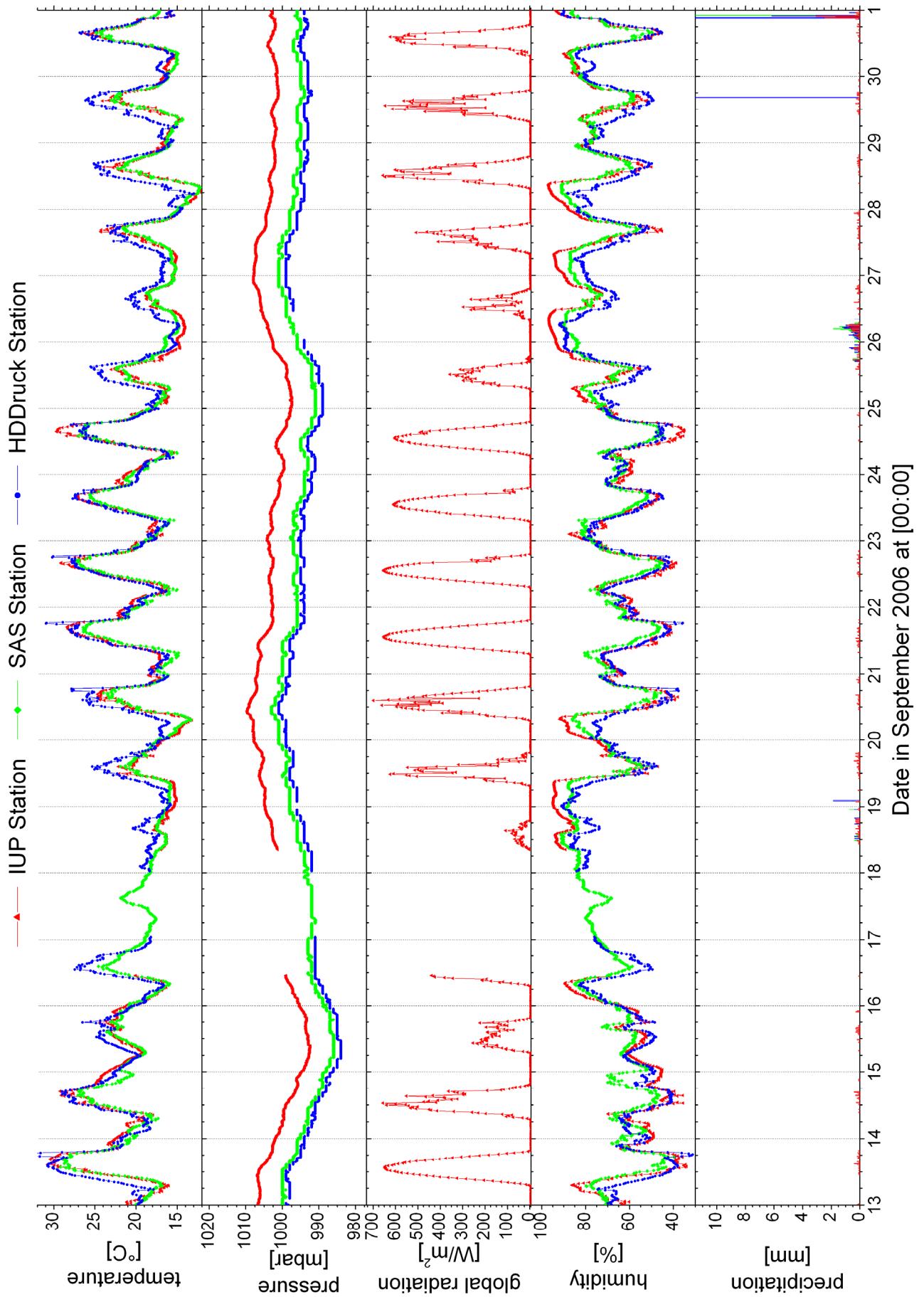
12.6 Data February 2006 (selected plots)

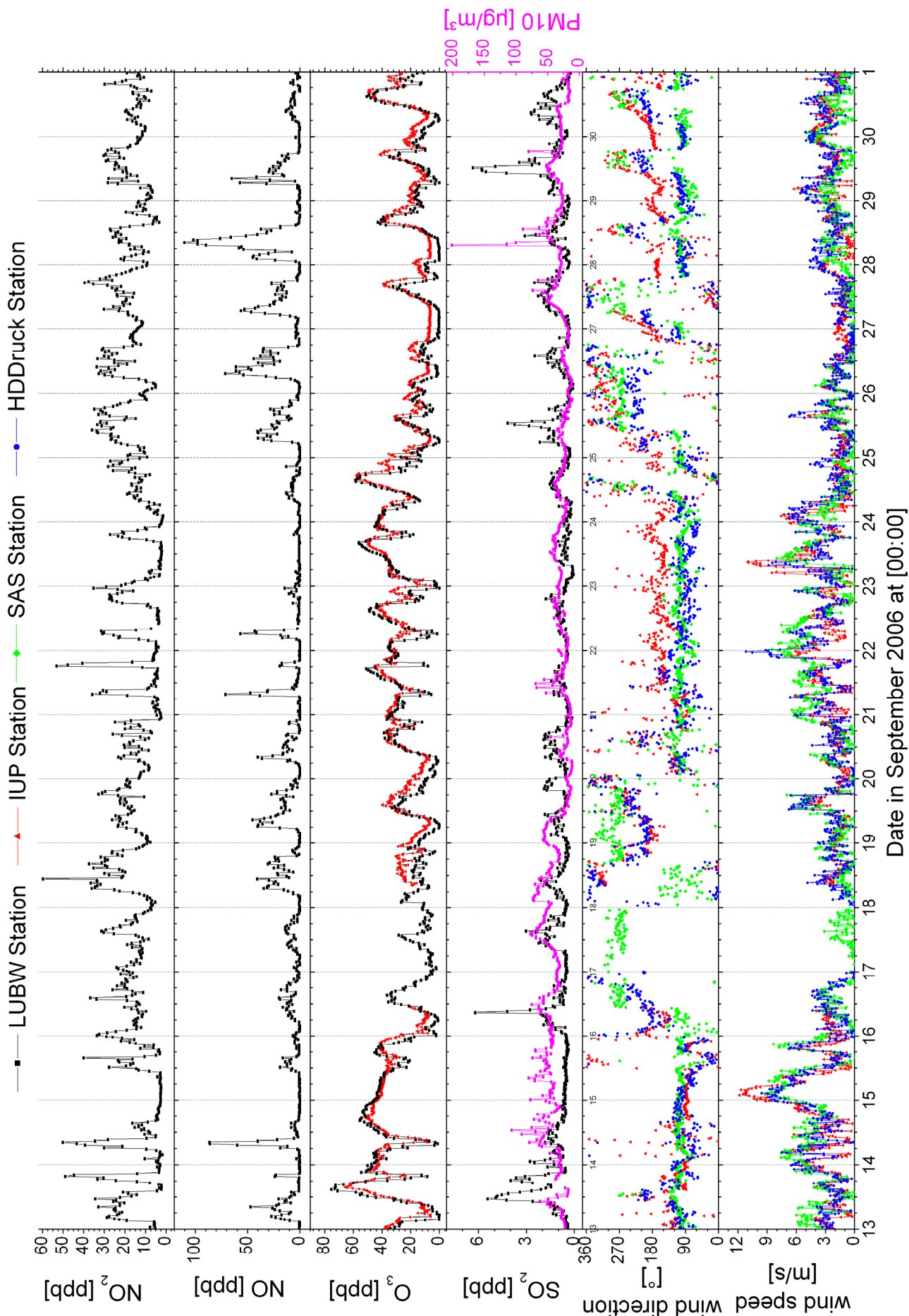


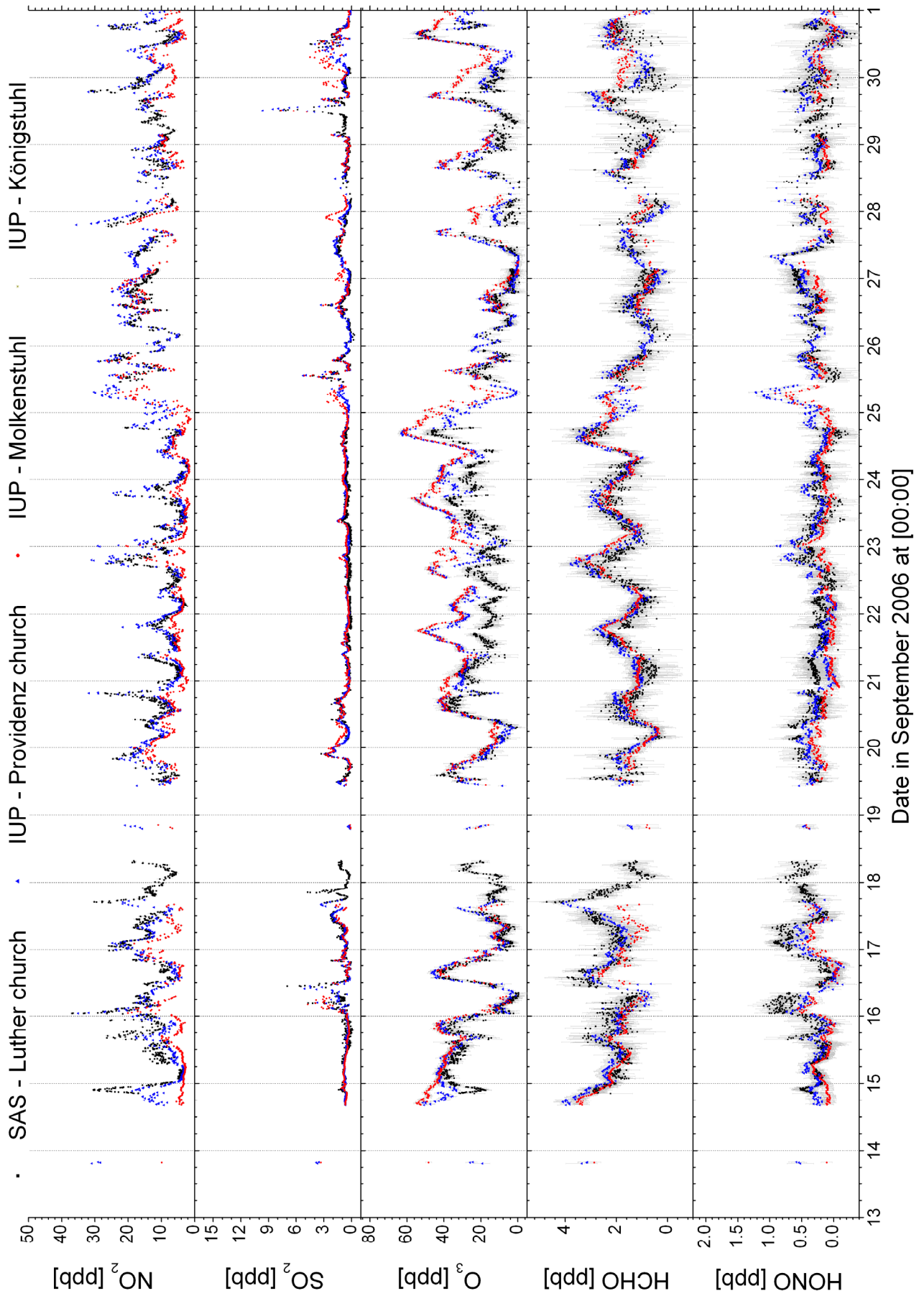




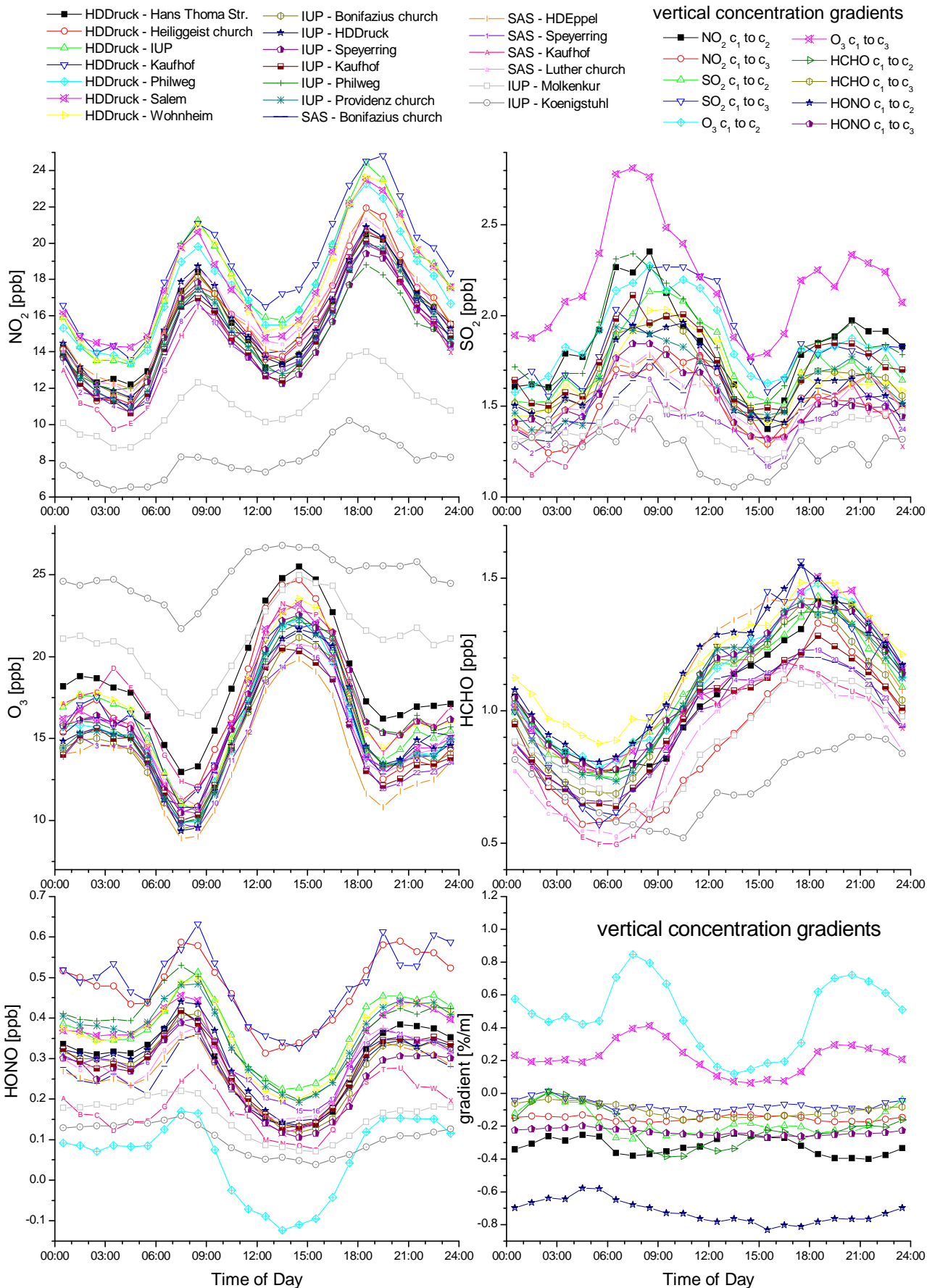
12.7 Data September 2006 (selected plots)



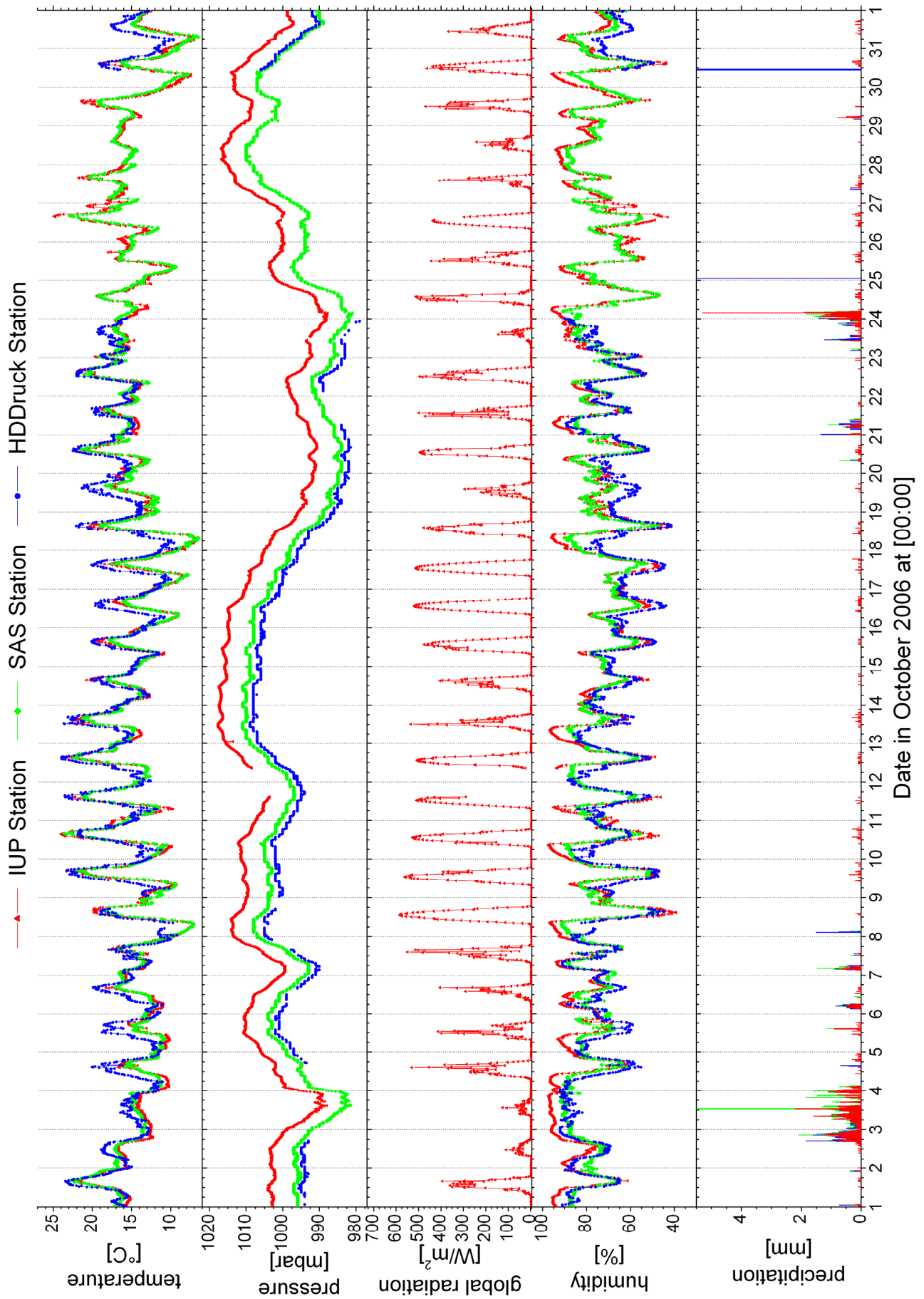


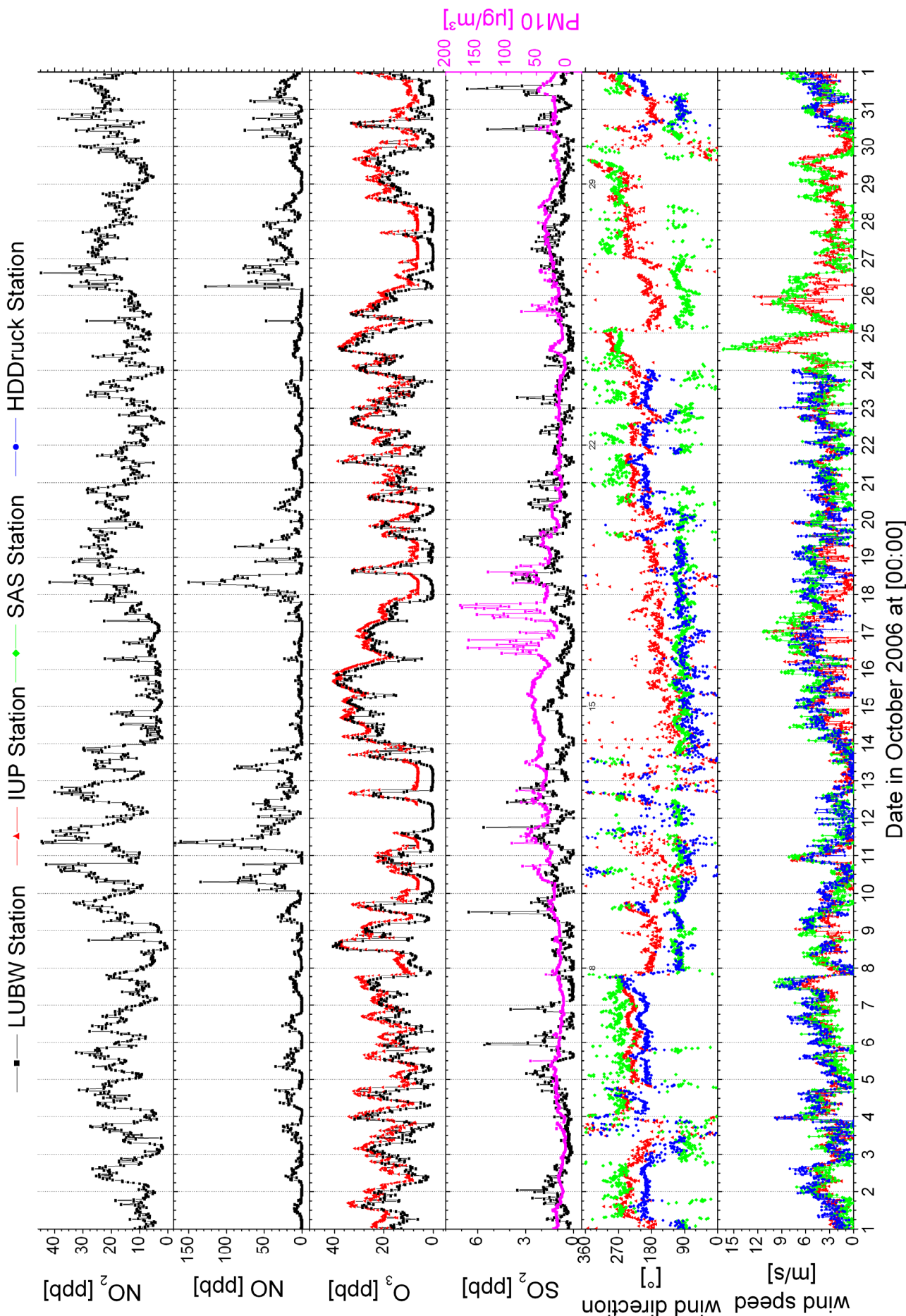


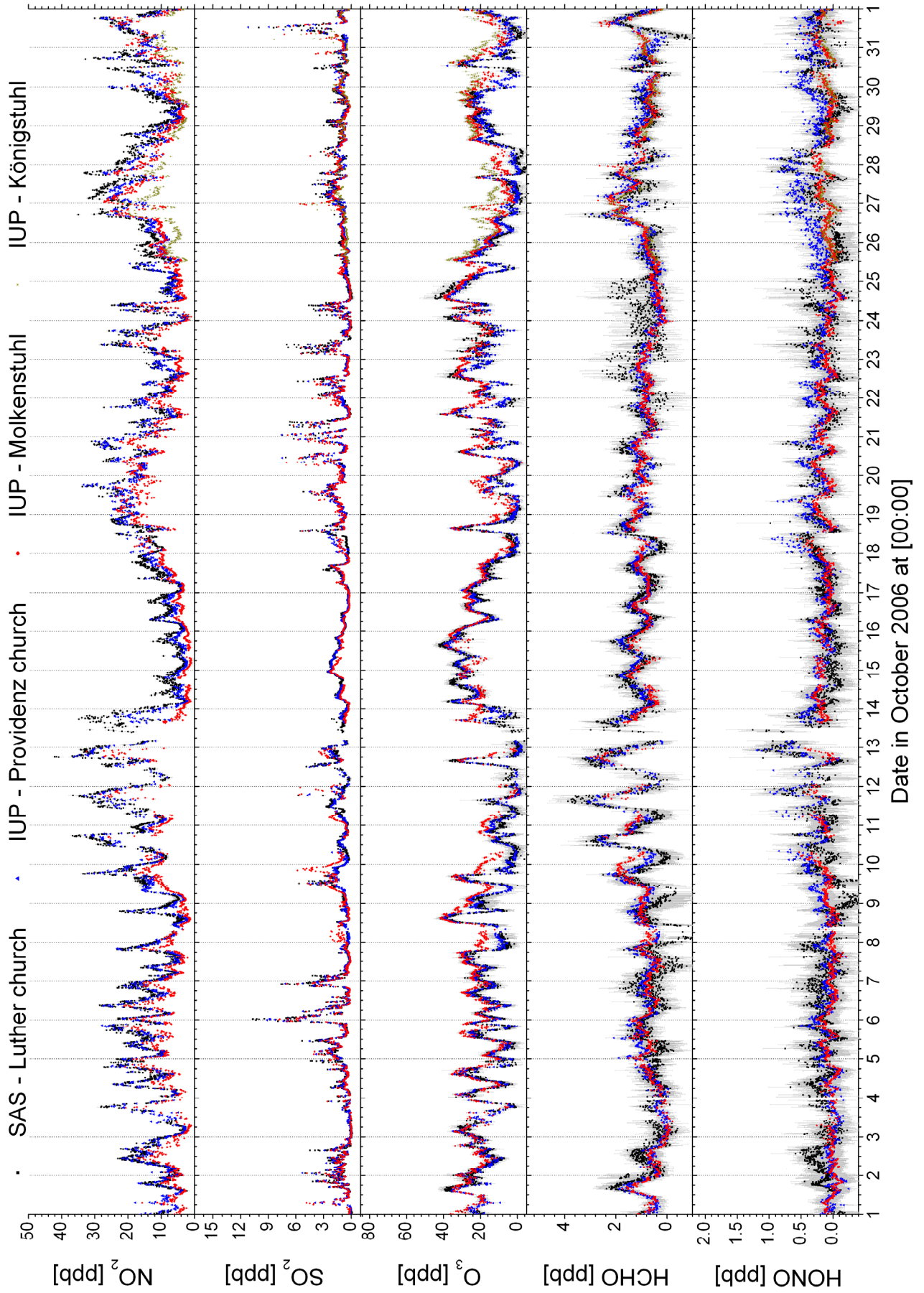
### mean daily cycle



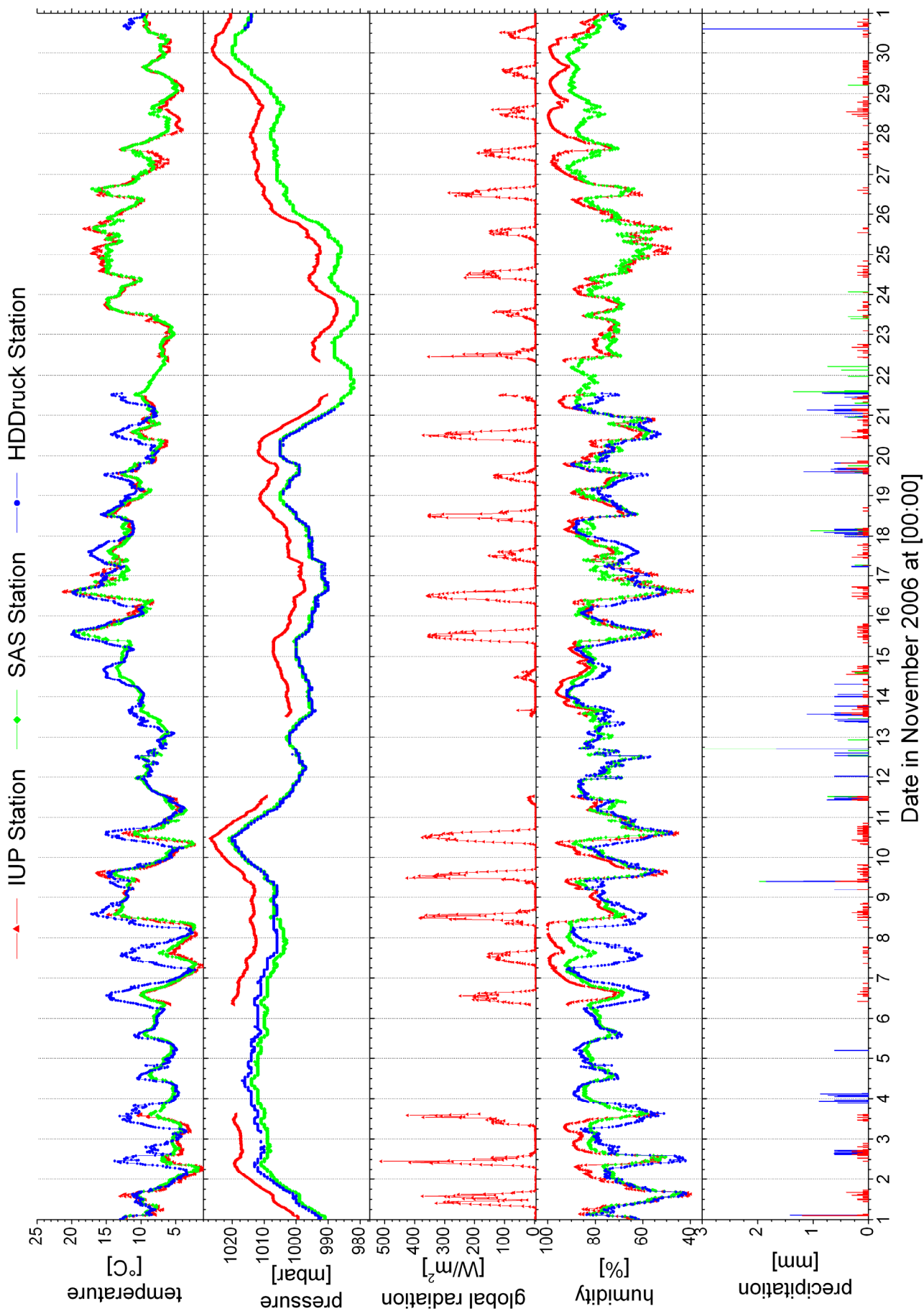
### 12.8 Data October 2006 (selected plots)

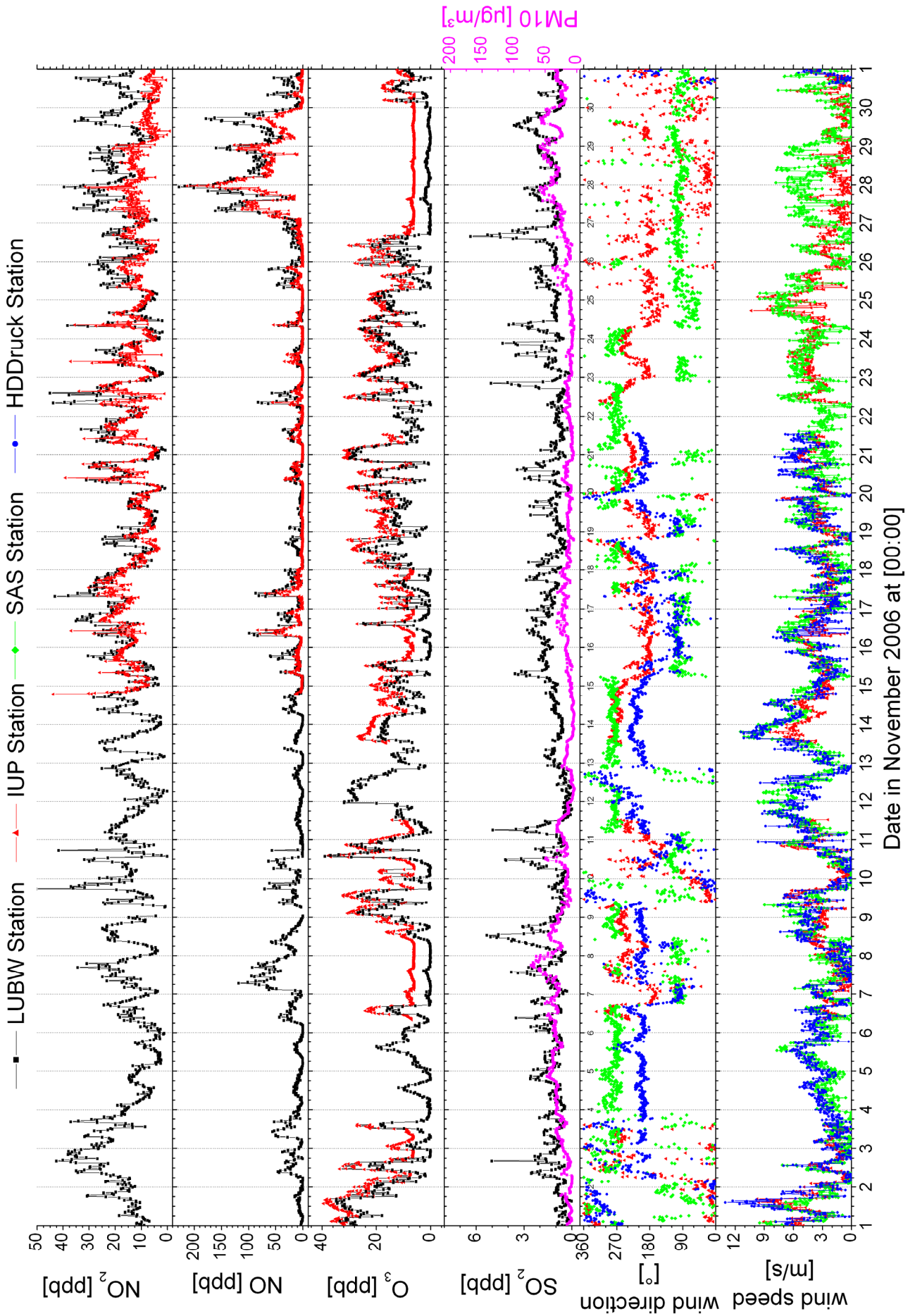


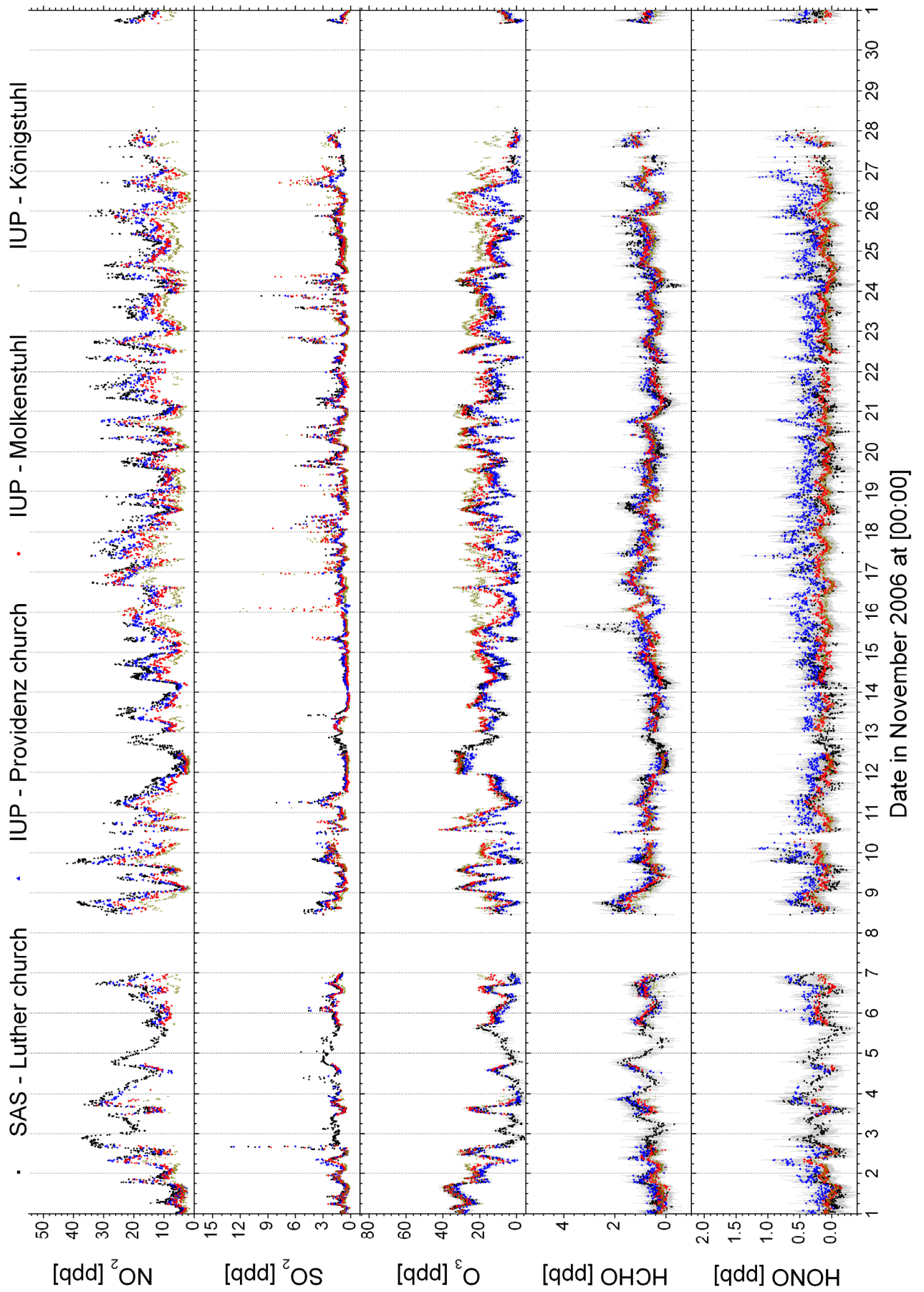




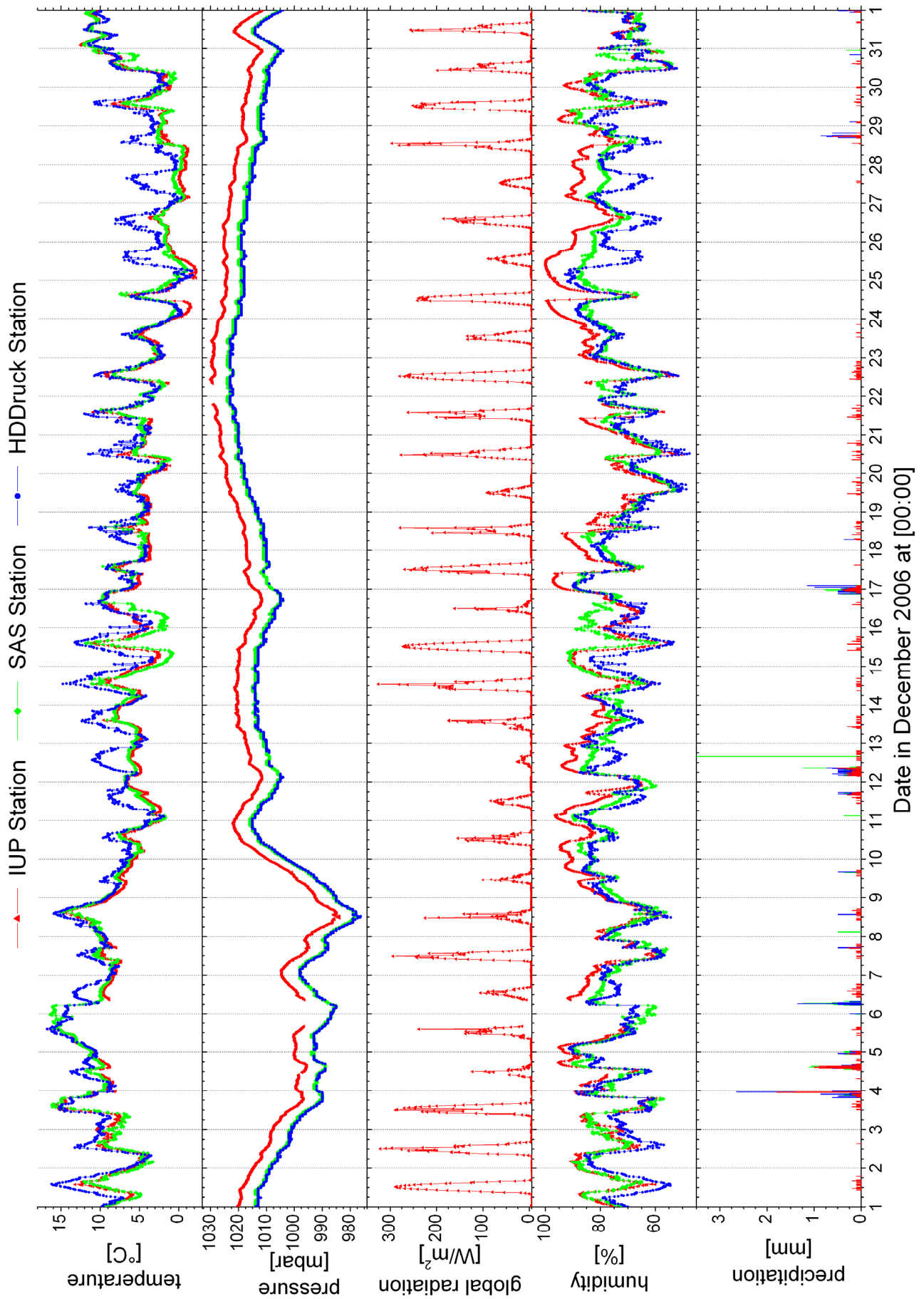
### 12.9 Data November 2006 (selected plots)

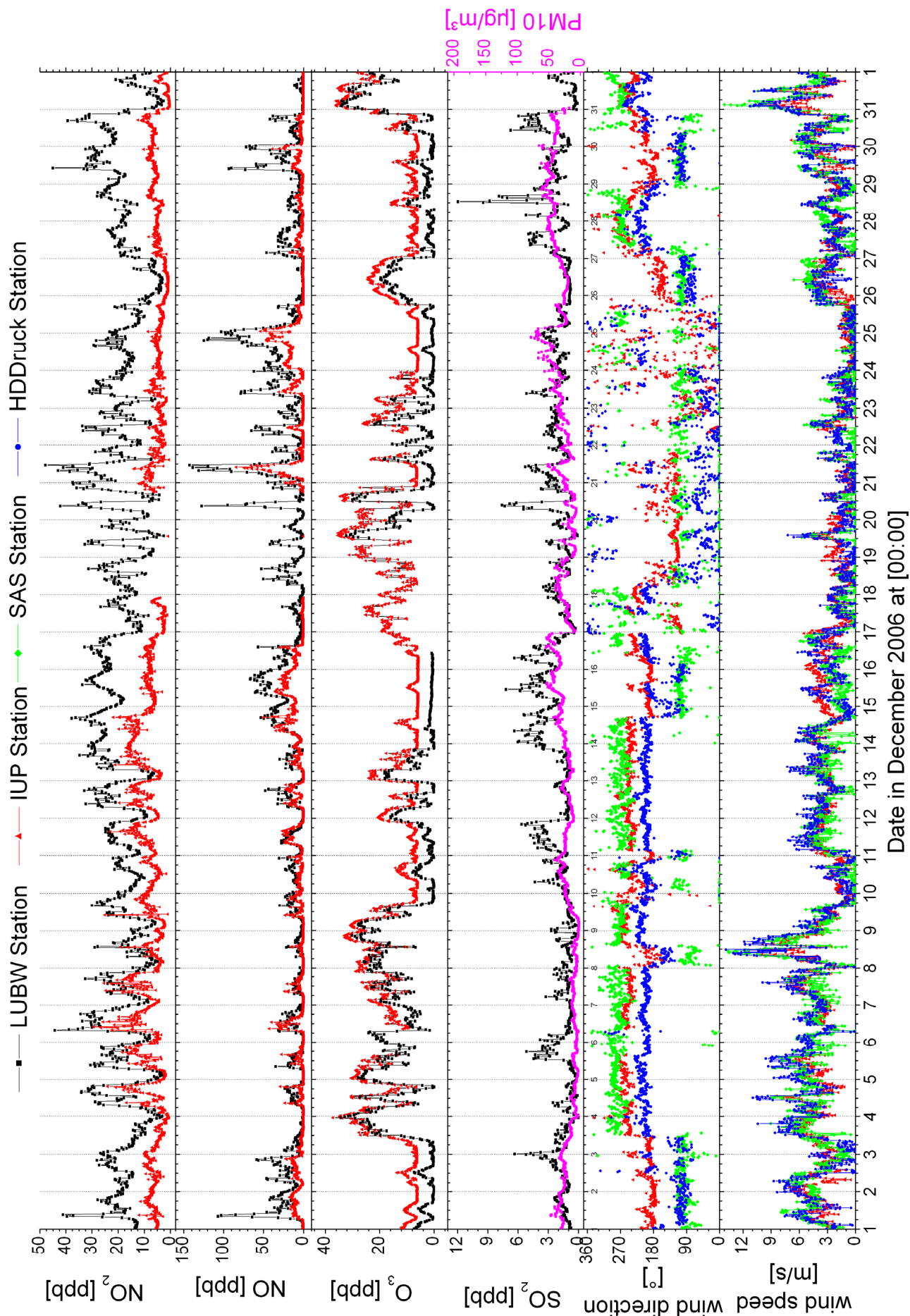


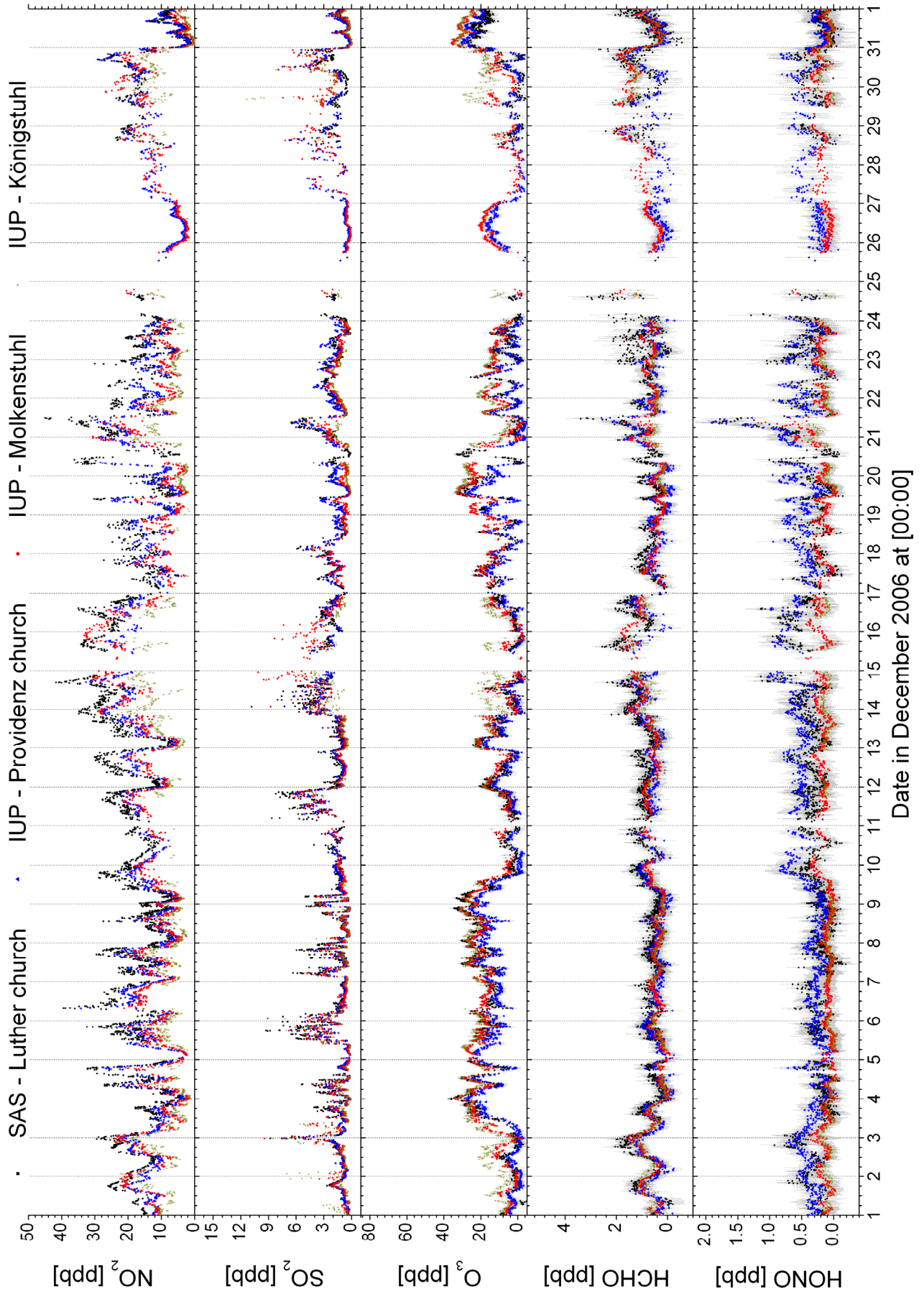




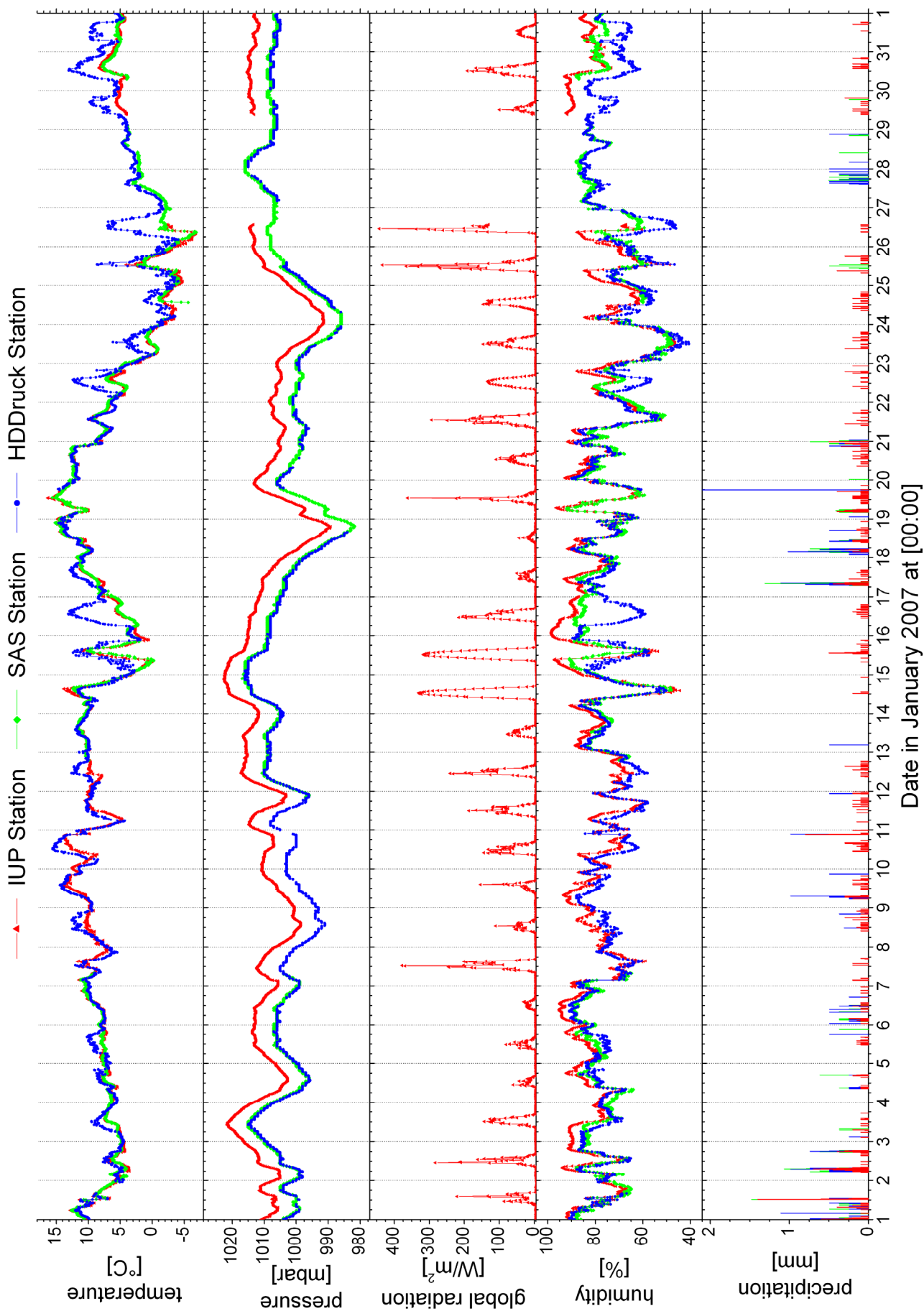
12.10 Data December 2006 (selected plots)

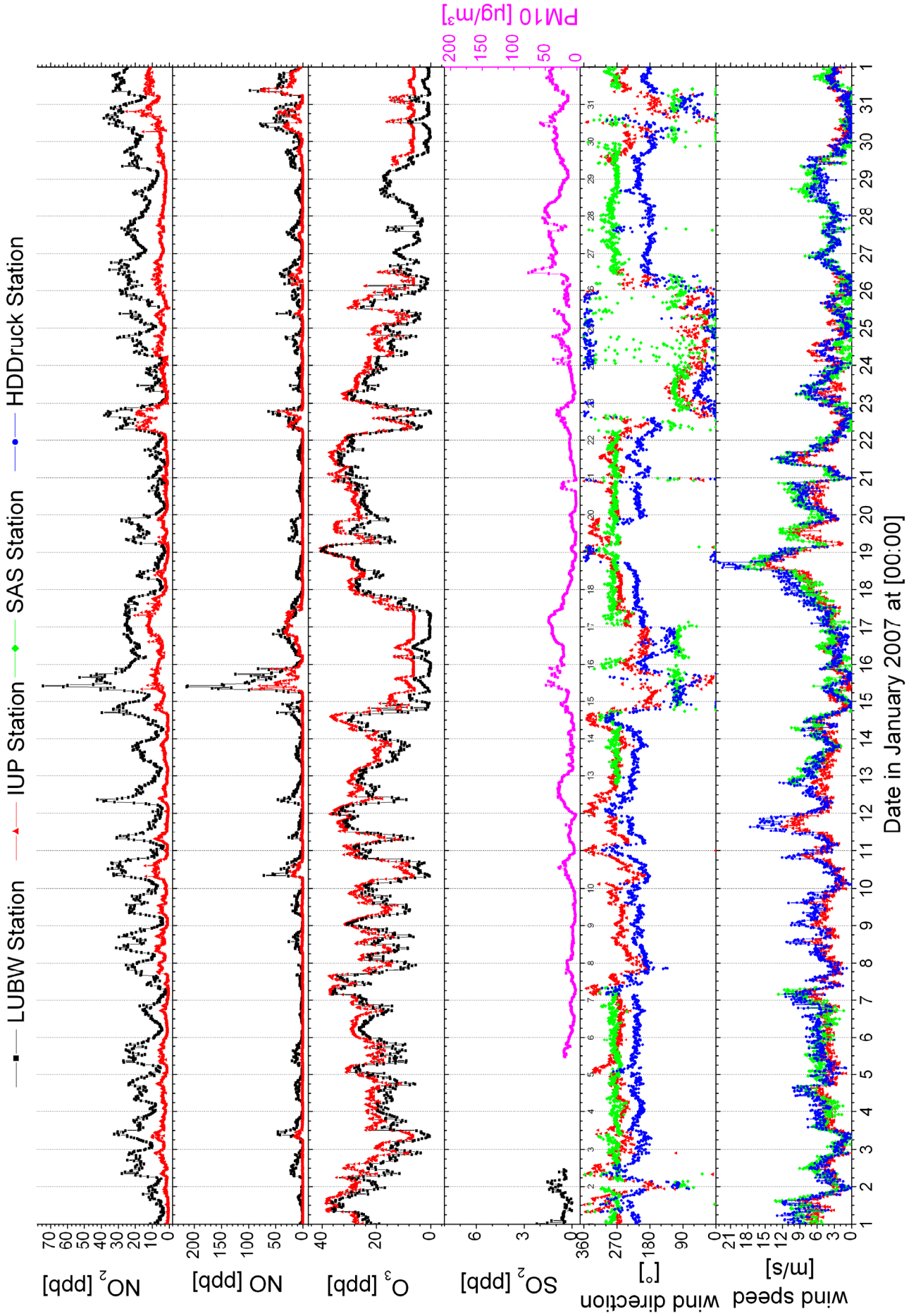


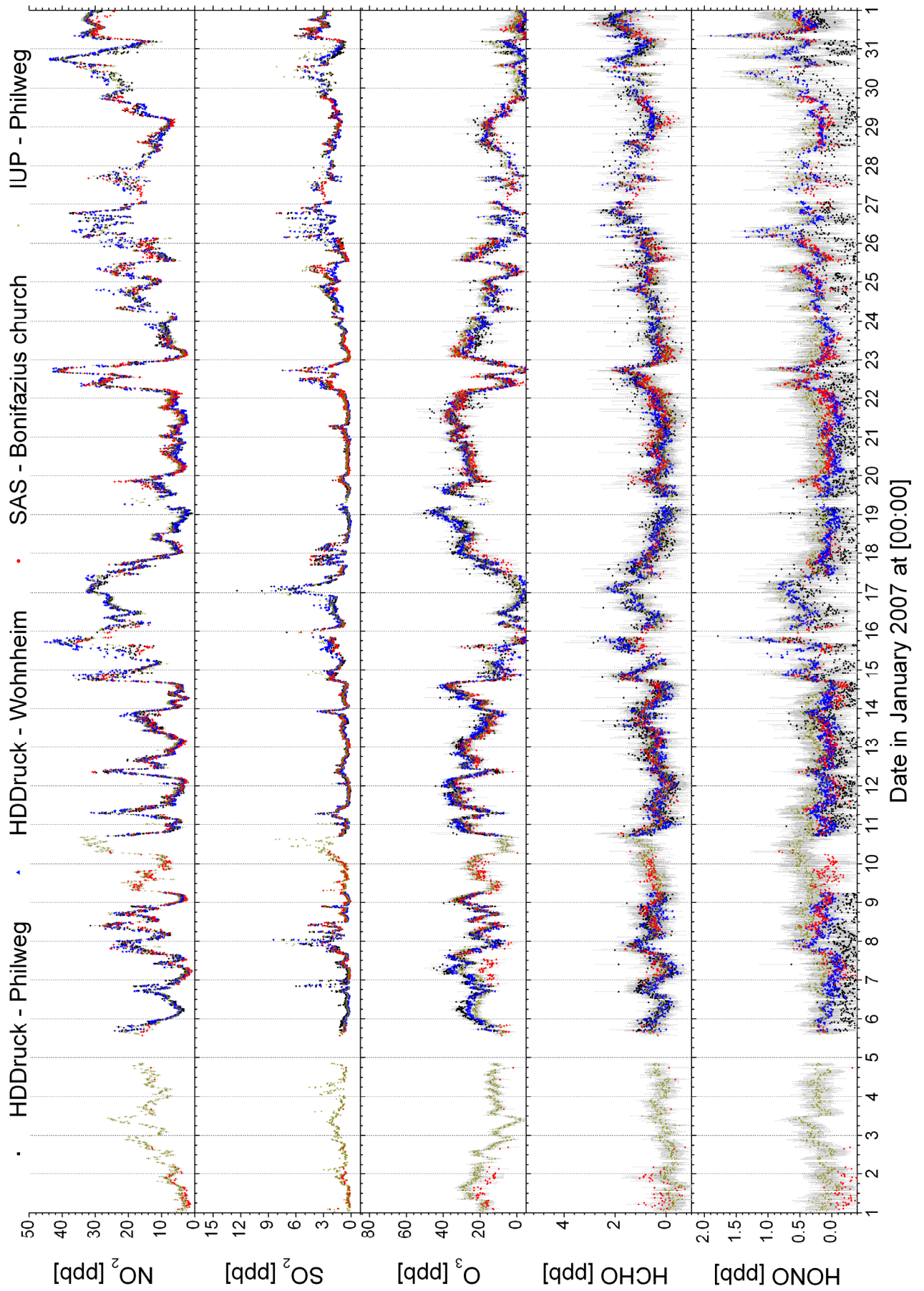


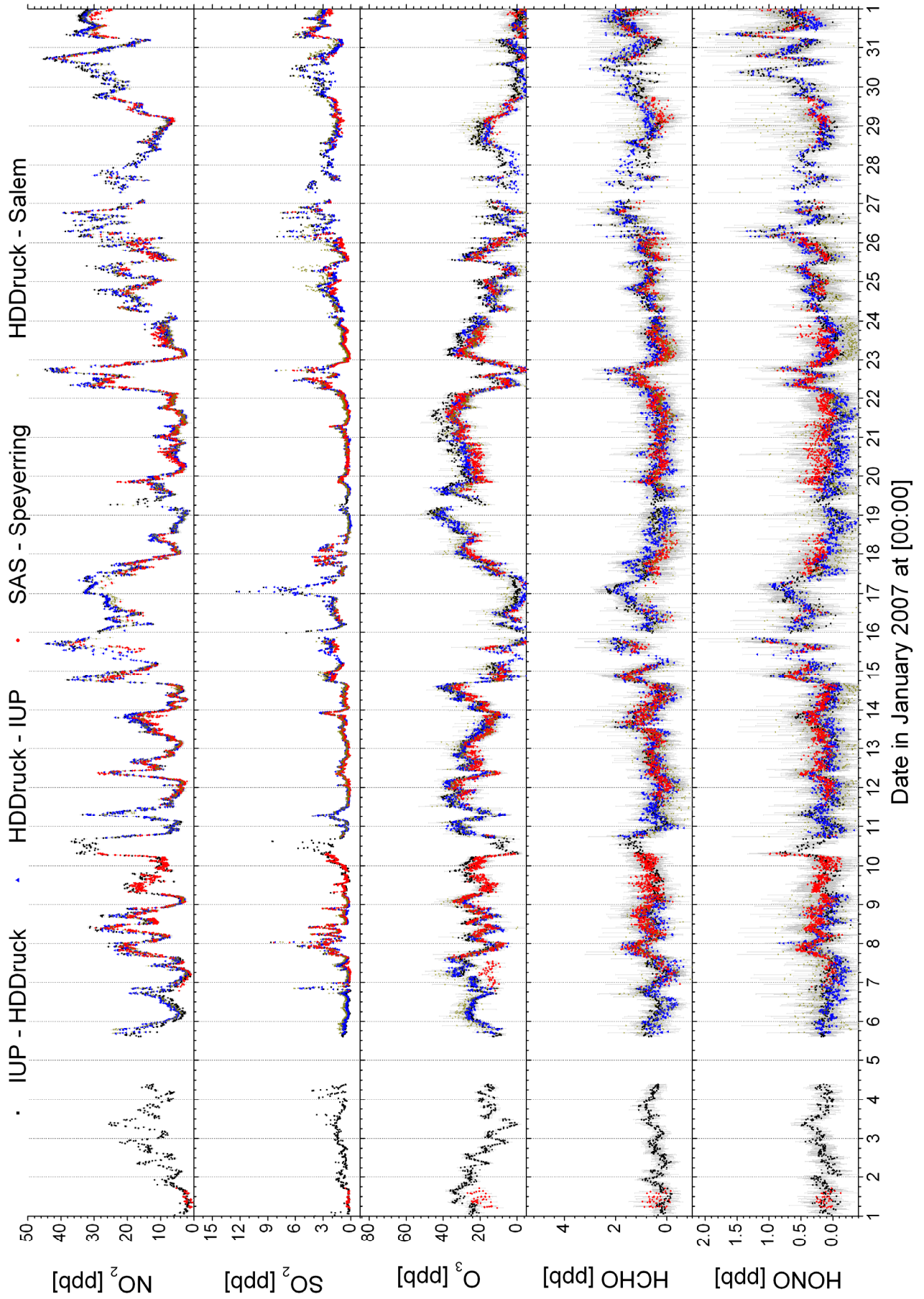


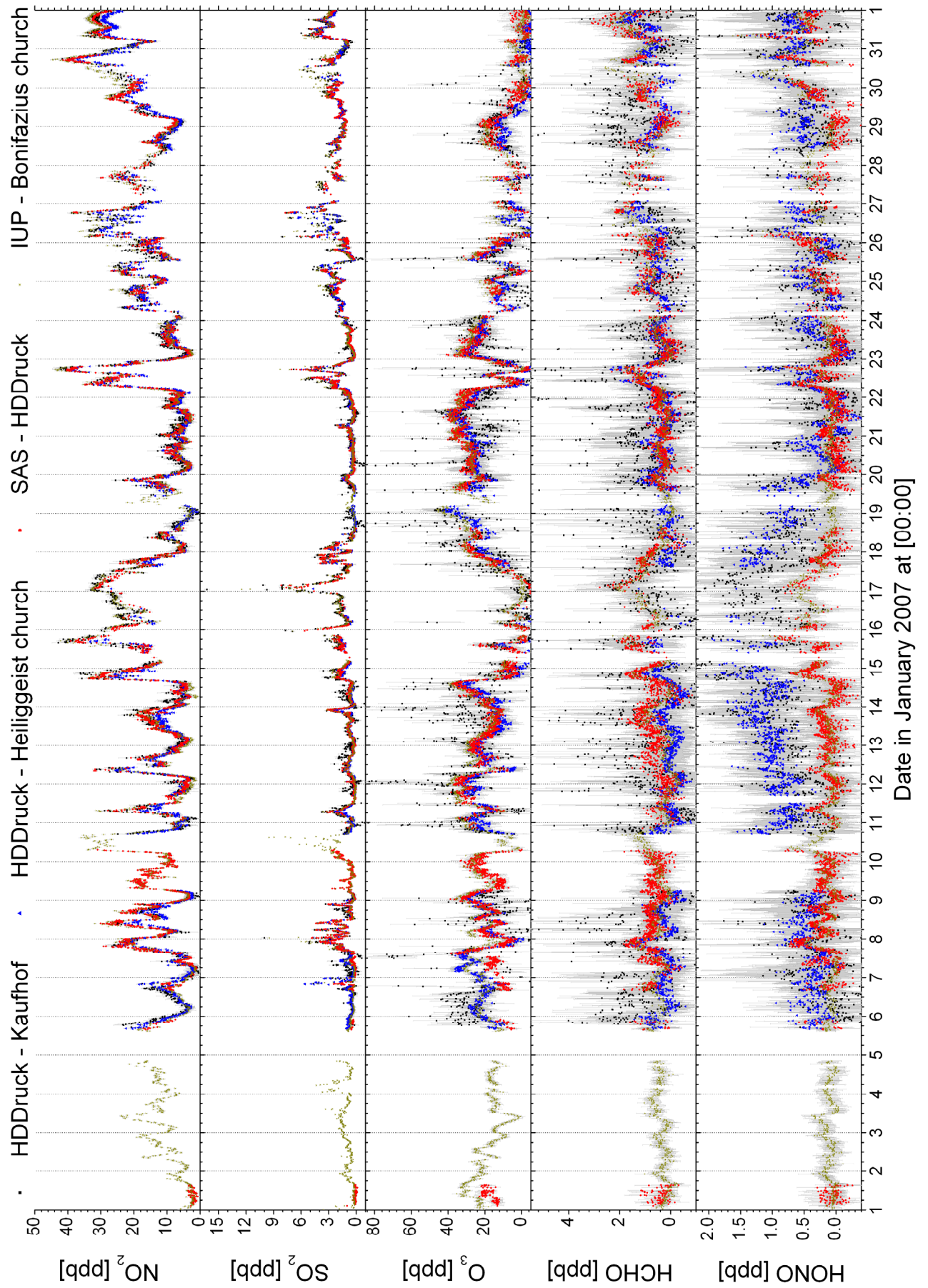
# 12.11 Data January 2007

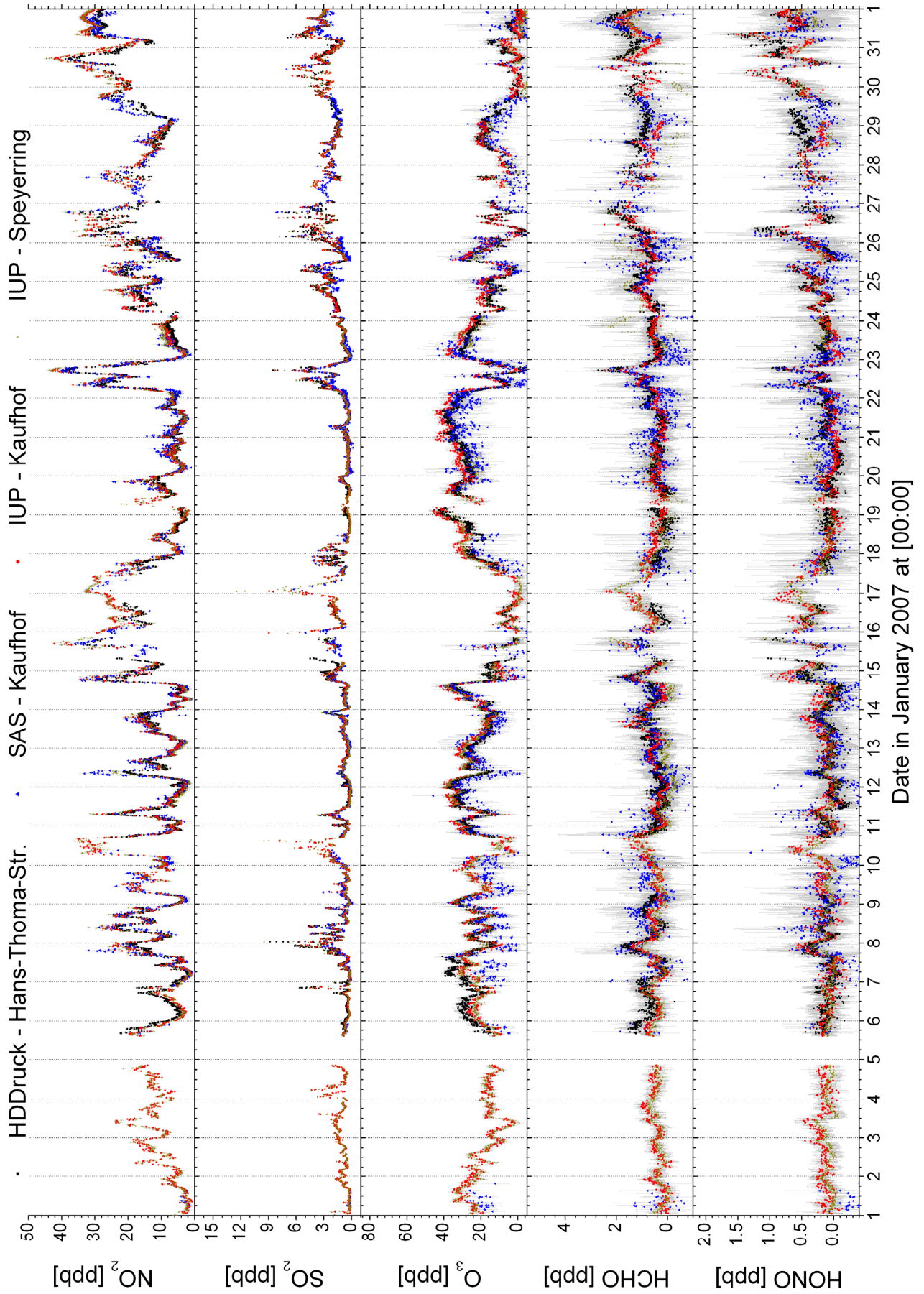


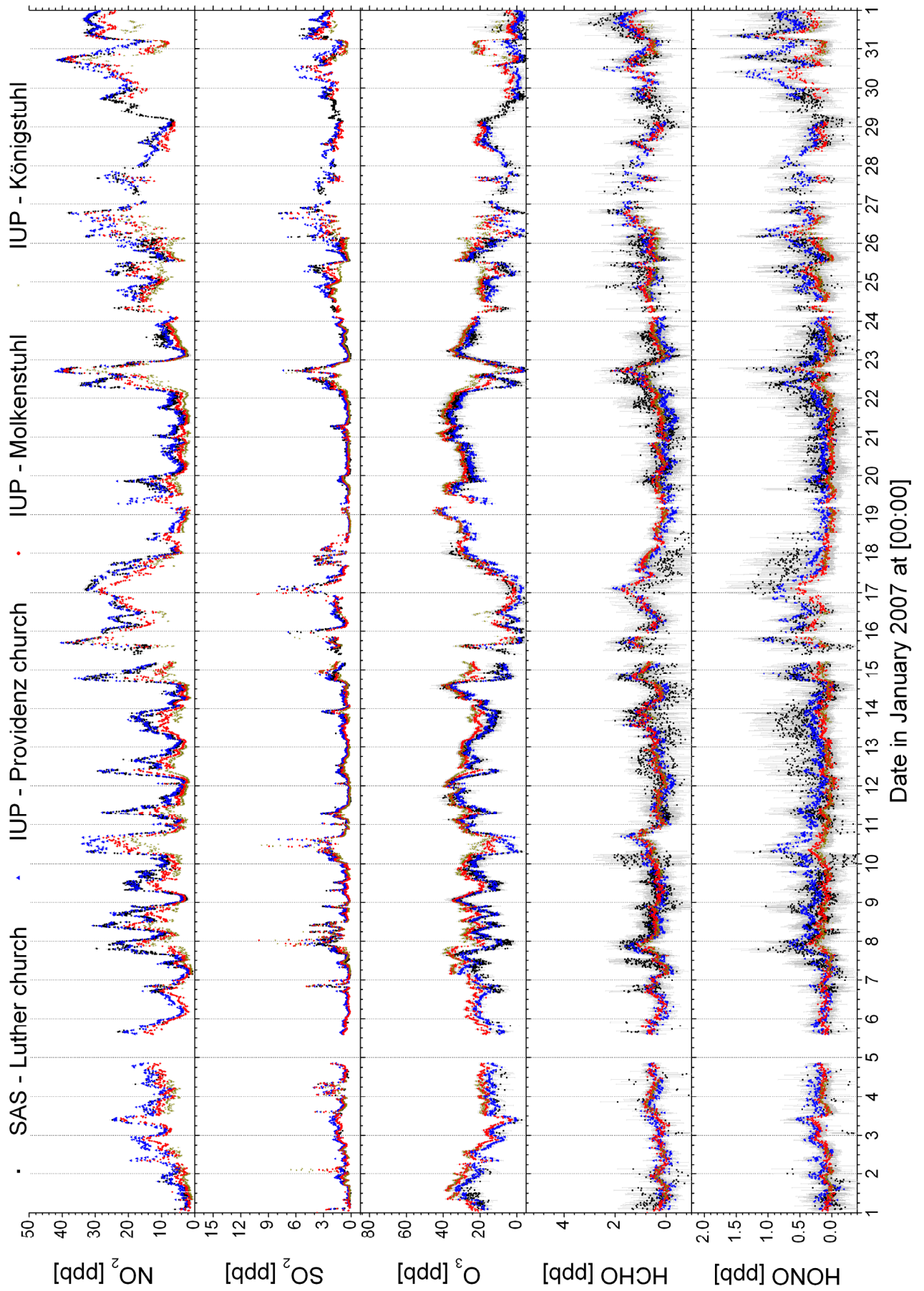






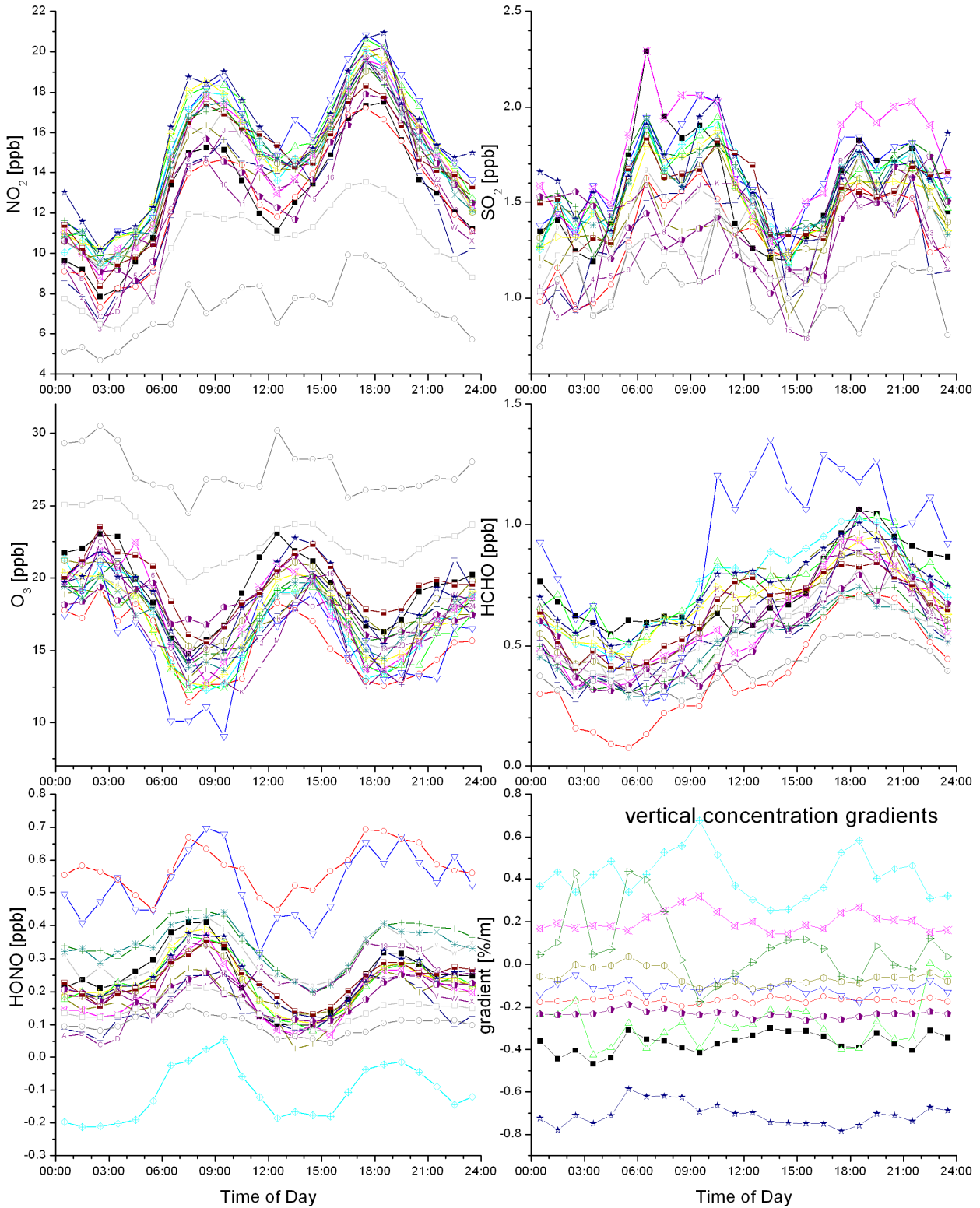




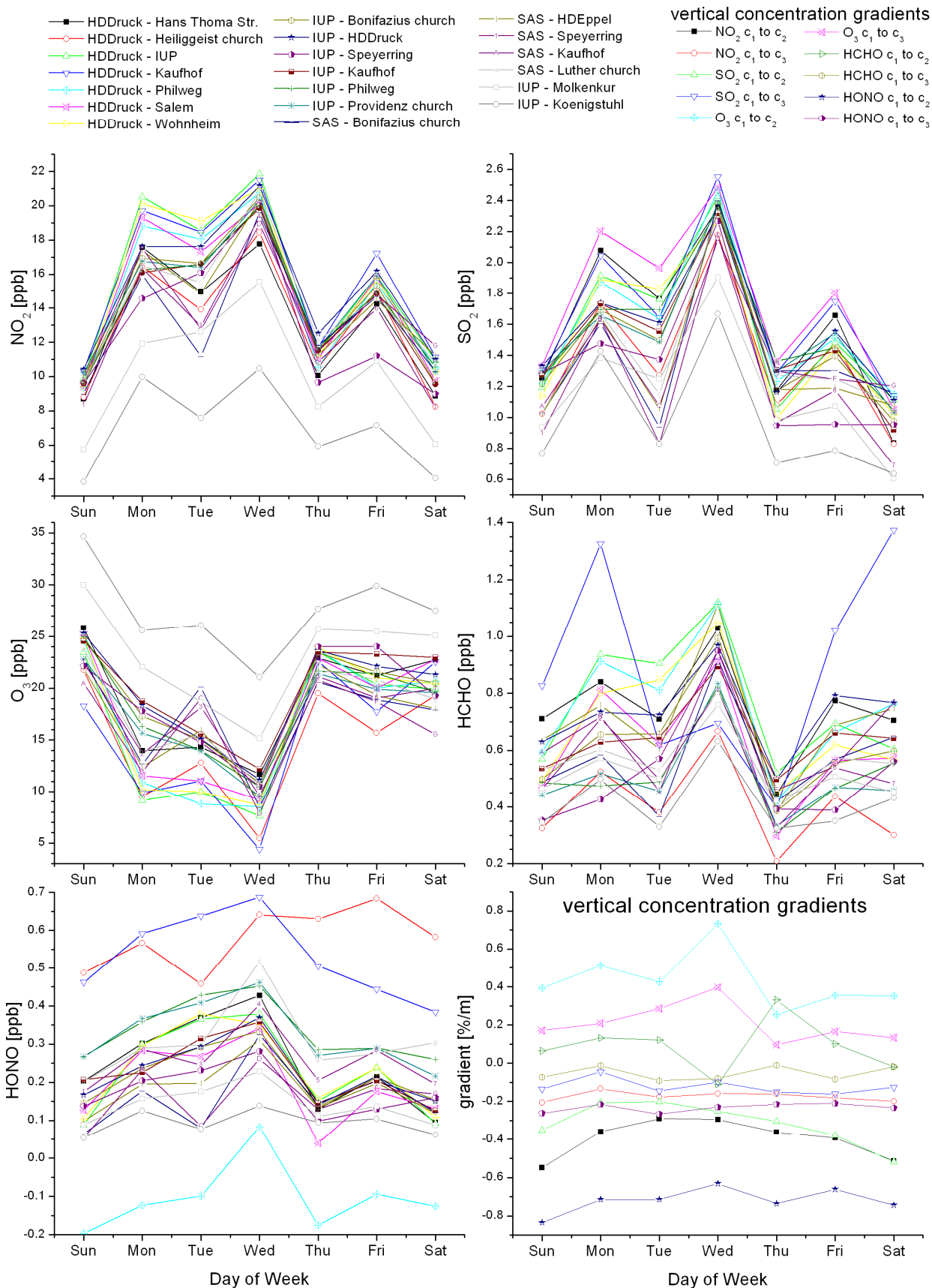


### mean daily cycle January 2007

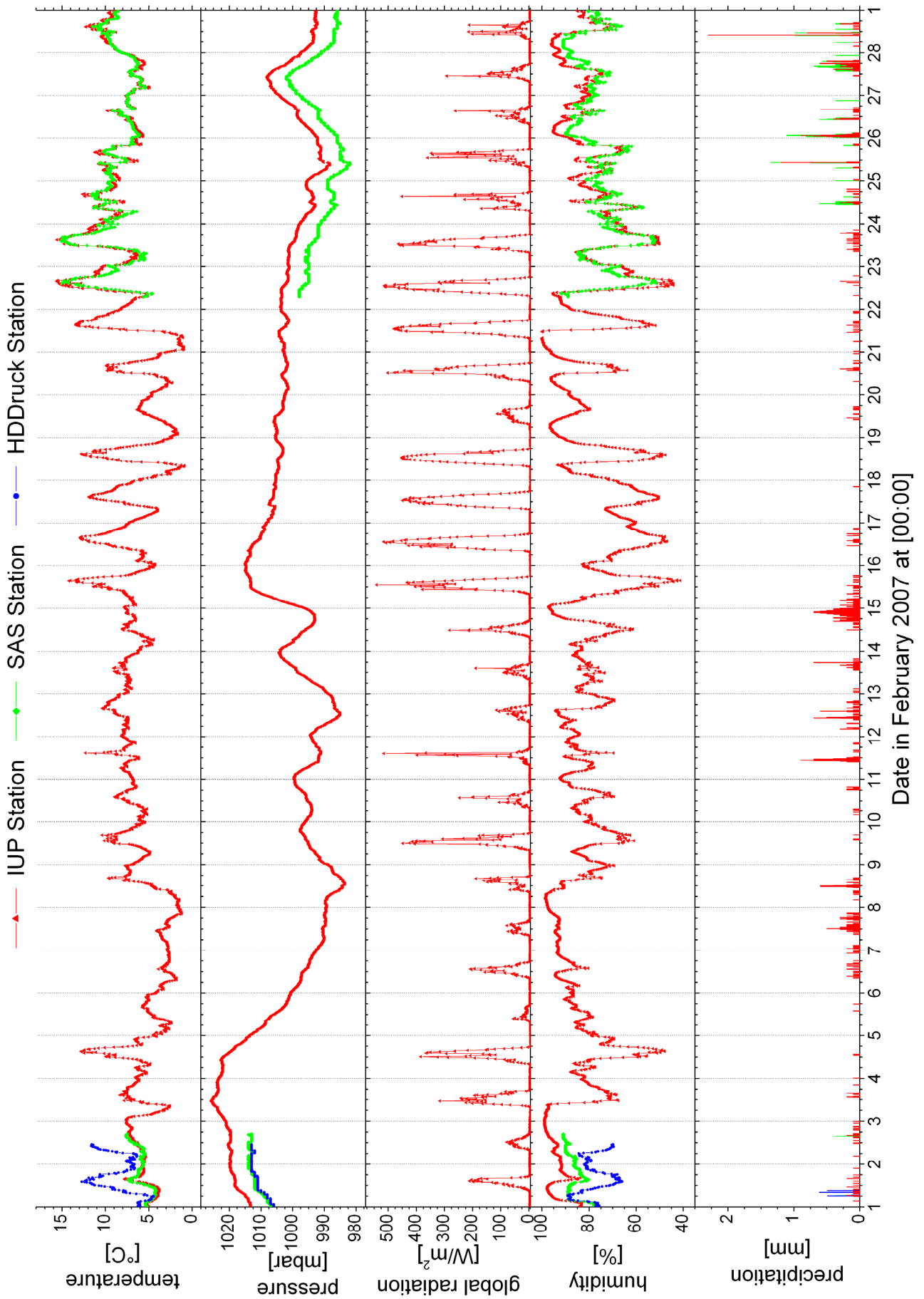
- |                                                                                                                                                                                                                                                                   |                                                                                                                                                                                                                                                                                                                 |                                                                                                                                                                                                               |                                                                                                                                                                                                                                                                                                                                                                                                                                                                                                                                                                                                                                         |
|-------------------------------------------------------------------------------------------------------------------------------------------------------------------------------------------------------------------------------------------------------------------|-----------------------------------------------------------------------------------------------------------------------------------------------------------------------------------------------------------------------------------------------------------------------------------------------------------------|---------------------------------------------------------------------------------------------------------------------------------------------------------------------------------------------------------------|-----------------------------------------------------------------------------------------------------------------------------------------------------------------------------------------------------------------------------------------------------------------------------------------------------------------------------------------------------------------------------------------------------------------------------------------------------------------------------------------------------------------------------------------------------------------------------------------------------------------------------------------|
| <ul style="list-style-type: none"> <li>■ HDDruck - Hans Thoma Str.</li> <li>○ HDDruck - Heiliggeist church</li> <li>△ HDDruck - IUP</li> <li>▽ HDDruck - Kaufhof</li> <li>◇ HDDruck - Philweg</li> <li>× HDDruck - Salem</li> <li>◇ HDDruck - Wohnheim</li> </ul> | <ul style="list-style-type: none"> <li>◇ IUP - Bonifazius church</li> <li>★ IUP - HDDruck</li> <li>◇ IUP - Speyerring</li> <li>◇ IUP - Kaufhof</li> <li>◇ IUP - Philweg</li> <li>◇ IUP - Providenz church</li> <li>◇ IUP - Molkenkur</li> <li>◇ IUP - Koenigstuhl</li> <li>◇ SAS - Bonifazius church</li> </ul> | <ul style="list-style-type: none"> <li>◇ SAS - HDEppel</li> <li>◇ SAS - Speyerring</li> <li>◇ SAS - Kaufhof</li> <li>◇ SAS - Luther church</li> <li>◇ IUP - Molkenkur</li> <li>◇ IUP - Koenigstuhl</li> </ul> | <p><b>vertical concentration gradients</b></p> <ul style="list-style-type: none"> <li>■ NO<sub>2</sub> c<sub>1</sub> to c<sub>2</sub></li> <li>○ NO<sub>2</sub> c<sub>1</sub> to c<sub>3</sub></li> <li>△ SO<sub>2</sub> c<sub>1</sub> to c<sub>2</sub></li> <li>▽ SO<sub>2</sub> c<sub>1</sub> to c<sub>3</sub></li> <li>◇ O<sub>3</sub> c<sub>1</sub> to c<sub>2</sub></li> <li>× O<sub>3</sub> c<sub>1</sub> to c<sub>3</sub></li> <li>◇ HCHO c<sub>1</sub> to c<sub>2</sub></li> <li>◇ HCHO c<sub>1</sub> to c<sub>3</sub></li> <li>★ HONO c<sub>1</sub> to c<sub>2</sub></li> <li>◇ HONO c<sub>1</sub> to c<sub>3</sub></li> </ul> |
|-------------------------------------------------------------------------------------------------------------------------------------------------------------------------------------------------------------------------------------------------------------------|-----------------------------------------------------------------------------------------------------------------------------------------------------------------------------------------------------------------------------------------------------------------------------------------------------------------|---------------------------------------------------------------------------------------------------------------------------------------------------------------------------------------------------------------|-----------------------------------------------------------------------------------------------------------------------------------------------------------------------------------------------------------------------------------------------------------------------------------------------------------------------------------------------------------------------------------------------------------------------------------------------------------------------------------------------------------------------------------------------------------------------------------------------------------------------------------------|

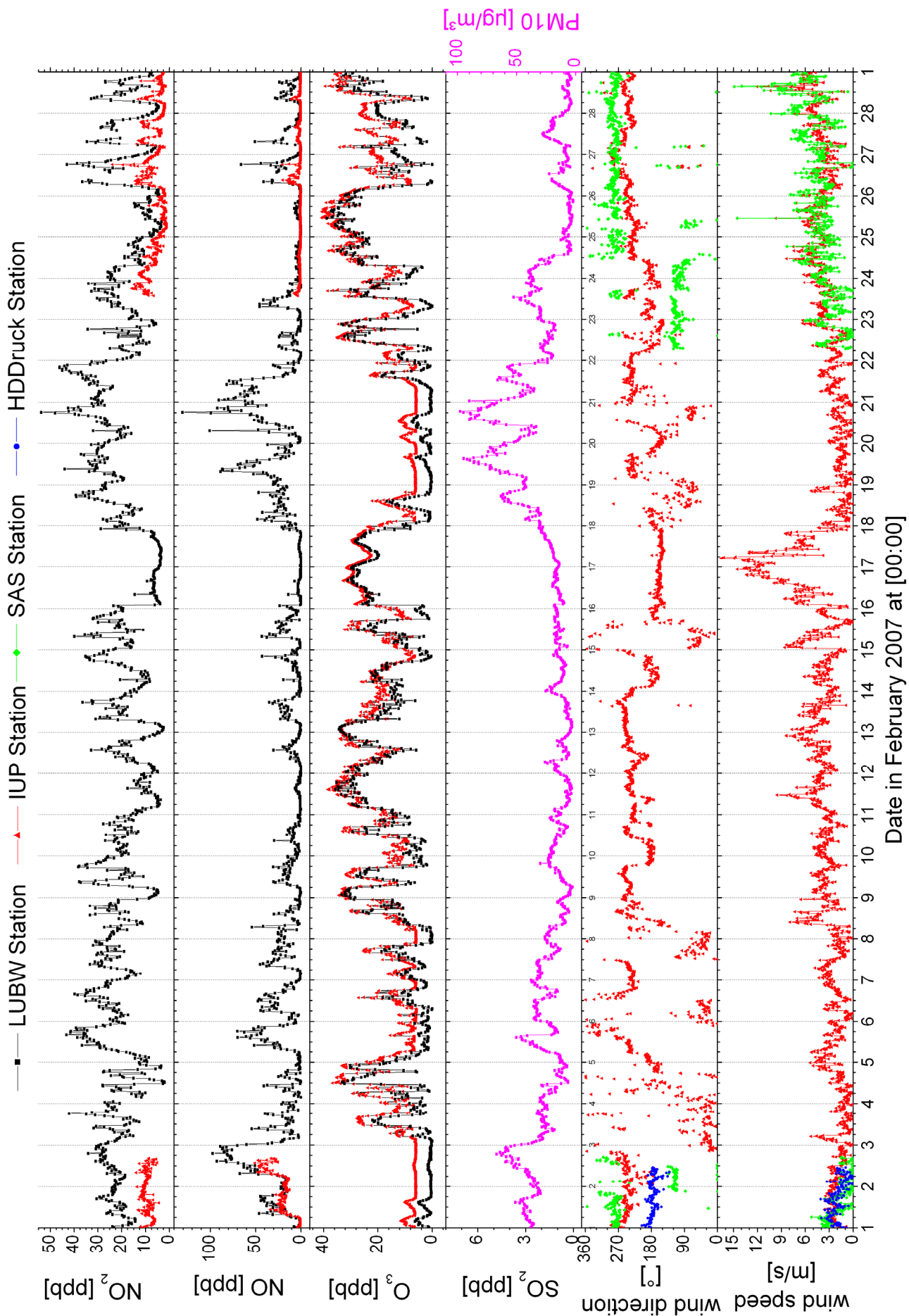


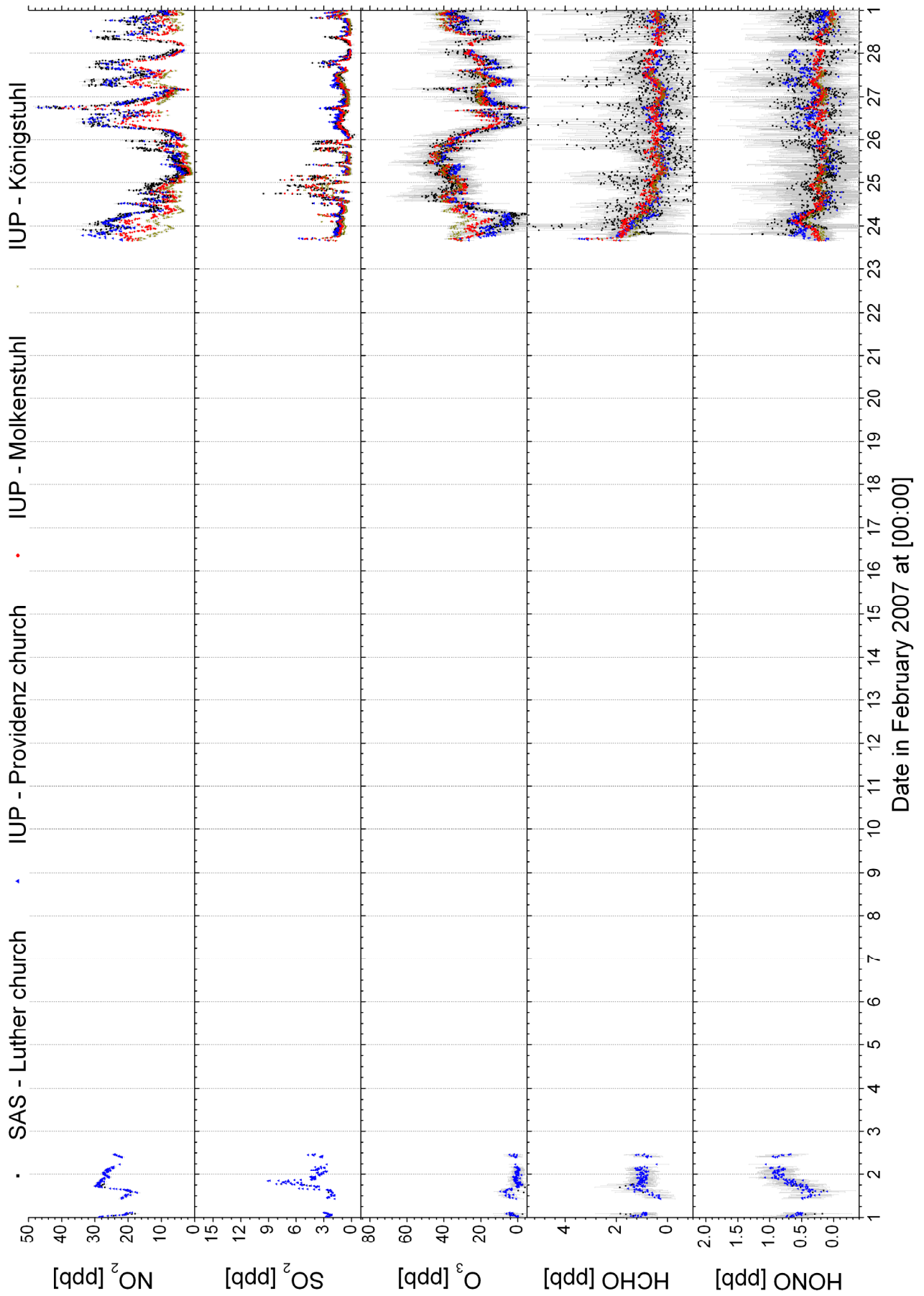
### mean weekly cycle January 2007



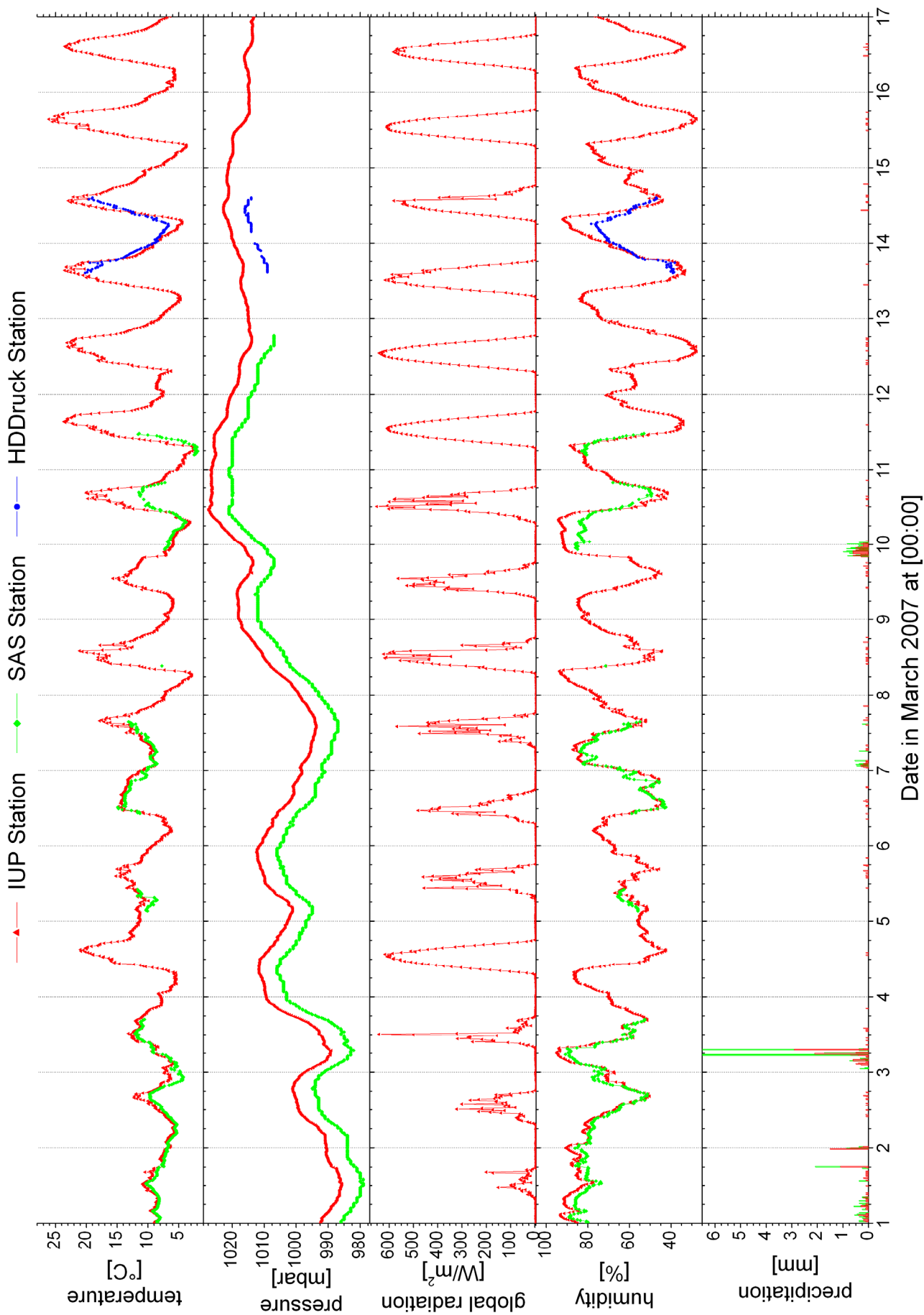
12.12 Data February 2007 (selected plots)

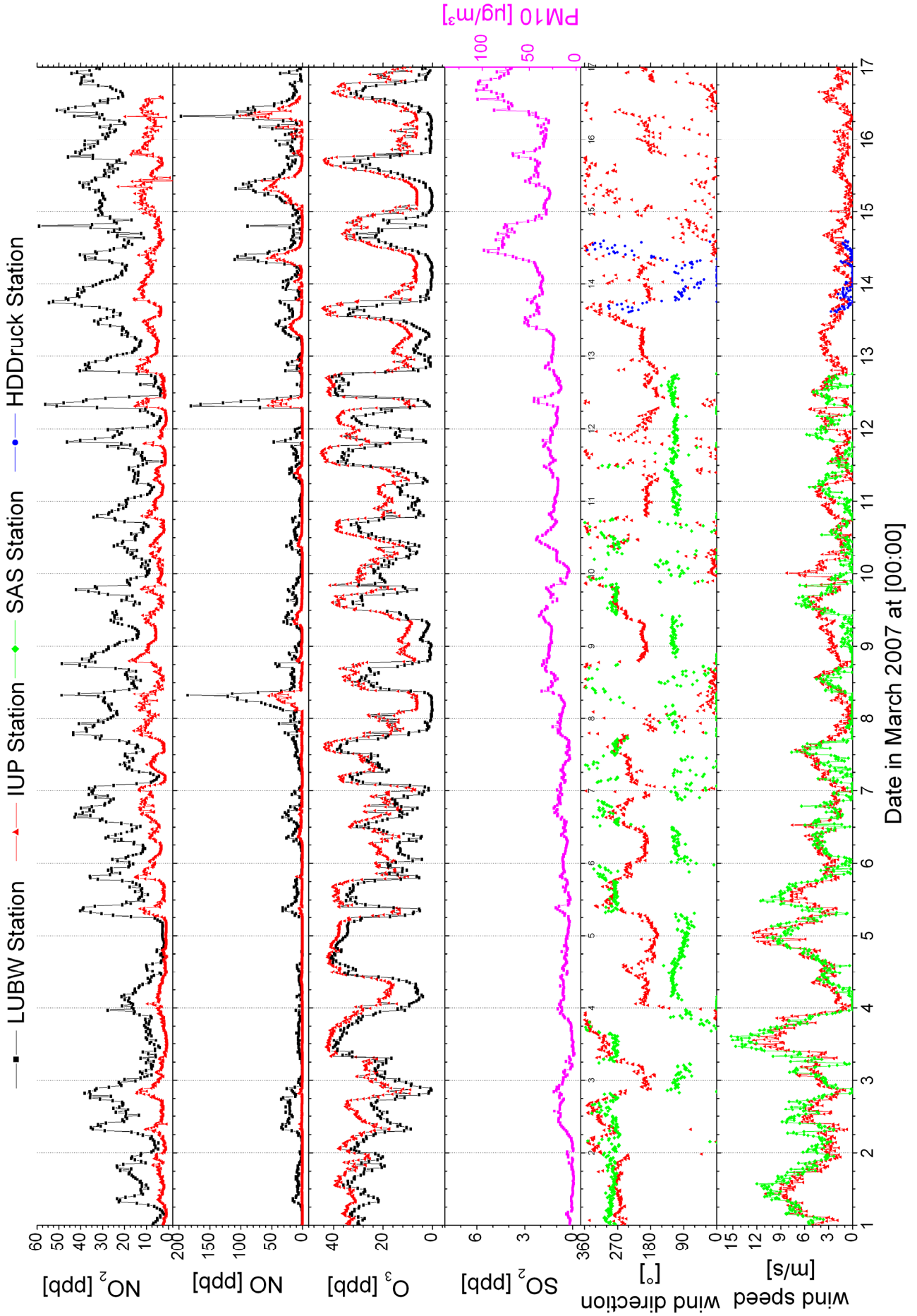


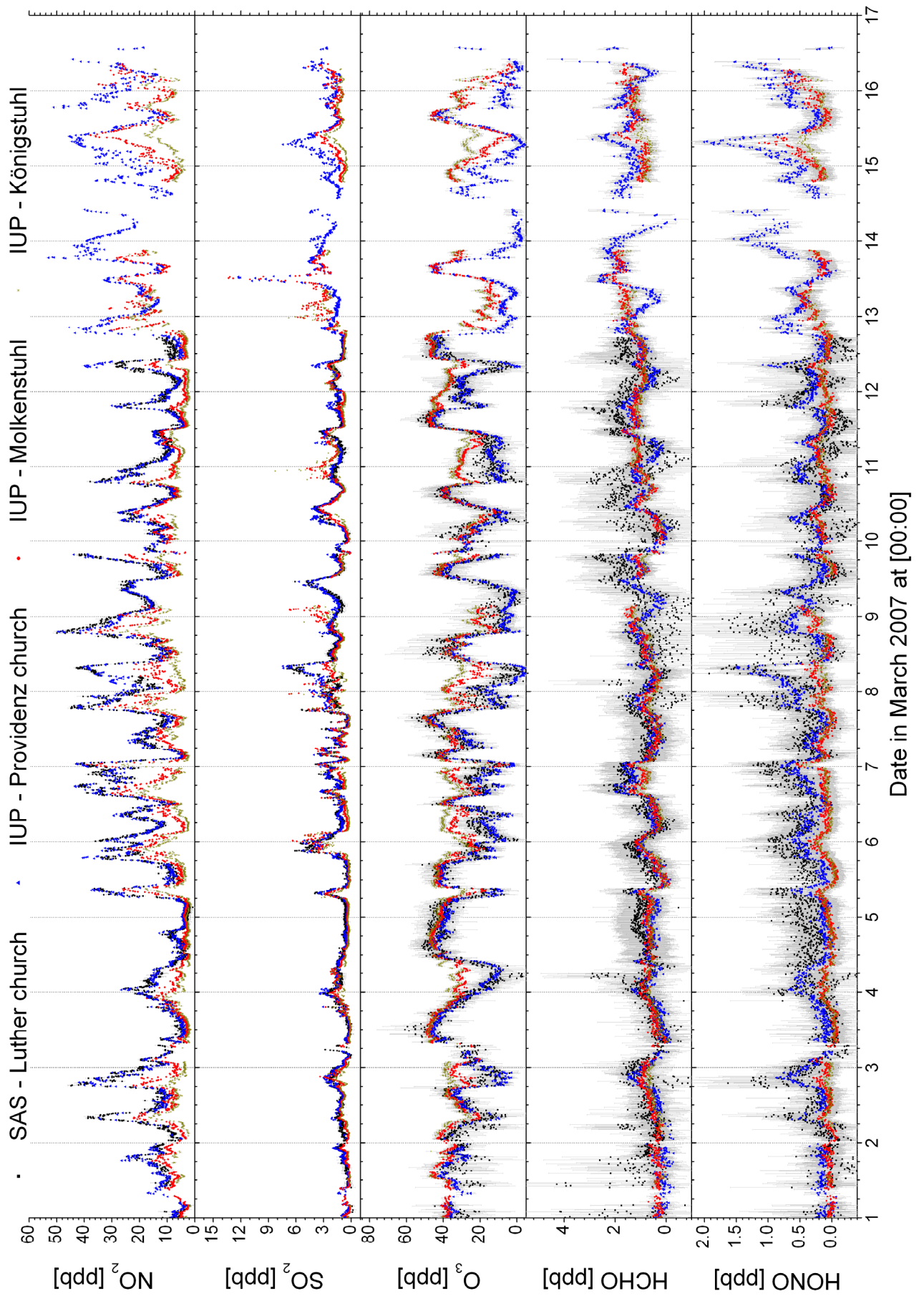




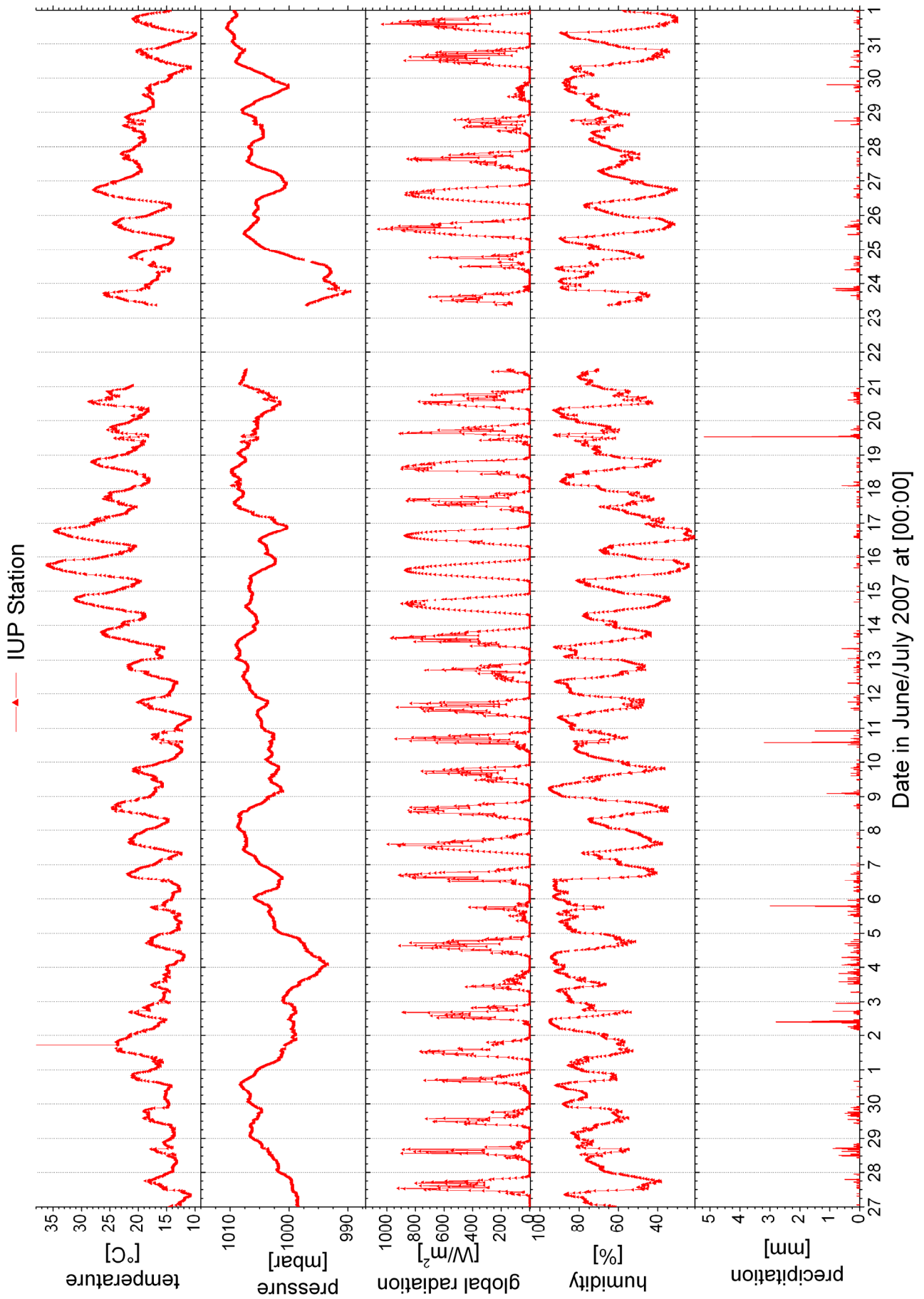
12.13 Data March 2007 (selected plots)

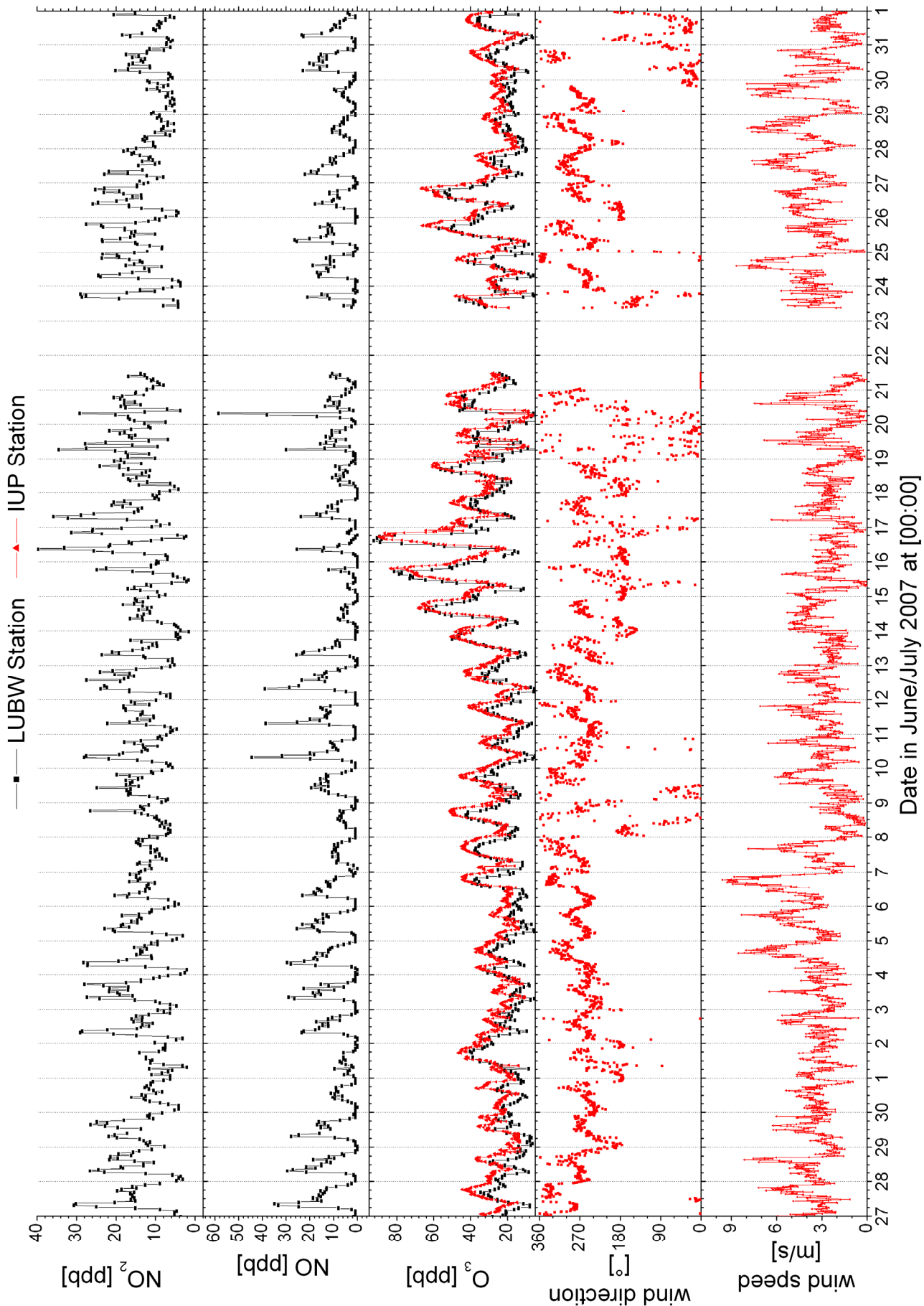


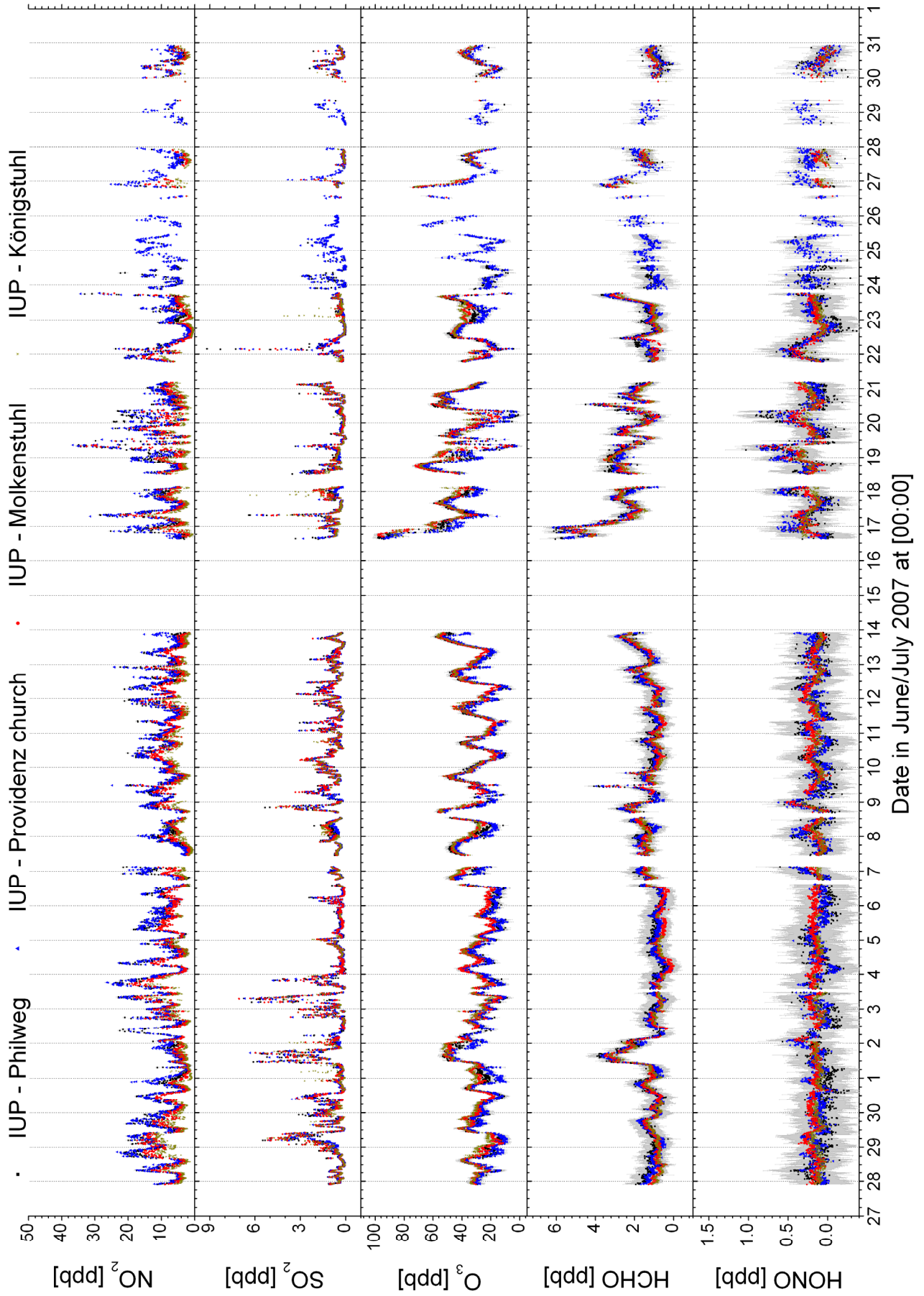




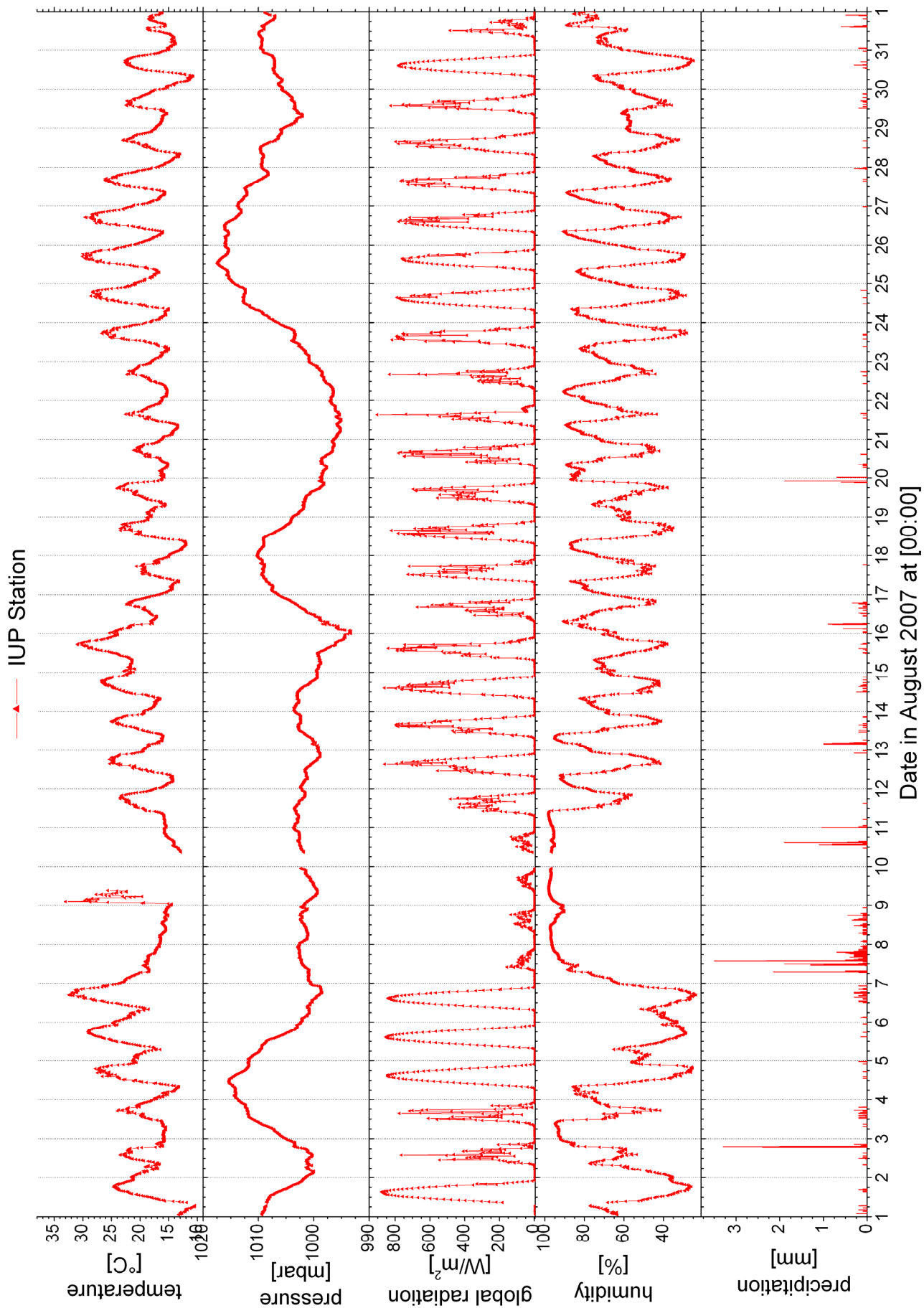
### 12.14 Data June/July 2007 (selected plots)

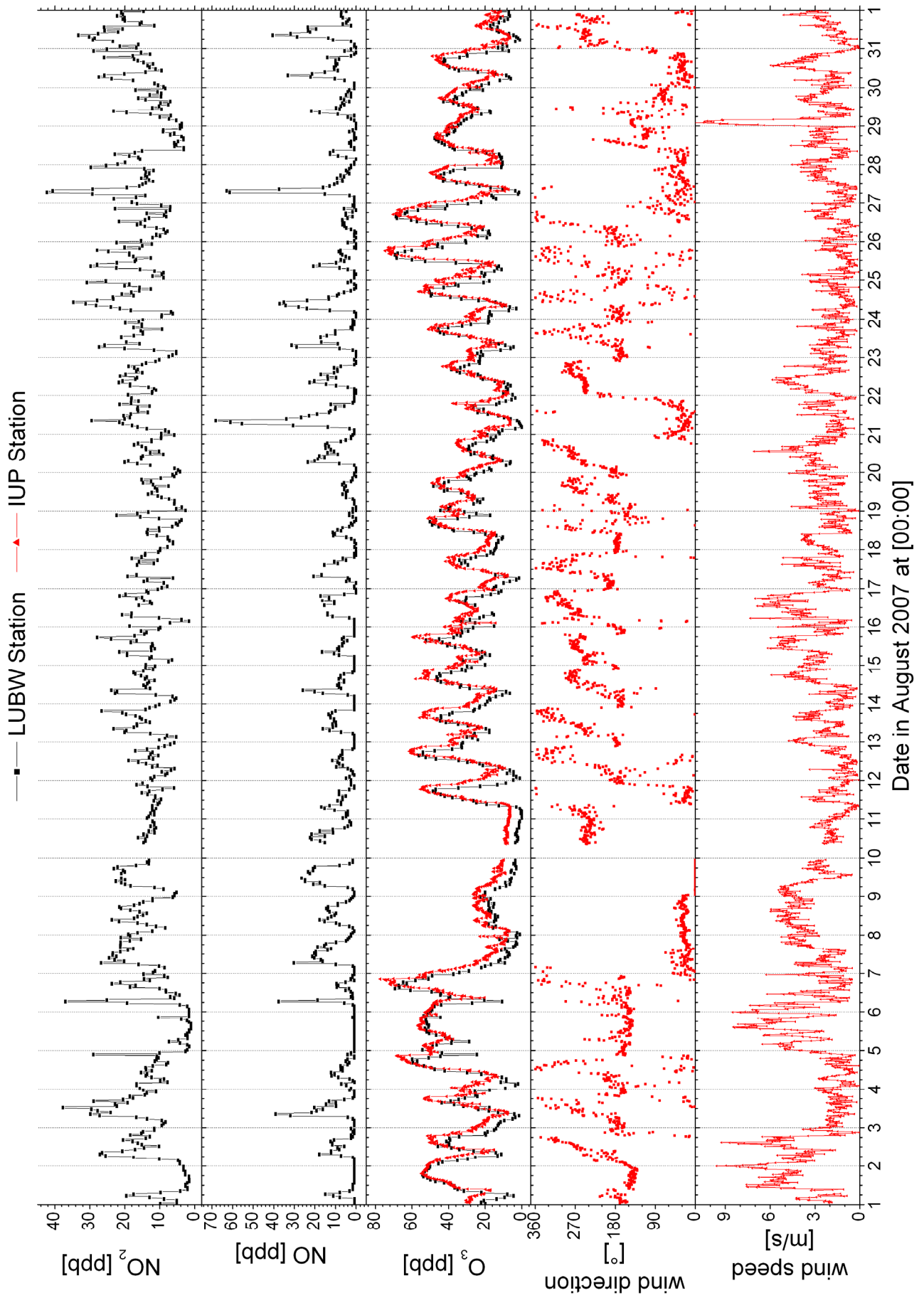


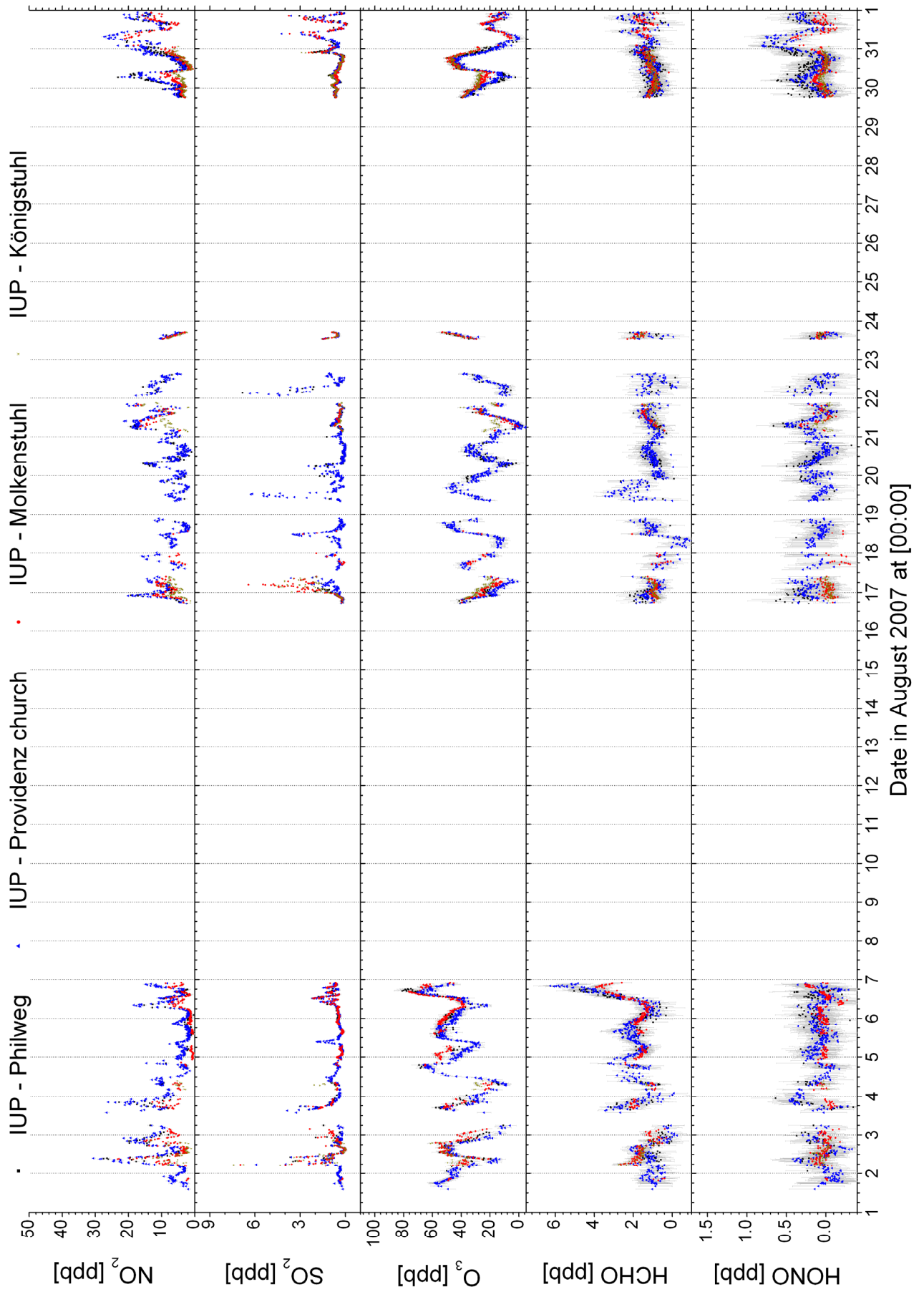




12.15 Data August 2007 (selected plots)







### 12.16 Data September 2007 (selected plots)

